ABSTRACT

Title of dissertation: GRAVITY GRADIOMETER AIDED INERTIAL NAVIGATION WITHIN NON-GNSS ENVIRONMENTS

Justin A. Richeson
Doctor of Philosophy, 2008

Dissertation directed by: Professor Darryll J. Pines
Department of Aerospace Engineering

Gravity gradiometer aiding of a strapdown inertial navigation system (INS) in the event of Global Navigation Satellite System (GNSS) signal loss, or as a complement to an INS/GNSS system, is proposed. Gravity gradiometry is ideal for covert military applications where a self contained, passive, spoof-free aid is desirable, and for space navigation near planetary bodies and moons where GNSS is unavailable. This dissertation provides the first comprehensive discussion on gravity gradiometry fundamentals, map modeling, and regional and altitude effects on the gravitational gradient signal for use as a navigation aid. A thorough methodology to implement strapdown and stabilized gravity gradiometer instruments (GGIs) into an autonomous extended Kalman filter is also presented in the open literature for the first time. Lastly, a brief discussion on extraterrestrial navigation using gravity gradiometry is given.

To quantify the potential performance for future gravity gradiometer instruments as an INS aid, extensive Monte Carlo simulations of a hypersonic scramjet

cruise missile were performed. The results for the 1000 km range mission indicate that GGI updates significantly improve the navigation accuracy of the autonomous INS. The sensitivities of the system to variations in inertial measurement unit (IMU) quality, gravity field variation, GGI noise, update rate, and type are also investigated along with a baseline INS/Global Positioning System (GPS). Given emerging technologies that have the potential to drastically decrease gradiometer noise levels, a hypothetical future grade gravity gradiometer aided INS is shown to bound root-mean-square (RMS) position errors at 0.336 m, velocity errors at 0.0069 m/s, and attitude errors at 0.00977°, which is comparable to the nominal INS/GPS system with 10 sec updates.

The performance of two subsonic cases is also investigated and produced impressive passive navigation accuracy. A commercial aircraft simulation using a future grade GGI provided RMS errors of 0.288 m in position, 0.0050 m/s in velocity, and 0.0135° in attitude. A low altitude and velocity gravity gradiometer based survey simulation similarly showed sub-meter RMS position errors of 0.539 m, velocity errors of 0.0094 m/s, and attitude errors of 0.0198°.

GRAVITY GRADIOMETER AIDED INERTIAL NAVIGATION WITHIN NON-GNSS ENVIRONMENTS

by

Justin A. Richeson

Dissertation submitted to the Faculty of the Graduate School of the
University of Maryland, College Park in partial fulfillment
of the requirements for the degree of
Doctor of Philosophy
2008

Advisory Committee:
Professor Darryll J. Pines, Chair & Adviser
Professor Mark J. Lewis, Co-Adviser
Associate Professor Kenneth Yu
Assistant Professor J. Sean Humbert
Professor Shapour Azarm, Dean's Representative
Adjunct Faculty Ryan P. Starkey, Currently at University of Colorado, Boulder

ACKNOWLEDGMENTS

There are many people who have encouraged and aided me throughout my life, and ultimately in achieving my doctorate, and to those people I would like to say "Thank you." The list of people that follow is fairly extensive, but is by no means intended to be complete. For that reason, if I have forgotten to include someone, I apologize in advance.

First, I would like to express my gratitude to my family for their support throughout my life's ambitions. I'd particularly like to thank my brother, Chase, for sticking by my side through the good and bad times. I'd like to thank my mother, Jackie, for her constant support and encouragement (and also for the laptop that's been the workhorse throughout my graduate years). And lastly, I'd like to thank my father, Glen(n), for constantly pushing me in life to be the best I could be and for instilling me with a hardy work ethic. Without your "perseverance," few of my academic accomplishments would have been possible.

Along the same lines, I'd like to thank my grandparents Alice and Scottie Lacy ("Ma" and "Pa") and Margot "Grandma" Marmor for everything they have done for me over the past twenty-six years. All three of you have shown by example how to be strong independent people no matter the circumstances. Ma and Pa, you have taught me that an academic education can never be a substitute for common sense, and that even the most educated individual can be humbled by someone

with less "book smarts." And to Grandma, thank you for the countless trips to the Smithsonian museums in D.C., and specifically to the National Air and Space Museum which undoubtedly lay the seed for my current profession.

And while not related biologically, I would like to thank Harry Walker who ran the Child's Garden day care center where my brother and I spent countless hours before and after elementary school and during summer breaks. Chase and I joke that you were like a second father to us, but in all seriousness, the lessons you taught me in my formative years have definitely shaped my entire life. And for that, I deeply thank you.

On a less serious note, I'd like to thank my high school friends who made those years much more enjoyable. In particular, Don and the Kunkels, Matt and the Palmers, Vince and the Beachleys, Matt Heron, Dave Bilbrough, and Darrin Malfi, thank you for all the good times. I'd also like to acknowledge my high school calculus and physics teachers, Mrs. Kubic and Mr. Hopkins, for encouraging me to pursue engineering in college and being the best teachers in high school.

In my eight-and-a-half years at the University of Maryland (undergraduate and graduate), I have been influenced by countless people who I would like to thank for helping me succeed and for making this time of my life so memorable. Starting with people from undergrad, I'd like to thank Jesse Colville, Matt Strube, Andy Zang, Ben Hein, Tim Beasman, Dan Shafer, Dave Giger, Suzanne Ruddy (MacKusick), Sadie Micheal, Kirstin Hollingsworth, Alexandra Langley, Will Becker, Jackie Rielly (Schmoll), and everyone else in the 2003 ENAE class who put in the long hours with me to try and excel in every team project and homework assignment thrown

at us. I'd also like to thank Chad Tucker, Will Becker, Chris Wei, Pat Taylor, Joe Sivak, Mike "Jerome" McAndrew, Lenny Reisner, and Maurice for the "non-academic" college experiences. From my junior and senior years in the rotorcraft center, I'd like to thank Nick Rosenfeld, Julie Blondeau (Samuel), Ben Berry, Alice Ryan, and many others for their camaraderie, and to Jinsong Bao, Paul Samuel, Felipe Bohorquez, Matt Tarascio, and Ron Couch (among others) for showing me the required work ethic and leadership needed to be a successful graduate student.

In graduate school, there have been countless officemates and classmates who have helped me immensely with my coursework and research. In particular, Jesse Colville, Kerrie Smith, and Andy Zang, if it weren't for you three working together with me on homework and projects, the first two years of grad school would have been a nightmare. Also, to all of my officemates from JMP 1116 (Rama Balar, Adam Beerman, Josh Clough, Qina Diao, Amardip Ghosh, Dan Hoult, Andrew Johnston, Inna Kurits, Jamie Meeroff, Dave Minton, Vijay Ramasubramanian, Marc Ruppel, Neal Smith, Greg Stamp, and the honorary officemate, Falcon Rankins), thank you for the long random discussions at the conference table and for the input on the office caricature murals. Specifically, Adam—thank you for keeping up on entertainment gossip so I had someone to talk to about the newest episode of *The Office* or *Heroes* and for the memorable Friday night WiiWas; Neal—thank you for being up for any much needed distraction to go get coffee or talk outside, and for explaining numerous fundamental compressible flow concepts to me; and Vijay—thank you for being more than willing to proofread something I wrote or bounce ideas off of, and more importantly, there to vent to and offer advice on any number of topics you

may (or may not) have been familiar with.

While technically a fellow graduate student for several years, I'd like to thank Suneel Sheikh for his immeasurable aid and mentorship in completing this dissertation (and for the extra discretionary income through ASTER Labs). Thank you for the many hours helping me grasp Kalman filtering concepts, IMU error models, and your invaluable advice on living life in general. But even more so, I'd like to thank you for your uncompromising values and endless supply of encouragement, support, and all around positivity (including acknowledging my very modest contributions to the flag football team). I hope that in my lifetime I am able to learn even a small part of the interpersonal skills I've seen you exhibit.

I would also like to thank Ryan Starkey for all the same reasons I mentioned above with Suneel. Even when you were staring down a deadline, you were always more than willing to let someone sit down with you and talk about their research or any non-technical issue at length. Your work ethic, down-to-Earth personality, and all-around generosity are truly amazing characteristics that have become a template in my mind of what a true scholar is.

And to my dissertation committee (including Ryan), I am sincerely grateful for the praises, recommendations, and criticisms I have received from you all throughout this process. The feedback in my pre-defense and defense truly made this a sounder dissertation. On a more personal note, I would like to thank Dr. Yu for his friendliness and many long discussions on my long-term aspirations. To Dr. Lewis, thank you for allowing me to attend you group meetings even though I wasn't technically your student, being happy to answer any question I might ask, and for

"re-vectoring" my research topic into the field of navigation which has been a much more rewarding experience. And last, but definitely not least, I would like to thank Dr. Pines for the countless hours spent discussing any and every topic imaginable, for being a good friend, and for tasking me with the novel gravity gradiometer aided INS topic.

To the aerospace engineering staff, I would like to give a collective thank you. And specifically, I'd like to thank Becky Sarni for helping me track down Dr. Pines, and to Pat Baker for solving every problem I had in record time (*e.g.* campaigning the graduate school for my MS/BS credits).

On a non-technical note, there are many caricature artists I have had the fortune of working with and/or for over the past 8+ years. The summers, weekends, and late night gigs were always a welcome break from my engineering day job. Starting with my mentors at Kaman's at Six Flags America, thank you Jim Toth and Ryan Holeman for teaching me the art and business of "big-heads-and-little-bodies." And to everyone from the 1999 season (Don Kunkel, Jerry Gaylord, Luci Pereira, Jason Vaughn, Richard Warr, Reggie Butler, Charles Matthews, Lindsey Bailey Harris, Mia, etc.), thank you for the memorable summer. Don and Jerry, thanks for being amazing friends, two of the nicest people I've ever known, and for serving as a constant reminder that I should leave the artwork to professionals. Luci, thank you for everything and for the best back-handed compliment of all time when you told me "your picture would be great, if you knew how to draw." Also, thank you to the other Kaman's employees I worked with over the remaining years: Kevin and Katie Grey, Craig, Domo, *et al.* Lastly, I'd like to thank all the local Washington

D.C. area caricature artists who've shared some laughs (and often good sketches) with me: Mike Hassan, Chris Metzger, Dan Smith, Peter Scott, Rick Wright, Jason Levinson, and everyone else I've worked with the past several years.

The last person I must thank is my girlfriend of the past 4+ years, Lauren Belliveau. Thank you for taking a chance on me when I was just starting grad school, and for putting up with me the past 50 months (including my long hours, late nights, cranky sleep-deprived mornings, stressed out times, coffee overdoses, loud drumming, and countless other things I've annoyed you with). Thank you for also picking up the chores when I've been busy with work or just plain burnt out. Thank you for making me take vacations and see different parts of the world even when I initially resisted. Thank you for convincing me to get Houdini. Thank you for coming out to L.A. with me for an uncertain future. In general, thank you for everything.

This research was supported by the Space Vehicle Technology Institute (SVTI), one of the NASA Constellation University Institute Projects (CUIP), under grant NCC3-989, with joint sponsorship from the U.S. Department of Defense. Appreciation is expressed to Dr. Darryll Pines, director of the SVTI at the University of Maryland; Claudia Meyer of the NASA Glenn Research Center, program manager of CUIP; and to Dr. John Schmisseur and Dr. Walter Jones of the U.S. Air Force Office of Scientific Research.

TABLE OF CONTENTS

LIST OF TABLES

LIST OF FIGURES

LIST OF SYMBOLS

A	=	Area, m^2
A_{bw}	=	Wetted body area, m^2
$A_{c_{le}}$	=	Cowl lip leading edge area, m^2
$A_{c_{surf}}$	=	Cowl surface area, m^2
A_{c_x}	=	Axially projected cowl area, m^2
$(A_i/A_1)_{max}$	=	Maximum geometric contraction ratio
A_q	=	Quanternion 4×4 skew symmetric matrix of $\boldsymbol{\omega}_{nb}^b$, rad/s
A_{wall}	=	Combustor wall area, m^2
A_0	=	Capture area, m^2
(A_0/A_i)	=	Capture area ratio
(A_0/A_1)	=	Inlet contraction ratio
(A_4/A_2)	=	Combustor expansion ratio
(A_5/A_i)	=	Base-to-inlet area ratio
(A_5/A_0)	=	Base-to-capture area ratio
$\mathbf{a}$	=	Specific force vector, m/s^2
a_e	=	Semimajor axis of Earth, m
a_{GPS}	=	Semimajor axis of GPS orbit, m
a_T	=	Amplitude of Gaussian height distribution, m^2
a_∞	=	Freestream speed of sound, m/s^2
a, b, c	=	Polynomial curve-fit coefficients (Ch. 3)
b	=	Bias
$\dot{b}$	=	Drift
b_e	=	Semiminor axis of Earth, m
C_D	=	Total drag coefficient, referenced to A_5

$C_{D_{add}}$	=	Additive drag coefficient, referenced to A_5
$C_{D_{cw}}$	=	Cowl wave drag coefficient, referenced to A_5
C_{D_f}	=	Body skin friction drag coefficient, referenced to A_5
$C_{D_{le}}$	=	Cowl leading edge drag coefficient, referenced to A_5
$C_{D_{tw}}$	=	Tail wave drag coefficient, referenced to A_5
$C_{D_{tf}}$	=	Tail skin friction drag coefficient, referenced to A_5
$C_{D,0}$	=	Profile drag coefficient, referenced to A_5
C_{D_α}	=	Induced drag coefficient, referenced to A_5
C_N	=	Normal force coefficient, referenced to A_5
$\overline{C}_{n,m}$, $\overline{S}_{n,m}$	=	Fully normalized spherical harmonic coefficients
C_T	=	Thrust coefficient, referenced to A_5
C_s^t	=	Coordinate transformation matrix from s-frame to t-frame
c	=	Speed of light, m/s^2
c_{ij}	=	ith row and jth column element of coordinate transformation
$cov()$	=	Covariance operator
D	=	Drag, N
d_{le}	=	Cowl lip leading edge diameter, m
$E[\,]$	=	Expectation operator
E_{min}	=	Minimum elevation angle for GPS satellite visibility, rad
Eö	=	Eötvös unit, = 10^{-9} s^{-2}
ER	=	Equivalence ratio
e	=	Error quantity, ≡ estimated - truth
e^2	=	First eccentricity of the Earth ellipsoid squared
e_{GPS}	=	First eccentricity of GPS orbit
$\mathbf{F}$	=	Externally applied force vector, N
F	=	Linearized state error dynamics matrix

F_∞, F_5	=	Freestream and Nozzle exit stream thrust, respectively, N
$\mathbf{f}$	=	Nonlinear state dynamics vector
$f()$	=	Arbitrary function
	=	Probability density function (App. C)
f_e	=	Flatness of the Earth ellipsoid
f_{stoich}	=	Stoichiometric fuel-to-air ratio
G	=	Universal gravitational constant, $m^3/(kg\text{-}s^2)$
GM	=	Gravitational constant of Earth, m^3/s^2
$\mathbf{g}$	=	Gravitational acceleration vector, m/s^2
$\overline{\mathbf{g}}$	=	Gravity acceleration vector, m/s^2
H	=	Linearized measurement error matrix
(H/C)	=	Hydrogen-to-Carbon ratio
$\mathbf{h}$	=	Nonlinear measurement vector
h	=	Altitude, m
h_T	=	Height of Gaussian terrain distribution, m
h_0, h_{-1}, h_{-2}	=	Allan variance parameters
I	=	Identity matrix
i_{GPS}	=	Inclination of GPS orbit, rad
J_n	=	n^{th} unnormalized zonal harmonic
K	=	Kalman gain matrix
$\mathbf{k}$	=	Slope evaluation of nonlinear dynamics
$\mathbf{L}$	=	GGI measurement vector equivalent of L, Eö
L	=	Length, m (Ch. 3)
	=	GGI measurement tensor, Eö (Ch. 5)
L'	=	GGI tensor measurement with angular accelerations, Eö
L_{total}	=	Total scramjet missile length, m

$\mathbf{l}_b$	=	GGI accelerometer baseline vector, m
l_b	=	Magnitude of GGI accelerometer baseline, m
M	=	Mach number
M_{des}	=	Inlet design Mach number
M_e	=	Radius of curvature in the meridian, m
m	=	Mass, kg
	=	Order of spherical harmonic model (Ch. 2)
$\dot{m}_f$, $\dot{m}_0$	=	Fuel and Capture mass flow rate, respectively, kg/s
N	=	Number of grid nodes (Ch. 2)
	=	Normal force, N (Ch. 3)
N_e	=	Radius of curvature in the prime vertical plane, m
n	=	Gyro noise state, rad/s
	=	Degree of spherical harmonic model (Ch. 2)
n_{max}	=	Maximum degree of spherical harmonic model
nl	=	Nonlinearity
P	=	Error covariance matrix
$\mathcal{P}_{GPS}$	=	Period of GPS orbit
$\overline{P}_{n,m}$	=	Fully normalized associated Legendre function
P_∞	=	Freestream static pressure, Pa
Q	=	Discrete process noise covariance matrix
$\mathbf{q}$	=	Body-to-navigation frame quaternion
q_w	=	White noise power spectral density
q_∞	=	Freestream dynamic pressure, Pa
R	=	Measurement noise covariance matrix
R_e	=	Mean curvature, m
R_i	=	Rotation matrix about the ith axis

R_∞	=	Gas constant for air, J/kg-K
$\mathbf{r}$	=	Position state vector
$\mathbf{r}_j$	=	Position of jth GPS satellite vehicle, m
r	=	Radius, m
$r_{iso,in}$, $r_{iso,out}$	=	Interior and exterior isolator boundary, respectively, m
S_f	=	GPS receiver clock frequency PSD, s^2/s^3
S_ϕ	=	GPS receiver clock phase PSD, s^2/s
SF	=	Scale factor
s	=	Horizontal or axial distance, m
T	=	Thrust, N
T_n^a	=	6×6 vector transition matrix from n- to a-frame
T_∞	=	Freestream temperature, K
t	=	Time, s
u_{GPS}	=	Argument of latitude of GPS satellite vehicle, rad
V	=	Volume, m^3
(V_f/V_{total})	=	Fuel volume fraction
V_L	=	GGI white noise matrix, Eö
V_{total}	=	Total scramjet missile volume, m^3
$\mathbf{v}_j$	=	Velocity of jth GPS satellite vehicle, m/s
v	=	Velocity, m/s^2
w	=	White process noise
w_{fin}	=	Tail fin width, m
$\mathbf{x}$	=	State vector
x, y	=	Arbitrary state variables (App. C)
$\mathbf{y}$	=	Measurement vector

Greek

α	=	Angle of attack, rad
α_{GPS}	=	Satellite half-angle for GPS SV visibility test, rad
β	=	First order Gauss-Markov process time constant, 1/s
β_{GPS}	=	Earth half-angle for GPS SV visibility test, rad
β_s	=	Cone shock angle, rad
$\mathbf{\Gamma}$	=	Gravitational gradient vector equivalent of Γ, Eö
Γ	=	Gravitational gradient tensor, Eö
γ_{fpa}	=	Flight path angle, rad
γ_∞	=	Ratio of specific heats in freestream
Δ	=	Discrete incremental quantity
	=	Laplacian operator (Ch. 2)
	=	Small-angle misalignment matrix, rad (Ch. 4)
∇	=	Gradient operator
δ	=	Perturbation (small error) quantity
θ_b	=	Pitch angle, rad
$\theta_{GPS,j}$	=	GPS satellite-to-user visibility angle, rad
θ_g	=	Accelerometer-to-gradiometer frame rotation angle, rad
θ_s	=	Scramjet forebody half-cone angle, $^\circ$
λ	=	Longitude, rad
μ	=	Mean
ν	=	White measurement noise
ρ	=	Density, kg/m^3
	=	GPS pseudorange measurement, m (Ch. 6 & App. D)
$\dot{\rho}$	=	GPS pseudorange rate measurement, m/s
σ	=	Standard deviation

Φ	=	Error state transition matrix
ϕ	=	Latitude, rad
ϕ_b	=	Roll angle, rad
ϕ_g	=	Gravitational potential, m^2/s^2
Ψ^n	=	Skew symmetric matrix equivalent of $\boldsymbol{\psi}^n \times ()$, rad
Ψ^n_{in}	=	Skew symmetric matrix equivalent of $\boldsymbol{\psi}^n_{in} \times ()$, rad
ψ_b	=	Yaw angle, rad
$\boldsymbol{\psi}^n$	=	Small-angle body-to-navigation frame rotation error, rad
$\boldsymbol{\psi}^n_{in}$	=	Small-angle inertial-to-navigation frame rotation error, rad
Ω_{GPS}	=	Right ascension of the ascending node of GPS SV, rad
Ω^t_{sr}	=	Skew symmetric matrix equivalent of $\boldsymbol{\omega}^t_{sr} \times ()$, rad/s
ω_e	=	Earth's rotation rate, rad/s
$\boldsymbol{\omega}^t_{sr}$	=	Angular velocity of the r-frame with respect to the s-frame, with coordinates in the t-frame, rad/s

Superscripts

a	=	Accelerometer
b	=	Body frame or Strapdown instrument
e	=	Earth Centered, Earth Fixed frame
g	=	Gyro or GGI frame (Ch. 5)
i	=	Earth Centered Inertial frame or Stabilized instrument
n	=	North-East-Down Navigation frame
PQW	=	Perifocal frame
T	=	Transpose
*	=	Trim value
$^-$	=	A priori quantity

$^+$	=	A posteriori quantity
$\widehat{}$	=	Estimated quantity
$\widetilde{}$	=	Measured quantity

Subscripts

$comb$	=	Scramjet combustor
$cone$	=	Scramjet inlet cone
$cowl$	=	Scramjet cowl
cyl	=	Scramjet external, constant-radius portion of body
D	=	Down
	=	Drag (Ch. 3)
E	=	East
f	=	Final
	=	Fuel (Ch. 3)
	=	GPS clock drift (App. D)
fin	=	Scramjet tail fin
fin, tip	=	Scramjet tail fin tip
gm	=	Gauss-Markov
H	=	Homogeneous solution
i	=	ith array element
	=	Scramjet inlet (Ch. 3)
iso	=	Scramjet isolator
j	=	jth array element or jth satellite vehicle
k	=	kth time epoch
L	=	GGI
N	=	North

	=	Normal force (Ch. 3)
noz	=	Scramjet nozzle
P	=	Particular solution
r	=	Position
ref	=	Reference
str	=	Structural
$surf$	=	Scramjet surface (area)
T	=	Terrain
u	=	GPS user receiver clock
v	=	Velocity
w	=	White noise
∞	=	Freestream
0	=	Initial
1	=	Scramjet isolator entrance (Ch. 3)
2	=	Scramjet isolator exit / combustor entrance (Ch. 3)
4	=	Scramjet combustor exit / nozzle entrance (Ch. 3)
5	=	Scramjet nozzle exit / base (reference) (Ch. 3)
ϕ	=	GPS clock phase
ψ	=	Orientation error
ω	=	Angular rate

Acronyms

AGARD	=	Advisory Group for Aeronautical Research and Development
CHAMP	=	CHAllenging Minisatellite Payload
DCR	=	Dual Combustor Ramjet
ECI	=	Earth Centered Inertial

ECEF	=	Earth Centered, Earth Fixed
EGM96	=	Earth Geopotential Model, 1996
EKF	=	Extended Kalman Filter
ESA	=	European Space Agency
FFT	=	Fast Fourier Transform
FTG	=	Full Tensor Gradiometer
GDOP	=	Geometric Dilution of Precision
GGI	=	Gravity Gradiometer Instrument
GNSS	=	Global Navigation Satellite System
GOCE	=	Gravity Field and Steady-State Ocean Circulation Explorer
GPS	=	Global Positioning System
GRACE	=	Gravity Recovery and Climate Experiment
IMU	=	Inertial Measurement Unit
INS	=	Inertial Navigation System
JHU/APL	=	Johns Hopkins University / Applied Physics Laboratory
LEO	=	Low Earth Orbit
MRSE	=	Mean Radial Spherical Error
NASA	=	National Aeronautics and Space Administration
NED	=	North, East, Down
NGS	=	National Geodetic Survey
NOAA	=	National Oceanic and Atmospheric Administration
RMS	=	Root Mean Square
SQUID	=	Superconducting QUantum Interference Device
SV	=	Satellite Vehicle
UERE	=	User Equivalent Range Error
WGS84	=	1984 World Geodetic System

Chapter 1

Introduction

1.1 Motivation

High accuracy position, velocity, and attitude estimation is required for many aerospace vehicle mission objectives. Such accuracy requirements are typically achieved by an integrated inertial navigation system (INS) consisting of inertial measurement units (IMUs) and an external aid to prevent error accumulation due to uncompensated instrument errors and geodetic/geophysical uncertainties,[1–6] See Fig. 1.1 from Ritland.[6] Of the common available aids, all-weather Global Navigation Satellite Systems (GNSS), specifically the Global Positioning System (GPS), have become the most popular means to limit INS errors.[1,2,4,6–9] GNSS aiding does have the noted disadvantages that it relies on expensive segments (space, control, and user) that require constant maintenance and monitoring, data rates are relatively low, the greatest accuracy requires constant satellite tracking, satellite geometry can yield poor performance (especially in altitude), orientation information requires multiple antennas, and the weak signal can be easily jammed or spoofed. Furthermore, GNSS aiding is ineffective for exploration missions far from Earth, such as the Moon or Mars.

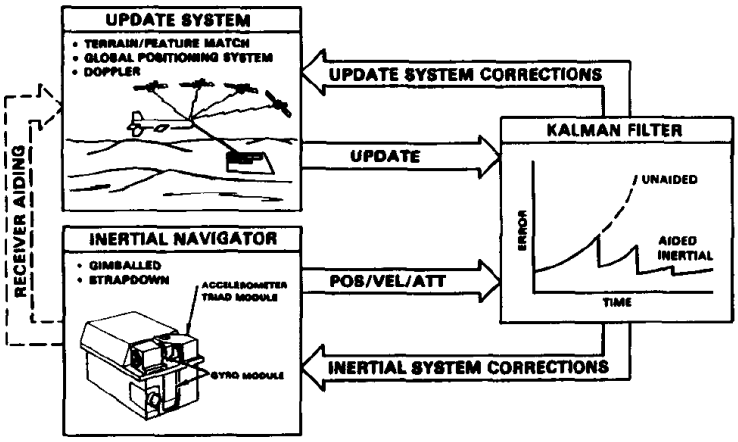

Figure 1.1: Aided Inertial Navigation using an Extended Kalman Filter, from Ref. [6]

In the event of non-GNSS environments, the INS must integrate the inertial measurements with any uncompensated errors which can produce unacceptable state estimation, divergence, and/or loss of vehicle. During these periods, several other aids may be used for robustness.[6] Vision based systems, which are becoming increasingly prevalent with unmanned reconnaissance vehicles, require optical access that may be infeasible aboard some systems such as hypersonic cruise vehicles, and are susceptible to weather variations. Vision aids may also have high computational requirements that are prohibitive with current technology. Terrain aids typically emit a radar or laser that can be sensed by other users which is undesirable for covert military missions. And like optical systems, terrain aiding often relies on matching the sensor measurement to a pre-surveyed map that may be sensitive to temporal variations and anomalies, such as fluctuations in water or sand. This dissertation proposes the use of a completely self contained, passive system that relies on gravity gradiometry for INS aiding that exhibits none of the issues above.

Figure 1.2: Recent Scramjet Research Programs

An airbreathing hypersonic cruise vehicle was chosen as the primary example mission for such a system due to the interest following the successful X-43A,[10–12] HyShot,[13–15] and HyFly/FASST tests,[16] and its relevance to the X-51 Scramjet Engine Demonstrator – WaveRider (SED-WR) program.[17,18] Furthermore, gravity gradiometer instrument (GGI) aiding for scramjet applications has two distinct advantages over low-speed/low-altitude flight. First, because the vehicle is traveling at high speeds (Mach 6–8) and the GGI produces only a moderate update rate (∼1 Hz), the gravitational gradients are sampled at position intervals >1500 m that allow for greater gravity variations than those that would be observed for low velocity vehicles. Second, the high altitudes required for scramjet cruise (∼22–26 km) attenuates high frequency gravity anomalies found at lower altitude so the system is less susceptible to terrain anomalies.[19,20]

Unfortunately, current gradiometer systems are too massive and sizeable for many airborne applications, so continued improvements must be made to make

GGIs a viable airborne INS aid. For these reasons, and to show applicably to a wider range of missions, two subsonic cases are also simulated with less rigor. The first represents a commercial aircraft at cruise conditions, and the second is a low speed and altitude gravity survey mission.

1.2 Previous Work

1.2.1 Gravity Gradiometer Instruments

The first gravity gradiometer instrument (GGI) was invented by Hungarian physicist Loránd (Roland von) Eötvös in the late 1880s using a specialized torsion balance to investigate gravitational phenomenon.[21] His extensive and groundbreaking research in gravitational gradiometry led to the naming of the Eötvös as the fundamental unit of the gravitational gradient. (1Eö $\equiv 10^{-9}\text{s}^{-2}$, which is physically equivalent to measuring the gradient of 10 grains of sand 1 cm away, assuming 1 grain of sand $\approx$ 1 milligram.)[22] Over the past century, gravity gradiometer instruments have evolved from torsion balances to precisely machined sensors that are typically based on finite differencing linear accelerometers or torsion beams.

This subsection summarizes the history and research in developing airborne and space-borne gravity gradiometer instruments for navigation aiding and surveying. The original 1960s airborne GGIs are described first, followed by the current generation airborne GGIs. Superconducting and cold atom interferometer GGIs are also discussed as they are believed to be the enabling technologies to improve future

generation gradiometer sensitivities.

1.2.1.1 First Generation Airborne GGIs

The 1960s brought about many innovative technological breakthroughs in the field of inertial navigation systems. As the error sources of inertial measurement units became better understood, and more precise and accurate accelerometers and gyroscopes became available, "the Air Force Geophysics Laboratory (then called Air Force Research Laboratory) sought to develop efficient approaches for mapping the short-wavelength features of the Earth's gravity field over large geographic areas" to improve the navigation performance of autonomous inertial systems.[23] This issue arises due to Einstein's equivalence principle which states that inertial accelerations are indistinguishable from accelerations caused by a gravitational field. Therefore, accelerometers are unable to measure acceleration, and instead measure specific forces which is the acceleration of the system in an inertial frame minus the gravitational acceleration in the inertial frame:

$$\mathbf{a}^i = \dot{\mathbf{v}}^i - \mathbf{g}^i. \tag{1.1}$$

Because of this issue, an INS using accelerometers must include an estimate of the true gravitational field in which the vehicle operates in order to calculate the true vehicle accelerations. Until this point in time, the uncertainty attributed to the accelerometer errors, $\delta\mathbf{a}$, was sufficiently large that the gravitational modeling errors, even for simple models, were safely negligible. Mathematically,

$$\delta\dot{\mathbf{v}}^i = \delta\mathbf{a}^i + \delta\mathbf{g}^i \approx \delta\mathbf{a}^i. \tag{1.2}$$

With improvements in accelerometer design and fabrication, INS analysts began to speculate that gravitational errors would need to be modeled and compensated for.[5] One approach was to use a gravity gradiometer instrument to update the INS's gravity model, usually by spatial integration of the gravitational gradients in real time (See Sec. 1.2.2.1).

However, with the publication of Kalman's seminal papers,[24,25] the growth of other INS aids, and the difficulty in design and manufacture of a robust, sensitive, small GGI, gravity gradiometer aided inertial navigation became largely forgotten. Fortuitously, with the rise of oil prices and the potential profit of mineral exploration (specifically diamond mines), GGI development is being actively pursued by several commercial enterprises to provide a fast, low cost surveying and prospecting service to these industries. (The current exploration instruments are discussed in detail in the next section.)

Here, the first generation airborne gravity gradiometer instruments developed simultaneously in the 1960s and 1970s by the Charles S. Draper Laboratories, Hughes Research Laboratories, and Bell Aerospace / Textron are reviewed. All three GGIs were pursued under Department of Defense (DoD) funding as a potential airborne INS aid with the goal of producing an airborne GGI with a noise level of 10 Eö moving-window averaged at a data rate of 10 sec.[26]

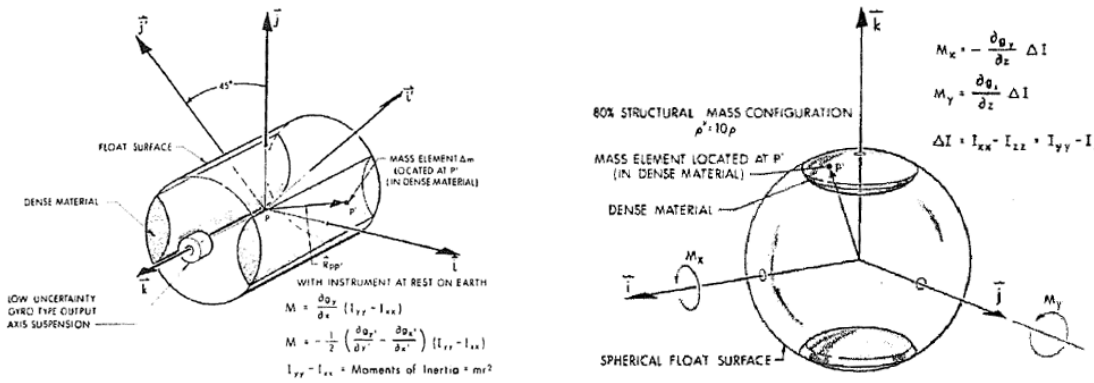

Figure 1.3: Draper Cylindrical and Spherical GGI Schematics, from Ref. [28]

Charles S. Draper Laboratory Floated GGI

The Draper Lab's floated gravity gradiometer instrument was initially developed as a "feasibility" cylindrical model[27] and later into a spherical model. Trageser[28] describes the feasibility model in detail along with test results which proved its surprising sensitivity to puddles on the roof of the laboratory.Because the instrument was stationary (unlike the other two 1960s GGIs), its noise level was limited primarily by the thermal noise floor. For benchtop tests using a human fist the cylindrical Draper GGI produced a 0.99 Eö mean root-mean-square (RMS) error. When using a 100 kg lead ball the RMS was 1.15 Eö with a 10 sec integration and 0.50 Eö for a 120 sec integration.

Draper's spherical GGI built on lessons learned from their cylindrical model and focused on "attaining [a] high degree of mass balance, temperature control and material stabilities" to meet the DoD specifications.[29] The spherical design was also relatively immune to platform jitter compared to the feasibility model. The 10 cm, 0.7 kg spherical GGI used two silver-filled tungsten proof masses attached to either

end of a sphere floated in Freon 113 to produce a pair of torques that could be used to measure two off-diagonal elements of the gravitational gradient tensor, see right portion of Fig. 1.3.[30] A cluster of three GGIs in an umbrella configuration could then be used to measure the full tensor.[26,28] The spherical GGI development began in 1974 and was first tested in Septemeber 1976. In laboratory experiments with a 100 kg lead mass, this second Draper GGI produced near-thermal noise noise limits (0.085 Eö experimental vs. 0.045 Eö theory) with a bias stability less than 1 Eö over several days.[30]

Grubin later proposed adding a second pair of proof masses to the Draper GGI in order to measure three components of the gravitational gradient tensor.[31] This would also allow the use of only two floated GGIs to measure the full gradient tensor, and the orientation of the instruments could be optimized for robustness. While current airborne GGIs are all based off of the Bell/Textron instrument, as described shortly, the Draper Lab notion of producing an extremely sensitive non-rotating gradiometer is the basis for research of superconducting and cold atom interferometer GGIs.

Hughes Research Laboratory Rotating Torsional GGI

Hughes Research Laboratory took a drastically different approach to developing its gradiometer sensor. Hughes quickly rotated a precisely manufactured cruciform shape of four proof masses and thin arms to measure the gravitational gradients using torque differences. The premise was to measure the gravitational

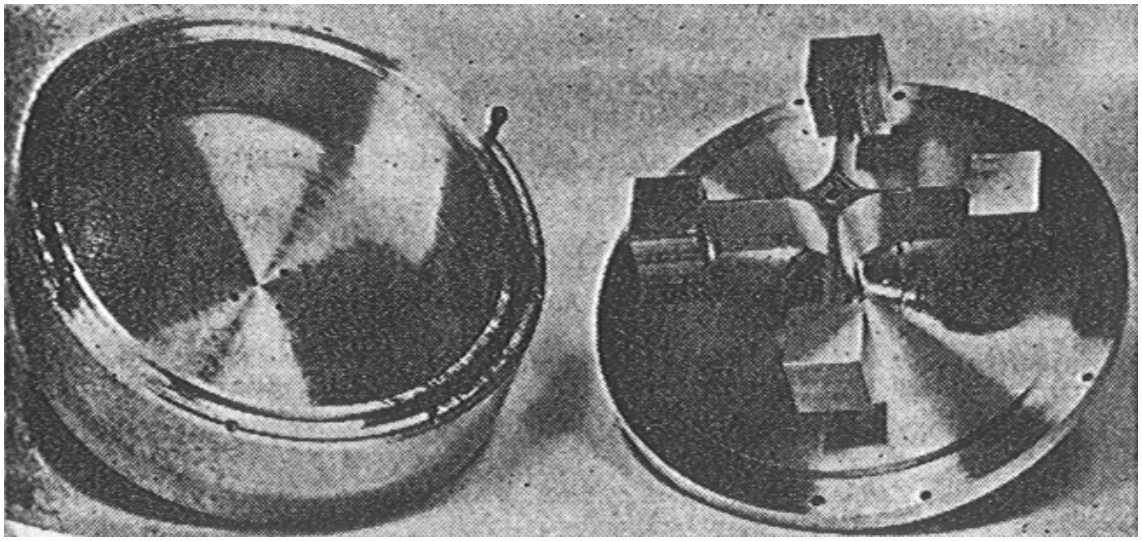

Figure 1.4: Hughes Rotating Torsional GGI, from Ref. [33]

gradients at a sufficiently high frequency that the linear and angular motions had negligible error contributions.[32] This resulted in Hughes having to overcome various precision manufacturing issues, and to contend with bearing noise, a highly isoelastic structure, and material stabilities.[29]

A summary of the instrument and its idealized performance (perfectly matched masses and lengths) is presented by Bell *et al.*[32] They show that the GGI measurement dynamics are uniquely driven by the gravitational gradients at twice the instrument rotation rate. Berman continued this analysis in two papers where he investigated errors that occur at multiples of the rotation rate since they would be seen as gravitational gradients.[33,34] The four rotating proof mass modes (gravitational gradient, torsional, and two orthogonal translations) are also modeled along with the error due to a center of gravity offset and general asymmetry.

A summary of the Hughes rotating torsional GGI is as follows. The overall instrument has an approximately 4.5" (12 cm) diameter, the proof masses are 0.75"

(2 cm) cubed, and the arms connecting the masses are 1.5" (4 cm) long × 0.75" (2 cm) wide × 0.050" (.13 cm) thick. The cruciform sensor has a resonance frequency of 200 cycle per second and is rotated at 6000 revolutions per minute.[32]

Bell Aerospace / Textron Rotating Accelerometer GGI

The rotating finite differenced accelerometer gravity gradiometer instrument developed and tested by the Bell Aerospace Division of Textron, Inc. is easily the most published first generation airborne GGI, and has continued to live on to the present day.[20,26,29,35–41] The Bell / Textron GGI is based on summing two finite differenced accelerometer pairs tangentially mounted on a (relatively slow) rotating disc. The instrument was originally used aboard Trident fleet submarines for improved navigation accuracy during periods of prolonged submersion,[42] and later tested for surveying feasibility on land, rail, and in the air.[38] Most recently, it has been developed into an airborne surveying tool for prospecting and mineral exploration as detailed in the next subsection.

Metzger[29] presented a thorough review of research and development practices for the Bell / Textron GGI. He explained that this gradiometer had a 15 cm baseline between accelerometers and was rotated at a 1/4 Hz frequency to decrease the power of the Bell Model IV accelerometer's turn-on bias as seen in Fig. 1.5. The scale factor error then became the predominant source of GGI error and was corrected with two feedback loops: one that balances the accelerometers in each pair, and one that balances the two pairs. This effectively matched the scale factor error of

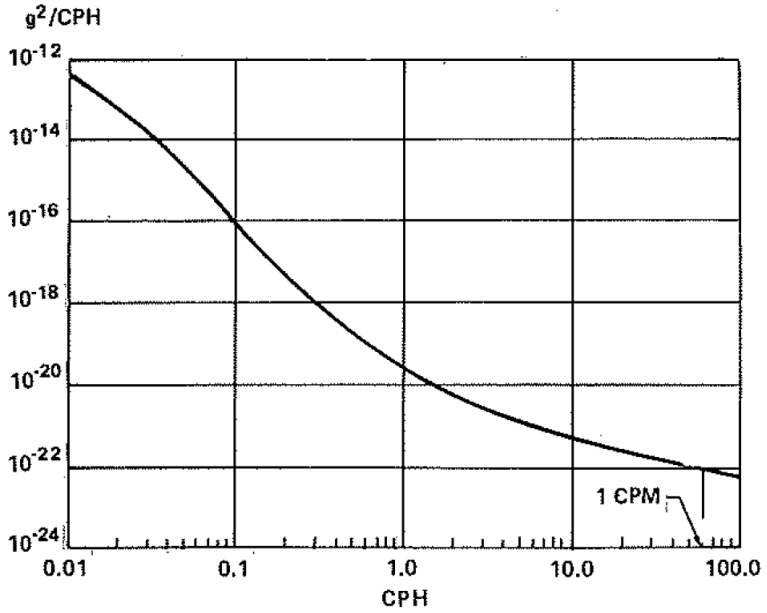

Figure 1.5: Accelerometer Null Bias vs. Rotation Rate (Cycles/Hour), from Ref. [29]

three accelerometers to that of the fourth at every revolution. Misalignments were also corrected at 1/4 Hz, and further error compensation was achieved by shaking and dithering the instrument at specific frequencies.[20] Laboratory tests conducted in the mid 1970s showed that this instrument was able to produce noise levels of 2 Eö with a 10 sec moving window average.[29]

The Bell / Textron GGI, like the Hughes instrument, measured the difference of two on-diagonal gravitational gradients and another off-diagonal gradient as a result of the instrument's rotation, see Fig. 1.6 and Sec. 5.1.3 for details. In order to measure the full gravitational gradiometer tensor, three instruments were "symmetrically positioned about the vertical axis, with each gradiometer inclined at the same 'umbrella' angle; i.e., the spin axis of each instrument is oriented at the same angle away from the vertical, analogous to the spindles of an umbrellas,"[23] as shown

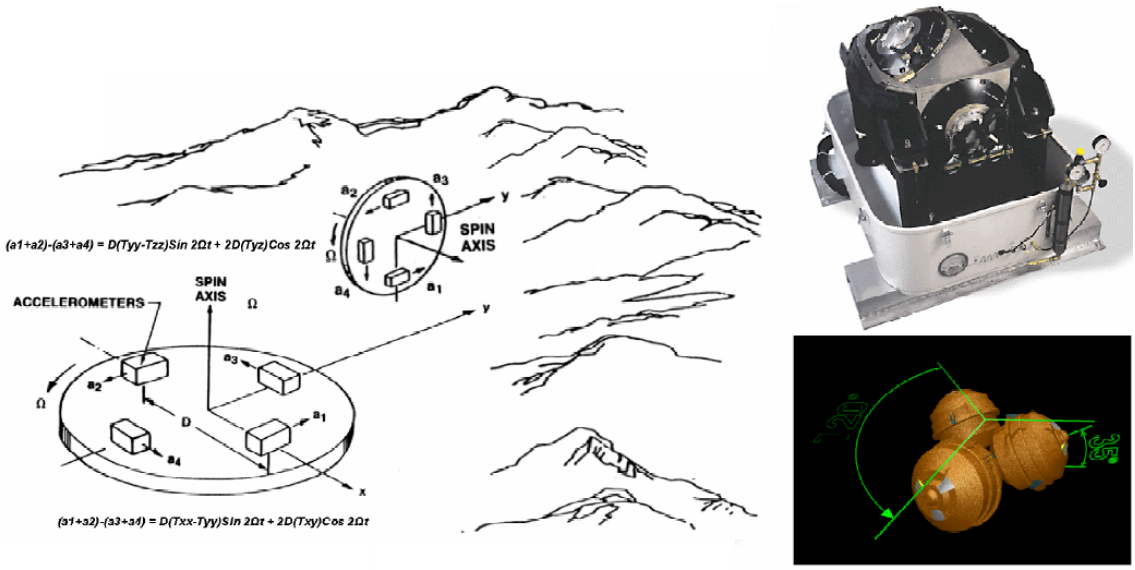

Figure 1.6: Bell / Textron Rotating Accelerometer GGI, (Schematic, GGI w/ Stabilized Platform, and Internal Umbrella Configuration) from Ref. [47]

in the bottom right of Fig. 1.6. The entire umbrella configuration was also rotated at a much slower 500°/hr.[40]

Richman[43] proposed a finite differenced accelerometer GGI that was based on using two separated IMUs on an airplane. The issues of aircraft flexure, among others, likely prohibited this concept from being developed further.

1.2.1.2 Current Generation GGIs

Bell / Textron Derived GGIs

The Bell / Textron instrument technology was eventually acquired by Lockheed Martin which has since produced several current-generation rotating GGIs including eight-accelerometer partial tensor GGIs (BHP Billiton's Falcon Airborne Gravity Gradiometer (AGG)[44,45] and the Arms Control Verification Gravity Gra-

diometer (ACVGG)[39,46]), and full tensor GGIs similar to the original Bell / Textron GGI (Bell Geospace's 3-D Full Tensor Gradiometer (3D-FTG)[47,48] and ARKeX's FTGeX[45]).

The BHP Billiton Falcon^{TM} AGG[44,49–51] was the first commercial system to use a gradiometer for airborne surveying and mineral deposit exploration. The instrument development began in 1993 with initial studies. Although the results weren't very promising, the decision to move forward with construction of the Falcon AGG was made in March 1994. The first mission was flown in late 1997, and the first system, *Einstein*, was operational in 1999 using a Cessna Grand Caravan airplane. Since then three other systems have been delivered, including one aboard a helicopter for improved spatial resolution because of the reduced flight speed. One major drawback of this airborne GGI is that it only includes one rotating disc, so that only a partial-tensor measurement is made.

The Arms Control Verification Gravity Gradiometer is similar to the Falcon AGG in that it is comprised of a single rotating disc with eight-accelerometers that produces a partial-tensor measurement. The ACVGG was developed under funding by the Defense Threat Reduction Agency[46] and the Defense Nuclear Agency[20] for surface gravity surveys. While little has been published on this instrument, it is reported to have a 30 cm baseline between accelerometer pairs (twice that of the Bell / Testron GGI) and it's rotation rate is "dramatically increased" compared to the original 1/4 Hz frequency.[20] From these improvements, the projected stationary survey noise is said to be 1 Eö at a 1 Hz update rate.[46] A similar instrument was patented in 1994 by Hoffmeyer and Affleck that provides some further detail into

eight rotating accelerometer GGIs.[39]

Bell Geospace, who had acquired exclusive rights to the Bell / Textron technology and performed several marine surveys, took notice at the potential profit of BHP Billiton's airborne survey system and began work on their own.[52] The primary advantage of Bell Geospace's Airborne 3D Full Tensor Gradiometer (Air-FTG®) to the Falcon AGG is the ability to measure the full gravitational gradient tensor.[53] Like the original Bell / Textron GGI, the 3D FTG sensor uses three GGIs each with four rotating accelerometers to provide a full gravitational tensor observation aboard either airborne or marine missions (Marine-FTG®). Also, like the Falcon AGG, the Air-FTG system performs airborne surveys on a Cessna Grand Caravan equipped with various technologies to accurately map terrain variations and eliminate their gravitational contributions to the GGI signal during post-processing. The result is a detailed map of gravitational anomalies below the survey area that warrant further investigation if they exhibit mineral or oil deposit characteristics.[48,54] Unfortunately, current airborne GGI exploration systems are able to discriminate only major diamond formations because smaller formations are masked by the instrument's noise floor.[54]

ARKeX is another commercial organization that has developed an airborne full-tensor gradiometer for mineral exploration (FTGeX) with the aid of Lockheed Martin. This Oxford Instruments Superconducting Ltd. spin-off reports that their Cessna-based survey system has been used extensively since its deployment in Spring 2005.[55–57] And currently, ARKeX is pursuing the development of a superconducting GGI that will decrease the instrument's noise floor at least a factor of ten so that

smaller mineral formations may be discovered.

Lastly, a room temperature, stationary GGI was briefly mentioned by Gleason[20] to have been investigated by researchers at the Johns Hopkins University / Applied Physics Laboratory around 1995. The goal noise level was reported to be 0.1 Eö up to a 100 Hz data rate. Unfortunately, to the present author's knowledge, this instrument has never been discussed again in the open literature.

Superconducting Airborne GGIs

Gravity gradiometer instruments saw over an order-of-magnitude improvement in noise sensitivity with the use of superconducting technologies in the early 1980s. With the incorporation of superconducting quantum interference devices (SQUIDs) and wire electric discharge machining (EDM), incredibly precise measurements of accelerometer proof masses were possible. A revolutionary single axis superconducting gravity gradiometer (SGG) at the University of Maryland produced a noise floor of 1 Eö/$\sqrt{Hz}$ in 1987.[58,59] Further development provided by NASA funding led to a three-axis SGG with an improved noise of 0.02 Eö/$\sqrt{Hz}$, Fig. 1.7.[60–63] This NASA SGG was meant for a global survey mission aboard a satellite, and was able to reduce its noise three orders of magnitude below the room-temperature Bell / Textron derived GGIs by keeping the instrument at a cryogenic temperature of $\sim$4 K which enhances the mechanical linearity of the proof mass deflections.

The University of Maryland's Superconducting Angular Accelerometer (UMD SAA, Fig. 1.8 (a)) and the University of Western Australia's Orthogonal Quadrupole

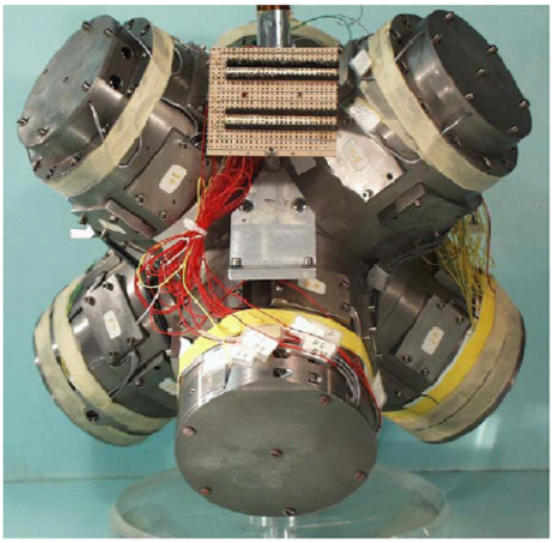

Figure 1.7: University of Maryland Superconducting Gravity Gradiometer, from Ref. [63]

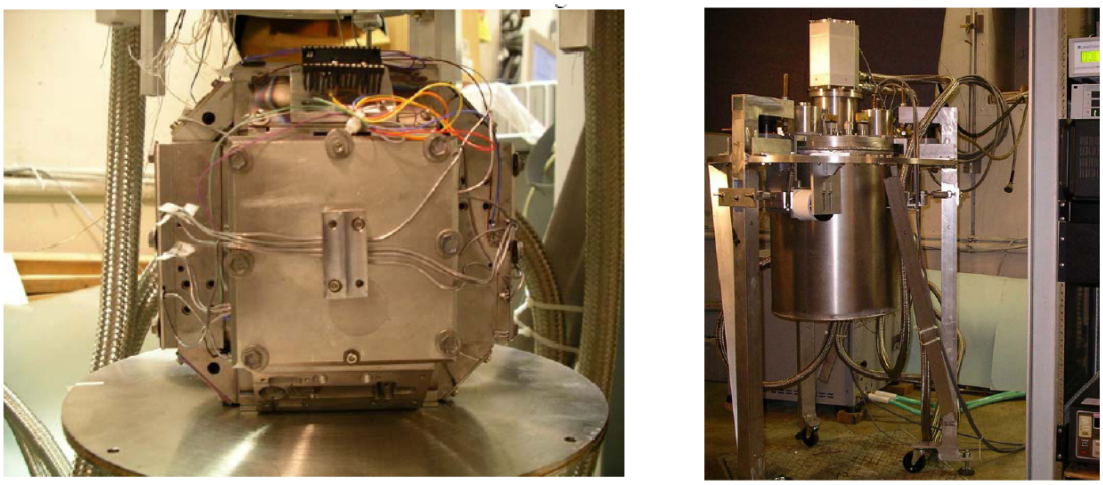

(a) (b)

Figure 1.8: UMD SAA (a) and Cryostat (b), from Ref. [66]

Responder (UWA OQR, Fig. 1.9) are two superconducting GGIs designed for airborne surveying.[19,64–66] Both instruments use angular, instead of linear, accelerometers as their basic means of measuring the gravitational gradients because the angular accelerometers are more robust to demanding aircraft dynamics. The UMD SAA has a predicted airborne surveying performance of 0.34 Eo at a 1 sec update rate.[64] The main issue with both of these systems is the need to enclose the GGI in a closed-loop refrigerant system, or *cryostat*, to maintain the ∼4 K operating temperature, as shown in Fig. 1.8 (b). Also, a sophisticated stabilized platform must be incorporated to isolate the GGI from the vehicle's dynamics.

Both the UMD SAA and UWA OQR are being pursued by ARKeX and Gedex to design an airborne survey system with a 1 Eö/$\sqrt{Hz}$ design goal. The ARKeX Exploration Gravity Gradiometer (EGG) is reported to only measure the vertical gravitational gradient,[45,55,56,67] while the Gedex High-Definition Airborne Gravity Gradiometer (HD-AGG$^{\text{TM}}$) is likely a full-tensor GGI based primarily on the UMD SAA that includes funding support from De Beers.[68–73]

The European Space Agency's Gravity Field and Steady-State Ocean Circulation Explorer (ESA GOCE) satellite will incorporate an Electrostatic Gravity Gradiometer (EGG) as its primary payload to map Earth's gravitational field spatially and temporally.[74,75] The difference between the GOCE EGG and many of the other superconducting GGIs is that the EGG uses capacitance (*i.e.* voltage) to measure the accelerometer's proof mass displacements whereas the UMD and UWA GGIs rely on inductance (*i.e.* current).[74] The noise specification for this 137 kg, 1.32 m × 0.9 m × 0.9 m state-of-the-art instrument is an impressive 3mEö/$\sqrt{Hz}$

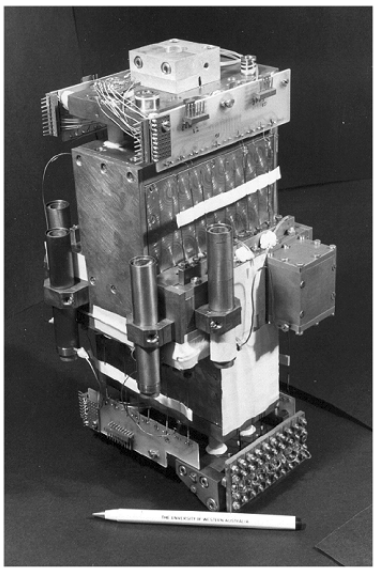

Figure 1.9: UWA OQR, from Ref. [19]

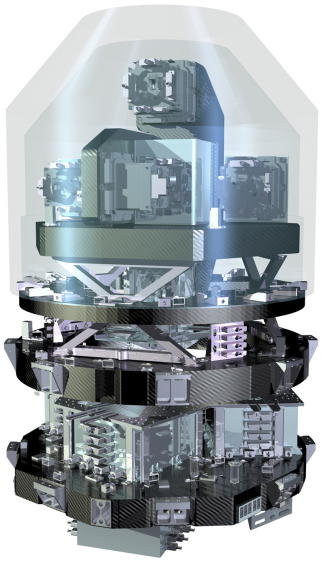

Figure 1.10: ESA GOCE EGG, from Ref. [75]

with a data rate of up to 10 sec.[74]

The University of Texas's operational Gravity Recovery and Climate Experiment (GRACE) mission uses twin satellites as the proof masses of an effective gravity gradiometer instrument with a 220 km baseline.[76] While not a superconducting GGI per se, this novel system shows the current state of the art in satellite gravity gradiometry.

The last superconducting GGI to mention is a novel sensor from Gravitec that is based on measuring the behavior of a superconducting string.[45,77–80] The size (400 $\times$ 30 $\times$ 30 mm) and mass (0.5 kg) of this gradiometer is tremendously smaller than the other surveyed instruments and its goal noise level of 5 Eö/$\sqrt{Hz}$ at 5–10 Hz measuring all off-diagonal graviational gradients is also encouraging. Unfortunately, the open literature does not provide much detailed information on how exactly this

GGI is intended to perform, nor how it will overcome the challenges present in the others sensors. But, if this GGI comes to fruition, it could revolutionize current airborne GGI survey systems.

Cold Atom Interferometer GGIs

Innovative research in cold atom interferometry (based on work that has already garnered two Nobel Prizes in Physics)[81,82] may lead to dramatically reduced GGI noise levels.[83–85] The premise of a cold atom accelerometer is to cool $\sim 10^9$ cesium atoms to 2μK so that their wave-like properties can be exploited when the atoms are launched vertically. Then using interferometric methods, the gravitational acceleration on the drag-free atoms can be measured with laser light pulses. A vertical GGI that incorporates two such cold atom accelerometers using the same cesium atoms produced a noise of 30 Eö/$\sqrt{Hz}$ with its 1.4 m baseline. If the baseline were increased to 10 m, the noise floor is predicted to decrease to 4 mEö/$\sqrt{Hz}$.[85]

1.2.1.3 Gravity Gradiometer Instrument Specifications

Table 1.1 summarizes the instruments above and their specifications.

1.2.2 Gravity Gradiometer Aided Inertial Navigation

The use of gravity gradiometer instruments as an INS aid has been identified and investigated since the 1960s. Most of the early research focused on real-time determination of the gravity anomaly to provide improved un-aided inertial naviga-

Table 1.1: Gravity Gradiometer Instruments

Gradiometer	Developer	Noise, 1-σ Eö	Data Rate, sec
Rotating Accel. GGI	Bell Aerospace / Textron	2 (Lab.), 10 (Air)	10
Rotating Torque GGI	Hughes Research Laboratory	0.5 (Goal)	10
Floated GGI	Draper Laboratory	1 (Lab.)	10
Falcon AGG	Lockheed Martin / BHP Billiton	3	Post Survey
ACVGG	Lockheed Martin	1	1
3D FTG	Lockheed Martin / Bell Geospace	5	Post Survey
FTGeX	Lockheed Martin / ARKeX	10 (Goal)	1
UMD SGG (Space)	Univ. of Maryland	0.02 (Lab.)	1
UMD SAA (Air)	Univ. of Maryland	0.3 (Lab.)	1
UWA OQR	Univ. of Western Australia	1 (Lab.)	1
Exploration GGI	ARKeX	1 (Goal)	1
HD-AGG	Gedex / UMD / UWA	1 (Goal)	1
Electrostatic GGI	European Space Agency	0.001 (Goal)	10
Cold Atom Interferometer	Stanford Univ. / JPL	30 (Lab.)	1

tion (*i.e.* dead-reckoning) accuracy. Eventually, GGI-based gravity mapping missions were proposed and researched so that these high accuracy and resolution maps could be stored onboard non-GGI aided INSs. Then, once these gravity field maps

were available, it was identified that they could be used for matching onboard GGI measurements to the stored map for position updating. While the work in this dissertation is focused on simulating map-matched GGI/INS systems, a high accuracy gravity field model is a necessity. Therefore, a review of the literature pertaining to the determination of gravity anomalies using a GGI/INS (which is a precursor to mapping missions), GGI/INS mapping and surveying, and map-matched GGI/INS technology is presented in the subsequent subsections. A brief summary of some other novel applications of gravity gradiometer instruments is also given.

1.2.2.1 Real-Time Determination of the Gravity Anomaly

The 1975 AIAA Guidance and Control conference in Boston, MA held a special session on gravity gradiometry technology that produced many seminal papers in this field.[28,35,86–88] Gerber[86] investigated the effect of GGI errors (white noise, time-correlated noise, random constant bias, and random constant drift) on a one-dimensional integrated INS. He found that transient errors were dominated by GGI biases and long-term errors were governed by noise near the Schuler frequency. Grubin,[87] the next paper in the session, presented a similar paper with 1-D simulations that looked at the effect of gravity anomalies on an INS's position accuracy with and without an onboard GGI. Grubin examined the effects of GGI biases, scale factors, and misalignments along with gravity anomaly bias and Schuler resonance, and he concluded that the GGI bias produced the largest INS position error. One primary difference between these two papers is in their modeling of the gravity field. Gerber

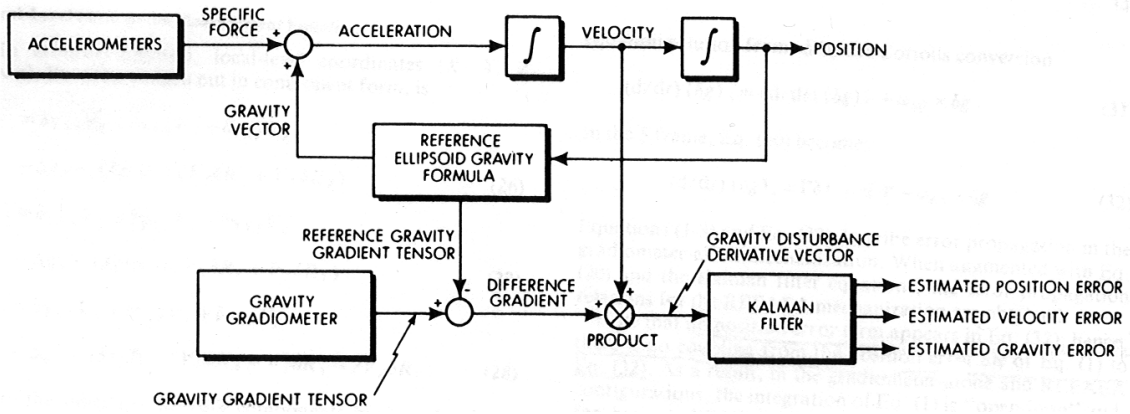

Figure 1.11: Block Diagram of INS/GGI for Real-Time Determination of Gravity Anomaly, from Ref. [88]

chose to take a stochastic approach while Grubin used a simple deterministic model with several randomly placed masses.

The third paper in the session, by Heller and Jordan,[88] proved that GGI aiding of a reference gravity field was optimal (Fig. 1.11), as had been assumed by the previous two papers. The authors compared the simulated INS performance of a reference ellipsoidal gravity model aided with GGI updates and the performance of direct integration of the GGI signal with the reference gravity model acting as an aid with a finite update rate. They concluded that the main issue with the latter system is that the error growth exhibits a diverging random walk trend because of the integration of the GGI noise. The other two papers in this 1975 session are reviewed elsewhere in this chapter. Trageser's paper[28] on the Draper GGI was discussed on pg. 7, and Metzger and Jircitano's paper[35] on a map-matching GGI/INS will be discussed on pg. 28.

Over the years, the interest in a GGI-aided INS for real-time gravity anomaly

determination has decreased as the difficulty in the instrument design was identified. Occasionally, people have revisited the subject and added some modest gains to the state of the art. Zondek[89] is notable for extending this use of a GGI/INS to an Earth-orbiting satellite as a means to improve its ephemerides. Specifically, the paper focuses on measuring and correcting for high-frequency orbit errors due to unmodeled gravitational phenomenon. Wells and Breakwell[90] derived several one-dimensional filters (one Kalman and two Weiner-Hoph) to blend GGI and Doppler velocity measurements into an INS. The Weiner-Hoph filters were necessary to implement a higher-order nonlinear gravity model that would be impossible to include in a Kalman filter due to its inherent assumption of linearized error dynamics.

Hopkins[91] investigated the effect of a GGI-aided INS to reduce anomalous gravitational errors during GPS outages. Unlike the work in this dissertation, *there is no comparison of the GGI measurement to a stored gravity map.* Instead, Hopkins only looks at whether or not to model the gravitational errors in a GPS/INS by using a gradiometer as an additional sensor. He shows that the gravity error modeling and the added GGI provide further refinement of the navigation solution during GPS blackouts.

Shingu[92,93] simulated a GGI-aided INS to *estimate unmodeled gravity errors for a more robust inertial navigation.* His chosen application was a long-range autonomous rocket trajectory where a portion of the Earth's mass was concentrated in a single location unbeknownst to the rocket's INS.

Most recently, Jekeli[94] simulated a GGI-aided INS consisting of future-grade IMUs for accurate long term dead-reckoning as part by a Defense Advanced Research

Projects Agency (DARPA) concept. He showed that the unmodeled gravitational disturbances from a simulated mountainous region would produce ∼5 km of horizontal position error after one hour dead-reckoning with future-grade IMUs. However, with an integrated, onboard GGI with 0.1 Eö noise updating at 1 Hz, *the position errors decreased to only 5 m—a three order of magnitude improvement.* This reference is particularly notable for its clear derivation of a strapdown gradiometer's linearized measurement errors and the integration of a GGI into a 6 degree of freedom INS. This dissertation extends Jekeli's work by including map-matching of the GGI measurement to a stored gravity map, adding orientation effects to the derivation of the GGI measurement errors, and derivation of a stabilized GGI with its linearized error measurement. Furthermore, the system error state transition matrix is calculated more computationally efficient in this work as compared to Jekeli.

Kwon and Jekeli[95] also investigated the DARPA problem of accurate long-term dead reckoning from the viewpoint of using a high-resolution onboard gravity map instead of an onboard GGI. Using the future-grade IMUs, they showed by simulation that ground data needed to be gridded at a 2 arcmin resolution with accuracy of 5 mgal (5×10^{-5} m/s^2) or better in order to provide the goal of 5 m position error after one hour of free-inertial dead reckoning.

1.2.2.2 Gravity Gradiometer Surveying

Gravity gradiometry technology has been proposed as an alternative or replacement to traditional gravimeter surveying. The major advantages to a GGI-

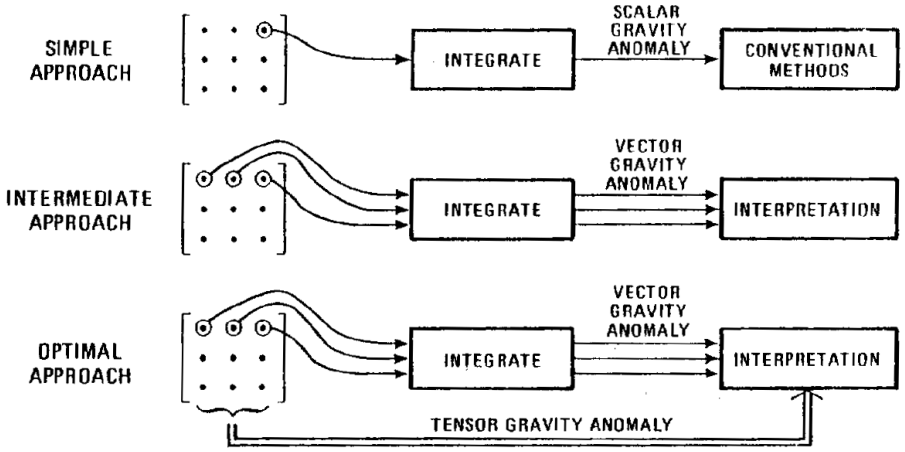

Figure 1.12: Gravitational Gradient Survey Integration Methodologies, from Ref. [96]

based survey system are:

- Improved high frequency observability due to the gravitational gradients being the derivative of the gravitational acceleration.
- More information available since Γ^n is a 3×3 tensor measurement while the gravimeter's acceleration is at most a 3-element array.
- GGI, unlike gravimeter, measurements are decoupled from linear accelerations so that accurate estimation of these accelerations is unnecessary.

Jordan[96] was the first to research using an airborne gradiometer for fast, large-scale survey missions. He compared three methods of using the GGI measurements, see Fig. 1.12: a simple integration of only the gradient of the vertical gravitational acceleration with respect to the velocity vector (Γ_{xD}) to yield scalar gravity anomalies; integration of the gradients of the gravitational acceleration with respect to the velocity vector ($\Gamma_{\mathrm{xN}}, \Gamma_{\mathrm{xE}}, \Gamma_{\mathrm{xD}}$) to yield a vector of the gravity anomaly; and optimal integration of the full tensor. By simulating a mission over a salt dome field, Jordan

showed that at least three components of the gradient tensor should be measured, but that the accuracy improvement from using three to nine elements was rather small. He also concluded that a GGI-based survey can save time and money because a 18 km-spaced GGI survey was comparable to a 8 km- spaced airborne gravimeter survey. Sensitivities to track spacing, GGI noise, vehicle speed, and survey altitude were also presented.

A decade later, Brzezowski and Heller[23] discussed the error sources of a GGI survey mission in detail. The error contributions are, in summary:

- **Gradiometer System Errors:** GGI noise; environmentally induced errors; navigation, attitude, and attitude-rate uncertainties; and gimbal, vehicle, and limited nearby-object compensation.
- **Discrete Sampling Effects:** aliasing of frequencies higher than half the sampling frequency, which determines the spatial resolution of the survey when multiplied by the aircraft speed.
- **Limited Data Extent:** the limitation in determining the low frequency signal content because the far-field gravity is not measured.

Then, using three gravity field characteristics (low, medium, and high variations), Brzezowski and Heller showed that it is easier to compute the deflections of the vertical of the gravitational vector than to compute the magnitude of the gravitational disturbance. Furthermore, "rougher," or highly variant, gravity fields caused larger survey errors. And surprisingly, limited data extent produced about half the modeled survey error.

Jekeli[38] summarized the Gravity Gradiometer Survey System (GGSS) experimental test program of 1983–1989. The GGSS used a full tensor Bell / Textron GGI mounted in a large conversion van to investigate the usefulness of the system for airborne, road, and rail surveying. The airborne GGI tests were the first of their kind and were accomplished by loading the van aboard an aircraft and then flying tracks over a 315 km $\times$ 315 km area at a 700 m altitude. The test was plagued by poor GPS coverage and of the 128 tracks flown, only 19 were chosen for analysis. Rather surprisingly, this first flight test of an airborne GGI produced average noise levels of only $\sim$10 Eö with a 10 sec average, while 3–6 Eö was expected. Moreover, the results of the GGSS program likely motivated early development of the commercial airborne GGI survey systems.

Jekeli[97,98] later compared airborne gravimetry and gradiometry survey errors in the frequency domain. He reiterated the potential benefits of an airborne GGI system but noted that the current limitation is the self-generating noise of the instrument, which is over an order of magnitude of other GGI system errors. He concluded that the future of gravity surveys would preferably lie with GGIs because future gradiometer-based surveys only require improvements in IMU quality, while gravimeter-based surveys also require improvements in real time kinematic (RTK) GPS to compensate for the vehicle's accelerations. (A full technical report on this work is also available from Ohio State University.)[99]

1.2.2.3 Gravitational Gradient Map-Matching

Although not much has been published in the open literature, map-matched gravity gradiometer aiding dates back to the 1975 AIAA Guidance and Control conference. A one-dimensional covariance analysis by Metzger and Jircitano[35,100] estimated INS position accuracy based on gravity and gradient map-matching for mobile systems (4–240 m/s). The premise was to simulate an initial mapping mission and then compare the steady state lag of a second GGI/INS mission following the same trajectory. They show that the gravitational gradients are preferable for map-matching since their shorter correlation distances (4,600 m vs. 37,000 m) produced higher frequency signals and thus finer spatial resolutions. Increases in instrument noise and vehicle velocity, or decreases in map record length, are shown to degrade performance. The velocity effects are due to the assumption that the GGI produces measurements at every 10 seconds, so the initial mapping mission produces coarser maps when simulated at higher velocities. For the work presented in this dissertation, the gravity map is a fixed resolution regardless of vehicle velocity so position error is less sensitive to cruise speed.

In 1990, Affleck and Jircitano[36] presented three-dimensional results of an integrated INS/GGI simulation for low speed airborne and submarine systems. Unfortunately, the depth of the presented analysis was minimal, most likely due to the proprietary nature of the original work and the classification of some of the technology. Indeed, the vast majority of their simulations are shown as simple block diagrams. Nevertheless, the results are quite promising as shown in Fig. 1.13. This

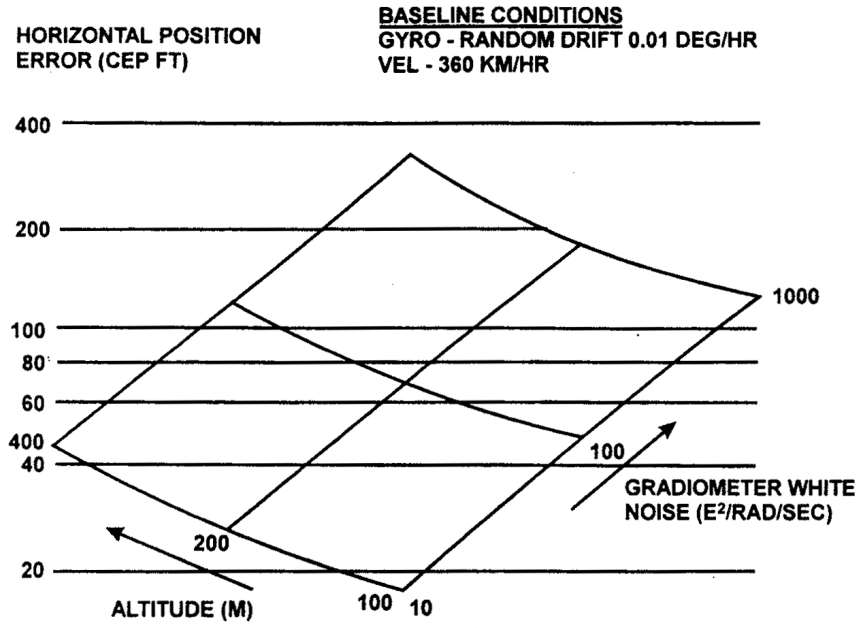

(a)

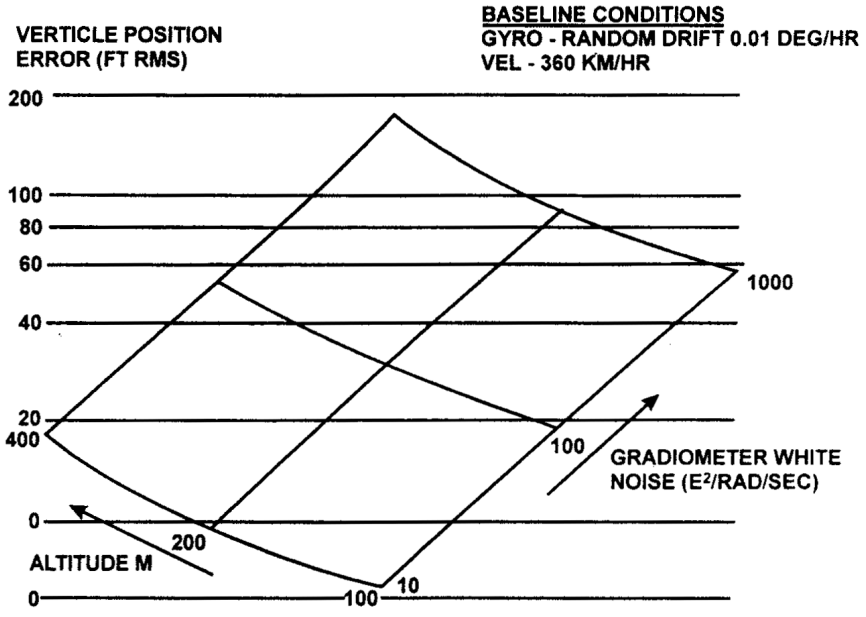

(b)

Figure 1.13: Horizontal (a) and Vertical (b) Position Error vs. Cruise Altitude, from Ref. [20]; originally from Ref. [36]

dissertation's research is essentially a continuation of Affleck and Jircitano's work but with the noted difference that the current work presents the detailed analyses that are omitted in the reference. Furthermore, this present work extends the analysis to the hypersonic regime and includes simulation of future-grade GGIs that the reference did not consider.

The following year Jircitano and Dosch proposed and patented a Gravity Aided INS (GAINS) using a GGI and a vertical gravimeter for covert submarine navigation.[37,101] This concept built on the prior two references and includes specifics in the modeling of the gravity field, but their filter implementation is again shown as only a block diagram. From the schematic, the filter states included GGI, gravimeter, depth sensor, and IMU instrument errors along with the standard INS position, velocity, and attitude error dynamics. The filter also includes states for the estimated gravitational field potential, acceleration, gradient and third order derivative. With their covert navigation system, the authors showed that modern submarines could produce position errors as low as $\sim$30 m.

More recently, Zhang *et al.*[102] simulated a map-matched GGI/INS for an autonomous underwater vehicle (AUV), similar to the prior papers. Unfortunately, like the previously cited papers, the presented analysis consists of only flow charts and results. Their results show an estimated position accuracy of tens of meters for their AUV concept.

A different GGI/INS map-matching approach was taken by Archibald for his doctoral work.[103] He implemented neural networks to match large-area noisy and truth gravitational gradient and magnetic field maps. While INS simulations were

shown to motivate his research, the neural network was not integrated with the INS. Regardless, the novel concept of matching large-scale geophysical quantities could be used as an initial estimate of a user's position state.

Lastly, Gleason[20] discussed many of the practical issues of a GGI/INS for navigation and terrain avoidance at length. The paper focuses on extrapolation of gridded gravity data at a given altitude using Fast Fourier Transforms (FFTs), terrain elevation, and density assumptions. He also showed that the at-altitude gravitational field can be optimally estimated when ground gravity data is available. Some of the other issues discussed were the effects of vehicle velocity and altitude, gradiometer noise level and data rate, and the design of a low-pass filter to reduce high frequency instrument errors.

1.2.3 Other Gravity Gradiometer Instrument Applications

Some other novel applications for gravity gradiometer instruments are summarized below to show the versatility of this relatively unknown sensor.

1.2.3.1 Close-Loop Satellite Attitude Refinement

Roberson[104] proposed using a hypothetical differenced accelerometer GGI to compute the radial (*i.e.* vertical) gravitational gradient of the Earth so that fine tilt orientation could be achieved aboard an orbiting satellite. He motivated his research by the discovery that the primary radial gradient produced a torque on satellites that caused their long axis to be aligned with the gradient. Thus, because

the orientation of this gradient is well known, it could be exploited for high accuracy attitude determination. He also derived error equations for the GGI assuming scale factor, bias, and misalignments in accelerometer pairs that pointed radially away from the Earth's center. While his derivations are informative to show the effects of the accelerometer errors on the overall GGI error, their derivation is rather confusing and limited to a partial-tensor measurement ($\Gamma_{\mathrm{ND}}, \Gamma_{\mathrm{ED}}, \Gamma_{\mathrm{DD}}$).

Diesel[105] showed that a single rotating accelerometer could theoretically provide a measurement of the gravitational gradient as the IMU sensor records measurements at various locations. The periodic measurement could then be used to finely estimate the spacecraft's tilt errors because the tangential gradient signal is zero in the vertical and horizontal directions. Diesel also comments on a controller to stabilize the system, the filter power spectral density, sensor dynamics and an error analysis.

1.2.3.2 Arms Treaty Verification

The use of a GGI to estimate the mass properties of arms treaty-limited systems was first proposed by Parmentola.[106] He investigated using a GGI to take an effective gravitational X-ray of two Tomahawk-scale cruise missiles; one with a simulated conventional warhead, and one with a nuclear warhead. By unobtrusively scanning the gravitational gradients 0.5 m away from the missile, the warhead type could be unambiguously determined.

Gray, Parmentola, and LeSchack[22] expanded this work by using a least squares

approach to invert noisy GGI measurements to estimate the mass properties of an object. The paper discusses the numerical issues of calculating the measurement matrix pseudo-inverse and provides background on the multipole expansion for the mass properties. Then by simulating objects moving on an assembly line near a GGI, it was shown that this system could be a viable tool in monitoring arms treaty-limited objects. Moreover, it was concluded that the GGI estimated non-uniform and less spherical objects less accurately than a uniform sphere; however, this result may be heavily dependent on their choice of a multipole expansion in estimating the object's mass distribution.

Determination of asteroid and comet mass distributions using a GGI has also been proposed.[107] Although this is not a treaty-limited object, the problem formulation is quite similar.

1.2.3.3 Underground Bunker or Void Detection

The notion of using a GGI system for underground bunker or void detection is essentially the same as using it for surveying or exploration. The premise is to take a gravitational survey of an area along with its terrain elevation and back out any anomalous features. The difference is now that instead of an increased gravitational potential for the exploration missions, there is a decrease due to the void.

Romaides *et al.*[46] undertook an experimental ground-based validation study using the ACVGG (see pg. 13) and these principles. Preliminary tests were performed over a subway car storage facility in Cambridge, MA that showed the clear

presence of the underground tunnel. A full-scale survey was then performed at Vandenberg Air Force Base over the Missile Alert Facility (MAF) bunkers using the ACVGG and a state of the art gravimeter. Although the bunkers were heavily reinforced with concrete that helped compensate for the absence of mass, the GGI-based survey unambiguously resolved the MAF location, unlike the gravimeter survey. The results from this study are particularly promising since they show a viable tool for determining the location of underground bunkers in the global war on terror.

1.2.3.4 All Accelerometer Inertial Navigation

Gravity gradiometer instruments have also been proposed as an extension to gyro-less all-accelerometer inertial navigation systems.[108] Zorn presented two paper on this topic that envisioned a 12-accelerometer GGI to measure specific force, angular accelerations, and the full-tensor gravitational gradient tensor (Section 5.2 discusses a similar GGI, and pg. 186 explains how the angular acceleration is observable). Zorn's first paper[40] summarizes the concept and derives the applicable measurements for the system. The second paper[41] continues the work by simulating two INS/GPS systems to investigate the sensor requirements for the all-accelerometer INS to be comparable to a tactical-grade INS with gyros. For a constant altitude, speed, and turning radius simulation, it was shown that the all-accelerometer INS (which is essentially a GGI) needed a 10^{-6} improvement in the accelerometer bias stability and white noise level to yield a comparable tactical-grade INS/GPS navi-

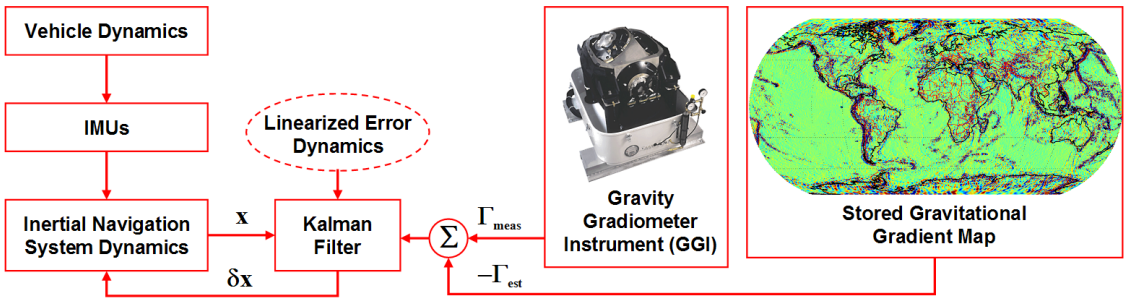

Figure 1.14: Map-Matching GGI/INS using an Extended Kalman Filter

gation accuracy. This vast reduction in accelerometer error is directly attributed to the need to accurately measure the angular acceleration of the vehicle so that the attitude could be determined after integrating twice.

1.3 Objective

The objective of this dissertation is to show the potential benefit of a novel gravity gradiometer aided inertial navigation system. *The premise is to compare GGI measurements with an onboard gravity field map to produce delta-position corrections through an extended Kalman filter implementation*, as shown schematically in Fig. 1.14. Conceptually, this system functions in much the same manner as a terrain-based map-matching INS aid. The main difference is that the emitting radar or laser sensor of a terrain-based system is replaced with the self-contained, passive gravity gradiometer instrument. Furthermore, instead of making a single range measurement (or possibly a Doppler as well), a GGI can make up to six non-symmetric measurements of the gravitational gradient tensor.

In order to quantify the performance of the INS/GGI system a characterization

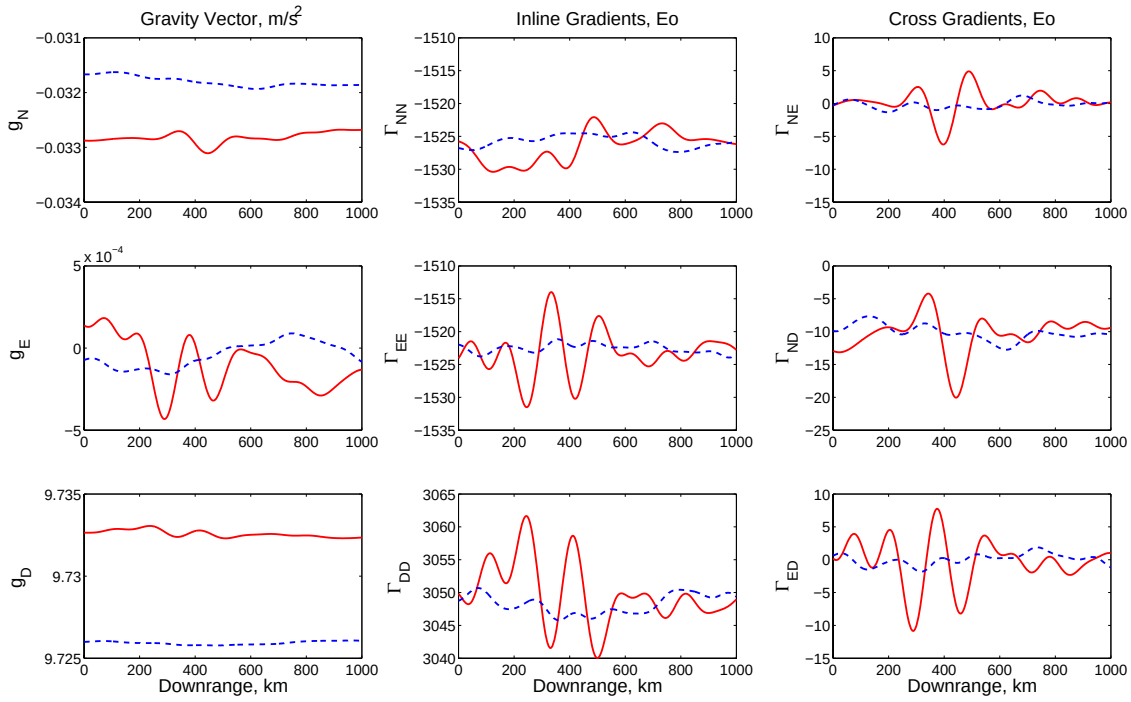

Figure 1.15: Simulated Gravity at Nominal Latitude and Altitude for Mach 7 Trajectories, "High" Variation (solid), "Low" Variation (dashed)

of the gravitational gradients is first undertaken. Of utmost importance are the gradient variations since the slope of the gravitational gradients are used for the position updates. In other words, if the gradients were constant, there would be no discernable features in the signal to derive position knowledge, see dashed gradients in Fig. 1.15 compared to the solid curves. Conversely, if the gradient variation is sufficiently large compared to the GGI noise level, these changes may be exploited to update the INS position estimate. The primary questions to be answered are:

- How much do the gravitational gradients vary?
- Which gravitational gradient varies the most?
- Where do the gravitational gradients most?
- How does altitude effect the gradient variations?

As a corollary to the gravitational gradient characterization study, and the lack of available terrain elevation data for this work, a first-order analysis of when one may neglect local terrain effects is carried out. In order to broaden the applicability of this study, a parametric "mountain" is simulated and its vertical gravitational gradient is computed for a variety of dimensions and user altitudes. Then, to reduce one of the independent variables, the "mountain" width is optimized to provide the maximum gravitational gradient so that the terrain contributions may be estimated as a function of terrain peak and user altitude.

After these fundamental gravitational gradient questions are answered, the map-matching GGI-aided INS simulations are performed to quantify the potential performance and sensitivities of future INS/GGI systems. The first objective to this goal is the modeling of the inertial measurement unit signals. A hypersonic

scramjet is chosen for the majority of the simulations. The off-design aerodynamics and propulsion characteristics are used to calculate the trim conditions over a 1000 km range cruise. Then, the trim angles are finite differenced to calculate the body-to-navigation frame portion of the gyro signal. The assumed trajectory and cruise velocity and altitude are used to calculate the accelerometer signals for the simulation.

The details of integrating a gravity gradiometer instrument into an inertial navigation system using an extended Kalman filter implementation are also presented thoroughly for the first time. Extensions and modifications to traditional INS simulations are documented to enable stable filter performance. In the event of filter divergence, the reason (numerical truncation error) is identified and solutions are proposed.

Furthermore, the simulated gravity gradiometer instrument measurement and their linearized errors are derived thoroughly for the first time in the open literature. Specifically, the inclusion of tilt errors and the conversion from the GGI tensor measurements to vector measurements to allow for the filter implementation is performed for the first time. Completely new derivations for a stabilized GGI are also performed for this dissertation work.

The hypersonic INS/GGI navigation system sensitivities are identified through the use of numerous Monte Carlo simulation configurations. The varied design parameters are: instrument noise, update rate, and type (strapdown or stabilized); gravitational gradient variation; IMU quality (navigation or tactical grade); and Mach number. Also, to compare with current technologies, an INS/GPS system

is simulated. The effects of GPS measurements (pseudorange with or with out pseudorange rate), update rate, and IMU quality are also quantified.

Two subsonic INS/GGI cases are also simulated to show the potential performance on current platforms. A commercial aircraft mission and a GGI-survey mission are both simulated using the "best" INS/GGI design parameters from the hypersonic simulations. These cases are also important because current GGIs are too large and heavy for missile-class vehicles, but can be used aboard these two current subsonic vehicles.

1.4 Dissertation Outline

This dissertation consists of seven chapters and five appendices, organized as follows.

Chapter 2 discusses some fundamental aspects of gravity gradiometry including the gravitational potential and acceleration, and the centripetal components of gravity. A brief review of how the gravity field is typically modeled and how it was modeled for this work is presented. The parametric terrain study to estimate when local terrain contributions may be negelected from the computed gravity map is also undertaken in this chapter. Then the gravitational gradient sensitivities to altitude and location on the Earth are shown. Lastly, the simulated trajectories used in the Monte Carlo simulations are detailed along with a study to estimate the stored map's linear interpolation error as a function of grid resolution.

The third chapter presents the hypersonic vehicle model used for the ma-

jority of the simulations. The aerodynamic and propulsion characteristics from a JHU/APL reference are described and the implemented curve-fit calculations are given. A simple mass model is then determined so that the trim conditions can be computed over the assumed trajectories. The trim pitch and roll angles are lastly finite differenced to produce part of the simulated gyro signals for the INS simulations.

Chapter 4 details the intertial navigation system model. Standard coordinate frames and transformations are reviewed, then the navigation equations are derived from first principles. The INS linearized error dynamics are also derived thoroughly. And lastly, the simulated acclerometer and gyro measurement errors are presented along with a survey of current tactical and navigation grade IMU specifications. The modifications to traditional INS simulations in order to integrate a GGI aid is also identified in this chapter.

The fifth chapter presents a thorough methodology for modeling many gravity gradiometer instruments. Then the rotating, stabilized GGI measurements are derived clearly for reference purposes since many references provide at most a confusing derivation of this type of GGI measurement. Next, the assumed twelve-accelerometer GGI is described. Strapdown and stabilized GGI measurements and their linearized error equations are also derived comprehensively for the first time.

Chapter 6 explains the Monte Carlo simulation set up and assumptions. A parametric analysis on the effect of Monte Carlo set size is undertaken, and then the INS/GGI and baseline INS/GPS results are presented for numerous system configurations.

Chapter 7 summarizes the contributions of this work to the state-of-the-art and recommends a set of work for future study.

Several appendices are also included in this dissertation to supplement the content of the main body. Appendix A consists of additional global gravitational gradient maps at various altitudes, which are used in the analyses of Ch. 2. Appendix B supplements Ch. 3 with additional polynomial curve fits for the thrust coefficient propulsion calculations. Appendix C presents an overview of the extended Kalman filter model implemented for this work. A review of the Kalman filter assumptions, stochastic processes, and linear system dynamics are also shown. And a new method to calculate the gyro noise portion of the error state transition matrix is discussed as well. Appendix D details the modeled nominal 24-satellite GPS constellation and the assumed measurements for the baseline INS/GPS analyses. Lastly, App. E lists the extensive mean-radial-spherical-error results from the Monte Carlo simulations.

Chapter 2

Gravity Map Model

This chapter presents the model used to simulate the gravity field for this work. Section 2.1 first presents a brief review of the gravity potential and its derivatives. Section 2.2.1 and 2.2.2 then describe how the gravity field is typically modeled using spherical harmonic and local terrain models. Section 2.2.3 next estimates when the local terrain effects may be omitted from the gravitational field model, and Sec. 2.2.4 discusses and estimates other vehicle self-generated bias sources. A global-scale characterization of the gravitational gradients using a spherical harmonic model is performed in Sec. 2.3 to identify trends in the gradients for use as a navigation map-matching aid. Then the two chosen simulation trajectories are detailed in Sec. 2.4 along with studies to determine the stored gravity field grid spacing. Lastly, Sec. 2.5 summarizes the contributions and results from this chapter.

2.1 Gravity Gradiometry

The gravitational potential is defined as[109,110]

$$\phi_g \equiv \iiint_V \frac{\rho(\mathbf{r}')}{|\mathbf{r}-\mathbf{r}'|} dV, \tag{2.1}$$

where ρ is the density of the attracting mass at $\mathbf{r}'$ and $\mathbf{r}$ is the vehicle (or "user") location. The first derivative of the the potential yields the gravitational vector:

$$\mathbf{g}^n \equiv \nabla\phi_g = \begin{pmatrix} g_N \\ g_E \\ g_D \end{pmatrix}, \tag{2.2}$$

where it has been assumed that the coordinates are in the local North-East-Down navigation frame, see Sec. 4.1.3. The second derivative produces the gravitational gradient tensor:

$$\Gamma^n \equiv \nabla\nabla^T\phi_g = \begin{pmatrix} \Gamma_{\mathrm{NN}} & \Gamma_{\mathrm{NE}} & \Gamma_{\mathrm{ND}} \\ \Gamma_{\mathrm{NE}} & \Gamma_{\mathrm{EE}} & \Gamma_{\mathrm{ED}} \\ \Gamma_{\mathrm{ND}} & \Gamma_{\mathrm{ED}} & \Gamma_{\mathrm{DD}} \end{pmatrix}. \tag{2.3}$$

The trace of Γ^n, or equivalently the Laplacian of the potential, is equal to Fourier's equation:[109]

$$\triangle\phi_g = \Gamma_{\mathrm{NN}} + \Gamma_{\mathrm{EE}} + \Gamma_{\mathrm{DD}} = -4\pi G\rho(\mathbf{r}), \tag{2.4}$$

where G is Newton's gravitational constant and ρ here is the density at the user. Because the density of the Earth (mean crust $\sim$2,670 kg/m^3)[110] is much greater than the atmosphere (at sea level $\sim$1.2 kg/m^3), it is common to assume a "free-air" gravitational potential so that the gravitational attraction of the air is neglected. Thus, Fourier's equation is now

$$\triangle\phi_g = \Gamma_{\mathrm{NN}} + \Gamma_{\mathrm{EE}} + \Gamma_{\mathrm{DD}} = 0, \tag{2.5}$$

which is Laplace's equation. The general solution to Laplace's equation is an infinite harmonic summation, to be discussed in the next section.

Before continuing, a word on nomenclature is in order. Throughout much of the literature the term "gravity gradient" has been used. In the strict sense, the quantity that is being referred to is the *gravitational* gradient—not the gravity gradient. Gravity is defined as the sum of the gravitational and centrifugal potentials (or accelerations, or gradients). It will be shown later that the measurement made by a gravity gradiometer is a combination of the gravitational gradient and noise in the form of angular rates and accelerations, see Sec. 5.1. The terms "gravity gradient" and "gravity gradiometer" in some sense are misnomers, as the quantities that are being used are more accurately *gravitational* gradients.

For completeness, the centripetal potential is the analytic function:[111]

$$\phi_c = \frac{\omega_e^2}{2} \left(r \cos \phi \right)^2 , \tag{2.6}$$

where ω_e is Earth's rotation rate, ϕ is the latitude of the user, and r is the radius from the user to the center of the Earth. The first derivative of Eq. (2.6) is then the centripetal acceleration due to the Earth's rotation.

2.2 Gravity Map Modeling

Gravitational field maps are typically computed by the summation of a spherical harmonic model to capture low frequency, long range gravitational effects and integration of local terrain elevation to capture the high frequency, short range effects.[95] The centripetal portion is then added to compute the gravity acceleration vector. And since the centripetal effects are simple analytical functions, this section will focus solely on the more complicated modeling of the gravitational potential

and its derivatives.

2.2.1 Spherical Harmonics

The general solution to Laplace's equation, Eq. (2.5), is an infinite harmonic summation. In spherical coordinates:[109,112]

$$\phi_g(r,\theta,\lambda) = \frac{GM}{r}\Big[1 + \sum_{n=2}^{\infty}\Big(\frac{a_e}{r}\Big)^n \sum_{m=0}^{n}\big(\bar{C}_{nm}\cos(m\lambda) + \bar{S}_{nm}\sin(m\lambda)\big)\bar{P}_{nm}(\theta)\Big], \tag{2.7}$$

where θ is the colatitude ($= \pi/2-$ latitude), λ is the longitude, n and m are the degree and order of the fully normalized coefficients ($\bar{C}_{nm}$,$\bar{S}_{nm}$), and $\bar{P}_{nm}(\theta)$ is the fully normalized associated Legendre function. The equation is referenced to a given gravitational parameter GM which is the universal gravitational constant times the total mass of the attracting body, and a_e is a reference radius (for Earth a_e = 6,378,137 m).[113,114] In practice, the series is truncated at a maximum degree, n_{max}, based on the available coefficient set.

There are three designations for spherical harmonics.[109,115] The first designation is a *zonal* harmonic when $m = 0$, Fig. 2.1 (a). These harmonics are independent of λ and related to the well known unnormalized J harmonics by (Vallado,[115] pg. 518):

$$J_n = -\bar{C}_{n,0}\sqrt{2n+1}. \tag{2.8}$$

The J_2 term is by far the largest harmonic term (zonal or otherwise) as it accounts for the bulk ellipsoidal shape of the Earth. The second special designation is a *sectoral* harmonic which occurs when $m = n$, Fig. 2.1 (b). These harmonics are

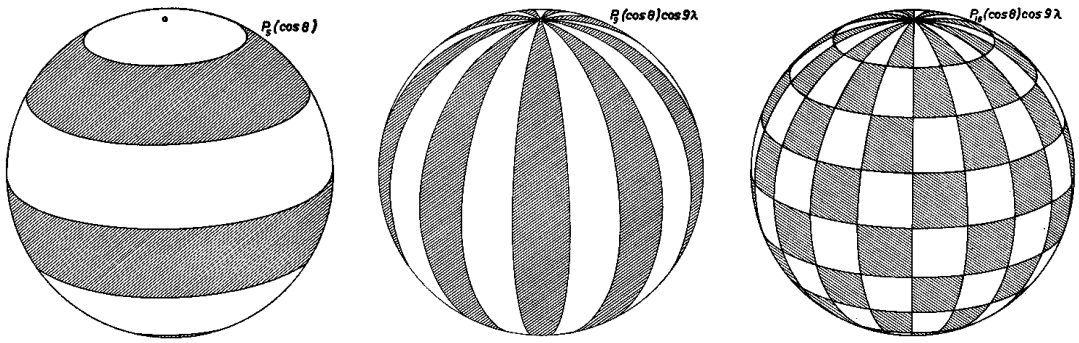

(a) (b) (c)

Figure 2.1: Spherical Harmonic Classifications (a) Zonal (b) Sectoral (c) Tesseral, from Ref. [109]

independent of latitude and account for gravitational variations in slices parallel to the meridian. Lastly, when $0 < m < n$ the harmonics are designated as *tesseral* and essentially account for potential variations in a checkerboard-like pattern of alternating mass distributions, Fig. 2.1 (c).

While spherical harmonic models allow for calculation of global gravitational potentials, their usefulness is limited primarily by the finite spatial resolution of the model. And although there is no universal definition for the spherical harmonic model's resolution, a convenient and common definition is the half wavelength of the maximum zonal harmonic with respect to the equatorial radius:[116]

$$S.H.M._{res} = \frac{\pi a_e}{n_{max}} \approx \frac{20 \times 10^6 \ m}{n_{max}}. \tag{2.9}$$

Many spherical harmonic gravity models have been published for Earth with the most extensive being the EGM96 set that includes coefficients up to degree and order 360.[114] Recent work such as the GFZ Potsdam CHAMP (Challenging Minisatellite Payload) and the University of Texas GRACE (Gravity Recovery and

Climate Experiment) satellite missions are producing higher accuracy coefficients; however, their maximum degree and order is currently only 140 (CHAMP)[117] or 200 (GRACE).[118] And since the resolution is proportional to $1/n_{max}$, EGM96 is about twice as fine as GRACE's GGM02C.[118] Therefore, to produce the highest resolution gravitational maps, the EGM96 coefficient set was chosen.

The calculation of the spherical harmonic potential and its derivatives (vector and gradient tensor) is rather straight forward except for the calculation of the associated Legendre functions.[111,119] For the present work, the National Oceanic and Atmospheric Administration (NOAA) / National Geodetic Survey (NGS) program `geopot97.v0.4e.f` was modified to produce gridded gravity accelerations and gravitational gradients at user defined latitude, longitude, and altitude ranges.[120,121] The code calculates the Legendre functions and derivatives using an efficient iterative Clenshaw summation.[119,122] However, this version of the program may not work or be as efficient for future higher degree coefficient sets because of numerical precision limitations. Instead, the new `geopot07.f`[123] may be used for $n_{max} \leq 2190$, or the Fortran 95 package SHTOOLS by Wieczorek[124] may be used up to $n_{max} \approx 2800$. Another approach would be to implement one of the algorithms presented by Holmes and Featherstone.[125]

As mentioned, the spherical harmonic models alias higher frequency (and finer resolution) terrain contributions due to its finite summation of Eq. (2.7). A discussion on methods to account for the terrain effects is presented in the next section, and a fundamental investigation as to when the terrain effects may be neglected is performed in Sec. 2.2.3. Section 2.2.4 then discusses other gravitational gradient

biases.

2.2.2 Terrain Elevation Contributions

Referring back to the spherical harmonic gravitational potential, Eq. (2.7), and the gradient tensor definition, Eq. (2.3), one can show that to first order the gravitational gradients are inversely proportional to the cube of the distance between the vehicle and attracting mass because the gradients are the second derivative of the potential, which is itself inversely proportional to the distance. Mathematically,

$$\phi_g \approx \frac{GM}{r} \quad \rightarrow \quad \frac{\partial^2 \phi_g}{\partial r^2} = \Gamma_{\mathrm{DD}} \approx \frac{2GM}{r^3}. \tag{2.10}$$

Therefore, because the gradients attenuate proportional to distance cubed, local terrain elevation variations will be negligible at sufficiently high altitudes compared to a given gradiometer instrument's noise level. Conversely, for low altitude applications, such as surveying missions, the signal-to-noise ratio due to the local terrain variation is large enough that it should be included in the computed gravity map.

In these latter cases digital elevation maps and an assumption of the terrain's density can be used to account for local terrain contributions. Jekeli and Zhu surveyed several algorithms including prism, fast Fourier transform (FFT), and ordinary numerical integration methods for two terrain data sets and found that FFTs can produce accurate models at a constant gridded altitude with low computation time.[110] Gleason also presented an FFT method that included several discrete density layers and showed that one can optimally estimate gravity at altitude with knowledge of surface gravity data and terrain elevation.[20] Thus, when terrain ef-

fects are not negligible (*i.e.* low altitudes and/or low GGI noise), an FFT model such as those described in the above references should be included in gravity field mapping. A limitation of the current work is the omission of such terrain effects in the simulated gravity field which causes a reduction in the available gradient signal frequencies. This is especially true for the subsonic GGI survey simulation since its assumed altitude is only 100 m.

2.2.3 Minimum Altitude to Neglect Terrain Effects

This section presents a parametric study of when terrain effects may be neglected for a given GGI noise level and user altitude. To bound the analysis, a single hypothetical mountain directly below the user is simulated and its vertical gravitational gradient is calculated. The vertical component was chosen as it is the largest component of the gradient tensor as shown later in Fig. 2.11. The mountain is assumed to have a zero-mean, normal, Gaussian height distribution, see Eq. (C.8) on pg. 313:

$$h_T(s) = \frac{a_T}{\sigma_T\sqrt{2\pi}} \exp\left(-\frac{s^2}{2\sigma_T^2}\right), \tag{2.11}$$

where h_T is the height of the mountain, s is the horizontal distance from the origin of the mountain, a_T and σ_T are the amplitude and standard deviation of the distribution, respectively. Figure 2.2 shows a schematic of the mountain for several design parameters. A Gaussian distribution was chosen because it qualitatively estimates the shape of a mountain and its distribution is uniquely defined by only two parameters, thereby facilitating the parametric nature of this study.

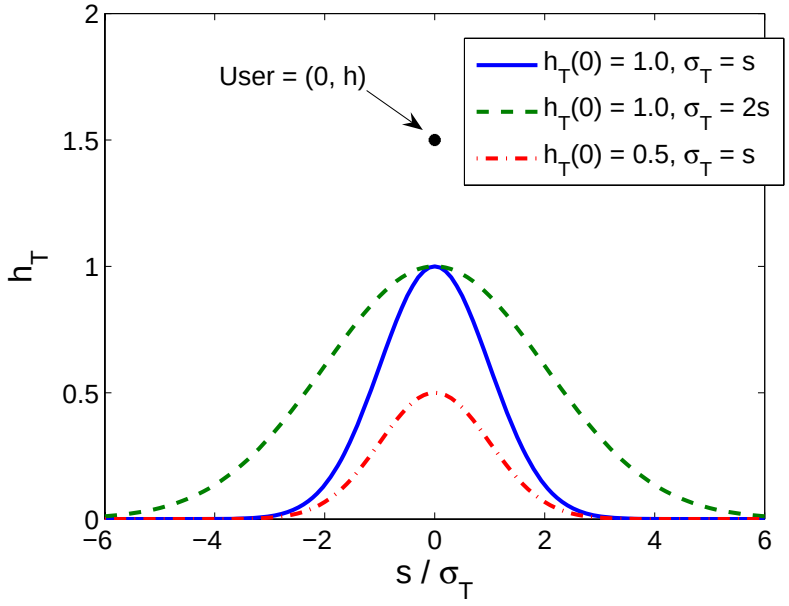

Figure 2.2: Schematic of Modeled Gaussian Mountain

The vertical gravitational gradient is calculated according to:[110]

$$\Gamma_{\mathrm{DD}} = G\rho_T \iint_A T_{33} dA, \tag{2.12}$$

where the integration in the vertical direction has been performed so that

$$T_{33} = \begin{cases} \dfrac{1}{(h-h_T)^2} - \dfrac{1}{h^2}, & s = 0 \\ \dfrac{1}{s^2}\left[\dfrac{h-h_T}{r_h} - \left(\dfrac{h-h_T}{r_h}\right)^3 - \dfrac{h}{r_0} + \left(\dfrac{h}{r_0}\right)^3\right], & s \neq 0 \end{cases} \tag{2.13}$$

where h is the user altitude, and

$$r_h^2 \equiv s^2 + (h-h_T)^2, \tag{2.14}$$

$$r_0^2 \equiv s^2 + h^2. \tag{2.15}$$

For a given peak altitude, $h_T(0)$, and standard deviation, σ_T, the amplitude is computed by

$$a_T = \sqrt{2\pi} h_T(0) \sigma_T. \tag{2.16}$$

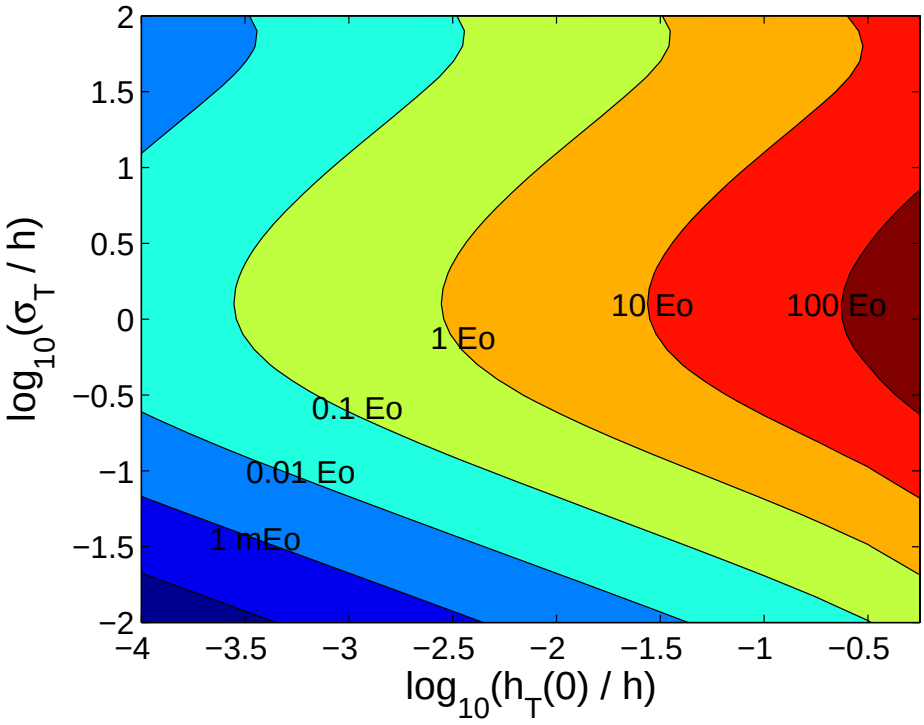

Figure 2.3: Terrain Contribution to Γ_{DD}

Then Γ_{DD} is calculated by numerically integrating Eq. (2.12) and (2.13) by:

$$\Gamma_{\mathrm{DD}} = \pi G \rho_T \sum_{s_i=0}^{6\sigma_T} \left(T_{33,i+1} + T_{33,i}\right) s_i \Delta s + \left(2T_{33,i+1} + T_{33,i}\right) \frac{\Delta s^2}{3}, \tag{2.17}$$

where s is a 2,001-element equispaced array of the horizontal distance from the origin to six times the standard deviation parameter and $T_{33,i}$ is the value from Eq. (2.13) at s_i. Also, it is assumed that $G = 6.6742 \times 10^{-11}$ m^3/(kg $\cdot$ s^2) and $\rho_T = 2{,}670$ kg/m^3.

To investigate a wide range of terrain possibilities, the simulated mountain's standard deviation and peak altitude were normalized by the user altitude and varied logarithmically. (Section 2.2.3.1 proves that the gradient calculation, as formulated, is uniquely defined by σ_T and $h_T(0)/h$.) The vertical gravitational gradient due to the simulated mountains are shown in Fig. 2.3. This plot can be used to estimate

when terrain effects may be neglected by:

1. Identifying the largest terrain object(s) from an elevation map and estimating the peak, $h_T(0)$, and standard deviation, σ_T, of the object.
2. Normalizing $h_T(0)$ and σ_T by the predicted user's flight altitude, h.
3. Locating the corresponding vertical gravitational gradient in Fig. 2.3 for the estimated $h_T(0)/h$ and σ_T/h.
4. Then, the terrain effects may be neglected for modeling purposes if the estimated Γ_{DD} is sufficiently less than the GGI noise.

It should be noted, that many mountains actually sit on large plateaus, which act as an altitude bias that has no effect on the terrain contribution of the gradient signal. Indeed, it can be shown that an infinite uniform sheet of mass has zero vertical gravitational gradient. In this regard, when estimating a mountain's characteristics, the peak should be referenced to the map's minimum elevation; not necessarily mean sea level.

Figure 2.3 also presents the interesting trend that the largest gravitational gradient occurs when $\sigma_T/h \approx 1.29$ for values of $h_T(0)/h < 10^{-2}$ and decreases to unity as $h_T(0)$ approaches h, as shown in Fig. 2.4. Therefore, low altitude surveys are more susceptible to more compact terrain variations, while higher applications are more sensitive to "wider mountains." The optimal σ_T/h ratios which maximize Γ_{DD} are a function of $h_T(0)/h$ only; however, at high altitudes σ_T grows large enough that these features would be accounted for in the spherical harmonic model. Thus, a constraint of $3\sigma_T \leq (\pi a)/n_{max} \approx 55$ km for n_{max} =360, from the spherical harmonic resolution definition of Eq. (2.9), can be set to limit the maximum standard deviation

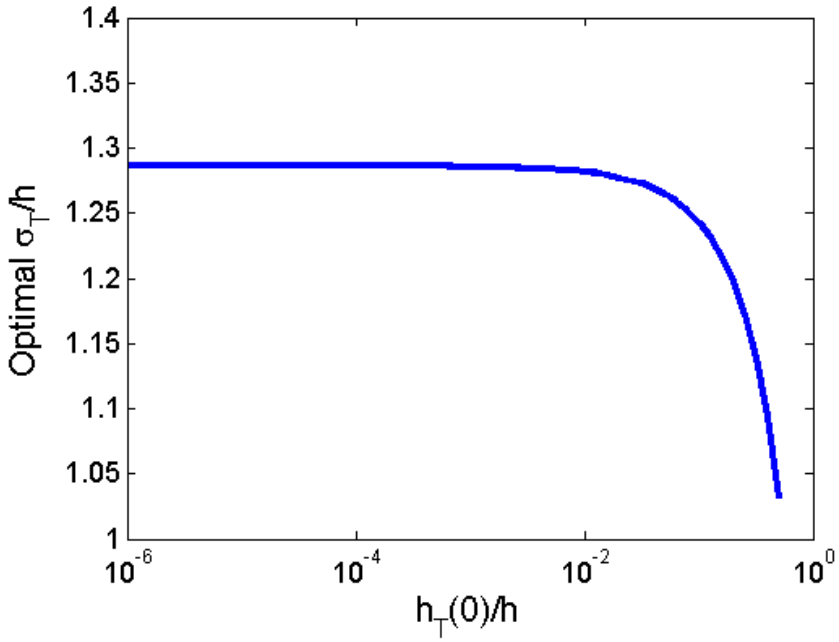

Figure 2.4: Optimal σ_T/h to Maximize Terrain Γ_{DD}

parameter.

Figure 2.5 uses the optimal σ_T/h ratios and the $\sigma_T \leq 18.6$ km constraint to calculate the maximum Γ_{DD} for a variety of peak terrain and user altitude configurations. This figure allows one to not have to estimate σ_T/h for a given mission and terrain elevation map. Therefore, using Fig. 2.5 one can estimate the terrain contribution to the vertical gravitational gradient for various missions given only the peak terrain and user altitude. Then, if the user's GGI noise level is sufficiently above the estimate in the figure, the terrain effects may be neglected.

For example, a commercial aircraft cruising at a 10 km altitude using a current-grade airborne GGI with an $\sim$5 Eö noise level would be affected by mountains approximately 100 m and taller. And a satellite in a 300 km altitude orbit with a space-grade 0.01 Eö GGI noise level would only be affected by terrain effects

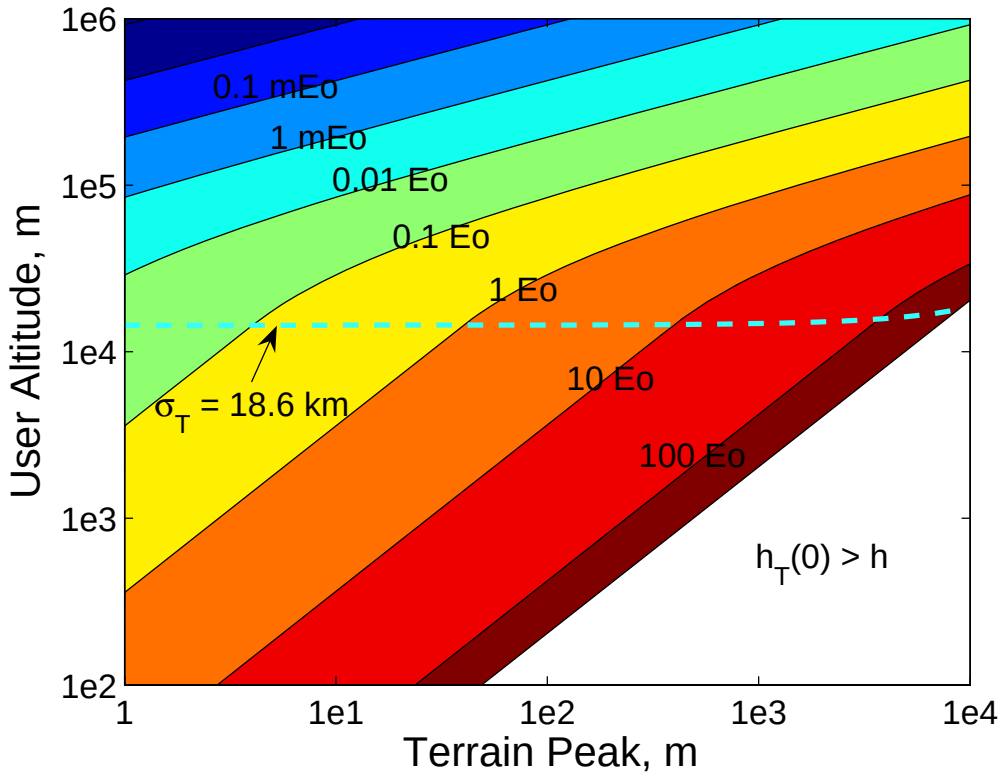

Figure 2.5: Terrain Contribution to Maximum Γ_{DD} for Various Peak Terrain and User Altitude Conditions

greater than about 500 m tall. The hypersonic cases simulated in this work are at an ∼24 km altitude and have GGI noise levels ≤0.1 Eö. Therefore, according to Fig. 2.5, terrain effects of 10 m and less should produce gradients above the noise GGI noise floor and should thus be included in future work. For reference purposes, a 100 m altitude corresponds to an ∼30 story building, the largest mountain in the contiguous United States is Mount Whitney at 4.4 km, and the largest in the world is Mount Everest at 8.8 km from sea level.

2.2.3.1 Normalization of Terrain Γ_{DD} Computation

The proof of non-dimensionalizing the Gaussian distribution parameters by the user altitude will be shown in parts. The dependence of $h_T(0)/h$ and σ_T/h on the horizontal distance (s), terrain elevation (h_T), r_h, r_0, and $T_{33,i}$ components will be derived in succession. Then these components will be substituted into Eq. (2.17) to show that, as posed, Γ_{DD} is indeed a function of only the two normalized Gaussian distribution design parameters.

The horizontal distance array is assumed to be equally-spaced from 0 to six times the standard deviation parameter:

$$s = \left[0 : \frac{6\sigma_T}{2000} : 6\sigma_T\right]. \tag{2.18}$$

This can be rewritten in terms of σ_T/h by factoring out the user altitude:

$$s = h\left[0 : \frac{6}{2000}\left(\frac{\sigma_T}{h}\right) : 6\left(\frac{\sigma_T}{h}\right)\right] \equiv h f_s\left(\frac{\sigma_T}{h}\right), \tag{2.19}$$

where the second equality denotes that s is equal to a function of only σ_T/h multiplied by the user altitude, h. Similarly, the increment of the horizontal distance

array is:

$$\Delta s = \frac{6\sigma_T}{2000} = h\frac{6}{2000}\left(\frac{\sigma_T}{h}\right) \equiv h f_{\Delta s}\left(\frac{\sigma_T}{h}\right). \tag{2.20}$$

The Gaussian terrain elevation is, from Eq. (2.11):

$$h_T(s) = h_T(0)\exp\left[-\frac{1}{2}\left(\frac{s}{\sigma_T}\right)^2\right], \tag{2.21}$$

where the amplitude a_T has been replaced by Eq. (2.16). Then, substituting the horizontal distance, Eq. (2.18), into the terrain elevation equation results in

$$h_T(s) = h_T(0)\exp\left(-\frac{1}{2}\left[0 : \frac{6}{2000} : 6\right]^2\right). \tag{2.22}$$

The exponential portion is now shown to be independent of the standard deviation parameter because of the choice of the assumed horizontal distance array. And the terrain elevation can be rewritten as:

$$h_T(s) = h\left(\frac{h_T(0)}{h}\right)\exp\left(-\frac{1}{2}\left[0 : \frac{6}{2000} : 6\right]^2\right) \equiv h f_{h_T}\left(\frac{h_T(0)}{h}\right). \tag{2.23}$$

The distances r_0 and r_h can then be derived as functions of only $h_T(0)/h$ and σ_T/h multiplied by the user altitude. Starting with Eq. (2.15), and substituting in Eq. (2.19),

$$r_0 = \sqrt{s^2 + h^2} = h\sqrt{f_s^2\left(\sigma_T/h\right) + 1} \equiv h f_{r_0}\left(\sigma_T/h\right) \tag{2.24}$$

And substituting Eq. (2.19) and (2.23) into (2.14) yields

$$\begin{aligned} r_h &= \sqrt{s^2 + (h - h_T)^2} = \sqrt{h^2 f_s^2(\sigma_T/h) + \left[h - h f_{h_T}(h_T(0)/h)\right]^2} \\ &= h\sqrt{f_s^2(\sigma_T/h) + \left[1 - f_{h_T}(h_T(0)/h)\right]^2} \equiv h f_{r_h}\left(\frac{h_T(0)}{h}, \frac{\sigma_T}{h}\right). \end{aligned} \tag{2.25}$$

Then these terms can be substituted into the calculations of $T_{33,i}$. For the singularity case of $s = 0$,

$$T_{33,0} = \frac{1}{(h-h_T)^2} - \frac{1}{h^2} = \frac{1}{h^2}\left\{\frac{1}{\left[1 - f_{h_T}\left(h_T(0)/h\right)\right]^2} - 1\right\} \equiv \frac{1}{h^2} f_{T_{33,0}}\left(\frac{h_T(0)}{h}\right). \tag{2.26}$$

When $s \neq 0$, there are two main components to $T_{33,i}$: $(h - h_T)/r_h$ and h/r_0. The first component can be rearranged as

$$\frac{h-h_T}{r_h} = \frac{h\left(1 - h_T/h\right)}{r_h} = \frac{h\left(1 - f_{h_T}\left(h_T(0)/h\right)\right)}{h f_{r_h}\left(h_T(0)/h, \sigma_T/h\right)} \equiv f_{T_{33,i_1}}\left(\frac{h_T(0)}{h}, \frac{\sigma_T}{h}\right). \tag{2.27}$$

The second component is

$$\frac{h}{r_0} = \frac{h}{h f_{r_0}\left(\sigma_T/h\right)} \equiv f_{T_{33,i_2}}\left(\frac{\sigma_T}{h}\right). \tag{2.28}$$

Then, from Eq. (2.13), T_{33} for $s \neq 0$ can be rewritten as

$$\begin{aligned} T_{33,i} &= \frac{1}{h^2 f_s^2(\sigma_T/h)}\left(f_{T_{33,i_1}} - f_{T_{33,i_1}}^3 - f_{T_{33,i_2}} + f_{T_{33,i_2}}^3\right) \\ &\equiv \frac{1}{h^2} f_{T_{33,i}}\left(\frac{h_T(0)}{h}, \frac{\sigma_T}{h}\right). \end{aligned} \tag{2.29}$$

Finally, the vertical gradient can be found from Eq. (2.17) using the change of integration variable from s to s/h and substitution of the relations above:

$$\begin{aligned} \Gamma_{\mathrm{DD}} &= \pi G \rho_T \sum_{(s/h)_i=0}^{6\sigma_T/h} \left(T_{33,i+1} + T_{33,i}\right)\left(\frac{s}{h}\right)_i \Delta\left(\frac{s}{h}\right) h^2 \\ &\qquad + \left(2T_{33,i+1} + T_{33,i}\right)\frac{1}{3}\Delta\left(\frac{s}{h}\right)^2 h^2 \\ &= \pi G \rho_T \sum_{(s/h)_i=0}^{6\sigma_T/h} h^2\left(\frac{1}{h^2} f_{T_{33,i+1}} + \frac{1}{h^2} f_{T_{33,i}}\right) f_s f_{\Delta s} \\ &\qquad + h^2\left(2\frac{1}{h^2} f_{T_{33,i+1}} + \frac{1}{h^2} f_{T_{33,i}}\right)\frac{f_{\Delta s}^2}{3} \\ &\equiv \pi G \rho_T \sum_{(s/h)_i=0}^{6\sigma_T/h} f_{\Gamma_{\mathrm{DD}}}\left(\frac{h_T(0)}{h}, \frac{\sigma_T}{h}\right). \end{aligned} \tag{2.30}$$

The altitude dependence in the T_{33} calculations are thus effectively canceled by the choice of defining s as a function of σ_T, which caused Γ_{DD} to be independent of h.

2.2.4 Gravitational Gradient Biases

Nearby masses, such as the vehicle's structure, fuel, and payload, must also be accounted for in the INS/GGI filter since they can produce non-negligible gravitational gradients. Many of these vehicle masses produce essentially constant gravitational gradient biases since they consist of constant masses that are positioned at a constant distance from the instrument. However, other self-generated gradients are time-varying such as fuel consumption and slosh, control surface (fin) deflections, and passenger movement in the case of a commercial aircraft system. To use the proposed INS/GGI navigation system effectively, the onboard filter must estimate and compensate each one of these additional biases accurately so that the external gravitational field may be used for position updates.

In order to estimate the gravitational gradient contribution from a variety of bias sources, the generating bodies are modeled as simple point masses. Then, using Eq. (2.10) on pg. 48:

$$\frac{\partial^2 \phi_g}{\partial r^2} = \Gamma \approx \frac{2GM}{r^3},$$

the gravitational gradient contribution from a point mass is a function of only the bias's mass, M, and its distance from the user, r. Figure 2.6 plots the magnitude of the gradient for masses from 0.1 kg to 1 metric ton (1,000 kg) at a distance of 10 cm to 100 m. Each mass has a slope of -3 on the log-log axes because of the

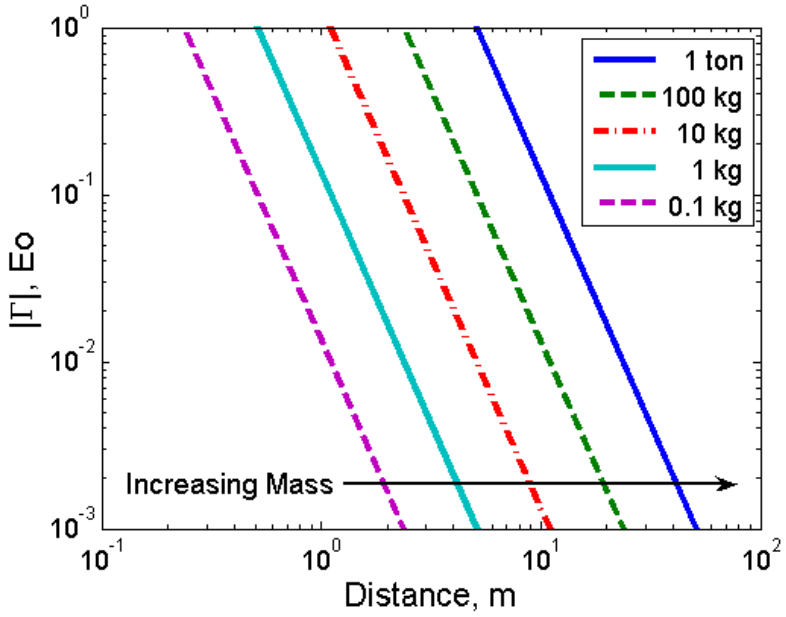

Figure 2.6: Point Mass Gravitational Gradient Contribution

inverse-cube relation of the point mass gradient to the displacement distance. For example, a 10 kg mass produces a 1 Eö gravitational gradient at 1 m and a 0.001 Eö gradient at 10 m. Furthermore, a 0.1 kg mass 1 m from a GGI is equivalent to a 100 kg mass at a 10 m distance. Also, as the displacement is increased 2.154× (*i.e.* $\sqrt[3]{10}\times$), the gravitational gradient bias decreases an order of magnitude. And lastly, for a given distance, the gravitational gradient is directly proportional to the bias source's mass, so that a larger mass produces a linearly proportionate larger gradient bias.

As another example, if a 100 kg (∼220 lb) person is 2.5 m from a GGI, they would produce ∼1 Eö gravitational gradient. Then, as the person walks away from the instrument, their gravitational gradient measurement would be 0.1 Eö at about 5.4 m, 0.01 Eö at ∼12 m, and 0.001 Eö at 25 m. Then, in terms of GGI noise levels, a

1 Eö sensor would have to account for all 100 kg and larger masses 2.5 m and closer, and a 0.001 Eö sensor would have to compensate for all masses $\geq$100 kg within 25 m of the GGI. The same 0.001 Eö GGI would also have to account for all 10 kg masses within $\sim$12 m, and 1 kg masses within $\sim$5.4 m of the instrument. Therefore, for a given GGI noise level, all self-generated vehicle biases should be taken into account, and ideally the largest time-varying biases should be placed farthest away from the GGI so that their errors are inherently reduced.

2.3 Gravitational Gradient Characterization

In this section the regional and altitude effects of the gravitational gradients are investigated on a global scale. The following figures plot components of the gradient tensor using the full 360 degree and order EGM96 spherical harmonic model and the modified geopot97 code at given altitudes. As discussed, the EGM96's finite resolution aliases high frequency terrain effects so that the true gravitational gradients at low altitudes are most likely larger than those presented. Nevertheless, the spherical harmonic model allows for identification of global areas of interest and trends.

Referring to Fig. 2.7 (c), the gravitational gradients are intuitively highest and vary most rapidly in mountainous ranges, as seen over the Rockies, coast of South America, and Himalayas. More surprisingly, areas in the Pacific Ocean also produce noticeable gradients, particularly around Indonesia and west of Japan. Therefore, it can be seen that unlike other map matching aids (*e.g.* terrain or vision), gravity

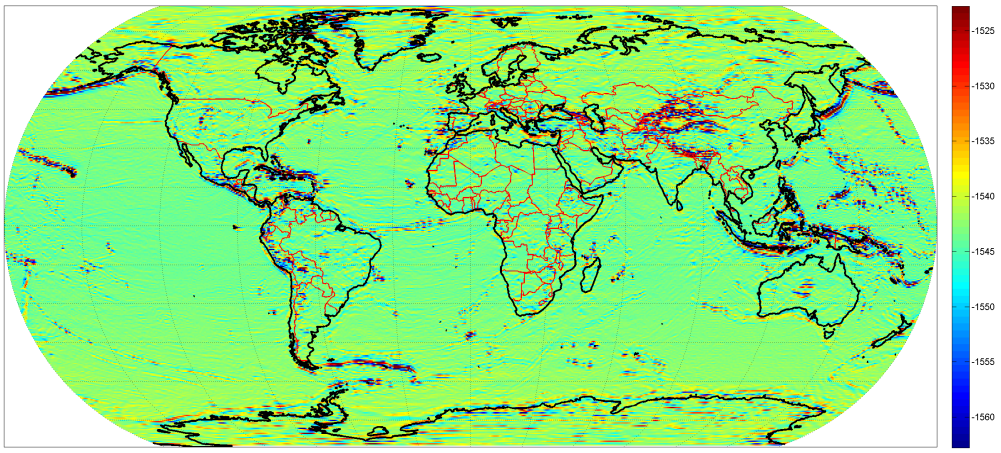

(a)

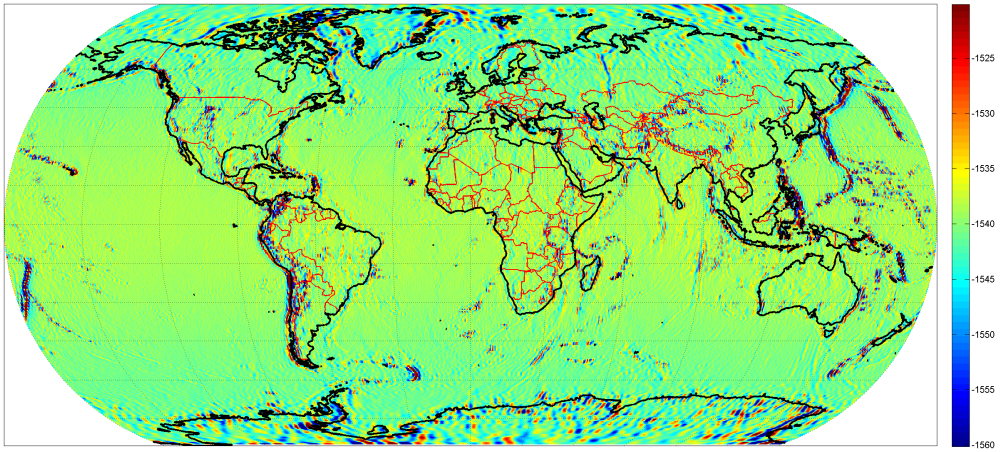

(b)

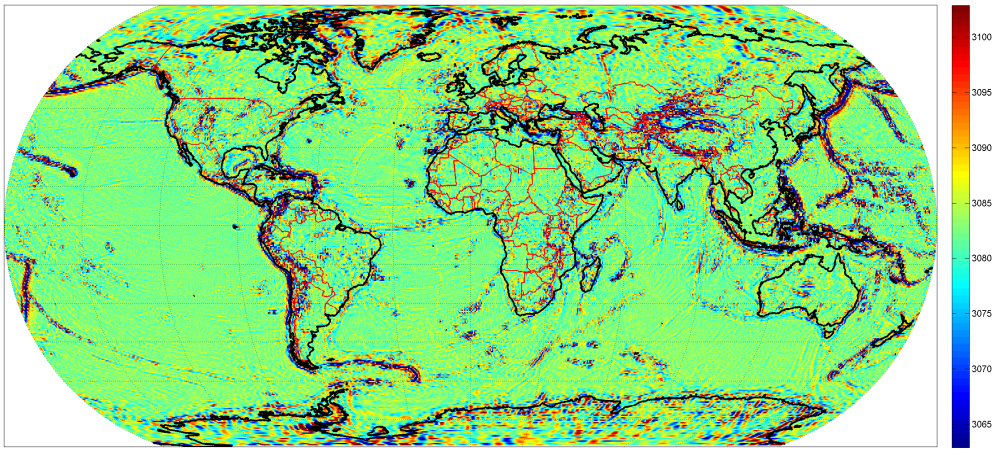

(c)

Figure 2.7: Inline Gravitational Gradients at Surface (a) Γ_{NN} (b) Γ_{EE} (c) Γ_{DD}

gradient aiding can be applicable over bodies of water.

Figures 2.7 and 2.8 plot all six gravitational gradients at the Earth's surface. The first set of figures correspond to three inline gradients, and the second set are the three off-diagonal gradients. The inline gradients are plotted with a colorbar varying from ±20 Eö from the mean, and the off-diagonal gradients are plotted with a ±10 Eö variation to compare how much the gradient signal varies.

Comparing the inline gradients, it is apparent that the vertical gravitational gradient varies more noticeably than either Γ_{NN} or Γ_{EE}. This result is due to the coupling of the three inline gradients by Laplace's equation, Eq. (2.5) on pg. 43, so that

$$\Gamma_{\mathrm{DD}} = -\left(\Gamma_{\mathrm{NN}} + \Gamma_{\mathrm{EE}}\right). \tag{2.31}$$

The regions where the gradients are the largest and vary the most is, however, relatively independent of the gradient. This is also true for the three off-diagonal gradients.

Comparing the off-diagonal components in Fig. 2.8, it is apparent that the North-East gravitational gradient varies the least while the North-Down and East-Down components have about the same variation. The reason for this is that the Γ_{ND} and Γ_{ED} gradients are the spatial derivatives of the vertical gravitational acceleration (g_D). The Γ_{NE} component, however, is the horizontal derivative of the other horizontal gravitational acceleration, which is typically orders of magnitude smaller than g_D. The North-Down component also has a prominent low-frequency variation in the latitudinal (North/South) direction due to the bulk oblateness of the Earth.

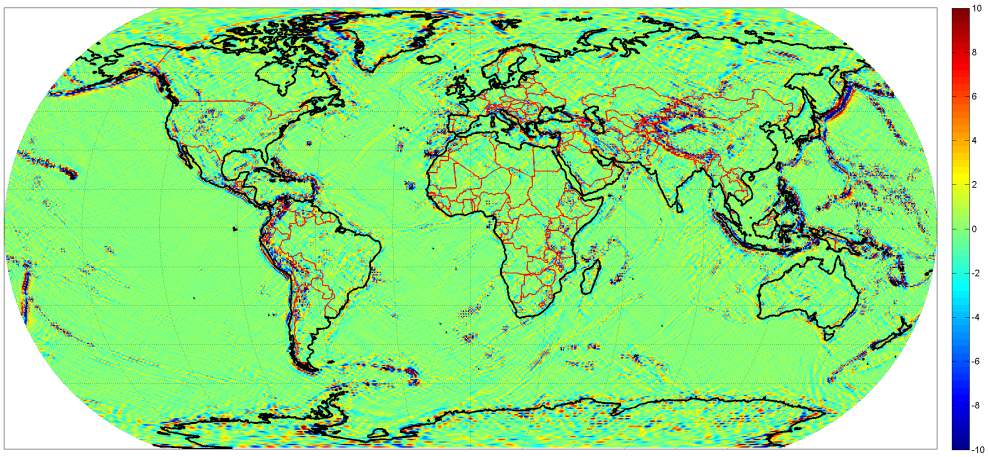

(a)

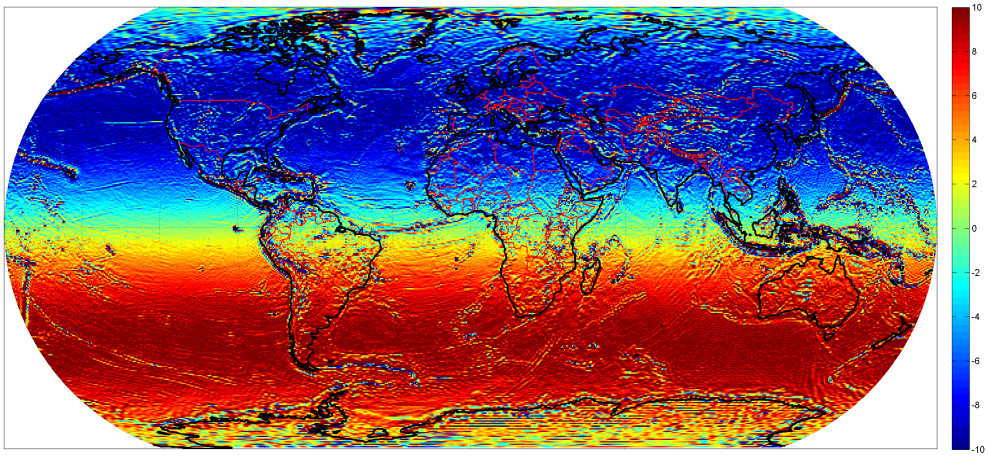

(b)

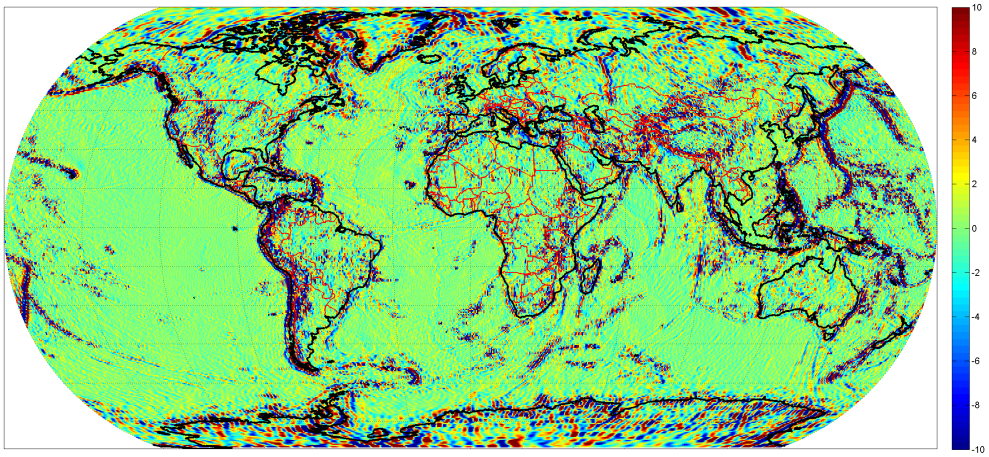

(c)

Figure 2.8: Off-Diagonal Gradients at Surface (a) Γ_{NE} (b) Γ_{ND} (c) Γ_{ED}

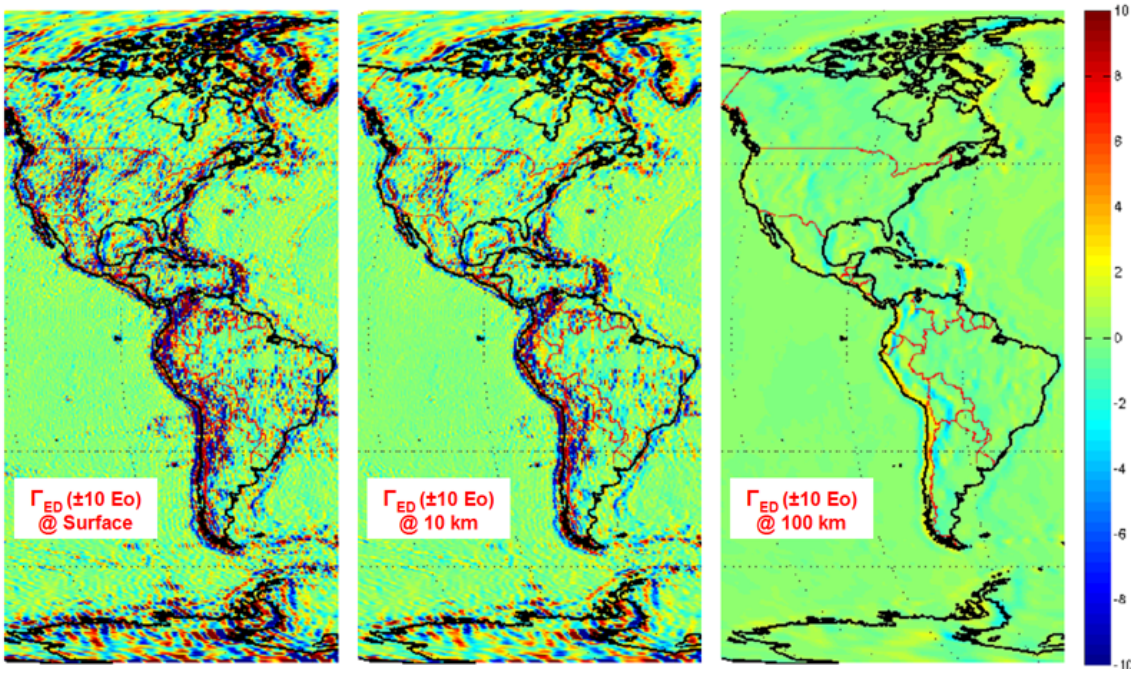

Figure 2.9: East-Down Gravitational Gradient at Three Altitudes

To qualitatively show the effects of altitude attenuation on the high frequency gravitational gradient signals, Fig. 2.9 plots the East-Down gradient at three altitudes focusing on North and South America. Comparing the surface and 10 km plots, it is apparent that many of the high frequency components of the gravitational signal have been removed as the altitude was increased. This is particularly noticeable in moderate areas like Canada and Brazil. As the altitude is increased from 10 km to 100 km, almost all distinguishable gravitational gradient variations are removed. At this altitude, only the largest mountain ranges produce subtle changes in the gravitational gradient. Thus, increasing one's altitude acts to smooth the gravitational gradient signal and thereby reduce its usefulness for map-matching. This trend is common for all six gradients. (Appendix A includes additional plots of the global gravitational gradients at various altitudes.)

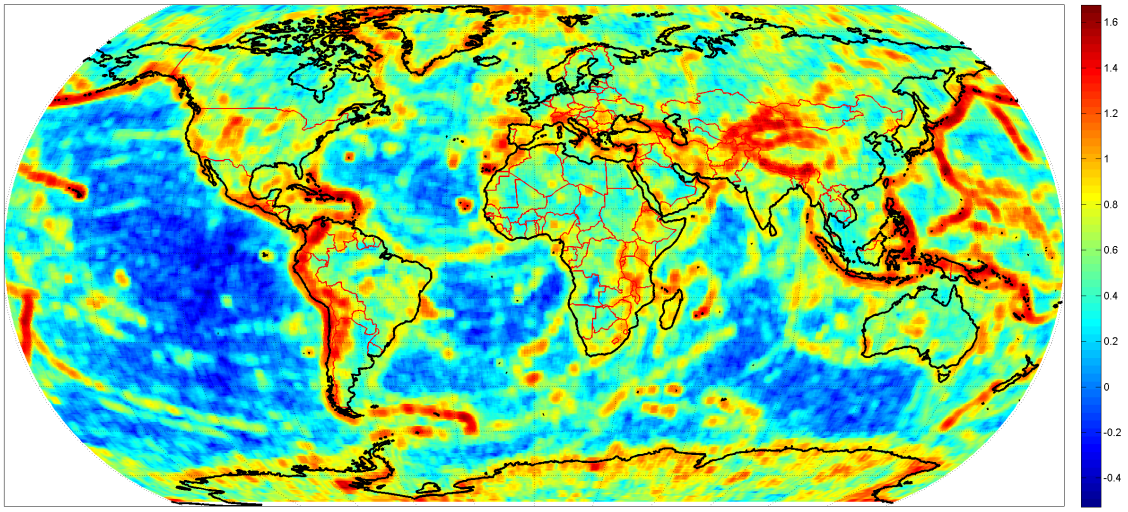

Figure 2.10: Γ_{DD} Standard Deviation, $\log_{10}$(Eö), at Surface

To further investigate the regional and altitude effects on the gradiometer aided INS system, standard deviations were computed over a horizontal ∼220 km × 220 km moving window (corresponding to 5 × 5 Γ^n grid points). This analysis aids in quantifying the expected gravitational gradient signal variations over a region of interest and helps to quantify the altitude trends. Figure 2.10 logarithmically plots the standard deviation of the vertical gradient at the Earth's surface, which was calculated from Fig. 2.7 (c). Similar standard deviation plots were computed for all six gradients at several altitudes and are shown in Appendix A. The geographical regions of high and low gradient variation are essentially the same for each Γ^n component, but the magnitude of the standard deviations are functions of the gradient components and altitude. Figure 2.11 summarizes the global minimum, mean, and maximum gravitational gradient standard deviations for the computed components as a function of altitude. The Γ_{EE} and Γ_{NN} standard deviations are approximately equal, so the East-East component is omitted in the figure.

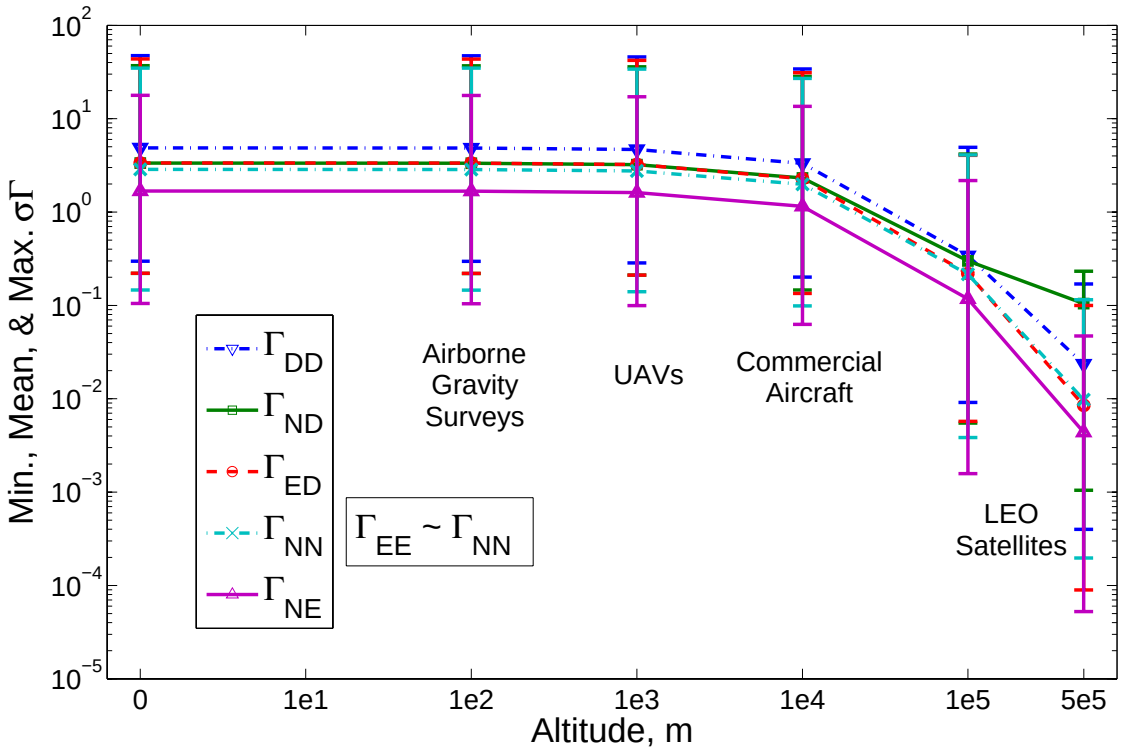

Figure 2.11: Minimum, Mean, and Maximum Gravitational Gradient Standard Deviation vs. Altitude

Referring to Fig. 2.11, the vertical gradient (Γ_{DD}) has the largest variation as expected because it is the largest component of the gradient tensor. The spatial derivatives of the vertical gravitational acceleration (*i.e.* $\partial g_D/\partial N = \Gamma_{\mathrm{ND}}$ and $\partial g_D/\partial E = \Gamma_{\mathrm{ED}}$) have the next largest variation due to g_D being the largest component of the gravitational vector. The other inline gradients, Γ_{NN} and Γ_{EE}, have variations that are about half those of Γ_{DD} due to the coupling of these gradients due to Laplace's constraint, as shown in Eq. (2.5) and (2.31). Lastly, the Γ_{NE} component has the least variation because it is the longitudinal derivative of g_N, which is itself quite small. The change in the Γ_{ND} trend at the highest altitudes is caused by Earth's oblateness which yields comparably large Γ_{ND} variations at the equator and poles, See Fig. A.10 (b) on pg. 299.

It should be noted that the gradient variations at lower altitudes in Fig. 2.11 are rather conservative because of the aliasing of terrain effects. However, even with this omission, the gradient signal variations are on the same order of magnitude as the airborne GGI noises in Table 1.1. The gradient signal variation is an important part of the navigation performance because it is what allows the Kalman filter to make delta corrections to the observable system states. As an analogy to terrain based systems, if the user is standing in a flat region, it is nearly impossible to gain any orientation or position information. Conversely, if the user is in a hilly terrain, one can estimate where they are in relation to their local elevation map. The same general concept holds for gradient navigation—that performance is proportional to signal variation. However, the notion of preferring high gravitational variations is in direct contrast with typical inertial navigation because gravity variations are usually

seen as sources of error to the INS.

Therefore, if the signal-to-noise ratio were to increase by decreasing the GGI noise, it appears that one could theoretically achieve an improvement in navigation performance using a GGI-aided INS for airborne applications, especially over regions with a strong gravitational gradient (high variations). The same can be said for Low-Earth-Orbit (LEO) satellites. The current primary issues limiting an INS/GGI system are:

1. The lack of high resolution, accurate gravitational maps over many regions.
2. The prohibitive size, weight, and noise floor of current GGIs.
3. The absence of open-literature algorithms to optimally blend GGI measurements into an inertial navigation system.

This dissertation makes the assumptions that the first two issues are solved at some point in the future and focuses on the algorithm development and quantification of the potential performance of future INS/GGI systems.

2.4 Simulation Trajectories

In order to investigate the sensitivity of the gravitational gradient signal variation on the INS/GGI navigation performance, two 1000 km constant latitude trajectories in the contiguous United States were chosen. The "High" gravity gradient variation trajectory follows the Northern border of Wyoming, and the "Low" gradient trajectory follows near the Northern border of Kansas into Missouri and Illinois. Figure 2.12 plots these two trajectories over the logarithmic standard deviation plot

Table 2.1: Simulated Trajectories

	Latitude	Longitude
High Gradient Variation	45.0°	[−113.0°:−100.3°]
Low Gradient Variation	38.0°	[−100.0°:−88.6°]

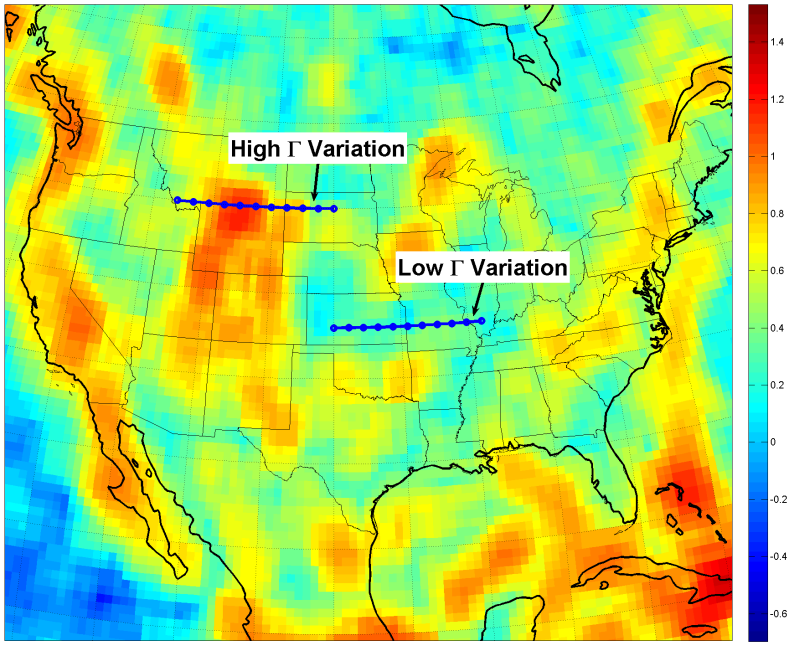

Figure 2.12: Simulated Trajectories

of the vertical gradient at a 10 km altitude. Figure 2.13 plots the gravity acceleration and the gravitational gradients for the two trajectories at the Mach 7 altitude. The constant latitude and the longitude ranges are summarized in Table 2.1.

The 1000 km range was chosen as it is approximately the maximum range that a cruise missile can travel without violating arms treaties. The choice of a constant latitude, Eastern cruise was so that the longitude rate is constant for a given velocity, see Eq. (4.51) on pg. 152. The two subsonic cases were simulated to

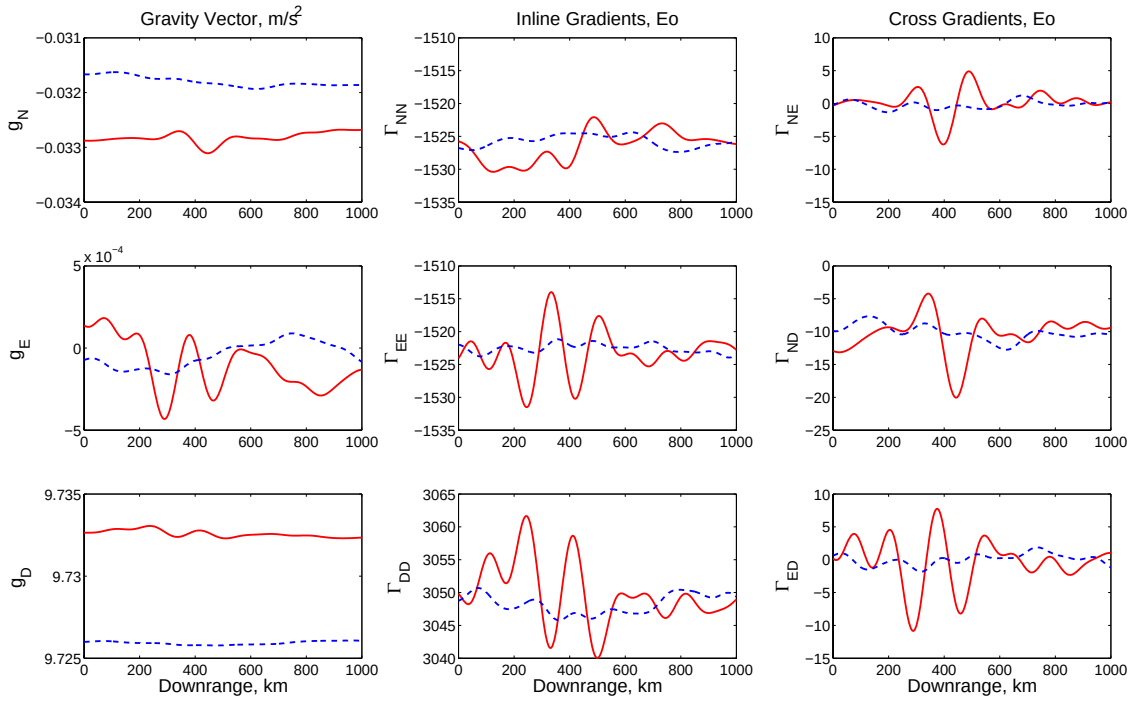

Figure 2.13: Simulated Gravity at Nominal Latitude and Altitude for Mach 7 Trajectories, High Γ Variation (solid), Low Γ Variation (dashed)

ranges such that the filter achieved steady state operation at about halfway into the simulation. The commercial aircraft range was set to 200 km, and the GGI-survey case range was 50 km.

For the hypersonic scramjet simulations, the cruise altitude was calculated so that the vehicle flew at a constant one-atmosphere dynamic pressure according to the 1976 standard atmosphere model.[126] The velocities and altitudes were calculated as follows. Given a freestream Mach number, the cruise velocity is

$$v_\infty = M_\infty a_\infty = M_\infty \sqrt{\gamma_\infty R_\infty T_\infty}, \tag{2.32}$$

where a_∞ is the freestream speed of sound at altitude, γ_∞ is the ratio of specific heats and is assumed to be 1.4, $R_\infty = 287$ J/kg-K is the gas constant for air, and the atmospheric temperature causes the altitude dependence. Then, using the definition of dynamic pressure, the velocity can also be found as

$$q_\infty \equiv \frac{1}{2}\rho_\infty(h) v_\infty^2 \quad \rightarrow \quad v_\infty = \sqrt{\frac{2q_\infty}{\rho_\infty(h)}}. \tag{2.33}$$

These two equations can be set equal to each other and squared to yield

$$2q_\infty = M_\infty^2 \gamma_\infty \left(\rho_\infty R_\infty T_\infty\right) = M_\infty^2 \gamma_\infty P_\infty(h), \tag{2.34}$$

where the ideal gas equation has been used for the second equality. This relation can now be solved for pressure as a function of the prescribed dynamic pressure and Mach number:

$$P_\infty(h) = \frac{2q_\infty}{\gamma_\infty M_\infty^2}. \tag{2.35}$$

A bisection method is used to numerically calculate the altitude so that the pressure as defined by the 1976 standard atmosphere model is equal to the given Mach

Table 2.2: Simulated Cruise Values

	Mach 6	Mach 7	Mach 8	747-100	GGI Survey
Altitude, m	22,043.8	24,040.2	25,785.3	10,000.0	100.0
Velocity, m/s	1,778.43	2,084.22	2,391.29	250.0	40.0
Range, km	1,000.0	1,000.0	1,000.0	500.0	300.0
Final Time, sec	565.20	482.45	420.60	802.60	1,252.15

number and the assumed dynamic pressure constraint. Equation (2.32) is then used to calculate the East velocity with the at-altitude freestream temperature from the standard atmosphere calculation. Table 2.2 summarizes the cruise altitudes, Eastern velocities, range, and total simulation time for the three cruise Mach numbers simulated and the two subsonic cases.

For the two subsonic cases, the velocities and altitudes were chosen to approximate a commercial aircraft and a GGI-based survey/exploration mission. The commercial aircraft mission is assumed to be a Boeing 747-100 class vehicle which cruises at approximately 250 m/s ($M_\infty \approx 0.84$) at a 10,000 m (∼33,000 ft) altitude.[127] The GGI survey mission assumes a 100 m altitude based on the Falcon AGG specification for their average fixed wing system.[†] The velocity is estimated to be 40 m/s, which is slightly higher than the stall speed of a Cessna Grand Caravan (61 knots $\approx$ 31.4 m/s)[128] since this is the platform for most airborne GGI exploration systems, and reduced speed improves the spatial resolution of the survey.

The details of the gravity field maps that were computed and stored for the INS simulations are summarized in Sec. 2.4.2. But first, the methodology to determine

[†]http://falcon.bhpbilliton.com/falcon/specifications.asp, cited 6 Nov. 2007

the map resolution is presented in the following section.

2.4.1 Gravity Map Resolution

2.4.1.1 Horizontal Resolution

For a given altitude, the gravitational potential and horizontal (latitudal and longitudal) derivatives are linear combinations of sine and cosine waves, see Eq. (2.7). To determine the chosen resolution on the gravity map in the horizontal directions, and to estimate the error due to the linear interpolation between grid points, a MATLAB script was written that calculated the residual error between a fine, "truth," cosine wave and the linearly interpolated, "estimated," cosine wave for various resolutions:

$$e_{horiz} = |\cos(s_T) - \widehat{\cos(s_T)}|, \tag{2.36}$$

where the truth resolution is

$$s_T = \left[0 : \frac{\pi}{100 N_{horiz}} : \pi\right]. \tag{2.37}$$

The number of node points for the coarse cosine wave was defined by

$$N_{horiz} = \frac{a_e \pi / n_{max}}{horiz_{map\ res}}, \tag{2.38}$$

where the numerator is the spherical harmonic resolution and the denominator is the variable gravity map resolution. The bounds of $[0 : \pi]$ for the independent cosine wave variable, s, were chosen because it is half a period and thus corresponds to the highest half-wavelength of the spherical harmonic resolution as defined in Eq. (2.9)

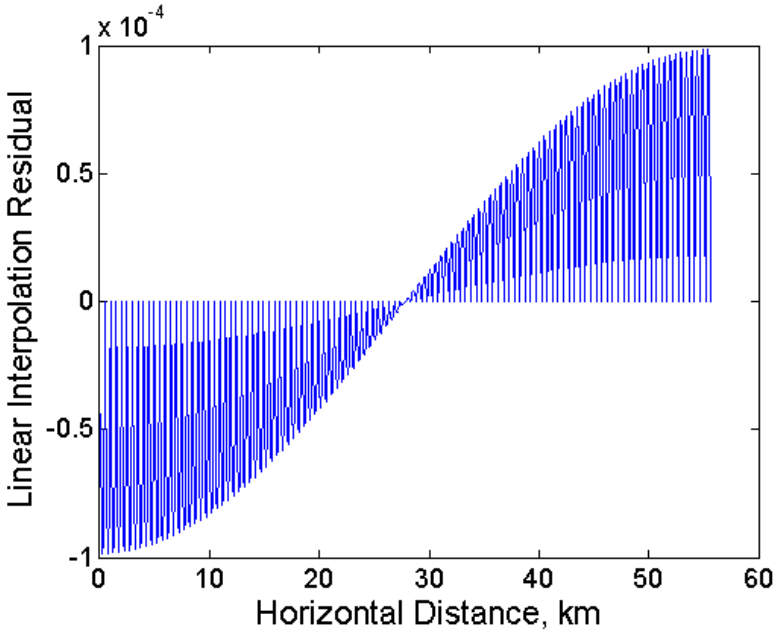

Figure 2.14: Horizontal Spherical Harmonic Error Due to Linear Interpolation, with 500 m Resolution

on pg. 46. The coarse cosine wave was created with a resolution of N_{horiz}, or

$$s = \left[0 : \frac{\pi}{N_{horiz}} : \pi\right]. \tag{2.39}$$

The estimated cosine wave was then linearly interpolated to each of the truth nodes by

$$\widehat{\cos(s_T)} = \cos(s)_i + \left(\frac{\cos(s)_{i+1} - \cos(s)_i}{s_{i+1} - s_i}\right)(s_T - s_i), \tag{2.40}$$

and the error residual between the coarse and fine cosine waves was computed by Eq. (2.36).

Figure 2.14 plots the horizontal residuals for the case of $horiz_{map\ res} = 500$ m, other resolutions exhibit similar trends but varying magnitudes and periods. For all cases, the maximum error occurs near the 0 and π locations of cos(s) because the slopes are most nonlinear at these points.

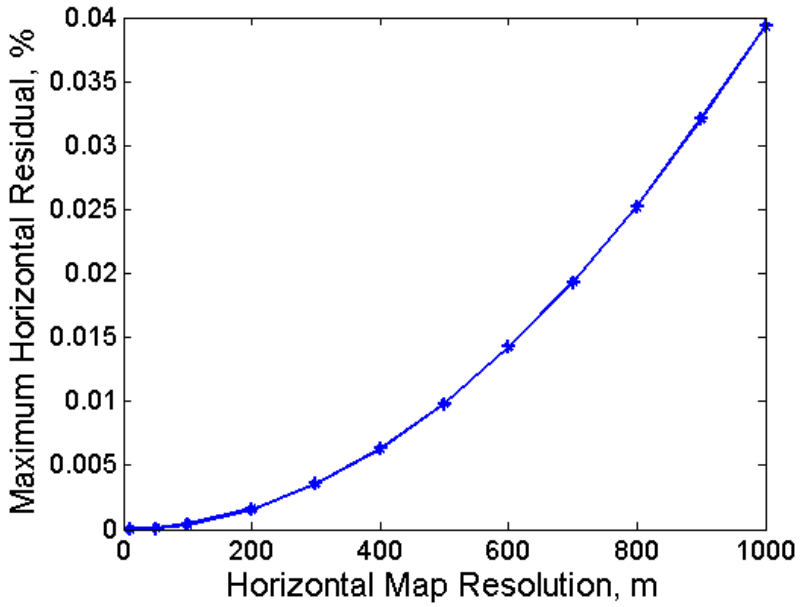

Figure 2.15: Horizontal Spherical Harmonic Error Due to Linear Interpolation vs. Map Resolution

The resolution of the estimated cosine curve, $horiz_{map\ res}$, was varied from 10 m to 1 km and the maximum residual for each case was stored and plotted as Fig. 2.15. As seen is this figure, as the map spacing decreases, the error due to linear interpolation decreases as one might expect. Also, it is apparent that as the map resolution continues to become more and more fine, there is diminishing returns in terms of the error residual. Therefore a compromise between acceptable error and gravity map storage size must be made (as the horizontal resolution is decreased by half, the storage requirements increase by a factor of four because of the two horizontal dimensions). For this work an error limit of 0.01% was chosen, which leads to a horizontal spacing of 500 m and an linear interpolation error of 0.00983%.

2.4.1.2 Vertical Resolution

The vertical resolution was determined by investigating the nominal magnitude of the vertical gravitational acceleration, gradient, and third order derivative as functions of altitude. Each of these functions were also normalized by the nominal altitude for the Mach 6 cruise trajectory (h_{nom} = 22,043.8 m) because the gravitational quantities are largest at lowest altitudes. (The subsonic cases are discussed at the end of this section.) The assumed simplistic normalized gravitational acceleration is

$$\frac{g_D(h)}{g_D(h_{nom})} \approx \left[g_0 \left(\frac{a_e}{a_e + h} \right)^2 \right] / \left[g_0 \left(\frac{a_e}{a_e + h_{nom}} \right)^2 \right] = \left(\frac{a_e + h_{nom}}{a_e + h} \right)^2, \qquad (2.41)$$

where $a_e = 6,378,137$ m for Earth's semimajor axis.[113,114] The normalized vertical gradient is

$$\frac{\Gamma_{\mathrm{DD}}(h)}{\Gamma_{\mathrm{DD}}(h_{nom})} \approx \left[\frac{-2g_0 a_e^2}{(a_e + h)^3} \right] / \left[\frac{-2g_0 a_e^2}{(a_e + h_{nom})^3} \right] = \left(\frac{a_e + h_{nom}}{a_e + h} \right)^3. \qquad (2.42)$$

And the normalized gradient derivative is

$$\frac{\partial \Gamma_{\mathrm{DD}}}{\partial h} \approx \left[\frac{6g_0 a_e^2}{(a_e + h)^4} \right] / \left[\frac{6g_0 a_e^2}{(a_e + h_{nom})^4} \right] = \left(\frac{a_e + h_{nom}}{a_e + h} \right)^4. \qquad (2.43)$$

The altitudes investigated were 1200 m below the nominal altitude to 1200 m above, which corresponds to approximately the final 1-σ filter altitude error for the Mach 6 cruise simulation with a tactical grade IMU and no external measurements.

Again, coarse and fine normalized gravitational parameters were computed using the relations above and the linear interpolation residuals were calculated. Figure 2.16 plots the residuals for the three gravitational quantities with a vertical

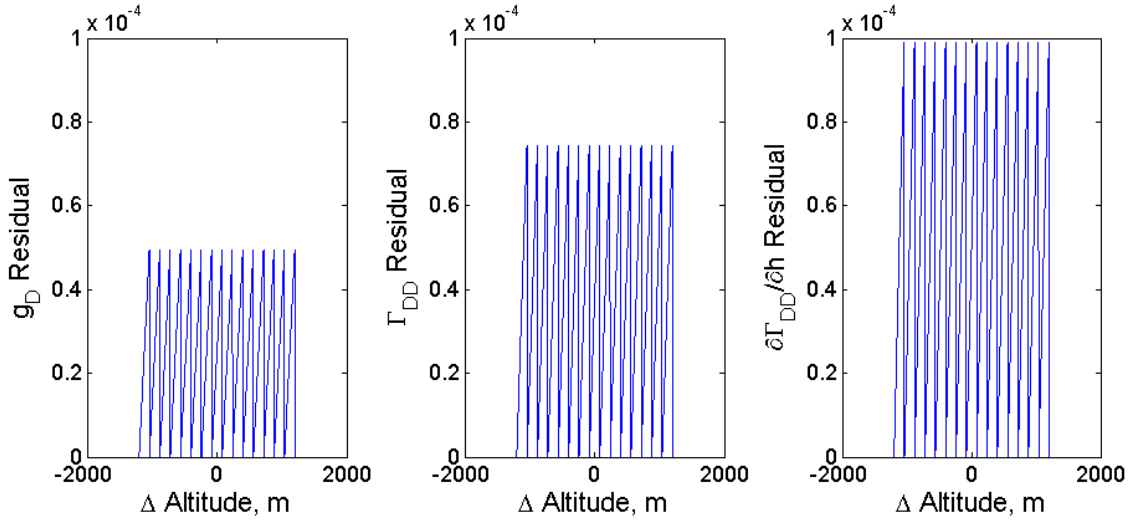

Figure 2.16: Vertical Spherical Harmonic Error Due to Linear Interpolation, with 160 m Resolution

resolution of 160 m ($N_{vert} = 16$). The third derivative of the gravitational potential, $\partial\Gamma_{\mathrm{DD}}/\partial h$, produces the largest linear interpolation errors because it has the greatest exponential compared to Γ_{DD} and g_D.

Instead of varying the vertical resolution, as done above with the horizontal resolution, the number of node points was varied. N_{vert} was investigated from 11 to 20, corresponding to a vertical resolution of 218 m to 120 m. The maximum residuals are summarized in Fig. 2.17 along with the 0.01% error constraint. From Fig. 2.17, the vertical resolution is set by the third derivative of the gravitational potential at a value of 160 m, or $N_{vert} = 16$, and the maximum linear interpolation error is 0.00991%.

For the commercial aircraft case with the assumed 10,000 m altitude, a 160 m grid resolution causes a linear interpolation error of 0.00992%. For this case, only the best INS/GGI system was simulated, which has position errors on the order of

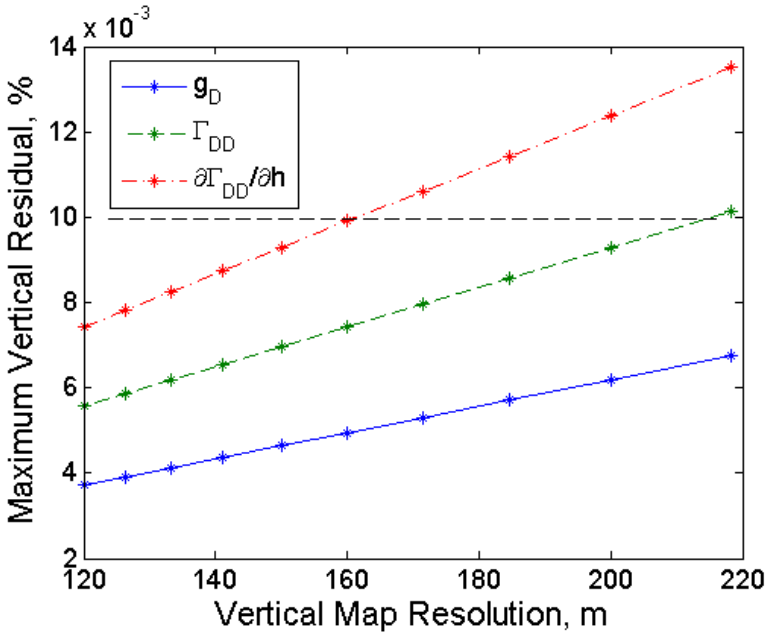

Figure 2.17: Vertical Spherical Harmonic Error Due to Linear Interpolation vs. Map Resolution

a meter. Therefore, only 3 altitude grid points were used for the map: one at the nominal altitude, and one each plus/minus the 160 m vertical grid resolution.

The gravity gradiometer instrument survey mission altitude is 100 m, so this was set as the grid resolution for this gravity field map since negative altitudes would not be physical. With the survey altitude of 100 m and the 100 m resolution, the linear interpolation error was calculated to be 0.00621%. Again, only 3 grid points were used for this case since only the best INS/GGI system was simulated and the position errors (< 1 m) are much less than the grid resolution.

Table 2.3: Gravitational Gradient Map Parameters

High Gravitational Gradient Variation Trajectory						
M_∞	Latitude, °	N_ϕ	Longitude, °	N_λ	Altitude, m	N_h
6	44.982 – 45.018	9	-113.0 – -100.2705	2005	20843.8 – 23243.8	16
7	44.9865 – 45.0135	7	-113.0 – -100.2768	2004	23080.2 – 25000.2	13
8	44.991 – 45.009	5	-113.0 – -100.2832	2003	25065.3 – 26505.3	10
Low Gravitational Gradient Variation Trajectory						
M_∞	Latitude, °	N_ϕ	Longitude, °	N_λ	Altitude, m	N_h
6	37.982 – 38.018	9	-100.0 – -88.5774	2005	20843.8 – 23243.8	16
7	37.9865 – 38.0135	7	-100.0 – -88.5831	2004	23080.2 – 25000.2	13
8	37.991 – 38.009	5	-100.0 – -88.5888	2003	25065.3 – 26505.3	10

2.4.2 Simulated Gravity Field Maps

Table 2.3 summarizes the inputs to the modified geopot97 code. The variation in the nominal latitude, final latitude, and nominal altitude parameters were computed from the final 1-σ filter position errors of these states using a tactical grade INS with no external updates. Because faster simulations traveled the 1,000 km range in a shorter period of time, their dead-reckoning position error has less time to grow and therefore the position errors are less. This also results in smaller storage requirements for the faster simulations because the finite spatial resolutions were held constant.

The latitude resolutions were converted from position to degrees by

$$\Delta\phi[^\circ] = \frac{\Delta\phi[m]}{a_e}\left(\frac{180^\circ}{\pi[rad]}\right). \tag{2.44}$$

Table 2.4: Gravitational Gradient Map Storage Requirements

M_∞	6	7	8
N_{grid}	288,720	182,364	100,150
File Size, KB	70,207	44,345	24,354

The longitude resolutions were converted by

$$\Delta\lambda[^\circ] = \frac{\Delta\lambda[m]}{a_e \cos\phi_{nom}} \left(\frac{180^\circ}{\pi[rad]}\right). \tag{2.45}$$

The storage requirements for the tabulated $\phi, \lambda, h, \phi_g, \overline{\mathbf{g}}^n$, and Γ^n components using eight significant figures is summarized in Table 2.4, where $N_{grid} = N_\phi + N_\lambda + N_h$. The files were saved as ASCII text, and the storage requirements could have been reduced if it were saved as a binary file.

The subsonic cases were simulated over only the high Γ^n variation trajectory. Their horizontal grid parameters were kept the same as the Mach 8 case and the altitude nodes were defined as described at the end of the last section.

2.5 Chapter Summary

This chapter presents a review of gravity gradiometry, spherical harmonics, and local terrain integration methods for the purpose of gravity field modeling in Sec. 2.1–2.2.2.

Section 2.2.3 then estimates when the high frequency local terrain effects may be neglected compared to a given GGI noise level. Using a parametric model for the analysis, it is shown that the gravitational gradient contribution of the mountain can

be computed by only two parameters (width and height of the terrain feature) since the user altitude can be used to normalize these values, as shown in Sec. 2.2.3.1. And it is found that wider mountains have a larger effect on higher altitude missions, whereas narrower features with the same peak height produce larger gradients for lower altitude missions. Also, the width parameter is then optimized to maximize the gravitational gradient so that the vertical gradient contribution from a terrain feature can be estimated by only the user altitude and the peak height of the feature, as shown in Fig. 2.5. If the estimated gradient is sufficiently less than the GGI noise level, then the terrain effects may be neglected from the computed gravitational map.

Section 2.2.4 next estimates the gravitational gradients due to a variety of point masses at various distances from a GGI. It is shown in Fig. 2.6 that when the GGI noise level is reduced an order of magnitude, the GGI is able to measure a mass 1/10 the original mass at the original distance or a mass the same size as the original mass but at a distance 2.154 times the original distance. Therefore, for the GGIs simulated later in Ch. 6 ($\sigma_{\nu_L} = 0.1$–0.001 Eö), almost all vehicle mass distributions would need to be accounted for in a real GGI navigation system. However, for the simulations preformed in this work, these additional vehicle-generated gradient contributions are ignored because of the low fidelity mass model in Sec. 3.2. Also, it is noted that stationary mass distributions produce a constant gravitational gradient bias that can be calibrated by the INS/GGI, and only moving masses need to be estimated and corrected for by the onboard filter. For this latter case, it is suggested to maximize the separation distance between the GGI and the moving mass so that

its measured gradient is reduced.

The gravitational gradient characterization studies in Sec. 2.3 serve to answer the four questions posed on pg. 37:

- First, it is shown that the gravitational gradient signal variation is on the same order of magnitude as current airborne and space-borne GGI noise levels, *i.e.* ∼1–10 and 0.001-0.01 Eö, respectively. The signal-to-noise ratio for lower altitude airborne applications is quite conservative, however, because the high frequency fluctuations from local terrain effects are not modeled. Therefore, there is enough information that an airborne gravity gradiometer map-matching aid should be able to provide position information to an INS.
- The order in which the gravitational gradient tensor components vary, from greatest to least, is Γ_{DD}, Γ_{ND} and Γ_{ED}, Γ_{NN} and Γ_{EE}, and Γ_{NE}; as shown in Fig. 2.11 on pg. 66.
- In the global gravitational gradient plots it is shown that Γ^n varies most in mountainous regions, as one might expect. However, it is also shown that there are noticeable areas of high gradient variation over certain bodies of water.
- Lastly, Fig. 2.11 shows that altitude does not attenuate the magnitude of the gradient variation below about 1,000 m. But, the low altitude trends shown in the figure would likely change if local terrain effects were included in the analysis.

Section 2.4 lastly discusses the two chosen trajectories over the USA ("high" and "low" gradient variations) for the simulations performed in Ch. 6. The calculation of the three hypersonic cruise vehicles' altitudes and velocities are also shown

in this section, as are the assumptions for the two subsonic simulations (see Table 2.2). Section 2.4.1 then details the gravity map resolution studies that determined the 500 m horizontal and 160 m vertical grid spacing so that the linear interpolation error is less than 0.01%. Lastly, Sec. 2.4.2 summarizes the stored gravity field maps that are needed for the computation of the hypersonic missile trim states in the following chapter, the gravity vector and the gravitational gradients for the INS in Ch. 4, and the gradient portion of the simulated GGI measurements in Ch. 5.

Chapter 3

Hypersonic Vehicle Model

The hypersonic vehicle modeled in this work is based primarily on a 1982 Advisory Group for Aeronautical Research and Development (AGARD) report by the Johns Hopkins University / Applied Physics Lab (JHU/APL) which presents a surprisingly candid, in-depth design methodology to model the propulsion system and aerodynamics of parametric scramjet missiles.[129] This dissertation digitized and curve-fit many of the results of this reference so that they may be implemented as a parametric first-order hypersonic missile design tool.

Several extensions to the original report are also derived and implemented to produce realistic truth inertial measurement unit signals. First, volume calculations and a parametric mass model are added. Then, trim state relations are newly derived for numerical computation of the missile's trim pitch, roll, and equivalence ratio at a point in time. The trim state calculations are used to numerically integrate the missile's mass properties over a 1,000 km (540 nautical mile) range simulation as fuel is being burned and the vehicle accounts for variations in the acceleration due to gravity. The pitch and roll trim states are lastly finite differenced so that they may be used as part of the gyro signals in the inertial navigation system simulation.

The following section describes the methodology to calculate the propulsion

and aerodynamic characteristics of the axisymmetric scramjet missile as set forth in the cited reference.[129] Appendix B supplements this section with numerous thrust coefficient curve fits. The last part of Sec. 3.1 then validates the implemented Fortran code with the reference's example calculations. Section 3.2 explains the parametric mass model used for the analysis and the calculation of the internal volume of the missile. This section also details some of the additional assumptions pertaining to the dimensions of the vehicle. Section 3.3 next derives the trim state relations and presents how these results are used to simulate the INS truth gyro and accelerometer signals, and the last section summarizes the chapter results.

3.1 JHU/APL Axisymmetric Scramjet Model

The JHU/APL AGARD report[129] presents a design study for a hypersonic scramjet missile that is boosted to Mach 4 on a first stage rocket and then accelerates to a Mach 8 cruise. The missile is assumed to be launched from a volume constrained box, so that the total length is a fixed 4.0 m and the diameter is a fixed 0.50 m. The inlet may be either a full axisymmetric chin inlet (as assumed in this work) an aft inlet, or a sector of one of these two inlets with an on-design Mach number, M_{des}, of 6, 7, or 8. In this work, the scramjet is assumed to cruise at its on-design Mach number at one of the three values in the report, *i.e.* $M_\infty = M_{des} = 6$, 7, or 8.

From analyzing the many tradeoffs in the inlet designs, the reference[129] concludes that the full axisymmetric chin inlet allows for maximum capture area and engine thrust. Therefore, this type of vehicle inlet is chosen for the scramjet models

in this dissertation. The effect of on-design inlet Mach number was not thoroughly investigated here because of the assumption that the cruise $M_\infty = M_{des}$. Also, for the simulations in this dissertation, the missiles are assumed to fly at their constant on-design Mach number so that the off-design M_∞ effects could have been neglected. However, for design purposes, the report's assumed operating range of Mach 4–8 and an angle of attack from 0–10° are maintained for calculating the maximum geometric contraction ratio in Sec. 3.1.1.2. Other design choices in the implemented scramjet model are detailed in their respective sections.

The results in the JHU/APL AGARD reference[129] were first scanned from a microfiche-sourced hard copy of the report and stored as image files. Engauge Digitizer 2.14,[†] a free software package, was then used to automatically and manually identify feature points on the graphical results of the image files. The software allows the user to define arbitrary axes on the image file so that rotation and scaling of the feature points are computed internally in the program. The data sets were then imported into MATLAB and curve fit using the `polyfit.m` function and an assumption of either quadratic polynomials or linear segments. The coefficients produced from the MATLAB curve fits are listed in the appropriate discussions below and in App. B for the thrust coefficient calculations. The interpolation between various curvefits is also discussed in the following subsections.

The first subsection describes the calculation of the propulsion system and the assumptions used in the reference report's analyses. The next subsection details the aerodynamic model and the multitude of drag terms included. The last subsection

[†]http://digitizer.sourceforge.net/

validates the implementation of these two subsections as a computer code with example calculations in the appendix of the reference report.

3.1.1 Propulsion

According to the 1982 JHU/APL report,[129] "the results presented and assumptions used ... are based on experimental data and analytical techniques developed from testing and analyzing scramjet engines over the past 20 years." And while this reference is somewhat dated when taking into account the developments in scramjet technologies over the past 25 years,[130–132] it is arguably the most in-depth open literature reference regarding the full design of a hypersonic scramjet. And the inclusion of the off-design propulsion and aerodynamics (which is absent from most references) allows for calculation of the trim states.

The reference uses the integral form of the mass, momentum, energy, and species conservation equations at several discrete thermodynamic stations to compute the thrust coefficient of the hypersonic scramjet.[129] The first station is the freestream, "∞," flow station that is unaffected by the hypersonic vehicle. The properties at this station are uniquely defined by the velocity of the vehicle and an assumption of the atmosphere at altitude. The reference states that all calculations were performed at a 15,240 m (50,000 ft) altitude for simplicity, and that variations in the altitude would have had only a minor effect on the overall thrust coefficient. For this work, the 1976 standard atmosphere is modeled to calculate the freestream pressure, density, and temperature for a given altitude.[126] The next station, "0,"

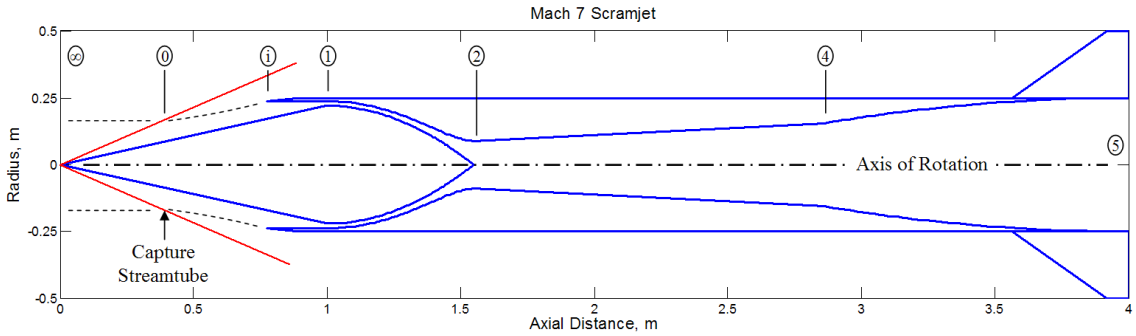

Figure 3.1: Scramjet Missile Geometry and Thermodynamic Stations

consists of the properties just behind the initial cone forebody's oblique shock. The area of this station, A_0, is the capture area that is ingested into the engine and is at most equal to the geometric inlet area, A_i. The "1" station is at the entrance of the constant area isolator (or diffuser) and accounts for the total pressure losses from the inlet shocks. The "2" station is at the exit of the constant-area isolator (or equivalently, the combustor entrance) and compensates for the shock train in the isolator. The combustor is modeled between stations "2" and "4" as a constant expansion area section. And lastly, the nozzle is modeled from station "4" to "5," with its exit area, A_5, serving as the reference area for all the propulsion and aerodynamic force coefficients. Figure 3.1 illustrates the thermodynamic stations on a Mach 7-designed scramjet.

The freestream and exit properties are then used to calculate the thrust coefficient referenced to the capture area, A_0, at a given freestream Mach number, angle of attack, and equivalence ratio by

$$(C_T)_{\text{ref}} = \frac{0.98\,F_5 - F_\infty - P_\infty\,(A_5 - A_0)}{q_\infty A_0} \tag{3.1}$$

where F_5 is the nozzle stream thrust with an 98% efficiency, F_∞ is the freestream

stream thrust using the calculated capture area, P_∞ is the freestream static pressure, and q_∞ is the freestream dynamic pressure. The reference plots the thrust coefficient as a function of the inlet contraction ratio, (A_0/A_1), for the following discrete design parameter configurations:

- **Base-to-capture area ratio**: $(A_5/A_0) = 1$, 2, 3, 4, 6, and 8.
- **Combustor expansion ratio**: $(A_4/A_2) = 2$, 3, and 4.
- **Freestream Mach number**: $M_\infty = 3$ to 8 in intervals of 1.
- **Equivalence ratio**: $ER = 0.25$, 0.50, 0.75, and 1.00 or the maximum ER to cause thermal choking.

Mathematically, the thrust coefficient as shown in the reference appendices is

$$\left(\frac{T}{q_\infty A_0}\right)_{\text{ref}} = f\left(\frac{A_0}{A_1}, \frac{A_5}{A_0}, \frac{A_4}{A_2}, M_\infty, ER\right). \tag{3.2}$$

There is also an implicit dependence on angle of attack in the thrust coefficient calculations because the inlet contraction ratio is calculated by

$$\left(\frac{A_0}{A_1}\right) = \left(\frac{A_0}{A_i}\right)\left(\frac{A_i}{A_1}\right)_{max}, \tag{3.3}$$

where the mass capture area ratio, (A_0/A_i), is a function of M_{des}, M_∞, and α as detailed in the following subsection. The maximum geometric contraction ratio, $(A_i/A_1)_{max}$ is calculated from the assumed range of operating conditions of $M_\infty =$ [4:8] and $\alpha =$ [0:10°] and is explained further in Sec. 3.1.1.2. The base-to-capture area ratio, (A_5/A_0), is also dependent on M_{des}, M_∞, and α because it is calculated by

$$\left(\frac{A_5}{A_0}\right) = \left(\frac{A_5}{A_i}\right) / \left(\frac{A_0}{A_i}\right), \tag{3.4}$$

and (A_0/A_i) is dependent on these parameters. (A_5/A_i) is a constant, user-defined design parameter, which in this work is set to 1.10 to maximize the capture area and thus engine thrust.

Therefore, for a given on-design inlet Mach number, M_{des}, and a current M_∞ and α, (A_0/A_1) and (A_5/A_0) are calculated by Eq. (3.3) and (3.4). Then, with the user-defined combustor expansion ratio, (A_4/A_2), and a given equivalence ratio, the thrust coefficient may be computed. The details of how these calculations are implemented is explained in Sec. 3.1.1.3.

Lastly, for the sake of completeness, the primary assumptions made in the reference's thrust coefficient computations are:[129]

1. A constant area isolator, so that $A_2 = A_1$.
2. RJ-5 fuel with a 100% combustion efficiency.
3. A combustor wall-to-entrance area ratio, (A_{wall}/A_4), of 40.
4. Inlet and combustor flows are in thermochemical equilibrium.
5. Combustor wall heat transfer is neglected.
6. Nozzle exit thrust efficiency of 98% for an expansion one-third between the frozen and equilibrium chemistry solutions.

3.1.1.1 Off-Design Mass Capture

The reference plots the off-design mass capture as a function of angle of attack from $-10°$ to $10°$ for the three on-design Mach numbers (M_{des} = 6, 7, 8) and six freestream Mach numbers (M_∞ = 3–8 in intervals of one). Because the scramjets in this work are assumed to have a full axisymmetric chin inlet, the off-design capture

area is a function of only the magnitude of the angle of attack. So, when the digitized graph was curve fit, the capture areas for the negative angles of attack were treated as if they were positive. The result is a quadratic function of angle of attack at a given M_{des} and M_∞:

$$\left(\frac{A_0}{A_i}\right)_{\text{ref}} = \begin{cases} 1.0 & if \quad M_\infty \geq M_{des} \;\&\; \alpha < \alpha_{min,M_{des},M_\infty} \\ a_{M_{des},M_\infty}\,\alpha^2 + b_{M_{des},M_\infty}\,\alpha + c_{M_{des},M_\infty} & else \end{cases} \tag{3.5}$$

where the coefficients for the quadratic are given in Table 3.1 along with the α_{min} values at the given M_{des} and M_∞ nodes. The first part of the if-statement in Eq. (3.5) is a constraint to ensure that the capture area ratio is never greater than 1, which may be calculated when the inlet is oversped ($M_\infty > M_{des}$) at low angles of attack.

After the capture area has been calculated at the desired angle of attack, cubic interpolation is used to compute (A_0/A_i) at the desired freestream Mach number using the four closest M_∞ nodes so that $(A_0/A_i) = f(M_\infty, \alpha)$.

3.1.1.2 Maximum Geometric Contraction Ratio

The maximum geometric contraction ratio is computed by taking the lowest geometric contraction ratio over the assumed operating range so that the inlet operating conditions are not violated for any point in the design space. The maximum contraction area ratio, $(A_0/A_1)_{max}$, is computed in the reference using an empirical relation for the inlet kinetic energy efficiency and an approximation of the total pressure recovery of the cone inlet.[129] The data points from the graphical representation of the maximum capture area are listed in Table 3.2. The geomet-

Table 3.1: Capture Area Curve-Fit Coefficients

Mach 6 Inlet				
M_∞	a_{6,M_∞}	b_{6,M_∞}	c_{6,M_∞}	$\alpha_{min,6,M_\infty}$
3	-0.50381096e-3	0.0	0.62345823	—
4	-0.92407015e-3	0.0	0.74196463	—
5	-0.13984166e-2	0.0	0.87788013	—
6	-0.10985493e-2	-0.10907126e-1	1.0184941	1.4761375
7	-0.35091049e-2	0.27913499e-1	0.94327056	3.9772961
8	-0.30688169e-2	0.24114687e-1	0.96142167	5.6218745

Mach 7 Inlet				
M_∞	a_{7,M_∞}	b_{7,M_∞}	c_{7,M_∞}	$\alpha_{min,7,M_\infty}$
3	-0.33911231e-3	0.0	0.55158020	—
4	-0.81493479e-3	0.0	0.66104957	—
5	-0.11643156e-2	0.0	0.77025633	—
6	-0.16964511e-2	0.0	0.89003444	—
7	-0.14945940e-2	-0.99412493e-2	1.0146784	1.24389711
8	-0.41068464e-2	0.29071650e-1	0.94410395	3.5394128

Mach 8 Inlet				
M_∞	a_{8,M_∞}	b_{8,M_∞}	c_{8,M_∞}	$\alpha_{min,8,M_\infty}$
3	-0.19959882e-3	0.d0	0.49430093	—
4	-0.67340679e-3	0.d0	0.58781782	—
5	-0.11137407e-2	0.d0	0.69188719	—
6	-0.14964941e-2	0.d0	0.79606842	—
7	-0.22808079e-2	0.d0	0.89916475	—
8	-0.19133374e-2	-0.60703864e-2	1.0059433	0.78489235

Table 3.2: Maximum Contraction Ratio

M_∞	3	4	5	6	7	8
$(A_0/A_1)_{max}$	3.15567	5.20698	7.15743	8.36812	8.50000	7.98145

ric contraction ratio, (A_i/A_1), is then calculated over the operating design space of $M_\infty = [4{:}8]$ and $\alpha = [0{:}10^\circ]$ using cubic interpolation of the nodes of Table 3.2 for $(A_0/A_1)_{max}$ and the analysis in the previous subsection for (A_0/A_i). The minimum value of the geometric contraction ratio over the entire operating regime is then used as the maximum allowable geometric contraction ratio. Mathematically,[129]

$$\left(\frac{A_i}{A_1}\right)_{max} = \min\left[\left(\frac{A_0}{A_1}\right)_{max} / \left(\frac{A_0}{A_i}\right)\right]. \tag{3.6}$$

3.1.1.3 Thrust Coefficient

The thrust coefficient is then calculated after the contraction ratio, (A_0/A_1), and base area-to-capture area, (A_5/A_0), values are computed at the free stream Mach number and angle of attack of interest. The contraction ratio, (A_0/A_1), is calculated by multiplying the capture area ratio in Sec. 3.1.1.1 at a given M_∞ and α with the maximum geometric contraction ratio in the previous subsection, as shown in Eq. (3.3) on pg. 89. And the base area-to-capture area ratio is computed by Eq. (3.4) again using the (A_0/A_i) at the desired Mach number and angle of attack.

The thrust coefficient (referenced to the capture area) is calculated as a function of (A_0/A_1) by the polynomial curve fits in App. B. The reference plots results for combustor expansion ratios, (A_4/A_2), of 2, 3, or 4. However, only the combustor

expansion ratios of 3 and 4 were curve fit in this work, since they are shown to prevent thermal choking over a much larger operating range than the $(A_4/A_2) = 2$ results. Also, this work assumes a value of $(A_4/A_2) = 3$ to allow for increased internal vehicle volume over $(A_4/A_2) = 4$, and because the higher combustor expansion ratio has little effect on the thrust levels.

The thrust coefficient is calculated at each of the four closest base area-to-capture ratio (A_5/A_0), freestream Mach number, and equivalence ratio nodes for the given combustor expansion ratio, $(A_4/A_2) = 3$. After the thrust coefficients are calculated for the 64 nodes (4 (A_5/A_0), 4 M_∞, and 4 ER), these values are re-referenced to the base area by

$$\left(\frac{T}{q_\infty A_5}\right) = \left(\frac{T}{q_\infty A_0}\right)_{\text{ref}} / \left(\frac{A_5}{A_0}\right)_{node} \tag{3.7}$$

and interpolated cubicly to the computed (A_5/A_0) at a given freestream Mach number and angle of attack, *i.e.* $(A_5/A_0) = f(M_\infty, \alpha)$. This process results in 16 thrust coefficients at 4 M_∞ and 4 ER nodes, which are then cubicly interpolated to the desired free stream Mach number and lastly the equivalence ratio. Thus, the thrust coefficient is

$$C_T \equiv \left(\frac{T}{q_\infty A_5}\right) = f\left(M_\infty, \alpha, ER\right). \tag{3.8}$$

3.1.2 Aerodynamics

The aerodynamics forces modeled in the reference[129] are comprised of three major sources: the profile drag coefficient, the inlet additive drag coefficient, and the normal force coefficient. Each component, and the profile drag subcomponents,

will be presented in detail in the following subsections. Many of the missile dimensions will also be presented in the profile drag subsection, and used again in the computation of the missile volume in Sec. 3.2.1.

3.1.2.1 Profile Drag Coefficient

The profile drag is the drag present at all angles of attack and is sometimes referred to as the axial force. For this model, the profile drag is the sum of the wave drag caused by the 6° cowl angle, the leading edge drag due to the 0.254 cm (0.1") bluntness of the cowl, the exterior body (skin) friction, and the wave and friction drag from the four tail surfaces. Each of the profile drag components are detailed below along with any assumptions made by the reference source.[129]

Cowl Wave Drag

The cowl wave drag is caused by the oblique shock from the 6° cowl angle assumed by the reference.[129] The cowl wave drag was calculated using "a finite difference solution of the hyperbolic equations of motion for a steady inviscid flow," (Waltrup *et al.*,[129] pg. 8-5) which is the same technique used for the off-design capture area and inlet additive drag calculations.

The cowl wave drag is normalized by the axially projected cowl area, A_{c_x}, and plotted in the report as a function of freestream Mach number for design Mach numbers from 4 to 8 in intervals of 1. The cowl wave drag exhibits two different trends, one when the inlet is undersped ($M_\infty \leq M_{des}$) which is a function of M_{des},

and one when the inlet is oversped ($M_\infty > M_{des}$) which is independent of M_{des}. The reason for this behavior is that when the inlet is flying slower than the shock-on-cowl-lip inlet-design Mach number, the initial shock off the 12.5° conical forebody is outside the cowl and the cowl sees a flow field dependent on this initial shock. When the inlet is oversped, the forebody shock is inside the cowl and the cowl wave drag is just a function of the freestream flow.

For a Mach 6 designed inlet flying at a freestream Mach number lower than Mach 6, the curve-fit cowl wave drag is

$$\left(\frac{C_{D_{cw}}}{A_{c_x}} \times 10^4 \frac{1}{in^2}\right)_{\text{ref}} = 0.020828418\, M_\infty^2 - 0.28005453\, M_\infty + 2.3813260. \quad (3.9)$$

For an undersped Mach 7 inlet, the curve-fit cowl wave drag is

$$\left(\frac{C_{D_{cw}}}{A_{c_x}} \times 10^4 \frac{1}{in^2}\right)_{\text{ref}} = 0.012006681\, M_\infty^2 - 0.19139457\, M_\infty + 2.0817794. \quad (3.10)$$

And for the Mach 8 inlet flying below Mach 8, the curve-fit cowl wave drag is

$$\left(\frac{C_{D_{cw}}}{A_{c_x}} \times 10^4 \frac{1}{in^2}\right)_{\text{ref}} = 0.011497814\, M_\infty^2 - 0.18189467\, M_\infty + 1.9660494. \quad (3.11)$$

Lastly, for an oversped inlet with any M_{des}, the curve-fit cowl wave drag is

$$\left(\frac{C_{D_{cw}}}{A_{c_x}} \times 10^4 \frac{1}{in^2}\right)_{\text{ref}} = 0.024652242\, M_\infty^2 - 0.44480915\, M_\infty + 3.2354515. \quad (3.12)$$

The reference's presented cowl wave drag coefficient is then re-referenced to the base area in terms of metric units by:

$$C_{D_{cw}} \equiv \left(\frac{D_{cw}}{q_\infty A_5}\right) = \left(\frac{C_{D_{cw}}}{A_{c_x}} \times 10^4 \frac{1}{in^2}\right)_{\text{ref}} (A_{c_x}) \left(10^{-4}\right) \left(\frac{in}{m}\right)^2, \quad (3.13)$$

where 1 inch equals 0.0254 meters, and A_{c_x} is the cowl area projected axially.

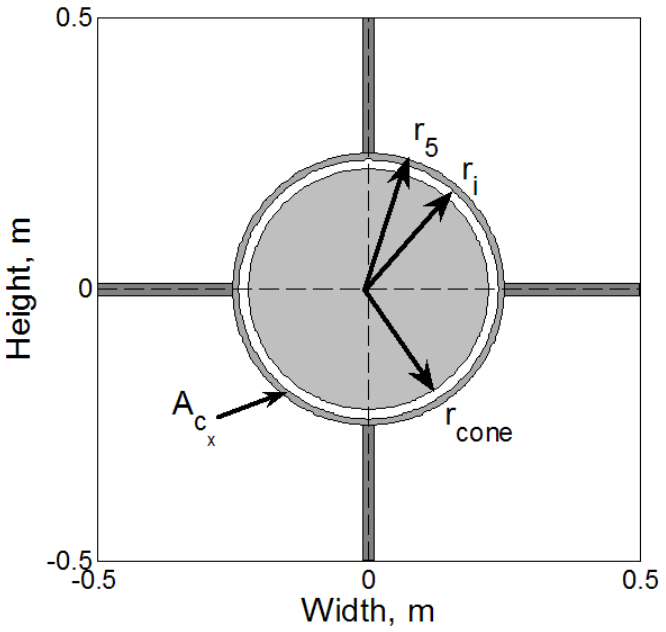

Figure 3.2: Scramjet Missile Front View

The axially projected cowl area is simply the difference between the base area and the inlet area, as shown in Fig. 3.2 of the front view of the modeled vehicle. From the given reference base area,

$$A_5 = \pi r_5^2 = 0.785 m^2, \tag{3.14}$$

(using the reference base radius $r_5 = 0.5$ m) and the user defined geometric design parameter, (A_5/A_i), the axial cowl area is

$$A_{c_x} = A_5 - A_i = A_5 \left(1 - (A_5/A_i)^{-1}\right). \tag{3.15}$$

For this work, (A_5/A_i) is assumed to be 1.1 so that the inlet is able to capture nearly all of the incoming flow. Therefore, $A_{c_x} = 0.0714$ m^2 for the scramjet designs in this dissertation.

Cowl Leading Edge Drag

The cowl leading edge drag is caused by the bow shock that is formed from the reference's assumed cowl lip diameter of 0.254 cm (0.1").[129] The way in which the reference calculates this quantity is not reported, but it is graphically represented as a function of M_∞ for the three inlet design Mach numbers and referenced to the cowl leading edge area. The relationships follow linear trends that include a sharp drop in the drag coefficient when the inlet is near the on-design Mach number because the initial cone shock is on the cowl at this condition. The drag is then essentially constant when the inlet is oversped because the cone shock no longer affects the cowl's leading edge drag.

For Mach 6 on-design inlets, the curve fits for the cowl leading edge drag are

$$\left(\frac{C_{D_{le}}}{A_{c_{le}}} \times 10^3 \frac{1}{in^2}\right)_{\text{ref}} = \begin{cases} 0.98467225\, M_\infty + 2.5726761, & M_\infty \leq 5.89020 \\ -14.454016\, M_\infty + 93.270209, & else \\ -0.0033134638\, M_\infty + 3.8911951, & M_\infty \geq 6.17372 \end{cases} \tag{3.16}$$

Similarly, the Mach 7 designed inlet curve fits are

$$\left(\frac{C_{D_{le}}}{A_{c_{le}}} \times 10^3 \frac{1}{in^2}\right)_{\text{ref}} = \begin{cases} 0.97465857\, M_\infty + 2.8212132, & M_\infty \leq 6.8018133 \\ -15.048172\, M_\infty + 111.33128, & else \\ -0.0042186311\, M_\infty + 3.8984785, & M_\infty \geq 7.1323400 \end{cases} \tag{3.17}$$

And the Mach 8 inlet polynomial-fit calculations are

$$\left(\frac{C_{D_{le}}}{A_{c_{le}}} \times 10^3 \frac{1}{in^2}\right)_{\text{ref}} = \begin{cases} 0.97924800\, M_\infty + 2.9478391, & M_\infty \leq 7.7620733 \\ -15.065858\, M_\infty + 127.50517, & else \\ 0.00093863892\, M_\infty + 3.8535373, & M_\infty \geq 8.1997933 \end{cases} \tag{3.18}$$

The cowl leading edge drag is then referenced to only the base area by

$$C_{D_{le}} \equiv \left(\frac{D_{le}}{q_\infty A_5}\right) = \left(\frac{C_{D_{le}}}{A_{c_{le}}} \times 10^3 \frac{1}{in^2}\right)_{\text{ref}} (A_{c_{le}}) \left(10^{-3}\right) \left(\frac{in}{m}\right)^2, \tag{3.19}$$

The cowl lip leading edge area, $A_{c_{le}}$, is calculated by multiplying the circumference of the inlet and the diameter of the cowl lip leading edge:

$$A_{c_{le}} = (2\pi\, r_i)\, d_{le}, \tag{3.20}$$

where $d_{le} = 0.00254$ m (0.1") and the inlet radius is computed from the inlet area,

$$r_i = \sqrt{A_i/\pi} = \sqrt{\frac{A_5}{\pi(A_5/A_i)}}, \tag{3.21}$$

which is 0.477 m following the $(A_5/A_i) = 1.1$ assumption in this work.

Body Friction Drag

The reference computes the exterior surface's body (skin) friction "assuming a smooth adiabatic wall with a fully developed turbulent boundary layer" (Waltrup *et al.*,[129] pg. 8-20). The reference's body friction is normalized by the wetted body area and plotted as a function of freestream Mach number. The quadratic polynomial curve fit for the skin friction is

$$\left(\frac{C_{D_f}}{A_{bw}} \times 10^6 \frac{1}{in^2}\right)_{\text{ref}} = 0.028936761\, M_\infty^2 - 0.83731029\, M_\infty + 6.3921607. \tag{3.22}$$

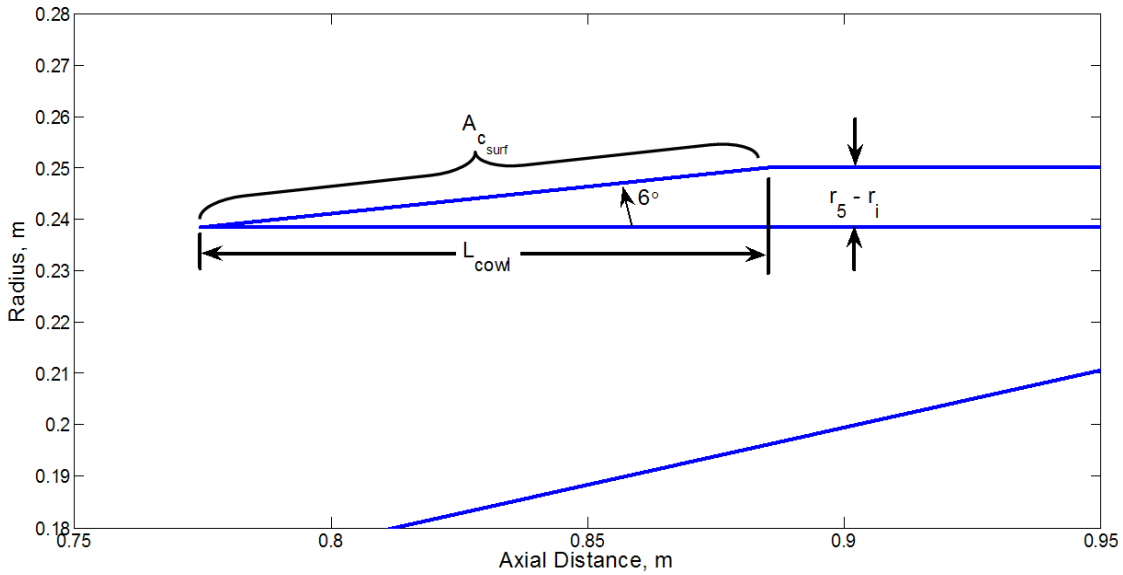

Figure 3.3: Detail of Scramjet Missile Cowl

And in metric units, referenced to the base area:

$$C_{D_f} \equiv \left(\frac{D_f}{q_\infty A_5}\right) = \left(\frac{C_{D_f}}{A_{bw}} \times 10^6 \frac{1}{in^2}\right)_{\text{ref}} (A_{bw}) \left(10^{-6}\right) \left(\frac{in}{m}\right)^2 \tag{3.23}$$

where A_{bw} is the wetted body area that consists of the sum of the cowl surface area and the constant radius, "cylinder," surface area.

The cowl surface area is found by using the reference's 6° cowl angle[129] and trigonometry to be

$$A_{c_{surf}} = \pi \left(r_i + r_5\right) \sqrt{L_{cowl}^2 + (r_5 - r_i)^2}, \tag{3.24}$$

where the cowl length is

$$L_{cowl} = \frac{r_5 - r_i}{\tan 6°}, \tag{3.25}$$

and the square root term in $A_{c_{surf}}$ is the hypotenuse of the cowl.

The "cylinder" surface area is the length of the missile excluding the cone

Table 3.3: Shock Angles for 12.5° Cone

Mach Number	6	7	8
Conical Shock Angle, °	16.63569672	15.90885885	15.41968796

forebody and cowl lengths multiplied by the circumference of the base:

$$A_{cyl_{surf}} = (2\pi\, r_5)\, L_{cyl}, \tag{3.26}$$

where

$$L_{cyl} = L_{total} - L_i - L_{cowl}, \tag{3.27}$$

$L_{total} = 4.0$ m is assumed in the reference,[129] L_{cowl} is calculated from Eq. (3.25), and L_i is calculated from the on-design shock on cowl lip condition (*i.e.* when $M_\infty = M_{des}$ and $\alpha = 0$). From geometry, see Fig. 3.5 on pg. 111, the inlet length is

$$L_i = \frac{r_i}{\tan\beta_s}, \tag{3.28}$$

where β_s is the oblique conical shock angle from the 12.5° cone forebody. The shock angle for the shock on cowl lip condition is a function of the on-design Mach number and the cone half-angle (12.5°). β_s can be found by numerically solving the Taylor-Maccoll equations from an initial shock angle to the cone surface and then iterating the shock angle until the computed cone surface angle converges to the desired cone angle (See Anderson,[133] Ch. 10 for details). For this work, an online java program developed by Chris Hood[134] at the University of Colorado, Boulder was used for these computations and the results are summarized in Table 3.3.

Now, using Eq. (3.24)–(3.28) and Table 3.3, the body wetted area is

$$A_{bw} = A_{c_{surf}} + A_{cyl_{surf}}. \tag{3.29}$$

Tail Drag

The last profile drag contributions come from the wave and skin friction from the four tail fins. The reference computes the tail wave drag based on two-dimensional flow over a 15° wedge with a 55° sweep angle using the freestream Mach number.[129] The tail's 0.2581 m^2 (400 in^2) surface area skin friction is computed with the same assumptions as the body friction above. From these assumptions, many higher-order effects are omitted including the flow distortion from the forebody, cowl and missile body, and the tail's contribution to the lift force. With these omissions, the tail wave drag, D_{tw}, and friction drag, D_{tf}, are only a function of the freestream Mach number:

$$\left(\frac{D_{tw}}{q_\infty A_5} \times 10^3 \frac{1}{in^2}\right)_{\text{ref}} = 0.010669708\, M_\infty^2 - 0.21896876\, M_\infty + 9.8720353, \tag{3.30}$$

$$\left(\frac{D_{tf}}{q_\infty A_5} \times 10^3 \frac{1}{in^2}\right)_{\text{ref}} = 0.026468258\, M_\infty^2 - 0.75490733\, M_\infty + 5.6466228, \tag{3.31}$$

The actual tail drag coefficients referenced to the base area ($C_{D_{tw}}$ and $C_{D_{tf}}$) are found by multiplying the curve fit calculations by 10^{-3} and $(\text{in/m})^2$.

Profile Drag Summary

To recapitulate, the total profile drag coefficient for a given inlet design Mach number and current freestream Mach number is

$$C_{D,0} \equiv \left(\frac{D_0}{q_\infty A_5} \right) = C_{D_{cw}} + C_{D_{le}} + C_{D_f} + C_{D_{tw}} + C_{D_{tf}}, \tag{3.32}$$

where Eq. (3.13), (3.19), (3.23), (3.30), and (3.31) are used for the components of the profile drag.

3.1.2.2 Additive Drag Coefficient

The inlet additive drag is the wave drag caused by the conical shock off of the inlet forebody. This quantity is calculated by integrating the pressure along the streamtube behind the forebody shock using the same numerical procedure as the capture area and cowl wave drag computations.[129]

The reference[129] plots the additive drag coefficient normalized by the inlet area for various design Mach number (M_{des} = 4, 6, 7, 8), freestream Mach number (M_∞ = 3–8 in intervals of 1), and angle of attack ($\alpha = 0°$, 5°, 10°) configurations as a function of inlet "smile" angle. The report[129] states that full axisymmetric chin inlets ($\phi_{smile} = 360°$) are the most efficient configuration since they maximize mass capture to the inlet, so only these inlets were curve fit and modeled.

For code implementation, the additive drag is calculated by quadratical interpolation from the design Mach number's α node values, Table 3.4, to the desired angle of attack at each of the M_∞ nodes. These values are then cubicly interpolated to the desired freestream Mach number. A constraint is also added to ensure the

Table 3.4: Additive Drag Coefficient Data

Mach 6 Inlet			
M_∞	$\alpha = 0°$	$\alpha = 5°$	$\alpha = 10°$
3	0.0397868	0.0398905	0.0398908
4	0.0246806	0.0252112	0.0265942
5	0.0117020	0.0122356	0.0141486
6	0.0	0.00372576	0.00787309
7	0.0	0.0	0.0
8	0.0	0.0	0.0

Mach 7 Inlet			
M_∞	$\alpha = 0°$	$\alpha = 5°$	$\alpha = 10°$
3	0.0491538	0.0491329	0.0496144
4	0.0342637	0.0349434	0.0372098
5	0.0215513	0.0225873	0.0250972
6	0.0102914	0.0112934	0.0148257
7	0.0	0.00395732	0.00901193
8	0.0	0.0	0.00610441

Mach 8 Inlet			
M_∞	$\alpha = 0°$	$\alpha = 5°$	$\alpha = 10°$
3	0.0565045	0.0561253	0.0548474
4	0.0417301	0.0425830	0.0454651
5	0.0298079	0.0307331	0.0341246
6	0.0186616	0.0201850	0.0241256
7	0.00881249	0.0109387	0.0154648
8	0.0	0.00130182	0.0108252

additive drag coefficient is at least zero and never negative, as might be calculated from the interpolation procedure.

After the interpolations, the additive drag is re-normalized from the inlet area to the base area by

$$C_{D_{add}} \equiv \left(\frac{D_{add}}{q_\infty A_5} \right) = \left(\frac{D_{add}}{q_\infty A_i} \right)_{\text{ref}} / \left(\frac{A_5}{A_i} \right), \tag{3.33}$$

where the base area to inlet area ratio, (A_5/A_i), is again one of the design parameters.

3.1.2.3 Normal Force Coefficient

The normal force coefficient is arguably the most deficient aspect of the aerodynamic model presented in the reference.[129] The simple analytic relation for the normal force coefficient is given as:

$$C_N \equiv \left(\frac{N}{q_\infty A_5} \right) = (-0.3 M_\infty + 5.4)\, \alpha, \tag{3.34}$$

where α is in radians. This relation is said to be "representative of those computed for other hypersonic missile designs," Waltrup *et al.*,[129] pg. 8-20. Improvements to this normal force coefficient could include the effects from the geometric design parameters and tail fin deflections. However, for the first order system analysis in this work, this relation was assumed to reasonably accurate.

3.1.3 Code Validation

This subsection validates the implemented Fortran 90/95 program using the previous two subsections' curve-fit aerodynamics and propulsion with several example calculations in the appendix of the JHU / APL reference.[129] The reference

Table 3.5: Scramjet Design Validation for $M_\infty = 4.0$, $\alpha = 0.0°$, $ER = 1.0$

Parameter	Code	Reference	Error, %
$C_{D_{cw}}$	0.028220	0.0281	0.4292
$C_{D_{le}}$	0.026047	0.0261	−0.2027
C_{D_f}	0.028290	0.0285	−0.7351
$C_{D_{tw}}$	0.009166	0.0092	−0.3600
$C_{D_{tf}}$	0.003050	0.0030	1.6828
$C_{D_{add}}$	0.010327	0.0104	−0.7057
C_D	0.105102	0.1053	−0.1879
C_T	0.490926	0.4872	0.7647

calculations use a Mach 6 inlet design ($M_{des} = 6$) and a base-to-inlet area ratio, (A_5/A_i), of 2.39 for the scramjet design parameters and investigates its Mach 4 and 8 performance. Specifically, the reference computes the drag and thrust coefficient values for Mach 4, 0° α; Mach 8, 0° α; and Mach 8, 5° α conditions with an equivalence ratio of 1.0. The trim equivalence ratio for the Mach 8, 5° angle of attack cruise is also estimated in the reference. For all cases, the assumed operating design range was $M_\infty = [4{:}8]$ and $\alpha = [0{:}10°]$, which dictates the maximum geometric contraction ratio as discussed in Sec. 3.1.1.2.

The results of the example calculation for the $M_{des} = 6$, $M_\infty = 4.0$, 0.0 angle of attack, 1.0 ER condition are listed in Table 3.5. The drag coefficient components, total drag coefficient, and thrust coefficient are listed for the Fortran code's calculated values, the reference's values,[129] and the percent error between the two.† As shown in Table 3.5, the computed drag coefficient components are less than

†There are two typographical errors in the reference's calculation of the drag coefficient.[129]

Table 3.6: Scramjet Design Validation for $M_\infty = 8.0$, $\alpha = 0.0°$, $ER = 1.0$

Parameter	Code	Reference	Error, %
$C_{D_{cw}}$	0.022209	0.0221	0.4927
$C_{D_{le}}$	0.015460	0.0155	−0.2599
C_{D_f}	0.012472	0.0123	1.4006
$C_{D_{tw}}$	0.008803	0.0088	0.0358
$C_{D_{tf}}$	0.001301	0.0013	0.1025
$C_{D_{add}}$	0.0	0.0	—
C_D	0.060245	0.0600	0.4089
C_T	0.198546	0.2043	−2.8166

1% in error except for the tail wave drag, which has a rather small contribution to the overall drag coefficient. Thus, the overall C_D error for this operating condition is only −0.188% compared to the reference's calculations. The thrust coefficient—which requires more extensive curve-fitting and interpolation in the Fortran program—produces a larger error of 0.765%.

The drag and thrust coefficient results for the Mach 8, 0° α, $ER = 1.0$ operating condition for the Mach 6 inlet design is listed in Table 3.6. The components of the drag coefficient are typically under 1% in error, and the overall C_D is over-predicted by only 0.409% from the reference.[129] The thrust coefficient, however, is under-predicted 2.82% compared to the reference's calculations. Considering the

The first typo is in the additive drag coefficient calculation. The reference reports that "$C_{D_{add}} = 0.248/2.39 = 0.0104$," which is mathematically incorrect. The first value should be 0.0248. The second typo is with the total drag coefficient, C_D. The reference reports it as 0.1503 instead of 0.1053, which is the value that is computed if the individual drag elements are summed.

error in computing the numerous curve-fits and interpolating between the 64 thrust coefficient nodes (see Sec. 3.1.1.3), the approximately 3% error is quite good. Furthermore, this under-prediction allows for a slightly conservative estimate of the scramjet's thrust level.

The third example calculation presented in the reference[129] is for a Mach 8 cruise at a 5° angle of attack and $ER = 1.0$. The only difference in the total drag coefficient between this case and the $M_\infty = 8$, $\alpha = 0$ case in Table 3.6 is the induced drag caused by the normal force coefficient. This drag term is

$$C_{D_\alpha} = C_N \sin(\alpha), \tag{3.35}$$

which equals 0.0228 for $M_\infty = 8$ and $\alpha = 5°$, where C_N is calculated by Eq. (3.34) on pg. 105. Therefore, the total drag coefficient as computed by the implemented code is 0.830627, the reference's $C_D = 0.828$, and the error is 0.3172%. The thrust coefficient for the $M_\infty = 8$, $\alpha = 5°$ configuration is the same as for the Mach 8, $\alpha = 0°$ case, so the error is again -2.82%.

Lastly, the reference[129] estimates the trim equivalence ratio, ER^*, for the $M_\infty = 8$, $\alpha = 5°$ condition. The trim ER as computed by the reference is the value when $C_D = C_T$ at the given M_∞ and α. As defined in this manner, the Fortran program's $ER^* = 0.448$ and the reference's trim equivalence ratio is 0.437 thus resulting in a 2.52% error between the two results. This error is primarily attributed to this dissertaion's code under-predicting the thrust coefficient as shown in Table 3.6.

Overall, the comparison with the Fortran program's calculation of the aerody-

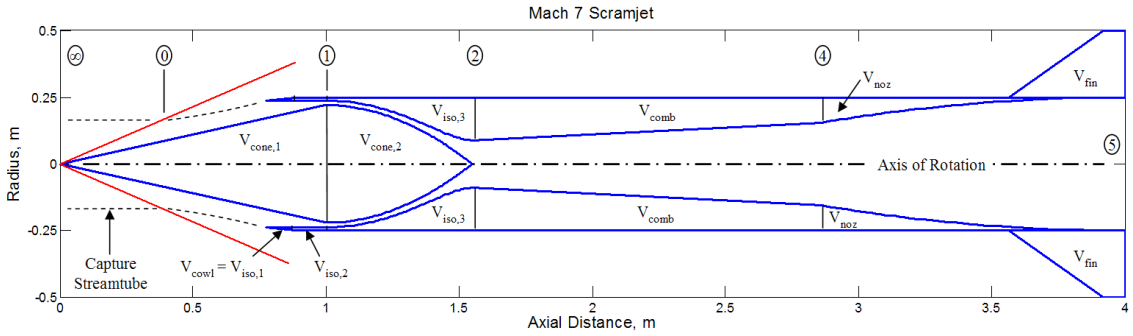

Figure 3.4: Scramjet Missile Volume Definitions

namic and propulsion forces are in excellent agreement with the example calculations in the source reference.[129] The total drag coefficients are predicted within 1% and the thrust coefficients are at worse in error of less than 3%.

3.2 Mass Model

The mass model implemented in this work is based off the parametric model used by Starkey in his doctoral work.[135] The model assumes that the initial total vehicle mass, $m(t_0)$, is comprised of only fuel and a constant density structure that ideally compensates for all subsystem masses that would be included on the vehicle. The division of the two mass components is defined by the fuel volume fraction, (V_f/V_{total}), and an assumption for the fuel density, ρ_f, and structural density, ρ_{str}:

$$m(t_0) = (1 - (V_f/V_{total}))\, V_{total}\rho_{str} + (V_f/V_{total})V_{total}\rho_f. \tag{3.36}$$

The total volume, V_{total}, is calculated from summing the internal volume of the scramjet missile. A summary of the different scramjet volumes is illustrated in Fig. 3.4. The cone volume consists of the 12.5° forebody, $V_{cone,1}$, and the internal

portion of the isolator, $V_{cone,2}$. The isolator volume is a sum of the 6° cowl volume, $V_{cowl} = V_{iso,1}$, the constant area cowl volume, V_{iso_2}, and the exterior portion of the isolator, $V_{iso,3}$. The combustor volume, V_{comb}, nozzle volume, V_{noz}, and the volume of the four tail fins, V_{fin}, are the other components of the total vehicle volume, V_{total}. The following subsection details how each of these components are evaluated.

Section 3.2.2 then presents a discussion on the fuel choice used in this work and how the structural density, ρ_{str}, and fuel volume fraction, (V_f/V_{total}), were chosen to meet the design goals of a approximately 1,100 kg initial mass and 25–30% initial fuel mass fraction.

3.2.1 Internal Volume Calculation

This subsection details the component volume calculations for the modeled scramjet. The dimensions and volumes are described in the following order: cone inlet, isolator and cone rear, combustor, nozzle, and tail fins. A summary of these volumes concludes this subsection.

Inlet

The inlet is a 12.5° cone whose maximum radius, r_{cone}, is calculated by first computing the isolator area:

$$A_1 = \left(\frac{A_i}{A_1}\right)^{-1}_{max} A_i = \pi(r_i^2 - r_{cone}^2), \tag{3.37}$$

where $(A_i/A_1)_{max}$ is the maximum geometric contraction ratio as defined in Eq. (3.6) on pg. 93, and the second equality is a result of the geometry, as shown in Fig. 3.5.

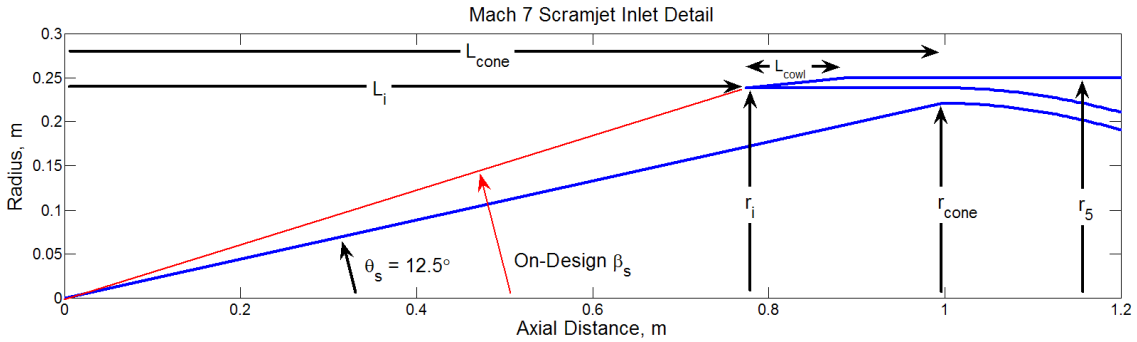

Figure 3.5: Detail of Scramjet Missile Inlet

Solving the second equality for the maximum cone radius yields

$$r_{cone} = \sqrt{r_i^2 - A_1/\pi}. \tag{3.38}$$

The length of the inlet cone from the tip to where the flow begins to be turned downwards is also found from geometry:

$$L_{cone} = \frac{r_{cone}}{\tan(12.5^\circ)}. \tag{3.39}$$

The volume of the 12.5° cone prior to turning the flow downward is then analytically

$$V_{cone,1} = \frac{\pi}{3} r_{cone}^2 L_{cone}. \tag{3.40}$$

Isolator / Rear of Cone

The volume of the 6° cowl from the inlet radius, r_i, to the base radius, r_5, is

$$V_{cowl} = V_{iso,1} = \frac{\pi}{3} L_{cowl}(r_i^2 + r_i r_5 + r_5^2) - \pi r_i^2 L_{cowl}, \tag{3.41}$$

where L_{cowl} is calculated in Eq. (3.25) on pg. 100. The volume of the constant cross-sectional area portion of the cowl/isolator between $L_i + L_{cowl}$ and L_{cone}, see Fig. 3.5 and 3.6, is

$$V_{iso,2} = \pi \left(r_5^2 - r_i^2\right) \left(L_{cone} - L_i - L_{cowl}\right). \tag{3.42}$$

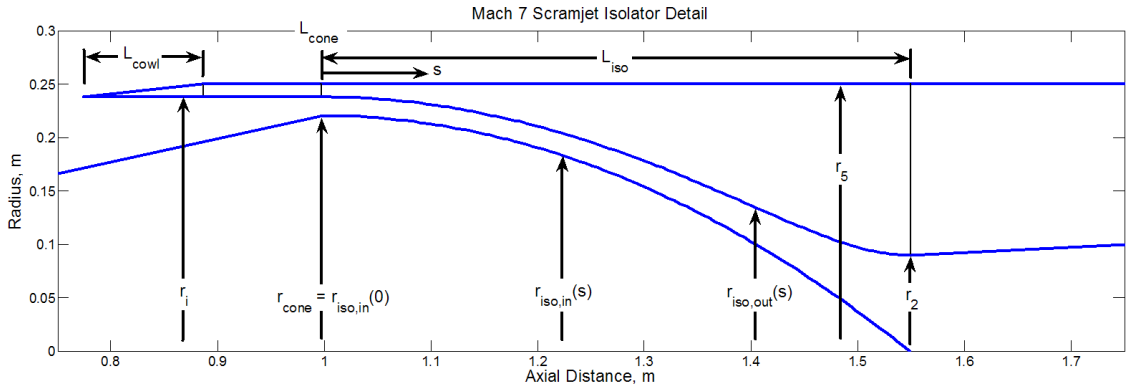

Figure 3.6: Detail of Scramjet Missile Isolator

The constant-area isolator dimensions are calculated with the assumption that the rear of the cone forebody (*i.e.* the inner portion of the isolator) is a quadratic polynomial:

$$r_{iso,in}(s) = a_{iso}\left(\frac{s}{L_{iso}}\right)^2 + b_{iso}\left(\frac{s}{L_{iso}}\right) + c_{iso}, \tag{3.43}$$

where s is the axial length of the isolator beginning where the cone directs the flow down ($s = [0{:}L_{iso}]$), see Fig. 3.6. The coefficients for the isolator's inner geometry are a result of known constraints and several assumptions to make the isolator appear similar to other JHU/APL designs.[136,137] The first constraint is that the initial value of the isolator equals the maximum cone radius:

$$r_{iso,in}(0) = r_{cone} = c_{iso}. \tag{3.44}$$

Then substituting Eq. (3.44) into (3.43) and adding the constraint that the cone radius at the end of the isolator is zero:

$$r_{iso,in}(L_{iso}) = a_{iso} + b_{iso} + r_{cone} = 0 \quad \rightarrow \quad a_{iso} = -b_{iso} - r_{cone}. \tag{3.45}$$

Now it is assumed that $b_{iso} = 0$, thus $a_{iso} = -r_{cone}$, to make the isolator look similar to the schematic presented in a 2001 JHU/APL design[137] which uses the

same methodologies as the original 1982 reference.[129] Substituting these coefficients into the isolator quadratic equation,

$$r_{iso,in}(s) = -r_{cone}\left(\frac{s}{L_{iso}}\right)^2 + r_{cone}. \tag{3.46}$$

Furthermore, the isolator length is assumed to be

$$L_{iso} = 2L_i - L_{cone}, \tag{3.47}$$

again so that the overall missile dimensions approximately correspond to the 2001 JHU/APL paper by Waltrup.[137]

Now that the interior curve of the isolator is defined, the exterior curve is calculated using the isolator's constant area assumption. Therefore,

$$A_1 = const = \pi\left(r_{iso,out}^2 - r_{iso,in}^2\right) \quad \rightarrow \quad r_{iso,out}(s) = \sqrt{A_1/\pi + r_{iso,in}(s)^2}, \tag{3.48}$$

where $r_{iso,in}(s)$ is given by Eq. (3.46). A close up of the isolator geometry for the Mach 7 inlet design is shown in Fig. 3.6 on pg. 112.

The volume of the rear of the cone is numerically integrated by

$$\begin{aligned} V_{cone,2} &= \int_0^{L_{iso}} \pi r_{iso,in}^2(s)ds \\ &= \sum_{s=0}^{L_{iso}} \left[\pi\left(\frac{r_{iso,in}(s_i) + r_{iso,in}(s_{i-1})}{2}\right)^2 (s_i - s_{i-1})\right], \end{aligned} \tag{3.49}$$

which is essentially summing small segments of a cylinder, and s_i is the ith element of the 100-element equispaced s array from zero to L_{iso}. The isolator's outer volume is similarly numerically integrated by

$$\begin{aligned} V_{iso,3} &= \pi r_5^2 L_{iso} - \int_0^{L_{iso}} \pi r_{iso,out}^2(s)ds \\ &= \sum_{s=0}^{L_{iso}} \left\{\pi\left[r_5^2 - \left(\frac{r_{iso,out}(s_i) + r_{iso,out}(s_{i-1})}{2}\right)^2\right](s_i - s_{i-1})\right\}. \end{aligned} \tag{3.50}$$

Combustor

The combustor is modeled as a linear expansion specified by (A_4/A_2) from the isolator exit to the nozzle entrance. The length of the combustor is calculated using the assumption that the combustor wall area is 40 times that of the combustor entrance area, *i.e.* $(A_{wall}/A_2) = 40$, as given in the primary reference.[129] The combustor wall's surface area is then

$$A_{wall} = \pi \left(r_2 + r_4\right) \sqrt{L_{comb}^2 + \left(r_4 - r_2\right)^2}, \tag{3.51}$$

where $r_2 = r_{iso,out}(L_{iso})$ and the combustor exit radius, r_4, is

$$\left(\frac{A_4}{A_2}\right) = \frac{\pi r_4^2}{\pi r_2^2} \quad \rightarrow \quad r_4 = r_2\sqrt{(A_4/A_2)} \tag{3.52}$$

Solving Eq. (3.51) for the combustor length gives

$$L_{comb} = \sqrt{\left[\frac{A_{wall}}{\pi(r_2 + r_4)}\right]^2 - \left(r_4 - r_2\right)^2}, \tag{3.53}$$

and the combustor volume is then

$$V_{comb} = \pi r_5^2 L_{comb} - \frac{\pi}{3} L_{comb}\left(r_2^2 + r_2 r_4 + r_4^2\right). \tag{3.54}$$

The figures in this chapter show the modeled combuster with an expansion ratio, (A_4/A_2), of three with a Mach 7 designed inlet.

Nozzle

The nozzle is modeled as a quadratic polynomial in a manner similar to the internal isolator geometry with two known boundary conditions, $r_{noz}(0) = r_4$ and

$r_{noz}(L_{noz}) = r_5$, and a known length:

$$L_{noz} = L_{total} - (L_{cone} + L_{iso} + L_{comb}) . \tag{3.55}$$

Using the quadratic polynomial equation,

$$r_{noz}(s_{noz}) = a_{noz} \left(\frac{s_{noz}}{L_{noz}} \right)^2 + b_{noz} \left(\frac{s_{noz}}{L_{noz}} \right) + c_{noz}, \tag{3.56}$$

where $s_{noz} = [0 : L_{noz}]$, substituting in the boundary conditions, and solving for the first and third coefficients yields

$$a_{noz} = r_5 - b_{noz} - r_4 \tag{3.57}$$

$$c_{noz} = r_4. \tag{3.58}$$

The midpoint value is then

$$r_{noz}(L_{noz}/2) = \frac{1}{4} a_{noz} + \frac{1}{2} b_{noz} + c_{noz} = \frac{1}{4} (r_5 + b_{noz} + 3r_4) = \frac{1}{4} (3r_5 + r_4) , \tag{3.59}$$

where the last equality is an assumed constraint so that the nozzle geometry is qualitatively similar to typical nozzles. Solving Eq. (3.59) for the second coefficient yields:

$$b_{noz} = 2 (r_5 - r_4) . \tag{3.60}$$

All three coefficients are then substituted into Eq. (3.56) to produce the geometry of the nozzle boundary:

$$r_{noz}(s_{noz}) = (r_4 - r_5) \left(\frac{s_{noz}}{L_{noz}} \right)^2 + 2 (r_5 - r_4) \left(\frac{s_{noz}}{L_{noz}} \right) + r_4. \tag{3.61}$$

The volume of this portion of the missile is the volume of an external cylinder

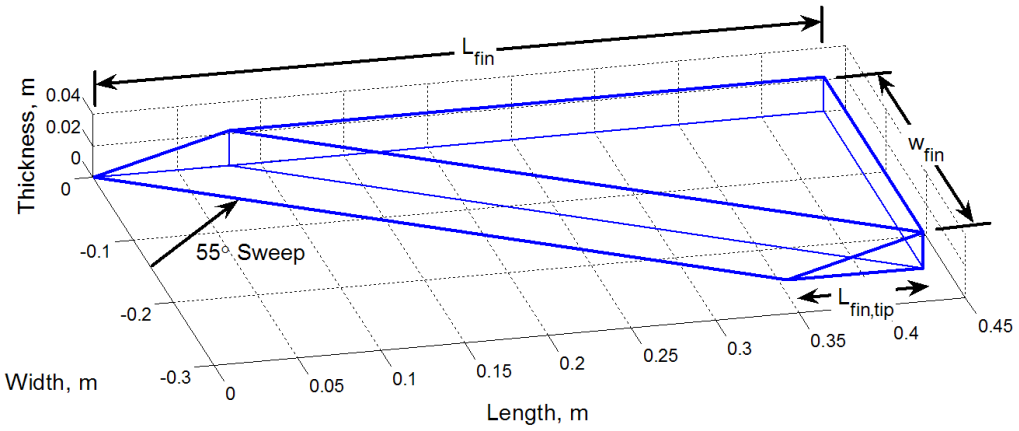

Figure 3.7: Scramjet Missile Fin Detail

of radius r_5 and length L_{noz} minus the internal volume of the nozzle:

$$\begin{aligned} V_{noz} &= \pi r_5^2 L_{noz} - \int_0^{L_{noz}} \pi r_{noz}^2(s_{noz}) ds_{noz} \qquad (3.62) \\ &= \pi r_5^2 L_{noz} - \sum_{s_{noz}=0}^{L_{noz}} \pi \left(\frac{r_{noz}(s_{noz,i}) + r_{noz}(s_{noz,i-1})}{2} \right)^2 (s_{noz,i} - s_{noz,i-1}), \end{aligned}$$

where $s_{noz,i}$ is the ith element in the 100-element equally spaced array from zero to L_{noz}, and L_{noz} as defined in Eq. (3.55).

Tail Fins

The volume of the four tail fins is the final component of the total volume of the modeled scramjet missile. Following the reference's assumptions of a 15° wedge angle,[129] the length of the fin at the tip is

$$L_{fin,tip} = \frac{t_{fin}}{\tan(15°)}, \qquad (3.63)$$

where t_{fin} is the thickness of the fin and Fig. 3.7 shows the fin dimensions. The reference[129] also assumes a 5% thickness for the tail. For this work it is assumed

that this constraint is in relation to the length of the fin at its base, so

$$t_{fin} = 0.05\, L_{fin}, \tag{3.64}$$

where L_{fin} is the tail fin's length where it is mounted to the missile body. Substituting the fin thickness into the tail's length at the tip, Eq. (3.63), yields

$$L_{fin,tip} = \frac{0.05}{\tan(15^\circ)} L_{fin}. \tag{3.65}$$

The width of the tail fin, w_{fin}, is computed from the reference's assumption that the fins have a 55° sweep angle.[129] Using the tangent of the sweep angle and the difference in the fin length at the base and tip, one has

$$\tan(55^\circ) = \frac{L_{fin} - L_{fin,tip}}{w_{fin}} \quad \rightarrow \quad w_{fin} = \frac{1 - (0.05/\tan(15^\circ))}{\tan(55^\circ)} L_{fin}, \tag{3.66}$$

where Eq. (3.65) has been used for $L_{fin,tip}$. From the reference,[129] the total planform area of the four fins is 400 in^2, so each fin's planform area is 100 in^2 or 0.06452 m^2. Using the dimensions calculated above, the planform area is

$$\begin{aligned} A_{fin} &= 0.5\,(L_{fin} + L_{fin,tip})\, w_{fin} = \frac{L_{fin} w_{fin}}{2}\left(1 + \frac{0.05}{\tan(15^\circ)}\right) \\ &= \frac{L_{fin}^2}{2\tan(55^\circ)}\left[1 - \left(\frac{0.05}{\tan(15^\circ)}\right)^2\right]. \end{aligned} \tag{3.67}$$

Rearranging, the fin base length can be solved for as:

$$L_{fin} = \sqrt{\frac{2A_{fin}\tan(55^\circ)}{1 - (0.05/\tan(15^\circ))^2}}. \tag{3.68}$$

With Eq. (3.64), (3.66), and (3.68), the volume of a single tail fin (which is the same for all missile designs) is

$$\begin{aligned} V_{fin} &= 0.5 L_{fin,tip} w_{fin} t_{fin} + 0.5\,(L_{fin} - L_{fin,tip})\, w_{fin} t_{fin} \\ &= 0.5 L_{fin} w_{fin} t_{fin} = 0.025 L_{fin}^2 w_{fin} = 0.00119\ m^3, \end{aligned} \tag{3.69}$$

where $L_{fin} = 0.437$ m from Eq. (3.68) and $w_{fin} = 0.249$ m from Eq. (3.66).

Internal Volume Summary

The total scramjet volume is calculated by

$$V_{total} = \sum_{i=1}^{2} V_{cone,i} + \sum_{i=1}^{3} V_{iso,i} + V_{comb} + V_{noz} + 4V_{fin}, \tag{3.70}$$

where Eq. (3.40)–(3.42), (3.49), (3.50), (3.54), (3.63), and (3.69) are used for the various component volumes.

3.2.2 Determination of Mass Model Design Parameters

Now that the total missile volume can be calculated for a given M_{des}, (A_5/A_i), and (A_4/A_2), there are three quantities that need to be determined to calculate the initial mass of the modeled scramjet using Eq. (3.36) on pg. 109: the fuel density, ρ_f, average structural density, ρ_{str}, and fuel volume fraction, (V_f/V_{total}).

JP-10 is assumed as the fuel for the scramjet missile. This fuel type was chosen based on Edwards' 2003 survey paper on aerospace propellants[138] which states that JP-10 is "the only airbreathing-missile fuel in operational use by the United States at the present time." Furthermore, the fuel assumed in the JHU/APL report (RJ-5),[129] had "cost and freeze-point limitations [that] prevented field use." In hindsight, JP-7, which was used by the Mach 3+ SR-71[138] and proposed for the Mach 5 X-51,[18] may have proven to be a better fuel choice because of its improved regenerative cooling properties over JP-10. Regardless, JP-10's density of 940 kg/m^3 is used for the scramjet mass model in this dissertation (Horning,[139] pg. 131). JP-10's hydrogen-

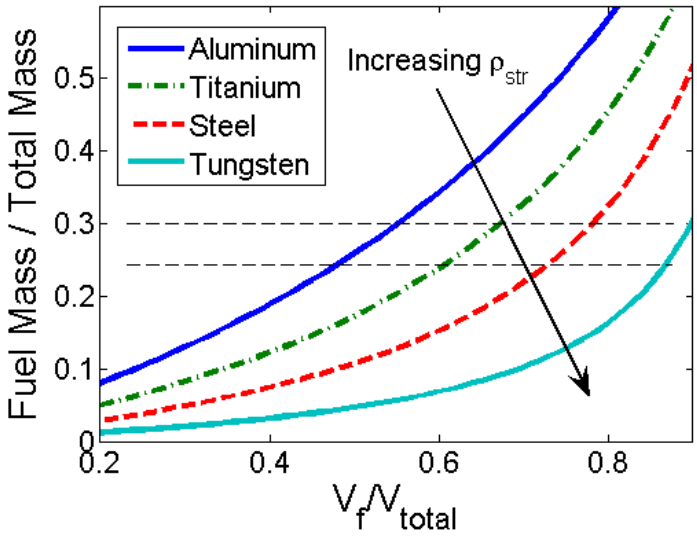

Figure 3.8: Scramjet Fuel Mass Fraction vs. (V_f/V_{total})

to-carbon ratio, (H/C), is 1.61 which results in a stoichiometric fuel-to-air ratio of 0.07066 using (Heiser and Pratt,[140] pg. 112):

$$f_{stoich} = \frac{36 + 3(H/C)}{103[4 + (H/C)]}, \tag{3.71}$$

which assumes air is comprised of 79% nitrogen and 21% oxygen.

Four average structural densities are considered for the mass model: aluminum (2,700 kg/m^3), titanium (4,507 kg/m^3), steel (7,850 kg/m^3), and tungsten (19,255 kg/m^3). Figure 3.8 plots the fuel mass fraction as a function of the fuel volume fraction from 20–90% for the four structural densities using the relation

$$\frac{m(t_0)}{m_f(t_0)} = \frac{m_{str} + m_f(t_0)}{m_f(t_0)} = \frac{(1 - (V_f/V_{total}))}{(V_f/V_{total})} \frac{\rho_{str}}{\rho_f} + 1, \tag{3.72}$$

and the JP-10 fuel density. Billig states, "The mass fraction of propellant for a rocket for a tactical missile is typically 50-70% of the initial weight as compared to 25-30% for the ramjet," (Jensen and Netzer,[141] pg. 12) so the modeled scramjet's

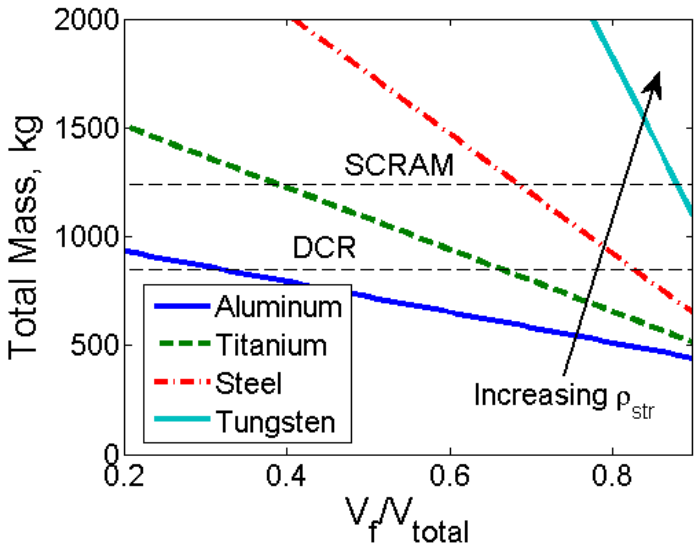

Figure 3.9: Scramjet Mass vs. (V_f/V_{total}), Mach 7 inlet

fuel mass fraction would ideally fall in this range, which is shown as dashed lines in the figure.

The second design constraint considered in the determination of the mass properties of the scramjet model is its initial mass, $m(t_0)$. The initial mass for the Mach 7 inlet design is plotted as Fig. 3.9 for fuel volume fractions between 20 and 90% using Eq. (3.36) on pg. 109. The estimated initial masses of two JHU/APL hypersonic missile designs (excluding their rocket booster masses) are plotted as dashed lines in the figure. The Mach 7.5 SCRAM missile initial mass is approximated as 850 kg and the Mach 4–6 Dual Combustor Ramjet (DCR) initial mass as 1,240 kg from Waltrup *et al.*'s survey of U.S. Navy high speed air-breathing propulsion systems.[142] Therefore, the second design constraint imposed is an initial wet mass of ∼1,100 kg which is the average of these two designs.

From Fig. 3.9, it is apparent that the initial mass of the scramjet is quite

sensitive to (V_f/V_{total}) near the $m(t_0)$ = 1,100 kg constraint. For an aluminum structure, the fuel volume fraction would be less than 20% which causes a fuel mass fraction of less than 10% as shown in Fig. 3.8. For a titanium structure, the fuel volume is about 50% for an initial mass of 1,100 kg and the resultant fuel mass fraction is 17.3%. A steel structure requires a 75% (V_f/V_{total}) to produce a 1,100 kg initial mass and thus a 22% fuel mass fraction. Lastly, the tungsten structure needs a fuel volume fraction over 90% to yield the desired initial mass, which is deemed unreasonably high. Although none of the modeled densities meet both design constraints, the titanium structure with a 50% fuel volume fraction was chosen as a compromise between the two constraints.

3.2.3 Modeled Axisymmetric Hypersonic Missile Summary

The primary design parameters used to model the hypersonic, axisymmetric scramjet missiles in this work are listed in Table 3.7. The top portion of the table summarizes the main geometric design parameters for the vehicles. The middle portion summarizes the fuel and mass properties of the vehicle. And the bottom portion summarizes the cruise dynamic pressure and the operating ranges used to calculate the maximum contraction ratio, $(A_i/A_1)_{max}$, and the gridded aerodynamic and propulsion data for the trim calculations in the next section. Table 3.8 lists the resultant maximum contraction ratios and the operating point that sets this value, the total volume of the three missile designs, the initial fuel mass, and the initial vehicle mass. Again, the fuel mass fraction is 17.3%.

Table 3.7: Modeled Scramjet Design Parameters

Design Parameter	Symbol	Value	Units
Total Length	L_{total}	4.0	m
Base (Reference) Radius	r_5	0.25	m
Base-to-Inlet Area Ratio	(A_5/A_i)	1.1	—
Combustor Expansion Area Ratio	(A_4/A_2)	3.0	—
Combustor Wall-to-Entrance Area Ratio	(A_{wall}/A_2)	40.0	—
Fuel Density (JP-10)	ρ_f	940.0	kg/m^3
Fuel Hydrogen-to-Carbon Ratio (JP-10)	(H/C)	1.61	—
Stoichiometric Fuel-to-Air Ratio (JP-10)	f_{stoich}	0.07066	—
Structural Density (Titanium)	ρ_{str}	4507	kg/m^3
Fuel-to-Total Volume Ratio	(V_f/V_{total})	0.5	—
Cruise Dynamic Pressure	q_∞	101325	Pa
Freestream Mach Number Range	M_∞	4–8	—
Angle of Attack Range	α	0–10	°
Equivalence Ratio Range	ER	0.25–1	—

Table 3.8: Scramjet Missile Design Summary

M_{des}	$(A_i/A_1)_{max}$	Total Volume	Fuel Mass	Total Mass
6	7.0178 at $M_\infty = 4.0$, $\alpha = 0°$	0.3887 m^3	182.7 kg	1058.5 kg
7	7.8768 at $M_\infty = 4.0$, $\alpha = 0°$	0.4034 m^3	189.6 kg	1098.7 kg
8	7.9814 at $M_\infty = 8.0$, $\alpha = 0°$	0.4102 m^3	192.8 kg	1117.1 kg

3.3 Trim State Calculation

Detailed trim conditions are used to compute the trim pitch, roll, and equivalence ratio profiles along the 1,000 km cruise trajectory as fuel is burned and the vehicle compensates for changes in the gravity vector. The trim Euler angles are then finite differenced to produce the body-to-navigation frame angular rates that are a portion of the overall simulated truth gyro signal. The accelerometer specific force measurements are more easily simulated for cruise since they are analytic functions of the trajectory.

The assumed cruise trajectories in this work are due East at a constant velocity and altitude, see Sec. 2.4. Therefore, the yaw angle of the vehicle is held at 90° throughout the duration of the simulation. Also, because of the constant altitude assumption, the flight path angle, γ_{fpa}, of the missile is always zero so that the pitch angle, θ_b, is equivalent to the angle of attack, *i.e.* $\theta_b \equiv \alpha + \gamma_{fpa} = \alpha$. The pitch angle, roll angle, and equivalence ratio are then the three variables used to trim the scramjet's accelerations at each simulation epoch. Because of the low fidelity aerodynamics of the tail fins, and the absence of a high-fidelity mass model, the moment dynamics are not trimmed in this work.

The next subsection derives the trim state calculations used in this work starting with the free-body diagram of the missile and the vehicle dynamics. The following subsection presents the results of finite differencing the trim pitch and roll angles along with the simulated navigation-frame specific forces.

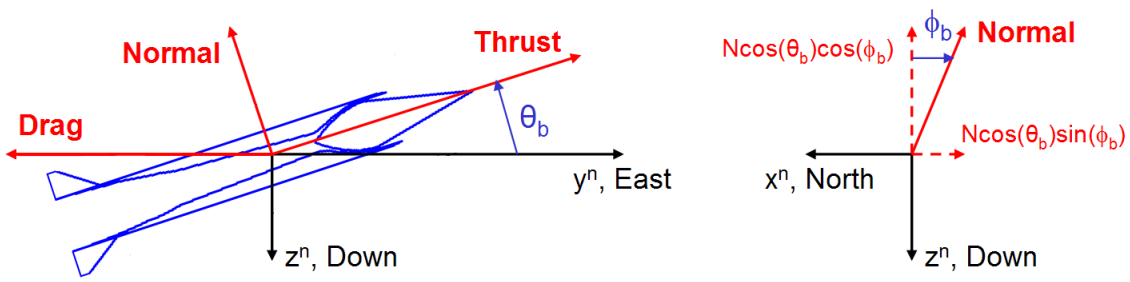

Figure 3.10: Scramjet Missile Free Body Diagram

3.3.1 Free Body Diagram & Cruise Dynamics

The dynamics of the missile are computed in the North-East-Down navigation frame (see Sec. 4.1.3 for details on the NED coordinate frame). The forces acting on the vehicle are the thrust, drag, and normal force as shown in Fig. 3.10. The gravitational, centripetal, and Coriolis accelerations are accounted for separately in the specific force term of the vehicle dynamics, see Eq. (3.84) on pg. 128. The scramjet thrust is assumed to be aligned with the body's line of symmetry which is inclined from the Easterly cruise by the pitch angle (or equivently α). The vehicle drag is defined as the sum of the profile drag and additive drag and is opposite of the velocity vector, *i.e.* in the West direction. The normal force is nominally in the body frame's "up" direction, but may also be rolled North or South to compensate for latitudinal gravitational variations during cruise. For all aerodynamic and propulsion force calculations, it is assumed that the vehicle is flying at a constant 1-atmosphere dyanmic pressure as discussed in Sec. 2.4.

The sum of these forces in the navigation frame are calculated as follows. The thrust is aligned predominately in the East direction, but also has a small component

in the negative Down ("up") direction, so that

$$\mathbf{T}^n = T(M_\infty, \alpha, ER)\,(0, \quad \cos\alpha, \quad -\sin\alpha)^T, \tag{3.73}$$

where the functional dependence of Mach number, angle of attack, and equivalence ratio on thrust is explicitly shown, and the angle of attack is used in place of the pitch angle to coincide with the standard aerodynamic/propulsion nomenclature in the majority of this chapter. The drag is simply in the West, and is a function of the freestream Mach number and angle of attack (due to the additive drag):

$$\mathbf{D}^n = (0, \quad -D(M_\infty, \alpha), \quad 0)^T. \tag{3.74}$$

Lastly, the normal force has a small component in the West direction due to the vehicle's angle of attack and its "up" component has a small portion of lift in the North/South axes:

$$\mathbf{N}^n = N(M_\infty, \alpha)\,(-\cos\alpha\sin\phi_b, \quad -\sin\alpha, \quad -\cos\alpha\cos\phi_b)^T. \tag{3.75}$$

Then setting the sum of these forces equal to the mass times the specific forces in the n-frame:

$$ma_N = -N(\alpha)\cos\alpha\sin\phi_b \tag{3.76a}$$

$$ma_E = T(\alpha, ER)\cos\alpha - D(\alpha) - N(\alpha)\sin\alpha \tag{3.76b}$$

$$ma_D = -T(\alpha, ER)\sin\alpha - N(\alpha)\cos\alpha\cos\phi_b, \tag{3.76c}$$

which is a set of three nonlinear equations with three unknowns (α, ϕ_b, and ER). The freestream Mach number dependence is dropped above because it will be assumed that the vehicle cruises at the constant, on-design Mach number throughout

the simulation. Also, the vehicle mass and specific forces on the left hand side of the equations are known quantities for a given position and velocity by Eq. (3.84) discussed in the following subsection. Therefore, the trim states $(\alpha^*, \phi_b^*, ER^*)$ are computed by solving Eq. (3.76a)–(3.76c) at each epoch along the trajectory given the calculated $m\mathbf{a}^n$.

The trim roll angle, ϕ_b^*, can be calculated as a function of the trim angle of attack, α^*, using Eq. (3.76a):

$$\phi_b^* = \sin^{-1}\left(\frac{-ma_N}{N(\alpha^*)\cos\alpha^*}\right). \tag{3.77}$$

The trim angle of attack (or trim pitch angle) is found by solving Eq. (3.76b) and (3.76c) for the thrust term and then dividing the Down equation from the East equation to remove the dependence on equivalence ratio:

$$\tan\alpha = \frac{-N(\alpha)\cos\alpha\cos\phi_b - ma_D}{N(\alpha)\sin\alpha + D(\alpha) + ma_E}. \tag{3.78}$$

Rearranging so that the roll angle term is isolated on the left hand side results in

$$-N(\alpha)\cos\alpha\cos\phi_b = (N(\alpha)\sin\alpha + D(\alpha) + ma_E)\tan\alpha + ma_D. \tag{3.79}$$

Squaring this equation, and then using the fact that $\sin^2\phi_b + \cos^2\phi_b = 1$ with Eq. (3.77) for the sine term, the roll dependence can be removed so that the entire expression is only a function of the trim angle of attack:

$$\begin{aligned} N^2(\alpha)\cos^2\alpha\cos^2\phi_b &= N^2(\alpha)\cos^2\alpha\left[1 - \left(\frac{ma_N}{N(\alpha)\cos\alpha}\right)^2\right] \\ N^2(\alpha)\cos^2\alpha - (ma_N)^2 &= \left[(N(\alpha)\sin\alpha + D(\alpha) + ma_E)\tan\alpha + ma_D\right]^2 \end{aligned} \tag{3.80}$$

Then rearranging slightly,

$$N^2(\alpha)\cos^2\alpha = \left[(N(\alpha)\sin\alpha + D(\alpha) + ma_E)\tan\alpha + ma_D\right]^2 + (ma_N)^2, \tag{3.81}$$

which is essentially a relationship for matching the lift and weight of the missile at the current epoch. This equation is only a function of the angle of attack and is numerically solved for the trim value, α^*, using a bisection method to bound the trim α from gridded aerodynamics tables of $N(\alpha)_{M_\infty=M_{des}}$ and $D(\alpha)_{M_\infty=M_{des}}$ and a false position method with cubic interpolation to refine the value.

The equivalence ratio is computing using Eq. (3.76b) after being rearranged slightly to

$$T(\alpha^*, ER)\cos\alpha^* = N(\alpha^*)\sin\alpha^* + D(\alpha^*) + ma_E. \tag{3.82}$$

This equation is effectively a higher-order $T = D$ constraint. The thrust's trim equivalence ratio is numerically calculated using a bisection and false position method with cubic interpolation and α^* from Eq. (3.81).

3.3.2 Simulated Pitch and Roll Rates

In order to calculate the trim states, the specific forces, $\mathbf{a}^n$, must be computed at each epoch along the trajectory. These quantities can be found from rearranging Eq. (4.47) on pg. 151 in terms of the specific force vector:

$$\mathbf{a}^n = \dot{\mathbf{v}}^n + (\Omega^n_{in} + \Omega^n_{ie})\,\mathbf{v}^n - \overline{\mathbf{g}}^n. \tag{3.83}$$

For the constant altitude, constant Eastern velocity trajectory assumed, $\dot{\mathbf{v}}^n = \mathbf{0}$, $\mathbf{v}^n = (0,\ v_E,\ 0)^T$, and $\dot{\phi} = \dot{h} = 0$. Then substituting these conditions into the expanded velocity dynamics of Eq. (4.49) on pg. 152 yields the trajectory's specific

force equation in the n-frame:

$$\mathbf{a}^n = \begin{pmatrix} a_N \\ a_E \\ a_D \end{pmatrix} = \begin{pmatrix} \left(\dot{\lambda} + 2\omega_e\right) v_E \sin\phi - \overline{g}_N \\ -\overline{g}_E \\ \left(\dot{\lambda} + 2\omega_e\right) v_E \cos\phi - \overline{g}_D \end{pmatrix}, \tag{3.84}$$

where $\dot{\lambda} = v_E / \left((N_e + h)\cos\phi\right)$. The details of these derivations and how the elements are calculated are explained in Ch. 4. The gravity acceleration vector, $\overline{\mathbf{g}}^n$, is calculated using the 360 degree and order EGM96 spherical harmonic model and the modified `geopot97` code as explained in Sec. 2.4. Table 2.2 on pg. 72 summarizes the cruise altitudes and velocities for the 1-atmosphere dynamic pressure, Mach 6, 7, and 8 designs.

Then, starting with the initial scramjet masses (Table 3.8 on pg. 122), the first trim state is computed from Eq. (3.81), (3.77), and (3.82). Using the trim equivalence ratio, ER^*, and the capture area at the design Mach number (which also equals the freestream Mach number) and trim angle of attack:

$$A_0^*(M_{des}, M_\infty, \alpha) = \left(\frac{A_0}{A_i}\right)_{M_{des}, M_\infty, \alpha^*} \left(\frac{A_i}{A_5}\right) A_5, \tag{3.85}$$

where $(A_5/A_i) = 1.1$ in this work and $A_5 = 0.785$ m^2 using $r_5 = 0.25$ m from the JHU/APL reference,[129] the fuel mass flow rate is

$$\dot{m}_f = \left(\frac{\dot{m}_f}{\dot{m}_0}\right) \dot{m}_0 = \left(ER^* f_{stoich}\right) \left(\rho_\infty v_E A_0^*\right), \tag{3.86}$$

where the stoichiometric fuel-to-air ratio is calculated by Eq. (3.71) on pg. 119 as 0.07066 and the freestream density at altitude is computed using the 1976 standard atmosphere model.[126] The mass of the scramjet is next reduced by Euler integration

at the 20 Hz simulation time step:

$$m(t + \Delta t) = m(t) - \dot{m}_f \Delta t. \tag{3.87}$$

The trim states are then recalculated and this process is repeated for the entire 1,000 km cruise trajectory.

The trim state and mass profiles are stored in memory and the pitch (angle of attack) and roll rates are computed by first-order forward finite differences of their respective trim values. The trim states, angular rates, and the mass profiles are written out as a text file for the 1,000 km downrange at the 20 Hz simulation time step. This file is then read in by the INS simulation and used as part of the simulated gyro signals.

The total simulated truth gyro signals are a sum of the navigation-to-inertial and the body-to-navigation frame rotations:

$$\boldsymbol{\omega}_{ib}^b = \boldsymbol{\omega}_{in}^b + \boldsymbol{\omega}_{nb}^b = C_n^b \boldsymbol{\omega}_{in}^n + \boldsymbol{\omega}_{nb}^b. \tag{3.88}$$

where C_n^b is computed using the INS truth quaternion as discussed in Sec. 4.3.3.1, $\boldsymbol{\omega}_{in}^n$ is calculated by Eq. (4.23) on pg. 144, and $\boldsymbol{\omega}_{nb}^b$ is found by Eq. (4.33) on pg. 147 using the roll and pitch rates ($\dot{\phi}_b$ and $\dot{\theta}_b$) calculated in this section. As a reminder, the yaw angle, ψ_b, is a constant 90° to ensure the Eastern flight, so its rate is always zero, *i.e.* $\dot{\psi}_b(t) = 0$.

Figure 3.11 plots the Mach 6, 7, and 8 trim roll and pitch rate profiles along with the trim equivalence ratio profile over the 1,000 km simulation. The high gravitational gradient variation trajectory results are shown in red solid lines and the low Γ^n variation trajectory is shown in blue dashed lines. (Section 2.4 details the

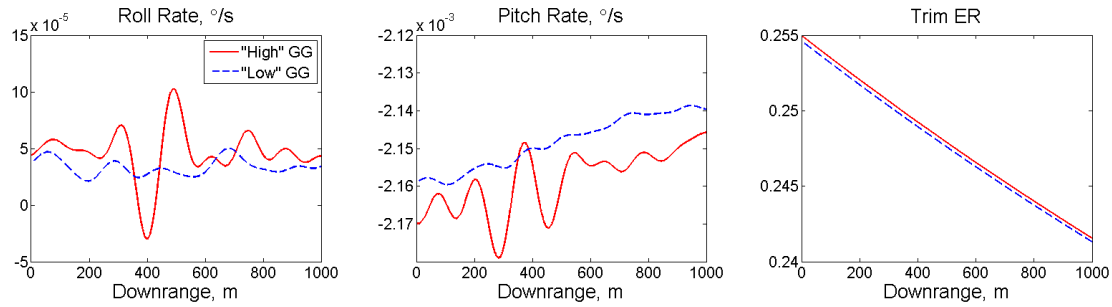

(a)

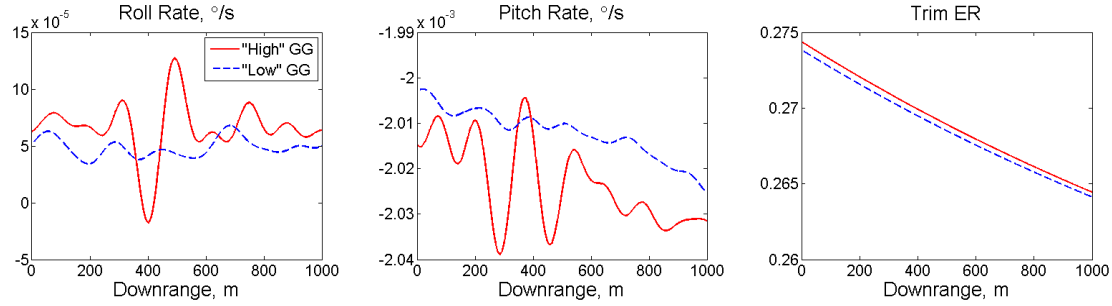

(b)

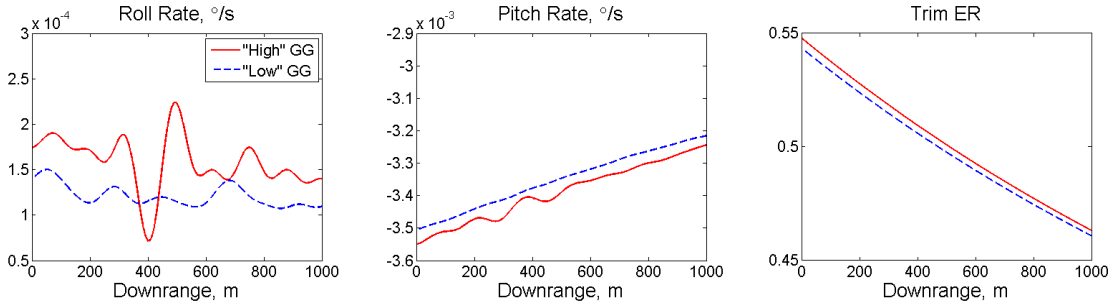

(c)

Figure 3.11: Trim Roll Rate, Pitch Rate, and Equivalence Ratio (a) Mach 6 (b) Mach 7 (c) Mach 8

Table 3.9: Scramjet Initial Trim Angles and Excess Fuel

M_{des}	Γ^n Var.	$\alpha^*(t_0)$	$\phi_b^*(t_0)$	$m_f(t_f)$
6	High	7.4721°	-4.6525°	2.70 kg
7	High	8.2970°	-6.2255°	54.38 kg
8	High	8.9666°	-8.1503°	6.51 kg
6	Low	7.4417°	-3.7964°	2.86 kg
7	Low	8.2524°	-5.0580°	54.43 kg
8	Low	8.9021°	-6.6034°	7.33 kg

two trajectories). The trim roll rates are quite insensitive to the simulation Mach number because they compensate for the (approximately same) small North/South deflections of the gravity vector. The trim pitch rate is negative throughout the simulation since the vehicle pitches down as fuel mass is expended and the lift required to match the weight of the vehicle is decreased. The equivalence ratio also decreases along the trajectory since the thrust level increases and the drag decreases as α^* decreases and also because the reduced vehicle mass requires less thrust compensation, as shown in Eq. (3.82).

Table 3.9 lists the initial trim pitch, $\alpha(t_0)$, and roll, $\phi_b^*(t_0)$, angles along with the excess fuel at the end of the simulation. The initial trim angles increase with higher Mach number primarily due to the increased initial mass of the higher speed vehicles which requires more lift and thus a higher α^*. The trim roll angle is coupled to the trim α by Eq. (3.77) on pg. 126 so that as the trim pitch angle increases the vehicle must roll more to compensate for the gravity vector deflection towards the South. The excess fuel mass is listed to show that the 17.3% fuel mass fraction is

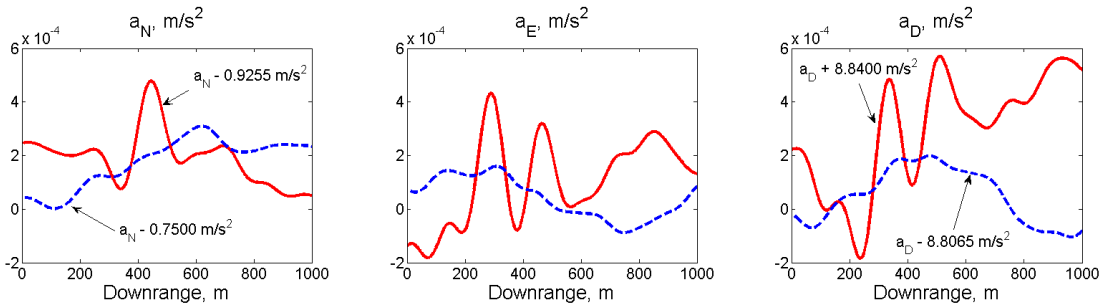

Figure 3.12: Trim Specific Forces, Mach 7

sufficient for each of the cruise simulations.

Figure 3.12 plots the simulated specific forces along the 1,000 km trajectory for the Mach 7 design. The Mach 6 and 8 systems are identical to these plots with the only difference being the bias of the North and Down specific forces caused by the $(\dot{\lambda} + 2\omega_e)v_E$ term in Eq. (3.84) on pg. 128. The variation of the signals in Fig. 3.12 are attributed solely to the gravitational field since the other terms in the specific force calculations are constant along the trajectory and the centripetal acceleration is constant for a constant latitude and altitude cruise.

3.4 Chapter Summary

This chapter details the hypersonic missile model used for the majority of the navigation simulations in Ch. 6. The first section consists of extensive curve fits from a JHU/APL reference[129] and an interpolation methodology to calculate the on- and off-design thrust, drag, and normal forces for several axisymmetric missile designs. (Appendix B includes additional thrust coefficient curve fits for the propulsion analysis.) Section 3.1.3 validates the implemented Fortran code to

the reference's[129] sample calculations and shows that the model used in this work is accurate to within 1% of the drag coefficient and 3% of the thrust coefficient computations.

Section 3.2 extends the original JHU/APL report to include a simple parametric mass model. Section 3.2.1 details the assumptions and calculations used to compute the total missile volume. Section 3.2.2 then explains the design constraints and assumptions used to determine the missile model's mass properties of 50% JP-10 fuel and 50% titanium structure by volume. The three scramjet designs ($M_\infty =$ 6, 7, and 8) are finally summarized in Sec. 3.2.3.

Section 3.3 incorporates the off-design angle of attack and equivalence ratio aerodynamic and propulsion performance developed in Sec. 3.1 and the mass model of Sec. 3.2 to compute the trim states along the 1,000 km cruise. Section 3.3.1 derives new trim relations to balance the forces of the vehicle using the angle of attack (pitch angle), roll angle, and equivalence ratio as the trim variables. Then Sec. 3.3.2 explains how the vehicle is numerically integrated along the 1,000 km range trajectory as mass is being expended and the vehicle is pitching, rolling, and throttling to maintain constant altitude and velocity cruise conditions. This section also details how the pitch (angle of attack) and roll angles are finite differenced to produce the navigation-to-body rotation rates needed for a portion of the simulated gyro signals in the INS dynamics, which are explained in the following chapter. Furthermore, the trim accelerometer specific forces are shown in this section, which are also derived thoroughly in the next INS chapter.

Chapter 4

Inertial Navigation System

In this chapter, the inertial navigation system (INS) model is derived. The chapter begins with a summary of the relevant coordinate frames needed and the transformations between these frames. Then the navigation equations used to numerically integrate the inertial measurements into velocity, position, and orientation information are derived. Lastly, the inertial measurement unit (IMU) characteristics are given along with the equations used to model their error behavior.

4.1 Coordinate Frames

4.1.1 Earth-Centered-Inertial Frame

The Earth-centered inertial, or "i-", frame is defined in such a way that Newton's laws of motion hold. According to his First Law, a body at rest (or constant velocity) will remain at rest (or constant velocity) in the absence of applied forces. And, according to his Second Law, the time rate of change of momentum is equal to the sum of forces applied:

$$\frac{d}{dt}\left(m_i \dot{\mathbf{r}}^i\right) = \mathbf{F}^i, \tag{4.1}$$

where m_i is the *inertial mass* of the object, $\dot{\mathbf{r}}^i$ is its linear velocity in the inertial frame, and $\mathbf{F}^i$ is the sum of the applied forces in the inertial frame. If the mass is constant, the more common

$$m_i \ddot{\mathbf{r}}^i = \mathbf{F}^i \tag{4.2}$$

expression is found, where $\ddot{\mathbf{r}}$ is now the linear acceleration of the object.

In order to use classical navigation theory, Newton's Second Law must be modified with a gravitational term. This modification is necessitated by the fact that the gravitational field is a *kinematic force* that induces accelerations that are independent of mass, which causes different behavior than the externally applied force, $\mathbf{F}^i$, that Newton described (Jekeli,[1] pg. 4). Thus, Eq. (4.2) becomes

$$m_i \ddot{\mathbf{r}}^i = \mathbf{F}^i + m_g \mathbf{g}^i \tag{4.3}$$

where the second term is the force due to the gravitational field from Earth's mass attracting the user. Specifically, m_g is the *gravitational mass* and $\mathbf{g}$ is the gravitational vector. Now, invoking the Weak Equivalence Principle, which essentially states that an object will accelerate at the same rate regardless of its mass, one can equate the inertial and gravitational masses $m_i = m_g = m$. This gives the relation:

$$\ddot{\mathbf{r}}^i = \mathbf{a}^i + \mathbf{g}^i, \tag{4.4}$$

where $\mathbf{a}^i = \mathbf{F}/m$ is the *specific force* or acceleration due to applied forces in the inertial frame. Furthermore, $\mathbf{a}$ is the sensed quantity measured by the accelerometers because the proof mass in the accelerometer behaves identically to linear and gravitational accelerations (except in opposite signs). For a more thorough discussion of these concepts, the reader may consult Jekeli[1] pg. 3–6.

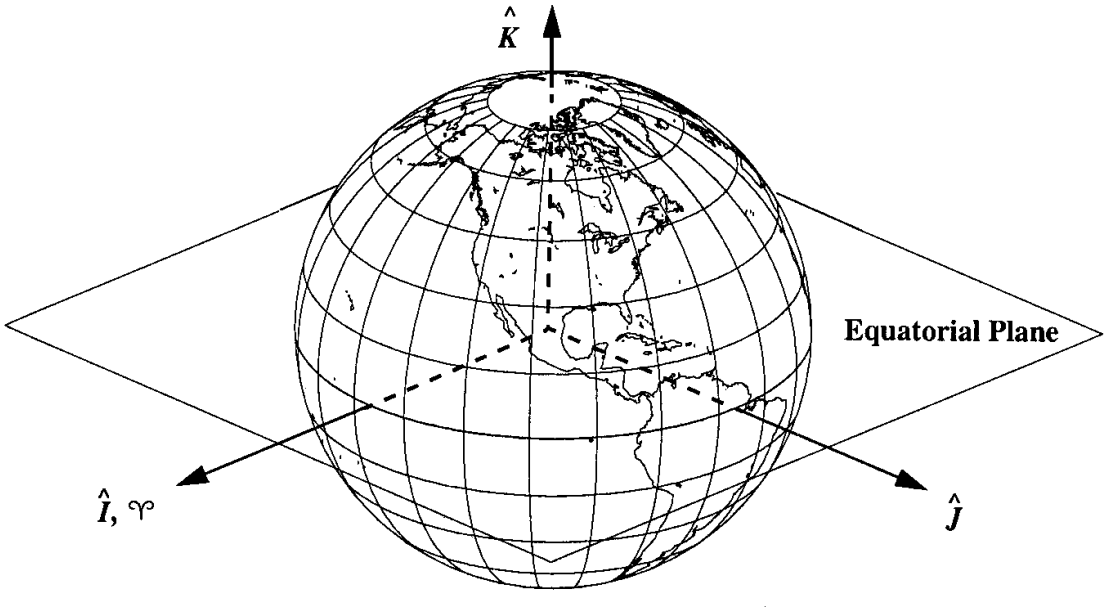

Figure 4.1: Earth-Centered-Inertial Coordinate System, from Ref. [115]

Now, the inertial frame is defined as follows for terrestrial navigation. The Earth-Centered-Inertial (ECI) frame is a non-rotating rectilinear coordinate system with its origin located at the Earth's center (See Fig. 4.1, from Vallado,[115] pg. 157). The 1-axis ($\widehat{I}$ in the figure) points to the mean vernal equinox, the 3-axis ($\widehat{K}$) is aligned with the Earth's spin axis through the North pole, and the 2-axis ($\widehat{J}$) completes the right hand orthogonal coordinate system. Technically, this frame is not truly inertial. Although the coordinate system does not rotate with respect to the stars, the frame's center is accelerating due to the Earth's rotation around the Sun.

4.1.2 Earth-Centered-Earth-Fixed Frame

The Earth-Centered-Earth-Fixed (ECEF) or "e-" frame is similar to the inertial frame except it rotates with the Earth. The coordinate system origin is still at

the Earth's center and the 3-axis is aligned with the spin axis through the North pole; however, the 1-axis now points through the mean Greenwich meridian at the equator. The 2-axis completes a right hand orthogonal frame. This frame is particularly notable for its use within the Global Positioning System's satellite broadcast (App. D).

4.1.3 Navigation Frame

The Navigation or "n-" frame is a local geodetic system that will serve as the primary frame of interest (See Fig. 4.2). The frame has its origin at the vehicle's center of mass and it's 1-axis points North, 3-axis points down (perpendicular to the local Earth ellipsoid's surface), and the 2-axis completes the right hand convention such that it points East. Other n-frame variations exist such as East-North-Up and South-East-Up; however, North-East-Down is the most common orientation and will be used throughout this work.

4.1.4 Body Frame

The Body or "b-" frame is also a local system whose origin is located at the vehicle's center of mass. The 1-axis is aligned to point through the front, the 2-axis through the right, and the 3-axis down through the floor, as shown in Fig. 4.3. The inertial measurement units (IMUs) used in this study are all assumed to be strap-down systems where the accelerometers and gyros are aligned the b-frame axes. As discussed later in Sec. 4.5.1, the truth accelerometer and gyro coordinate systems

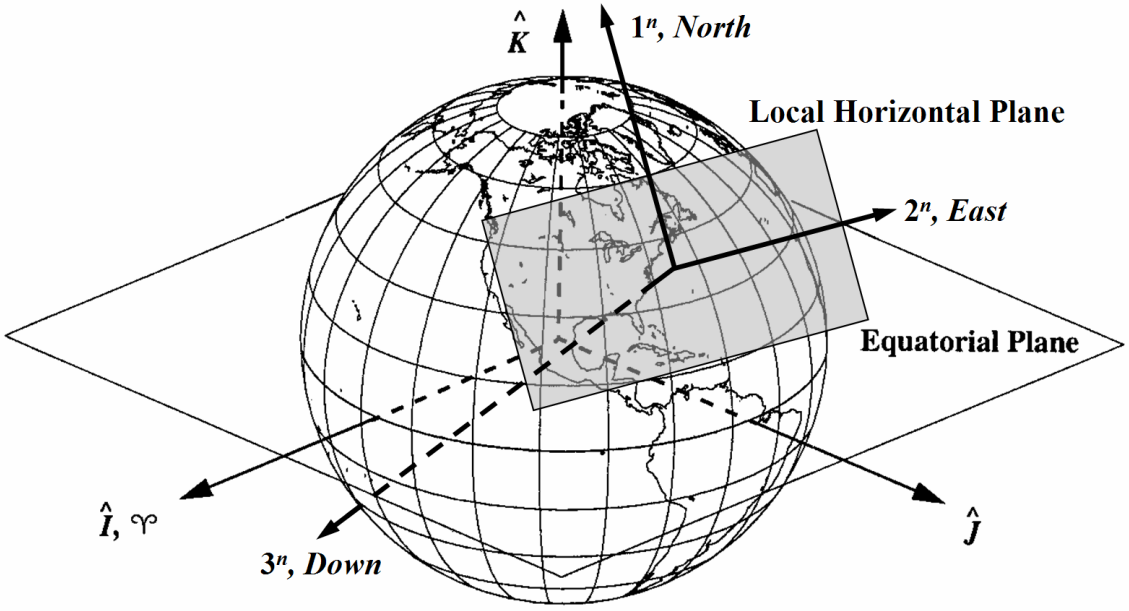

Figure 4.2: Navigation Frame (North-East-Down) Coordinate System, modified from Ref. [115]

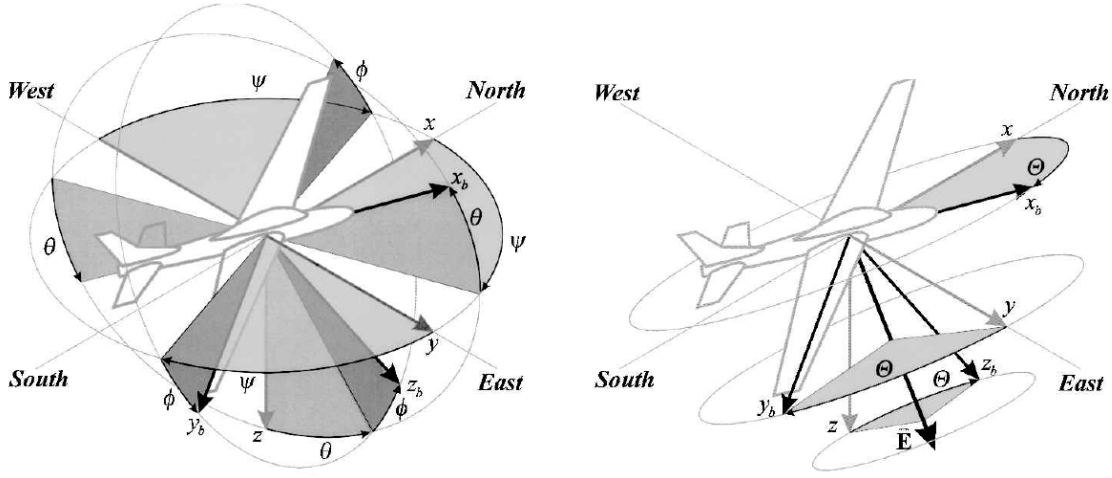

Figure 4.3: Body Frame Coordinate System and Euhler Angles, from Ref. [145]

were originally perturbed slightly from the true body frame to add uncompensated errors to the system. Unfortunately, this addition caused may of the INS/GGI simulations to diverge, so these errors were decided to be removed for the simulations.

4.2 Coordinate Transformations

4.2.1 Fundamental Concepts

This subsection explains the concepts used in the subsequent sections which describe specific coordinate transformations. First, transformation (direction cosine) matrices and their properties will be discussed. Then Euler angles and their small angle approximations will be presented. This section will conclude with the definition of the time rate of change of a coordinate transformation matrix.

Assume a single point defined in two frames so that its three-element position vector is defined as $\mathbf{r}^s$ in the first arbitrary frame and $\mathbf{r}^t$ in the second arbitrary frame. The transformation matrix from the first frame to the second, C_s^t, is defined to satisfy

$$\mathbf{r}^t = C_s^t \mathbf{r}^s. \tag{4.5}$$

And the elements of the transformation matrix are

$$c_{i,j} = \mathbf{e}_i^s \cdot \mathbf{e}_j^t = cos(\theta), \tag{4.6}$$

where $\mathbf{e}_i^s$ is the unit vector along the i^{th} axis of the s-frame, $\mathbf{e}_j^t$ is similarly defined, and θ is the angle between $\mathbf{e}_i^s$ and $\mathbf{e}_j^t$. Therefore, the elements of the transformation matrix are equivalent to the cosine of the angles between the frame axes, and thus

commonly referred to as a *direction cosine matrix*.

The transformation matrix is also an orthogonal matrix and has the property that its inverse is equivalent to its transpose, which is also equivalent to the transformation matrix from the t-frame to the s-frame. Mathematically,

$$\left(C_s^t\right)^{-1} = \left(C_s^t\right)^T = C_t^s. \tag{4.7}$$

The transformation matrix could also be formulated as a series of specific rotations about three axes. Assuming the first rotation is α about the 1-axis of the s-frame, the second rotation is β about the newly defined "2-axis," and the last rotation is γ about the newest "3-axis,"

$$\begin{aligned} C_s^t &= R_3(\gamma)R_2(\beta)R_1(\alpha) \qquad (4.8)\\ &= \begin{pmatrix} \cos\gamma & \sin\gamma & 0 \\ -\sin\gamma & \cos\alpha & 0 \\ 0 & 0 & 1 \end{pmatrix} \begin{pmatrix} \cos\beta & 0 & -\sin\beta \\ 0 & 1 & 0 \\ \sin\beta & 0 & \cos\beta \end{pmatrix} \begin{pmatrix} 1 & 0 & 0 \\ 0 & \cos\alpha & \sin\alpha \\ 0 & -\sin\alpha & \cos\alpha \end{pmatrix} \\ &= \begin{pmatrix} c(\gamma)c(\beta) & c(\gamma)s(\beta)s(\alpha)+s(\gamma)c(\alpha) & -c(\gamma)s(\beta)c(\alpha)+s(\gamma)s(\alpha) \\ -s(\gamma)c(\beta) & -s(\gamma)s(\beta)s(\alpha)+c(\gamma)c(\alpha) & s(\gamma)s(\beta)c(\alpha)+c(\gamma)s(\alpha) \\ s(\beta) & -c(\beta)s(\alpha) & c(\beta)c(\alpha) \end{pmatrix}, \end{aligned}$$

where $c()$ denotes cosine and $s()$ denotes sine in the last equality. The rotation angles can also be calculated from a given transformation matrix using its elements:

$$\alpha = tan^{-1}\left(\frac{-c_{3,2}}{c_{3,3}}\right), \quad \beta = sin^{-1}\left(c_{3,1}\right), \quad \gamma = tan^{-1}\left(\frac{-c_{2,1}}{c_{1,1}}\right). \tag{4.9}$$

If α, β, and γ are assumed to be small angles, then $\cos\theta \approx 1$ and $\sin\theta \approx \theta$

(where θ is an arbitrary small angle). Neglecting second-order small angles,

$$\begin{aligned} C_s^t &\approx \begin{pmatrix} 1 & \gamma & -\beta \\ -\gamma & 1 & \alpha \\ \beta & -\alpha & 1 \end{pmatrix} = \begin{pmatrix} 1 & 0 & 0 \\ 0 & 1 & 0 \\ 0 & 0 & 1 \end{pmatrix} - \begin{pmatrix} 0 & -\gamma & \beta \\ \gamma & 0 & -\alpha \\ -\beta & \alpha & 0 \end{pmatrix} \\ &\approx I - \Psi, \end{aligned} \tag{4.10}$$

where I is a 3×3 identity matrix and Ψ is the *skew symmetric matrix* of $\boldsymbol{\psi} = (\alpha, \beta, \gamma)^T$ which is equivalent to $\boldsymbol{\psi} \times ()$, see Eq. (4.18). Using Eq. (4.7),

$$C_t^s = \left(C_s^t\right)^T \approx I + \Psi \tag{4.11}$$

for small rotation angles.

The transformation of a second order tensor from one frame to another requires two direction cosine matrix multiplications. This can be proven as follows. Starting with an arbitrary linear equation in the arbitrary s-frame,

$$\mathbf{y}^s = A^s \mathbf{x}^s \tag{4.12}$$

and the transformations for each vector,

$$\mathbf{x}^s = C_t^s \mathbf{x}^t; \quad \mathbf{y}^s = C_t^s \mathbf{y}^t, \tag{4.13}$$

where the t-frame is also arbitrary, one can substitute these relations into Eq. (4.12) above to get

$$C_t^s \mathbf{y}^t = A^s C_t^s \mathbf{x}^t. \tag{4.14}$$

Then using the property that the inverse of the transformation matrix is equal to its transpose, Eq. (4.7), $\mathbf{y}^t$ can be solved as

$$\mathbf{y}^t = C_s^t A^s C_t^s \mathbf{x}^t = A^t \mathbf{x}^t. \tag{4.15}$$

Therefore, pre- and post-multiplication of a coordinate transformation matrix is needed to rotate a tensor from one frame to another, *i.e.*,

$$A^t = C_s^t A^s C_t^s. \tag{4.16}$$

The last concept to discuss is the time rate of change of C_s^t. It can be shown that (Jekeli,[1] pg. 21)

$$\dot{C}_s^t = C_s^t \Omega_{ts}^s, \tag{4.17}$$

where Ω_{ts}^s is the *skew symmetric matrix* for the transformation matrix's rotation rate $\boldsymbol{\omega}_{ts}^s$. If $\boldsymbol{\omega}_{ts}^s = (\omega_1, \omega_2, \omega_3)^T$, then Ω_{ts}^s is equivalent to $\boldsymbol{\omega}_{ts}^s \times ()$ and defined as

$$\Omega_{ts}^s = \begin{pmatrix} 0 & -\omega_3 & \omega_2 \\ \omega_3 & 0 & -\omega_1 \\ -\omega_2 & \omega_1 & 0 \end{pmatrix}. \tag{4.18}$$

The terminology of the angular rate subscripts and superscripts should be clarified at this point. An arbitrary rotation rate, $\boldsymbol{\omega}_{sr}^t$, is the angular velocity of the arbitrary r-frame with respect to the s-frame, but with coordinates in the t-frame. The terminology for an arbitrary skew symmetric matrix, Ω_{sr}^t, is the same.

4.2.2 ECEF to ECI Transformation

Neglecting Earth's polar axis motion and any nutation of its spin axis, the rotation between the Earth-Centered-Earth-Fixed (ECEF) and Earth-Centered-Inertial (ECI) frames can be estimated as a single rotation about the Earth's spin axis, *i.e.*, the 3-axis of both frames (Jekeli,[1] pg. 22). The rotation rate of the Earth can also be assumed a constant, ω_e, and the total rotation between the e-frame and i-frame

is then $\omega_e t$. The rotation rate vector from ECEF to ECI, with coordinates in the e-frame is

$$\boldsymbol{\omega}_{ie}^{e} = (0, \quad 0, \quad \omega_e)^T, \tag{4.19}$$

and the transformation matrix from the i-frame to the e-frame is

$$C_i^e = R_3(\omega_e t) = \begin{pmatrix} \cos\omega_e t & \sin\omega_e t & 0 \\ -\sin\omega_e t & \cos\omega_e t & 0 \\ 0 & 0 & 1 \end{pmatrix}. \tag{4.20}$$

4.2.3 Navigation to ECEF Transformation

The navigation frame can be transformed to the e-frame by two rotations. The first rotation is about the n-frame's 2-axis (East) to align the n-frame's 3-axis with the Earth's spin axis (ECEF 3-axis). A rotation about the spin axis is then performed to align the 1- and 2- axes. Denoting the geodetic latitude as ϕ and geodetic longitude as λ, the n-frame to e-frame transformation matrix is

$$C_n^e = R_3(-\lambda)R_2(\frac{\pi}{2} + \phi) = \begin{pmatrix} -\sin\phi\cos\lambda & -\sin\lambda & -\cos\phi\cos\lambda \\ -\sin\phi\sin\lambda & \cos\lambda & -\cos\phi\sin\lambda \\ \cos\phi & 0 & -\sin\phi \end{pmatrix}. \tag{4.21}$$

Solving Eq. (4.17) for the rotation rate vector gives

$$\boldsymbol{\omega}_{en}^{n} = \left(\dot{\lambda}\cos\phi, \quad -\dot{\phi}, \quad -\dot{\lambda}\sin\phi\right)^T, \tag{4.22}$$

where $\dot{\phi}$ is the angular rate of latitude and $\dot{\lambda}$ is the longitude rate.

The rotation rate of the navigation frame with respect to the inertial frame will also be used. This rotation rate is calculated by noting $\boldsymbol{\omega}_{in}^{n} = \boldsymbol{\omega}_{ie}^{n} + \boldsymbol{\omega}_{en}^{n}$ and

$\boldsymbol{\omega}_{ie}^{n} = C_{e}^{n}\boldsymbol{\omega}_{ie}^{e}$. Therefore, using Eq. (4.19), (4.21), and (4.22),

$$\boldsymbol{\omega}_{in}^{n} = \left((\dot{\lambda} + \omega_e)\cos\phi, \quad -\dot{\phi}, \quad -(\dot{\lambda} + \omega_e)\sin\phi\right)^{T}. \tag{4.23}$$

To conclude this subsection, the relationship between the navigation frame position coordinates (ϕ, λ, h) and the ECEF position coordinates will be given. This transformation will be useful in calculating the GPS measurements and the geometric dilution of precision (GDOP). This relationship is (Torge,[143] pg. 99–100 or Jekeli,[1] pg. 23)

$$\begin{pmatrix} r_1^e \\ r_2^e \\ r_3^e \end{pmatrix} = \begin{pmatrix} (N_e + h)\cos\phi\cos\lambda \\ (N_e + h)\cos\phi\sin\lambda \\ (N_e(1 - e^2) + h)\sin\phi \end{pmatrix}, \tag{4.24}$$

where N_e is the radius of curvature in the prime vertical plane and e^2 is the first eccentricity of the Earth ellipsoid squared. For completeness, M_e is the radius of curvature in the meridian, and all three properties are defined as

$$N_e = \frac{a_a}{\sqrt{1 - e^2\sin^2\phi}}, \tag{4.25}$$

$$e^2 = \frac{\sqrt{a_e^2 - b_e^2}}{a_e^2} = 2f_e - f_e^2, \tag{4.26}$$

where a_e is Earth's semimajor axis, b_e is the semimajor axis, f_e is the flatness of Earth's ellipsoid, and

$$M_e = \frac{a_e(1 - e^2)}{(1 - e^2\sin^2\phi)^{3/2}}. \tag{4.27}$$

Figure 4.4 illustrates several of these parameters with reference to a simplified Earth ellipsoid, from Jekeli,[1] pg. 23.

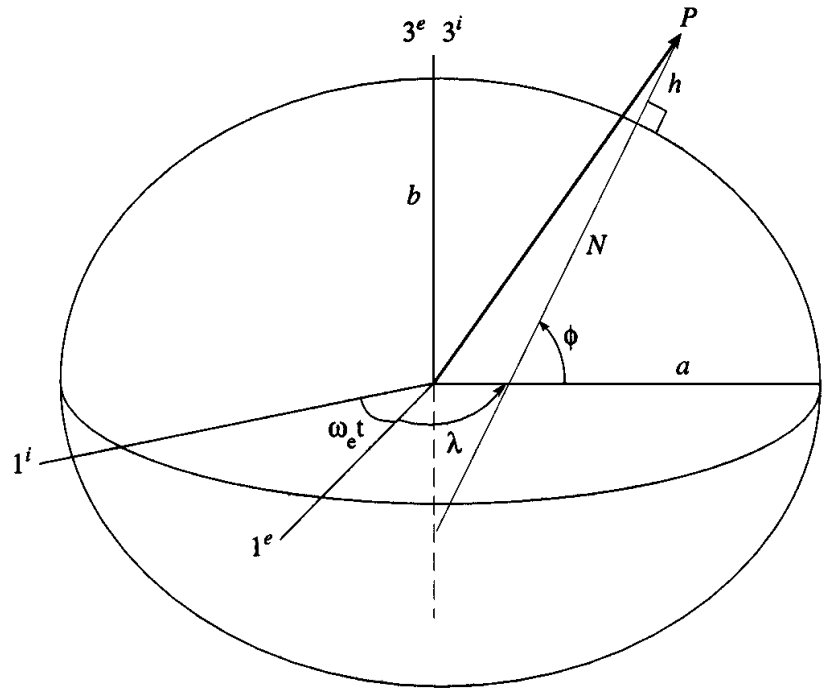

Figure 4.4: Coordinate System Transformation, from Ref. [1]

Table 4.1: World Geodetic System 1984 Properties

Parameter Name	Symbol	WGS84 Value
Semi-Major Axis	a_e	6,378,137.0 m
Semi-Minor Axis	b_e	6,356,752.3142 m
First Eccentricity Squared	e^2	$6.694\ 379\ 990\ 14 \times 10^{-3}$
Reciprocal of Flattening	$1/f_e$	298.257 223 563
Earth's Gravitational Constant	GM	$3.986\ 004\ 418 \times 10^{14}$ m^3/s^2
Earth's Rotation Rate	ω_e	$7.292\ 115\ 0 \times 10^{-5}$ rad/s

The values for the Earth ellipsoid, defined by the Department of Defense's World Geodetic System 1984 (and used in the EGM96 spherical harmonic model) are summarized in Table 4.1.[113]

4.2.4 Body to Navigation Transformation

The body to navigation frame transformation is comprised of three rotations. The first rotation is a negative roll ($-\phi_b$) about the b-frame's 1-axis, followed by a negative pitch ($-\theta_b$) rotation about the new 2-axis, and concluded with a negative yaw ($-\psi_b$) rotation about the newest 3-axis. Since matrix multiplication is not communicative (*i.e.*, $AB \neq BA$), the Euler angles of this transformation (roll, pitch, and yaw) are defined by the order of rotations above, as shown in Fig. 4.3 on pg. 138. Mathematically, the body to navigation rotation matrix is

$$C_b^n = R_3(-\psi_b)R_2(-\theta_b)R_1(-\phi_b), \tag{4.28}$$

or when expanded:

$$C_b^n = \begin{pmatrix} c(\psi_b)c(\theta_b) & c(\psi_b)s(\theta_b)s(\phi_b) - s(\psi_b)c(\phi_b) & c(\psi_b)s(\theta_b)c(\phi_b) + s(\psi_b)s(\phi_b) \\ s(\psi_b)c(\theta_b) & s(\psi_b)s(\theta_b)s(\phi_b) + c(\psi_b)c(\phi_b) & s(\psi_b)s(\theta_b)c(\phi_b) - c(\psi_b)s(\phi_b) \\ -s(\theta_b) & c(\theta_b)s(\phi_b) & c(\theta_b)c(\phi_b) \end{pmatrix}, \tag{4.29}$$

where $c()$ denotes cosine and $s()$ denotes sine. The Euler angles can also be found using the C_b^n coefficients, similar to Eq. (4.9), by

$$\phi_b = tan^{-1}\left(\frac{c_{3,2}}{c_{3,3}}\right), \quad \theta_b = -sin^{-1}\left(c_{3,1}\right), \quad \psi_b = tan^{-1}\left(\frac{c_{2,1}}{c_{1,1}}\right). \tag{4.30}$$

The relationship between the Euler angle rates and the rotation matrix rates are also based on the specific rotation order. If b_1 is defined as the frame that θ_b rotates about and b_2 as the frame that ψ_b rotates about, the transformation matrix can be rewritten as

$$C_b^n = C_{b_2}^n C_{b_1}^{b_2} C_b^{b_1}. \tag{4.31}$$

The rotation rate of the matrix can also be decomposed into the three rotations due to each of the Euler angle rates ($\dot{\phi}_b$,$\dot{\theta}_b$,$\dot{\psi}_b$):

$$\begin{aligned} \boldsymbol{\omega}_{nb}^b &= \boldsymbol{\omega}_{nb_2}^b + \boldsymbol{\omega}_{b_2b_1}^b + \boldsymbol{\omega}_{b_1b}^b = C_{b_1}^b C_{b_2}^{b_1} \boldsymbol{\omega}_{nb_2}^{b_2} + C_{b_1}^b \boldsymbol{\omega}_{b_2b_1}^{b_1} + \boldsymbol{\omega}_{b_1b}^b \\ &= C_{b_1}^b C_{b_2}^{b_1} \begin{pmatrix} 0 \\ 0 \\ \dot{\psi}_b \end{pmatrix} + C_{b_1}^b \begin{pmatrix} 0 \\ \dot{\theta}_b \\ 0 \end{pmatrix} + \begin{pmatrix} \dot{\phi}_b \\ 0 \\ 0 \end{pmatrix}. \end{aligned} \tag{4.32}$$

Using Eq. (4.28) and (4.31), it can be shown that $C_{b_2}^{b_1} = R_2(\theta_b)$ and $C_{b_1}^b = R_1(\phi_b)$. Then, substituting back in and arranging, the rotation rate of the body-to-navigation frame transformation matrix is

$$\boldsymbol{\omega}_{nb}^b = \begin{pmatrix} 1 & 0 & -\sin\theta_b \\ 0 & \cos\phi_b & \cos\theta_b \sin\phi_b \\ 0 & -\sin\phi_b & \cos\theta_b \cos\phi_b \end{pmatrix} \begin{pmatrix} \dot{\phi}_b \\ \dot{\theta}_b \\ \dot{\psi}_b \end{pmatrix}, \tag{4.33}$$

where the Euler angle rates are given by the time rate of change of the trim profiles as discussed in Sec. 3.3.2.

Sec. 4.3.3.1 dicusses the quaternion equivalent to this section, which is used for more stable numerical integration.

4.3 Inertial Navigation Equations

In this section, the inertial navigation equations are derived and their numerical mechanization is presented. The navigation equations illustrate how the measured specific forces and angular rates are integrated into meaningful position, velocity, and attitude information. The derivation of the equations are first presented for an arbitrary frame and then specified to the n-frame. Quaternions are also discussed as a means of integrating the body to navigation rotation matrix. Lastly, the classical fourth-order Runge-Kutta algorithm is described as it is used to integrate the inertial navigation system (INS) states and the rotation quaternion.

4.3.1 Arbitrary Frame Equations

Before focusing on the rotating n-frame navigation equations, the dynamic equations in an arbitrary frame will be investigated. This subsection will thus illuminate the acceleration sources present for any possible coordinate system. The next subsection will then use these results in the derivation of the n-frame navigation equations that were implemented in this work.

The derivation starts with a point in an arbitrary frame, $\mathbf{r}^a$, and the transformation from an initial arbitrary frame to an inertial frame, C_a^i, so that

$$\mathbf{r}^i = C_a^i \mathbf{r}^a. \tag{4.34}$$

Then, using the chain rule to differentiate Eq. (4.34) with respect to time gives

$$\dot{\mathbf{r}}^i = C_a^i \Omega_{ia}^a \mathbf{r}^a + C_a^i \dot{\mathbf{r}}^a, \tag{4.35}$$

where Eq. (4.17) on pg. 142 is used for the rotation matrix derivative term. Taking the derivative with respect to time again and arranging gives

$$\ddot{\mathbf{r}}^i = C_a^i \ddot{\mathbf{r}}^a + 2C_a^i \Omega_{ia}^a \dot{\mathbf{r}}^a + C_a^i \left(\Omega_{ia}^a \Omega_{ia}^a + \dot{\Omega}_{ia}^a \right) \mathbf{r}^a = \mathbf{a}^i + \mathbf{g}^i, \tag{4.36}$$

where Eq. (4.4) on pg. 135 is used for the second equality. Solving for the arbitrary-frame acceleration now gives

$$\ddot{\mathbf{r}}^a = -2\Omega_{ia}^a \dot{\mathbf{r}}^a - \left(\Omega_{ia}^a \Omega_{ia}^a + \dot{\Omega}_{ia}^a \right) \mathbf{r}^a + \mathbf{a}^a + \mathbf{g}^a, \tag{4.37}$$

where $\mathbf{a}^a \equiv C_i^a \mathbf{a}^i$ and $\mathbf{g}^a \equiv C_i^a \mathbf{g}^i$. The first term in Eq. (4.37) is the Coriolis acceleration due to an object having a velocity in a rotating frame. The first part of the parenthetic term is the centrifugal acceleration felt by the object as the frame rotates, and the second term in the parenthesis is due to the frame's angular acceleration.

Equation (4.37) is a second order differential equation describing the acceleration of a system that has the current velocity, $\dot{\mathbf{r}}^a$, and position states, $\mathbf{r}^a$, being forced be an $\mathbf{a}^a$ and $\mathbf{g}^a$. Most second order systems are solved by splitting the system into two first order systems as such:

$$\begin{aligned} \frac{d}{dt}\dot{\mathbf{r}}^a &= -2\Omega_{ia}^a \dot{\mathbf{r}}^a - \left(\Omega_{ia}^a \Omega_{ia}^a + \dot{\Omega}_{ia}^a \right) \dot{\mathbf{r}}^a + \mathbf{a}^a + \mathbf{g}^a, \\ \frac{d}{dt}\mathbf{r}^a &= \dot{\mathbf{r}}^a. \end{aligned} \tag{4.38}$$

The system states (position and velocity, along with the transformation matrix) can now be solved using a numerical integration algorithm for first order systems (Sec. 4.3.3). For strapdown accelerometers, the specific force in the a-frame is calculated

by transforming the accelerometer readings in the b-frame to the arbitrary frame with the current estimated C_b^a rotation matrix:

$$\mathbf{a}^a = C_b^a \mathbf{a}^b. \tag{4.39}$$

The rotation matrix, C_b^a, is integrated according to Eq. (4.17) on pg. 142, and the rotation rate vector is given by

$$\boldsymbol{\omega}_{ab}^b = \boldsymbol{\omega}_{ib}^b - C_a^b \boldsymbol{\omega}_{ia}^a, \tag{4.40}$$

where $\boldsymbol{\omega}_{ib}^b$ is the gyro measurement and $\boldsymbol{\omega}_{ia}^a$ is the calculated rotation rate of the arbitrary frame to the inertial with coordinates in the a-frame using the current INS states.

4.3.2 Navigation Frame Equations

This section uses the results from the previous section to derive the North-East-Down (n-frame) navigation equations. The navigation frame mechanization is noticeably different than other mechanizations[1,2] (namely the i-frame or e-frame) because the velocity variables, $\mathbf{v}^n = (v_N, v_E, v_D)^T$, are not the time rate of change of the position variables, $\mathbf{r}^n = (\phi, \lambda, h)^T$. Instead, the n-frame velocities are defined as

$$\mathbf{v}^n = C_e^n \dot{\mathbf{r}}^e, \tag{4.41}$$

where $\dot{\mathbf{r}}^e$ is the ECEF velocity vector. The n-frame position is similarly defined.

Taking the derivative of Eq. (4.41) and using Eq. (4.17) for the rotation matrix derivative,

$$\dot{\mathbf{v}}^n = C_e^n \Omega_{ne}^e \dot{\mathbf{r}}^e + C_e^n \ddot{\mathbf{r}}^e. \tag{4.42}$$

Substituting Eq. (4.37) on pg. 149 with the arbitrary frame now being the ECEF frame, noting that the Earth rotates at a constant rate ($\dot{\Omega}^e_{ie} = 0$) and, by definition, $\dot{\mathbf{r}}^e = C^e_n \mathbf{v}^n$, we now have

$$\dot{\mathbf{v}}^n = C^n_e \Omega^e_{ne} C^e_n \mathbf{v}^n - 2C^n_e \Omega^e_{ie} C^e_n \mathbf{v}^n - C^n_e \Omega^e_{ie} \Omega^e_{ie} \mathbf{r}^e + \mathbf{a}^n + \mathbf{g}^n, \tag{4.43}$$

where $\mathbf{a}^n = C^n_e \mathbf{a}^e$ and $\mathbf{g}^n = C^n_e \mathbf{g}^e$. Next, it can be shown that $C^n_e \Omega^e_{ne} C^e_n = \Omega^n_{ne}$ and similarly, $C^n_e \Omega^e_{ie} C^e_n = \Omega^n_{ie}$ using Eq. (4.16) on pg. 142. By inspection, one also has $\Omega^n_{ne} = -\Omega^n_{en}$. So,

$$\dot{\mathbf{v}}^n = -\left(\Omega^n_{en} + 2\Omega^n_{ie}\right) \mathbf{v}^n + \mathbf{a}^n + \overline{\mathbf{g}}^n, \tag{4.44}$$

where

$$\overline{\mathbf{g}}^n \equiv \mathbf{g}^n - C^n_e \Omega^e_{ie} \Omega^e_{ie} \mathbf{r}^e, \tag{4.45}$$

which is the sum of the gravitational acceleration due to mass attraction and the centrifugal acceleration, more commonly referred to as *gravity*. Lastly, we can rearrange the angular rate matrices because $\Omega^n_{ie} = \Omega^n_{in} + \Omega^n_{ne}$, so

$$\begin{aligned} \Omega^n_{en} + 2\Omega^n_{ie} &= \Omega^n_{en} + \Omega^n_{ie} + (\Omega^n_{in} + \Omega^n_{ne}) \\ &= \Omega^n_{en} + \Omega^n_{ie} + (\Omega^n_{in} - \Omega^n_{en}) \\ &= \Omega^n_{ie} + \Omega^n_{in}. \end{aligned} \tag{4.46}$$

Substituting back into Eq. (4.44), the velocity navigation equations are finally

$$\dot{\mathbf{v}}^n = -\left(\Omega^n_{in} + \Omega^n_{ie}\right) \mathbf{v}^n + \mathbf{a}^n + \overline{\mathbf{g}}^n, \tag{4.47}$$

where the gravity term is defined in Eq. (4.45).

The skew symmetric matrices that multiply the velocity vector are found as follows. The navigation frame to inertial frame rotation rate, $\boldsymbol{\omega}^n_{in}$, is given by Eq. (4.23)

on pg. 144, and the ECEF to ECI rotation, $\boldsymbol{\omega}_{ie}^{n}$, is calculated by multiplying the transpose of Eq. (4.21) and $\boldsymbol{\omega}_{ie}^{e}$ from Eq. (4.19) on pg. 143. With the skew symmetric definition, Eq. (4.18), the matrices are

$$-\left(\Omega_{in}^{n}+\Omega_{ie}^{n}\right)=\begin{pmatrix} 0 & -(\dot{\lambda}+2\omega_e)\sin\phi & \dot{\phi} \\ (\dot{\lambda}+2\omega_e)\sin\phi & 0 & (\dot{\lambda}+2\omega_e)\cos\phi \\ -\dot{\phi} & -(\dot{\lambda}+2\omega_e)\cos\phi & 0 \end{pmatrix}. \tag{4.48}$$

The velocity navigation equations are then

$$\dot{\mathbf{v}}^{n}=\begin{pmatrix} \dot{v}_N \\ \dot{v}_E \\ \dot{v}_D \end{pmatrix}=\begin{pmatrix} -(\dot{\lambda}+2\omega_e)v_E\sin\phi+v_D\dot{\phi}+a_N+\overline{g}_N \\ (\dot{\lambda}+2\omega_e)(v_N\sin\phi+v_D\cos\phi)+a_E+\overline{g}_E \\ -v_N\dot{\phi}-(\dot{\lambda}+2\omega_e)v_E\cos\phi+a_D+\overline{g}_D \end{pmatrix}. \tag{4.49}$$

The navigation equations for the position states are much simpler to derive. Starting with the navigation to ECEF position coordinate transformation, Eq. (4.24) on pg. 144, one substitutes the definitions of N_e, Eq. (4.25), and M_e, Eq. (4.27). Then differentiating with respect to time and pre-multiplying by C_e^n, the transpose of Eq. (4.21), one has

$$\mathbf{v}^{n}=\begin{pmatrix} v_N \\ v_E \\ v_D \end{pmatrix}=\begin{pmatrix} \dot{\phi}(M_e+h) \\ \dot{\lambda}(N_e+h)\cos\phi \\ -\dot{h} \end{pmatrix}. \tag{4.50}$$

Solving for the time rate of change of latitude, longitude, and altitude, the position navigation equations are:

$$\dot{\mathbf{r}}^{n}=\begin{pmatrix} \dot{\phi} \\ \dot{\lambda} \\ \dot{h} \end{pmatrix}=\begin{pmatrix} \dfrac{v_N}{M_e+h} \\ \dfrac{v_E}{(N_e+h)\cos\phi} \\ -v_D \end{pmatrix}. \tag{4.51}$$

With the velocity navigation equations, Eq. (4.49), there are now six nonlinear differential equations that will be used to integrate the accelerometer readings into the navigation frame velocity and position components.

However, the strapdown IMUs are rigidly fixed to the body frame, so the rotation matrix C_b^n must also be simultaneously computed to transform the accelerometer measurements into the n-frame (by $\mathbf{a}^n = C_b^n \mathbf{a}^b$). The differential equation for this rotation matrix is given by Eq. (4.17) on pg. 142, which specified to the body-to-navigation frame transformation is

$$\dot{C}_b^n = C_b^n \Omega_{nb}^b. \tag{4.52}$$

The angular rates for the rotation rate are found by subtracting the calculated navigation-to-inertial rate, $\boldsymbol{\omega}_{in}^n$ (Eq. (4.23) on pg. 144), from the gyro measurement, $\boldsymbol{\omega}_{ib}^b$:

$$\boldsymbol{\omega}_{nb}^b = \boldsymbol{\omega}_{ib}^b - C_n^b \boldsymbol{\omega}_{in}^n. \tag{4.53}$$

The specifics of the rotation matrix integration will be addressed in the mechanization section (Sec. 4.3.3).

The gravity acceleration vector, Eq. 4.45 on pg. 151, is linearly interpolated from the gridded, precomputed gravity map using the full 360 degree and order EGM95 spherical harmonic model for the gravitational acceleration. The geopot97 program used for the spherical harmonic calculations adds the centrifugal potential, acceleration, and gradients by default to give the full gravity quantities. For the gravitational gradient portion of the precomputed maps, the centrifugal gradient contribution was commented out from the source code. This was also done for the

global gravitational gradient maps shown in this dissertation.

4.3.3 Navigation Mechanization

This subsection addresses the numerical integration of the body-to-navigation frame transformation matrix and the six nonlinear navigation equations. The rotation matrix integration is performed by transforming the matrix into a quaternion, and a summary of its definition and use is presented first. The classical fourth-order Runge-Kutta method used to simultaneously integrate the quaternion, velocity, and position information is then described.

4.3.3.1 Body-to-Navigation Frame Quaternion

Quaternions are another way to present orientation information in lieu of a transformation matrix. A quaternion is a four-element vector similar to a complex number with three imaginary components. The three imaginary parts essentially make up a single axis of rotation and the lone real part defines the magnitude of the rotation about that axis.[144,145] This is in contrast to the transformation matrix that can be decomposed into three rotations about three orthogonal axes, see Eq. (4.8) on pg. 140. (For a thorough survey of attitude represenations and their history, one may consult Phillips et al.[145,146])

The transformation between the rotation matrix and a quaternion is straightforward and will be given without derivation (See Jekeli,[1] pg. 13–18 for a more detailed discussion). If the ith row and jth column component of C_b^n is $c_{i,j}$, then the

quaternion equivalent is[†]

$$\mathbf{q} = \begin{pmatrix} \frac{1}{2}\sqrt{1 + c_{1,1} + c_{2,2} + c_{3,3}} \\ (c_{2,3} - c_{3,2}) \ / \ (4q_1) \\ (c_{3,1} - c_{1,3}) \ / \ (4q_1) \\ (c_{1,2} - c_{2,1}) \ / \ (4q_1) \end{pmatrix}, \tag{4.54}$$

where q_1 is the first component of the quaternion and represents the magnitude of the rotation. The remaining quaternion components represent the elements of the single rotation axis. Given a quaternion, the equivalent transformation matrix is can be found to be

$$C_b^n = \begin{pmatrix} q_1^2 + q_2^2 - q_3^2 - q_4^2 & 2(q_2q_3 + q_1q_4) & 2(q_2q_4 - q_1q_3) \\ 2(q_2q_3 - q_1q_4) & q_1^2 - q_2^2 + q_3^2 - q_4^2 & 2(q_3q_4 + q_1q_2) \\ 2(q_2q_4 + q_1q_3) & 2(q_3q_4 - q_1q_2) & q_1^2 - q_2^2 - q_3^2 + q_4^2 \end{pmatrix}, \tag{4.55}$$

where q_i is the i$^{\text{th}}$ component of the quaternion. The quaternion equivalent of the rotation matrix time derivative is

$$\dot{\mathbf{q}} = \frac{1}{2} A_q \mathbf{q}, \tag{4.56}$$

where A_q is the 4×4 skew symmetric matrix for the angular rate $\boldsymbol{\omega}_{nb}^b$, Eq. (4.53) on pg. 153:

$$A_q = \begin{pmatrix} 0 & \omega_1 & \omega_2 & \omega_3 \\ -\omega_1 & 0 & \omega_3 & -\omega_2 \\ -\omega_2 & -\omega_3 & 0 & \omega_1 \\ -\omega_3 & \omega_2 & -\omega_1 & 0 \end{pmatrix}, \tag{4.57}$$

[†]This quaternion definition is based on Jekeli,[1] and it should be noted that other references may define the real and imaginary components of the quaternion in a slightly different manner.

and where ω_i is the i$^{\text{th}}$ component of $\boldsymbol{\omega}_{nb}^{b}$.

The body-to-navigation frame rotation matrix is integrated by first converting the direction cosine matrix into a quaternion using Eq. (4.54). Equations (4.56), (4.57), and (4.53) on pg. 153 for the calculated rotation rate are used to integrate the quaternion elements simultaneously with the position and velocity states using the Runge-Kutta algorithm in the next section. After the integration is completed, the new quaternion is transformed back into a direction cosine matrix using Eq. (4.55).

4.3.3.2 Fourth-Order Runge-Kutta Integration

This subsection describes the algorithm used to integrate the velocity, position, and attitude quaternion states. Numerical integration of a differential equation is typically conducted by estimating the slope of the dynamical equation over a small interval and then using an Eulerian update. The choice of how one estimates the slope over the interval can be arbitrary, but the desire is to minimize the error between the true and estimated slopes. The error is often found by taking the Taylor series expansion of the function, and then a finite number of terms are used to minimize the resultant Taylor series error. The most common numerical integration algorithms are of the Runge-Kutta family.

All Runge-Kutta methods are of the form (Chapra and Canale,[147] pg. 695):

$$\mathbf{x}_{k+1} = \mathbf{x}_k + \mathbf{f}(\mathbf{x}_k, t_k, \Delta t_k)\Delta t_k, \tag{4.58}$$

where $\mathbf{x}_k$ is the system state vector to be numerically integrated, Δt is the integration time step, and the subscripts denote the discrete time epoch. The term $\mathbf{f}$

is equivalent to the continuous dynamics of the system (*i.e.*, $\dot{\mathbf{x}}$) and is referred to as the *increment function*, which may be an explicit function of the current states, time, and time step. The increment function can also be envisioned as the estimated slope between the state vector at two epochs. Assuming there is no explicit dependence on time, as is the case for the dynamical systems in this work, and the time step is constant, the Runge-Kutta increment functions have the form (Chapra and Canale,[147] pg. 695):

$$\mathbf{f}(\mathbf{x}_k, \Delta t) = a_1\mathbf{k}_1 + a_2\mathbf{k}_2 + \cdots + a_n\mathbf{k}_n, \tag{4.59}$$

where the coefficients a_i and the vectors $\mathbf{k}_i$ (the slope evaluations at different conditions) are chosen to minimize the Taylor series error.

The most popular Runge-Kutta method is the classical Fourth-Order method (Chapra and Canale,[147] pg. 701):

$$\mathbf{x}_{i+1} = \mathbf{x}_i + \frac{1}{6}\left(\mathbf{k}_1 + 2\mathbf{k}_2 + 2\mathbf{k}_3 + \mathbf{k}_4\right)\Delta t, \tag{4.60}$$

and the slope evaluations are performed according to

$$\begin{aligned}
\mathbf{k}_1 &= \mathbf{f}(\mathbf{x}_k) \\
\mathbf{k}_2 &= \mathbf{f}(\mathbf{x}_k + \frac{1}{2}\mathbf{k}_1\Delta t) \\
\mathbf{k}_3 &= \mathbf{f}(\mathbf{x}_k + \frac{1}{2}\mathbf{k}_2\Delta t) \\
\mathbf{k}_4 &= \mathbf{f}(\mathbf{x}_k + \mathbf{k}_3\Delta t).
\end{aligned} \tag{4.61}$$

Thus, there are four slope evaluations for each integration interval. The first evaluation is done at the original point, the second and third slopes are calculated at

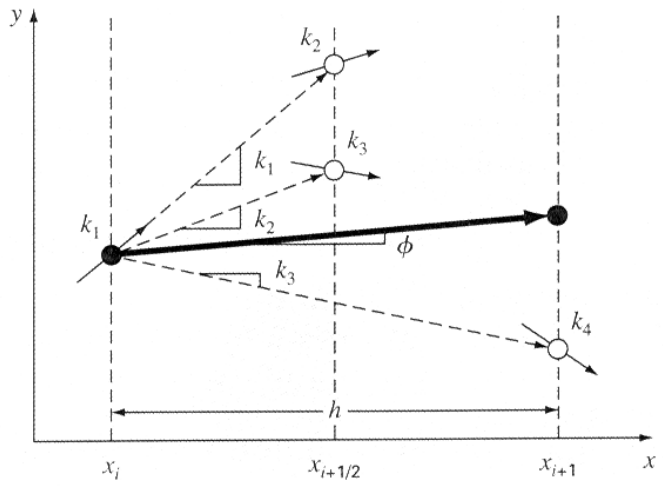

Figure 4.5: Fourth-Order Runge-Kutta Schematic, from Ref. [147]

the estimated midpoint, and the last slope is found from the estimated final point (as represented in Fig. 4.5, from Chapra and Canale,[147] pg. 701). These estimated slopes are then linearly combined using Eq. (4.60) to find the state vector at the new time epoch, $\mathbf{x}_{k+1}$, from Eq. (4.58) with fourth-order accuracy in time.

The state vector in this work, $\mathbf{x}$, consists of the navigation position and velocity states $(\phi, \lambda, h, v_N, v_E, v_D)^T$, the body-to-navigation frame quaternion, $\mathbf{q}$, and the IMU and GPS states, which will be described in Sec. 4.5.1 and D.4, respectively. The slope evaluation vector, $\mathbf{f}$, corresponds to the navigation equations given by Eq. (4.49) on pg. 152 and (4.51) on pg. 152, the quaternion time derivative given by Eq. (4.56) on pg. 155, and the IMU state rates in Sec. 4.5.2. The GPS states are integrated slightly differently using Eq. (D.41) and (D.42) because of the process noise added to these states. The gravity vector is also calculated at each slope evaluation for the given position using the stored gravity field map. And the simulated IMU specific forces, Eq. (3.84) on pg. 128, and angular rates, Eq. (3.88), pg. 129,

are assumed to be constant for each integration interval.

4.4 Inertial Navigation Error Equations

To derive the necessary linear error dynamics for the extended Kalman filter, the navigation error equations will be differentially perturbed. This perturbation technique follows the error definition in Eq. (C.38) on pg. 323, which can be rewritten as

$$\widehat{\mathbf{x}}(t) = \mathbf{x}(t) + \delta\mathbf{x}(t). \tag{4.62}$$

This equation defines the estimated states, $\widehat{\mathbf{x}}$, as the sum of the truth states, $\mathbf{x}$, and a linear perturbation, or error, from the truth, $\delta\mathbf{x}$. It should be noted that the δ operator is equivalent to the perturbation or linear error about the true non-linear navigation equations. Also, the δ operator is communicative with the time differential operator, d/dt (Jekeli,[1] pg. 141).

4.4.1 Position Error Equations

The position error equations are derived by a linear perturbation of the position navigation equations. To better explain the perturbation procedure, first take a Taylor series expansion of the position dynamics, Eq. (4.51), about the true position and velocity states and define this quantity as the estimated position dynamics:

$$\begin{aligned}\dot{\widehat{\mathbf{r}}}^n &= \dot{\mathbf{r}}^n + \left[\frac{\partial\dot{\mathbf{r}}^n}{\partial\mathbf{r}^n}\right]_{\mathbf{x}=\widehat{\mathbf{x}}}(\widehat{\mathbf{r}}^n - \mathbf{r}^n) + \frac{1}{2}\left[\frac{\partial^2\dot{\mathbf{r}}^n}{(\partial\mathbf{r}^n)^2}\right]_{\mathbf{x}=\widehat{\mathbf{x}}}(\widehat{\mathbf{r}}^n - \mathbf{r}^n)^2 + \cdots \\ &\quad + \left[\frac{\partial\dot{\mathbf{r}}^n}{\partial\mathbf{v}^n}\right]_{\mathbf{x}=\widehat{\mathbf{x}}}(\widehat{\mathbf{v}}^n - \mathbf{v}^n) + \frac{1}{2}\left[\frac{\partial^2\dot{\mathbf{r}}^n}{(\partial\mathbf{v}^n)^2}\right]_{\mathbf{x}=\widehat{\mathbf{x}}}(\widehat{\mathbf{v}}^n - \mathbf{v}^n)^2 + \cdots . \end{aligned} \tag{4.63}$$

Then, taking only the first order terms and rewriting in terms of errors, the perturbed position dynamics are

$$\hat{\dot{\mathbf{r}}}^n - \dot{\mathbf{r}}^n = \delta\dot{\mathbf{r}}^n = + \left[\frac{\partial \dot{\mathbf{r}}^n}{\partial \mathbf{r}^n}\right]_{\mathbf{x}=\hat{\mathbf{x}}} \delta\mathbf{r}^n + \left[\frac{\partial \dot{\mathbf{r}}^n}{\partial \mathbf{v}^n}\right]_{\mathbf{x}=\hat{\mathbf{x}}} \delta\mathbf{v}^n. \tag{4.64}$$

Introducing the shorthand notation of $F_{\dot{\mathbf{a}}\mathbf{b}}$ for the partial derivative matrix of $\dot{\mathbf{a}}$ with respect to $\mathbf{b}$, the error dynamics can be written as

$$\delta\dot{\mathbf{r}}^n = F_{\dot{\mathbf{r}}\mathbf{r}}\delta\mathbf{r}^n + F_{\dot{\mathbf{r}}\mathbf{v}}\delta\mathbf{v}^n. \tag{4.65}$$

And the coefficient matrices for the partial derivatives of the position dynamics with respect to position and velocity are

$$F_{\dot{\mathbf{r}}\mathbf{r}} \equiv \frac{\partial \dot{\mathbf{r}}^n}{\partial \mathbf{r}^n} = \begin{pmatrix} \frac{\partial \dot{\phi}}{\partial \phi} & \frac{\partial \dot{\phi}}{\partial \lambda} & \frac{\partial \dot{\phi}}{\partial h} \\ \frac{\partial \dot{\lambda}}{\partial \phi} & \frac{\partial \dot{\lambda}}{\partial \lambda} & \frac{\partial \dot{\lambda}}{\partial h} \\ \frac{\partial \dot{h}}{\partial \phi} & \frac{\partial \dot{h}}{\partial \lambda} & \frac{\partial \dot{h}}{\partial h} \end{pmatrix}, \quad F_{\dot{\mathbf{r}}\mathbf{v}} \equiv \frac{\partial \dot{\mathbf{r}}^n}{\partial \mathbf{v}^n} = \begin{pmatrix} \frac{\partial \dot{\phi}}{\partial v_N} & \frac{\partial \dot{\phi}}{\partial v_E} & \frac{\partial \dot{\phi}}{\partial v_D} \\ \frac{\partial \dot{\lambda}}{\partial v_N} & \frac{\partial \dot{\lambda}}{\partial v_E} & \frac{\partial \dot{\lambda}}{\partial v_D} \\ \frac{\partial \dot{h}}{\partial v_N} & \frac{\partial \dot{h}}{\partial v_E} & \frac{\partial \dot{h}}{\partial v_D} \end{pmatrix}. \tag{4.66}$$

For trajectories along an approximately constant latitude, the radii of curvature, M_e and N_e, are constant, and the coefficient matrices for the position error can be derived as

$$F_{\dot{\mathbf{r}}\mathbf{r}} = \begin{pmatrix} 0 & 0 & \frac{-v_N}{(M_e+h)^2} \\ \frac{v_E \sin\phi}{(N_e+h)\cos^2\phi} & 0 & \frac{-v_E}{(N_e+h)^2\cos\phi} \\ 0 & 0 & 0 \end{pmatrix} \tag{4.67}$$

$$F_{\dot{\mathbf{r}}\mathbf{v}} = \begin{pmatrix} \frac{1}{M_e+h} & 0 & 0 \\ 0 & \frac{1}{(N_e+h)\cos\phi} & 0 \\ 0 & 0 & -1 \end{pmatrix}. \tag{4.68}$$

For the attitude and velocity error dynamics that follow, the linear perturbations will be calculated directly without an explicit Taylor series expansion.

4.4.2 Attitude Error Equations

The errors in the attitude (*i.e.*, the rotation matrix) equations will be addressed next because these results will be used in the velocity error derivations of the following section. Three approaches are dominant in the literature to account for attitude errors: the $\boldsymbol{\psi}$-angle,[148,149] $\boldsymbol{\phi}$-angle,[149,150] and quaternion formulations.[151,152] The $\boldsymbol{\psi}$-angle approach uses the attitude errors between the estimated and true body frame while the $\boldsymbol{\phi}$-angle approach uses the angular errors between the navigation frame and the estimated platform frame as its error states, which is more typically used for stabilized IMU suites. It has been shown that these two methods are equivalent by simulation, and are analytically related by:[149]

$$\boldsymbol{\phi} = \boldsymbol{\psi} + \delta\boldsymbol{\theta}, \tag{4.69}$$

where $\delta\boldsymbol{\theta}$ is the angular error between the estimated n-frame and true b-frame. Between these formulations, the $\boldsymbol{\psi}$-angle approach was chosen because it produces simpler, and thus computationally faster, error dynamics.[149,153]

The quaternion formulation has also been shown to be equivalent to the $\boldsymbol{\phi}$-angle error with an additional scale factor proportional to acceleration, which can be removed by normalizing the quaternion.[151,152] The quaternion formulation was not chosen because its error dynamics are much more complicated than the other two approaches and it requires four, instead of three, error states with the added unit normalization constraint.

As mentioned above, $\boldsymbol{\psi}$ is the angular error between the estimated and true body frames, therefore its derivation comes from a perturbation about the true

body frame.[1,148,153] Perturbing the body-to-navigation rotation matrix differential, Eq. (4.52) on pg. 153, gives

$$\delta\dot{C}_b^n = \delta C_b^n \Omega_{nb}^b + C_b^n \delta\Omega_{nb}^b. \tag{4.70}$$

Also, if the estimated rotation matrix is a small rotation from the true C_b^n, then according to Eq. (4.10) on pg. 141,

$$\widehat{C}_b^n = (I - \Psi^n)\, C_b^n = C_b^n - \Psi^n C_b^n, \tag{4.71}$$

where Ψ^n is the skew symmetric matrix representation of $\boldsymbol{\psi} \times ()$, see Eq. (4.18) on pg. 142. Using the definition that the rotation error is the estimated rotation minus the truth, the body-to-navigation rotation error matrix is

$$\delta C_b^n \equiv \widehat{C}_b^n - C_b^n = -\Psi^n C_b^n. \tag{4.72}$$

Now, differentiating this error equation with respect to time gives an alternative relation for the rotation matrix error dynamics:

$$\delta\dot{C}_b^n = -\dot{\Psi}^n C_b^n - \Psi^n \dot{C}_b^n = -\dot{\Psi}^n C_b^n - \Psi^n C_b^n \Omega_{nb}^b, \tag{4.73}$$

where Eq. (4.52) on pg. 153 has been used for $\dot{C}_b^n$ in the last equality. Equating Eq. (4.70) and Eq. (4.73):

$$\delta C_b^n \Omega_{nb}^b + C_b^n \delta\Omega_{nb}^b = -\dot{\Psi}^n C_b^n - \Psi^n C_b^n \Omega_{nb}^b \tag{4.74}$$

$$C_b^n \delta\Omega_{nb}^b = -\dot{\Psi}^n C_b^n, \tag{4.75}$$

where Eq. (4.72) was used to cancel the two terms between lines. Solving for $\dot{\Psi}^n$,

$$\dot{\Psi}^n = -C_b^n \delta\Omega_{nb}^b C_n^b = -\delta\Omega_{nb}^n, \tag{4.76}$$

where Eq. (4.16) on pg. 142 is used for the second equality. Therefore, the right hand side is a skew-symmetric matrix, see Eq. (4.18), with elements equal to the vector $-\delta\boldsymbol{\omega}^n_{nb} = -C^n_b\delta\boldsymbol{\omega}^b_{nb}$.[154] The vector equivalent is then

$$\dot{\boldsymbol{\psi}}^n = -C^n_b\delta\boldsymbol{\omega}^b_{nb}. \tag{4.77}$$

To get the body-to-navigation frame angular rate errors, we perturb Eq. (4.53) on pg. 153 to get

$$\delta\boldsymbol{\omega}^b_{nb} = \delta\boldsymbol{\omega}^b_{ib} - \delta C^b_n\boldsymbol{\omega}^n_{in} - C^b_n\delta\boldsymbol{\omega}^n_{in}. \tag{4.78}$$

The rotation error matrix δC^n_b is equivalent to

$$\delta C^b_n = (\delta C^n_b)^T = (-\Psi^n C^n_b)^T = C^b_n\,(-\Psi^n)^T = C^b_n\Psi^n, \tag{4.79}$$

where the property that a symmetric matrix is equal to the negative of its transpose has been used.

Substituting Eq. (4.79) and (4.78) into (4.77), one has

$$\dot{\boldsymbol{\psi}}^n = -C^n_b\delta\boldsymbol{\omega}^b_{ib} + \Psi^n\boldsymbol{\omega}^n_{in} + \delta\boldsymbol{\omega}^n_{in}. \tag{4.80}$$

It can readily be shown that $\boldsymbol{\psi}^n \times \boldsymbol{\omega}^n_{in}$ is equivalent to $-\boldsymbol{\omega}^n_{in} \times \boldsymbol{\psi}^n$, see Eq. (4.97). Therefore, after some slight rearranging, the small error angles between the estimated body frame and the true body frame are governed by the dynamics:

$$\dot{\boldsymbol{\psi}}^n = \delta\boldsymbol{\omega}^n_{in} - \boldsymbol{\omega}^n_{in} \times \boldsymbol{\psi}^n - C^n_b\delta\boldsymbol{\omega}^b_{ib}. \tag{4.81}$$

The first term on the right hand side is the error due to the incorrect rotation of the navigation frame with respect to the inertial frame in n-frame coordinates, and is a function of the position and velocity states, see Eq. (4.23). The second term

is implemented as a skew symmetric matrix of $-\boldsymbol{\omega}_{in}^{n}$ that couples the estimated n-to-i frame rotation rate with the angular errors, and the third term is the gyro sensor errors rotated into the n-frame. Section 4.5.1 details the simulated gyro error models.

The $\boldsymbol{\omega}_{in}^{n}$ error is calculated by perturbing Eq. (4.23) on pg. 144, repeated here with the position rates substituted:

$$\boldsymbol{\omega}_{in}^{n} = \begin{pmatrix} \frac{v_E}{N_e + h} + \omega_e \cos\phi \\ -\frac{v_N}{M_e + h} \\ -\frac{v_E \tan\phi}{N_e + h} - \omega_e \sin\phi \end{pmatrix}. \tag{4.82}$$

Because the angular rate is a function of the position and velocity states, its perturbed (*i.e.*, linearized error) value has the from

$$\delta\boldsymbol{\omega}_{in}^{n} = F_{\dot{\boldsymbol{\psi}}\mathbf{r}}\delta\mathbf{r}^{n} + F_{\dot{\boldsymbol{\psi}}\mathbf{v}}\delta\mathbf{v}^{n}, \tag{4.83}$$

and the partial derivatives for the coefficient matrices are

$$F_{\dot{\boldsymbol{\psi}}\mathbf{r}} \equiv \frac{\partial\boldsymbol{\omega}_{in}^{n}}{\partial\mathbf{r}^{n}} = \begin{pmatrix} -\omega_e \sin\phi & 0 & -\frac{\dot{\lambda}\cos\phi}{N_e + h} \\ 0 & 0 & \frac{\dot{\phi}}{M_e + h} \\ -\frac{\dot{\lambda}}{\cos\phi} & 0 & \frac{\dot{\lambda}\sin\phi}{N_e + h} \end{pmatrix} \tag{4.84}$$

$$F_{\dot{\boldsymbol{\psi}}\mathbf{v}} \equiv \frac{\partial\boldsymbol{\omega}_{in}^{n}}{\partial\mathbf{v}^{n}} = \begin{pmatrix} 0 & \frac{1}{N_e + h} & 0 \\ -\frac{1}{M_e + h} & 0 & 0 \\ 0 & -\frac{\tan\phi}{N_e + h} & 0 \end{pmatrix}, \tag{4.85}$$

where the position dependence on N_e and M_e have been neglected (Jekeli,[1] pg. 154), and the position rates have been used for brevity, see Eq. (4.51) on pg. 152.

Using Eq. (4.81) to estimate the rotation errors, one can attempt to correct the estimated body-to-navigation rotation matrix, C_b^n (Shin,[155] pg. 46). With the small rotation assumption, Eq. (4.71) on pg. 162 can be solved for the true rotation matrix as

$$C_b^n = (I - \Psi^n)^{-1} \widehat{C}_b^n. \tag{4.86}$$

To first order, the true (or more accurately, the updated estimate of the) rotation matrix is

$$\widehat{C}_b^{n+} = C_b^n \approx (I + \Psi^n) \widehat{C}_b^{n-}, \tag{4.87}$$

where Eq. (4.11) on pg. 141 has been used. This relation is used within the Extended Kalman Filter to update the estimated rotation matrix after each measurement. Also, the $\boldsymbol{\psi^n}$-angle errors are reset to zero after the update because of the assumption that there are no known systematic errors.

4.4.3 Velocity Error Equations

The velocity error equations are also derived by a linear perturbation analysis. Beginning with the velocity dynamics, Eq. (4.47) on pg. 151, the velocity error dynamics have the form

$$\delta\dot{\mathbf{v}}^n = -\delta\left[\left(\Omega_{in}^n + \Omega_{ie}^n\right)\mathbf{v}^n\right] + \delta\mathbf{a}^n + \delta\overline{\mathbf{g}}^n. \tag{4.88}$$

We will first focus on the Coriolis error, which is a function of the position and velocity states only. Using Eq. (4.49) on pg. 152, neglecting the accelerometer readings and gravity acceleration, and substituting in the position rates from Eq. (4.51)

on pg. 152:

$$-\left(\Omega_{in}^{n}+\Omega_{ie}^{n}\right)\mathbf{v}^{n}=\begin{pmatrix}-\dfrac{v_E^2\tan\phi}{N_e+h}-2\omega_e v_E\sin\phi+\dfrac{v_N v_D}{M_e+h}\\ \dfrac{v_N v_E\tan\phi+v_E v_D}{N_e+h}+2\omega_e v_N\sin\phi+2\omega_e v_D\cos\phi\\ -\dfrac{v_N^2}{M_e+h}-\dfrac{v_E^2}{N_e+h}-2\omega_e v_E\cos\phi\end{pmatrix}. \quad (4.89)$$

Because of the dependence on position and velocity, the Coriolis error has the form

$$\begin{aligned}-\delta\left[\left(\Omega_{in}^{n}+\Omega_{ie}^{n}\right)\mathbf{v}^{n}\right] &= F_{\dot{\mathbf{v}}\mathbf{r}}\delta\mathbf{r}^{n}+F_{\dot{\mathbf{v}}\mathbf{r}}\delta\mathbf{v}^{n} \quad (4.90)\\ &= -\left[\frac{\partial[(\Omega_{in}^{n}+\Omega_{ie}^{n})\mathbf{v}^{n}]}{\partial\mathbf{r}^{n}}\right]\delta\mathbf{r}^{n}-\left[\frac{\partial[(\Omega_{in}^{n}+\Omega_{ie}^{n})\mathbf{v}^{n}]}{\partial\mathbf{v}^{n}}\right]\delta\mathbf{v}^{n}.\end{aligned}$$

Taking the partial derivates and assuming N and M are again constant,

$$-\frac{\partial[(\Omega_{in}^{n}+\Omega_{ie}^{n})\mathbf{v}^{n}]}{\partial\mathbf{r}^{n}}= \quad (4.91)$$
$$\begin{pmatrix}-\dfrac{v_E^2}{(N_e+h)\cos^2\phi}-2\omega_e v_E\cos\phi & 0 & \dfrac{v_E^2\tan\phi}{(N_e+h)^2}-\dfrac{v_N v_D}{(M_e+h)^2}\\ \dfrac{v_N v_E}{(N_e+h)\cos^2\phi}+2\omega_e(v_N\cos\phi-v_D\sin\phi) & 0 & -\dfrac{(v_N\tan\phi-v_D)v_E}{(N_e+h)^2}\\ 2\omega_e v_E\sin\phi & 0 & \dfrac{v_N^2}{(M_e+h)^2}+\dfrac{v_E^2}{(N_e+h)^2}\end{pmatrix},$$

$$-\frac{\partial[(\Omega_{in}^{n}+\Omega_{ie}^{n})\mathbf{v}^{n}]}{\partial\mathbf{v}^{n}}= \quad (4.92)$$
$$\begin{pmatrix}\dfrac{v_D}{M_e+h} & -\dfrac{2v_E\tan\phi}{N_e+h}-2\omega_e\sin\phi & \dfrac{v_N}{M_e+h}\\ \dfrac{v_E\tan\phi}{N_e+h}+2\omega_e\sin\phi & \dfrac{v_N\tan\phi+v_D}{N_e+h} & \dfrac{v_E}{N_e+h}+2\omega_e\cos\phi\\ -\dfrac{2v_N}{M_e+h} & -\dfrac{2v_E}{N_e+h}-2\omega_e\cos\phi & 0\end{pmatrix}.$$

Using the position rates for $\dot{\phi}$ and $\dot{\lambda}$, and defining the mean curvature $R_e\equiv\sqrt{M_eN_e}$,

the partial derivatives can be simplified to

$$
\begin{aligned}
F_{\dot{\mathbf{v}}\mathbf{r}} = &\equiv -\frac{\partial[(\Omega_{in}^n + \Omega_{ie}^n)\mathbf{v}^n]}{\partial \mathbf{r}^n} \qquad (4.93)\\
&= \begin{pmatrix} -\left(\dfrac{\dot{\lambda}}{\cos\phi} + 2\omega_e \cos\phi\right) v_E & 0 & \dfrac{v_E \dot{\lambda} \sin\phi - v_D \dot{\phi}}{R_e + h} \\ \dfrac{v_N \dot{\lambda}}{\cos\phi} + 2\omega_e \left(v_N \cos\phi - v_D \sin\phi\right) & 0 & -\dfrac{\dot{\lambda}\left(v_N \sin\phi + v_D \cos\phi\right)}{R_e + h} \\ 2\omega_e v_E \sin\phi & 0 & \dot{\phi}^2 + \dot{\lambda}^2 \cos^2\phi \end{pmatrix},
\end{aligned}
$$

$$
\begin{aligned}
F_{\dot{\mathbf{v}}\mathbf{v}} &\equiv -\frac{\partial[(\Omega_{in}^n + \Omega_{ie}^n)\mathbf{v}^n]}{\partial \mathbf{v}^n} \\
&= \begin{pmatrix} \dfrac{v_D}{R_e + h} & -2(\dot{\lambda} + \omega_e)\sin\phi & \dot{\phi} \\ (\dot{\lambda} + 2\omega_e)\sin\phi & \dfrac{v_N \tan\phi + v_D}{R_e + h} & (\dot{\lambda} + 2\omega_e)\cos\phi \\ -2\dot{\phi} & -2(\dot{\lambda} + \omega_e)\cos\phi & 0 \end{pmatrix}. \qquad (4.94)
\end{aligned}
$$

The velocity error dynamics due to the n-frame specific force errors are attributed to two parts: the body-to-navigation frame rotation and the accelerometer sensors. Symbolically:

$$\delta \mathbf{a}^n = \delta C_b^n \mathbf{a}^b + C_b^n \delta \mathbf{a}^b. \qquad (4.95)$$

The rotation matrix error is given by Eq. (4.72) on pg. 162, so

$$\delta C_b^n \mathbf{a}^b = -\Psi^n C_b^n \mathbf{a}^b = -\Psi^n \mathbf{a}^n. \qquad (4.96)$$

It can easily be verified that

$$
-\Psi^n \mathbf{a}^n = \begin{pmatrix} a_2^n \psi_3^n - a_3^n \psi_2^n \\ -a_1^n \psi_3^n + a_3^n \psi_1^n \\ a_1^n \psi_2^n - a_2^n \psi_1^n \end{pmatrix} = \begin{pmatrix} 0 & -a_3^n & a_2^n \\ a_3^n & 0 & -a_1^n \\ -a_2^n & a_1^n & 0 \end{pmatrix} = \mathbf{a}^n \times \boldsymbol{\psi}^n. \qquad (4.97)
$$

The error from the specific force term is now

$$\delta \mathbf{a}^n = \mathbf{a}^n \times \boldsymbol{\psi}^n + C_b^n \delta \mathbf{a}^b, \qquad (4.98)$$

where $\delta\mathbf{a}^b$ are the errors caused by the accelerometer sensor triad, which will be derived in Sec. 4.5.1.

The gravity error term is modeled by taking into account only the error in the gravitational acceleration. Because Earth's rotation rate is known with high precision, and the position error is typically small, the gravity error due to the centripetal acceleration is neglected. This term could be added in future work. Using the full gravitational gradient tensor, the gravity error is modeled as:

$$\delta\overline{\mathbf{g}}^n \approx \delta\mathbf{g}^n = \Gamma^n \begin{pmatrix} R_e & 0 & 0 \\ 0 & R_e & 0 \\ 0 & 0 & -1 \end{pmatrix} \delta\mathbf{r}^n \equiv F_{\mathbf{gr}}\delta\mathbf{r}^n, \tag{4.99}$$

where the middle matrix approximates the Jacobian between the North-East-Down positions and the navigation position states, and the mean curvature of Earth at the current estimated position is defined as $R_e \equiv \sqrt{M_e N_e}$. The values of the gravitational gradients are calculated by linearly interpolation from the stored, gridded gravity map to the current estimated position.

4.4.4 Summary

The linearized error dynamics are used to update the filter error covariance matrix. The error dynamics are not actually integrated numerically, instead they are only used to compute the error state transition matrix as discussed at the end of Sec. C.5.1. The position, velocity, and attitude errors constitute nine of the twenty-six states that the filter estimates in its covariance matrix. The linear errors of these

states can be summarized as

$$\frac{d}{dt}\begin{pmatrix} \delta\mathbf{r}^n \\ \delta\mathbf{v}^n \\ \boldsymbol{\psi}^n \end{pmatrix} = \delta\dot{\mathbf{x}}_{INS} = \begin{pmatrix} F_{\dot{\mathbf{r}}\mathbf{r}} & F_{\dot{\mathbf{r}}\mathbf{v}} & 0 \\ F_{\dot{\mathbf{v}}\mathbf{r}} + F_{\mathbf{gr}} & F_{\dot{\mathbf{v}}\mathbf{v}} & [\widehat{\mathbf{a}}^n\times] \\ F_{\dot{\boldsymbol{\psi}}\mathbf{r}} & F_{\dot{\boldsymbol{\psi}}\mathbf{v}} & [\widehat{\boldsymbol{\omega}}^n_{in}\times] \end{pmatrix} \delta\mathbf{x}_{INS} + \begin{pmatrix} 0 & 0 \\ \widehat{C}^n_b & 0 \\ 0 & -\widehat{C}^n_b \end{pmatrix} \begin{pmatrix} \delta\mathbf{a}^b \\ \delta\boldsymbol{\omega}^b_{ib} \end{pmatrix}, \tag{4.100}$$

where Eq. (4.67) and (4.68) define the position error matrices, $F_{\dot{\mathbf{r}}\mathbf{r}}$ and $F_{\dot{\mathbf{r}}\mathbf{v}}$; Eq. (4.93), (4.99), and (4.94) define the velocity errors, $F_{\dot{\mathbf{v}}\mathbf{r}}$, $F_{\mathbf{gr}}$, and $F_{\dot{\mathbf{v}}\mathbf{v}}$; and Eq. (4.84) and (4.85) define the attitude error matrices, $F_{\dot{\boldsymbol{\psi}}\mathbf{r}}$ and $F_{\dot{\boldsymbol{\psi}}\mathbf{v}}$. The term $[\widehat{\mathbf{a}}^n\times]$ is a skew symmetric matrix of the filter-corrected specific force measurements rotated from the body frame to the navigation frame using the current estimate of C^n_b, *i.e.*

$$\widehat{\mathbf{a}}^n = \widehat{C}^n_b\widehat{\mathbf{a}}^b. \tag{4.101}$$

The $[\widehat{\boldsymbol{\omega}}^n_{in}\times]$ term is another skew symmetric matrix whose components are calculated from Eq. (4.23) using the current estimates of the position and velocity states.

The last two terms on the right of Eq. (4.100) are due to the inertial measurement unit errors which are rotated into the navigation frame by $\widehat{C}^n_b$. The filter is augmented with the IMU error states as described in the following section. This allows the filter to reduce some of the IMU errors in-flight with the information from the external INS aid. Also, the strapdown gravity gradiometer instrument requires an estimate of the angular velocity of the body frame which is calculated from the estimated gyro readings as described later in Sec. 5.2.1.

4.5 Inertial Measurement Unit Model

This section presents the details of how the measured and filter-corrected IMU readings are simulated. The suite of inertial measurement units in this work consists of a triad of accelerometers and a triad of gyros. IMUs are able to produce uninterrupted specific force and angular rate measurements in highly dynamic environments. Unfortunately, direct integration of these measurements (dead-reckoning navigation) results in navigation state error growth that may reach unacceptably high levels and even loss of vehicle. To ensure safe and reliable performance, an external aid with a finite accuracy is often blended into the IMU-only navigation solution through a Kalman filter approach. However, to produce an optimal Kalman gain, the IMU error sources must be modeled accurately.

This next subsection describes the various IMU error sources and how they are modeled for this work. The following subsection surveys the current state-of-the-art in navigation and tactical grade inertial measurement unit specifications and details how these values are used for the simulated IMU readings.

4.5.1 IMU Error Model

The sources of error from an inertial measurement unit include uncompensated scale factors, biases, thermal effects, nonlinearities, misalignments, non-orthogonalities, and electronic measurement noise.[1,2] Each of these error sources are described as follows.

Scale Factor errors cause measurement errors that are proportional to the

true specific force of angular rate measurement. Theses errors are usually time invariant and are modeled as random constants.

Bias error, also referred to as *turn-on bias*, *bias repeatability*, *bias stability*, *drift bias* (for gyros), or *offset* (for accelerometers), is the initially offset constant sensor reading that changes each time the instrument is turned on. Because of this, it is often modeled as a simple random constant.

Thermal Effects in the mechanical properties of the IMUs can result in the scale factor and/or bias error to vary over time. In these cases, a correlated (Gauss-Markov) random walk process may be added to the random constant assumption of the scale factor and/or bias error.

Nonlinearities in the IMUs can cause the linear input/output relationship of the sensor to vary off nominal, particularly during periods of high dynamics. These errors are often modeled by a sum of linear and/or quadratic accelerations with random constant coefficients (Farrell and Barth,[2] pg. 216 & 218). For example, the accelerometer nonlinearity term may be modeled as

$$nl_j^a = k_{j,1}^a (a_1^a)^2 + k_{j,2}^a (a_2^a)^2 + k_{j,3}^a (a_3^a)^2 + k_{j,4}^a (a_1^a a_2^a) + k_{j,5}^a (a_1^a a_3^a) + k_{j,6}^a (a_2^a a_3^a). \quad (4.102)$$

where the a terms are the components of the truth specific forces and the k terms are random constants.

Misalignments and **Non-orthogonalities** result when the IMU package is not mounted perfectly along the body axes or when the IMU sensors themselves are not aligned sufficiently with respect to each other. Since strapdown IMUs and their package are assumed to by rigidly attached to the vehicle, these errors are

modeled as a small error rotation matrix with random constants. For example, if the accelerometers were misaligned and non-orthogonal to each other in an a-frame, the body-frame specific forces would be estimated as

$$\widetilde{\mathbf{a}}^b = (I - \Delta^a)\,\widetilde{\mathbf{a}}^a, \tag{4.103}$$

where

$$\Delta^a = \begin{pmatrix} 0 & d_1 & d_2 \\ d_3 & 0 & d_4 \\ d_5 & d_6 & 0 \end{pmatrix}, \tag{4.104}$$

and the d terms are random constants. Because of the non-orthogonalities, the Δ^a matrix is not necessarily skew symmetric.

Instrument Noise is usually due to high frequency electronic noise that varies from each measurement reading. Since these variations happen at a frequency faster than the update rate of the sensor, they are often modeled as zero-mean white noises. For the gyro noise in this work a first order Gauss-Markov is tuned with a small enough time constant that it approximates white noise. The accelerometer noise is modeled as white.

Including all the errors above, the measured specific force sensed by an accelerometer in its local a-frame is[2]

$$\widetilde{a}_j^a = \left(1 - SF_j^a\right)\left(a_j^a - b_j^a - nl_j^a - w_j^a\right), \tag{4.105}$$

where a_j^a is the truth specific force measurement, SF_j^a is the truth scale factor, b_j^a is the turn-on bias, nl_j^a is the measurement nonlinearity as defined above, and w_j^a is the white noise of the sensor. The triad of accelerometer specific forces would then be

estimated in the body frame by Eq. (4.103) using an estimate of the misalignments and non-orthogonalities. The gyro measurements would be implemented similarly.

The issue with including all the error terms is that the Kalman filter must account for each of these errors to operate optimally. This entails augmenting the filter state vector with each coefficient in each error term, which would drastically increase the size of the filter and the computational costs. As a compromise, it is common to include only the largest sources of error such as IMU biases and noise, and to a lesser extent scale factors. For this work, IMU scale factor and bias states are augmented to the filter state vector along with a noise state for each of the gyros.

Originally, misalignments and accelerometer nonlinearities were implemented into the simulation to provide uncompensated errors to the system that would test the filter robustness. Unfortunately, some of the INS/GGI simulations reduced the tilt errors to the point that the uncompensated misalignments caused divergence to occur. Therefore these errors were turned off for all Monte Carlo simulations presented. The non-orthogonalities and gyro nonlinearities are not widely reported in the surveyed IMU specifications and were thus never pursued for implementation into the simulation.

Following the assumption of no misalignments or non-orthogonalities, the IMUs are all aligned with the body frame axes. It is also implicitly assumed that the IMUs either reside at the center of mass of the vehicle or have already had compensation for any lever arm effects on the readings. Therefore, along with the

neglection of the nonlinearities, the accelerometer specific force measurement is

$$\widetilde{a}_j^b = \left(1 - SF_j^a\right)\left(a_j^b - b_j^a - w_j^a\right), \tag{4.106}$$

and the gyro measurement is similarly,

$$\widetilde{\omega}_{ib,j}^b = \left(1 - SF_j^g\right)\left(\omega_{ib,j}^b - b_j^g - n_j^g\right), \tag{4.107}$$

where n_j^g is the noise state that approximates a white noise process.

The filter estimates the scale factors and biases of the IMUs (and the gyro noise) so that it assumes the IMU readings are

$$\widetilde{a}_j^b = \left(1 - \widehat{SF}_j^a\right)\left(\widehat{a}_j^b - \widehat{b}_j^a\right), \tag{4.108}$$

where the noise is compensated for in the error process noise matrix, Q_k, and

$$\widetilde{\omega}_{ib,j}^b = \left(1 - \widehat{SF}_j^g\right)\left(\widehat{\omega}_{ib,j}^b - \widehat{b}_j^g - \widehat{n}_j^g\right). \tag{4.109}$$

These relationships can then be solved for the estimated specific forces and angular rates:

$$\widehat{a}_j^b = \frac{\widetilde{a}_j^b}{1 - \widehat{SF}_j^a} + \widehat{b}_j^a, \tag{4.110}$$

$$\widehat{\omega}_{ib,j}^b = \frac{\widetilde{\omega}_{ib,j}^b}{1 - \widehat{SF}_j^g} + \widehat{b}_j^g + \widehat{n}_j^g. \tag{4.111}$$

These estimated measurements are then processed by the INS when integrating the navigation states and computing the linearized navigation errors.

In order for the filter to update its estimate of the IMU errors (which are initialized to zero in the estimated state vector) their linearized errors must be derived

and the IMU states need to be added to the total filter state vector. The accelerometer specific force error can be derived by subtracting the truth measurement (from rearranging Eq. (4.106)) from the filter-estimated measurement:

$$\begin{aligned}\delta a_j^b &= \widehat{a}_j^b - a_j^b = \left(\frac{\widetilde{a}_j^b}{1-\widehat{SF}_j^a} + \widehat{b}_j^a\right) - \left(\frac{\widetilde{a}_j^b}{1-SF_j^a} + b_j^a + w_j^a\right) \\ &= \frac{(1-SF_j^a)-(1-\widehat{SF}_j^a)}{(1-\widehat{SF}_j^a)(1-SF_j^a)}\widetilde{a}_j^b + \delta b_j^a - w_j^a. \end{aligned} \tag{4.112}$$

Noting that scale factors are on the order of 1×10^{-4} for the surveyed IMUs, the accelerometer errors can be approximated as

$$\delta a_j^b \approx (\delta SF_j^a)\widetilde{a}_j^b + \delta b_j^a - w_j^a. \tag{4.113}$$

The gyro error can be similarly found, but with the slight difference of the noise state:

$$\delta \omega_{ib,j}^b \approx (\delta SF_j^g)\widetilde{\omega}_{ib,j}^b + \delta b_j^g + \delta n_j^a. \tag{4.114}$$

The IMU error states added to the Kalman filter state vector are then:

$$\delta \mathbf{x}_a = \left(\delta SF_x^a,\ \delta SF_y^a,\ \delta SF_z^a,\ \ \delta b_x^a,\ \delta b_y^a,\ \delta b_z^a\right)^T \tag{4.115}$$

$$\delta \mathbf{x}_g = \left(\delta SF_x^g,\ \delta SF_y^g,\ \delta SF_z^g,\ \ \delta b_x^g,\ \delta b_y^g,\ \delta b_z^g,\ \ \delta n_x^g,\ \delta n_y^g,\ \delta n_z^g\right)^T. \tag{4.116}$$

The accelerometer errors can also be re-written in vector form as

$$\delta \mathbf{a}^b = \left(\text{diag}(\widetilde{\mathbf{a}}^b),\ \ I\right)^T \delta \mathbf{x}_a - \mathbf{w}^a, \tag{4.117}$$

where $\text{diag}(\widetilde{\mathbf{a}}^b)$ is a diagonal matrix whose elements are the components of the uncorrected accelerometer measurements and I is a 3×3 identity matrix. The gyro errors in vector notation are

$$\delta \boldsymbol{\omega}_{ib}^b = \Big(\text{diag}(\widetilde{\boldsymbol{\omega}}_{ib}^b),\ \ I,\ \ I\Big)^T \delta \mathbf{x}_g. \tag{4.118}$$

Equation (4.117) and (4.118) are then substituted back into Eq. (4.100) to produce the total linearized INS error dynamics.

The dynamics for the scale factors and biases are all zero since they are modeled as random constants. The gyro noise dynamics follow the description in Sec. C.2.3 for the Gauss-Markov process estimating a white noise. In summary,

$$\frac{d}{dt}\delta\mathbf{x}_g = \mathbf{0}, \tag{4.119}$$

and

$$\frac{d}{dt}\delta\mathbf{x}_g = \frac{d}{dt}\begin{pmatrix} \delta\mathbf{SF}^g \\ \delta\mathbf{b}^g \\ \delta\mathbf{n}^g \end{pmatrix} = \begin{pmatrix} 0 & 0 & 0 \\ 0 & 0 & 0 \\ 0 & 0 & -\beta I \end{pmatrix}\delta\mathbf{x}_g + \begin{pmatrix} \mathbf{0} \\ \mathbf{0} \\ \mathbf{w}^g(t) \end{pmatrix}. \tag{4.120}$$

The discrete implementation of the gyro errors is, see Sec. C.2.3,

$$\delta\mathbf{x}_{g,k+1} = \begin{pmatrix} 1 & 0 & 0 \\ 0 & 1 & 0 \\ 0 & 0 & \exp(-\beta\Delta t) \end{pmatrix}\delta\mathbf{x}_{g,k} + \begin{pmatrix} \mathbf{0} \\ \mathbf{0} \\ \mathbf{w}_k^g \end{pmatrix}, \tag{4.121}$$

where the variance of the discrete driving noise is

$$\sigma_{w^g}^2 = (q_{w^g}/\Delta t)\left[1 - \exp(-2\beta\Delta t)\right], \tag{4.122}$$

where q_{w^q} is the power spectral density of the gyro white noise and $\beta = 2.146/(2\Delta t)$. The gyro noise states' portion of the filter discrete process noise covariance matrix is then

$$Q_{k,\mathbf{n}^g} = E\left[\left(\mathbf{w}_k^g\right)\left(\mathbf{w}_k^g\right)^T\right] = \sigma_{w^g}^2 I, \tag{4.123}$$

where I is a 3×3 identity matrix.

The accelerometer noise portion of the filter's discrete process noise covariance matrix is a little more complicated to calculate. Using the velocity error dynamics, Eq. (4.100) on pg. 169, and the accelerometer errors, Eq. (4.117) on pg. 175, the acceleration error due to the accelerometer noise is

$$\delta\dot{\mathbf{v}}^n_{w^a} = -C^n_b \mathbf{w}^a. \tag{4.124}$$

The resultant velocity error can then be approximated by a simple Euler integration, see Eq. (C.29) on pg. 317, so that

$$\delta\mathbf{v}^n_{w^a} \approx \dot{\mathbf{v}}^n_{w^a}\Delta t = -C^n_b \mathbf{w}^a \Delta t. \tag{4.125}$$

The discrete process noise covariance matrix for the velocity errors can now be calculated by

$$\begin{aligned} Q_{k,\delta\mathbf{v}^n} &= E\left[\left(\delta\mathbf{v}^n_{w^a}\right)\left(\delta\mathbf{v}^n_{w^a}\right)^T\right] \approx E\left[\left(-C^n_b\mathbf{w}^a\Delta t\right)\left(-C^n_b\mathbf{w}^a\Delta t\right)^T\right] \\ &= C^n_b E\left[\left(\mathbf{w}^a\right)\left(\mathbf{w}^a\right)^T\right] C^b_n \Delta t^2 = C^n_b C^b_n \sigma^2_{w^a}\Delta t^2 \\ &= \sigma^2_{w^a}\Delta t^2 I, \end{aligned} \tag{4.126}$$

where $E\left[\left(\mathbf{w}^a\right)\left(\mathbf{w}^a\right)^T\right] = \sigma^2_{w^a} I$ is used in the second line.

The rest of the discrete process noise covariance matrix is zero for the INS and IMU states. The GPS receiver clock states' process noise covariance is derived in Sec. D.4.

4.5.2 IMU Specifications

A survey of current IMU sensor specifications was conducted to provide realistic values for the simulated IMU instrument errors. Sensors manufactured by

Honeywell,[156,157] Northrop Grumman,[158] Astronautics Corporation of America's Kearfott,[159] BEI Technologies' Systron Donner,[160] and the German iMAR (Inertiale Mess-, Automatisierungs- und Regelsysteme)[161] are summarized in Tables 4.2 and 4.3, where the navigation grade IMUs are in the top portion of each table and the tactical grade sensors are in the bottom. This survey is not meant to be complete, but rather it is used to show the current (as of 2006) state-of-the-art in IMU sensor manufacturing. Using these IMU data sheets as reference, the navigation and tactical grade IMU specifications used in this study are listed in Table 4.4. The modeled specifications were chosen by taking the more aggressive performance specification in each IMU class. The units reported in the IMU specifications can be a source of confusion, so the values used in the Monte Carlo simulations are detailed below.

The truth uncompensated scale factor standard deviation is calculated by multiplying the value in Table 4.4 by 1×10^{-6}. This term is dimensionless and needs no unit conversion.

The standard deviation of the random constant accelerometer bias is converted to standard metric units by

$$\sigma_{b_j^a}\ \left[m/s^2\right] = \sigma_{b_j^a}\ [\mu g]\left(\frac{1\times10^{-6}}{1\mu}\right)\left(\frac{9.81m/s^2}{1g}\right) \tag{4.127}$$

The 1-σ value for the navigation grade accelerometer turn-on bias is then 0.00147 m/s^2 and the tactical grade value is 0.0491 $\times$ 10^{-3} m/s^2. The gyro bias standard deviation is similarly converted to radians per second by

$$\sigma_{b_j^g}\ [rad/s] = \sigma_{b_j^g}\ \left[\frac{^\circ}{Hr}\right]\left(\frac{\pi rad}{180^\circ}\right)\left(\frac{1Hr}{3600sec}\right). \tag{4.128}$$

Table 4.2: Navigation and Tactical Grade Acceleromter Specifications

Manufacturer	Model	Data Rate (Hz)	Bias (μg)	Random Walk ($\mu g/\sqrt{Hz}$)	Scale Factor (ppm)	Non-Linearity ($\mu g/g^2$)	Alignment ($mrad$)
Honeywell	HG9848	600	50	–	150	20	0.1–2
Honeywell	HG9900	300	25	–	100	–	0.1–2
iMAR	iNAV-FJI	1000	5–60	8	60–100	–	–
iMAR	iNAV-RQH	2000	15–100	8	60–100	–	–
Kearfott	KI-4901	–	400	85	500	15	0.1
Kearfott	KI-4921	–	200	68	350	15	0.1
BEI	DQI	600	200–1500	200	350	–	0.5
Honeywell	HG1700	600	1000–2000	–	300	500 (ppm)	–
Honeywell	HG1900	3600	1000	–	300	500 (ppm)	–
Honeywell	HG1930	2400	4000	–	700	30 (ppm)	–
Honeywell	HG9868	600	1000	–	300	20	0.4–12
iMAR	iNAV-FMS	400	1000	–	300	–	–
Northrop	LN-200	360	300–3000	–	100–5000	–	–
Northrop	LN-600	700	200	–	–	–	0.1
Kearfott	KI-4801	–	400	85	500	50	0.3
Kearfott	KI-4920	–	400	85	500	15	0.3

Table 4.3: Navigation and Tactical Grade Gyro Specifications

Manufacturer	Model	Data Rate (Hz)	Bias ($^\circ/Hr$)	Random Walk ($^\circ/\sqrt{Hr}$)	Scale Factor (ppm)	Non-Linearity (ppm)	Alignment ($mrad$)
Honeywell	HG9848	600	0.005	0.005	10	–	–
Honeywell	HG9900	300	0.003	0.002	5	–	–
iMAR	iNAV-FJI	1000	0.003–0.05	0.001–0.0025	30	5–10	–
iMAR	iNAV-RQH	2000	0.003–0.05	0.0013–0.005	10	–	–
Kearfott	KI-4901	–	0.005	0.003	50	–	0.07
Kearfott	KI-4921	–	0.04	0.01	75	–	0.1
BEI	DQI	600	3–10	0.035	350	–	0.5
BEI	DIGI-Q (est)	600	3–10	0.05	100	500	35
Honeywell	HG1900	3600	0.3–30	0.1	150	–	–
Honeywell	HG1930	2400	20	0.15	300	–	–
Honeywell	HG1700	600	1–10	0.125–0.5	150	–	–
Honeywell	HG9868	600	1	0.125	150	–	–
iMAR	iNAV-FMS	400	0.75–3	0.15	300	–	–
Kearfott	KI-4801	–	0.1–0.7	0.05	350	–	0.3
Kearfott	KI-4920	–	0.1–0.7	0.05	120	–	0.3
Norhtrup	FOG-200	500	1	0.02	500	–	–
Northrop	FOG-600	600	0.1–0.2	0.005	100	100–1000	1
Northrop	FOG-1000	600	0.1	0.0035	100	50–1000	1
Northrop	LN-200	360	0.1–1	0.02–0.15	100–500	–	–
Northrop	LN-600	700	0.1	–	–	–	0.1

Table 4.4: Simulated Navigation and Tactical Grade IMU Specifications

	Navigation Grade		Tactical Grade	
	Accel.	Gyro	Accel.	Gyro
Scale Factor	60 ppm	10ppm	300 ppm	200 ppm
Turn-On Bias	15 μg	0.003 $^\circ/Hr$	500 μg	1.0 $^\circ/Hr$
Sensor Noise	8 $\mu g/\sqrt{Hz}$	0.001 $^\circ/\sqrt{Hr}$	100 $\mu g/\sqrt{Hz}$	0.02 $^\circ/\sqrt{Hr}$
Misalignment	0.1 $mrad$	0.1 $mrad$	0.3 $mrad$	0.5 $mrad$
Non-Linearity	15 $\mu g/g^2$	—	20 $\mu g/g^2$	—

and the navigation grade 1-σ bias is 1.45×10^{-8} rad/s (0.833×10^{-6} $^\circ/s$). The tactical gyro bias is 4.85×10^{-6} rad/s (0.278×10^{-3} $^\circ/s$).

The instrument noise is sometimes referred to as the random walk parameter of the sensor because the result of integrating the noise is a random walk behavior of the sensor measurement. The actual value cited in most IMU data sheets is the square root of the white noise power spectral density (PSD). As shown in Eq. C.9 on pg. 313, the variance of a white process is equivalent to the PSD divided by the sampling rate. Therefore, the noise variance for each sensor is calculated as

$$\sigma^2_{w^a}\left[\left(m/s^2\right)^2\right] = \left[\sqrt{q_{w^a}}\left[\mu g/\sqrt{Hz}\right]\left(\frac{9.81\times10^{-6}m/s}{1\mu g}\right)\right]^2/\Delta t, \quad (4.129)$$

$$\frac{q_{w^g}}{\Delta t}\left[(rad/s)^2\right] = \left[\sqrt{q_{w^g}}[^\circ/\sqrt{Hr}]\left(\frac{\pi rad}{180^\circ}\right)\sqrt{\frac{1Hr}{3600sec}}\right]^2/\Delta t, \quad (4.130)$$

where $\sqrt{q_w}$ is the parameter specified in Table 4.4, and the gyro noise value above is implemented as described at the end of the previous subsection. As shown in the two equations above, the value of the simulated noise variance is proportional to the frequency of the updates. IMUs are able to produce data rates up to several

thousand Hz, but for this work the simulation is updated at a frequency of only 20 Hz to keep the computational costs fairly low. This results in an accelerometer 1-σ noise level of 0.000351 m/s^2 for nav.-grade IMUs and 0.00439 m/s^2 for tac.-grade IMUs. The gyro noise as calculated from (4.122) and (4.130) is 0.130×10^{-5} rad/s (0.745×10^{-4} $^\circ/s$) for the navigation grade IMUs and 0.260×10^{-4} rad/s (0.149×10^{-2} $^\circ/s$) for the tactical grade gyros. (David Gaylor's research report "Simulation of an Unaided INS in Orbit" was used as a reference for this discussion.)[162]

4.6 Chapter Summary

This chapter reviews inertial navigation system fundamentals in Sec. 4.1 and 4.2. The INS state dynamics are then derived in Sec. 4.3, followed by their linearized errors in Sec. 4.4. These four sections follow standard INS formulations with only one modification for the use with a GGI aid—the velocity error dynamics due to gravity acceleration registration errors. This error source must include the full gravitational gradient tensor and a Jacobian between the coordinate frame of the gravity map and the n-frame's latitude, longitude, and altitude states, as shown in Eq. (4.99) on pg. 168. This term differs from typical INSs which only account for the vertical gravitational gradient of a point mass Earth.

Section 4.5 next discusses the accelerometer and gyro error models simulated in this work. Section 4.5.1 reviews typical IMU error sources and details the scale factor, bias, and noise models used to corrupt the truth IMU measurements. For this work, the scale factor and bias of each accelerometer and gyro is augmented to the

filter state vector to allow for in-flight calibration of the IMU errors and for optimal calculation of the Kalman gain. The second modification to a traditional INS for GGI aiding is the need to model the gyro noise as a Gauss-Markov process that estimates white noise, and to augment the filter state with the gyro noises so that strapdown GGIs are able to estimate all gyro angular velocity errors. This results in the calculation of the gyro noise portion of the error state transition matrix having to include a full exponential term instead of just a first order Taylor series expansion of the matrix exponential (as shown in Eq. (4.121) on pg. 176 and discussed further at the end of Sec. C.5.1). This estimation of the error state transition matrix is an improvement on Jekeli's method[94] which used a more computationally expensive procedure that truncated the matrix exponential expansion at 30 terms.

Section 4.5.2 then surveys current navigation and tactical grade IMU error specifications. The IMU errors simulated for the navigation analyses in Ch. 6 are then summarized in Table 4.4.

The INS dynamics and error models presented in this chapter are used as the basis for the Monte Carlo simulations in Ch. 6 for both the INS/GGI and INS/GPS systems. The noisy GGI or GPS measurements are blended into the INS-estimated states through an extended Kalman filter as explained in App. C. The measurements are detailed in the next chapter for the gravity gradiometer instrument updates, and in App. D for the baseline GPS updates.

Chapter 5

Gravity Gradiometer Instrument Model

As surveyed in Sec. 1.2.1, gravity gradiometer instruments (GGIs) have been manufactured in a multitude of configurations. This chapter presents and derives the measurement observables and linearized error models for several finite-differenced accelerometer-based GGIs. The first section derives a general accelerometer-based GGI measurement formulation. These results are then used to derive the stabilized, rotating disc GGI measurements that many references state without derivation. Next, the envisioned non-rotating, 12-accelerometer GGI is discussed and its measurements are derived assuming the instrument is either strapped down to the body or stabilized with respect to inertial. The linearized strapdown and stabilized error equations are lastly comprehensively derived for the first time so that they may be used in the extended Kalman filter simulations.

5.1 Accelerometer-Based GGI Measurements

In an arbitrary, rotating "a-" frame, the sensed specific force measured by a 3-axis accelerometer triad is, see Eq. (4.37) on pg. 149,

$$\mathbf{a}^a = \ddot{\mathbf{r}}^a + 2\Omega_{ia}^a \dot{\mathbf{r}}^a + \left(\Omega_{ia}^a \Omega_{ia}^a + \dot{\Omega}_{ia}^a\right) \mathbf{r}^a - \mathbf{g}^a, \tag{5.1}$$

where $\mathbf{r}^a$ is the accelerometer triad's position, $\mathbf{g}^a$ is the gravitational acceleration vector, Ω^a_{ia} is the skew symmetric matrix (see Eq. (4.18) on pg. 142) of the angular velocity from the a-frame to the i-frame, and $\dot{\Omega}^a_{ia}$ is the corresponding angular acceleration, all with coordinates in the a-frame. Now, assuming that two accelerometer triads are rigidly fixed at a specified baseline ($\mathbf{l}_b \equiv \mathbf{r}^a_2 - \mathbf{r}^a_1$) so that $\dot{\mathbf{l}}_b = \ddot{\mathbf{l}}_b = 0$, and the angular rates and accelerations are equivalent, these triads may be differenced to yield

$$\begin{aligned} \mathbf{a}_1 - \mathbf{a}_2 &= -\ddot{\mathbf{l}}_b - 2\Omega^a_{ia}\dot{\mathbf{l}}_b - \left(\Omega^a_{ia}\Omega^a_{ia} + \dot{\Omega}^a_{ia}\right)\mathbf{l}_b - \mathbf{g}_1 + \mathbf{g}_2 \\ &= \left(\Gamma^a - \Omega^a_{ia}\Omega^a_{ia} - \dot{\Omega}^a_{ia}\right)(\mathbf{r}^a_2 - \mathbf{r}^a_1) \\ &\equiv L'^a\,(\mathbf{r}^a_2 - \mathbf{r}^a_1)\,. \end{aligned} \tag{5.2}$$

The second equality uses the assumption that the gravitational acceleration has a linear variation between the two accelerometer triads so that $\mathbf{g}^a_2 - \mathbf{g}^a_1 = \Gamma^a(\mathbf{r}^a_2 - \mathbf{r}^a_1)$. This linear assumption is quite valid since typical GGI baselines are less than one meter (See Sec. 1.2.1), whereas gradient correlation distances are on the order of kilometers.[87,88]

With knowledge of the accelerometer positions, the gradiometer measurement can now be made:

$$(\mathbf{a}_1 - \mathbf{a}_2)\,/\,(\mathbf{r}_2 - \mathbf{r}_1) = \Gamma^a - \Omega^a_{ia}\Omega^a_{ia} - \dot{\Omega}^a_{ia} \equiv L'^a. \tag{5.3}$$

It is important to note that the gravitational gradient tensor cannot be directly measured; instead, the gradients are masked by centripetal and angular accelerations. To exploit the gravitational gradients for position aiding, these rotational effects must be estimated or removed.

The angular acceleration may be easily removed, at least in theory, by averaging the GGI measurement with its transpose:

$$\frac{1}{2}\left(L'^{a} + (L'^{a})^{T}\right) = \Gamma^{a} - \Omega^{a}_{ia}\Omega^{a}_{ia} \equiv L^{a}. \tag{5.4}$$

Or equivalently, the six non-symmetric tensor component measurements can be represented in vector notation as

$$\mathbf{L}^{a} \equiv \begin{pmatrix} L^{a}_{11} \\ L^{a}_{12} \\ L^{a}_{13} \\ L^{a}_{22} \\ L^{a}_{23} \\ L^{a}_{33} \end{pmatrix} = \begin{pmatrix} \Gamma^{a}_{11} + \omega_y^2 + \omega_z^2 \\ \Gamma^{a}_{12} - \omega_x\omega_y \\ \Gamma^{a}_{13} - \omega_x\omega_z \\ \Gamma^{a}_{22} + \omega_x^2 + \omega_z^2 \\ \Gamma^{a}_{23} - \omega_y\omega_z \\ \Gamma^{a}_{33} + \omega_x^2 + \omega_y^2 \end{pmatrix}, \tag{5.5}$$

where $\boldsymbol{\omega}^{a}_{ia} = (\omega_x, \omega_y, \omega_z)^{T}$ is the angular velocity. The angular accelerations may be removed in this manner because they are the only asymmetric term in the raw GGI measurement, whereas the gravitational gradient and the centripetal acceleration matrices are both symmetric.

Another interesting corollary is that the angular accelerations can be observed directly by averaging the raw GGI measurement with the negative of its transpose:

$$\frac{1}{2}\left(L'^{a} - (L'^{a})^{T}\right) = \dot{\Omega}^{a}_{ia}. \tag{5.6}$$

The observability of the angular accelerations, which may be integrated twice to produce orientation information, is the basis for using a GGI for all-accelerometer inertial navigation. For more on this topic see Sec. 1.2.3 on pg. 31 and the papers by Zorn.[40,41]

A short word on nomenclature is necessary at this point. The GGI measurement observable, $\Gamma^a - \Omega^a_{ia}\Omega^a_{ia} - \dot{\Omega}^a_{ia}$, is not typically given a dedicated symbol. Therefore, this work essentially follows the terminology used by Jekeli[94] because his derivation was used as a starting point for many of the derivation in this chapter. The primary difference between the nomenclature in this work and Jekeli's is that he uses L to denote this GGI measurement. However, Jekeli notes that the gravitational gradient tensor is more easily observed when the angular acceleration term, $\dot{\Omega}^a_{ia}$, is not estimated. Thus, this work exclusively uses $L^a \equiv \Gamma^a - \Omega^a_{ia}\Omega^a_{ia}$ as the primary GGI measurement and L'^a as the raw, uncorrected measurement observable that includes the angular accelerations.

To complete the generic GGI measurement formulation, two items need to be addressed: The calculation of the gravitational gradients from the stored navigation frame to the measured accelerometer frame, and the contributions to $\boldsymbol{\omega}^a_{ia}$. The gradient transformation will be discussed first, and the rotation rates will follow.

5.1.1 Gravitational Gradient Transformation Matrix

The pre-computed gravitational gradient tensor map is rotated transformed into the measurement frame by pre- and post-multiplication of a navigation-to-accelerometer frame direction cosine matrix, see Eq. (4.16) on pg. 142,

$$\Gamma^a = C^a_n \Gamma^n C^a_n. \tag{5.7}$$

The coordinate transformation matrices may also be expanded to include an intermediate gravity gradiometer instrument ("g-") frame so that rotating disc GGIs

may be investigated. The expanded transformation is then:

$$\Gamma^a = C_n^a \Gamma^n C_a^n = C_g^a C_n^g \Gamma^n C_g^n C_a^g. \tag{5.8}$$

This new g-frame can be specialized to the body frame for a strapdown GGI:

$$\Gamma^a = C_b^a C_n^b \Gamma^n C_b^n C_a^b. \tag{5.9}$$

or to the inertial frame for a stabilized instrument:

$$\Gamma^a = C_i^a C_n^i \Gamma^n C_i^n C_a^i. \tag{5.10}$$

The body-to-navigation frame rotation matrix is tracked by the INS. The C_n^i transformation is uniquely a function of position and time:

$$\begin{aligned} C_n^i &= C_e^i C_n^e \\ &= (C_i^e)^T C_n^e = R_3(-\lambda - \omega_e t) R_2(\pi/2 + \phi) \\ &= \begin{pmatrix} -\sin\phi\cos(\lambda+\omega_e t) & -\sin(\lambda+\omega_e t) & -\cos\phi\cos(\lambda+\omega_e t) \\ -\sin\phi\sin(\lambda+\omega_e t) & \cos(\lambda+\omega_e t) & -\cos\phi\sin(\lambda+\omega_e t) \\ \cos\phi & 0 & -\sin\phi \end{pmatrix}, \end{aligned} \tag{5.11}$$

where Eq. (4.20) and (4.21) on pg. 143 have been used. The C_b^a and C_i^a rotations are based on the orientation of the accelerometer pairs. These gradient transformations will be further specified in the following sections.

The coordinate transformation $\Gamma^a = C_n^a \Gamma^n C_a^n$ can be alternatively written in vector notation as

$$\boldsymbol{\Gamma}^a = T_n^a \boldsymbol{\Gamma}^n, \tag{5.12}$$

where

$$\boldsymbol{\Gamma}^a \equiv (\Gamma_{11}^a, \Gamma_{12}^a, \Gamma_{13}^a, \Gamma_{22}^a, \Gamma_{23}^a, \Gamma_{33}^a)^T \tag{5.13}$$

and

$$\mathbf{\Gamma}^n \equiv (\Gamma^n_{11}, \Gamma^n_{12}, \Gamma^n_{13}, \Gamma^n_{22}, \Gamma^n_{23}, \Gamma^n_{33})^T \tag{5.14}$$

are vectors of the diagonal and upper-diagonal elements of the gravitational gradient tensor. This new 6×6 transformation matrix, T^a_n, is comprised of the components of C^a_n and can be derived in two ways as follows.

The first way to derive T^a_n is to symbolically compute $\Gamma^a = C^a_n \Gamma^n C^n_a$ and then rearrange the components of Γ^a into $\mathbf{\Gamma}^a$ and factor out Γ^n into $\mathbf{\Gamma}^n$. This results in

$$T^a_n = \begin{pmatrix} c^2_{11} & 2c_{11}c_{12} & 2c_{11}c_{13} & c^2_{12} & 2c_{12}c_{13} & c^2_{13} \\ c_{11}c_{21} & c_{11}c_{22} + c_{12}c_{21} & c_{11}c_{23} + c_{13}c_{21} & c_{12}c_{22} & c_{12}c_{23} + c_{13}c_{22} & c_{13}c_{23} \\ c_{11}c_{31} & c_{11}c_{32} + c_{12}c_{31} & c_{11}c_{33} + c_{13}c_{31} & c_{12}c_{32} & c_{12}c_{33} + c_{13}c_{32} & c_{13}c_{33} \\ c^2_{21} & 2c_{21}c_{22} & 2c_{21}c_{23} & c^2_{22} & 2c_{22}c_{23} & c^2_{23} \\ c_{21}c_{31} & c_{21}c_{32} + c_{22}c_{31} & c_{21}c_{33} + c_{23}c_{31} & c_{22}c_{32} & c_{22}c_{33} + c_{23}c_{32} & c_{23}c_{33} \\ c^2_{31} & 2c_{31}c_{32} & 2c_{31}c_{33} & c^2_{32} & 2c_{32}c_{33} & c^2_{33} \end{pmatrix}, \tag{5.15}$$

where c_{ij} is the ith row and jth column of C^a_n.[†]

Looking at Eq. (5.15), it appears that there are some patterns imbedded in the matrix. To better understand where these patterns arise from, and to develop a more robust shorthand notation for populating T^a_n, start with a single component

[†]The transformation matrix elements here are in the opposite order as those in the author's conference papers.[163,164] This is because the elements were based on C^n_b which is tracked by the INS quaternion. Here, it is based on C^a_n which is essentially the transpose of C^n_b if the GGI is a strapdown sensor, thus causing the c_{ij} in the conference papers to become c_{ji} here. Also, it was discovered after the conference proceedings that there is a small typo in these two references. The element in the first row, second column of T^b_n should be $2c_{11}c_{21}$ in these papers.

of Γ^a, say Γ^a_{ij}. One can then say that this component is equal to the summation of $\mathbf{\Gamma}^n$ and some coefficients that may be written as partial derivatives:

$$\Gamma^a_{ij} = \sum_{k=1}^{3}\sum_{l=1}^{3}\left(\frac{\partial x^a_i}{\partial x^n_k}\right)\left(\frac{\partial x^a_j}{\partial x^n_l}\right)\Gamma^n_{kl}, \tag{5.16}$$

where the partial derivative coefficients will be explained shortly. Expanding out this summation and combining coefficients for the symmetric elements of Γ^n, *i.e.* $\Gamma^n_{kl} = \Gamma^n_{lk}$, gives

$$\begin{aligned}
\Gamma^a_{ij} &= \left(\frac{\partial x^a_i}{\partial x^n_1}\right)\left(\frac{\partial x^a_j}{\partial x^n_1}\right)\Gamma^n_{11} + \left[\left(\frac{\partial x^a_i}{\partial x^n_1}\right)\left(\frac{\partial x^a_j}{\partial x^n_2}\right) + \left(\frac{\partial x^a_i}{\partial x^n_2}\right)\left(\frac{\partial x^a_j}{\partial x^n_1}\right)\right]\Gamma^n_{12} \\
&+ \left[\left(\frac{\partial x^a_i}{\partial x^n_1}\right)\left(\frac{\partial x^a_j}{\partial x^n_3}\right) + \left(\frac{\partial x^a_i}{\partial x^n_3}\right)\left(\frac{\partial x^a_j}{\partial x^n_1}\right)\right]\Gamma^n_{13} + \left(\frac{\partial x^a_i}{\partial x^n_2}\right)\left(\frac{\partial x^a_j}{\partial x^n_2}\right)\Gamma^n_{22} \\
&+ \left[\left(\frac{\partial x^a_i}{\partial x^n_2}\right)\left(\frac{\partial x^a_j}{\partial x^n_3}\right) + \left(\frac{\partial x^a_i}{\partial x^n_3}\right)\left(\frac{\partial x^a_j}{\partial x^n_2}\right)\right]\Gamma^n_{23} + \left(\frac{\partial x^a_i}{\partial x^n_3}\right)\left(\frac{\partial x^a_j}{\partial x^n_3}\right)\Gamma^n_{33}.
\end{aligned} \tag{5.17}$$

Now, the partial derivative coefficients may be thought of as the components of C^a_n because $\mathbf{x}^a = C^a_n\mathbf{x}^n$ so each element of x^a is

$$\begin{aligned}
x^a_i &= c_{i1}x^n_1 + c_{i2}x^n_2 + c_{i3}x^n_3 \\
&= \left(\frac{\partial x^a_i}{\partial x^n_1}\right)x^n_1 + \left(\frac{\partial x^a_i}{\partial x^n_2}\right)x^n_2 + \left(\frac{\partial x^a_i}{\partial x^n_3}\right)x^n_3,
\end{aligned} \tag{5.18}$$

where c_{ij} is again the ith row and jth column of C^a_n, and the second equality is using the notion that the transformation matrix is like a partial derivative of one element in one frame to another element in another state. Finally, substituting this notion that $\left(\partial x^a_i/\partial x^n_j\right) = c_{ij}$ into Eq. (5.17), one has

$$\begin{aligned}
\Gamma^a_{ij} &= \left(c_{i1}c_{j1}\right)\Gamma^n_{11} + \left(c_{i1}c_{j2} + c_{i2}c_{j1}\right)\Gamma^n_{12} + \left(c_{i1}c_{j3} + c_{i3}c_{j1}\right)\Gamma^n_{13} \\
&+ \left(c_{i2}c_{j2}\right)\Gamma^n_{22} + \left(c_{i2}c_{j3} + c_{i3}c_{j2}\right)\Gamma^n_{23} + \left(c_{i3}c_{j3}\right)\Gamma^n_{33},
\end{aligned} \tag{5.19}$$

which is essentially a row of T^a_n multiplied by $\mathbf{\Gamma}^n$. This equation is useful because it is a more convenient, and less error prone, way to implement T^a_n as compared to

Eq. (5.15) where all the rows have been written out. (Deriving this version of the T_n^a transformation matrix for the dissertation is how the errors in the conference paper T_n^b transformations were discovered.)

This T_n^a transformation matrix is a generic coordinate transformation for any n-frame symmetric matrix whose components are ordered as $(11, 12, 13, 22, 23, 33)^T$ to the corresponding a-frame vector. The initial and final coordinate frames are arbitrary as long as the c_{ij} coefficients used to populate the transformation matrix are consistent. In other words, if two arbitrary frames are used, say the "s" and "t" frames, then T_s^t can be computed using either formulation above by using the c_{ij} components of the known or calculated 3×3 C_s^t direction cosine matrix. Furthermore, this transformation matrix is computationally efficient because it exploits the tensor symmetry and is, most importantly, necessary for the linearized error formulations that follows.

5.1.2 Inertial-to-Accelerometer Frame Rotation Rate

The inertial-to-accelerometer angular velocity, $\boldsymbol{\omega}_{ia}^a$, can be decomposed into three components:

1. The inertial-to-body frame rotation rate, $\boldsymbol{\omega}_{ib}^b$, which is measured by the on-board strapdown gyros.
2. The body-to-accelerometer frame rotation rate, $\boldsymbol{\omega}_{bg}^g$, which accounts for rotation of the overall GGI with respect to the body axes.
3. The gradiometer-to-accelerometer frame rotation rate, $\boldsymbol{\omega}_{ga}^a$, which accounts for rotating disc GGIs, like the Bell/Textron models.

Mathematically, and including the appropriate coordinate frame transformations,

$$\boldsymbol{\omega}_{ia}^{a} = C_{g}^{a} C_{b}^{g} \boldsymbol{\omega}_{ib}^{b} + C_{g}^{a} \boldsymbol{\omega}_{bg}^{g} + \boldsymbol{\omega}_{ga}^{a}. \tag{5.20}$$

This angular velocity can now be specified to strapdown and stabilized GGIs with either rotating or stationary accelerometers.

For the strapdown GGI case, the gradiometer frame is assumed to be aligned with the body axes so that the "g" subscripts and superscripts may be replaced with "b." This results in

$$\begin{aligned} \boldsymbol{\omega}_{ia}^{a} &= C_{b}^{a} C_{b}^{b} \boldsymbol{\omega}_{ib}^{b} + C_{b}^{a} \boldsymbol{\omega}_{bb}^{b} + \boldsymbol{\omega}_{ba}^{a} \\ &= C_{b}^{a} \boldsymbol{\omega}_{ib}^{b} + \boldsymbol{\omega}_{ba}^{a}, \end{aligned} \tag{5.21}$$

since $C_{b}^{b} = I$ and $\boldsymbol{\omega}_{bb}^{b} = \mathbf{0}$. Therefore, a strapdown GGI must estimate the gyro measurements correctly and account for any accelerometer-to-body frame rotations and their rates to observe the gravitational gradient tensor.

The stabilized GGI instead assumes that the g-frame is aligned with the inertial i-frame so that the "g-"scripts becomes "i"s:

$$\begin{aligned} \boldsymbol{\omega}_{ia}^{a} &= C_{i}^{a} C_{b}^{i} \boldsymbol{\omega}_{ib}^{b} + C_{i}^{a} \boldsymbol{\omega}_{bi}^{i} + \boldsymbol{\omega}_{ga}^{a} \\ &= C_{i}^{a} \left(\boldsymbol{\omega}_{ib}^{i} + \boldsymbol{\omega}_{bi}^{i} \right) + \boldsymbol{\omega}_{ga}^{a} \\ &= \boldsymbol{\omega}_{ga}^{a}. \end{aligned} \tag{5.22}$$

This equation essentially states that the rotation rate of the accelerometers with respect to the gradiometer frame is the only rate that needs to be estimated and removed from the GGI measurement in order to exploit the gradient tensor for position updates.

The last portion of the rotation rate that needs to be addressed is the accelerometer-to-gradiometer frame rotation. As explained in the first chapter, the Bell/Textron based GGIs use rotating accelerometers to modulate the gradient signal to a higher frequency that exhibits lower system error. These instruments typically rotate the accelerometers at a nominally constant angular velocity, $\boldsymbol{\omega}^a_{ga}$, in the direction out of the plane made by the four accelerometers. This results in

$$\boldsymbol{\omega}^a_{ga} = (0, \quad 0, \quad \omega_{\text{rot}})^T , \tag{5.23}$$

where ω_{rot} is the nominal rotation rate of the disc. For non-rotating GGIs, as is the focus of this work, $\boldsymbol{\omega}^a_{ga} = \mathbf{0}$ nominally.

5.1.3 Rotating, Stabilized GGI Measurements

This subsection uses the previous section's results to derive the GGI measurement made by the Bell/Textron based instruments. (The Hughes Research Laboratory's GGI also has the same resultant measurement; however, it is based on torque differences.) The purpose of this subsection is, to attempt, to provide a straightforward derivation of this instrument's measurement observable because most papers which reference this gradiometer either present a confusing derivation or none at all. It is the hope to also show the flexibility of the previous section in deriving current and future gradiometer measurements.

Beginning with the differenced accelerometer equation, Eq. (5.2), in the accelerometer-frame:

$$(\mathbf{a}_1 - \mathbf{a}_2) = \left(\Gamma^a - \Omega^a_{ia}\Omega^a_{ia} - \dot{\Omega}^a_{ia}\right)(\mathbf{r}_2 - \mathbf{r}_1) = L'^a\,(\mathbf{r}_2 - \mathbf{r}_1)\,.$$

Then assuming the accelerometer triads are single accelerometers whose sensitive axes are in opposite directions and are displaced from the gradiometer disc's origin by one-half the instrument baseline in either direction (See Fig. 5.1), the accelerometer measurements and positions are

$$\mathbf{a}_1^a = \begin{pmatrix} 0 \\ a_1 \\ 0 \end{pmatrix}, \quad \mathbf{r}_1^a = \begin{pmatrix} l_b/2 \\ 0 \\ 0 \end{pmatrix}, \quad \mathbf{a}_2^a = \begin{pmatrix} 0 \\ -a_2 \\ 0 \end{pmatrix}, \quad \mathbf{r}_2^a = \begin{pmatrix} -l_b/2 \\ 0 \\ 0 \end{pmatrix}. \tag{5.24}$$

Substituting these into the finite differenced accelerometer equation above,

$$\begin{pmatrix} 0 \\ a_1^a + a_2^a \\ 0 \end{pmatrix} = L'^a \begin{pmatrix} -l_b \\ 0 \\ 0 \end{pmatrix} = -l_b \begin{pmatrix} L'^a_{11} \\ L'^a_{21} \\ L'^a_{31} \end{pmatrix}. \tag{5.25}$$

Since the accelerometers are only measuring the second entry of the this array, the GGI measurement can by found by taking that component and dividing it by the instrument baseline:

$$(a_1^a + a_2^a)/l_b = -L'^a_{21} = -\left(\Gamma^a_{21} - \omega^a_x \omega^a_y - \dot{\omega}^a_z\right), \tag{5.26}$$

where the definition of L'^a has been used, and $(\omega^a_x, \omega^a_y, \omega^a_z)^T = \boldsymbol{\omega}^a_{ia}$.

The rotating gravitational gradient tensor in the accelerometer frame is calculated from the gradiometer frame by

$$\Gamma^a = C^a_g \Gamma^g C^g_a, \tag{5.27}$$

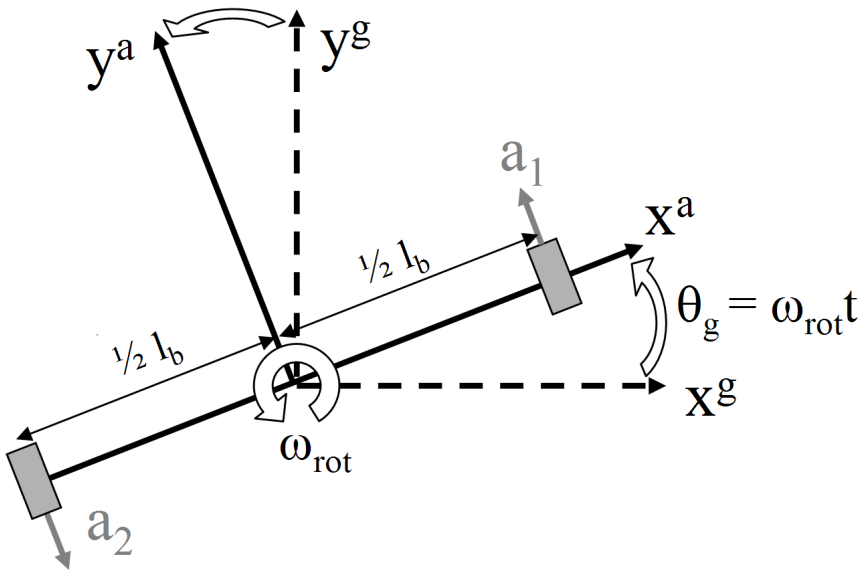

Figure 5.1: Schematic of GGI with 2 Rotating Accelerometers

where the gradiometer-to-accelerometer frame rotation matrix is, from Fig. 5.1,

$$C_g^a = R_3(\theta_g) = \begin{pmatrix} \cos\theta_g & \sin\theta_g & 0 \\ -\sin\theta_g & \cos\theta_g & 0 \\ 0 & 0 & 0 \end{pmatrix}. \tag{5.28}$$

Carrying out the multiplication and only keeping the Γ_{21}^a element,

$$\begin{aligned} \Gamma_{21}^a &= -\Gamma_{11}^g \sin\theta_g \cos\theta_g - \Gamma_{12}^g \sin^2\theta_g + \Gamma_{12}^g \cos^2\theta_g + \Gamma_{22}^g \sin\theta_g \cos\theta_g \\ &= (1/2)\left(\Gamma_{22}^g - \Gamma_{11}^g\right)\sin 2\theta_g + \Gamma_{12}^g \cos 2\theta_g, \end{aligned} \tag{5.29}$$

and $\theta_g = \omega_{\rm rot} t$, where $\omega_{\rm rot}$ is the nominally constant rotation rate of the GGI disc.

The Bell/Textron instrument is built and used on a stabilized platform, so its accelerometer-to-inertial angular velocity is just the rotation rate of the accelerometers with respect to the gradiometer frame. In other words,

$$\boldsymbol{\omega}_{ia}^a = \boldsymbol{\omega}_{ga}^a = (0, \quad 0, \quad \omega_{\rm rot})^T. \tag{5.30}$$

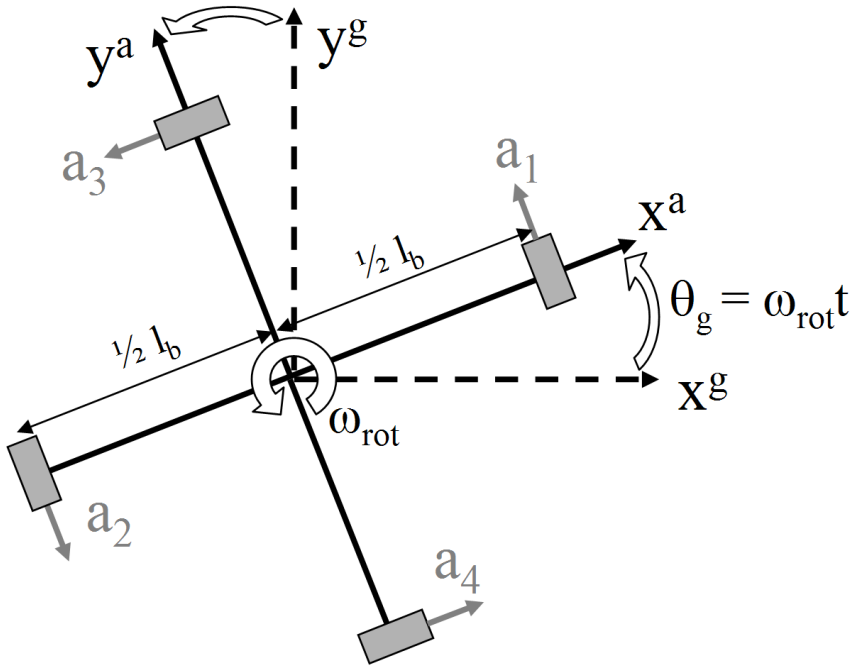

Figure 5.2: Schematic of GGI with 4 Rotating Accelerometers

Thus, there is essentially no angular motion in the x-y plane of the a- or g-frames, and the only angular acceleration in the a-frame is caused by deviations from the nominal disc rotation rate. Mathematically,

$$\omega_x = \omega_y = 0, \tag{5.31}$$

$$\dot{\omega}_z = \delta\dot{\omega}_{rot}. \tag{5.32}$$

Therefore, after substituting Eq. (5.29) and (5.32) into Eq. (5.26), the stabilized, rotating disc gradiometer measurement is

$$(a_1^a + a_2^a)/l_b = -L_{21}'^a = (1/2)\left(\Gamma_{11}^g - \Gamma_{22}^g\right)\sin 2\theta_g - \Gamma_{12}^g \cos 2\theta_g + \delta\dot{\omega}_{\rm rot}.$$

Furthermore, if a second pair of accelerometers are mounted 90° from the first set

in the x^a-y^a frame (Fig. 5.2), they would measure

$$\begin{aligned}(a_3^a + a_4^a)/l_b &= (1/2)\left(\Gamma_{11}^g - \Gamma_{22}^g\right)\sin(2\theta_g + 180^\circ) - \Gamma_{12}^g \cos(2\theta_g + 180^\circ) + \delta\dot{\omega}_{\text{rot}} \\ &= -(1/2)\left(\Gamma_{11}^g - \Gamma_{22}^g\right)\sin 2\theta_g + \Gamma_{12}^g \cos 2\theta_g + \delta\dot{\omega}_{\text{rot}}. \end{aligned} \tag{5.33}$$

Subtracting the second pair of accelerometers from the first pair produces a gradiometer measurement with twice the magnitude of a single accelerometer pair and with no angular acceleration errors (at least theoretically):

$$\left[(a_1^a + a_2^a) - (a_3^a + a_4^a)\right]/l_b = \left(\Gamma_{11}^g - \Gamma_{22}^g\right)\sin 2\theta_g - 2\Gamma_{12}^g \cos 2\theta_g. \tag{5.34}$$

The above equation is the measurement presented in many Bell/Textron GGI references with obtuse or absent derivations. However, because current laboratory gradiometers use non-rotating inertial measurement units, this type of sensor's linearized error equation was not pursued. But for completeness sake, it was presented so that is could be used for reference purposes.

5.2 Modeled Twelve-Accelerometer GGI

This section describes the envisioned gravity gradiometer instrument that was used in this research. The GGI is a set of three orthogonal accelerometer triads equally displaced from a central accelerometer in each of the gradiometer frame's cardinal directions. Figure 5.3 illustrates this notional gradiometer where each arrow represents a single accelerometer. The location and normalized specific force measurement for each of the twelve accelerometers are:

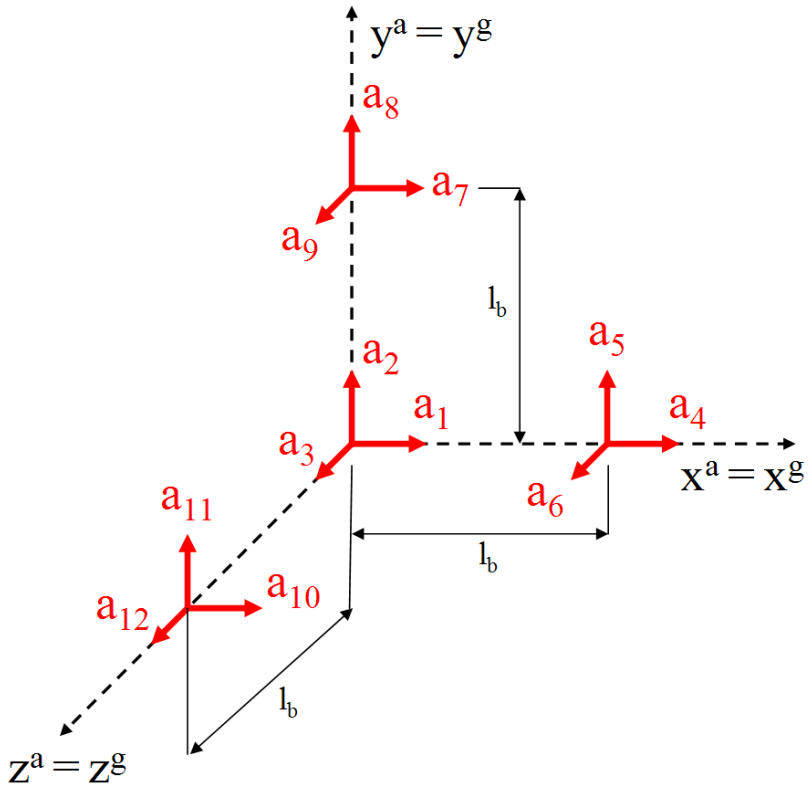

Figure 5.3: Schematic of Modeled Twelve-Accelerometer GGI

$$\mathbf{r}_1^a = \mathbf{r}_2^a = \mathbf{r}_3^a = (0, \quad 0, \quad 0)^T, \tag{5.35a}$$

$$\mathbf{r}_4^a = \mathbf{r}_5^a = \mathbf{r}_6^a = (l_b, \quad 0, \quad 0)^T, \tag{5.35b}$$

$$\mathbf{r}_7^a = \mathbf{r}_8^a = \mathbf{r}_9^a = (0, \quad l_b, \quad 0)^T, \tag{5.35c}$$

$$\mathbf{r}_{10}^a = \mathbf{r}_{11}^a = \mathbf{r}_{12}^a = (0, \quad 0, \quad l_b)^T, \tag{5.35d}$$

and

$$\mathbf{a}_1^a/a_1 = \mathbf{a}_4^a/a_4 = \mathbf{a}_7^a/a_7 = \mathbf{a}_{10}^a/a_{10} = (1, \quad 0, \quad 0)^T, \tag{5.36a}$$

$$\mathbf{a}_2^a/a_2 = \mathbf{a}_5^a/a_5 = \mathbf{a}_8^a/a_8 = \mathbf{a}_{11}^a/a_{11} = (0, \quad 1, \quad 0)^T, \tag{5.36b}$$

$$\mathbf{a}_3^a/a_3 = \mathbf{a}_6^a/a_6 = \mathbf{a}_9^a/a_9 = \mathbf{a}_{12}^a/a_{12} = (0, \quad 0, \quad 1)^T. \tag{5.36c}$$

By differencing pairs of accelerometers that are located at different locations and dividing by the instrument's baseline distance, the full L'^a tensor can be computed. For example, the L'^a_{11} component of the uncorrected GGI measurement matrix is found by differencing the two x^a accelerometers that are separated in the x^a direction, *i.e.* $\mathbf{a}_4$ and $\mathbf{a}_1$. Mathematically,

$$\begin{aligned} \mathbf{a}_4 - \mathbf{a}_1 &= L'^a \left(\mathbf{r}_4^a - \mathbf{r}_1^a\right), \\ \begin{pmatrix} a_4 - a_1 \\ 0 \\ 0 \end{pmatrix} &= \begin{pmatrix} L'^a_{11} & L'^a_{12} & L'^a_{13} \\ L'^a_{21} & L'^a_{22} & L'^a_{23} \\ L'^a_{31} & L'^a_{32} & L'^a_{33} \end{pmatrix} \begin{pmatrix} l_b - 0 \\ 0 \\ 0 \end{pmatrix} = l_b \begin{pmatrix} L'^a_{11} \\ L'^a_{21} \\ L'^a_{31} \end{pmatrix}, \end{aligned} \tag{5.37}$$

where Eq. (5.2) on pg. 185 has been used. Because only the first element of the array is measured by the accelerometers, one has

$$a_4 - a_1 = l_b L'^a_{11} \quad \rightarrow \quad L'^a_{11} = (a_4 - a_1)/l_b. \tag{5.38}$$

Similar pairs of accelerometers may be differenced to calculate all the elements in L'^a:

$$L'^a = \frac{1}{l_b} \begin{pmatrix} (a_4 - a_1) & (a_7 - a_1) & (a_{10} - a_1) \\ (a_5 - a_2) & (a_8 - a_2) & (a_{11} - a_2) \\ (a_6 - a_3) & (a_9 - a_3) & (a_{12} - a_3) \end{pmatrix} = \Gamma^a - \Omega^a_{ia}\Omega^a_{ia} - \dot{\Omega}^a_{ia}. \tag{5.39}$$

As shown by Eq. (5.4) on pg. 186, the angular accelerations can be eliminated by averaging the L'^a measurement with its transpose, which is equivalent to averaging off-diagonal elements. For example,

$$\begin{aligned}(1/2)(L'^a_{12} + L'^a_{21}) &= [(a_7 - a_1) + (a_5 - a_2)]/(2l_b) \\ &= (1/2)\left[(\Gamma^a_{12} - \omega_x\omega_y + \dot{\omega}_z) + (\Gamma^a_{21} - \omega_x\omega_y - \dot{\omega}_z)\right] \\ L^a_{12} &= [(a_7 - a_1) + (a_5 - a_2)]/(2l_b) = \Gamma^a_{12} - \omega_x\omega_y \end{aligned} \tag{5.40}$$

The full L^a tensor is similarly found by

$$L^a = \frac{1}{l_b}\begin{pmatrix} (a_4 - a_1) & \frac{1}{2}[(a_7 - a_1) + (a_5 - a_2)] & \frac{1}{2}[(a_{10} - a_1) + (a_6 - a_3)] \\ & (a_8 - a_2) & \frac{1}{2}[(a_{11} - a_2) + (a_9 - a_3)] \\ sym & & (a_{12} - a_3) \end{pmatrix}. \tag{5.41}$$

Therefore, it is apparent that the on-diagonal elements of L^a require only two accelerometers to measure, whereas the off-diagonal elements require four.

The individual accelerometers' specific force measurements of the GGI are not actually simulated. Instead, the overall measurement is computed for a given position (and orientation and rotation rate for a strapdown GGI). This modeling choice was made because the gradiometer's manufacturer typically employs special feedback loops to correct the GGI's internal accelerometer errors and only the overall instrument noise is specified. Also, because the accelerometers are stationary with respect to the gradiometer frame, it is assumed that $C^a_g = C^g_a = I$, as shown in Fig. 5.3. Thus, the noisy gradiometer measurement is simulated as

$$\widetilde{L}^a = \widetilde{L}^g = C^g_n \Gamma^n C^n_g - \Omega^a_{ia}\Omega^a_{ia} + V_L, \tag{5.42}$$

where $\Gamma^n = \Gamma^n(\mathbf{r}^n)$ is linearly interpolated from the gridded, stored gravitational gradient map to the user's true position, $\boldsymbol{\omega}_{ia}^a$ is calculated according to the discussion in Sec. 5.1.2, and V_L is a matrix of uncorellated, white Gaussian measurement noise of specified variance. It is implicitly assumed that the GGI is at the vehicle's center of mass so that lever arm effects are neglected. Also, higher order interpolation methods such as least-squares collocation, which optimally accounts for the error in the estimated gravity field, could be implemented in place of the simplistic linear interpolation.[95, 165]

The gradiometer matrix measurement, Eq. (5.42), can be alternatively written in vector form as

$$\widetilde{\mathbf{L}}^a = \begin{pmatrix} L_{11}^a \\ L_{12}^a \\ L_{13}^a \\ L_{22}^a \\ L_{23}^a \\ L_{33}^a \end{pmatrix} = T_n^a \begin{pmatrix} \Gamma_{\mathrm{NN}} \\ \Gamma_{\mathrm{NE}} \\ \Gamma_{\mathrm{ND}} \\ \Gamma_{\mathrm{EE}} \\ \Gamma_{\mathrm{ED}} \\ \Gamma_{\mathrm{DD}} \end{pmatrix} + \begin{pmatrix} \omega_y^2 + \omega_z^2 \\ -\omega_x\omega_y \\ -\omega_x\omega_z \\ \omega_x^2 + \omega_z^2 \\ -\omega_y\omega_z \\ \omega_x^2 + \omega_y^2 \end{pmatrix} + \boldsymbol{\nu}_L, \tag{5.43}$$

where ω_j is the j^{th} component of $\boldsymbol{\omega}_{ia}^a$, T_n^a is calculated by Eq. (5.15) on pg. 189 using $C_n^a = C_n^g$, and $\boldsymbol{\nu}_L$ is the vector of measurement noise. The estimated GGI measurement is computed similarly, but using the INS's estimated position (and for the case of the strapdown GGI, orientation and rotation rate) and without an estimate of the noise vector.

The overall twelve-accelerometer instrument may be physically strapped down to the body or stabilized on an inertial platform. Each configuration has its own

advantages and disadvantages, much like the tradeoffs between strapdown of stabilized IMUs. The benefit of a strapdown GGI is that a massive, complex stabilized platform is unnecessary for the instrument-vehicle integration. The drawbacks are that the sensor must now be able to estimate the angular errors of the vehicle, which may cause numerical issues as will be shown in the Results chapter, and that the instrument must be robust enough to perform in a dynamic environment. When considering the precision of current GGI's proof mass displacement measurement and the dynamics of the airborne environment, the second issue (increased robustness) is probably the most difficult to overcome. This leads to why almost all gradiometers are integrated with a stabilized platform that isolates the sensor from the body dynamics. These platforms, currently, are on the order of a washing machine in size, and their isolation characteristics, along with the GGI fragility, are the limiting factors on noise level reduction for airborne gravity gradiometry (H. J. Paik, Personal Communication, University of Maryland, College Park, May 14, 2007). The future potential performance of both classes of sensors are investigated and reported in the following chapters. But first, their measurements and linearized error dynamics are derived for use by the extended Kalman filter in the next subsections.

5.2.1 Strapdown Gravity Gradiometer Instrument

As mentioned above, the strapdown GGI is assumed to make measurements in the body frame with stationary accelerometers aligned to the body frame. Symbolically, the strapped down gradiometer measurement is found by substituting Eq. (5.9)

and (5.21) into Eq. (5.4) with $C_g^a = I$ and $\boldsymbol{\omega}_{ba}^a = \mathbf{0}$. The result is

$$L^b = C_n^b \Gamma^n C_b^n - \Omega_{ib}^b \Omega_{ib}^b. \tag{5.44}$$

The body-to-navigation frame rotation matrix, C_b^n, is calculated by the truth inertial navigation system quaternion, and Ω_{ib}^b is the calculated by the truth simulated gyros.

The modeled GGI measurement is corrupted by white, Gaussian noise and uses the truth INS and gyro states to calculate $\widetilde{L}^b$ at a given data rate. The strapdown GGI's estimated measurement is modeled as

$$\widehat{L}^b = \widehat{C}_n^b \widehat{\Gamma}^n \widehat{C}_b^n - \widehat{\Omega}_{ib}^b \widehat{\Omega}_{ib}^b. \tag{5.45}$$

Where $\widehat{C}_n^b$ is the INS estimate, $\widehat{\Gamma}^n = \Gamma^n(\mathbf{r}^n)$, and $\widehat{\Omega}_{ib}^b$ is calculated from the gyro measurement after it has been corrected for by scale factor, bias, and noise errors (see Eq. (4.111) on pg. 174). The strapdown GGI residual is then

$$\delta \mathbf{L}^b = \widehat{\mathbf{L}}^b - \widetilde{\mathbf{L}}^b, \tag{5.46}$$

after being reorganized into vector notation.

The simulated strapdown gradiometer measurement and estimate could also by calculated using Eq. (5.43) with the appropriate transformation matrix (C_n^b or $\widehat{C}_n^b$), position ($\mathbf{r}^n$ or $\widehat{\mathbf{r}}^n$) for the gradient interpolation, and gyro signal ($\boldsymbol{\omega}_{ib}^b$ or $\widetilde{\boldsymbol{\omega}}_{ib}^b$). Of course, the noise vector would only by included in the simulated measurement, not the estimate. The linearized error will now be derived for the Kalman filter update equations.

Typically, the gravity gradient errors consist of registration errors due to incorrect position knowledge, stored map errors, and instrument errors such as scale

factors, biases, nonlinearities, noise, etc.[20,36] The simplifying assumption will be made that there are no map errors which implies that the spherical harmonic model is sufficiently accurate at altitude. The assumption that the GGI errors are only a product of white noise is also made. (Red noise is sometimes used for low frequency deviations,[99] but is neglected here because of the relatively fast update rates.) Since a GGI is an extremely sensitive instrument, the manufacturer would employ its own means to internally monitor and correct most other error sources. Therefore, only the registration and white noise instrument error are considered from this set.

Other error sources occur due to incorrect rotation knowledge from the navigation frame to the gradiometer frame and centripetal errors due to imprecise rotation rate knowledge. Jekeli[94] included the centripetal terms, but the rotation matrix error contribution has not been thoroughly derived or investigated to the authors' knowledge. The following formulations will include both of these error sources along with the registration and white noise errors for use with a strapdown GGI. The case of a simulated stabilized GGI will then be derived from this expression.

To derive the strapdown GGI Kalman filter measurement form, we will begin by linearly perturbing the gradiometer measurement, Eq. (5.44), to get

$$\begin{aligned} \delta L^b &= C_n^b \left(\Psi^n \Gamma^n + \delta\Gamma^n - \Gamma^n \Psi^n\right) C_b^n - \delta\Omega_{ib}^b \Omega_{ib}^b - \Omega_{ib}^b \delta\Omega_{ib}^b + V_L \\ &= C_n^b \left(\delta\Gamma^n + L_\psi^n\right) C_b^n - L_\omega^b + V_L, \end{aligned} \tag{5.47}$$

where

$$L_\psi^n \equiv \Psi^n \Gamma^n - \Gamma^n \Psi^n, \tag{5.48}$$

$$L_\omega^b \equiv \delta\Omega_{ib}^b \Omega_{ib}^b + \Omega_{ib}^b \delta\Omega_{ib}^b \tag{5.49}$$

are both symmetric matrices, Ψ^n is the skew-symmetric matrix of rotation errors $\boldsymbol{\psi}^n = (\psi_N, \psi_E, \psi_D)^T$, and V_L is a matrix of instrument errors that includes the accelerometer differencing errors.

Following the assumptions above, the n-frame gravity gradients are only in error due to incorrect position knowledge, or *registration errors*. Mathematically,

$$\delta\boldsymbol{\Gamma}^n = \left[\frac{\partial\boldsymbol{\Gamma}^n}{\partial\phi}\right]\delta\phi + \left[\frac{\partial\boldsymbol{\Gamma}^n}{\partial\lambda}\right]\delta\lambda + \left[\frac{\partial\boldsymbol{\Gamma}^n}{\partial h}\right]\delta h \equiv \left[\frac{\partial\boldsymbol{\Gamma}^n}{\partial\mathbf{r}^n}\right]\delta\mathbf{r}^n. \tag{5.50}$$

Since six observations are made for each full tensor GGI measurement, $[\partial\boldsymbol{\Gamma}^n/\partial\mathbf{r}^n]$ is a 6×3 matrix that represents the third-order tensor of the gravity potential. Due to symmetry and Laplace's constraint, this matrix could be computationally reduced to only include its seven independent components.[36] However, for simple implementation purposes, the partial derivatives of $\boldsymbol{\Gamma}^n$ with respect to latitude, longitude and altitude are computed by second-order central finite differences and linear interpolation to the estimated position. As mentioned before, higher order methods such as least-squares collocation would be preferable for a real system to account for errors in the estimated gravity field.[95,165]

The error in the navigation-to-body frame rotation can be found by multiply-

ing out L_ψ^n:

$$L_\psi^n \equiv \Psi^n\Gamma^n - \Gamma^n\Psi^n$$

$$= \begin{pmatrix} 2(\Gamma_{\mathrm{ND}}\psi_E - \Gamma_{\mathrm{NE}}\psi_D) & \begin{matrix} -\Gamma_{\mathrm{ND}}\psi_N + \Gamma_{\mathrm{ED}}\psi_E \\ +(\Gamma_{\mathrm{NN}} - \Gamma_{\mathrm{EE}})\psi_D \end{matrix} & \begin{matrix} \Gamma_{\mathrm{NE}}\psi_N + (\Gamma_{\mathrm{DD}} - \Gamma_{\mathrm{NN}})\psi_E \\ -\Gamma_{\mathrm{ED}}\psi_D \end{matrix} \\ & 2(-\Gamma_{\mathrm{ED}}\psi_N + \Gamma_{\mathrm{NE}}\psi_D) & \begin{matrix} (\Gamma_{\mathrm{EE}} - \Gamma_{\mathrm{DD}})\psi_N - \Gamma_{\mathrm{NE}}\psi_E \\ +\Gamma_{\mathrm{ND}}\psi_D \end{matrix} \\ sym & & 2(\Gamma_{\mathrm{ED}}\psi_N - \Gamma_{\mathrm{ND}}\psi_E). \end{pmatrix} \tag{5.51}$$

Then, rearranging the diagonal and upper-diagonal elements into the equivalent vector notations and factoring out $\boldsymbol{\psi}^n$:

$$\begin{pmatrix} L_{\psi,11}^n \\ L_{\psi,12}^n \\ L_{\psi,13}^n \\ L_{\psi,22}^n \\ L_{\psi,23}^n \\ L_{\psi,33}^n \end{pmatrix} = \begin{pmatrix} 0 & 2\Gamma_{ND} & -2\Gamma_{NE} \\ -\Gamma_{ND} & \Gamma_{ED} & \Gamma_{NN} - \Gamma_{EE} \\ \Gamma_{NE} & \Gamma_{DD} - \Gamma_{NN} & -\Gamma_{ED} \\ -2\Gamma_{ED} & 0 & 2\Gamma_{NE} \\ \Gamma_{EE} - \Gamma_{DD} & -\Gamma_{NE} & \Gamma_{ND} \\ 2\Gamma_{ED} & -2\Gamma_{ND} & 0 \end{pmatrix} \begin{pmatrix} \psi_N \\ \psi_E \\ \psi_D \end{pmatrix}, \tag{5.52}$$

or more compactly

$$\mathbf{L}_\psi^n = \left[\frac{\partial \mathbf{L}_\psi^n}{\partial \boldsymbol{\psi}^n}\right] \boldsymbol{\psi}^n. \tag{5.53}$$

Following a similar procedure, the rotation rate error contribution to the grav-

ity measurement is calculated using Eq. (5.49), which when expanded out is

$$L^b_\omega \equiv \delta\Omega^b_{ib}\Omega^b_{ib} + \Omega^b_{ib}\delta\Omega^b_{ib}$$

$$= \begin{pmatrix} -2(\omega_y\delta\omega_y + \omega_z\delta\omega_z) & \omega_y\delta\omega_x + \omega_x\delta\omega_y & \omega_z\delta\omega_x + \omega_x\delta\omega_z \\ & -2(\omega_x\delta\omega_x + \omega_z\delta\omega_z) & \omega_z\delta\omega_y + \omega_y\delta\omega_z \\ sym & & -2(\omega_x\delta\omega_x + \omega_y\delta\omega_y) \end{pmatrix}, \tag{5.54}$$

where $(\omega_x, \omega_y, \omega_z)^T = \boldsymbol{\omega}^b_{ib}$ here. Then the vector form is

$$\mathbf{L}^b_\omega \equiv \begin{pmatrix} L^b_{\omega,11} \\ L^b_{\omega,12} \\ L^b_{\omega,13} \\ L^b_{\omega,22} \\ L^b_{\omega,23} \\ L^b_{\omega,33} \end{pmatrix} = \begin{pmatrix} 0 & -2\omega_y & -2\omega_z \\ \omega_y & \omega_x & 0 \\ \omega_z & 0 & \omega_x \\ -2\omega_x & 0 & -2\omega_z \\ 0 & \omega_z & \omega_y \\ -2\omega_x & -2\omega_y & 0 \end{pmatrix} \begin{pmatrix} \delta\omega_x \\ \delta\omega_y \\ \delta\omega_z \end{pmatrix} \equiv \left[\frac{\partial \mathbf{L}^b_\omega}{\partial \boldsymbol{\omega}^b_{ib}}\right] \delta\boldsymbol{\omega}^b_{ib}. \tag{5.55}$$

The linearized measurement errors for a strapdown gravity gradiometer can now be found. Substituting Eqs. (5.50), (5.52), & (5.55) into Eq. (5.47) with the transformation matrix T^b_n (Eq. (5.15) using C^b_n), and the gyro error states, Eq. (4.114) on pg. 175, gives

$$\begin{aligned} \delta\mathbf{L^b} &= T^b_n \left[\frac{\partial \boldsymbol{\Gamma}^n}{\partial \mathbf{r}^n}\right] \delta\mathbf{r}^n + T^b_n \left[\frac{\partial \mathbf{L}^n_\psi}{\partial \boldsymbol{\psi}^n}\right] \boldsymbol{\psi}^n \\ &\quad - \left[\frac{\partial \mathbf{L}^b_\omega}{\partial \boldsymbol{\omega}^b_{ib}}\right] \left[\widetilde{\boldsymbol{\omega}}^b_{ib}\cdot\right] \delta\mathbf{SF}^g - \left[\frac{\partial \mathbf{L}^b_\omega}{\partial \boldsymbol{\omega}^b_{ib}}\right] \delta\mathbf{b}^g - \left[\frac{\partial \mathbf{L}^b_\omega}{\partial \boldsymbol{\omega}^b_{ib}}\right] \delta\mathbf{n}^g + \boldsymbol{\nu}_L, \end{aligned} \tag{5.56}$$

where $[\widetilde{\boldsymbol{\omega}}^b_{ib}\cdot]$ is a diagonal matrix whose components are the measured rotation rate, and $\boldsymbol{\nu}_L$ is the vector of uncorrelated white measurement noise. The Kalman filter update matrix is implemented by using the coefficient matrices of Eq. (5.56) above

in the appropriate columns of the H_L^b matrix, and the remaining columns are filled with zeros.

5.2.2 Stabilized Gravity Gradiometer Instrument

The stabilized gravity gradiometer instrument assumes that the stabilized platform continually aligns the gradiometer's axes to the Earth-Centered-Inertial frame. Using Eq. (5.10) and (5.22) with the assumption that the accelerometers are stationary with respect to the g-frame so that $C_g^a = I$ and $\boldsymbol{\omega}_{ga}^a = \mathbf{0}$, the stabilized GGI truth measurement is

$$L^i = C_n^i \Gamma^n C_i^n, \tag{5.57}$$

because there are no GGI angular rates with respect to the inertial frame. The navigation-to-inertial frame direction cosine matrix is calculated by Eq. (5.11) on pg. 188 using the truth position.

The stabilized GGI residual is calculated by subtracting the noisy measurement from the inertial navigation system's estimated gradiometer reading:

$$\delta L^i = \widehat{L}^i - \left(L^i + V_L\right), \tag{5.58}$$

where $L^i + V_L \equiv \widetilde{L}^i$ is the simulated measurement with error, and V_L is a matrix of uncorrelated measurement noise.

The linearized error between the GGI measurement and INS estimate is found by linearly perturbing Eq. (5.57):

$$\begin{aligned} \delta L^i &= C_n^i \left(\Psi_{in}^n \Gamma^n + \delta\Gamma^n - \Gamma^n \Psi_{in}^n\right) C_i^n + V_L \\ &= C_n^i \left(\delta\Gamma^n + L_\psi^i\right) C_i^n + V_L, \end{aligned} \tag{5.59}$$

where

$$L^i_\psi \equiv \Psi^n_{in}\Gamma^n - \Gamma^n\Psi^n_{in}, \tag{5.60}$$

and Ψ^n_{in} is the skew symmetric rotation error matrix from the navigation-to-inertial frame with coordinates in the n-frame. This matrix is different than the traditional matrix Ψ^n which is equivalent to Ψ^n_{bn}, or the n-to-b-frame rotation error.

The navigation-to-inertial frame error can be calculated as follows. First, using the definition of a small-error rotation, Eq. (4.72) on pg. 162, and taking its transpose, one has

$$\delta C^i_n = C^i_n \Psi^n_{in}. \tag{5.61}$$

Using Eq. (5.11) and linearly perturbing each element results in

$$\delta C^i_n = \begin{pmatrix} \begin{matrix} -\cos\phi\cos\lambda\delta\phi \\ +\sin\phi\sin\lambda(\delta\lambda+\omega_e\delta t) \end{matrix} & -\cos\lambda(\delta\lambda+\omega_e\delta t) & \begin{matrix} \sin\phi\cos\lambda\delta\phi \\ +\cos\phi\sin\lambda(\delta\lambda+\omega_e\delta t) \end{matrix} \\ \begin{matrix} -\cos\phi\sin\lambda\delta\phi \\ -\sin\phi\cos\lambda(\delta\lambda+\omega_e\delta t) \end{matrix} & -\sin\lambda(\delta\lambda+\omega_e\delta t) & \begin{matrix} \sin\phi\sin\lambda\delta\phi \\ -\cos\phi\cos\lambda(\delta\lambda+\omega_e\delta t) \end{matrix} \\ -\sin\phi\delta\phi & 0 & -\cos\phi\delta\phi \end{pmatrix}, \tag{5.62}$$

which can be factored into C^i_n and the resultant small error rotation matrix:

$$\Psi^n_{in} = \begin{pmatrix} 0 & \sin\phi(\delta\lambda+\omega_e\delta t) & -\delta\phi \\ -\sin\phi(\delta\lambda+\omega_e\delta t) & 0 & -\cos\phi(\delta\lambda+\omega_e\delta t) \\ \delta\phi & \cos\phi(\delta\lambda+\omega_e\delta t) & 0 \end{pmatrix} \tag{5.63}$$

which is the skew symmetric matrix of the error rotation vector

$$\boldsymbol{\psi}^n_{in} = \left(\cos\phi(\delta\lambda+\omega_e\delta t), \quad -\delta\phi, \quad -\sin\phi(\delta\lambda+\omega_e\delta t)\right)^T, \tag{5.64}$$

This error rotation vector is essentially the same as $\boldsymbol{\omega}_{in}^{n}$ rotation rate (Eq. (4.23) on pg. 144), but where the time differential operator, $d()/dt$, has been replaced with the linear perturbation operator, $\delta()$. $\boldsymbol{\psi}_{in}^{n}$ can also be decomposed into INS error states:

$$\boldsymbol{\psi}_{in}^{n} = \begin{pmatrix} 0 & \cos\phi & 0 \\ -1 & 0 & 0 \\ 0 & -\sin\phi & 0 \end{pmatrix} \begin{pmatrix} \delta\phi \\ \delta\lambda \\ \delta h \end{pmatrix} + \begin{pmatrix} (\omega_e/c)\cos\phi \\ 0 \\ -(\omega_e/c)\sin\phi \end{pmatrix} (c\delta b_u) \tag{5.65}$$

or, more compactly as

$$\boldsymbol{\psi}_{in}^{n} = \left[\frac{\partial \boldsymbol{\psi}_{in}^{n}}{\partial \mathbf{r}^{n}}\right] \delta\mathbf{r}^{n} + \left[\frac{\partial \boldsymbol{\psi}_{in}^{n}}{\partial c b_u}\right] c\delta b_u, \tag{5.66}$$

where ω_e is Earth's rotation rate, c is the speed of light, and $c\delta b_u$ is the user's clock error, which for this work has the same dynamics as the GPS clock from Sec. D.4.

The linearized stabilized gradiometer measurement error can now be found using a formulation similar to Eq. (5.56) but using the new rotation error equation above and omitting the gyro errors:

$$\delta\mathbf{L}^{i} = T_{n}^{i} \left\{ \left[\frac{\partial \boldsymbol{\Gamma}^{n}}{\partial \mathbf{r}^{n}}\right] + \left[\frac{\partial \mathbf{L}_{\psi}^{n}}{\partial \boldsymbol{\psi}^{n}}\right] \left[\frac{\partial \boldsymbol{\psi}_{in}^{n}}{\partial \mathbf{r}^{n}}\right] \right\} \delta\mathbf{r}^{n} + T_{n}^{i} \left[\frac{\partial \mathbf{L}_{\psi}^{n}}{\partial \boldsymbol{\psi}^{n}}\right] \left[\frac{\partial \boldsymbol{\psi}_{in}^{n}}{\partial c b_u}\right] c\delta b_u + \boldsymbol{\nu}_L, \tag{5.67}$$

where T_{n}^{i} is calculated using Eq. (5.15) on pg. 189 with C_{n}^{i} as calculated in Eq. (5.11) on pg. 188.

5.3 Chapter Summary

This chapter presents a methodology to derive the measurements for a vast array of GGI configurations in Sec. 5.1. The methodology includes a new transformation matrix for converting on- and off-diagonal symmetric tensor components

from the North-East-Down navigation frame to an arbitrary frame in Sec. 5.1.1. And Sec. 5.1.2 includes the second part of the GGI measurement methodology which accounts for angular velocity effects which essentially mask the gravitational gradients in the GGI measurements. Section 5.1.3 then uses the presented methodology to derive the rotating, stabilized GGI measurement produced by the Bell/Textron-derived GGIs as an example of its applicability.

Section 5.2 details an envisioned 12-accelerometer, full-tensor GGI and derives the most comprehensive open-literature GGI linearized error models to date, including a new formulation for stabilized GGIs. As shown in Eq. (5.41) on pg. 200, for the 12-accelerometer GGI only two accelerometers are required to measure the inline (on-diagonal) gravitational gradients, but four accelerometers are necessary to measure the off-diagonal gradients and remove the angular accelerations from the GGI observable. Section 5.2.1 then derives the measurement of a strapdown GGI and its linearized error model. The error derivation is based on Jekeli,[94] however Eq. (5.56) on pg. 207 extends his derivation to include both the effect of the navigation-to-body frame transformation, T_n^b, and the error associated with this rotation, $\boldsymbol{\psi}^n$. Section 5.2.2 lastly derives a new stabilized GGI measurement formulation and its linearized errors. This error model, Eq. (5.67), again includes rotation effects and errors (T_n^i and $\boldsymbol{\psi}_{in}^n$), however this rotation error is comprised of position and time errors instead of orientation errors. Therefore, the error derivations of the strapdown and stabilized GGIs show that the strapdown sensor has direct observability of orientation and gyro errors, whereas the stabilized sensor has better observability of registration (position) errors through its rotation error term. These results produce a tradeoff

between the two sensor types:

- A strapdown GGI-aided INS produces lower orientation and gyro errors over a stabilized sensor, but increased position errors because of the need to continually estimate the orientation and gyro errors.
- A stabilized GGI-aided INS produces lower position errors than a strapdown sensor, but reduced orientation performance and gyro calibration because of the lack of observability of these states.

The next chapter thoroughly quantifies the tradeoffs between these two GGI types through extensive Monte Carlo simulations.

Chapter 6

Monte Carlo Simulation Results

This chapter presents and discusses the Monte Carlo simulation and results to quantify the performance of the gradiometer aided inertial navigation system and the baseline INS/GPS system. The first section gives an overview of how the simulations were run and how the data was reduced. The second section compares three Monte Carlo simulation set sizes and their effect on how closely they model the Gaussian errors of the navigation system. The next section presents the INS/GGI and INS/GPS results. The first half of each of the navigation aid's results show a representative time history of a simulation and a detailed analysis of the navigation state errors. These results are shown as a preface to the second half of the results where the sensitivities of various system parameters are quantified in terms of their steady state mean-radial-spherical-errors (MRSEs). The conclusions from these results are then summarized in Sec. 6.4.

6.1 Monte Carlo Simulation

For each Monte Carlo set and prior to any simulation run in the set, the stored gravity field map and the body rate files (for the hypersonic cases) are opened and

read into memory.This allows each simulation of the Monte Carlo set to run faster because the file input is only required once. The only minor issue is that there is now an initial time lag on the order of several seconds for the code to read in these full files. For the subsonic cases, the body rates are set to zero along with the initial pitch and roll angles and the time lag is shortened slightly. The yaw angle for all cases is a constant 90° to ensure the Eastern cruise.

After reading the file inputs, the inertial measurement unit specifications were set to either use the navigation or tactical grade values from Table 4.4 on pg. 181.

Next, the initial filter covariance matrix, $P(0)$ was chosen to be a diagonal matrix with the following values for the diagonal elements. The filter position state variance was set to $(10.0 \text{ m})^2$, and the latitude and longitude states were converted to radians by dividing by a, Earth's equatorial radius. The velocity variances were set to $(1.0 \text{ m/s})^2$, and the attitude states to $(0.05°)^2$. The filter variances for the IMU scale factors and biases, and gyro noises, were set to their simulated IMU specifications. The GPS receiver clock bias and drift variances were set to $(15 \text{ m})^2$ and $(0.5 \text{ m/s})^2$, respectively. This initial filter covariance was constant for all Monte Carlo sets and was tuned so that the filter would reach steady state operation as soon as possible for a wide variety of INS/GGI and INS/GPS configurations. As discussed later in the results sections, this was not always the case.

Following the set up of the initial covariance matrix, 1,000 Monte Carlo simulations were run for a given set of system design parameters. (The sensitivity of increasing the set size to 10,000 simulations or decreasing to 100 simulations is discussed in the following section.) Each simulation in the set has its initial truth

position, velocity, and attitude states set so that they correspond to the correct Mach number, initial latitude and longitude for a given trajectory, and initial trim angles. The filter's estimated position, velocity, and attitude states are also set to these values so that there are no initial errors for these nine states. The truth IMU states are then randomly initialized according to the IMU specifications in Table 4.4. Misalignments and nonlinearities were originally implemented into the simulated IMU measurements to add uncompensated errors to the filter, but it was quickly discovered that the INS/GGI simulations were too sensitive to prevent divergence with these additional errors. Therefore, the misalignments and nonlinearities errors were not simulated in any of the following simulations. The GPS receiver's truth bias and drift are randomly initialized with a 15 m and 0.5 m/s standard deviation, respectively. The last term randomly initialized for each simulation is a constant time offset between the simulation time and the GPS constellation time to allow for a variety of GPS geometries.

The truth and estimated state vectors and the filter covariance matrix are numerically integrated at 20 Hz with the truth and estimated IMU measurements according to Ch. 4, and App. C and App. D. Then the simulated GGI or GPS measurements are made at a given update rate that is constant for a given Monte Carlo set. The noisy truth measurements are calculated using the current truth states and white noise is added. The filter also estimates a noise-free measurement at the same time using its current state estimate. The residual between these two measurements and the linearized measurement errors are then used to compute the Kalman gain to correct the estimated state vector and covariance matrix. The

process of propagating the truth and estimated states and updating the estimated states at a finite rate is continued until the truth longitude passes the given range requirement.

In order to quantify the filter performance, the error in the 26 truth and filter-estimated states are computed at each epoch. The maximum error, sum of the error, and sum squared of the error of each state at each epoch are tallied for each of the simulations in the Monte Carlo set. Once all 1000 simulations are completed for a given set the mean, standard deviation, and maximum error of each state is computed at each epoch and written to a file. The same process is done with the filter's 1-σ estimate of each state's error using the diagonal elements of the filter covariance matrix, see Eq. (C.7) on pg. 312:

$$\widehat{\sigma}_{x_i} = \sqrt{P(i,i)}. \tag{6.1}$$

The data in the Monte Carlo error file is reduced further by calculating the root-mean-square (RMS) error of each state at each epoch using:

$$RMS_i = \sqrt{\overline{x}_i^2 + \sigma_{x_i}^2}, \tag{6.2}$$

where $\overline{x}_i$ is the mean error of the ith state at a given epoch, and σ_{x_i} is the standard deviation of the error at the same epoch. The RMS of the filter estimates are computed as well to identify if the filter is performing correctly.

The mean RMS for the position, velocity, and attitude states are then calculated for several filter settling times and the presented results are tabulated as follows. The top half of each table calculates the mean RMS from 1/10 of the final simulation time until the end of the simulation as a way of quantifying the

performance of the system while neglecting the initial filter settling transient. The bottom half of each table quantifies the steady-state navigation performance by calculating the mean RMS over only the last half of the simulation. The filter's estimated 1-σ standard deviations are denoted as "Cov." and are included to identify the effectiveness of the filter and illuminate the presence of any divergence issues. The mean-radial-spherical-error (MRSE) is also calculated to quantify the overall position, velocity, and attitude error. The velocity MRSE is computed by:

$$v_{\text{MRSE}} = \sqrt{v_N^2 + v_E^2 + v_D^2}, \tag{6.3}$$

and the position and attitude MRSEs are found similarly. The latitude error is converted to crossrange error by multiplication of a, and the downrange error is found by multiplying the longitude error by $a\cos(\phi_{nom})$, where ϕ_{nom} is the constant truth latitude. (Appendix E tabulates the position, velocity, and attitude MRSEs for each of the Monte Carlo sets with the two filter settling times above and the MRSE for the entire simulation.)

The hypersonic un-aided INS results are presented as Table 6.2 in a slightly different fashion. Without external aiding, the navigation filter propagates the inertial navigation states with the initialized uncompensated accelerometer and gyro errors. These errors cause the position, velocity, and attitude errors to grow steadily over time so that the mean RMS errors are less informative than for the aided cases. Instead, the RMS error states at the end of the simulation (at the 1,000 km downrange) are presented along with the maximum error encountered for the entire 1,000 simulation set. The navigation and tactical grade IMUs are presented as the top

Table 6.1: Steady State Error Versus Monte Carlo Set Size

Set Size	State	Units	North / Pitch RMS	North / Pitch Cov.	East / Roll RMS	East / Roll Cov.	Down / Yaw RMS	Down / Yaw Cov.
100	Pos.	m	0.1929	0.2049	0.2311	0.2221	0.1145	0.1148
	Vel.	m/s	0.0044	0.0045	0.0041	0.0038	0.0016	0.0015
	Att.	$^\circ\times10^{-3}$	1.2851	1.2965	1.0427	0.9934	7.5255	7.4114
1,000	Pos.	m	0.2055	0.2049	0.2229	0.2221	0.1144	0.1148
	Vel.	m/s	0.0045	0.0045	0.0038	0.0038	0.0016	0.0015
	Att.	$^\circ\times10^{-3}$	1.2945	1.2965	0.9892	0.9935	7.1992	7.4121
10,000	Pos.	m	0.2039	0.2049	0.2220	0.2221	0.1148	0.1148
	Vel.	m/s	0.0045	0.0045	0.0038	0.0038	0.0015	0.0015
	Att.	$^\circ\times10^{-3}$	1.2885	1.2965	0.9982	0.9935	7.3265	7.4119

and bottom half of the table, respectively.

6.2 Monte Carlo Set Size

Three Monte Carlo set sizes were compared to investigate the effect of increasing or decreasing the number of simulation runs per a given INS configuration. The chosen test case was the Mach 6, high Γ^n variation trajectory INS/GGI system with navigation grade IMUs aided by a stabilized 0.001 Eö gradiometer at 1 Hz. This configuration was picked because it yields the best INS/GGI performance and has an increased simulation duration versus the Mach 7 "Best" case presented in Sec. 6.3.1.1.

The computed steady state error and filter estimate for each of the nine navigation states is summarized in Table 6.1 for Monte Carlo sets of 100, 1,000 and

10,000 simulations. The figure of merit that is used for this steady is how closely the Monte Carlo steady state errors predict the optimal filter performance since this estimates how closely the simulations capture all random processes of the simulation. Quantitatively, this term is

$$\frac{RMS_i}{\widehat{RMS_i}} - 1, \tag{6.4}$$

where RMS_i is the ith state's steady state RMS computed from the Monte Carlo set and $\widehat{RMS_i}$ is the steady state filter estimate of the error. The quantity would be zero for an infinite number of random simulations assuming the filter is optimal. The value of $\widehat{RMS}$ for each state was chosen to be the average of the three steady state filter values, *i.e.* from the 100, 1,000, and 10,000 sets. Figure 6.1 plots the 100 and 1,000 set steady state filter error normalized by the 10,000 simulation set values for each of the nine navigation states $(\phi, \lambda, h, v_N, v_E, v_D, \psi_N, \psi_E, \psi_D)$. From this plot, it is apparent that the filter estimate error is essentially constant regardless of Monte Carlo set size.

Figure 6.2 then plots the normalized steady state error RMS as calculated by Eq. (6.4). The 100 Monte Carlo set has the largest deviation from the filter estimate because there are not enough simulations to accurately capture a full Gaussian distribution of all the random states. The 1,000 set, on the other hand, has less than a 1% variation from the filter estimate for all states except the Eastern velocity (1.35%) and yaw angle, ψ_D (2.87%). And the 10,000 simulation set better captures only five of the nine navigation states compared to the 1,000 simulation set.

The mean-radial-spherical-error for the normalized position, velocity, and at-

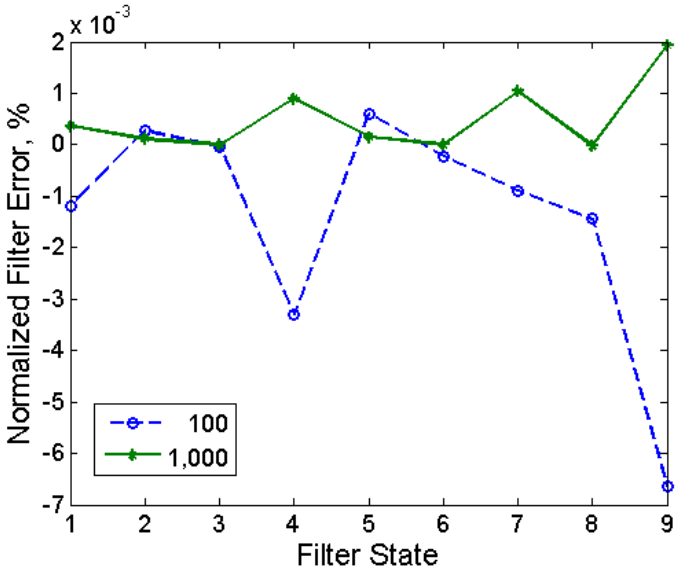

Figure 6.1: Normalized Steady State Filter Error vs. Monte Carlo Set Size

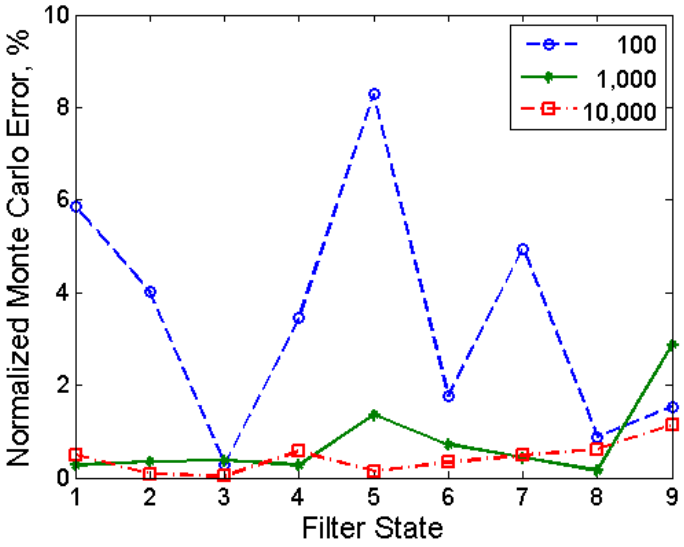

Figure 6.2: Normalized Steady State Error vs. Monte Carlo Set Size

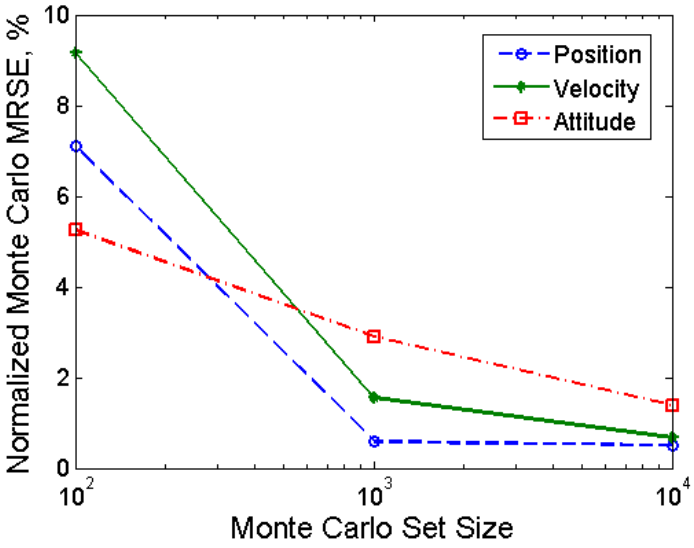

Figure 6.3: Normalized Steady State MRSE vs. Monte Carlo Set Size

titude states are plotted in Fig. 6.3 as a function of the Monte Carlo set size. The position and velocity errors are much better estimated when the number of simulations is increased from 100 to 1,000. However, increasing the set size from 1,000 to 10,000 has diminishing returns. The attitude error linearly decreases as the set size is increased by an order of magnitude.

It should be noted that while increasing the number of simulations better captures all the randomness of the system, the computational effort increases substantially. For the hypersonic simulations, a 1,000 simulation Monte Carlo set took about 16–20 minutes to run on a dual processor 64-bit AMD 2.2 GHz Opteron 246 with 2 GB of RAM. The 10,000 simulation set took on the order of 3–4 hours to complete, and the 100 simulation set several minutes. Taking the computation time, number of Monte Carlo configurations simulated, and the trends in Fig. 6.3 into account, the nominal 1,000 simulation set size was deemed a good compromise for this

work.

6.3 Results

Before presenting the Monte Carlo sensitivity results, several single simulation results will be shown to better understand the later discussions. The Monte Carlo errors and filter estimates are tabulated for the nine navigation states for the two settling times discussed above, and the columns of the tables are organized as follows. The North / Pitch columns constitute the crossrange, Northern velocity, and ψ_N (pitch) errors, the East / Roll columns similarly constitute the downrange, Eastern velocity, and ψ_E (roll) errors, and the Down / Yaw columns the altitude, Downward velocity, and yaw errors.

In order to limit the scope of the sample simulation results presented, the "Best" or "Nominal" case for each INS aid, GGI and GPS, will be first shown. Then one of the system design parameters will be deviated from this best or nominal case. The gradiometer cases are presented first, followed by the GPS cases.

The Monte Carlo steady state MRSE sensitivities to numerous parameters are then presented. These results are first shown by comparing the main system design parameters (IMU quality and GGI type or GPS measurement) as a function of GGI noise of GPS update interval. Then, the sensitivity to Mach number and Γ^n variation (for the hypersonic cases) are shown. The two subsonic cases are discussed in the single simulation result sections.

As motivation for the need of an external aid to the INS, the dead reckoning

inertial navigation results are listed in Table 6.2 for the mean and maximum RMS at the end of the hypersonic 1,000 km simulations. These results are only for the high gravitational gradient variation trajectories. The low Γ^n variation trajectory free-inertial errors are given in Tables E.2 and E.4 on pg. 358.

As shown in Table 6.2, after the Mach 7 free inertial 1,000 km cruise, the position errors grow to 25 m in the horizatal and 65 m in the vertical for a navigation grade IMU with no initial position, velocity, or attitude errors. The maximum error for the free inertial Monte Carlo simulations are approximately 4 times as large. The tactical grade IMUs produce nearly 1 km horizontal errors and 700 m vertical error for a total position error of 1.5 km due to only IMU error sources. The Mach 6 cases produce dead reckoning errors since the simulation is run longer and the error growth is a function of time. The Mach 8 case is simulated for a shorter duration and therefore has lower free-inertial errors. To enable safe operation of such systems and to meet precision strike goals (on the order og 3 m),[166] an external aid is a necessity.

6.3.1 Gravity Gradiometer Aided INS

Table 6.3 summarizes the 162 hypersonic gravity gradiometer aided inertial navigation system configurations tested in this work. The subsonic cases were only simulated along the high gravitational gradient variation trajectories with navigation grade IMUs and a stabilized GGI with 0.1, or 0.001 Eö updates at 1 Hz.

Table 6.2: Dead Reckoning Navigation Accuracy after 1000 km Cruise, High Γ^n Variation Trajectory

M_∞			North / Pitch		East / Roll		Down / Yaw	
IMU	State	Units	RMS	Max	RMS	Max	RMS	Max
Mach 6	Pos.	m	31.635	107.96	34.665	109.35	97.457	356.11
Nav.	Vel.	m/s	0.0925	0.2941	0.1081	0.3388	0.3635	1.3564
	Att.	$^\circ\times10^{-3}$	0.6222	2.0768	0.6595	2.3628	0.7135	2.6651
Mach 6	Pos.	m	1428.9	4323.4	1452.3	5107.9	945.93	3586.6
Tac.	Vel.	m/s	6.9633	20.405	7.0990	24.955	3.7091	14.651
	Att.	$^\circ\times10^{-3}$	144.47	447.63	148.02	485.69	159.95	613.88
Mach 7	Pos.	m	23.823	85.192	26.542	88.183	65.974	278.82
Nav.	Vel.	m/s	0.0817	0.2394	0.0965	0.3456	0.2787	0.9450
	Att.	$^\circ\times10^{-3}$	0.5744	2.4795	0.5459	2.2561	0.6129	1.9046
Mach 7	Pos.	m	918.82	3468.8	952.09	3095.8	703.89	2878.8
Tac.	Vel.	m/s	5.0600	19.586	5.2833	16.942	3.1409	12.570
	Att.	$^\circ\times10^{-3}$	126.02	437.87	121.19	434.81	132.75	443.72
Mach 8	Pos.	m	21.588	104.31	20.740	66.693	48.893	158.06
Nav.	Vel.	m/s	0.0770	0.2786	0.0821	0.2667	0.2323	0.7725
	Att.	$^\circ\times10^{-3}$	0.5110	1.8697	0.4941	1.6466	0.5351	1.6637
Mach 8	Pos.	m	655.86	2338.8	680.45	2722.5	500.13	1771.4
Tac.	Vel.	m/s	4.1040	15.929	4.2188	15.004	2.5330	8.9636
	Att.	$^\circ\times10^{-3}$	113.97	458.36	113.18	417.27	116.21	408.02

Table 6.3: INS/GGI Monte Carlo Test Matrix

Parameter	Values	#
IMU Grade	Navigation, Tactical (Stab. only)	2
Mach Number	6, 7, 8	3
Gradient Variation	"High," "Low"	2
Instrument Noise	0.1, 0.01, 0.001 Eö (1-σ)	3
Instrument Type	Stabilized, Strapdown	2
Data Rate	1, 5, 10 sec	3

6.3.1.1 Monte Carlo Results

For the single simulation runs, only the Mach 7 cases will be shown since they represent the same trends as the other two hypersonic cases. The "best" INS/GGI system configuration is summarized in Table 6.4 along with the varied parameter values chosen to give a brief discussion of some of the system sensitivities. The subsonic 0.1 and 0.001 Eö INS/GGI cases will be presented and discussed at the end of this subsection.

Table 6.4: INS/GGI "Best" and Off-Nominal Simulation Parameters

	IMU	Trajectory	Noise	Type	Data Rate
"Best" Value	Nav.	High Γ^n Variation	0.001 Eö	Stabilized	1 sec
Perturbed Value	Tac.	Low Γ^n Variation	0.1 Eö	Strapdown	10 sec

Hypersonic Cases

Figure 6.4 plots a single "Best" case stabilized gradiometer simulation error and 1-σ filter envelope for the nine navigation states. As shown, the filter accurately predicts the errors for each state with this future-grade gradiometer. Compared to the free inertial final position error, the covert GGI-aided INS reduces the steady state MRSE by a factor of 220 from 75.0 to 0.336 m. The steady state (500 km settling time) velocity error is also reduced remarkably to 0.0069 m/s, a factor of nearly 45 below the free-inertial case.

The attitude states surprisingly increase in error from the unaided simulations. This result is somewhat misleading as it is actually due to the simulation formulation—not the INS/GGI filter performance. Because the simulations were conducted without any initial position, velocity, or attitude errors, the free-inertial attitude errors are governed primarily by the uncompensated gyro errors. The navigation grade gyros have a simulated turn-on bias of 0.003°/Hr, which therefore cause only a $0.4\times10^{-3\circ}$ attitude error after the 482 sec Mach 7 simulation; close to the values reported in Table 6.2. Had the free-inertial simulation introduced initial attitude errors, the final errors would have grown much larger, and the improvement in attitude determination by GGI-aiding would be more obvious.

Some trends that are apparent for all simulated gradiometer-aided systems can be identified by Table 6.5. First, the vertical position and velocity errors are typically one-half the horizontal errors. This performance characteristic is attributed to the fact that the vertical gravitational gradient, Γ_{DD}, is approximately twice that

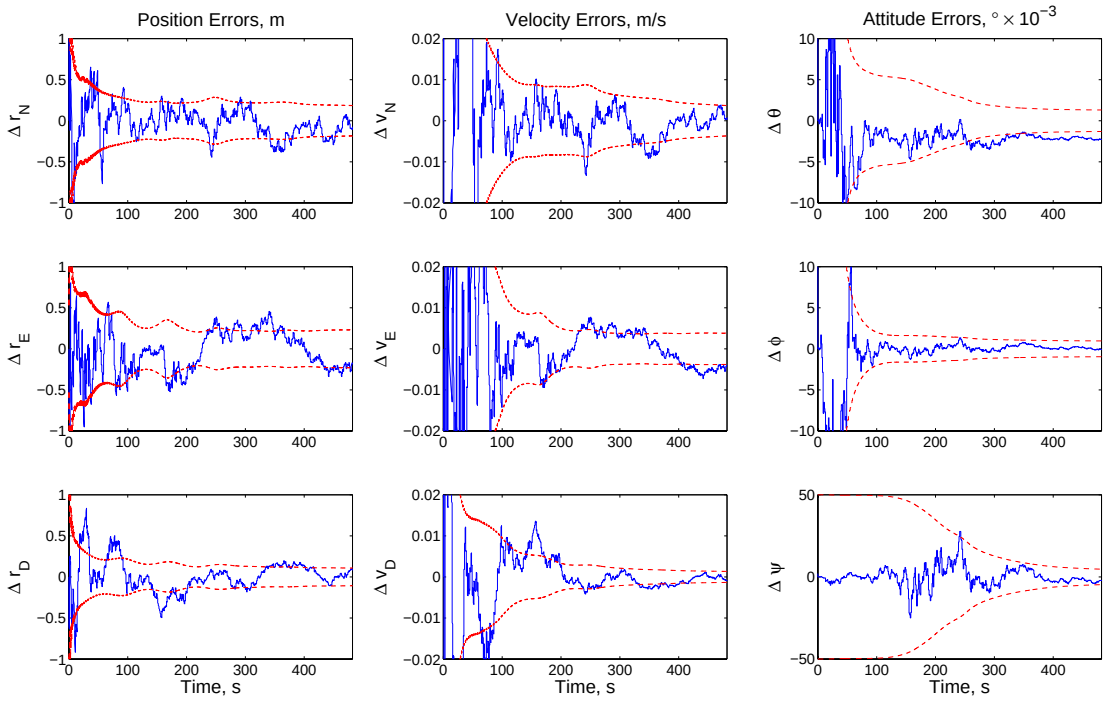

Figure 6.4: Sample "Best" Stabilized Gradiometer-Aided INS Simulation

Table 6.5: "Best" Gradiometer-Aided INS Case

Settling Time	State	Units	North / Pitch Error	North / Pitch Cov.	East / Roll Error	East / Roll Cov.	Down / Yaw Error	Down / Yaw Cov.
100 km	Pos.	m	1.2069	1.2692	0.3331	0.3469	0.4711	0.4770
	Vel.	m/s	0.0124	0.4474	0.0151	0.4466	0.0103	0.4455
	Att.	$^\circ\times10^{-3}$	0.9076	23.138	0.6166	22.820	5.3159	27.662
500 km	Pos.	m	0.2172	0.2172	0.2244	0.2259	0.1239	0.1229
	Vel.	m/s	0.0054	0.0054	0.0039	0.0039	0.0019	0.0019
	Att.	$^\circ\times10^{-3}$	1.6298	1.6488	1.1060	1.0763	9.5646	9.7920

of Γ_{NN} or Γ_{EE} by Laplace's constraint, Eq. (2.5) on pg. 43. Hence, variations in the inline horizontal gradients cause greater variations in the vertical component. Second, the tilt errors, ψ_N (pitch for Eastern flight) and ψ_E (roll), are reduced to an error floor of $\sim 0.001^\circ$ while the yaw error dominates the total attitude error. This phenomenon occurs because the gradiometer acts as essentially a gravitational compass to hone in on the vertical gradient and reduce the tilt errors. Furthermore, due to Earth's oblateness, the gravitational gradients are more sensitive to latitude than longitude variations so the ψ_E (roll) error has slightly better performance than the ψ_N (pitch) error.

Figure 6.5 shows a single simulation using the "Best" case parameters but with the navigation grade IMUs replaced by a tactical grade suite. Table 6.6 lists the 1,000 Monte Carlo navigation results. For this case the filter again accurately estimates the navigation errors. The INS/GGI produces position errors only slightly greater than those of the "Best" case, and corresponds to a three order-of-magnitude improvement from the free inertial tactical grade IMU errors. Velocity errors are reduced by over two orders-of-magnitude. The attitude errors are only reduced by a factor of two, however this is again caused by the simulation formulation.

The "Best" case parameter set is next flown over the "Low" gravity gradient variation trajectory to investigate the sensitivity of the system on signal strength. As seen in Fig. 6.6 and Table 6.7, there is minimal change in navigation performance between the two chosen trajectories. The most apparent difference between these two cases is that the lobe pattern of the filter 1-σ envelope is less pronounced compared to Fig. 6.4 and 6.5. The North (crossrange) position error is essentially the

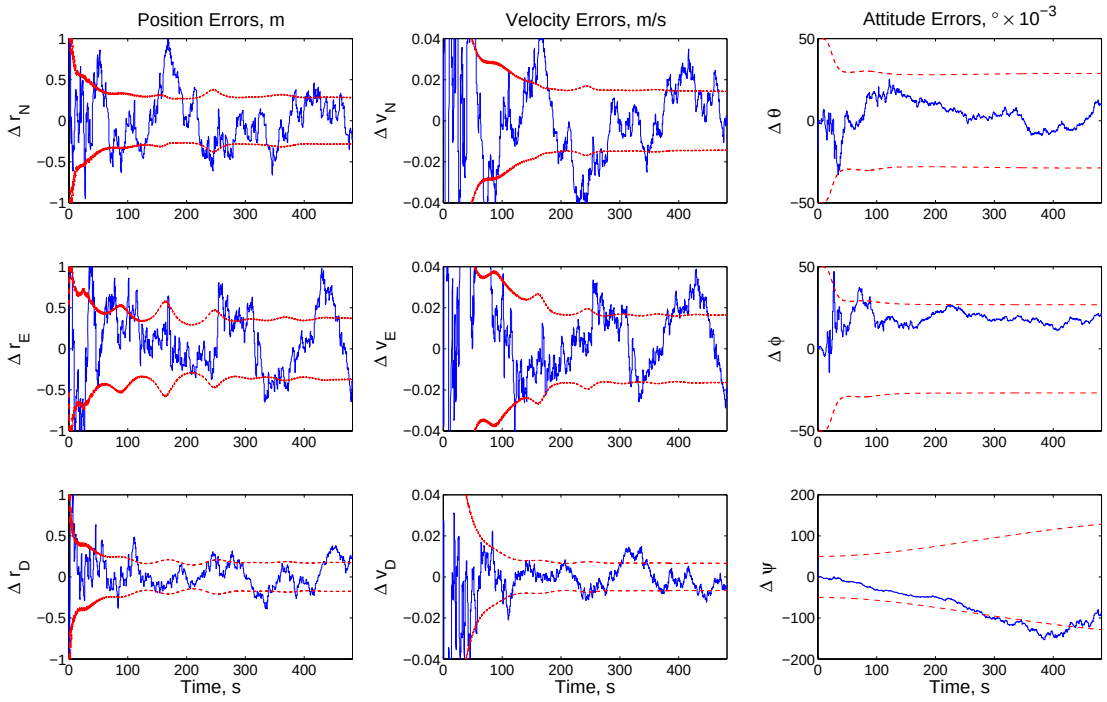

Figure 6.5: Sample Tactical Grade IMU Gradiometer-Aided INS Simulation

Table 6.6: Tactical Grade IMU, Gradiometer-Aided INS Case

Settling Time	State	Units	North / Pitch Error	North / Pitch Cov.	East / Roll Error	East / Roll Cov.	Down / Yaw Error	Down / Yaw Cov.
100 km	Pos.	m	1.2911	1.3136	0.4212	0.4264	0.5151	0.5080
	Vel.	m/s	0.0176	0.4527	0.0220	0.4537	0.0129	0.4482
	Att.	$^\circ \times 10^{-3}$	13.726	38.116	13.095	37.154	55.708	81.951
500 km	Pos.	m	0.2991	0.2970	0.3701	0.3690	0.1777	0.1787
	Vel.	m/s	0.0150	0.0148	0.0167	0.0166	0.0068	0.0068
	Att.	$^\circ \times 10^{-3}$	24.626	28.610	23.492	26.878	100.19	107.51

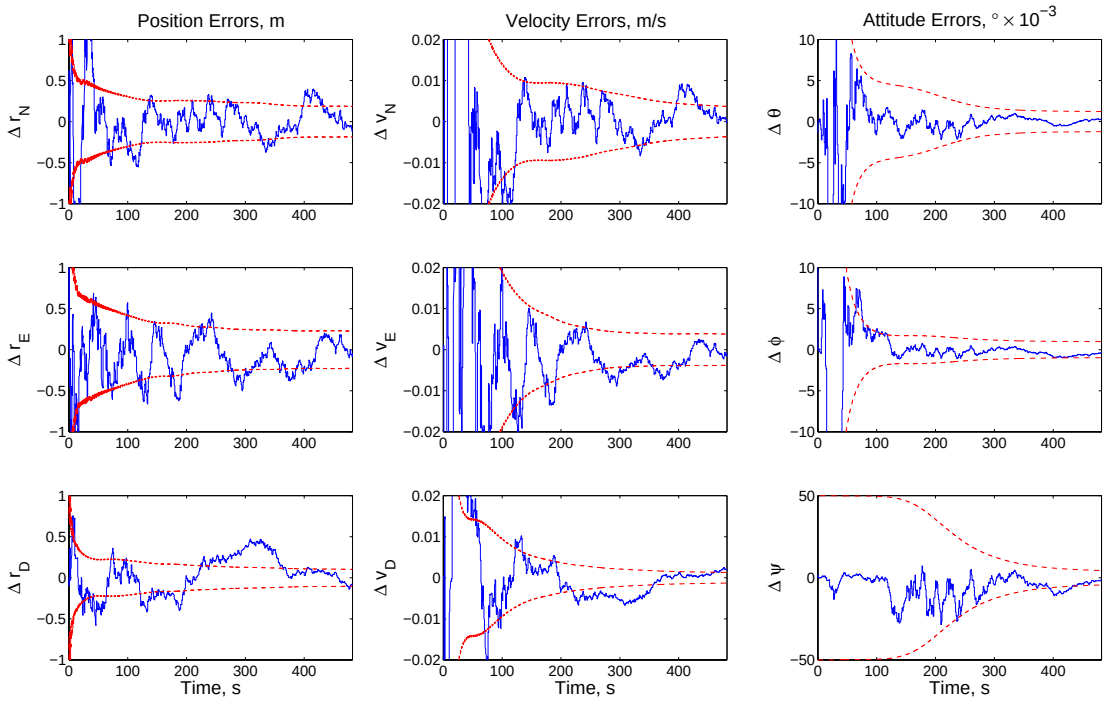

Figure 6.6: Sample "Low" Gravity Gradient Trajectory Gradiometer-Aided INS Simulation

Table 6.7: "Low" Gravity Gradient Variation Gradiometer-Aided INS Case

Settling Time	State	Units	North / Pitch Error	North / Pitch Cov.	East / Roll Error	East / Roll Cov.	Down / Yaw Error	Down / Yaw Cov.
100 km	Pos.	m	0.5544	0.5456	0.7716	0.7762	0.3811	0.3899
	Vel.	m/s	0.0115	0.4474	0.0032	0.4467	0.0253	0.4454
	Att.	$^\circ\times10^{-3}$	0.8298	23.039	0.6211	22.829	5.0592	27.503
500 km	Pos.	m	0.2102	0.2092	0.2499	0.2488	0.1165	0.1176
	Vel.	m/s	0.0054	0.0054	0.0041	0.0041	0.0018	0.0018
	Att.	$^\circ\times10^{-3}$	1.4896	1.4739	1.1139	1.0950	9.1022	9.5086

same for both trajectories, the East (downrange error) is about 10% higher for the "Low" trajectory, and the altitude error is surpisingly 6% lower for the "Low" trajectory. Again the vertical errors are approximately half those of the horizontal and the attitude errors are dominated by the yaw error. These results are quite promising. Initially it was believed that the gradiometer-aided INS would only be viable over regions with large gradient variations. But from this analysis it is now believed that the INS/GGI navigation package can yield exceptional performance with minimum sensitivity to the region of interest if the GGI noise floor can be reduced to 0.001 Eö/$\sqrt{Hz}$. A more complete investigation is performed and discussed in the following subsection that shows that signal variation does indeed affect navigation performance for other configurations and higher GGI noise levels.

Figure 6.7 plots a sample simulation over the "High" gradient variation trajectory, but now with increased gradiometer noise. The noise was increased from 0.001 Eö to 0.1 Eö with updates still simulated at 1 Hz. This increased noise value is still more than an order of magnitude lower than any currently planned airborne gradiometer. However, simulations performed with a 1 Eö simulated noise level showed negligible improvement over the free-inertial simulations, so a noise value of 0.1 Eö was chosen to show the effect of greater instrument noise on overall system performace. With the two order-of-magnitude increase in noise, the total steady state position error increased by a factor of 75 over the "Best" case INS/GGI. The velocity error increased by a factor of 40. The total attitude error is approximately the same regardless of noise level. Yet again, this result is slightly misleading. The tilt errors increased by a factor of 5 with the increased noise as one might expecet,

but the yaw error was halved over the low noise case. The reason for the decrease in yaw angle error is that the filter covariance was initially high enough that it never attempted to update the yaw estimate, thus allowing the yaw to propagate as if it were a free-inertial case with errors occurring from the gyro bias and a random walk from integrating its noise. As mentioned above, with the lack of initial position, velocity, and attitude errors, the attitude errors remain quite small without updates. If the initial filter covariance were tuned differently, the yaw angle error would have likely increased over the "Best" case yaw error. The yaw error issue will be even more apparent in the sensitivity study results.

Next, the "Best" case INS/GGI was simulated with 10 sec updates insead of the 1 sec updates in the other cases. By sampling at longer intervals, the filter processes fewer measurements over the cruise profile and thus the filter requires more time to reach steady state. Moreover, the decreased update rate effectively increases the noise in terms of its simulated power spectral density, see Eq. (6.5) on pg. 244. Figure 6.8 illustrates that the filter undergoes many saw-tooth error spikes between measurement updates in the initial portion of the 10 sec update INS/GGI simulation. After about halfway through the simulation the filter has converged to steady state position, velocity, and tilt errors. At this point, the filter begins to remove the yaw error until the simulation ends. The speed that the filter reaches steady state could be improved by additional filter tuning. Referring to Table 6.9, the position errors grew consistently by a factor of 3 over the 1 sec update results, however the total position error was still less than a meter (0.9789 m). The velocity errors for the 10 sec update case are about twice those of the nominal 1 Hz case

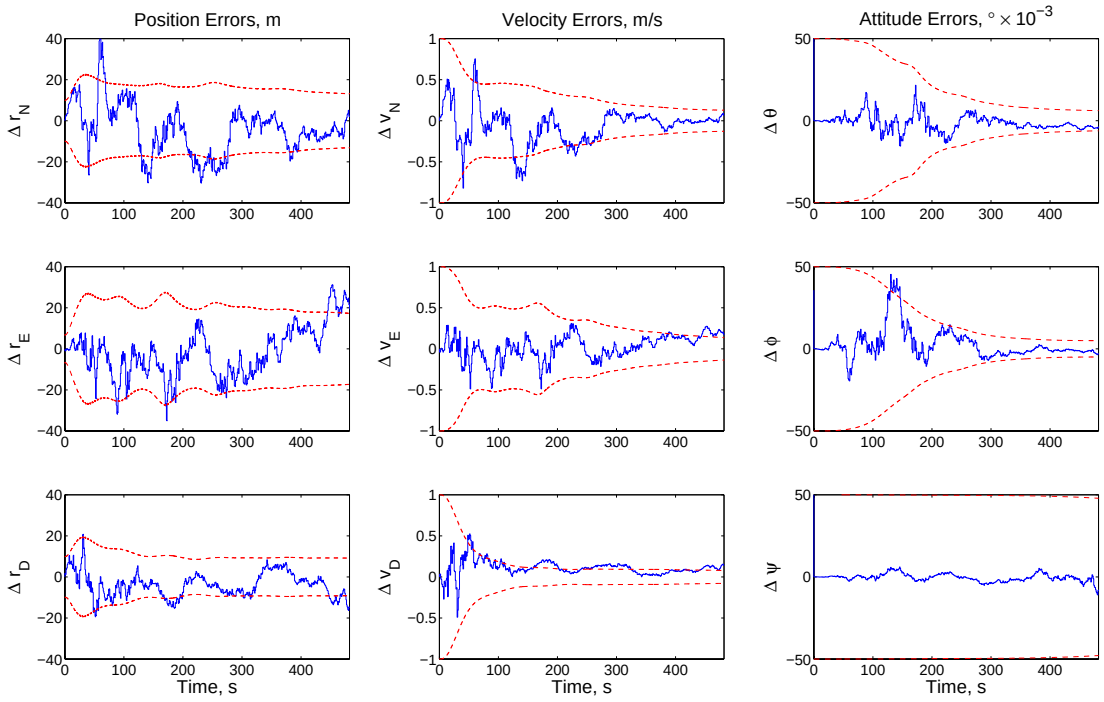

Figure 6.7: Sample Increased Noise Gradiometer-Aided INS Simulation

Table 6.8: Increased Noise Gradiometer-Aided INS Case

Settling Time	State	Units	North / Pitch Error	North / Pitch Cov.	East / Roll Error	East / Roll Cov.	Down / Yaw Error	Down / Yaw Cov.
100 km	Pos.	m	8.6561	12.969	11.476	13.665	5.7341	9.5701
	Vel.	m/s	0.0988	0.5453	0.1299	0.5654	0.0577	0.4940
	Att.	$^\circ\times10^{-3}$	3.6155	27.152	2.8556	26.061	2.9739	49.546
500 km	Pos.	m	14.919	15.376	18.833	19.307	9.2399	9.3009
	Vel.	m/s	0.1616	0.1815	0.2101	0.2178	0.0875	0.0891
	Att.	$^\circ\times10^{-3}$	6.5040	8.8750	5.1360	6.9104	5.3491	49.183

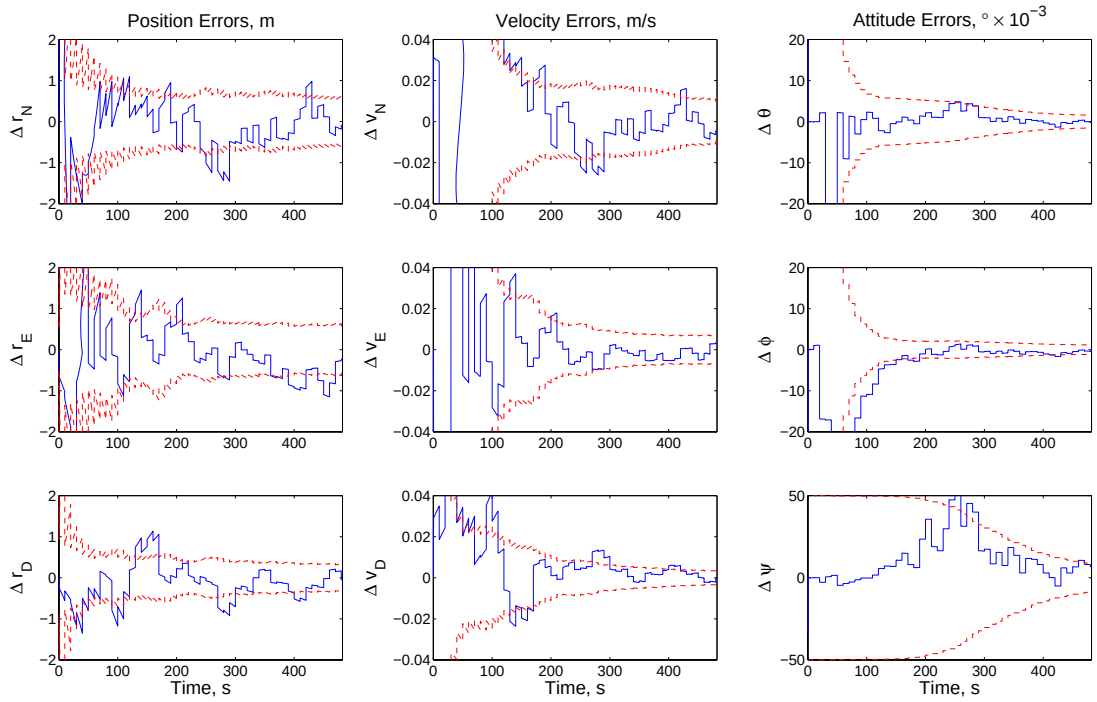

Figure 6.8: Sample Stabilized Gradiometer-Aided INS Simulation with 10 sec Updates

Table 6.9: Stabilized Gradiometer-Aided INS Case with 10 sec Updates

Settling Time	State	Units	North / Pitch Error	North / Pitch Cov.	East / Roll Error	East / Roll Cov.	Down / Yaw Error	Down / Yaw Cov.
100 km	Pos.	m	1.4780	1.5096	0.5849	0.5765	0.6223	0.6194
	Vel.	m/s	0.0164	0.4525	0.0171	0.4490	0.0119	0.4473
	Att.	$^\circ\times10^{-3}$	1.2480	23.743	0.8191	23.099	9.8083	34.572
500 km	Pos.	m	0.6152	0.6499	0.6601	0.6392	0.3796	0.3792
	Vel.	m/s	0.0129	0.0146	0.0084	0.0082	0.0052	0.0052
	Att.	$^\circ\times10^{-3}$	2.2424	2.7375	1.4705	1.5795	17.651	22.230

(0.0163 vs. 0.0069 m/s), and similarly the attitude errors grew by a factor of 2 (17.85 vs. 9.765°).

The final gradiometer-aided INS parameter to be perturbed is the use of a strapdown GGI instead of a stabilized GGI. The benefits of a strapdown version of a gradiometer versus a stabilized version is similar to the tradeoffs between strapdown and stabilized IMU sensors. A strapdown system provides for a smaller and, ideally, a mechanically less complicated sensor at the cost of additional computing requirements to address the angular rate and angular acceleration issues. Because angular rates and accelerations present themselves as false gravitational gradients, see Eq. (5.3) and (5.4) on pg. 185, all airborne gradiometers have been built with a stabilized platform in mind. If the angular accelerations and rates could be sufficiently estimated by either gyros (as assumed in this work) or by the gradiometer measurements itself (see Eq. (5.6) on pg. 186), a strapdown gradiometer could be built with reduced mass and volume. As explained next, the strapdown INS/GGI simulated here brings up unexpected computional issues.

Figure 6.9 plots a representative strapdown gradiometer-aided INS simulation. It is quite apparent that in this configuration the filter diverges, most noteably in altitude. This divergence is believed to be caused by numerical truncation error in the filter covariance propagation, Eq. (C.40) on pg. 324, and Kalman gain calculation, Eq. (C.49) on pg. 326:

$$\begin{aligned} P_{k+1} &= \Phi_k P_k \Phi_k^T + Q_k \\ K_{k+1} &= P_{k+1}^- H_{k+1}^T \left(H_{k+1} P_{k+1}^- H_{k+1}^T + R_{k+1} \right)^{-1}. \end{aligned}$$

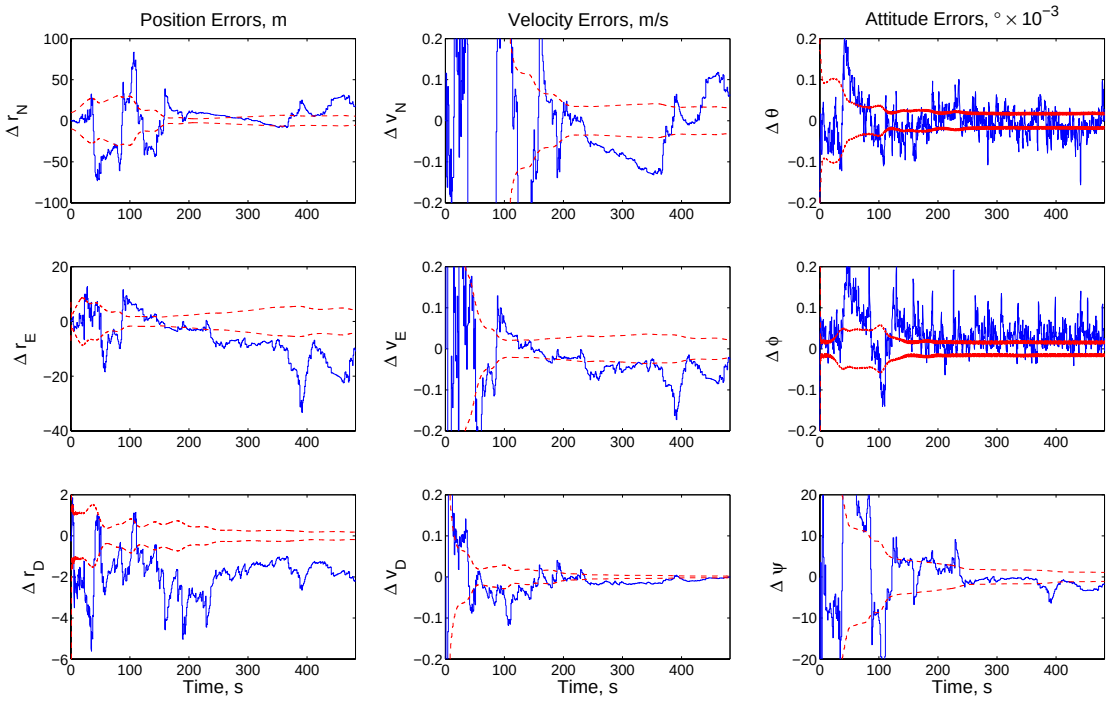

Figure 6.9: Sample Strapdown Gradiometer-Aided INS Simulation

Table 6.10: Strapdown Gradiometer-Aided INS Case

Settling Time	State	Units	North / Pitch Error	North / Pitch Cov.	East / Roll Error	East / Roll Cov.	Down / Yaw Error	Down / Yaw Cov.
100 km	Pos.	m	7.0255	7.4693	6.5463	4.6380	2.2185	3.3934
	Vel.	m/s	0.0464	0.4645	0.0450	0.4613	0.0108	0.4463
	Att.	$^\circ\times10^{-3}$	0.0349	0.0854	0.0483	0.1033	2.2739	23.039
500 km	Pos.	m	12.617	5.4450	10.730	4.4720	2.6048	0.2349
	Vel.	m/s	0.0735	0.0360	0.0669	0.0304	0.0095	0.0033
	Att.	$^\circ\times10^{-3}$	0.0285	0.0176	0.0468	0.0157	3.6020	1.5141

All real quantities in the FORTRAN simulations use double precision data types, however the gyro process noise variance in Q_k and P_k is many orders-of-magnitude larger than the gradiometer measurement noise variance in R_k and therefore numerical truncation occurs in the Kalman gain calculation. This truncation essentially causes the filter to ignore some of the GGI measurement noise matrix, $R_{GGI} = \text{diag}(\sigma^2_{\nu_L})$, and therefore the Kalman gain is not calculated optimally. For cases where the GGI noise is increased or the gyro noise is reduced so their variances are closer, no divergence exists. Furthermore, filter divergence occurs almost instantly when the GGI noise is decreased below 0.001 Eö with navigation grade gyros. In order to alleviate this issue, higher numerical precision could be used in the simulation, and/or a square-root Kalman filter implementation could be chosen instead of the standard filter implemented in this research. This divergence issue also caused all strapdown gradiometer aided INS simulations with tactical grade IMUs to diverge instantly. Regardless of the slow filter divergence, the strapdown gradiometer INS results are listed in Table 6.10. Surprisingly, the position errors are less than 17 m even with filter divergence. For the Monte Carlo sensitivities in the next subsection, the actual diverging errors are presented along with an extrapolation of the converged filter results into the 0.001 Eö GGI configurations.

Subsonic Cases

A representative time history of the commercial aircraft INS/GGI is shown in Fig. 6.10 and the Monte Carlo results are listed in Table 6.11. This case uses the

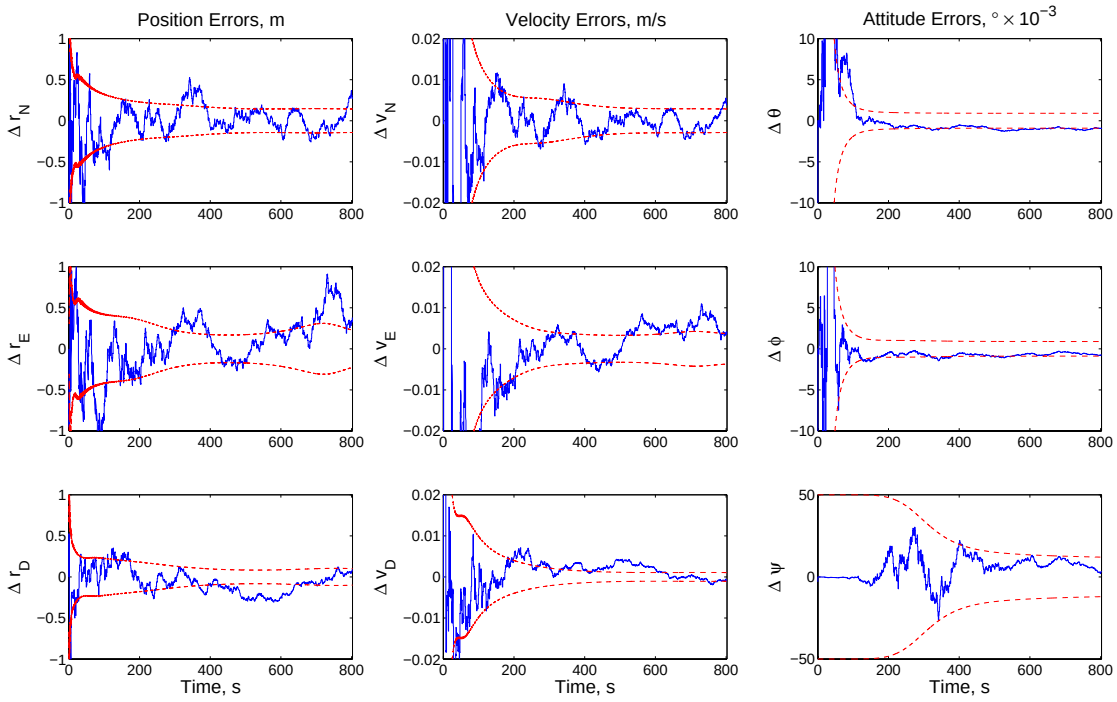

Figure 6.10: Sample Commercial Aircraft INS/GGI Simulation

Table 6.11: Commercial Aircraft INS/GGI Case

Settling Time	State	Units	North / Pitch Error	North / Pitch Cov.	East / Roll Error	East / Roll Cov.	Down / Yaw Error	Down / Yaw Cov.
50 km	Pos.	m	0.5459	0.5522	0.6386	0.6225	0.3091	0.3516
	Vel.	m/s	0.0174	0.4462	0.0141	0.4465	1.4869	0.4451
	Att.	$^\circ\times10^{-3}$	0.5209	22.729	0.5003	22.722	7.4570	30.0509
250 km	Pos.	m	0.1479	0.1476	0.2291	0.2252	0.0933	0.0923
	Vel.	m/s	0.0031	0.0031	0.0037	0.0037	0.0011	0.0011
	Att.	$^\circ\times10^{-3}$	0.9338	0.9082	0.8968	0.8970	13.420	14.088

"best" parameters as listed in Table 6.4 with the only difference being the reduced altitude of 10,000 m and East velocity of 250 m/s. The simulation is also run to a downrange of 500 km instead of 1,000 km. As shown in both Fig. 6.10 and Table 6.11, the filter is accurately estimating the simulation errors.

Comparing this simulation with the Mach 7 "best" INS/GGI system shows surprisingly little change in navigation performance. The downrange and East velocity errors are practically identical. The crossrange error is about 2/3 the hypersonic case, and the altitude error is about 3/4. The crosstrack (North) and downward velocity errors are both approximately half those of the Mach 7 simulation. And lastly, all steady state errors are comparable. These results are encouraging because they show that a future-grade gradiometers can provide exceptional navigation aiding even if their size and mass were not reduced to missile-class sizes.

Figure 6.11 and Table 6.12 show the results of the commercial aircraft case if its noise level were increased to 0.1 Eö with a 1 Hz update rate. The navigation performance is similar to the hypersonic case shown in Fig. 6.7 and Table 6.8. These results give an estimate as what a nearer-future INS/GGI system's navigation accuracy might be. It should be noted that the local terrain effects have not been included in any of the simulations, so this INS/GGI navigation accuracy would likely be improved if more signal frequencies were included.

The GGI-based survey mission results are presented in Fig. 6.12 and Table 6.13. This system is the closest to the current environment of airborne gradiometry. However, the simulations here are presented with space-grade noise levels which are three orders of magnitude lower than currently proposed airborne gradiometers.

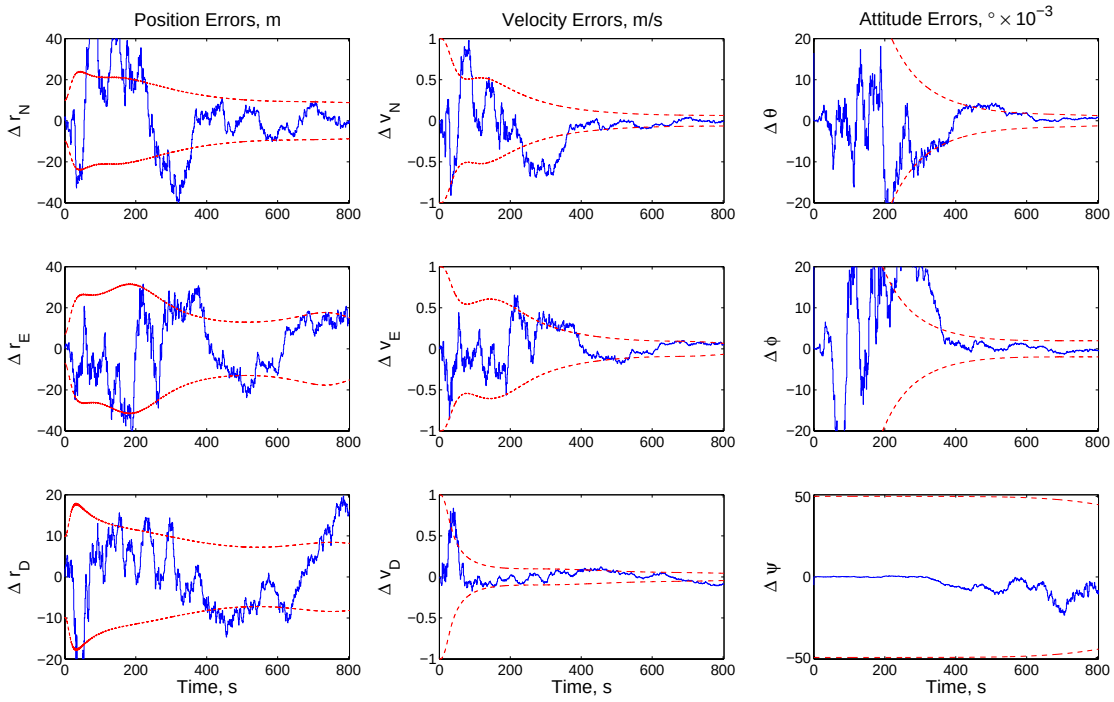

Figure 6.11: Sample Commercial Aircraft INS/GGI Simulation w/ Increased Noise

Table 6.12: Commercial Aircraft INS/GGI Case w/ Increased Noise

Settling Time	State	Units	North / Pitch Error	North / Pitch Cov.	East / Roll Error	East / Roll Cov.	Down / Yaw Error	Down / Yaw Cov.
50 km	Pos.	m	5.7697	9.8692	8.3473	11.382	4.9747	8.7136
	Vel.	m/s	0.0609	0.4909	0.0720	0.5040	2.9411	0.4786
	Att.	$^\circ \times 10^{-3}$	1.1469	23.398	0.9617	23.486	5.0887	49.220
250 km	Pos.	m	9.6523	9.7997	14.681	14.842	7.9068	7.7713
	Vel.	m/s	0.0753	0.0835	0.1087	0.1072	0.0635	0.0614
	Att.	$^\circ \times 10^{-3}$	2.0607	2.1133	1.7274	2.2715	9.1567	48.596

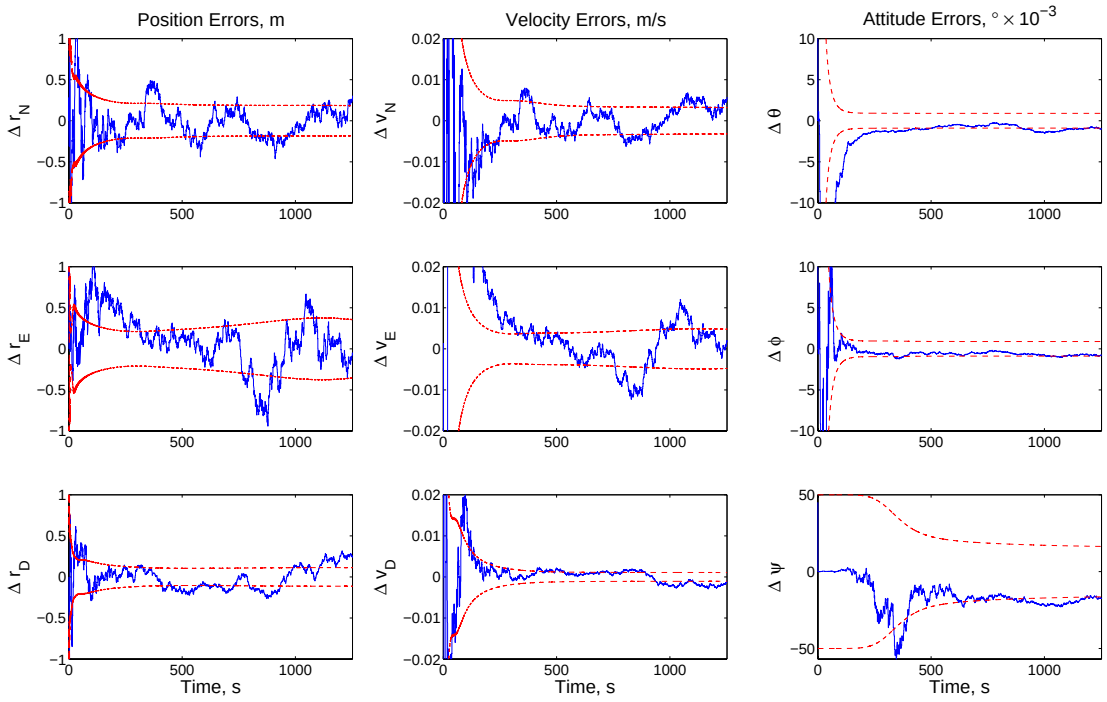

Figure 6.12: Sample GGI Survey INS/GGI Simulation

Table 6.13: GGI Survey INS/GGI Case

Settling Time	State	Units	North / Pitch Error	North / Pitch Cov.	East / Roll Error	East / Roll Cov.	Down / Yaw Error	Down / Yaw Cov.
30 km	Pos.	m	0.5568	0.5740	0.7188	0.6438	0.3760	0.3352
	Vel.	m/s	0.0569	0.4463	0.0357	0.4470	4.2667	0.4451
	Att.	$^\circ\times10^{-3}$	0.5459	22.722	0.5356	22.716	10.9640	32.003
150 km	Pos.	m	0.1917	0.1869	0.4885	0.3345	0.1217	0.1106
	Vel.	m/s	0.0034	0.0033	0.0086	0.0046	0.0013	0.0011
	Att.	$^\circ\times10^{-3}$	0.9788	0.8999	0.9601	0.8885	19.731	17.604

The simulation is also run for 300 km at a velocity of 40 m/s and a 100 m cruise altitude.

From Table 6.13, this low altitude and velocity system has degraded performance in its downrange and alongtrack (East) velocity accuracy. Comparing the filter estimates of these states to the Monte Carlo simulation errors, it also appears that the filter may not be performing correctly since the simulation errors are noticeably higher than the filter's estimates. The errors of these East states are also about twice those of the commercial aircraft and comparable scramjet cases. The other position errors are about 30% higher than the other subsonic case, and the North and Downward velocity errors are about the same.

The case where the GGI noise is simulated at 0.1 Eö at 1 Hz is shown in Fig. 6.13 and the Monte Carlo results are listed in Table 6.14. These results show that a future-grade airborne GGI aided INS can provide reasonable covert, passive navigation. If terrain effects were included in the gravitational field, these results would like be improved. The velocity accuracy is also improved over the comparable high-noise INS/GGI simulations because the truth velocity is decreased to only 40 m/s for the GGI-survey simulations.

6.3.1.2 Sensitivity Results

This section investigates many of the sensitivities of future INS/GGI systems. The first set of plots (Fig. 6.14 and 6.15) compares the performance of the gravity gradiometer instrument type and the effect of the IMU grade on the system

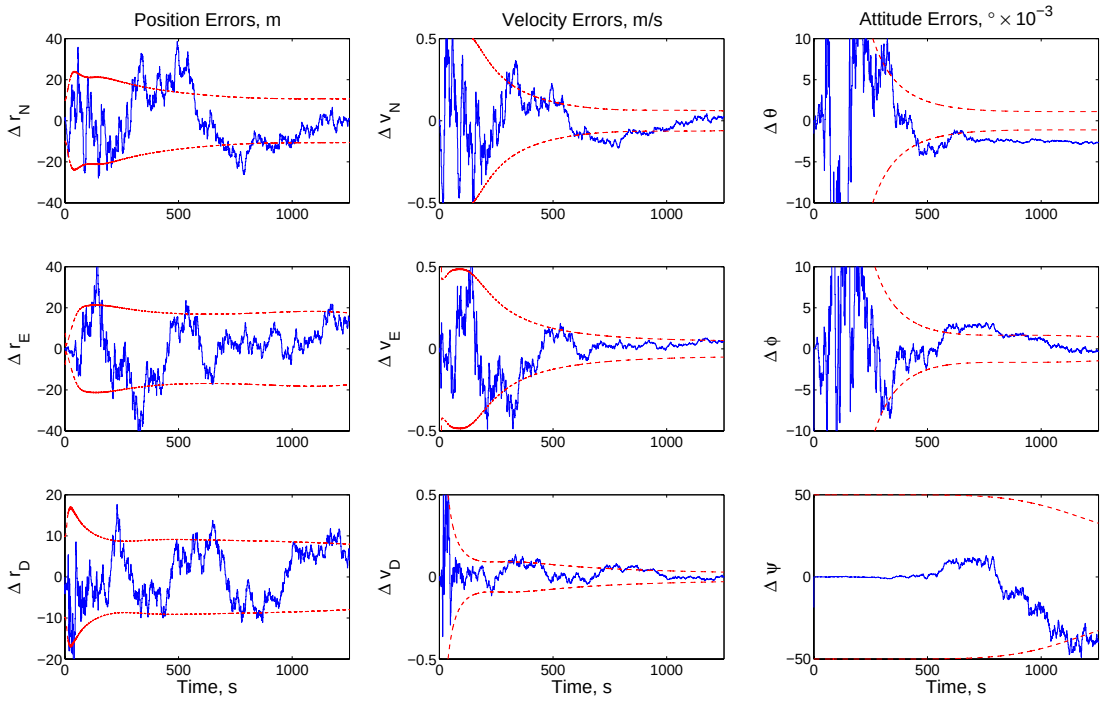

Figure 6.13: Sample GGI Survey INS/GGI Simulation w/ Increased Noise

Table 6.14: GGI Survey INS/GGI Case w/ Increased Noise

Settling Time	State	Units	North / Pitch Error	North / Pitch Cov.	East / Roll Error	East / Roll Cov.	Down / Yaw Error	Down / Yaw Cov.
30 km	Pos.	m	6.3029	10.573	10.675	13.010	5.4411	9.1511
	Vel.	m/s	0.0640	0.4813	0.0534	0.4812	5.3278	0.4674
	Att.	$^\circ\times10^{-3}$	0.6774	22.894	0.7255	23.130	9.3193	46.656
150 km	Pos.	m	10.580	11.068	18.833	17.774	8.6461	8.5760
	Vel.	m/s	0.0563	0.0664	0.0729	0.0661	0.0433	0.0413
	Att.	$^\circ\times10^{-3}$	1.2154	1.2094	1.3021	1.6341	16.771	43.982

performance. Only the steady state mean-radial-spherical-errors for the Mach 7 simulations are presented in this analysis as a baseline for the following plots. Figures 6.16–6.21 then focus on one of the three INS/GGI system configurations and investigates the sensitivities of speed/altitude on the system and the gravity gradient signal variations. Each of these figures are normalized by the Mach 7, high Γ^n variation trajectory cases that are presented in Fig. 6.14 and 6.15. Because the MRSE attitude errors from the Monte Carlo simulations were found to be somewhat misleading due to the initial filter covariance matrix, the filter's estimate of the attitude errors are also included in the results.

The GGI update rate and noise are combined in terms of the sensor's effective power spectral density (PSD) in an effort to reduce the results that are presented. Referring to Eq. (C.9) on pg. 313, the square root of the instrument's PSD can be written as

$$\sqrt{q_{GGI}} = \sigma_{\nu_L} \sqrt{\Delta t_{GGI}}, \tag{6.5}$$

which has units of Eö$\sqrt{s}$, or equivalently Eö/$\sqrt{Hz}$ (similar to the IMU noise specifications). Therefore, increasing the time between instrument updates causes an effective increase in the GGI noise by a factor of $\sqrt{\Delta t_{GGI}}$. All the INS/GGI results are plotted with this parameter as the abscissa (x-axis).

Figure 6.14 plots the position and velocity MRSE for the nominal Mach 7 INS/GGI cases along the high gradient variation trajectory. Referring to part (a) of the figure, the stabilized GGI cases have improved position accuracy over the strapdown GGI case because the stabilized sensor does not estimate the gyro or

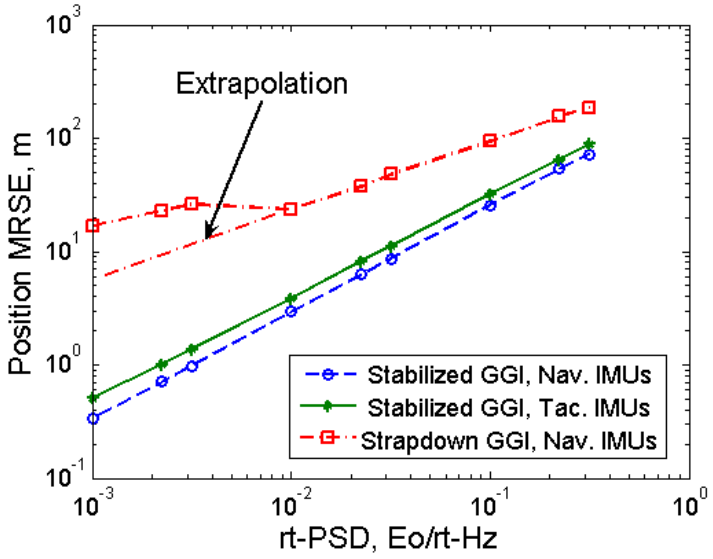

(a)

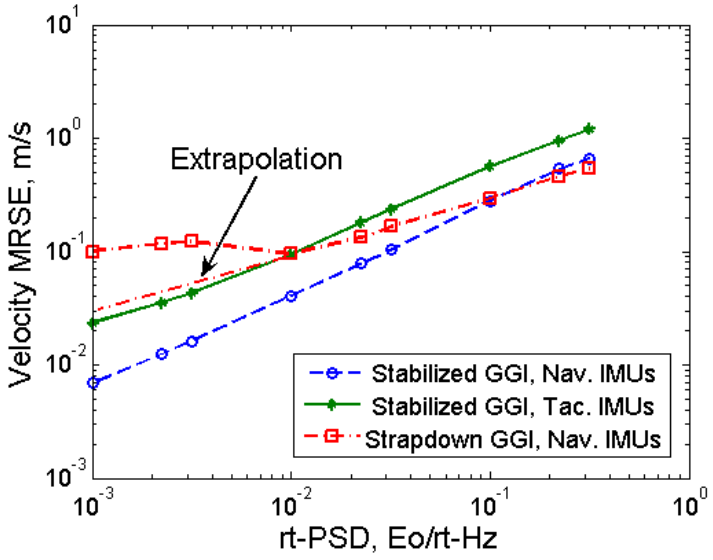

(b)

Figure 6.14: INS/GGI Steady State MRSEs for Mach 7, High Γ^n Variation, (a) Position (b) Velocity

attitude errors in order to observe the gravitational gradients, see Eq. (5.67) on pg. 210. The strapdown GGI has approximately 2.4–8.1 times the position MRSE compared to the navigation grade IMU / stabilized GGI system, with the largest sensitivity occurring at the lowest noise levels. For GGI noise <0.01 Eö/$\sqrt{Hz}$, the strapdown GGI filter begins to diverge, which causes increased error. The stabilized GGI with tactical grade IMUs produces position accuracy only 19–56% more than that of the stabilized GGI with navigation grade IMUs, with the largest sensitivity at the lowest GGI noise levels.

Neither GGIs have direct observability of the velocity errors (Eq. (5.67) and Eq. (5.56) on pg. 207). Thus, the velocity error corrections are made by way of the position and attitude error observability. And since a stabilized GGI has better position accuracy but worse attitude accuracy, whereas the strapdown GGI has reduced position accuracy and improved attitude accuracy, the velocity errors of both sensors are somewhat similar. From Fig. 6.14 (b), the stabilized GGIs have superior velocity performance for the lowest GGI noise levels even with the non-diverging strapdown GGI extrapolation. At higher noise levels, the navigation grade INS/GGI systems are comparable. The tactical grade IMU / stabilized GGI system has approximately 1.7–2.8 times the velocity error of the comparable INS/GGI with navigation grade IMUs. And again, the largest error sensitivity occurs for the lowest GGI noises.

The attitude errors for the three INS/GGI configurations are shown in Fig. 6.15 with the actual steady state MRSE (a) and the filter estimated MRSE (b). Because of the attitude and gyro error observability, the strapdown GGI produces about

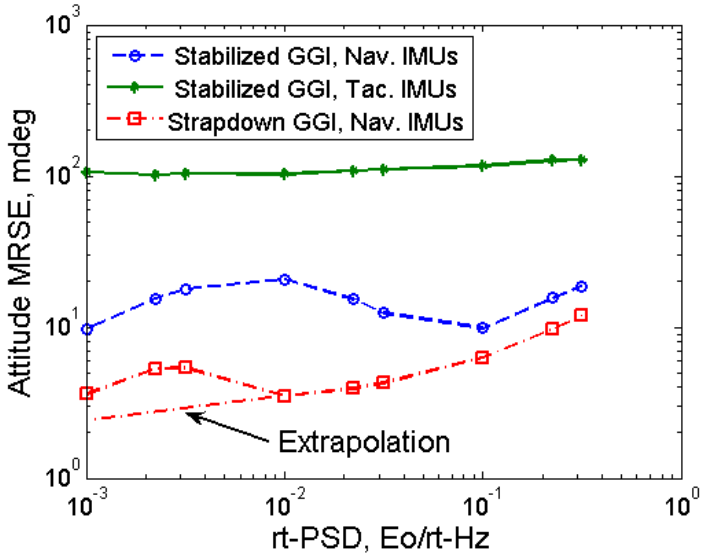

(a)

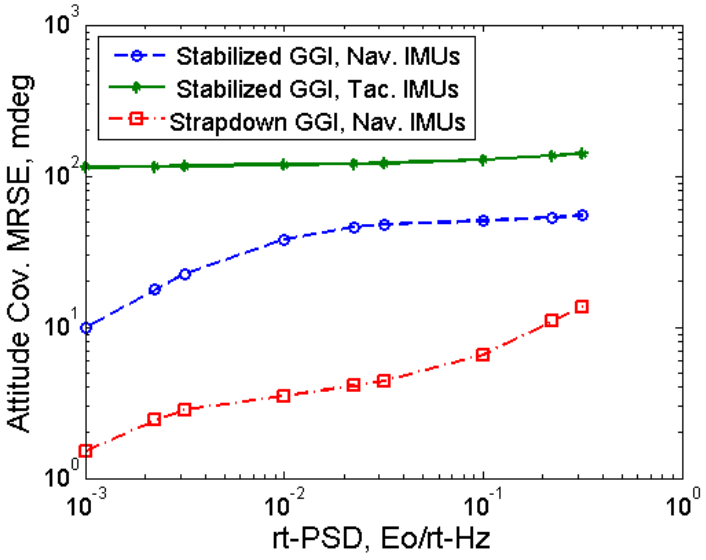

(b)

Figure 6.15: INS/GGI Steady State Attitude MRSEs for Mach 7, High Γ^n Variation, (a) Monte Carlo (b) Filter

an order of magnitude lower orientation error than the comparable stabilized GGI / navigation grade IMU case. Even for the low noise, diverging simulations, the strapdown GGI outperforms the stabilized GGI. The tactical grade IMU / stabilized GGI case has a steady 0.1° total attitude error for all simulated noise levels which is due to the yaw error not reaching steady state by the end of the simulation, as can be seen in Fig. 6.5. Had the filter been tuned differently, these INS/GGI systems would have reached a steady state yaw error faster and would have most likely changed the results. Also, the chosen initial filter covariance caused the stabilized GGI with navigation grade IMUs to overestimate the attitude errors at high noise levels and thereby allowed the gyros to run without corrections, thus causing lower errors when $\sqrt{q_{GGI}} < 0.01$ Eö$/\sqrt{Hz}$.

Stabilized GGI, Navigation Grade IMU

Figures 6.16 and 6.17 show the GGI/INS steady state MRSE sensitivities for the INS with navigation grade IMUs and a stabilized GGI aid. All the plot are normalized by the $M_\infty = 7$, high Γ^n variation cases shown in Fig. 6.14. The high gradient variation trajectories are plotted with solid lines and the low gradient trajectories are plotted with dashed lines. Furthermore, the Mach 6 cases use circles for data point markers, Mach 7 use asterisks, and Mach 8 uses squares.

Referring to Fig. 6.16 (a), increasing speed and altitude (larger Mach number) increases the overall position error on average 5%. This performance degradation is due to two main factors. First, the faster trajectories travel the 1000 km range in

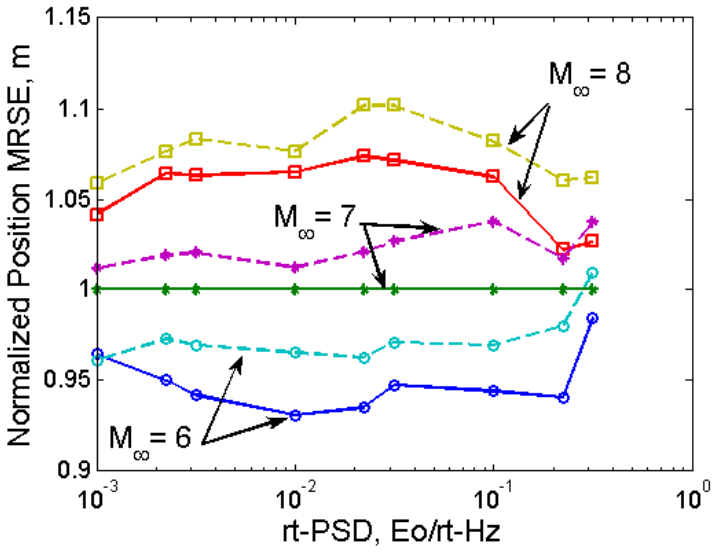

(a)

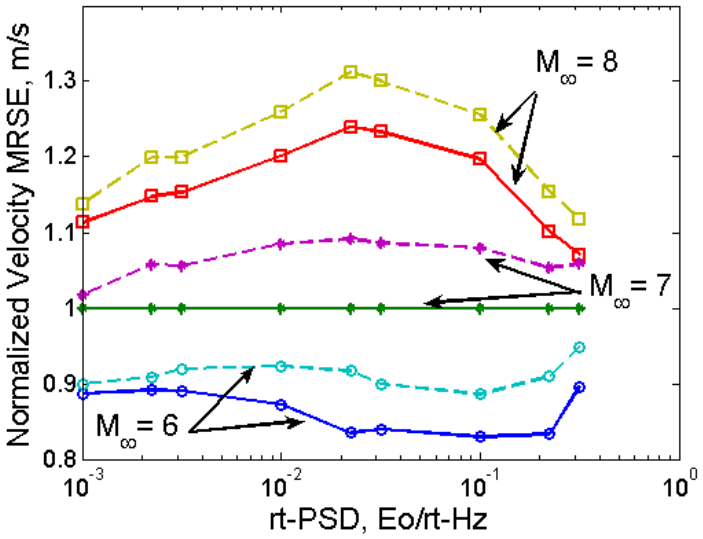

(b)

Figure 6.16: Normalized INS/GGI Steady State MRSE for Stabilized GGI w/ Nav. Grade IMUs, (a) Position (b) Velocity

a shorter time span so fewer measurements are made during a simulation. Second, the increase in cruise altitude reduces the magnitude of the gravitational gradient variations. And comparing the gradient variation simulations, the dashed lines, the position errors increase about 2% over the comparable high Γ^n variation cases. At the highest noise levels, the results are less sensitive to these effects because the GGI is relatively ineffective as a map-matching INS aid.

The velocity sensitivities follow the same trends as the position errors but have approximately twice the magnitude in their variations. Increasing or decreasing the cruise Mach number causes 7–24% change in velocity MRSE (∼15% on average). The lower signal variation results in about a 5% increase in the total error. Also, GGI noise levels near 0.02 Eö/$\sqrt{Hz}$ are most sensitive to these changes. These results are quite promising because they show that a future GGI with a noise level of 0.001 Eö$\sqrt{Hz}$ is essentially insensitive to the magnitude of the signal variation so that it could be an effective INS aid worldwide—not just over regions with high gradient variations.

Figure 6.17 plots the attitude sensitivities for this configuration. Referring back to Fig. 6.15, the filter overestimates the attitude error for GGI noises greater than 0.01 Eö. Therefore, the Monte Carlo error in part (a) of the Fig. 6.17 exhibits odd trends above this noise level. For the lower noise cases, the filter performs optimally and the trends in Fig. 6.17 (a) and (b) are similar. Referring to the filter estimated attitude MRSE, part (b), increasing the cruise velocity and altitude increases the attitude MRSE up to 30%. This sensitivity reduced as GGI noise increases and the gyros tend toward their dead-reckoning, free-inertial values. Sur-

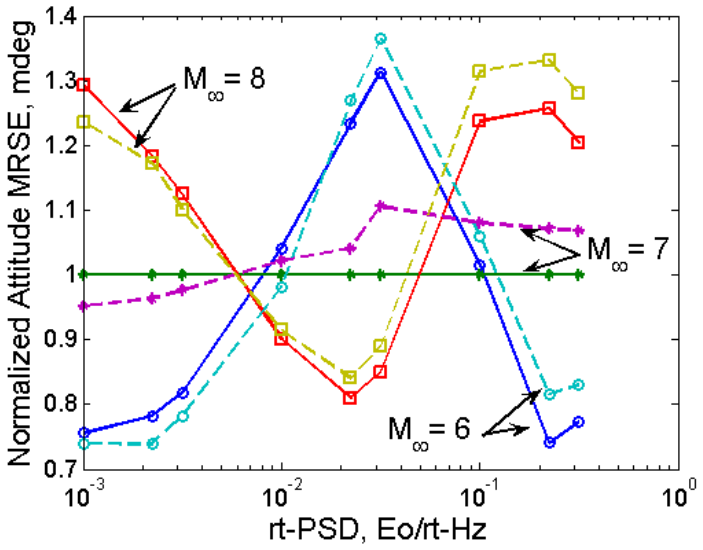

(a)

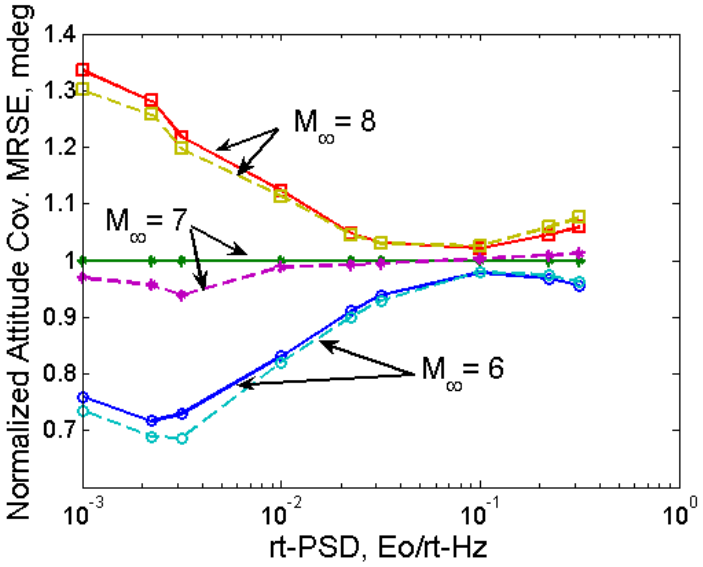

(b)

Figure 6.17: Normalized INS/GGI Steady State Attitude MRSE for Stabilized GGI w/ Nav. Grade IMUs, (a) Monte Carlo (b) Filter

prisingly, the lower Γ^n variation trajectories reduce the attitude error by almost 5%. The cause of this improvement in attitude accuracy is unknown, but may be due to the gravity vector being more stable so that the attitude errors are less affected by gravity errors.

Stabilized GGI, Tactical Grade IMU

Figure 6.18 plots the position and velocity sensitivities for the INS/GGI cases with tactical grade IMUs and a stabilized gradiometer. The position MRSE is less sensitive to Mach number and gradient variation changes compared to the previous navigation grade IMU / stabilized GGI system, especially at the lower and higher GGI noise levels. At the lowest GGI noise level, the position accuracy varies less than 2% from the nominal Mach 7, high gradient trajectory simulation. For GGI noise levels in the 0.01–0.1 Eö/$\sqrt{Hz}$ range, an increase in Mach number causes the position MRSE to rise about 5%. The trajectories cause on average about a 1% change in the position MRSE. For the low GGI noise levels, the lower Γ^n variation trajectories produces lower errors, but for $\sqrt{q_{GGI}} \geq 0.01$ Eö/$\sqrt{Hz}$ this trend reverses.

The velocity sensitivities are similar to the navigation grade IMU / stabilized GGI trends. The primary difference is that the tactical grade IMU system performance is almost entirely insensitive to speed / altitude or gradient signal variation at the lowest GGI noise levels. For a 0.001 Eö/$\sqrt{Hz}$ stabilized GGI, there is less than a 1% change in the velocity MRSE. For a 0.01 Eö/$\sqrt{Hz}$ sensor, the velocity MRSE has about 15% variation due to Mach number changes and about 5% sensitivity to

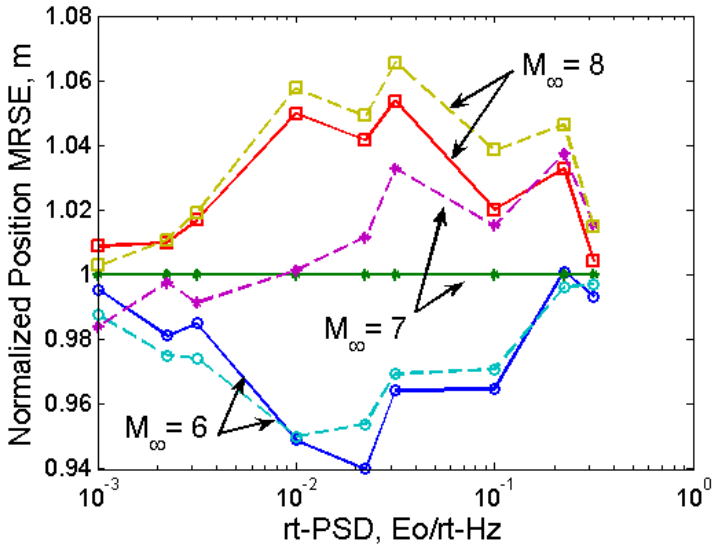

(a)

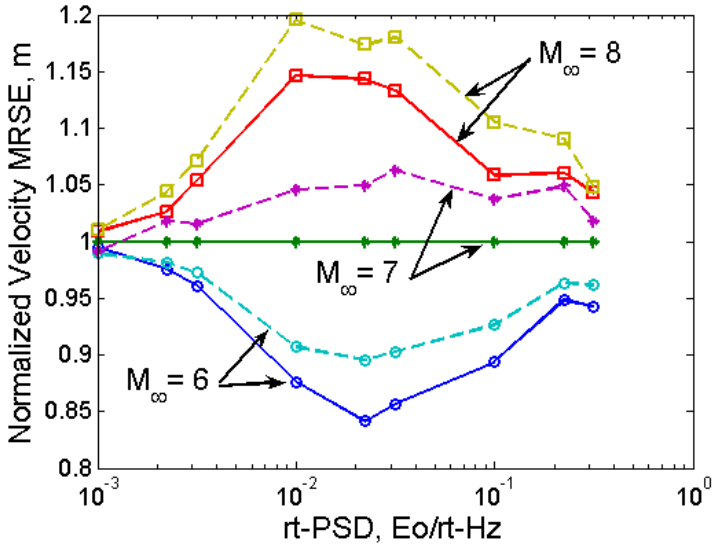

(b)

Figure 6.18: Normalized INS/GGI Steady State MRSE for Stabilized GGI w/ Tac. Grade IMUs, (a) Position (b) Velocity

signal variation. At the higher noise levels, the INS/GGI becomes less sensitive to these changes as it again starts to act more like a dead-reckoning, GGI-less INS.

Comparing the Monte Carlo and filter-estimated attitude MRSE in Fig. 6.19, it is evident that the filter is working optimally. Also, these plots show that the attitude errors are insensitive to the trajectory's gradient signal variation. According to the filter estimates, there is only a small increase in the error for high gravity field variations at low GGI noise levels and the trend reverses at higher GGI noises. The Mach number affects the attitude errors 5–10% with an increase in error as the speed decreases. This result is caused by the yaw error not reaching steady state by the end of the simulation (see Fig. 6.5). Therefore, since the lower Mach number cases run for a longer time, the yaw error increases to a higher value. If the initial filter covariance matrix were tuned differently these results would likely be different.

Navigation Grade IMU, Strapdown GGI

The normalized MRSE for the strapdown GGI with navigation grade IMUs are plotted in Fig. 6.20 and 6.21. The trends below the 0.01 Eö/$\sqrt{Hz}$ GGI noise levels will not be discussed in depth because they include the numerical divergence issues discussed on pg. 235. Furthermore, all strapdown GGI / tactical grade IMU systems diverged immediately due to the increased gyro noise of the tactical IMUs. Therefore only the navigation grade IMUs could be simulated with the strapdown gradiometer.

As shown in Fig. 6.20, the strapdown GGI system is very sensitive to the

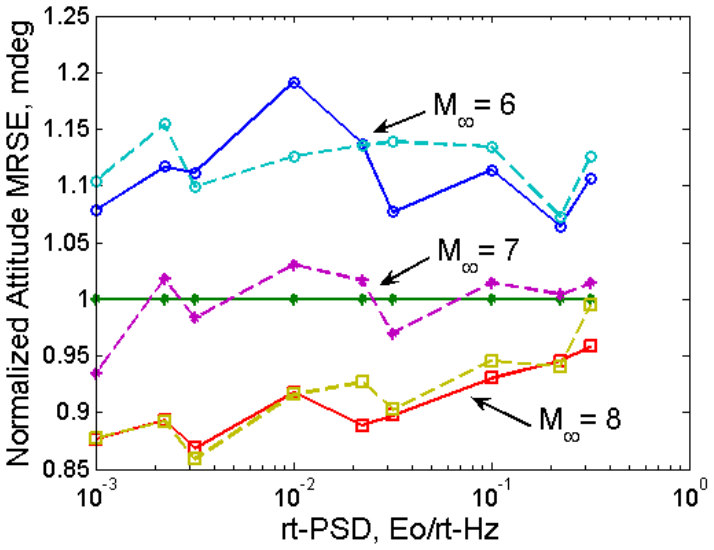

(a)

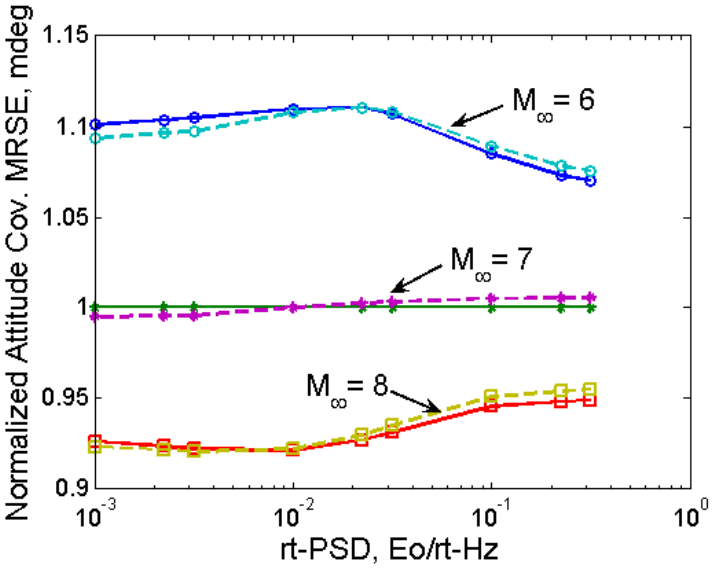

(b)

Figure 6.19: Normalized INS/GGI Steady State Attitude MRSE for Stabilized GGI w/ Tac. Grade IMUs, (a) Monte Carlo (b) Filter

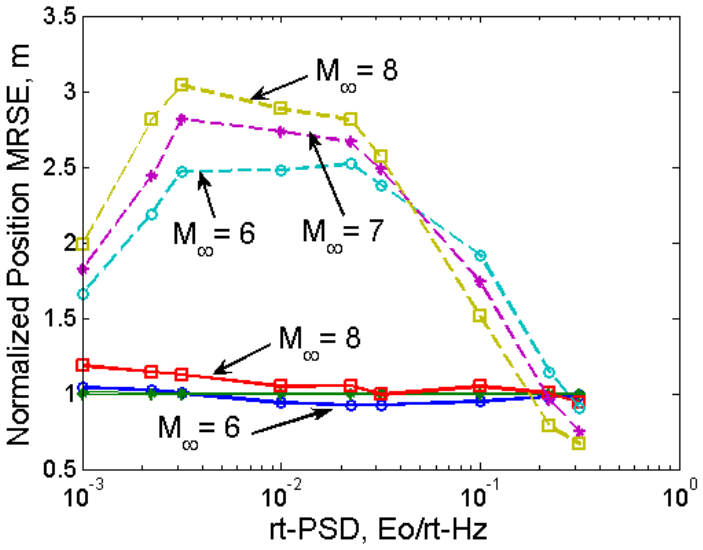

(a)

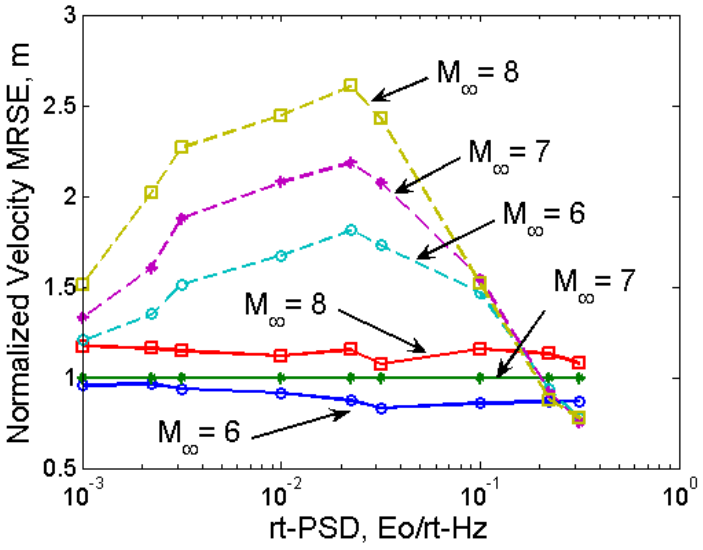

(b)

Figure 6.20: Normalized INS/GGI Steady State MRSE for Strapdown GGI w/ Nav. Grade IMUs, (a) Position (b) Velocity

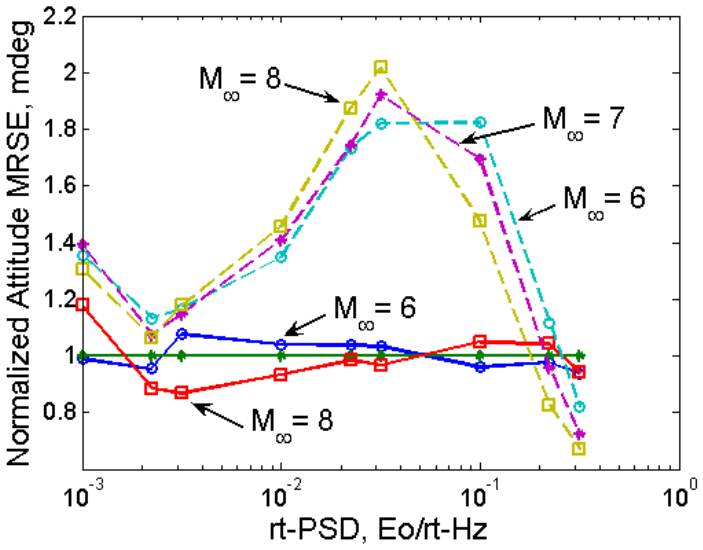

(a)

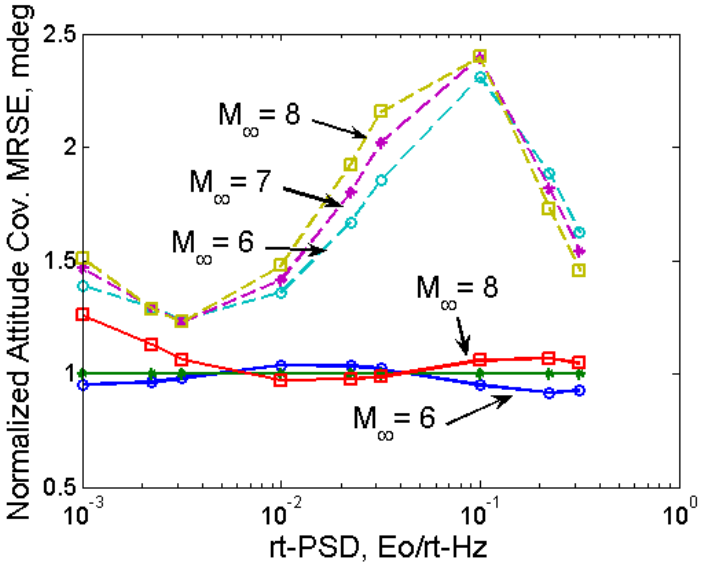

(b)

Figure 6.21: Normalized INS/GGI Steady State Attitude MRSE for Strapdown GGI w/ Nav. Grade IMUs, (a) Monte Carlo (b) Filter

gravitational gradient signal variation. At a GGI noise of 0.01 Eö/$\sqrt{Hz}$ the lower Γ^n variation trajectories have over 2.5 times the position error and between 1.5–2.5 the velocity error as the corresponding high Γ^n variation trajectory cases. The navigation performance is less sensitive at high GGI noise levels because the GGI is less efficient as an INS aid. And at the two highest GGI noise levels, the low Γ^n variation cases produce lower position and velocity MRSE since the gravity errors contributing to the velocity errors are smaller. Increasing the Mach number is shown to degrade position and velocity accuracy by up to 20%. This trend is reversed for the position MRSE at high GGI noise levels.

Figure 6.21 shows that the attitude errors for the strapdown GGI system are also quite sensitive to the gravitational gradient signal strength. At worse, the lower gradient variation trajectory doubles the total attitude error. The attitude sensitivity to Mach number is much lower, but follows some rather odd trends. The Monte Carlo errors show that increasing M_∞ increases the error for the low Γ^n variation cases with GGI noises $<$0.1 Eö/$\sqrt{Hz}$ and the high Γ^n cases with GGI noise $\geq$0.1 Eö. For the other cases, the Mach number sensitivity trends are reversed. It is unknown why these trends occur, but the magnitude of these sensitivities ($\sim$10%) are large enough to warrant further investigation.

6.3.2 Global Positioning System Aided Navigation

Like the INS/GGI results, the INS/GPS results are first presented and discussed in terms of single representative simulations and their detailed errors. The

Table 6.15: INS/GPS Nominal and Off-Nominal Simulation Parameters

	IMU	Trajectory	Measurements	Data Rate
Nominal Value	Nav.	High Γ^n Variation	ρ and $\dot{\rho}$	1 sec
Perturbed Value	Tac.	High Γ^n Variation	ρ-Only	1 sec

Monte Carlo sensitivity results are shown and discussed afterwards. The nominal INS/GPS simulation set parameters are listed in Table 6.15 along with their perturbed values. The full hypersonic INS/GPS text matrix used for the sensitivity analyses is summarized in Table 6.16. The subsonic INS/GPS simulations were only performed with navigation grade IMUs and GPS pseudorange and range-rate measurements at a 1 Hz update rate to provide a baseline to the INS/GGI simulations.

The primary concern with an INS/GPS system is the update rate or blackout duration of the GPS receiver. This rate is a function of the receiver design and the vehicle dynamics. For the atmospheric, hypersonic cruise simulations, the update intervals were varied from 1 sec to 300 sec. The subsonic systems' sensitivity to update rate was not investigated since they are used as only a baseline comparison

Table 6.16: INS/GPS Monte Carlo Test Matrix

Parameter	Values	#
IMU Grade	Navigation, Tactical	2
Mach Number	6, 7, 8	3
Measurement Type	ρ Only, ρ and $\dot{\rho}$	2
Data Rate	1, 10, [30:30:120], [180:60:300] sec	9

to the proposed future INS/GGI system. Also, all the INS/GPS simulations were performed over only the high gravitational gradient variation trajectory because the effect of GPS visibility and GDOP on the two trajectories is small, as shown in Fig. D.3 on pg. 341 and Fig. D.4 on pg. 350.

6.3.2.1 Monte Carlo Results

Hypersonic Cases

A sample simulation of the nominal Global Positioning System case is given in Fig. 6.22. The simulation uses the nominal 24-satellite GPS constellation and simulates pseudorange and pseudorange rate measurements to aid a navigation-grade INS at Mach 7. As shown in Fig. 6.22, the INS/GPS filter is stable and quickly reaches steady state in the horizontal and tilt states. The altitude, vertical velocity, and yaw states are less observable to the filter and therefore take slightly longer to correct and reach steady state values. The horizontal position state error envelopes have a discontinuous jump at 72 sec because the number of visible satellites increases from 6 to 7. This increase in measurement observables causes the geometric dilution of precision (GDOP) to drop from 11 to 3.4 instanteously and the filter covariance to reduce accordingly. Compared to the "Best" gradiometer-aided INS case, the nominal GPS performance is approximately twice as good, see Table 6.5 and 6.17. The North (crossrange) position error is half that of the INS/GGI case, and the East (downrange) error is one-quarter the gradiometer case, but the altitude is much closer to the nav.-grade IMU / stabilized GGI scenario. The overall velocity

error is about half the INS/GGI error (0.0031 vs. 0.0069 m/s), as is the yaw error. The tilt errors are only slightly lower then the gradiometer-aided case.

Figure 6.23 and Table 6.18 present results for the INS/GPS with tactical grade IMUs and both GPS measurements. The odd filter envelope towards the end of the simulation is due to two satellites going out of view, one at 407 sec and another at 426 sec. This tactical-grade case follows trends similar to the previous navigation grade case in relation to the comparable GGI cases. The tactical gradiometer crossrange position error is a factor of 2 larger than the current GPS case, the downrange error is a factor of 4 larger, and the altitude is only about 20% larger. The total velocity error for the tactical GPS is about half that of the tactical GGI case (0.0129 vs. 0.0234 m/s), and the total attitude error is comparable to the gradiometer case (0.0950 vs. 0.106°).

The last sample GPS case to be presented is the effect of measurement observables. If only pseudorange measurements (*i.e.* position information) were available, the performance is significantly degraded because of the lack of velocity and precise position knowledge from the pseudorange rate measurements, see Eq. (D.20) on pg. 345. Referring to Fig. 6.24 and Table 6.19, the total position error increases to almost 10 times that of the nominal navigation grade INS/GPS case. The velocity error is a little less sensitive, and only increases by a factor of 7. The attitude error also increases, but only by a factor of 3 over the case when pseudorange rate measurements are also made.

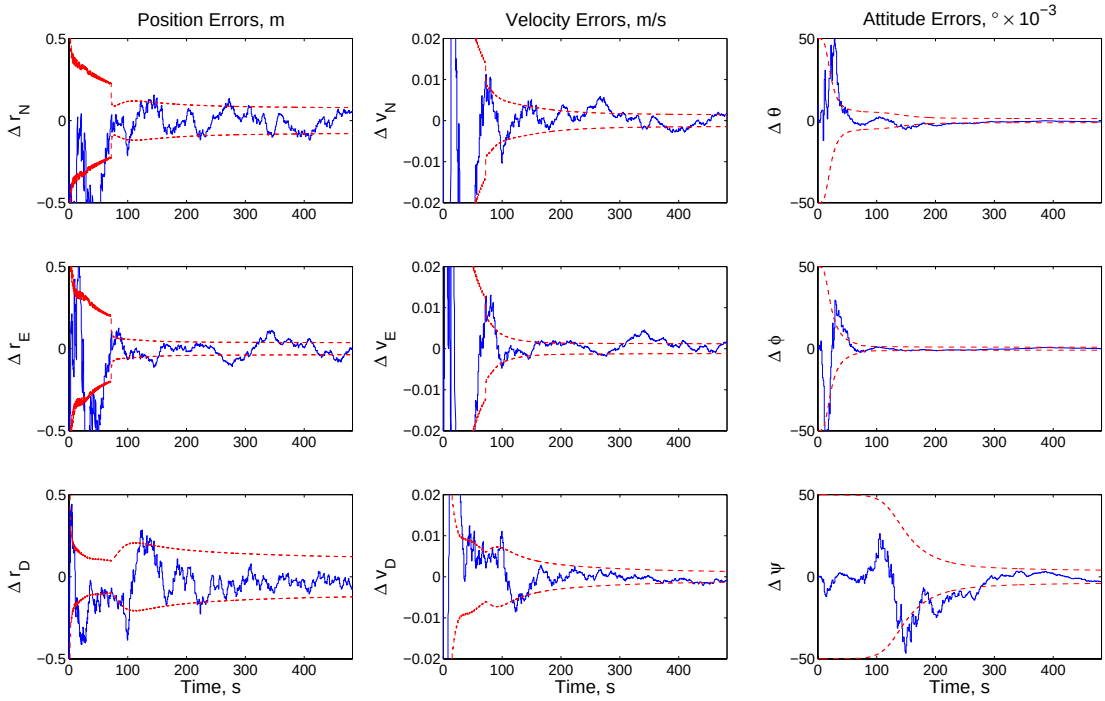

Figure 6.22: Sample Nominal Global Positioning System Simulation

Table 6.17: Nominal Global Positioning System Case

Settling Time	State	Units	North / Pitch Error	North / Pitch Cov.	East / Roll Error	East / Roll Cov.	Down / Yaw Error	Down / Yaw Cov.
100 km	Pos.	m	0.5487	0.3908	0.2848	0.2363	0.6372	0.4076
	Vel.	m/s	0.1394	0.1561	0.1140	0.1125	0.1143	0.1260
	Att.	$^\circ \times 10^{-3}$	0.7448	22.969	0.5160	22.751	3.1799	25.347
500 km	Pos.	m	0.1031	0.0953	0.0594	0.0540	0.1030	0.0869
	Vel.	m/s	0.0024	0.0024	0.0016	0.0015	0.0015	0.0014
	Att.	$^\circ \times 10^{-3}$	1.3350	1.3442	0.9228	0.9517	5.7198	5.6250

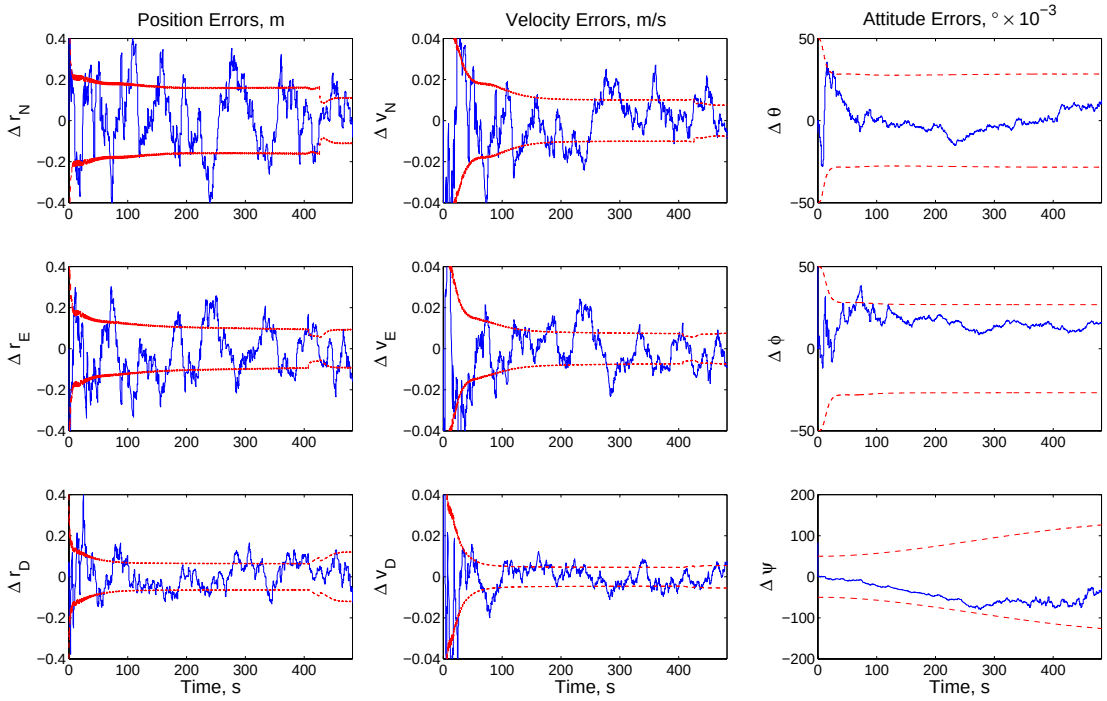

Figure 6.23: Sample Tactical Grade IMU Global Positioning System Simulation

Table 6.18: Tactical Grade IMU Global Positioning System Case

Settling Time	State	Units	North / Pitch Error	North / Pitch Cov.	East / Roll Error	East / Roll Cov.	Down / Yaw Error	Down / Yaw Cov.
100 km	Pos.	m	0.5405	0.4089	0.2773	0.2495	0.6456	0.4273
	Vel.	m/s	0.1398	0.1562	0.1183	0.1126	0.1209	0.1271
	Att.	$^\circ \times 10^{-3}$	13.439	37.976	12.768	37.120	49.469	81.184
500 km	Pos.	m	0.1496	0.1402	0.0942	0.0862	0.1429	0.1288
	Vel.	m/s	0.0091	0.0089	0.0071	0.0069	0.0058	0.0057
	Att.	$^\circ \times 10^{-3}$	24.110	28.357	22.898	26.816	88.961	106.13

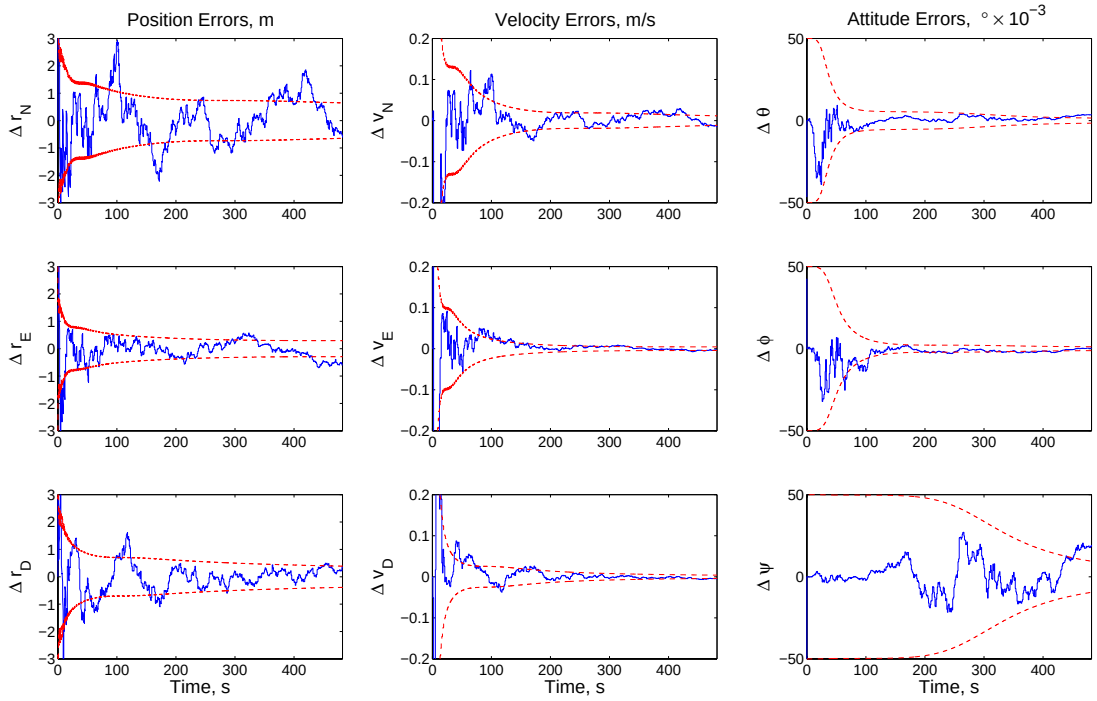

Figure 6.24: Sample Pseudorange Only Global Positioning System Simulation

Table 6.19: Pseudorange Only Global Positioning System Case

Settling Time	State	Units	North / Pitch Error	North / Pitch Cov.	East / Roll Error	East / Roll Cov.	Down / Yaw Error	Down / Yaw Cov.
	Pos.	m	4.8386	2.2330	1.8196	1.3189	3.2582	1.6642
100 km	Vel.	m/s	0.0197	0.4545	0.0178	0.4480	0.0157	0.4490
	Att.	$^\circ\times10^{-3}$	1.2829	23.806	0.8624	23.166	10.358	35.401
	Pos.	m	1.0518	0.9264	0.4696	0.4216	0.8063	0.5913
500 km	Vel.	m/s	0.0182	0.0181	0.0071	0.0065	0.0112	0.0082
	Att.	$^\circ\times10^{-3}$	2.3054	2.8519	1.5483	1.6996	18.640	23.722

Subsonic Cases

A commercial aircraft INS/GPS simulation is shown in Fig. 6.25 and the Monte Carlo set results are listed in Table 6.20. From the figure, the position, velocity, and attitude states reach steady-state conditions at or before the 250 km (∼400 sec) settling period. The position MRSE is almost half the low-noise INS/GGI simulation (0.1521 vs. 0.2281 m), with the crossrange (North) error being halved and the downrange (East) error being reduced to a third the INS/GGI value, see Table 6.11. The altitude error is approximately the same for both the INS/GPS and INS/GGI cases since the gradiometer-aiding system has improved performance in the vertical channel. The total velocity error for this GPS-aided case is 60% that of the INS/GGI (0.0029 vs. 0.0050 m/s). And again, the improvement is almost exclusively due to the reduced horizontal errors. The attitude error is similar to the INS/GGI simulation.

The GGI survey INS/GPS case is presented in Fig. 6.26 as a sample time history and in Table 6.21 for the full 1,000 simulation Monte Carlo set. This low-altitude, low-velocity INS/GPS case has a remarkable improvement in the navigation accuracy over the comparable INS/GGI case shown on pg. 241. The overall position MRSE decreases by a factor of four (0.1441 vs. 0.5387 m) primarily due to the downrange error decreasing by a factor of 7. The difference in performance of these two systems may be due to the shorter range of the simulation (300 km) which reduces the amount of variation of the gravitational gradient signal compared to the other cases (which end at 500 or 1,000 km). If the local terrain effects were

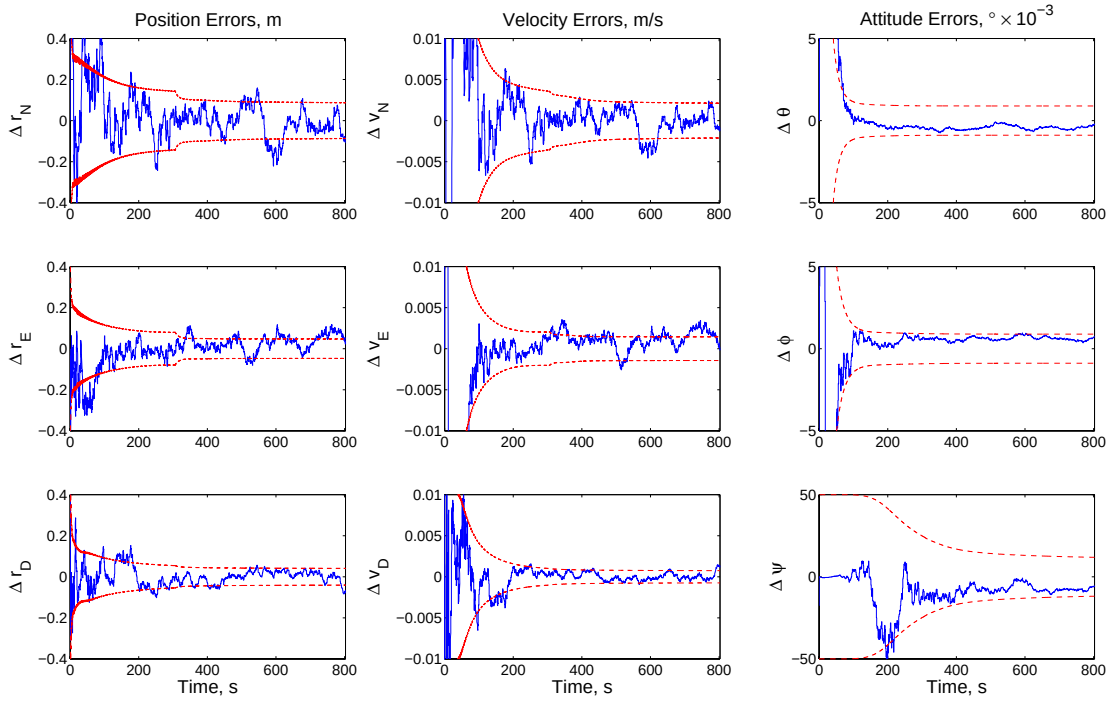

Figure 6.25: Sample Commercial Aircraft Global Positioning System Simulation

Table 6.20: Commercial Aircraft INS/GPS Case

Settling Time	State	Units	North / Pitch Error	North / Pitch Cov.	East / Roll Error	East / Roll Cov.	Down / Yaw Error	Down / Yaw Cov.
50 km	Pos.	m	0.5966	0.3750	0.2899	0.2343	0.6597	0.3923
	Vel.	m/s	0.1365	0.1526	0.1120	0.1092	2.4688	0.1233
	Att.	$^\circ \times 10^{-3}$	0.5081	22.719	0.4887	22.716	7.7545	29.476
250 km	Pos.	m	0.0999	0.0880	0.0640	0.0569	0.0952	0.0739
	Vel.	m/s	0.0021	0.0020	0.0016	0.0015	0.0011	0.0010
	Att.	$^\circ \times 10^{-3}$	0.9091	0.8916	0.8733	0.8849	13.955	13.054

included in the gravitational gradient signal model, the INS/GGI error should be reduced to a value closer to that of the INS/GGI case. The velocity error is about a third of the INS/GGI value (0.0028 vs. 0.0094 m/s) with the largest decrease in the alongtrack (East) component. And the tilt errors are about the same for both navigation aids. The INS/GPS yaw error, however, increases to twice the value of the INS/GGI error.

6.3.2.2 Sensitivity Results

The INS/GPS sensitivities are presented in a similar fashion to the INS/GGI cases. First, the Mach 7 steady state MRSEs will be compared for INS/GPS configurations with either navigation or tactical grade IMUs and GPS pseudorange with and without pseudorange rate updates. After these results, the sensitivity of Mach number on the navigation performance is discussed for the four INS/GPS systems.

Figure 6.27 plots the steady state Mach 7 position and velocity MRSE for the four INS/GPS systems simulated and update intervals from 1 to 300 sec. From part (a), the position error is strongly a function of GPS measurement. When pseudorange rate measurements are simulated, the position MRSE decreases on average by a factor 8 for the navigation grade IMU INS/GPS, and a factor of 7 for the tactical grade IMU system. The effect of IMU quality on the position error is less severe. For the ρ and $\dot{\rho}$ simulations, the tactical grade IMUs increase the error 35%, and for the ρ-only cases the error increases 25% for $\Delta t_{GPS} < 90$ sec.

The velocity errors exhibit similar trends, but with the noted difference that

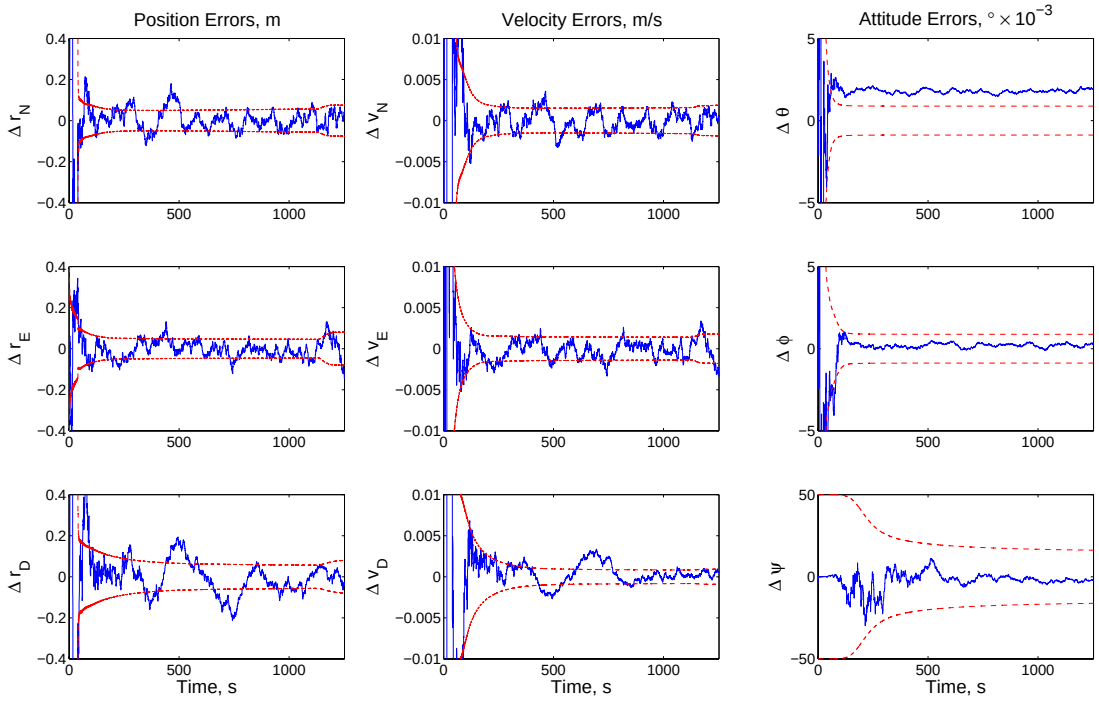

Figure 6.26: Sample GGI Survey Global Positioning System Simulation

Table 6.21: GGI Survey INS/GPS Case

Settling Time	State	Units	North / Pitch Error	North / Pitch Cov.	East / Roll Error	East / Roll Cov.	Down / Yaw Error	Down / Yaw Cov.
30 km	Pos.	m	0.5980	0.3753	0.2791	0.2266	0.7167	0.3881
	Vel.	m/s	0.1374	0.1537	0.1144	0.1114	5.6713	0.1260
	Att.	$^\circ \times 10^{-3}$	0.5039	22.712	0.4992	22.710	21.861	31.739
150 km	Pos.	m	0.0964	0.0861	0.0630	0.0556	0.0866	0.0692
	Vel.	m/s	0.0021	0.0019	0.0016	0.0015	0.0010	0.0009
	Att.	$^\circ \times 10^{-3}$	0.9015	0.8807	0.8921	0.8780	39.346	17.129

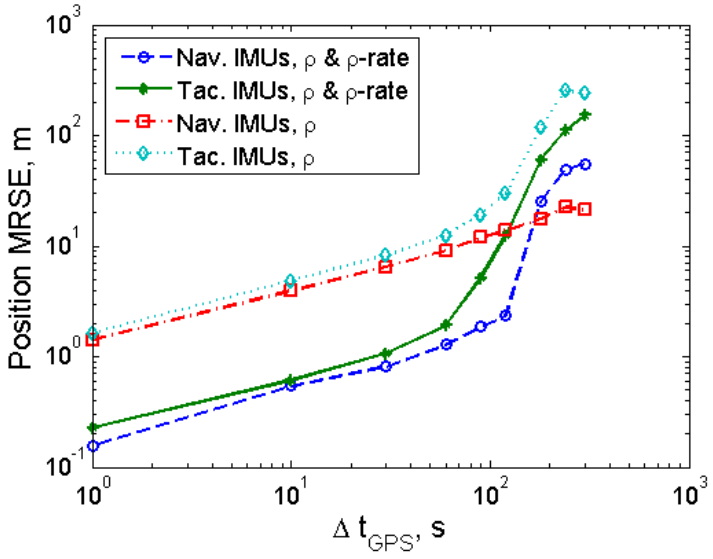

(a)

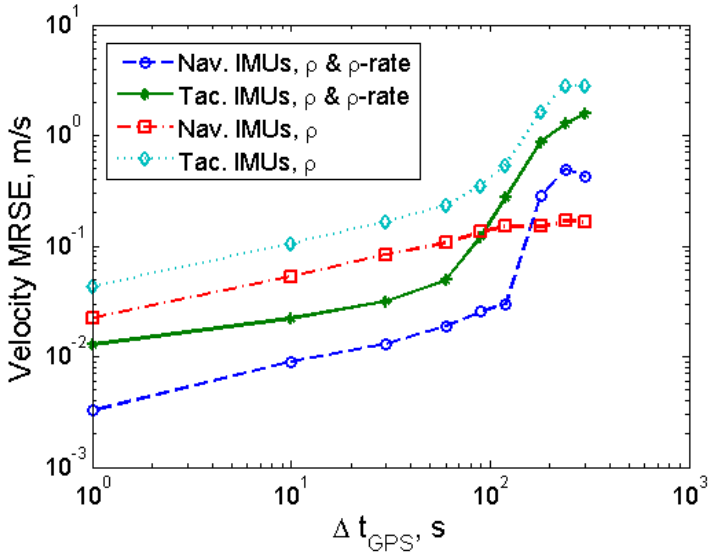

(b)

Figure 6.27: INS/GPS Steady State MRSE for Mach 7 Simulations, (a) Position (b) Velocity

the IMU quality causes larger variations. The increase in velocity error due to a tactical grade IMU is about 150% for the ρ and $\dot{\rho}$ simulations and 90% for the ρ-only simulations. The sensitivity to measurement type is 400–590% for the navigation grade INS/GPS and 80–420% for the tactical grade configuration.

There is a substantial increase in the position and velocity errors when the GPS update interval is greater than about 90 sec. The reason for this is that the GPS measurements are made so infrequent that the in-flight calibration of the IMU errors can not be performed as efficiently. For low Δt_{GPS}, the GPS-aiding allows the INS to reduce the accelerometer and gyro bias and (to a lesser extent) scale factor errors so that between updates the dead reckoning navigation accuracy is improved. In other words, the INS/GPS in-flight calibration essentially improves the quality of the IMUs. The pseudorange-only / navigation grade IMU system does not follow this trend at long update intervals because the filter overestimates the attitude errors here, which causes the filter to perform suboptimally as seen in Fig. 6.28.

Comparing the Monte Carlo and filter-estimated errors of Fig. 6.28, it is apparent that the INS/GPS is accurately predicting the errors for all cases except the navigation grade IMUs at high update intervals. For $\Delta t_{GPS} > 30$ sec, the ρ-only attitude errors start to be overestimated. The ρ and $\dot{\rho}$ navigation grade INS/GPS begins to perform suboptimally at $\Delta t_{GPS} \geq 90$ sec. Comparing these errors before these times, the attitude error increases 170–300% with a lack of pseudorange rate measurements. Because there is no direct observability of the attitude errors from the GPS measurements, the INS/GPS must use the estimated velocity vector to

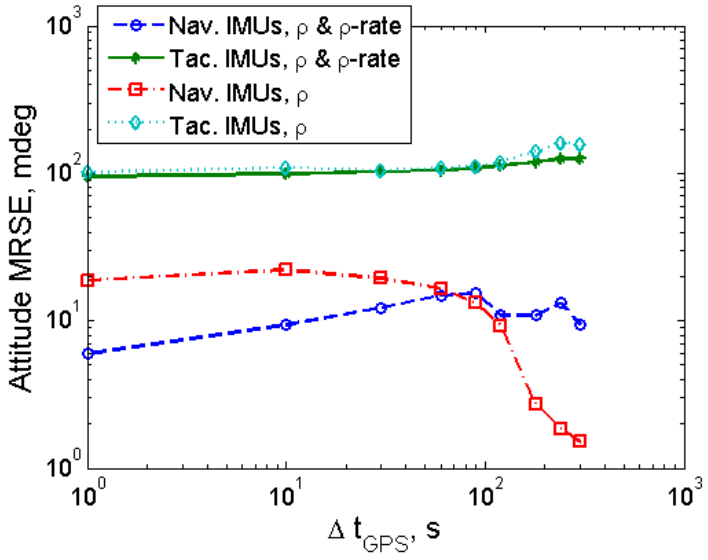

(a)

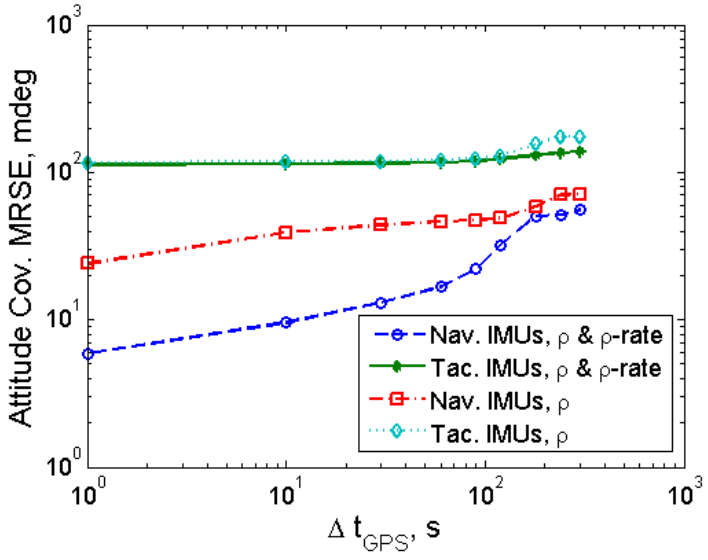

(b)

Figure 6.28: INS/GPS Steady State Attitude MRSE for Mach 7 Simulations, (a) Monte Carlo (d) Filter

estimate the attitude states. So, when the velocity observability is decreased, *i.e.* no $\dot{\rho}$ measurements, the performance is degraded. The tactical IMU systems both have an approximately constant 0.1° attitude error because the yaw error has not reached steady state by the end of the simulation. Furthermore, because of this poor tuning of the initial filter covariance of the yaw state, the attitude sensitivities to Mach number with not be presented. The total attitude MRSE is tabulated, however, in App. E for the interested reader.

Navigation Grade IMU, Pseudorange & Pseudorange Rate

The position and velocity sensitivities to Mach number are plotted in Fig. 6.29 for the navigation grade INS/GPS with pseudorange and range-rate measurements. The first noticeable characteristic of these plots is the spike at 120 sec for the Mach 8 simulation. This spike is a result of the in-flight IMU calibration issue. Because the Mach 8 case is simulated for the shortest amount of time to reach its 1000 km range, fewer updates are made than for the other two cases. Therefore, the faster simulation transitions to higher errors at a lower Δt_{GPS} because fewer overall measurements are made in the simulation. Neglecting this phenomenon, the position MRSE produces an 8% change in error for a change in Mach number. The velocity errors have an average sensitivity of 15% for changes in Mach number.

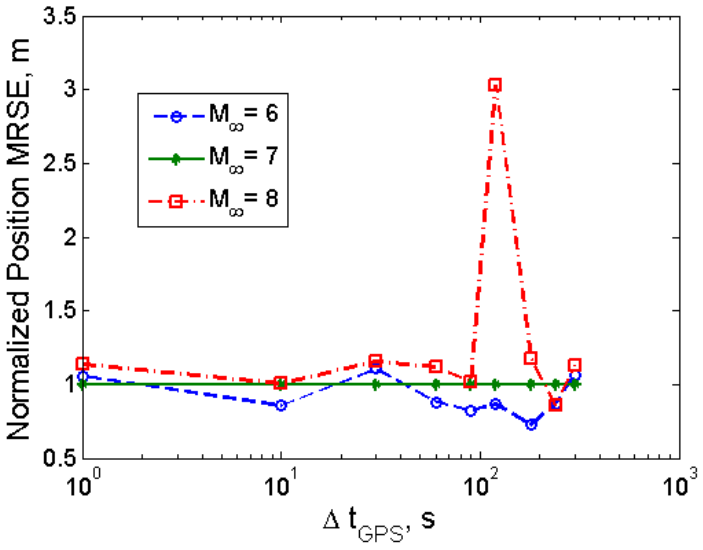

(a)

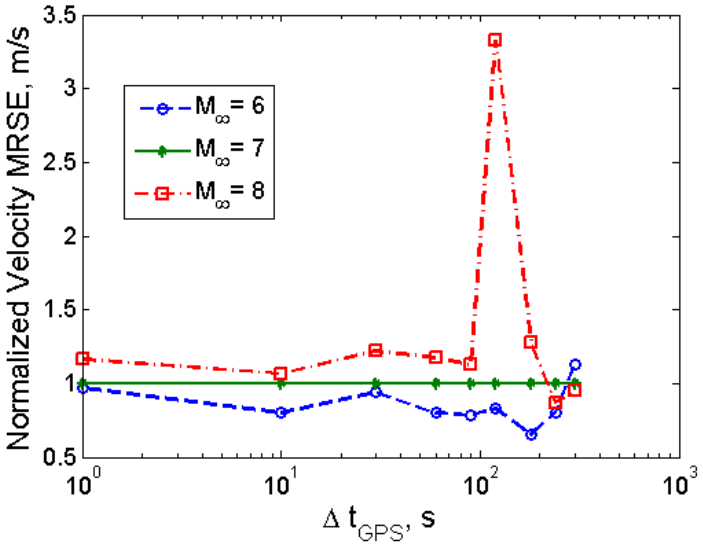

(b)

Figure 6.29: Normalized INS/GPS Steady State MRSE w/ ρ & $\dot{\rho}$ Measurements and Nav. Grade IMUs, (a) Position (b) Velocity

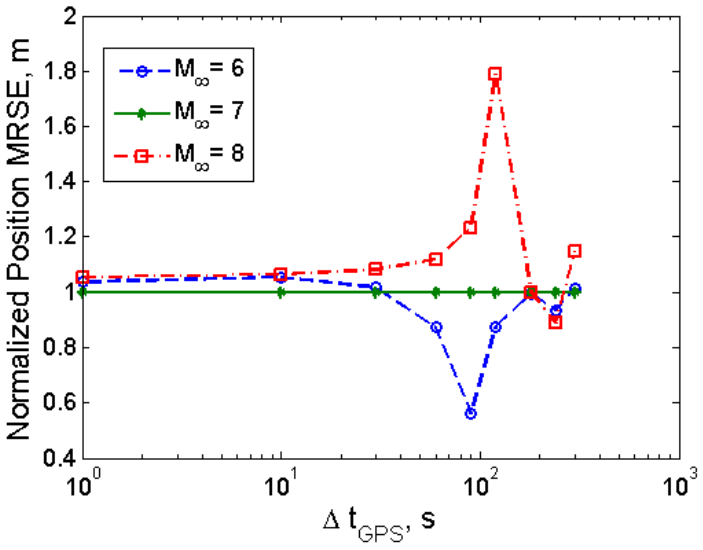

(a)

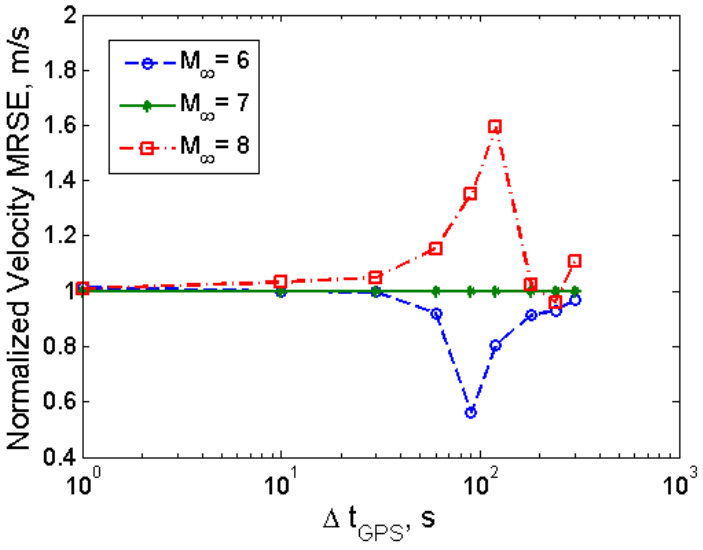

(b)

Figure 6.30: Normalized INS/GPS Steady State MRSE w/ ρ & $\dot{\rho}$ Measurements and Tac. Grade IMUs, (a) Position (b) Velocity

Tactical Grade IMU, Pseudorange & Pseudorange Rate

The MRSE of the tactical grade INS with pseudorange and pseudorange rate measurements is plotted in Fig. 6.30. Like the navigation grade INS/GPS above, the sensitivities have spikes due to the transition from efficient calibration of the IMU errors to less efficient calibration. This results in the negative spike at $\Delta t_{GPS} = 90$ sec for the Mach 6 case since the baseline (Mach 7) simulation has increased error occuring at an earlier update interval than the Mach 6 baseline. The positive spike at $\Delta t_{GPS} = 120$ sec for the Mach 8 case follows the same reasoning. At the highest measurement intervals, the INS/GPS is essentially a dead-reckoning system. Prior to the two spikes mentioned, the position error increases about 5% for an increase or decrease in Mach number from the $M_\infty = 7$ baseline. The reason why both the Mach 6 and 8 cases increase error is unknown. The Mach 6 position errors may have increased because the yaw errors are greater than the Mach 7 or 8 cases which may act to offset the additional updates made. Conversely, the Mach 8 simulations have less updates over their mission duration, but the yaw error has less time to accumulate as well. The velocity errors follow the same trends but with reduced sensitivity to Mach number.

Navigation Grade IMU, Pseudorange-Only

The GPS pseudorange-only updates to a navigation grade IMU INS/GPS produce unusual sensitivities to changes in Mach number, as shown in Fig. 6.31. The position and velocity errors typically increase for higher Mach numbers, but the

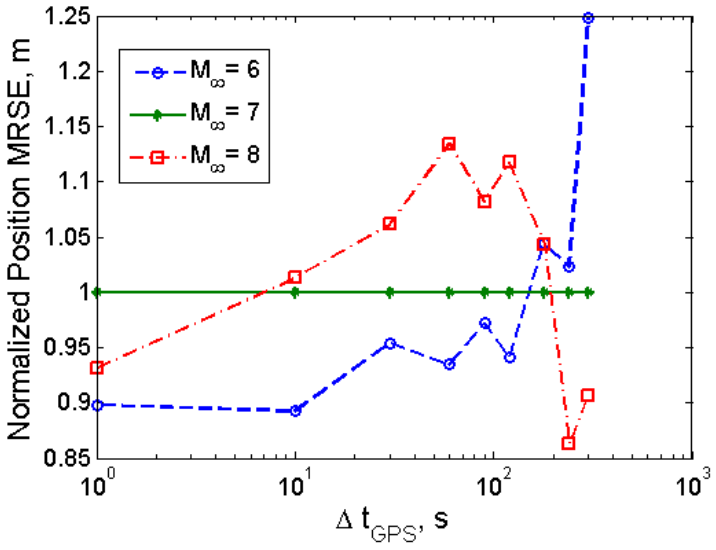

(a)

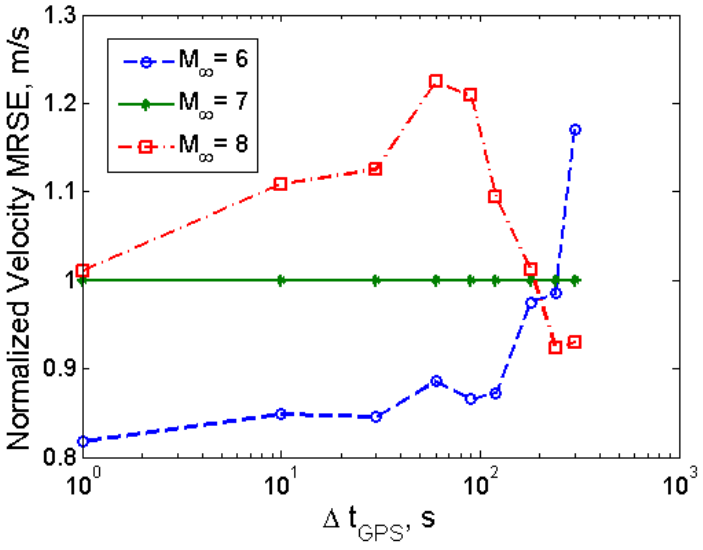

(b)

Figure 6.31: Normalized INS/GPS Steady State MRSE w/ ρ Measurements and Nav. Grade IMUs, (a) Position (b) Velocity

Mach 8 case at the fastest data rate cause less position error than the corresponding Mach 7 simulation set. The cause of this outlier is unknown. The over estimation of the yaw errors in the filter cause a suboptimal Kalman gain calculation which may be partially responsible. On average, the Mach 6 position errors decrease about 5% from the baseline, and the Mach 8 errors increase around 5% when the lowest and highest update interval results are ignored. The velocity errors are much more sensitive to Mach number. The Mach 6 velocity MRSE drops ∼15% and the Mach 8 rises 10–20% for most cases. The longest Δt_{GPS} results are almost dead reckoning case because so few measurements are made.

Tactical Grade IMU, Pseudorange-Only

The Mach number sensitivities of the tactical grade IMU, ρ-only INS/GPS is less ambiguous than the preceding system. The lower quality IMUs cause the gyro and attitude to increase more rapidly so that the filter performs optimally even at the longest Δt_{GPS}, unlike the previous nav.–grade configuration. The higher Mach numbers produce larger position and velocity errors because fewer GPS updates are processed during a simulation run. The position errors vary less than 10% for updates occurring at least every 30 seconds. For longer update intervals, the errors can increase over 20-57%. The velocity error sensitivities increase about 10–15% for the Mach 8 case and decrease about the same percentage when the Mach number is decreased to 6.

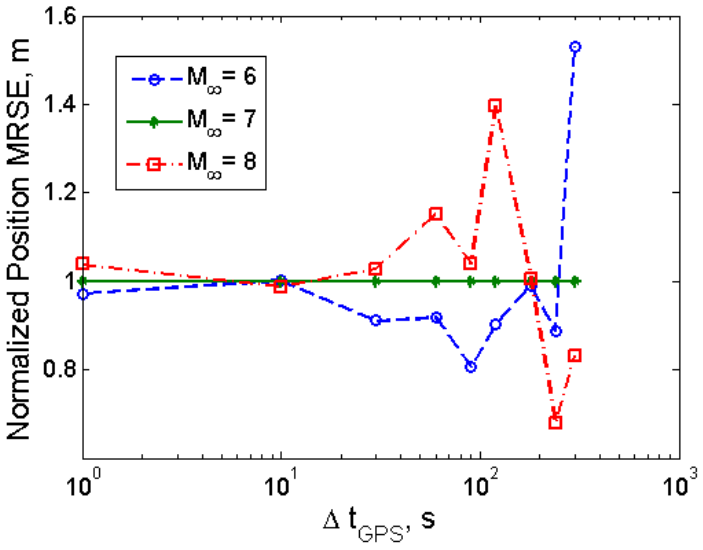

(a)

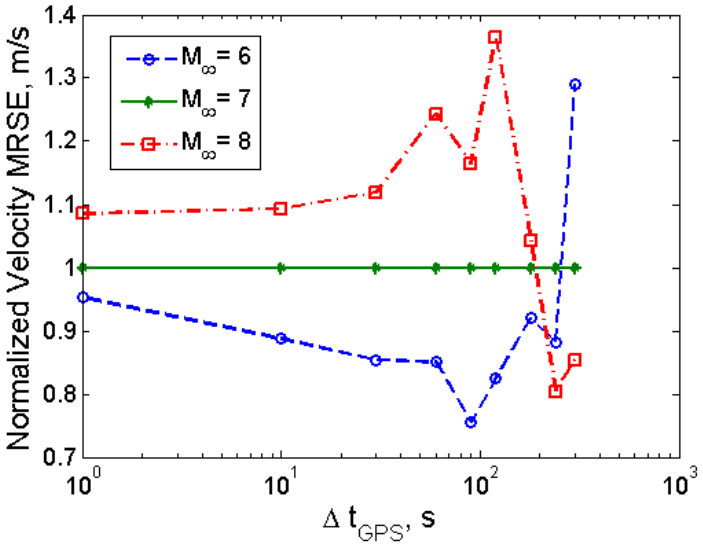

(b)

Figure 6.32: Normalized INS/GPS Steady State MRSE w/ ρ Measurements and Tac. Grade IMUs, (a) Position (b) Velocity

6.4 Chapter Summary

The results from the 1,000-set Monte Carlo INS/GGI and INS/GPS simulations are presented and discussed in this chapter. Section 6.1 discusses how the Monte Carlo simulations are performed using the elements of the previous chapters and first four appendices. The following section studies the effect of set size on how well the Monte Carlo simulations capture all the random processes of a sample INS/GGI simulation. It is shown in Sec. 6.2 that the filter-estimated errors are insensitive to Monte Carlo set size, and that the Monte Carlo derived errors capture the random processes more accurately as the set size is increased. However, increasing the Monte Carlo set size corresponds to an approximately linear increase in the computational expense with diminishing returns in the effectiveness of capturing the random processes (see Fig. 6.3 on pg. 221).

Section 6.3 then quantifies the navigation accuracy and sensitivities of the completely inertial, passive, covert INS/GGI and baseline INS/GPS systems. The INS/GGI results show surprisingly impressive sub-meter, INS/GPS-like total position error for a system with a space-grade stabilized GGI and current navigation grade IMUs for both hypersonic and subsonic missions. The INS/GGI also typically has half the vertical position and velocity errors compared to it horizontal errors because of the stronger signal variation in altitude.

The hypersonic INS/GGI system sensitivities to noise level, Mach number and gravitational gradient variation are also thoroughly investigated through extensive Monte Carlo simulations in Sec. 6.3.1. The main conclusions from these analyses

are as follows:

- A stabilized GGI with navigation grade IMUs at Mach 7 over the high Γ^n variation trajectory produces a total position MRSE of 0.336 m when the GGI noise level is 0.001 Eö at an update rate of 1 Hz.
- A strapdown GGI aided INS produces up to an order of magnitude increase in the position error of a comparable stabilized GGI, with the largest sensitivity occuring at the lowest noise levels.
- Conversely, the stabilized GGI produces attitude (*i.e.* orientation) errors that are an order of magnitude higher than the strapdown sensor.
- Reducing the quality of the IMUs with a stabilized GGI aided INS causes a 20–50% increase in position error and a 70–180% increase in velocity error.

The strapdown GGI is also shown to cause filter divergence when estimating gyro noise that is much larger than its own instrument noise. Two solutions are suggested to combat the numerical truncation issue that is at the root of the divergence:

1. Higher precision data types may be used to compute the Kalman gain matrix. (Double precision is used exclusively in this work.)
2. A square-root Kalman filter may be implemented instead of the traditional filter used in this work. The premise is that a square-root filter uses standard deviations instead of variances in its calculations, so that the values of the gyro and GGI noises are more similar in magnitude and thus numerical truncation is less likely to occur.

Table 6.22 summarizes the steady-state position MRSE as a function of GGI noise level through power law regressions. The conclusions resulting from these

Table 6.22: Hypersonic INS/GGI Postion MRSE (m) Sensitivity to GGI Noise

GGI Type	IMU	Γ^n Var.	Mach 6	Mach 7	Mach 8
Stabilized	Nav.	High	$209\sqrt{q_{GGI}}^{0.939}$	$219\sqrt{q_{GGI}}^{0.938}$	$227\sqrt{q_{GGI}}^{0.934}$
Stabilized	Tac.	High	$244\sqrt{q_{GGI}}^{0.903}$	$250\sqrt{q_{GGI}}^{0.902}$	$258\sqrt{q_{GGI}}^{0.904}$
Strapdown	Nav.	High	$376\sqrt{q_{GGI}}^{0.620}$	$377\sqrt{q_{GGI}}^{0.602}$	$359\sqrt{q_{GGI}}^{0.580}$
Stabilized	Nav.	Low	$217\sqrt{q_{GGI}}^{0.943}$	$226\sqrt{q_{GGI}}^{0.941}$	$235\sqrt{q_{GGI}}^{0.937}$
Stabilized	Tac.	Low	$246\sqrt{q_{GGI}}^{0.905}$	$260\sqrt{q_{GGI}}^{0.910}$	$263\sqrt{q_{GGI}}^{0.907}$
Strapdown	Nav.	Low	$286\sqrt{q_{GGI}}^{0.302}$	$212\sqrt{q_{GGI}}^{0.211}$	$164\sqrt{q_{GGI}}^{0.138}$
GGI noise level, $\sqrt{q_{GGI}}$, is in Eö/$\sqrt{Hz}$ units					

analyses are:

- Future improvements in GGI noise levels will lead to greater improvements in position error if the gradiometer is stabilized than if it is a strapdown sensor. This is shown in the exponential coefficients, which are the slopes of results such as Fig. 6.14 (a) on pg. 245. The main reason for the lower performance of the strapdown GGI/INS is its need to account for the IMU gyro errors.
- The stabilized GGI, navigation grade IMU system produces about a factor of 8.5 steady state position MRSE sensitivity to a 10× change in GGI noise level. The stabilized GGI, tactical grade IMU system is slightly less sensitive at about a factor of 8 for an order of magnitude change in $\sqrt{q_{GGI}}$.
- The strapdown GGI/INS produces only a factor of 4 improvement in position MRSE with a ten-fold improvement in GGI noise level when flying over the high Γ^n variation trajectory. And the sensitivity is reduced further to a factor of 1.4–2 when the system is flown over the low gradient variation trajectory

Table 6.23: Hypersonic INS/GGI Sensitivities to Γ^n Variation and Mach Number

		Γ^n Variation			Mach Number		
GGI Type	IMU	Pos.	Vel.	Att.	Pos.	Vel.	Att.
Stabilized	Nav.	1	1	1	1	2	2
Stabilized	Tac.	1	1	1	1	2	2
Strapdown	Nav.	3	3	3	2	2	1
Error Sensitivity:		1) <10%,		2) 10–100%,		3) >100%	

and $\sqrt{q_{GGI}}$ is varied by a factor of 10.

The system specific INS/GGI sensitivities are summarized in Table 6.23 in terms of the order of magnitude of the error variation. The primary conclusions are:

- The stabilized GGI aided INS is insensitive to changes in the gravitational gradient signal variation. The position, velocity, and attitude errors typically vary less than 10% between the high and low Γ^n trajectory results.
- The stabilized GGI aided INS position error is also insensitive to Mach number variations. However, the velocity and attitude errors are more sensitive and increase over 10% when the Mach number is increased or decreased.
- The strapdown GGI aided INS, however, is extremely sensitive to changes in the gravitational gradient signal. Position, velocity, and attitude errors can increase over 100% the high Γ^n trajectory values when the same configuration is flown over the low gradient variation trajectory.
- The strapdown GGI aided INS is noticeably less sensitive to Mach number variations. The position and velocity errors can increase up to 20% when the

Mach number is increased by 1, and the attitude error is least sensitive and changes at most 10% because most of the strapdown GGI update information is used to correct attitude and gyro errors.

Section 6.3.2 investigates the nominal integrated INS/GPS navigation performance. The Monte Carlo simulation results show sub-meter position errors for GPS update intervals of 30 seconds or faster when pseudorange and pseudorange rate measurements are available. However, the absence of pseudorange rate measurements produces almost an order of magnitude increase in the total position error. The effect of IMU quality is much less severe, and position MRSE only increases about 30% when tactical grade IMUs are simulated.

Compared to the INS/GGI results, the INS/GPS system with ρ and $\dot{\rho}$ updates at 1 Hz produces about half the position MRSE of a 0.001 Eö stabilized GGI aided INS with 1 Hz updates, regardless of the IMU quality. Also, the INS/GPS system needs ρ and $\dot{\rho}$ measurements only once every 10 sec to produce the same position MRSE as the 0.001 Eö stabilized GGI/INS with 1 Hz updates.

The main unexpected result from the INS/GPS simulations is the large error growth when GPS updates occur less than every minute. The inability to reduce the IMU errors in-flight produces about an order of magnitude increase in position and velocity error when the GPS update interval increases from 60 to 90 seconds.

Chapter 7

Conclusions and Future Work

This dissertation presents the first complete open literature methodology, derivation, implementation, and simulation of a map-matching gravity gradiometer aided inertial navigation system. Gravity gradiometer aiding is particularly applicable to military applications where GNSS signals may be jammed, spoofed, or otherwise unavailable. A hypersonic atmospheric cruise missile was thus chosen as an ideal application since its first use will be for a high speed cruise missile, and the high velocities and temperatures of flight may cause traditional aids to perform poorly or be impractical. Moreover, the increased velocity allows for greater gravitational variation between measurements, and the relatively high altitudes attenuate small terrain anomalies and fluctuations. However, the current size ($\sim$1 m^3) and weight ($\sim$250 kg without additional electronics cabinet) of current commercial airborne GGIs is prohibitively large. Therefore, further research and development is required to reduce future generation gradiometers to the point where they may be integrated into size and weight constrained air vehicles. For the nearer future, two subsonic missions which can accomodate the mass and volume of current GGIs are also simulated.

7.1 Summary of Contributions

The following are the primary contributions that this dissertation makes to the state of the art.

- The characterization of gravitational gradients for use as a map-matching navigation aid is performed for the first time.
- A parametric analysis is presented to estimate when local terrain effects may be neglected from a computed gravitational field map.
- Improvements to an integrated INS/GGI using a Kalman filter approach are identified and implemented.
- A thorough methodology to determine the measurement of a strapdown / stabilized, stationary / rotating accelerometer, stationary / rotating gravity gradiometer instrument is derived.
- This work provides the first linearized error derivation of a strapdown GGI that includes attitude errors and a means to convert tensor measurements from the body frame to the navigation frame.
- This work also derives a new formulation and linearized error equation for a stabilized GGI whose attitude and attitude rate errors are included in the sensor noise specification.
- This work is the first to simulate an INS/GGI system at hypersonic speeds and altitudes. And the first to simulate an airborne INS/GGI with space-grade GGI noise levels.
- The hypersonic INS/GGI sensitivities to noise level, Mach number, and gradient signal variation are investigated for the first time.

- The first comprehensive study of a hypersonic INS/GPS system and it's sensitivities to Mach number, IMU quality, GPS update interval, and available measurements is also performed.

7.2 Recommendations for Future Work

Some areas of future work are proposed below pertaining to an integrated INS/GGI system. Other applications for gravity gradiometer instruments are discussed afterwards along with a brief mention of the similarity of the current work to magnetometer-based map-matching navigation.

- The gravitational gradient field could be characterized with local terrain effects included. This analysis would be infeasible on a global scale, but could be useful over moderate regions of interest.
- The gravitational potential, acceleration, gradients, and possibly third order gradients could be augmented to the filter state vector. This would allow the filter to essentially update the state estimates using an optimal fit of the gravity field instead of a single point measurement as done in this work. This would, however, involve implementing a possibly complex linearized gravitational field model.[94, 167–171]
- To alleviate the strapdown GGI divergence issue, a square-root Kalman filter or higher precision floating point operations may be implemented.
- The centripetal errors in the velocity error dynamics could be added. Also, the effect of Earth's oblateness could be included in the Jacobian from the gravity map coordinates to the navigation frame position states.

- INS/GGI simulations could be performed that included local terrain effects in the gravitational field map. This is particularly important for lower altitude missions since the spherical harmonic model severely aliases the true signal content.
- The sensitivity of the INS/GGI system to gravitational field errors in the onboard gravity map could be investigated. In such cases, the inclusion of a higher order method for interpolating the gravity field data from the pre-computed map could be implemented and its benefit could be assessed.[95,165]

Gravity gradiometer based navigation is also viable for extraterrestrial applications where navigation satellites are unavailable. Spherical harmonic models for the Moon, Mars, and Venus are available online[†], and can be used to assess the navigation performance on and around these bodies. An ideal extraterrestrial mission would be to first send a satellite with a gradiometer payload to perform high resolution gravity maps of the planetary bodies. Then, future gradiometer-equipped missions would not only be able to improve the gravity model, but eventually navigate using the gravitational gradient map and the tools described herein. Low temperature, exo-atmospheric applications are particularly appealing because gradiometer instruments can yield higher precision due to reduced noise having to be filtered from vehicle motion and the improved mechanical stability at low temperatures.

Some other extensions to this work could be the use of a gravity gradiometer instrument for obstacle avoidance. In theory, as a GGI-equipped system moves

[†]http://pds-geosciences.wustl.edu/dataserv/index.htm

toward an obstacle it would measure an increase in the gravitational potential of the obstruction and could move to avoid collision. Similarly, a GGI system could traverse a corridor by avoiding the increased gravitational gradients as it nears one of the boundaries.

One last application for a gravity gradiometer instrument that could have near-future impact is its use as a warning system. If a GGI were properly calibrated, it could be used to measure large masses moving toward or near the instrument. This could be implemented as a missile defense system if the sensor noise is low enough and the gravitational gradients caused by the incoming missile is large enough to be unambiguously detected.

As one final comment, because the magnetic potential field possesses many of the same properties as the gravitational field, the methodology presented within this work may be useful in magnetometer-based map-matching inertial navigation systems.[172]

Appendix A

Global Gravitational Maps

This appendix provides additional global gravitational gradient plots at various altitudes. The first four sets of plots, Fig. A.1–A.4, illustrate the gradients as computed by the modified NGS/NOAA `geopot97.v0.4.e.f` program for all six gradients at 10 km and 100 km altitudes. (The gravitational gradient plots at the Earth's surface are shown in Fig. 2.7 & 2.8 on pg. 61 & 63.) The inline gradients are plotted with a 20 Eö variation from the global mean of the gradient component and the off-diagonal gradients are plotted with a 10 Eö variation from their means.

The second set of figures are the 5×5 grid point ($\sim$220 $\times$ 220 km) moving-window standard deviation plots that quantify the variation of the gravitational gradient signal. All six components of the gradient tensor are shown at 0, 10, and 100 km altitudes in terms of $\log_{10}$(Eö). Similar plots were computed for altitudes of 100 m, 1 km, and 500 km. These figures are not shown because they are qualitatively simular to Fig. A.5–A.9, and their magnitudes are summarized in Fig. 2.11 on pg. 66.

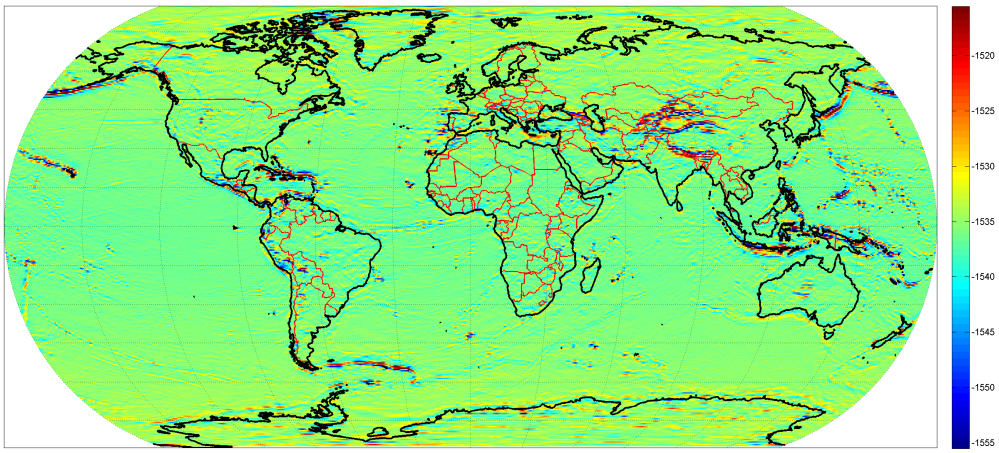

(a)

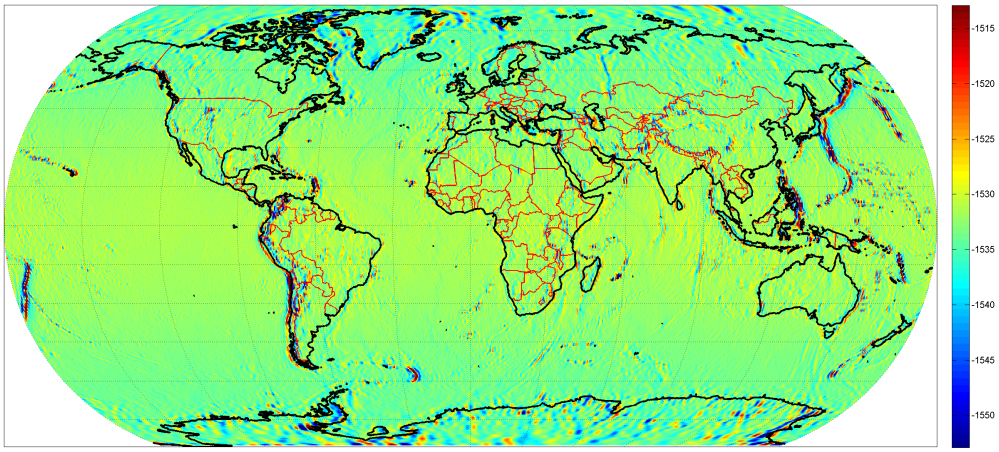

(b)

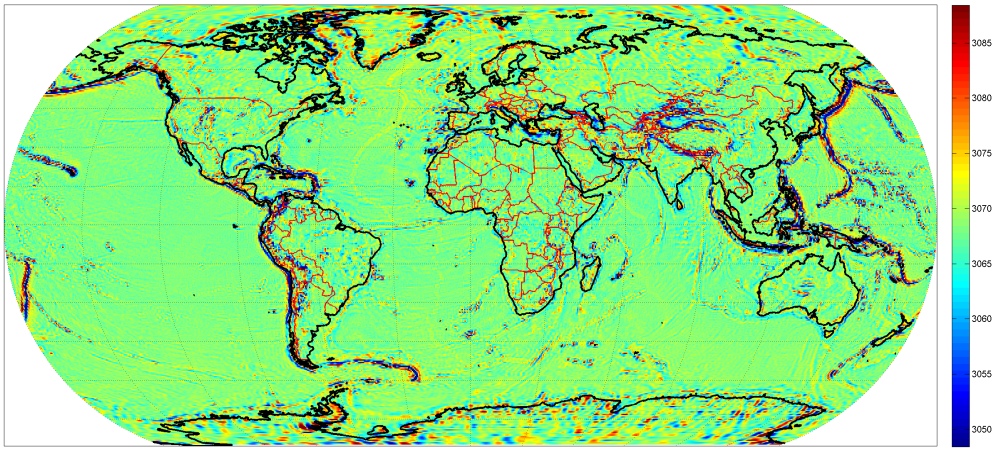

(c)

Figure A.1: Inline Gravitational Gradients at 10 km (a) Γ_{NN} (b) Γ_{EE} (c) Γ_{DD}

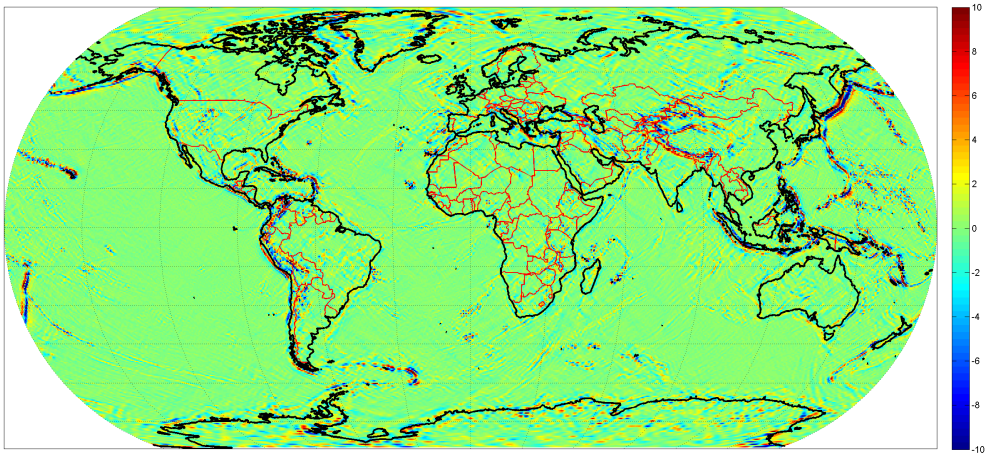

(a)

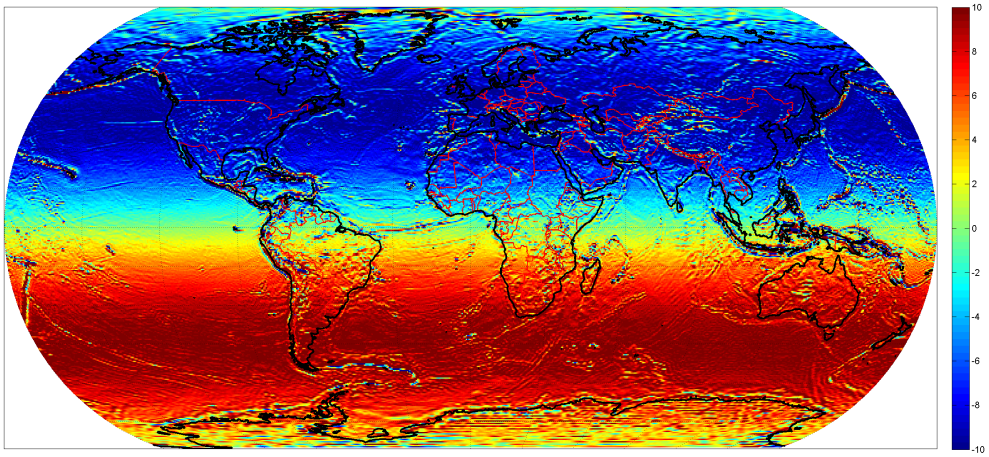

(b)

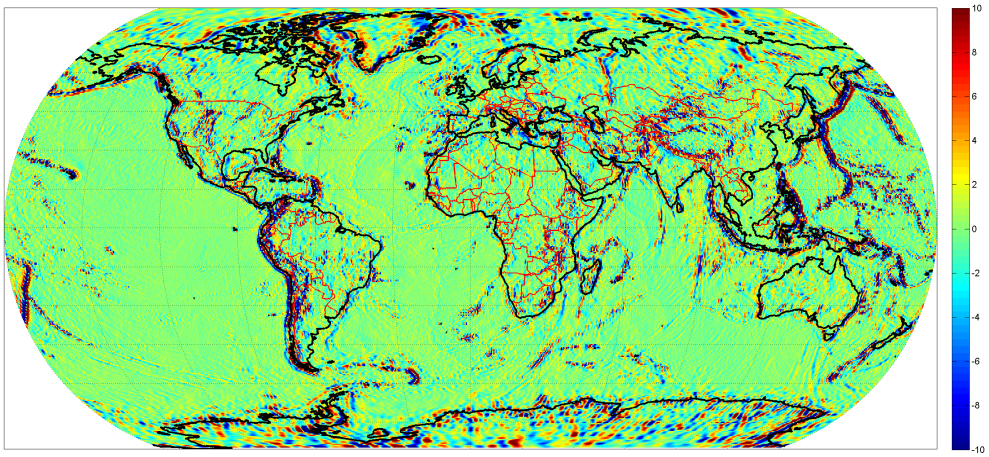

(c)

Figure A.2: Off-Diagonal Gradients at 10 km (a) Γ_{NE} (b) Γ_{ND} (c) Γ_{ED}

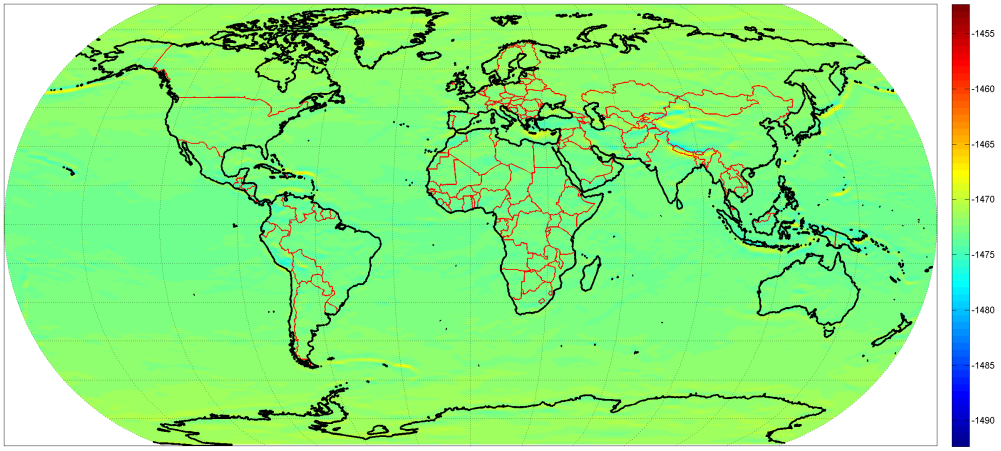

(a)

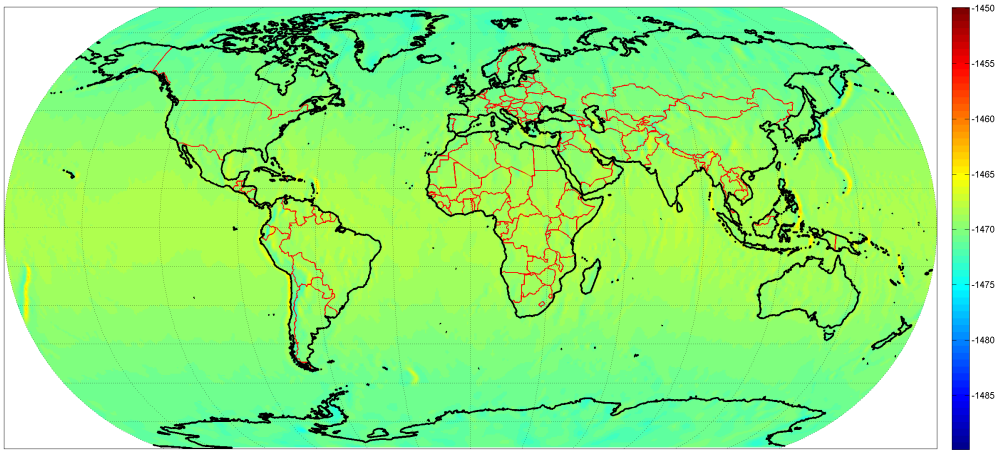

(b)

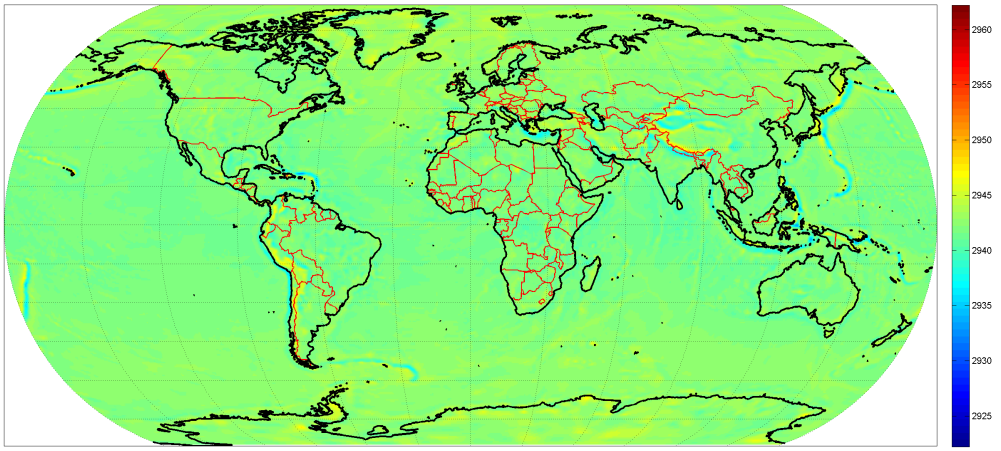

(c)

Figure A.3: Inline Gravitational Gradients at 100 km (a) Γ_{NN} (b) Γ_{EE} (c) Γ_{DD}

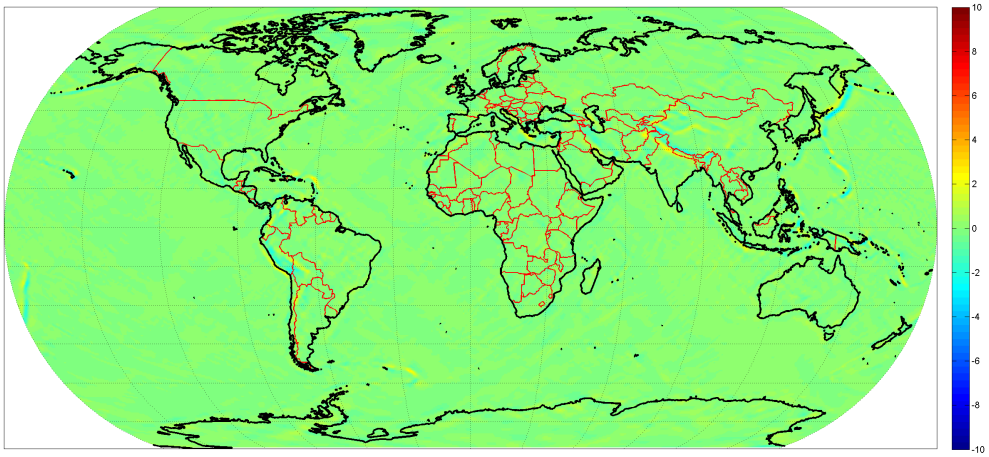

(a)

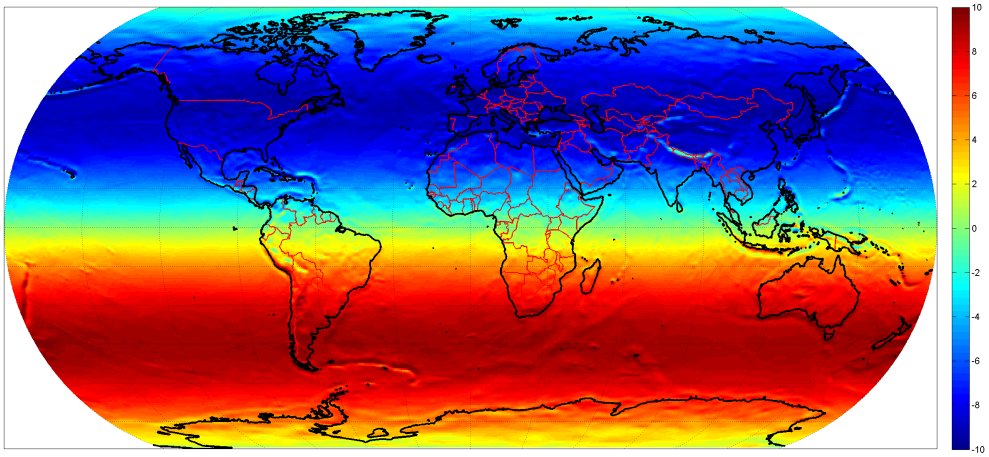

(b)

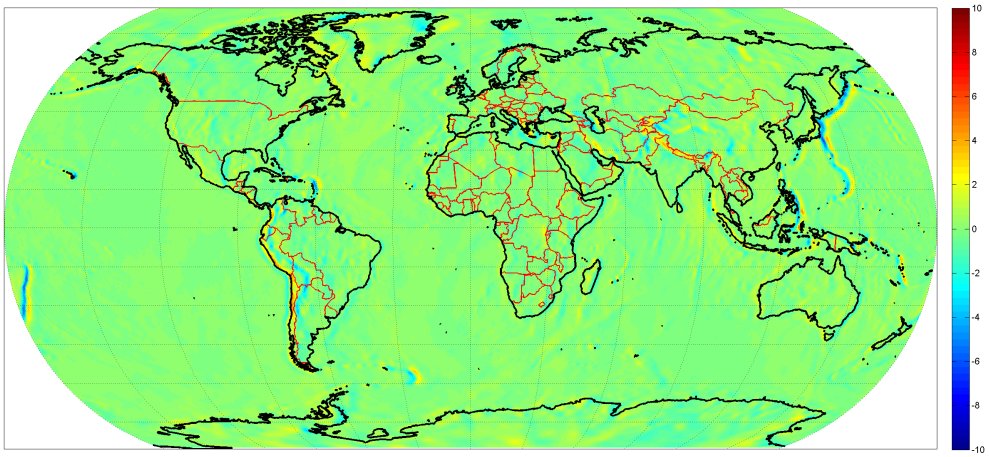

(c)

Figure A.4: Off-Diagonal Gradients at 100 km (a) Γ_{NE} (b) Γ_{ND} (c) Γ_{ED}

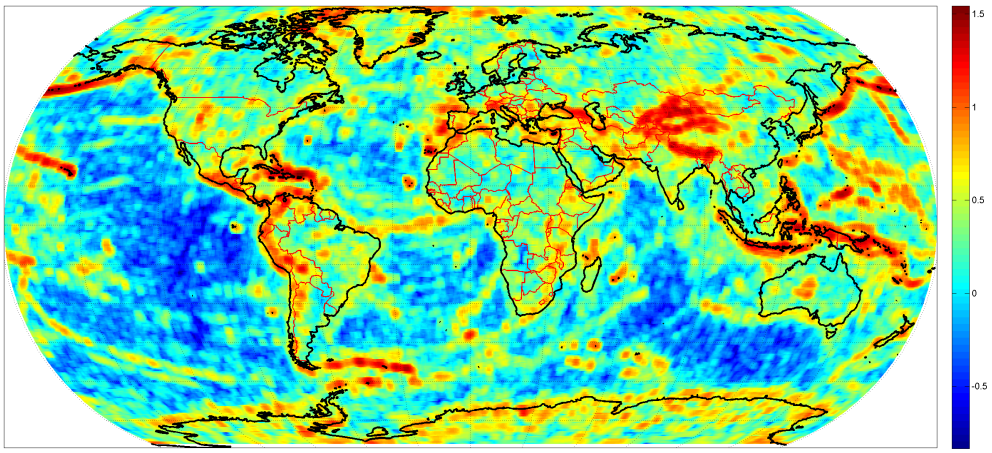

(a)

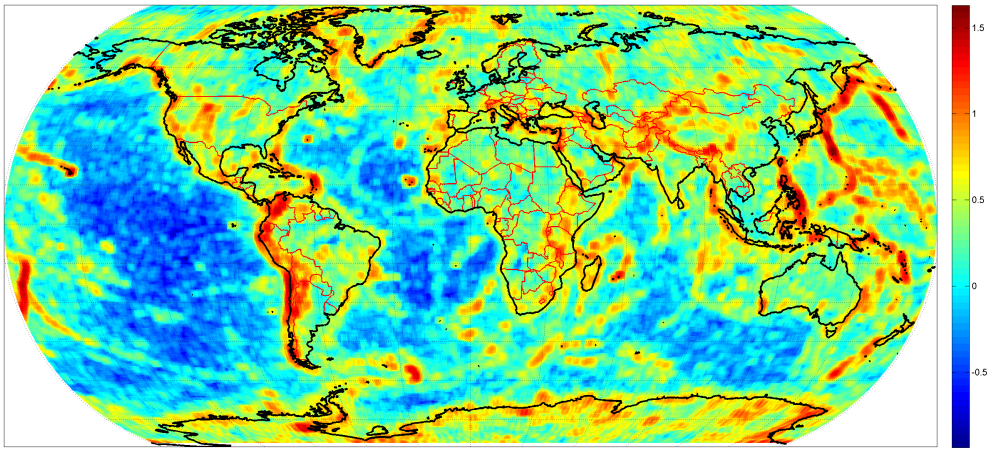

(b)

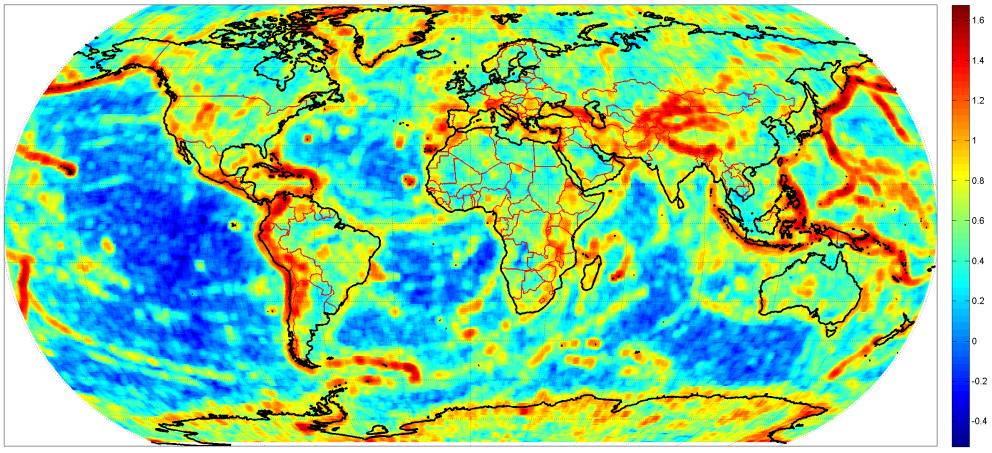

(c)

Figure A.5: Inline $\sigma\Gamma^n$, $\log_{10}$(Eö), at Surface (a) Γ_{NN} (b) Γ_{EE} (c) Γ_{DD}

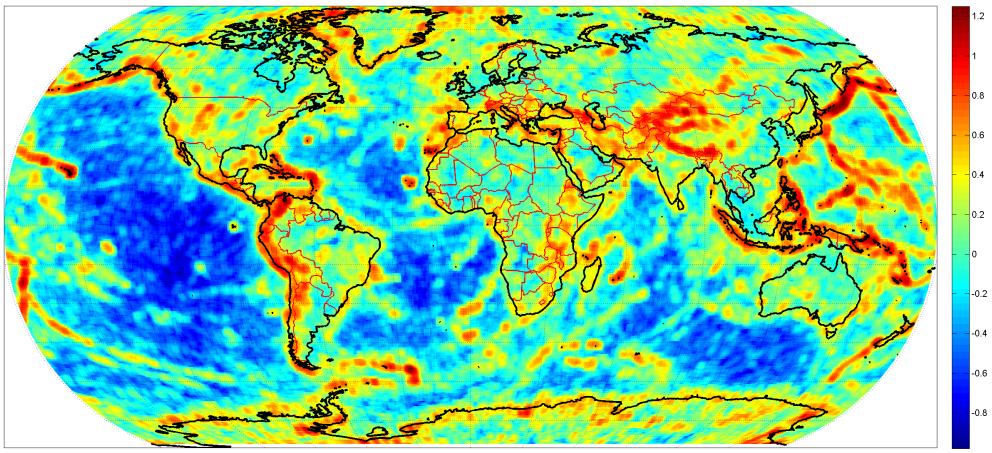

(a)

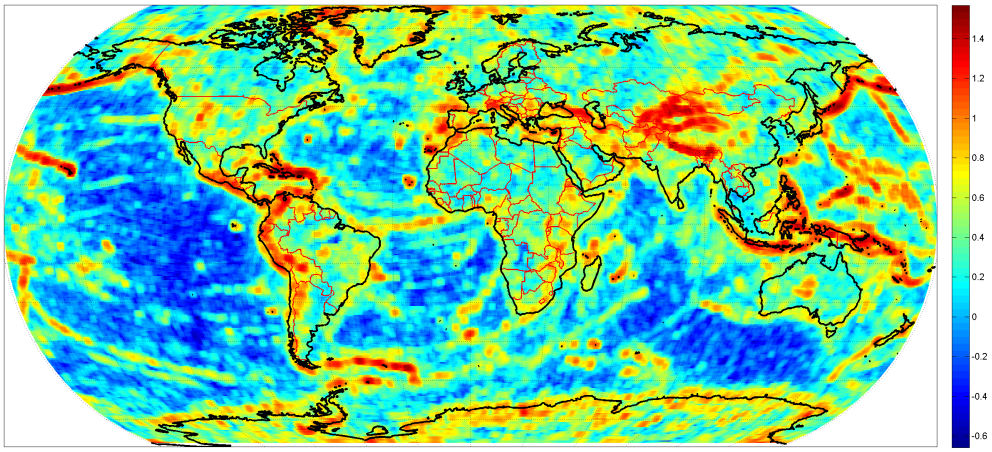

(b)

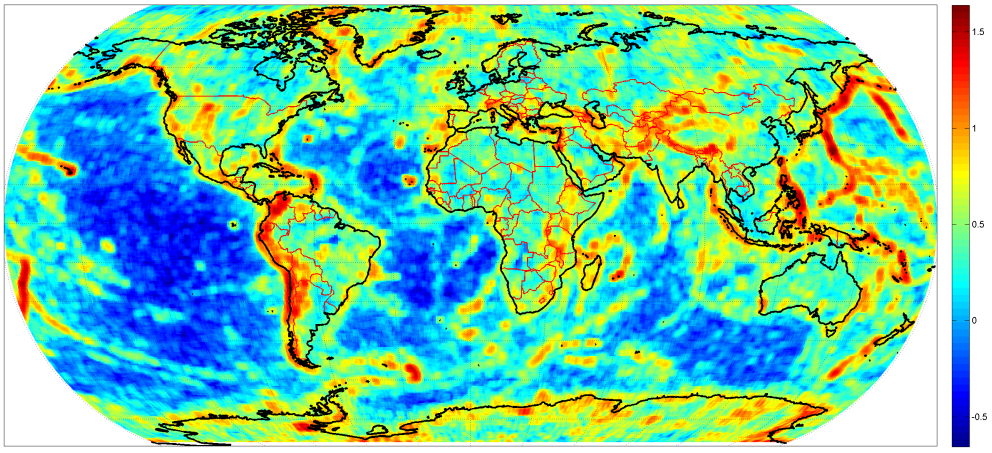

(c)

Figure A.6: Off-Diagonal $\sigma\Gamma^n$, $\log_{10}$(Eö), at Surface (a) Γ_{NE} (b) Γ_{ND} (c) Γ_{ED}

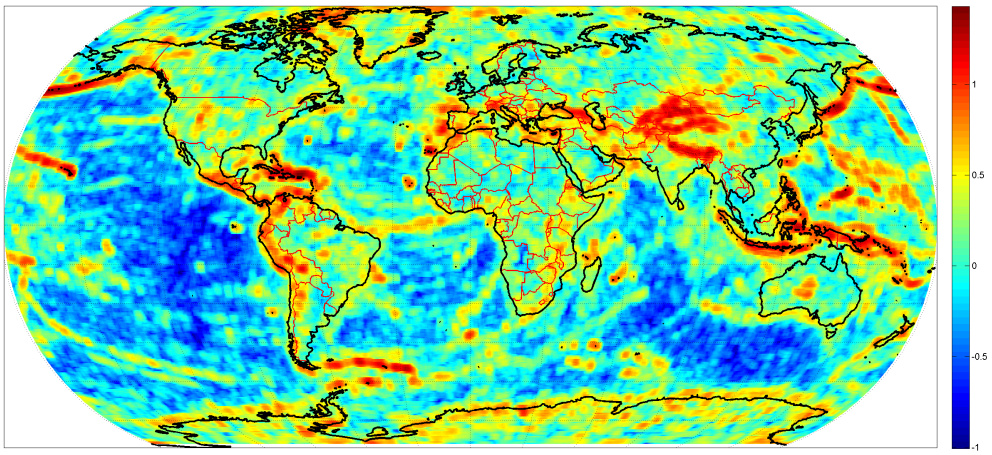

(a)

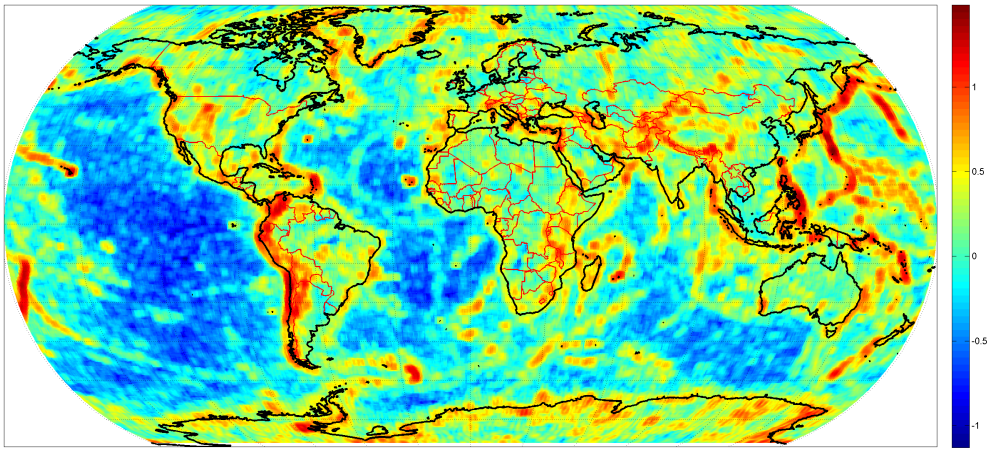

(b)

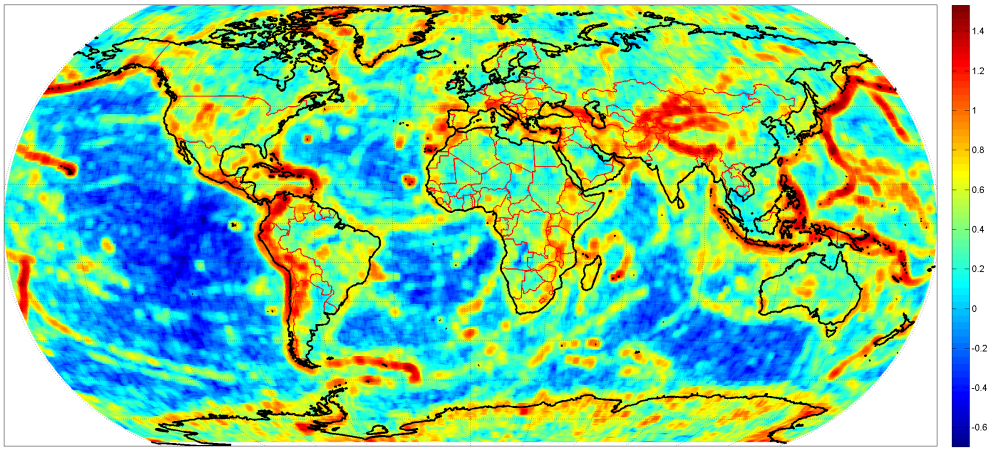

(c)

Figure A.7: Inline $\sigma\Gamma^n$, $\log_{10}$(Eö), at 10 km (a) Γ_{NN} (b) Γ_{EE} (c) Γ_{DD}

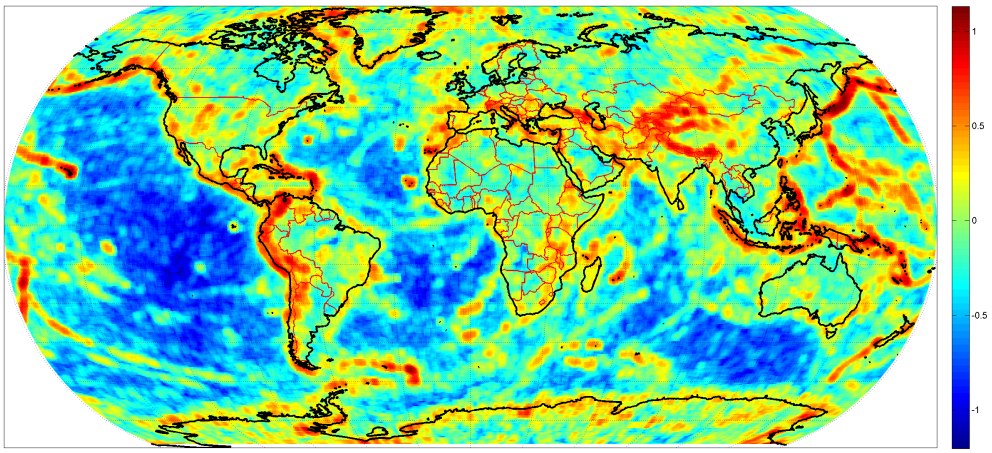

(a)

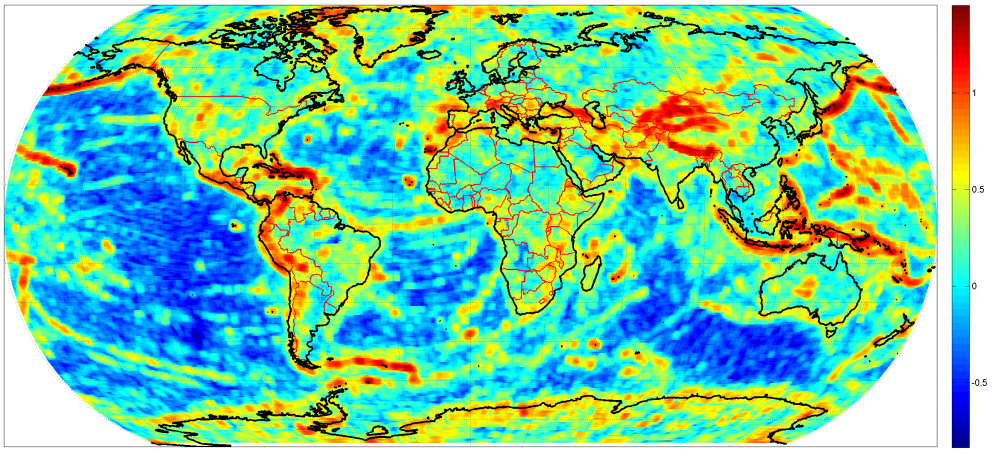

(b)

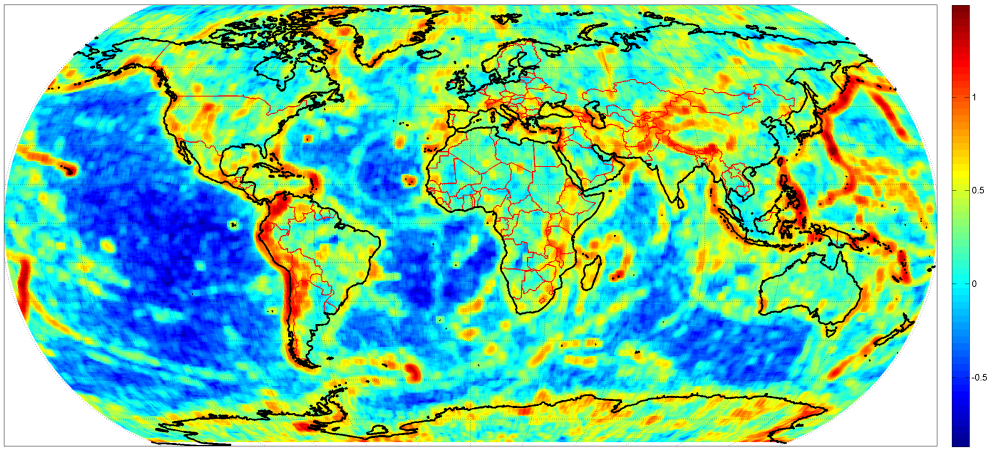

(c)

Figure A.8: Off-Diagonal $\sigma\Gamma^n$, $\log_{10}$(Eö), at 10 km (a) Γ_{NE} (b) Γ_{ND} (c) Γ_{ED}

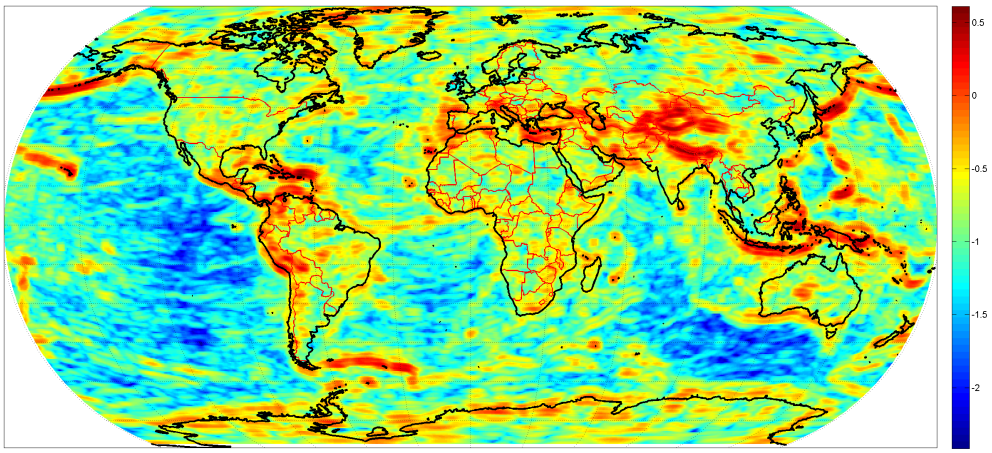

(a)

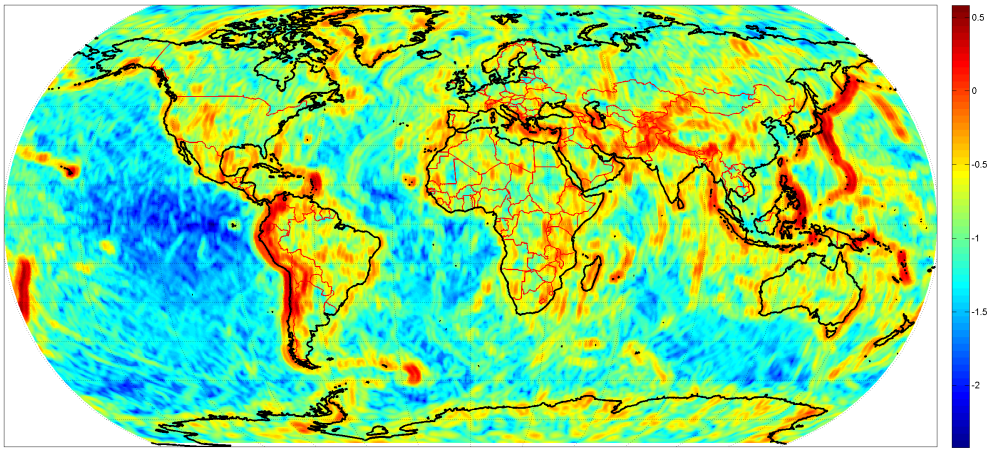

(b)

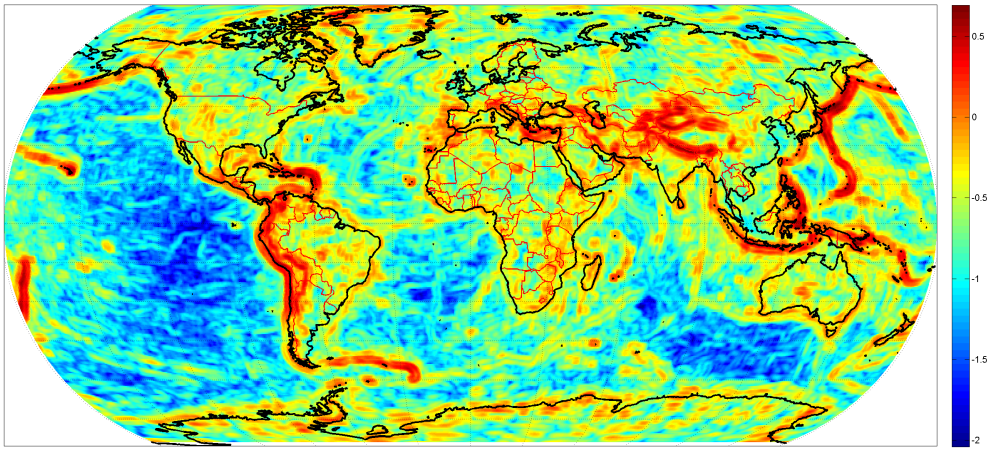

(c)

Figure A.9: Inline $\sigma\Gamma^n$, $\log_{10}$(Eö), at 100 km (a) Γ_{NN} (b) Γ_{EE} (c) Γ_{DD}

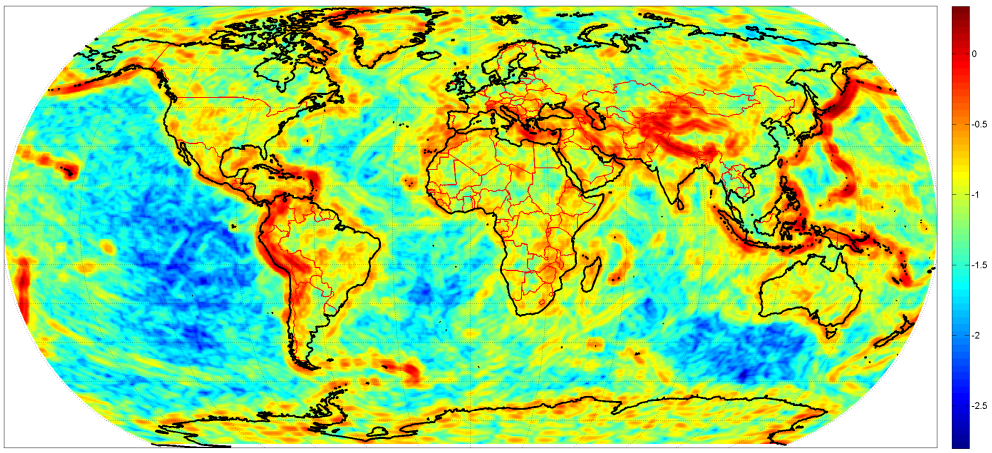

(a)

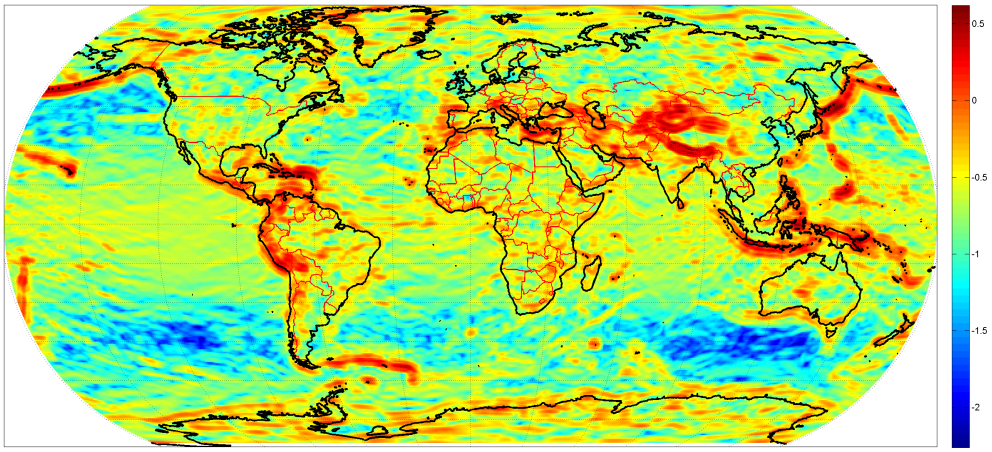

(b)

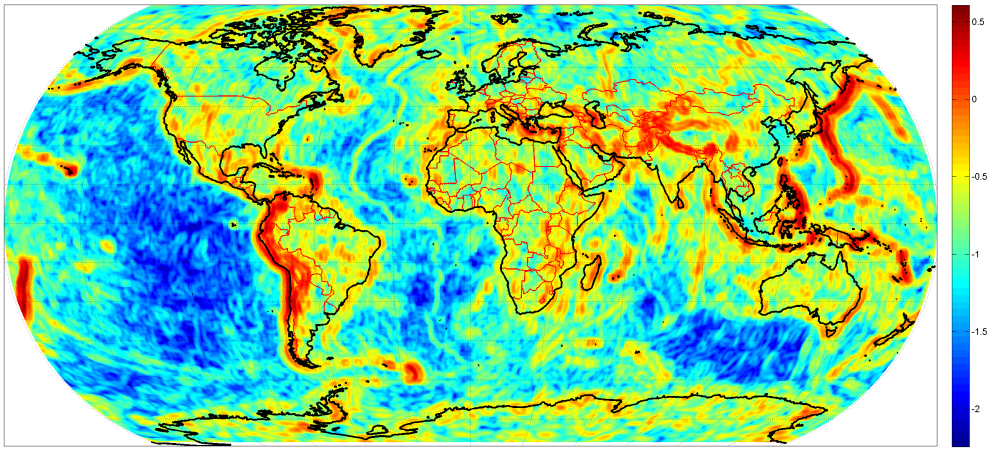

(c)

Figure A.10: Off-Diagonal $\sigma\Gamma^n$, $\log_{10}$(Eö), at 100 km (a) Γ_{NE} (b) Γ_{ND} (c) Γ_{ED}

Appendix B

Thrust Coefficient Curve Fits

The thrust coefficient is calculated as a function of the inlet compression ratio, (A_0/A_1), at a given design Mach number, freestream Mach number, and angle of attack by the quadratic polynomial curve-fit:

$$C_{T,\text{ref}} = \left(\frac{T}{q_\infty A_0}\right)_{\text{ref}} = \begin{cases} a\left(\frac{A_0}{A_1}\right)^2 + b\left(\frac{A_0}{A_1}\right) + c, & if\ \left(\frac{A_0}{A_1}\right) \leq \left(\frac{A_0}{A_1}\right)_{max} \\ 0, & else \end{cases} \tag{B.1}$$

where the coefficients a, b, and c are defined for the following configurations:

- **Base Area-to-Capture Area Ratio**: $(A_5/A_0) = 1$, 2, 3, 4, 6, and 8.
- **Equivalence Ratio**: $ER = 0.25$, 0.50, 0.75, and 1.00 or ER_{max} to cause thermal choking.
- **Freestream Mach Number**: $M_\infty = 4$, 5, 6, 7, and 8.
- **Combustor Expansion Ratio**: $(A_4/A_2) = 2$, 3, and 4.

The thrust coefficients were only curve fit for combustor expansion ratios of 3 and 4. Tables B.1–B.6 list the curve fit coefficients for the $(A_4/A_2) = 4$ scramjets and each of the (A_5/A_0), ER, and M_∞ configurations along with the maximum contraction ratio, $(A_0/A_1)_{max}$, values where the fits are valid.

Table B.7 then lists the curve-fit coefficients that are different for a combustor expansion ratio of 3. The $(A_0/A_1)_{max}$ values are the same as those in the $(A_4/A_2) = 4$

tables. The changes are primarily in the lower Mach number regime where the thrust coefficient is most sensitive to the combustor expansion. At the other conditions, the two combustor expansion ratios result in essentially the same thrust level so that the $(A_4/A_2) = 4$ fits are valid for the $(A_4/A_2) = 3$ designs.

Table B.1: Thrust Coefficient Curve-Fits, $(A_4/A_2) = 4$, $(A_5/A_0) = 1$

ER	M_∞	a	b	c	$(A_0/A_1)_{max}$
	4	-0.49869841e-1	0.49430349	-0.82621644	5.34124
	5	-0.68479882e-2	0.99125012e-1	-0.10943232	7.22688
0.25	6	-0.45458090e-2	0.66848095e-1	-0.10020729	8.36429
	7	-0.67763083e-2	0.96744182e-1	-0.25636996	8.51539
	8	-0.74915009e-2	0.98622305e-1	-0.27782115	7.95164
	4	-0.76991209e-1	0.73788027	-1.0082527	5.29383
	5	-0.89241822e-2	0.14105697	0.51239270e-2	7.21112
0.50	6	-0.71480649e-2	0.11498241	-0.93289771e-1	8.41051
	7	-0.49207419e-2	0.80802043e-1	-0.97280841e-1	8.57179
	8	-0.68767250e-2	0.10346300	-0.23251623	7.98609
	4	-0.83692969e-1	0.80721960	-0.94895952	5.25097
	5	-0.14337469e-1	0.21505580	0.16144186e-1	7.16958
0.75	6	-0.76123522e-2	0.13438755	-0.10170729e-1	8.35844
	7	-0.38090162e-2	0.74719918e-1	0.35054487e-1	8.52622
	8	-0.78741334e-2	0.12091532	-0.19482288	8.00242
	4	-0.95907300e-1	0.96465505	-1.2327463	5.28320
1.00	5	-0.18608201e-1	0.26443796	0.75892441e-1	6.90048
or	6	-0.76161545e-2	0.14704879	0.67975813e-1	8.20316
ER_{max}	7	-0.52199660e-2	0.10007825	0.62896756e-1	8.53903
	8	-0.76527114e-2	0.12160603	-0.12667565	7.94352

Table B.2: Thrust Coefficient Curve-Fits, $(A_4/A_2) = 4$, $(A_5/A_0) = 2$

ER	M_∞	a	b	c	$(A_0/A_1)_{max}$
	4	-0.14723606e-1	0.15796242	0.51099570e-1	5.14437
	5	-0.61912328e-2	0.81047984e-1	0.49456662e-1	7.44221
0.25	6	-0.41471505e-2	0.59300713e-1	-0.10809633e-2	8.30857
	7	-0.32666482e-2	0.45973194e-1	-0.30536811e-1	8.52718
	8	-0.37074063e-2	0.47618649e-1	-0.72715650e-1	7.97840
	4	-0.31959459e-1	0.30944616	0.15479222	5.24959
	5	-0.73712938e-2	0.11021194	0.23658088	7.19087
0.50	6	-0.54228444e-2	0.85381017e-1	0.12362564	8.35794
	7	-0.42692735e-2	0.67897666e-1	0.46325748e-1	8.44007
	8	-0.52866323e-2	0.73192206e-1	-0.35329442e-1	7.97164
	4	-0.29631520e-1	0.29916407	0.48348068	5.28796
	5	-0.93505382e-2	0.14449643	0.40529337	7.28516
0.75	6	-0.67267738e-2	0.10948393	0.25521763	8.41082
	7	-0.49389437e-2	0.85813169e-1	0.13326497	8.53236
	8	-0.50788323e-2	0.79375985e-1	0.46574283e-1	7.96868
	4	-0.36879008e-1	0.37874472	0.51512400	5.28645
1.00	5	-0.14375675e-1	0.19316592	0.52549549	7.23138
or	6	-0.72949267e-2	0.12302538	0.36783282	8.36721
ER_{max}	7	-0.52483802e-2	0.93660064e-1	0.22848722	8.61187
	8	-0.64503764e-2	0.99332058e-1	0.76087323e-1	8.16626

Table B.3: Thrust Coefficient Curve-Fits, $(A_4/A_2) = 4$, $(A_5/A_0) = 3$

ER	M_∞	a	b	c	$(A_0/A_1)_{max}$
	4	-0.11146619e-1	0.12005949	0.13773469	5.24767
	5	-0.34334492e-2	0.51767211e-1	0.10856734	7.21186
0.25	6	-0.28067197e-2	0.41974676e-1	0.39753387e-1	8.26063
	7	-0.24956469e-2	0.35852152e-1	-0.26626258e-2	8.49547
	8	-0.27291409e-2	0.35642461e-1	-0.38064314e-1	7.89869
	4	-0.22256065e-1	0.21882103	0.38402274	5.26673
	5	-0.73835782e-2	0.10376249	0.31873785	7.22574
0.50	6	-0.51619733e-2	0.77800273e-1	0.18304066	8.26729
	7	-0.36059536e-2	0.57763705e-1	0.10704738	8.52998
	8	-0.41643449e-2	0.59162080e-1	0.27658310e-1	7.85842
	4	-0.20878524e-1	0.21415689	0.74281116	5.19420
	5	-0.79771064e-2	0.12288176	0.52224229	7.21105
0.75	6	-0.70450758e-2	0.10813795	0.29998903	8.24834
	7	-0.50225198e-2	0.79620912e-1	0.20958715	8.49802
	8	-0.55665969e-2	0.81268786e-1	0.80020500e-1	7.95805
	4	-0.33413460e-1	0.33764979	0.72563305	5.21640
1.00	5	-0.14096373e-1	0.18317335	0.64149865	7.13521
or	6	-0.54601094e-2	0.95317851e-1	0.51840686	8.23574
ER_{max}	7	-0.63256723e-2	0.10099417	0.27526047	8.46407
	8	-0.59622853e-2	0.88468574e-1	0.17026105	7.97723

Table B.4: Thrust Coefficient Curve-Fits, $(A_4/A_2) = 4$, $(A_5/A_0) = 4$

ER	M_∞	a	b	c	$(A_0/A_1)_{max}$
	4	-0.11735694e-1	0.12017128	0.10247929	5.15165
	5	-0.39596504e-2	0.54340433e-1	0.85155807e-1	7.18347
0.25	6	-0.27058573e-2	0.39683807e-1	0.34540011e-1	8.18063
	7	-0.22989753e-2	0.32597252e-1	0.12484620e-2	8.54976
	8	-0.32100665e-2	0.39236480e-1	-0.46205128e-1	7.84728
	4	-0.26173887e-1	0.24413133	0.32844282	5.19329
	5	-0.73612348e-2	0.10218527	0.29417668	7.09964
0.50	6	-0.38172068e-2	0.61641187e-1	0.22316541	8.16017
	7	-0.36021941e-2	0.55258603e-1	0.12305535	8.45813
	8	-0.35772045e-2	0.50520919e-1	0.59264004e-1	7.94291
	4	-0.22675460e-1	0.22457780	0.72504452	5.25161
	5	-0.65538781e-2	0.10185956	0.57817918	7.19310
0.50	6	-0.41582314e-2	0.71822435e-1	0.41713740	8.26676
	7	-0.53155034e-2	0.81314672e-1	0.21679152	8.52047
	8	-0.47039122e-2	0.68863229e-1	0.13574411	8.02259
	4	-0.27615043e-1	0.28026860	0.87356171	5.22439
1.00	5	-0.93552788e-2	0.13103816	0.77145709	7.33966
or	6	-0.61425042e-2	0.98500147e-1	0.52539729	8.21213
ER_{max}	7	-0.39304571e-2	0.70793960e-1	0.36916636	8.49806
	8	-0.59267952e-2	0.87243640e-1	0.18333127	7.94496

Table B.5: Thrust Coefficient Curve-Fits, $(A_4/A_2) = 4$, $(A_5/A_0) = 6$

ER	M_∞	a	b	c	$(A_0/A_1)_{max}$
	4	-0.12529136e-1	0.12206898	-0.14968492e-1	5.27252
	5	-0.34291034e-2	0.44775234e-1	0.50857793e-1	7.23918
0.25	6	-0.17723672e-2	0.27413365e-1	0.27566069e-1	8.32048
	7	-0.22768270e-2	0.31015937e-1	-0.20237576e-1	8.49832
	8	-0.29900442e-2	0.36468051e-1	-0.53566511e-1	7.95358
	4	-0.17822279e-1	0.16317851	0.43083852	5.26965
	5	-0.41700614e-2	0.63750064e-1	0.36001300	7.23207
0.50	6	-0.36742344e-2	0.55665557e-1	0.22172396	8.36120
	7	-0.28725371e-2	0.45126210e-1	0.14099377	8.51603
	8	-0.41147649e-2	0.53997072e-1	0.54505152e-1	8.01917
	4	-0.73027373e-2	0.85815793e-1	0.96204392	4.89482
	5	-0.71594565e-2	0.10308161	0.56938533	7.16355
0.75	6	-0.32037931e-2	0.58435989e-1	0.44438378	8.29234
	7	-0.33599537e-2	0.57076361e-1	0.28317578	8.52126
	8	-0.47533838e-2	0.67321569e-1	0.14667716	7.94179
	4	-0.24566725e-1	0.24658399	0.90865333	5.25089
1.00	5	-0.12409402e-1	0.15827602	0.69721794	7.13662
or	6	-0.50926776e-2	0.85637217e-1	0.55995518	8.27444
ER_{max}	7	-0.37227053e-2	0.64248349e-1	0.40919142	8.38862
	8	-0.41636836e-2	0.64323415e-1	0.27021240	7.93855

Table B.6: Thrust Coefficient Curve-Fits, $(A_4/A_2) = 4$, $(A_5/A_0) = 8$

ER	M_∞	a	b	c	$(A_0/A_1)_{max}$
	4	-0.81368756e-2	0.83305787e-1	-0.78812864e-1	5.26415
	5	-0.24273038e-2	0.37205281e-1	-0.28679517e-1	7.08101
0.25	6	-0.27358687e-2	0.37034942e-1	-0.49023916e-1	8.25361
	7	-0.21923976e-2	0.29228660e-1	-0.52145408e-1	8.56251
	8	-0.18622312e-2	0.23863216e-1	-0.60198579e-1	7.91689
	4	-0.15535548e-1	0.15076497	0.29289183	5.25000
	5	-0.49321370e-2	0.69684983e-1	0.27020668	7.14472
0.50	6	-0.28437544e-2	0.45463429e-1	0.19738206	8.24510
	7	-0.22132714e-2	0.35625016e-1	0.12808787	8.57162
	8	-0.30407192e-2	0.41748329e-1	0.54903349e-1	7.95809
	4	-0.20904792e-1	0.19666099	0.63291311	5.26652
	5	-0.43906829e-2	0.68583118e-1	0.60015736	7.04946
0.75	6	-0.32898975e-2	0.55867996e-1	0.42090689	8.23280
	7	-0.33136575e-2	0.54277481e-1	0.26759355	8.51059
	8	-0.37348158e-2	0.54625293e-1	0.16373794	7.95528
	4	-0.31442963e-1	0.32812950	0.63112734	5.56779
1.00	5	-0.10250625e-1	0.13090870	0.72675794	7.16425
or	6	-0.33573140e-2	0.62001513e-1	0.59820948	8.34410
ER_{max}	7	-0.39744570e-2	0.63993267e-1	0.41216060	8.55414
	8	-0.42656742e-2	0.64204486e-1	0.26598943	8.03373

Table B.7: Thrust Coefficient Curve-Fit Corrections when $(A_4/A_2) = 3$

(A_0/A_1)	ER	M_∞	a	b	c
1	0.25	4	-0.20378066e-1	0.21893979	-0.17174159
		5	-0.61046225e-2	0.91499066e-1	-0.68965469e-1
	0.50	4	-0.33391996e-1	0.34025251	-0.83416244e-1
		5	-0.92850269e-2	0.14476685	0.19757637e-1
		6	-0.33391996e-1	0.34025251	-0.83416244e-1
		7	-0.92850269e-2	0.14476685	0.19757637e-1
	0.75	4	-0.37944022e-1	0.41943896	-0.83230792e-1
		5	-0.14127845e-1	0.20846118	0.71733448e-1
		6	-0.37944022e-1	0.41943896	-0.83230792e-1
1.00 or ER_{max}		4	-0.58856104e-1	0.63578795	-0.40942939
		5	-0.20862734e-1	0.27915649	0.77373924e-1
		6	-0.91072104e-2	0.15896258	0.76438585e-1
2	0.25	4	-0.14047642e-1	0.14979141	0.85859973e-1
	0.50	4	-0.29743597e-1	0.28007699	0.25672616
		5	-0.62390492e-2	0.98860848e-1	0.28015185
	0.75	4	-0.21746194e-1	0.24603850	0.59721737
		5	-0.92268944e-2	0.13712409	0.45986089
1.00 or ER_{max}		4	-0.29013543e-1	0.32770909	0.63977507
3	0.50	4	-0.26227989e-1	0.24948865	0.34706481
	0.75	4	-0.21193622e-1	0.23135170	0.70716066
		5	-0.81680616e-2	0.12046957	0.55572720
1.00 or ER_{max}		4	-0.26329484e-1	0.29179985	0.82637599
4	0.75	4	-0.15057494e-1	0.17001544	0.84237894
		5	-0.62919768e-2	0.94912554e-1	0.62820260
1.00 or ER_{max}		4	-0.31547564e-1	0.31857302	0.81193267
6	0.50	4	-0.18223755e-1	0.16971610	0.41201838
	0.75	4	-0.90162669e-2	0.11241800	0.90180647
1.00 or ER_{max}		4	-0.18108766e-1	0.19886729	1.0167907
8	1.00	4	-0.24920003e-1	0.26817736	0.78188375

Appendix C

Extended Kalman Filter Model

This chapter describes the process of filtering and the derivation of the Kalman filter gain to minimize the error of a dynamical system. The first section provides a definition for filtering and assumptions used in the following sections. The next section briefly discusses the Wiener filter as a segue into the importance of Kalman's work in the early 1960's. The third section derives the the Kalman filter with a preface on linear system dynamics. The last section describes the extended Kalman filter, the linearization of the system dynamics, and a summary of the implemented model.

C.1 Filtering Assumptions

The problem of accurately estimating the states of a system can be broken into three categories.[1,9] The first, and the focus of this chapter, is *filtering* where the goal is to estimate the states at the current time with information up to and including the current time. The second category is *prediction* where the goal is to estimate the states at a future time. And the last category is that of *smoothing* where the estimated states at a given time of interest is based on information before

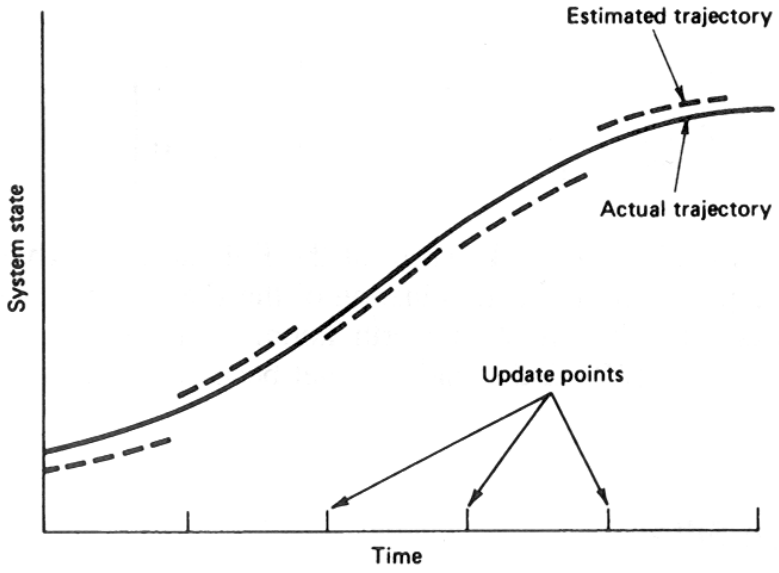

Figure C.1: Extended Kalman Filter, from Ref. [9]

and after this time epoch. Filtering is the main concern for navigation systems because one wishes to continually have an accurate estimate of the states of the system with minimal computational load to allow real time processing.

A number of reasonable assumptions must be made pertaining to the system modeling in order to make the mathematics tractable and ultimately derive the optimal Kalman gain.[1,9] The first assumption will be that the system can be modeled by linear dynamics. This assumption will be used through the majority of the derivations but will be extended to include nonlinear systems whose dynamics have been linearized about the current state estimate (*i.e.* an extended Kalman filter as shown in Fig. C.1 from Brown and Hwang,[9] pg. 344). The other main assumption is that the random processes and measurement noises are driven by uncorrelated white Gaussian variables. This assumption is based on the *Central Limit Theorem* of statistics which states that the summation of a set of random variables

with finite variance will tend to a normal, Gaussian distribution.Since the process and measurement noises are typically small variations about a true unbiased (*i.e.*, zero-mean) value, this assumption holds well. Also, the assumption that the noises are uncorrelated is reasonable since each noise is typically produced by a different sensor or system. And furthermore, the white noise assumption holds as long as we concern ourself with a finite band of system frequencies which is sufficiently less than the highest system frequencies.

C.2 Random Processes

This section provides several definitions used in the derivation of the Kalman filter gain. First, the *probability density function* is defined as (Jekeli,[1] pg. 166):

$$\int_a^b f_x(x)dx \equiv \mathscr{P}(a \leq x_k \leq b) \tag{C.1}$$

Or in words, this function defines the probability that a random variable, x_k, will have a particular value in the interval $[a, b]$. The *mean*, μ_x, or *expectation*, $E[x]$, of a random variable is defined as its first moment (Jekeli,[1] pg. 168 and Brown and Hwang,[9] pg. 26):

$$\mu_x = E[x] \equiv \int_{-\infty}^{\infty} x f_x(x)dx. \tag{C.2}$$

The *variance*, or degree that the random number's value deviates from the mean is defined as the second moment:

$$\begin{aligned} \sigma_x^2 &\equiv E[(x_k - \mu_x)^2] = E[x_k^2] - \mu_x^2 \\ &= \int_{-\infty}^{\infty} (x - \mu_x)^2 f_x(x)dx. \end{aligned} \tag{C.3}$$

The *standard deviation* is commonly used in place of the variance and is defined as the square-root of the variance, σ_x. The last definition is that of the *covariance* between two random variables x_k and y_k:

$$cov(x_k, y_k) \equiv E[(x_k - \mu_x)(y_k - \mu_y)] = E[x_k y_k] - \mu_x \mu_y, \tag{C.4}$$

where $E[xy] = \int_{-\infty}^{\infty} \int_{-\infty}^{\infty} xyf(x,y)dxdy$ and $f(x,y)$ is the *joint density function*. If the two random variables are *uncorrelated*,

$$cov(x_k, y_k) = 0, \quad \therefore \quad E[x_k y_k] = \mu_x \mu_y. \tag{C.5}$$

For a vector of random variables, $\mathbf{x}$, the *vector mean* is defined like before:

$$\mu_x = E[\mathbf{x}]. \tag{C.6}$$

The *covariance matrix* of a random vector with itself is defined as

$$P_x = cov(\mathbf{x}, \mathbf{x}) = \begin{pmatrix} cov(x_1, x_1) & \cdots & cov(x_1, x_N) \\ \vdots & \ddots & \vdots \\ cov(x_N, x_1) & \cdots & cov(x_N, x_N) \end{pmatrix}, \tag{C.7}$$

where x_1 denotes the first random variable and x_N denotes the last random variable in the vector $\mathbf{x}$. Also, because $cov(x_i, x_j) = cov(x_j, x_i)$, the covariance matrix is symmetric ($P_x = P_x^T$). And furthermore, the diagonal elements of the covariance matrix are equal to the variances of the random variable vector.

Following the assumptions given in Sec. C.1, zero-mean white Gaussian random processes will be used to model the forcing noises in the system dynamics. A *Gaussian* or *normal* process is defined by the probability density function (Brown

and Hwang,[9] pg. 25–26):

$$f_N(x) = \frac{1}{\sigma_x\sqrt{2\pi}} \exp\left[-\frac{1}{2\sigma_x^2}\left(x-\mu_x\right)^2\right]. \tag{C.8}$$

As shown, the Gaussian distribution is defined completely by its mean and variance. This distribution can then be specialized to a zero-mean *white noise* process, denote as $w(t)$ or $v(t)$. By definition, the noise will have a mean of zero. The variance, however, is harder to quantify. White noise is characterized by having zero covariance over any non-zero time interval (Jekeli,[1] pg. 177), meaning the variance is only defined at an infinitesimal period of time. This un-physical definition is mathematically realized using the Dirac delta function, and it can be shown that the variance of a white noise process is (Jekeli,[1] pg. 179):

$$\sigma_w^2 = q_w/\Delta t, \tag{C.9}$$

where q_w is the amplitude of the *power spectral density*, which is constant for all frequencies and the impetus for the process being labeled *white*.

The next subsections define three stochastic models that will be used in the accelerometer, gyro, and GPS receiver clock error models.

C.2.1 Random Constant

A random constant is usually used to model a random bias or any other constant that does not have a predetermined value. The differential equation that describes a random constant is

$$\dot{x}(t) = 0, \quad x(t_0) = x_0, \tag{C.10}$$

where the initial condition (x_0) has a given variance (σ_x^2) and zero mean.

C.2.2 Random Walk

A random walk is a process whose value varies, or "walks," stochastically over time. This process is modeled as an integrated white Gaussian noise, $w(t)$, with a mean of zero and a known variance (σ_w^2):

$$\dot{x}(t) = w(t), \quad x(t_0) = 0. \tag{C.11}$$

The initial value of the random walk process is assumed to be zero. However, if the system being modeled has a random initial condition, the system may be modeled as the combination of a random walk and a random constant.

C.2.3 First Order Gauss-Markov Process

A Gauss-Markov process is a random process whose characteristics are correlated from one time to another. A first order Gauss-Markov is defined by the linear differential equation:

$$\dot{x}(t) = -\beta x(t) + w(t), \quad x(t_0) = 0, \tag{C.12}$$

where β is a time constant that describes the level of correlation. For low β, the correlation is reduced so that the signal begins to resemble a white noise process. The gyro noise is modeled in this manner so that its contribution to the angular velocity error can be accounted for in the strapdown gravity gradiometer instrument measurement updates, see Sec. 5.2.1.

For this work, the first order Gauss-Markov process is discretely modeled by

$$x_{k+1} = \exp\left(-\beta \Delta t\right) x_k + w_k, \tag{C.13}$$

where $\beta = 2.146/(0.5\Delta t)$ is the prescribed time constant,[94] and the discrete white process variance is (Brown and Hwang,[9] pg. 124)

$$\sigma_{gm}^2 = \left(q_w/\Delta t\right)\left[1 - \exp(-2\beta\Delta t)\right]. \tag{C.14}$$

C.3 Linear Dynamic Systems

An n-dimensional linear system is one whose dynamics can be written as

$$\dot{\mathbf{x}}(t) = A(t)\mathbf{x}(t) + B(t)\mathbf{u}(t) + M(t)\mathbf{w}(t) \tag{C.15a}$$

$$\mathbf{y}(t) = C(t)\mathbf{x}(t) + D(t)\mathbf{u}(t) + N(t)\boldsymbol{\nu}(t), \tag{C.15b}$$

where $\mathbf{x}(t)$ is the n-dimensional continuous state vector of the system, $\mathbf{u}(t)$ is the command control input to the the system, $\mathbf{y}(t)$ is the output measurement vector, and $\mathbf{w}(t)$ and $\boldsymbol{\nu}(t)$ are the continuous random process and measurement noises, respectively. The matrices on the right hand side of the equations may be time varying, and essentially map the current states, controls, and noises into the state derivatives and measurements. The general theory of linear dynamic systems can be found in references such as Chen.[173] The discussion here will now be focused to the filtering problem at hand.

With the assumptions that there are no explicit control inputs and the noises are mapped directly to the state derivatives and measurements, the linear dynamics

can be rewritten as

$$\dot{\mathbf{x}}(t) = F(t)\mathbf{x}(t) + \mathbf{w}(t) \tag{C.16a}$$

$$\mathbf{y}(t) = H(t)\mathbf{x}(t) + \boldsymbol{\nu}(t). \tag{C.16b}$$

A change in notation has also been performed to coincide with typical filtering terminology. To derive the discrete form of the linear dynamics, we first solve for $\mathbf{x}(t)$. The general solution to a differential equation is the summation of its homogeneous and particular solutions. The homogeneous solution to Eq. (C.16a), *i.e.*

$$\dot{\mathbf{x}}_H(t) = F(t)\mathbf{x}_H(t), \quad \mathbf{w}(t) = \mathbf{0} \tag{C.17}$$

is given as

$$\mathbf{x}_H(t) = \Phi(t, t_0)\mathbf{x}_H(t_0), \tag{C.18}$$

where $\Phi(t, t_0)$ is the *state transition matrix* from time t_0 to t. The particular solution is found by assuming the form

$$\mathbf{x}_P(t) = \Phi(t, t_0)\boldsymbol{\nu}_P(t), \quad \text{and} \quad \mathbf{x}_P(t_0) = \mathbf{0}, \tag{C.19}$$

where $\mathbf{v_P}(t)$ is a time varying forcing vector that will be found. Substitution of the particular solution into the dynamic equation yields

$$\dot{\Phi}(t, t_0)\boldsymbol{\nu}_P(t) + \Phi(t, t_0)\dot{\boldsymbol{\nu}}_P(t) = F(t)\Phi(t, t_0)\boldsymbol{\nu}_P + \mathbf{w}(t). \tag{C.20}$$

With the properties that the state transition matrix is by definition invertible and its time derivative is:[1,173]

$$\dot{\Phi}(t, t_0) = F(t)\Phi(t, t_0), \tag{C.21}$$

one can solve for $\dot{\boldsymbol{\nu}}_P(t)$ and integrate to get

$$\boldsymbol{\nu}_P(t) = \int_{t_0}^{t} \Phi^{-1}(\tau, t_0)\mathbf{w}(\tau)d\tau. \tag{C.22}$$

Substituting $\boldsymbol{\nu}_P(t)$ back into Eq. (C.19), adding the particular and homogeneous solutions together, and using the properties that

$$\Phi^{-1}(\tau, t_0) = \Phi(t_0, \tau), \quad \text{and} \tag{C.23}$$

$$\Phi(t, t_0)\Phi(t_0, \tau) = \Phi(t, \tau), \tag{C.24}$$

the general solution to Eq. (C.16a) is found to be

$$\mathbf{x}(t) = \Phi(t, t_0)\mathbf{x}(t_0) + \int_{t_0}^{t} \Phi(t, \tau)\mathbf{w}(\tau)d\tau. \tag{C.25}$$

Applying the solution and Eq. (C.16b) to two discrete times $t = t_{k+1}$ and $t_0 = t_k$, the discrete linear dynamics are then

$$\mathbf{x}_{k+1} = \Phi_k \mathbf{x}_k + \mathbf{w}_k \tag{C.26a}$$

$$\mathbf{y}_{k+1} = H_{k+1}\mathbf{x}_{k+1} + \boldsymbol{\nu}_{k+1}, \tag{C.26b}$$

where the subscripts refer to the time of interest (t_k or t_{k+1}), and

$$\Phi_k \equiv \Phi(t_{k+1}, t_k) \tag{C.27}$$

$$\mathbf{w}_k \equiv \int_{t_k}^{t_{k+1}} \Phi(t, \tau)\mathbf{w}(\tau)d\tau. \tag{C.28}$$

For "small" time increments, the state transition matrix tends to the identity matrix so that the discrete process noise can be approximated as

$$\mathbf{w}_k \approx \int_{t_k}^{t_{k+1}} \mathbf{w}(\tau)d\tau \approx \mathbf{w}(t_k)\Delta t. \tag{C.29}$$

C.4 Wiener Filter

Filtering has its roots in the field of electronics.[9] The goal there, and in some degree universally, is to produce the greatest signal to noise separation when the characteristics of both processes are known. In electronics, this was usually implemented as a way to keep a certain range of frequencies and filter out all others, as in the removal of noise from an amplitude or frequency modulated radio signal.

Norbert Wiener, during World War II, addressed this signal to noise filter problem and produced the Wiener filter, first published in 1949.[174] With the assumption that the signal and noise were random processes with known characteristics, the Wiener filter solved for the optimal filter weighting function to minimize the mean-square error.

A limitation to the Wiener filter is its assumption that the signal and noise are both "noise-like" processes. In many cases, the signal is partially deterministic and hence the Wiener filter is no longer optimal. Also, the Wiener filter assumes a single-input-single-output (SISO) system, which greatly restricts its usefulness. The complementary Wiener filter attempts to extend the Wiener filter for use in multiple-input-multiple-output (MIMO) systems, however the noise-like assumption persists. The last major hindrance in the Wiener filter is its lack of recursion, especially when formulated for a discrete system. The discrete Wiener filter solves for the optimal weight factors (*i.e.*, gains) for a state at a given time by using all the measurements prior to and including the current time. When many measurements are made or the state is estimated at many times, the Wiener filter solution becomes computationally

infeasible. To alleviate some of the burden, only a set of measurements can be used for each state estimate, but this then limits the filter knowledge in calculating the optimal estimate.

C.5 Extended Kalman Filter

Rudolf E. Kalman in 1960 and 1961 published two papers that solved the major problems relevant in the Wiener filter by formulating the problem in a state-space manner.[24,25] Kalman did not assume that both the signal and its corrupting source were noise-like. Instead, it was only assumed that they were driven by uncorrelated process and measurement noises. The state-space derivation removed the SISO assumption of the Wiener filter so that any number of inputs and outputs could be modeled. And arguably the largest contribution of Kalman's filter was its use of recursion. Now, only the previous states and covariances were needed to estimate the current state and covariance, which allowed for a much more efficient implementation.

The only major restriction left in Kalman's formulation was the assumption of linear dynamics. Since most system dynamics are actually modeled with nonlinear relations, the Kalman filter will not optimally produce the best state estimates. One common solution to this problem is to linearize the system about a given state trajectory. If a nominal trajectory is chosen, the Kalman gains can be computed offline and the implementation is referred to as a *Linear Kalman Filter*. The major downfall of this method is that the guidance law must keep the true trajectory near

the pre-computed nominal one or the filter will diverge. However, is the system is continuously linearized with the current estimated states, an *Extended Kalman Filter (EKF)* is implemented. This typically results in better performance than the Linear Kalman filter since the estimates are usually closer to the true values than the nominal trajectory. This work uses the EKF implementation for this reason, and will be explained in the next sections. It should be noted, though, that the EKF is slightly riskier because divergence will result when the errors between the true and estimated trajectories grow too large, as shown with some of the strapdown GGI aided INS simulations.

The following three subsections derive the various components of the Extended Kalman Filter. The first subsection explains the process of linearizing the true nonlinear equations with respect to the current states. The next subsection defines an error as used in this dissertation and the Kalman filter propagation and update equations. And the last section summarizes the initialization, propagation, and update of the Extended Kalman Filter.

C.5.1 System Linearization

The Kalman filter was originally derived to give the optimal gain for the blending of noisy measurements into corrections for the estimated states given a linear dynamical system. Unfortunately, most system dynamics are nonlinear (*i.e.*, the navigation equations in Sec. 4.3). One popular way to still use the Kalman filter methods is to *linearize* the nonlinear system dynamics. The linearization is a good

approximation of the true system dynamics as long as the higher order terms and time increment are sufficiently "small".

For a generic nonlinear system, the dynamical equations are

$$\dot{\mathbf{x}}(t) = \mathbf{f}\left(\mathbf{x}(t), \mathbf{u}(t), t\right) + \mathbf{w}(t) \tag{C.30a}$$

$$\mathbf{y}(t) = \mathbf{h}\left(\mathbf{x}(t), t\right) + \boldsymbol{\nu}(t), \tag{C.30b}$$

where $\mathbf{f}$ is the nonlinear time rate of change of the states and $\mathbf{y}$ is the nonlinear measurement. Taking a Taylor series expansion of the dynamics about the estimated states, assuming $\mathbf{u} = \mathbf{0}$, and temporarily dropping the explicit time dependence notation, gives

$$\dot{\mathbf{x}} = \mathbf{f}\left(\widehat{\mathbf{x}}\right) + \left[\frac{\partial \mathbf{f}}{\partial \mathbf{x}}\right]_{\mathbf{x}=\widehat{\mathbf{x}}} \left(\mathbf{x} - \widehat{\mathbf{x}}\right) + \frac{1}{2}\left[\frac{\partial^2 \mathbf{f}}{\partial \mathbf{x}^2}\right]_{\mathbf{x}=\widehat{\mathbf{x}}} \left(\mathbf{x} - \widehat{\mathbf{x}}\right)^2 + \cdots + \mathbf{w} \tag{C.31a}$$

$$\mathbf{y} = \mathbf{h}\left(\widehat{\mathbf{x}}\right) + \left[\frac{\partial \mathbf{h}}{\partial \mathbf{x}}\right]_{\mathbf{x}=\widehat{\mathbf{x}}} \left(\mathbf{x} - \widehat{\mathbf{x}}\right) + \frac{1}{2}\left[\frac{\partial^2 \mathbf{h}}{\partial \mathbf{x}^2}\right]_{\mathbf{x}-\widehat{\mathbf{x}}} \left(\mathbf{x} - \widehat{\mathbf{x}}\right)^2 + \cdots + \boldsymbol{\nu}, \tag{C.31b}$$

where $\mathbf{x}$ is the vector of truth states and $\widehat{\mathbf{x}}$ is the vector of estimated states. Neglecting the second and higher order terms, the linearized dynamics are

$$\dot{\mathbf{x}}(t) \approx \mathbf{f}(\widehat{\mathbf{x}}(t), t) + F(t)\left(\mathbf{x}(t) - \widehat{\mathbf{x}}(t)\right) + \mathbf{w}(t) \tag{C.32a}$$

$$\mathbf{y}(t) \approx \mathbf{h}(\widehat{\mathbf{x}}(t), t) + H(t)\left(\mathbf{x}(t) - \widehat{\mathbf{x}}(t)\right) + \boldsymbol{\nu}(t), \tag{C.32b}$$

where the linearized dynamic equations and measurement matrices are

$$F(t) \equiv \left[\frac{\partial \mathbf{f}(t)}{\partial \mathbf{x}(t)}\right]_{\mathbf{x}(t)=\widehat{\mathbf{x}}(t)} \tag{C.33a}$$

$$H(t) \equiv \left[\frac{\partial \mathbf{h}(t)}{\partial \mathbf{x}(t)}\right]_{\mathbf{x}(t)=\widehat{\mathbf{x}}(t)}. \tag{C.33b}$$

If the estimated nonlinear state dynamics and measurement are defined as

$$\dot{\widehat{\mathbf{x}}}(t) \equiv \mathbf{f}(\widehat{\mathbf{x}}(t), t) \tag{C.34a}$$

$$\widehat{\mathbf{y}}(t) \equiv \mathbf{h}(\widehat{\mathbf{x}}(t), t), \tag{C.34b}$$

and an error state is defined as the perturbation between the estimated state and the true state, see Eq. (C.38), the linear dynamics become

$$\dot{\widehat{\mathbf{x}}}(t) - \dot{\mathbf{x}}(t) = \delta\dot{\mathbf{x}}(t) = \; F(t)\delta\mathbf{x}(t) - \mathbf{w}(t) \tag{C.35a}$$

$$\widehat{\mathbf{y}}_{k+1} - \mathbf{y}_{k+1} = \delta\mathbf{y}(t) = \; H(t)\delta\mathbf{x}(t) - \boldsymbol{\nu}(t). \tag{C.35b}$$

And the discrete error dynamics are (from Sec. C.3)

$$\delta\mathbf{x}_{k+1} = \; \Phi_k\delta\mathbf{x}_k - \mathbf{w}_k \tag{C.36a}$$

$$\widehat{\mathbf{y}}_{k+1} - \mathbf{y}_{k+1} = \delta\mathbf{y}_{k+1} = \; H_{k+1}\delta\mathbf{x}_{k+1} - \boldsymbol{\nu}_{k+1}. \tag{C.36b}$$

The state transition matrix is often calculated using a first order Taylor series expansion of the matrix exponential of the linearized dynamics, F, matrix:

$$\Phi_k = e^{F_k\Delta t} \approx I + F_k\Delta t, \tag{C.37}$$

where it has been assumed that F_k is constant over the time interval. Unfortunately, this approximation is poor for the exponential in the Gauss-Markov process. Jekeli addressed this problem by increasing the series truncation to 30 terms.[94] This approach was implemented initially, but the run times were drastically increased. It was then found that setting the gyro noise portion of the state transition matrix to $\mathrm{diag}(\exp(-\beta\Delta t))$ was as effective as the higher order series but without the added computational burden.

The linearized state dynamics matrix, $F(t)$, is summarized in Sec. 4.4.4 for the inertial navigation states, Sec. 4.5.1 for the IMU states, and in Sec. D.4 for the GPS receiver clock states. The linearized measurement matrix, $H(t)$, is derived in Sec. 5.2.1 and 5.2.2 for gravity gradiometer instrument aiding and Sec. D.3.2 and D.3.3 for the global positioning system aiding.

C.5.2 Discrete Kalman Filter

The derivation of the discrete Kalman filter propagation and update equations will liberally use the error states, which are defined as

$$\delta\mathbf{x} \equiv \widehat{\mathbf{x}} - \mathbf{x}, \tag{C.38}$$

where $\delta\mathbf{x}$ is a small perturbation (or error) from the true state, $\mathbf{x}$, and $\widehat{\mathbf{x}}$ is the filter-estimated state. It should be noted that this definition of the error is not universal. Many papers define the error as the true value minus the estimated value; however, in this work all errors will be consistently defined as those in Eq. (C.38). These error states are also assumed to propagate in time according to the discrete linear system dynamics of Eq. (C.36a).

The *error covariance matrix* is also of significant importance in the Kalman filter equations because it provides the filter a current estimate of all the system errors. This covariance matrix at time t_k is defined as

$$\begin{aligned} P_k &\equiv cov(\delta\mathbf{x}_k, \delta\mathbf{x}_k) \\ &= E[(\delta\mathbf{x}_k - \mu_{\delta x})(\delta\mathbf{x}_k - \mu_{\delta x})^T] = E[(\delta\mathbf{x}_k)(\delta\mathbf{x}_k)^T], \end{aligned} \tag{C.39}$$

where the last equality holds assuming the errors have zero-mean, which is a result of the forcing white process noise having zero mean. The propagation of the error covariance is found by substituting in the linear error dynamics with the assumption that the process noise and error states are uncorrelated so $E[\delta\mathbf{x}_k\mathbf{w}_k] = \mathbf{0}$. Therefore,

$$\begin{aligned} P_{k+1} &= E[(\delta\mathbf{x}_{k+1})(\delta\mathbf{x}_{k+1})^T] = E[(\Phi_k\delta\mathbf{x} - \mathbf{w}_k)(\Phi_k\delta\mathbf{x} - \mathbf{w}_k)^T] \\ &= \Phi_k E[\delta\mathbf{x}_k\delta\mathbf{x}_k^T]\Phi_k^T - E[\mathbf{w}_k\delta\mathbf{x}_k^t]\Phi_k^T - \Phi_k E[\delta\mathbf{x}_k\mathbf{w}_k^T] + E[\mathbf{w}_k\mathbf{w}_k^T] \\ &= \Phi_k P_k\Phi_k^T + Q_k, \end{aligned} \tag{C.40}$$

where the *discrete process noise covariance* is defined as

$$Q_k \equiv E[\mathbf{w}_k\mathbf{w}_k^T]. \tag{C.41}$$

Without external measurements, Eq. (C.36a) and (C.40) can be propagated deterministically from their initial conditions to yield the error and covariance at any time in the future. Only knowledge of the discrete error process noise, Q_k, and the error state transition matrix, Φ_k, are required for the calculations.

When external measurements are collected, for example by a GGI or GPS, a feedback loop is used to blend the noisy measurements with the current state estimates to produce the best updated estimate of the state vector. The derivation that follows minimizes the mean square error the of the state vector, and then is used to update the whole estimated states. Starting with the measurement update feedback form:

$$\delta\mathbf{x}_{k+1}^+ = \delta\mathbf{x}_{k+1}^- + K_{k+1}\left(\mathbf{y}_{k+1} - \widehat{\mathbf{y}}_{k+1}\right) = \delta\mathbf{x}_{k+1}^- + K_{k+1}\delta\mathbf{y}_{k+1}, \tag{C.42}$$

where the superscript "+" means the updated or *a posteriori* error state, "−" is the *a*

priori error, and K_{k+1} is the *Kalman gain matrix* to be derived. Then, substituting the discrete measurements, Eq. (C.36b), yields

$$\begin{aligned}\delta\mathbf{x}_{k+1}^{+} &= \delta\mathbf{x}_{k+1}^{-} - K_{k+1}\left(H_{k+1}\delta\mathbf{x}_{k+1}^{-} - \boldsymbol{\nu}_{k+1}\right) \\ &= \left(I - K_{k+1}H_{k+1}\right)\delta\mathbf{x}_{k+1}^{-} + K_{k+1}\boldsymbol{\nu}_{k+1}. \end{aligned} \tag{C.43}$$

The *a posteriori* error state is next substituted back into the definition of the error covariance matrix to get the updated error covariance:

$$\begin{aligned} P_{k+1}^{+} &= E\left[(\delta\mathbf{x}_{k+1}^{+})(\delta\mathbf{x}_{k+1}^{+})^{T}\right] \\ &= \left(I - K_{k+1}H_{k+1}\right)E\left[(\delta\mathbf{x}_{k+1}^{-})(\delta\mathbf{x}_{k+1}^{-})^{T}\right]\left(I - K_{k+1}H_{k+1}\right)^{T} \\ &\quad + \left(I - K_{k+1}H_{k+1}\right)E\left[(\delta\mathbf{x}_{k+1}^{-})(\boldsymbol{\nu}_{k+1})^{T}\right]K_{k+1}^{T} \\ &\quad + K_{k+1}E\left[(\boldsymbol{\nu}_{k+1})(\delta\mathbf{x}_{k+1}^{-})^{T}\right]\left(I - K_{k+1}H_{k+1}\right)^{T} \\ &\quad + K_{k+1}E\left[(\boldsymbol{\nu}_{k+1})(\boldsymbol{\nu}_{k+1})^{T}\right]K_{k+1}^{T}. \end{aligned} \tag{C.44}$$

Assuming the errors and measurement noises are uncorrelated, $E\left[(\delta\mathbf{x}^{-})(\boldsymbol{\nu})^{T}\right] = 0$, and the updated covariance matrix is now simply

$$P_{k+1}^{+} = \left(I - K_{k+1}H_{k+1}\right)P_{k+1}^{-}\left(I - K_{k+1}H_{k+1}\right)^{T} + K_{k+1}R_{k+1}K_{k+1}^{T}, \tag{C.45}$$

where P_{k+1}^{-} is the *a priori* error covariance and the *measurement noise covariance* is defined as

$$R_{k+1} \equiv E\left[\boldsymbol{\nu}_{k+1}\boldsymbol{\nu}_{k+1}^{T}\right]. \tag{C.46}$$

The updated covariance in Eq. (C.45) is also referred to as the *Joseph Form*. Other forms can be derived by substituting the Kalman gain into the Joseph form that are less computationally expensive. However, the Joseph form is used in this research

because it has better numerical properties (Brown and Hwang,[9] pg. 261). Also, after each iteration, the covariance matrix is recalculated by

$$P_{k+1} = \frac{1}{2}\left(P_{k+1} + P_{k+1}^T\right) \tag{C.47}$$

to reenforce the symmetric property to hold.

Like the Wiener filter, the goal of the Kalman filter is to minimize the mean-square error of the states by optimally blending the measurement with the estimated states. Mathematically, the Kalman gain is found by minimizing the trace (sum of diagonal elements) of the error covariance matrix since this is the sum of the error variances, see Eq. (C.7) on pg. 312. It can be shown that (Brown and Hwang,[9] pg. 217):

$$\frac{d\left(trace\ P_{k+1}^+\right)}{d\ K_{k+1}} = -2\left(H_{k+1}P_{k+1}^-\right)^T + 2K_{k+1}\left(H_{k+1}P_{k+1}^-H_{k+1}^T + R_{k+1}\right). \tag{C.48}$$

Setting this derivative equal to zero and solving for the Kalman gain matrix gives

$$K_{k+1} = P_{k+1}^-H_{k+1}^T\left(H_{k+1}P_{k+1}^-H_{k+1}^T + R_{k+1}\right)^{-1}, \tag{C.49}$$

which is the optimal gain used in Eq. (C.42).

While the discussion throughout this section has focused on the error states, what we are truly concerned with is how the "whole" state estimates are updated using the noisy measurement information and the Kalman gain. Using the error update equation, Eq. (C.42) and substituting the definition of the error terms, Eq. (C.38):

$$\widehat{\mathbf{x}}_{k+1}^+ - \mathbf{x}_{k+1}^+ = \widehat{\mathbf{x}}_{k+1}^- - \mathbf{x}_{k+1}^- + K_{k+1}\left(\mathbf{y}_{k+1} - \widehat{\mathbf{y}}_{k+1}\right). \tag{C.50}$$

Since $\mathbf{x}_{k+1}$ is the true state at time t_{k+1}, its *a priori* and *a posteriori* values are

equivalent, so the estimated states are updated using

$$\widehat{\mathbf{x}}_{k+1}^{+} = \widehat{\mathbf{x}}_{k+1}^{-} + K_{k+1}\left(\mathbf{y}_{k+1} - \widehat{\mathbf{y}}_{k+1}\right). \tag{C.51}$$

C.5.3 Summary

The Extended Kalman filter algorithm is summarized in this section. The summary is separated into the three major EKF components.

Initial Conditions

The Extended Kalman filter is initialized with an estimated and truth state vector and rotation matrix. The initial error covariance is typically defined as a diagonal matrix whose elements correspond to the initial state error variances.

$$\mathbf{x}(t_0) = \mathbf{x}_0 \tag{C.52}$$

$$\widehat{\mathbf{x}}(t_0) = \widehat{\mathbf{x}}_0 \tag{C.53}$$

$$C_b^n(t_0) = C_{b,0}^n \tag{C.54}$$

$$\widehat{C}_b^n(t_0) = \widehat{C}_{b,0}^n \tag{C.55}$$

$$P(t_0) = P_0 \tag{C.56}$$

Propagation

The nonlinear system dynamics are used to numerically integrate the truth and estimated state vectors and the rotation matrices using the simulated accelerometer and gyro measurements, see Ch. 4 and Sec. 3.3.2. The rotation matrix is integrated

using its equivalent quaternion as discussed in Sec. 4.3.3.1, and the GPS receiver dynamics are integrated according to Sec. D.4. The INS states use a fourth-order Runge-Kutta algorithm (Sec. 4.3.3.2) to numerically integrate the states at a constant rate of 20 Hz. At each time step the system dynamics are also linearized about the current state estimates and the error covariance is propagated using the error state transition matrix as discussed at the end of Sec. C.5.1. The IMU process noises are derived in Sec. 4.5.2, and the GPS clock process noises are explained in Sec. D.4.

$$\dot{\mathbf{x}}(t_k) = \mathbf{f}\left(\mathbf{x}\left(t_k\right)\right) + \mathbf{w}(t_k) \tag{C.57}$$

$$\dot{\mathbf{q}}(t_k) = \frac{1}{2} A_q \mathbf{q} \tag{C.58}$$

$$\dot{\widehat{\mathbf{x}}}(t_k) = \mathbf{f}\left(\widehat{\mathbf{x}}\left(t_k\right)\right) \tag{C.59}$$

$$\dot{\widehat{\mathbf{q}}}(t_k) = \frac{1}{2} \widehat{A}_q \widehat{\mathbf{q}} \tag{C.60}$$

$$F_k = \left[\frac{\partial \mathbf{f}}{\partial \mathbf{x}}\right]_{\mathbf{x}=\widehat{\mathbf{x}}(t_k)} \tag{C.61}$$

$$\Phi_k = I + F_k \Delta t \tag{C.62}$$

$$\Phi_{k,gyro\ noise} = \mathrm{diag}(e^{-\beta \Delta t}) \tag{C.63}$$

$$P_{k+1} = \Phi_k P_k \Phi_k^T + Q_k \tag{C.64}$$

Measurement Update

When an external measurement is made using the GGI or GPS, the linearized measurement matrix is calculated and the Kalman gain is computed. The estimated states are then updated using the Kalman gain and the residual of the noisy truth measurement and the estimated measurement. All measurements are simulated

using nonlinear equations, see Eq. (5.44), (5.57), (D.14), and (D.19). And their linearized errors are given in Eq. (5.56), (5.67), (D.15), and (D.20) respectively. The estimated rotation matrix is also updated using the calculated rotation angle errors, and then these states are reset to zero, as explained in Sec. 4.4.2.

$$\mathbf{y}_{k+1} = \mathbf{h}(\mathbf{x_{k+1}}) + \boldsymbol{\nu}_{k+1} \tag{C.65}$$

$$\widehat{\mathbf{y}}_{k+1} = \mathbf{h}(\widehat{\mathbf{x}}_{k+1}) \tag{C.66}$$

$$H_{k+1} = \left[\frac{\partial \mathbf{h}}{\partial \mathbf{x}}\right]_{\mathbf{x}=\widehat{\mathbf{x}}_{k+1}} \tag{C.67}$$

$$K_{k+1} = P_{k+1}H_{k+1}^T\left(H_{k+1}P_{k+1}H_{k+1}^T + R_{k+1}\right)^{-1} \tag{C.68}$$

$$\widehat{\mathbf{x}}_{k+1} = \widehat{\mathbf{x}}_{k+1} + K_{k+1}\left(\mathbf{y}_{k+1} - \widehat{\mathbf{y}}_{k+1}\right) \tag{C.69}$$

$$\widehat{C}_b^n = \left(I + \Psi^n\right)\widehat{C}_b^n \tag{C.70}$$

$$\boldsymbol{\psi}^n = \mathbf{0} \tag{C.71}$$

$$\begin{aligned} P_{k+1}^+ = {} & \left(I - K_{k+1}H_{k+1}\right)P_{k+1}\left(I - K_{k+1}H_{k+1}\right)^T \\ & + K_{k+1}R_{k+1}K_{k+1}^T \end{aligned} \tag{C.72}$$

Appendix D

Global Positioning System Model

The nominal United States of America's twenty-four satellite Global Positioning System (GPS) was modeled and integrated with the inertial navigation system (INS) to provide baseline navigation performance for various GPS dropouts and measurements. This chapter describes the modeling of the nominal constellation and the determination of each satellite vehicle's (SV) position and velocity as a function of time. The simulated measurements and their Kalman filter models are described in Sec. D.3 along with the visibility test to determine which SVs provide measurements and the importance of the geometric dilution of precision. The user's GPS receiver clock model is presented in the following section with the simulated noise values. Lastly, Sec. D.5 summarizes the Fortran module implementation of this chapter and its use in the overall simulation.

D.1 GPS Satellite Constellation

The position and velocity of each satellite in the nominal 24-satellite GPS constellation can be calculated by the following orbital parameters. The nominal design values are an eccentricity $e_{GPS} = 0.00$, inclination $i_{GPS} = 55°$, and semimajor

axis $a_{GPS} = 26,561.75km$. In reality, the eccentricity is generally less than 0.02 (Parkinson and Spilker,[7] pg. 179), thus for modeling purposes it will be assumed that the eccentricity is always zero . Also, due to the assumption of a circular orbit, the semimajor axis is equivalent to the semiminor axis, and orbital radius is therefore constant. It should be noted that the stated orbital radius above has been corrected for Earth's bulk oblateness (Parkinson and Spilker,[7] pg. 178–181). Each SV's position and velocity can then be determined by these assumed nominal values, a value of the Earth's gravitational constant, each SV's initial right ascension of the ascending node and argument of latitude at a given reference time, and the time offset between the current time and the initial reference time.

Earth's gravitational constant is modeled as the more accurate 1984 World Geodetic System (WGS84) value, $GM = 3.986004418 \times 10^{14}\ m^3/s^2$, than the original GPS value of $GM = 3.9860050 \times 10^{14}\ m^3/s^2$ (Ref. [113], pg. 3-3). According to the WGS84 report,[113] the GPS Operational Control Segment began using the improved value during the fall of 1994 and removed a radial bias of 1.3 m for the orbit estimators. In an effort to maintain consistency between previous and future GPS receivers, the GPS interface control document[175] continues to use the original, less accurate gravitational constant. However, for the purposes of simulating the GPS satellite vehicles' (SV) position and velocity, the current and more accurate WGS84 gravitational value is used.

The orbital period of the nominal GPS constellation can be found from the

Table D.1: Simulated GPS Parameters

Parameter Name	Symbol	Value	Units
Semimajor Axis	a_{GPS}	26,561.75	km
Eccentricity	e_{GPS}	0.00	—
Inclination	i_{GPS}	55.0	$^\circ$
Earth's Gravitational Constant	GM	$3.986\ 004\ 418 \times 10^{14}$	m^3/s^2
Orbital Period	$\mathcal{P}_{GPS}$	43,082.015	s
Initial Reference Time	t_0	Midnight, July 1, 1993	—
Earth's Rotation Rate	ω_e	$7.292\ 115\ 1467 \times 10^{-5}$	rad/s
Speed of Light	c	2.99792458×10^8	m/s

orbital radius and Earth's gravitational constant by[115]

$$\mathcal{P}_{GPS} = 2\pi\sqrt{a_{GPS}^3/GM} = 43,082.015s, \tag{D.1}$$

using the values of a_{GPS} and GM above. The GPS period is approximately one half a sidereal day $= 0.5 * (2\pi)/\omega_e = 43,082.050s$. The minimal difference between the two values is due to the correction of Earth's oblateness in the value of a_{GPS}, and truncation error with the GPS definition[175] of π. The parameters used for the simulated GPS module are summarized in Table D.1 which includes the initial reference time and the ICD-GPS-200[175] values of Earth's rotation, ω_e, (which is equivalent to the International Astronomical Union value stated in WGS84 reference[113]) and speed of light, c. These parameters are constant for each satellite in the constellation, and the remainder of this section explains the two parameters that uniquely define a specific SV's position and velocity.

The twenty-four satellites of the GPS-24 constellation are divided into six orbit planes with four satellite vehicles each. The orbit planes are defined by six right ascensions of the ascending node, Ω_{GPS}, which are the angles in the equatorial plane measured positively from the Earth-Centered-Inertial frame's x-axis (the mean vernal equinox) to the location of the ascending node. The ascending node is defined as the point on the equatorial plane at which the satellite crosses the equator from South to North (Vallado,[115] pg. 107). The right ascension of the ascending node is constant in the ECI frame, and the GPS constellation planes are equispaced by 60° starting at 32.847° as tabulated in Table D.2 (from Parkinson and Spilker,[7] pg. 181).

For each Ω_{GPS}, four satellites are "phased" by having various mean anomalies, M_{GPS}, that have been optimized to minimize the effects of a single SV failure on the total system performance.[7] For the idealized circular inclined SV orbit, the mean anomaly is equivalent to the true anomaly, ν_{GPS}, and the argument of latitude, u_{GPS} (Vallado,[115] pg. 108–111). The argument of latitude will be used for the remainder of this dissertation, but it should be noted that the actual GPS signal broadcast includes information to correct for deviations from this ideal scenario. For these more realistic situations, these three orbital angles are not equal and the method to calculate the SV position is more complicated (see ICD-GPS-200,[175] pg. 98–100 or Parkinson and Spilker,[7] pg. 138[†]). For both the idealized and realistic cases, the mean anomaly varies linearly in time, and continuing with the assumption of the

[†]It should be noted that on pg. 138 of Parkinson and Spilker, there is a slight typo in the calculation of "y_k." The correct equation is $y_k = x'_k \sin\Omega_k + y'_k \cos i_k \cos\Omega_k$, not $y_k = y'_k \sin\Omega_k + y'_k \cos i_k \cos\Omega_k$.

Table D.2: GPS-24 Satellite Constellation, from Ref. [7]

SV	ID	Ω_{GPS}, °	$u_{GPS}(t_0)$, °	SV	ID	Ω_{GPS}, °	$u_{GPS}(t_0)$, °
1	A3	272.847	11.676	13	D1	92.847	135.226
2	A4	272.847	41.806	14	D4	92.847	167.356
3	A2	272.847	161.786	15	D2	92.847	265.446
4	A1	272.847	268.126	16	D3	92.847	35.156
5	B1	332.847	80.956	17	E1	152.847	197.046
6	B2	332.847	173.336	18	E2	152.847	302.596
7	B4	332.847	204.376	19	E4	152.847	333.686
8	B3	332.847	309.976	20	E3	152.847	66.066
9	C1	32.847	111.876	21	F1	212.847	238.886
10	C4	32.847	241.556	22	F2	212.847	345.226
11	C3	32.847	339.666	23	F3	212.847	105.206
12	C2	32.847	11.796	24	F4	212.847	135.346

nominal circular inclined orbit the argument of latitude does as well. The value of the argument of latitude for the jth SV at a given time is

$$u_{GPS,j}(t) = u_{GPS,j}(t_0) + (t - t_0)\sqrt{\frac{GM}{a_{GPS}^3}} = u_{GPS,j}(t_0) + (t - t_0)\frac{2\pi}{\mathcal{P}_{GPS}}, \qquad \text{(D.2)}$$

where u_{GPS} is in radians, and t is the current time in relation to t_0 (defined as midnight, July 1, 1993) (Parkinson and Spilker,[7] pg. 138, 180). The arguments of latitude for the nominal reference constellation at the reference time are tabulated in Table D.2 (from Parkinson and Spilker,[7] pg. 181).

D.2 GPS Satellite Vehicle Position and Velocity

The Global Positioning System's satellite vehicle position and velocity are first computed in each satellite's orbital plane and then rotated into the Earth-Centered-Earth-Fixed (ECEF) coordinate frame. The Kalman filter later accounts for the transformation from the ECEF frame into the navigation frame through appropriate transformation matrices.

The Perifocal coordinate system (PQW) is a satellite-based frame with its origin at the Earth's center. The 1-axis ($\widehat{P}$ in Fig. D.1) typically points toward the orbit perigee, but because the orbit is circular the perigee is undefined and the x-axis is thus defined to point toward $\Omega_{GPS,j}$, *i.e.*, the mean vernal equinox of the jth SV orbit. The 2-axis ($\widehat{Q}$) is in the orbital plane and 90° from $\Omega_{GPS,j}$ in the direction of satellite motion. The 3-axis ($\widehat{W}$) completes the right hand coordinate system and is out of the orbit plane so that there is no position or velocity component in this

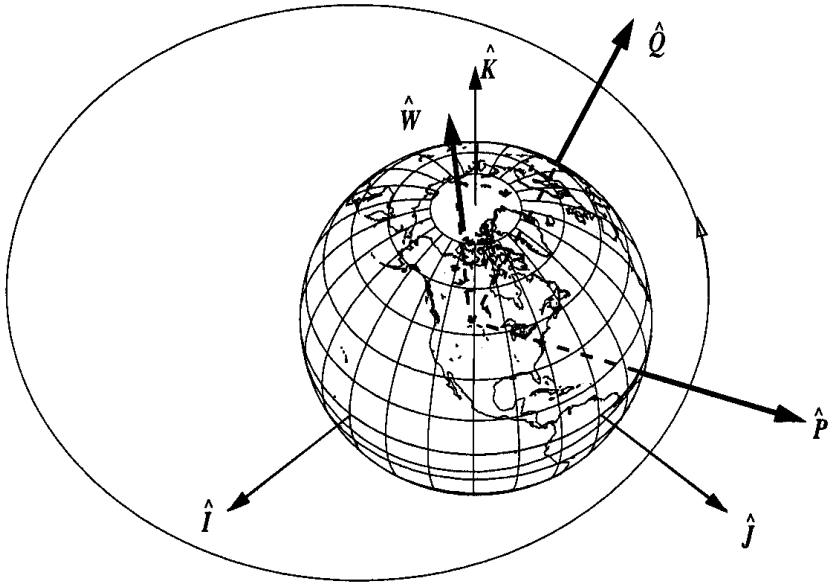

Figure D.1: Perifocal Coordinate System, from Ref. [115]

direction (Vallado,[115] pg. 161–162).

The jth GPS satellite's position and velocity as a function of the true anomaly and orbit semi-parameter, p_{GPS}, is (Vallado,[115] pg. 122–125)

$$\mathbf{r}_j^{PQW_j} = \left(\frac{p_{GPS}\cos(\nu_{GPS,j}(t))}{1+e_{GPS}\cos(\nu_{GPS,j}(t))},\ \frac{p_{GPS}\sin(\nu_{GPS,j}(t))}{1+e_{GPS}\cos(\nu_{GPS,j}(t))},\ 0 \right) \tag{D.3}$$

$$\mathbf{v}_j^{PQW_j} = \left(-\sqrt{\frac{GM}{p_{GPS}}}\sin(\nu_{GPS,j}(t)),\ \sqrt{\frac{GM}{p_{GPS}}}\left[e_{GPS}+\cos(\nu_{GPS,j}(t))\right],\ 0 \right) \tag{D.4}$$

For the assumed circular inclined orbit, several simplifications can be made to the expressions above. First, the semi-parameter is equal to the orbit radius and semi-major axis since $e_{GPS} = 0.00$.[115] Second, the true anomaly can be replaced by the argument of latitude as explained on page 333. The circular inclined orbit position and velocity of the jth SV in its PQW coordinate frame is now

$$\mathbf{r}_j^{PQW_j} = \left(a_{GPS}\cos(u_{GPS,j}(t)),\quad a_{GPS}\sin(u_{GPS,j}(t)),\ 0 \right) \tag{D.5}$$

$$\mathbf{v}_j^{PQW_j} = \left(-\sqrt{\frac{GM}{a_{GPS}}}\sin(u_{GPS,j}(t)),\ \sqrt{\frac{GM}{a_{GPS}}}\cos(u_{GPS,j}(t)),\ 0 \right). \tag{D.6}$$

The PQW to ECEF coordinate transformation generally consists of four rotations. The first three rotations transform the position and velocity vectors to the ECI frame, and the last rotation transforms from the ECI to the ECEF frame. The general PQW to ECI transformation is (Vallado,[115] pg. 173)

$$C_{PQW_j}^{i} = R_3(-\Omega_{GPS,j})R_1(-i_{GPS})R_3(-\omega_{GPS,j}), \tag{D.7}$$

where $\omega_{GPS,j}$ is the argument of perigee of the jth SV. For a circular orbit, this $\omega_{GPS,j}$ is undefined and thus set to zero.[115] The ECEF to ECI transformation is a single rotation due to Earth's spin:

$$C_i^e = R_3\big(\omega_e(t-t_0)\big),$$

repeated from Eq. (4.20). The rotations about Earth's spin axis can be combined, and the total PQW to ECEF transformation for the jth SV is now

$$\begin{aligned} C^e_{PQW_j} &= R_3\big(-\Omega_{GPS,j} + \omega_e(t-t_0)\big)R_1(-i_{GPS}) \qquad \text{(D.8)} \\ &= R_3(-\Omega_j(t))R_1(-i_{GPS}) \\ &= \begin{pmatrix} \cos(\Omega_j(t)) & -\sin(\Omega_j(t))\cos(i_{GPS}) & \sin(\Omega_j(t))\sin(i_{GPS}) \\ \sin(\Omega_j(t)) & \cos(\Omega_j(t))\cos(i_{GPS}) & -\cos(\Omega_j(t))\sin(i_{GPS}) \\ 0 & \sin(i_{GPS}) & \cos(i_{GPS}) \end{pmatrix}, \end{aligned}$$

using the definitions of the rotation matrices from Eq. (4.8) and defining the shorthand notation of $\Omega_j(t) \equiv \Omega_{GPS,j} - \omega_e(t-t_0)$.

The position and velocity for the GPS SVs can now be found in the ECEF frame. Multiplying Eq. (D.8) by Eq. (D.5) yields the position of the jth satellite:

$$\mathbf{r}^e_j = a_{GPS} \begin{pmatrix} \cos(\Omega_j)\cos(u_{GPS,j}) - \sin(\Omega_j)\cos(i_{GPS})\sin(u_{GPS,j}) \\ \sin(\Omega_j)\cos(u_{GPS,j}) + \cos(\Omega_j)\cos(i_{GPS})\sin(u_{GPS,j}) \\ \sin(i_{GPS})\sin(u_{GPS,j}) \end{pmatrix}, \qquad \text{(D.9)}$$

where the explicit time dependency of Ω_j and $u_{GPS,j}$ has been dropped for brevity. The jth satellite velocity is similarly found from Eq. (D.6) and (D.8) to be

$$\mathbf{v}^e_j = \sqrt{\frac{GM}{a_{GPS}}} \begin{pmatrix} -\cos(\Omega_j)\sin(u_{GPS,j}) - \sin(\Omega_j)\cos(i_{GPS})\cos(u_{GPS,j}) \\ -\sin(\Omega_j)\sin(u_{GPS,j}) + \cos(\Omega_j)\cos(i_{GPS})\cos(u_{GPS,j}) \\ \sin(i_{GPS})\cos(u_{GPS,j}) \end{pmatrix}. \qquad \text{(D.10)}$$

D.3 GPS Measurements

This section describes the simulated GPS measurement observables. The first subsection explains the method to calculate which satellites are visible to the user.

The next subsection defines the primary code-based GPS measurement denoted as pseudorange. The following subsection defines a carrier-phase based measurement equivalent to the time rate of change of the pseudorange which is used to yield velocity and precise position information. And the final subsection defines and discusses the important geometric dilution of precision quantity.

D.3.1 Visibility Test

The GPS satellites only present information to the user when their broadcast line-of-sight to the user is unobstructed. The primary obstruction source is the Earth, *i.e.*, when the user and the satellite are on opposite sides of the Earth. Local terrain, buildings, and an assortment of other features may also obstruct the GPS signal between the user and a given satellite vehicle. Furthermore, satellites with low elevation angles relative to the user transmit farther through the atmosphere than SVs with high elevation angles, thereby causing increased error effects associated with the ionosphere and troposphere. For these reasons, GPS receivers typically ignore SVs below a minimum elevation angle, E_{min}. Determining when a SV is "in-view" and able to produce measurement information is therefore important to correctly simulate the GPS constellation's usefulness, and is the subject of this subsection.

According to Parkinson and Spilker[7] pg. 183, "Each GPS satellite broadcasts to the Earth with an antenna coverage pattern that somewhat exceeds the angle $\alpha_{GPS} = 13.87^\circ$ subtended by the Earth." The satellite half-angle, α_{GPS}, is also a

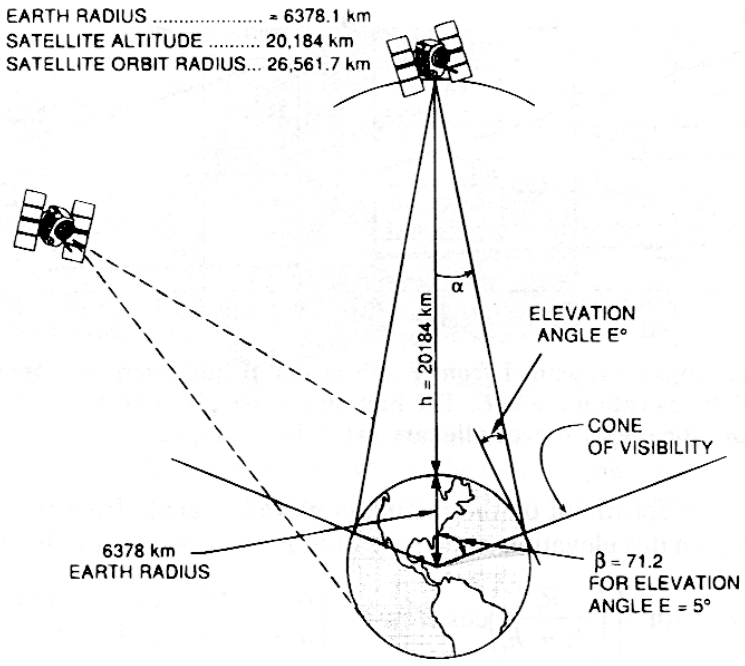

Figure D.2: GPS Visibility Angles, From Ref. [7]

function of minimum elevation angle (Parkinson and Spilker,[7] pg. 184):

$$\alpha_{GPS} = \sin^{-1}\left(\frac{a_e}{a_{GPS}}\cos\left(E_{min}\right)\right), \tag{D.11}$$

where $a_e = 6,378,137.0$ m is the semimajor axis of Earth, given in Table 4.1 on page 145.

The Earth half-angle, β_{GPS}, is the maximum angle between the user and satellite where a satellite is still visible. Referencing Fig. D.2 from Parkinson and Spilker,[7] pg. 183, and using the fact that the sum of angles in a triangle is π, the Earth half-angle can be found from $\beta_{GPS} + (\pi/2 + E_{min}) + \alpha_{GPS} = \pi$ to be

$$\beta_{GPS} = \frac{\pi}{2} - E_{min} - \alpha_{GPS}. \tag{D.12}$$

It should be noted that this expression and Fig. D.2 both assume that the altitude of the user is much less than Earth's radius so that α_{GPS} intersects the user's position.

This is a reasonable assumption for the current work because the nominal altitudes are ∼25 km, so that altitude is approximately 0.4% the Earth's semimajor axis.

The actual angle between the user, $\mathbf{r}^e$, and a given satellite, $\mathbf{r}^e_j$, (in ECEF coordinates) with the Earth's center as the vertex can be found from the dot product of the two vectors:

$$\theta_{GPS,j} = \cos^{-1}\left(\frac{\mathbf{r}^e \cdot \mathbf{r}^e_j}{||\mathbf{r}^e||\ ||\mathbf{r}^e_j||}\right). \tag{D.13}$$

The visibility test is then to compute $\theta_{GPS,j}$ for all 24 SVs at the given epoch, and if $\theta_{GPS,j} \leq \beta_{GPS}$, the jth GPS satellite is visible to the user. (The user's position in ECEF coordinates is calculated using Eq. (4.24) and the current n-frame position states, and the $\mathbf{r}^e_j$ calculation was given in the previous section).

In this research the altitudes of the hypersonic scramjet simulations are relatively high (∼25 km) so that local terrain and building obstructions are neglected. Therefore, a zero-degree elevation limit is used when determining the visibility of a GPS satellite. This results in a satellite half-angle, α_{GPS}, equal to 13.89° and an Earth half-angle, β_{GPS}, of 76.11°. (For lower altitudes, it is common to use a 5° elevation angle[7] and thus the reduced $\alpha_{GPS} = 13.84°$ and $\beta_{GPS} = 71.16°$.)

The percentage of satellite vehicles visible is shown in Fig. D.3. The figure was obtained by propagating the GPS constellation over two periods (∼24 hours) using 100,000 time steps. The user's position was held constant at the initial longitude, latitude, and altitude for the Mach 6 cases (See Table D.3). The Mach 7 and 8 cases produced higher altitudes, but negligibly different results than the Mach 6 cases. As shown in the figure, typically 8 or 9 satellites are visible. Ten satellites are

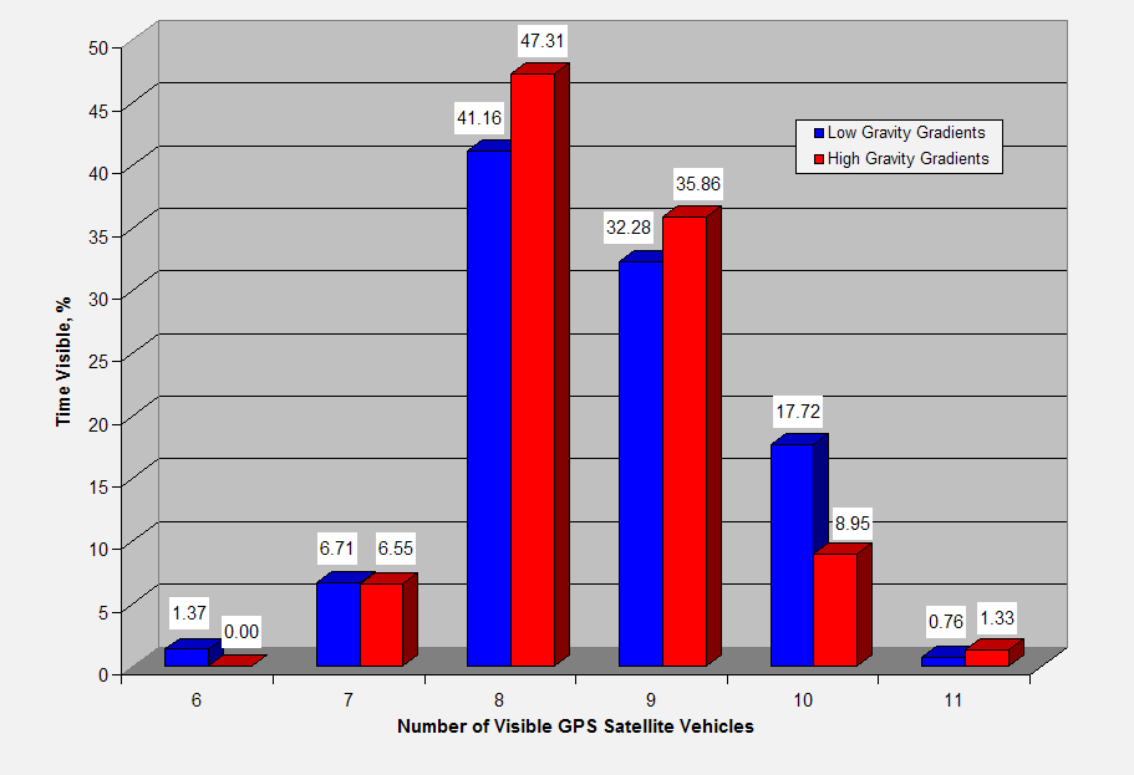

Figure D.3: Simulated GPS Satellite Visibility

somewhat common, however 11 satellites and less than 8 satellites are quite rare. Furthermore, there were no cases when less than 6 or more than 11 satellites were in view. The sensitivity to user position is also moderately small as shown by the similar trends for the two assumed user positions. The "High Gravity Gradients" cases are more focused at the 8 or 9 SV range whereas the "Low" cases are more likely to have 10 visible satellites.

D.3.2 Pseudorange

Pseudorange is the the principal measurement observable produced by the Global Positioning System. The term "pseudo"-range is used because the measurement is comprised of the range between the satellite and user with an additional error

Table D.3: User Position for GPS Satellite Visibility Analysis

Case	Longitude, °	Latitude, °	Altitude, m
High Gravity Gradients	45.0	-113.0	22043.8
Low Gravity Gradients	38.0	-100.0	22043.8

due to the user's receiver clock bias. This clock bias between the user's on-board receiver and the satellite constellation time is the largest error source in determining the true range between user and satellite, and is therefore explicitly determined in the measurement. Other sources of error, such as the atmosphere, ephemeris data, satellite clock bias, multipath, and receiver noise are accounted for in the User-Equivalent-Range-Error (UERE) whose error budget is tabulated at the end of this subsection.

The pseudorange measurement, using the user's position transformed into ECEF coordinates, $\mathbf{r}^e$, and the jth satellite vehicle, is nominally

$$\rho_j = ||\mathbf{r}_j^e - \mathbf{r}^e|| + cb_u, \tag{D.14}$$

where the speed of light is taken as $c = 2.99792458 \times 10^8$ m/s (ICD-GPS-200,[175] pg. 89), and b_u is the user's GPS receiver clock bias.

The Kalman Filter measurements are calculated by a small perturbation analysis. Neglecting broadcast, atmospheric, multipath, and receiver errors, pseudorange is a function of only position and clock bias. The small perturbation of the jth pseudorange measurement is then

$$\delta\rho_j = \left[\frac{\partial\rho_j}{\partial\mathbf{r}^e}\right]\left[\frac{\partial\mathbf{r}^e}{\partial\mathbf{r}^n}\right]\delta\mathbf{r}^n + c\cdot\delta b_u + \nu_\rho, \tag{D.15}$$

where $\delta\mathbf{r}^n$ is the user position error in the n-frame, δb_u is the user clock bias error, and ν_ρ is a white noise process that captures the additional uncompensated error sources. The partial derivatives of Eq. (D.14) with respect to user's ECEF position are

$$\left[\frac{\partial \rho_j}{\partial \mathbf{r}^e}\right] = \frac{\left(\mathbf{r}^e - \mathbf{r}_j^e\right)^T}{||\mathbf{r}_j^e - \mathbf{r}^e||}, \tag{D.16}$$

which is equivalent to the transpose of the jth satellite to user line-of-sight unit vector.

The position Jacobian from the navigation frame to the ECEF frame is found by taking the partial derivatives of the ECEF position vector with respect to the navigation frame variables. Recalling Eq. (4.24) on page 144:

$$\begin{pmatrix} r_1^e \\ r_2^e \\ r_3^e \end{pmatrix} = \begin{pmatrix} (N_e + h)\cos\phi\cos\lambda \\ (N_e + h)\cos\phi\sin\lambda \\ (N_e(1-e^2) + h)\sin\phi \end{pmatrix},$$

the Jacobian is then found to be

$$\begin{aligned} \left[\frac{\partial \mathbf{r}^e}{\partial \mathbf{r}^n}\right] &= \begin{pmatrix} \partial r_1^e/\partial\phi & \partial r_1^e/\partial\lambda & \partial r_1^e/\partial h \\ \partial r_2^e/\partial\phi & \partial r_2^e/\partial\lambda & \partial r_2^e/\partial h \\ \partial r_3^e/\partial\phi & \partial r_3^e/\partial\lambda & \partial r_3^e/\partial h \end{pmatrix} \\ &= \begin{pmatrix} -(N_e+h)\sin\phi\cos\lambda & -(N_e+h)\cos\phi\sin\lambda & \cos\phi\cos\lambda \\ -(N_e+h)\sin\phi\sin\lambda & (N_e+h)\cos\phi\cos\lambda & \cos\phi\sin\lambda \\ (N_e\,(1-e^2)+h)\cos\phi & 0 & \sin\phi \end{pmatrix}, \end{aligned} \tag{D.17}$$

where it has been assumed that the change in radius of curvature, N_e, due to latitude, ϕ, is negligible (Jekeli,[1] pg. 154). Also, the ECEF position vector is independent of

Table D.4: Precise Positioning System Error Model, P/Y Code, from Ref. [7]

Error Source	One-Sigma Error, m Bias	Random	Total
Ephemeris Data	2.1	0.0	2.1
Satellite Clock	2.0	0.7	2.1
Ionosphere	1.0	0.7	1.2
Troposphere	0.5	0.5	0.7
Multipath	1.0	1.0	1.4
Receiver Measurement	0.5	0.2	0.5
RMS User Equivalent Range Error (UERE)	3.3	1.5	3.6
Filtered RMS UERE	3.3	0.4	3.3

the navigation frame velocity vector, $\mathbf{v}^n$, so this Jacobian has been omitted in the pseudorange linear perturbation in Eq. (D.15).

Lastly, the uncompensated errors, ν_ρ, are modeled as a white noise process with a standard deviation of 3.6 meters, which corresponds to the unfiltered root-mean-square (RMS) UERE. The individual error sources are given in Table D.4 (from Parkinson and Spilker,[7] pg. 483). Parkinson and Spilker,[7] Jekeli,[1] and Farrell and Barth[2] provide further discussions on the cause of the pseudorange errors as well as some ways to model and reduce them.

D.3.3 Pseudorange Rate

The user's GPS receiver can measure the frequency shift of the carrier wave from the nominal broadcast values. The observed frequency differs due to Doppler shifts produced by satellite and user motion as well as frequency drift (bias time rate

of change) of the satellite and user clocks. The idealized Doppler shift caused by the velocity difference in the jth satellite and user along their line of sight is (Parkinson and Spilker,[7] pg. 411)

$$D_j = -\left\{ \left(\frac{\mathbf{v}_j^e - \mathbf{v}^e}{c} \right) \cdot \left(\frac{\mathbf{r}_j^e - \mathbf{r}^e}{||\mathbf{r}_j^e - \mathbf{r}^e||} \right) \right\} f_{carrier}, \tag{D.18}$$

where the user's ECEF velocity is found by $\mathbf{v}^e = C_n^e \mathbf{v}^n$ and C_n^e is given in Eq. (4.21) on page 143. The nominal carrier frequency has been denoted $f_{carrier}$. For the Global Positioning System two signals are transmitted at different frequencies: $L_1 =$ 1575.42 MHz and $L_2 = 1227.60$ MHz.

The Doppler shift can be converted into a pseudorange rate (also known as carrier phase Doppler) measurement by scaling the idealized Doppler by the speed of light and the carrier frequency, and including the user's clock bias rate. Mathematically, the jth pseudorange rate measurement is then (Parkinson and Spilker,[7] pg. 411)

$$\begin{aligned} \dot{\rho}_j &= -D_j \frac{c}{f_{carrier}} + c\dot{b}_u \\ &= \left(\mathbf{v}_j^e - \mathbf{v}^e \right) \cdot \left(\frac{\mathbf{r}_j^e - \mathbf{r}^e}{||\mathbf{r}_j^e - \mathbf{r}^e||} \right) + c\dot{b}_u. \end{aligned} \tag{D.19}$$

The pseudorange rate Kalman Filter measurements are found by a small perturbation analysis similar to the pseudorange measurements above. Again, neglecting the broadcast, atmospheric, multipath, and receiver errors, the pseudorange rate measurement is a function of only user position, velocity, and clock bias rate. Therefore the small perturbation of the jth measurement is of the form

$$\delta\dot{\rho}_j = \left\{ \left[\frac{\partial \dot{\rho}_j}{\partial \mathbf{r}^e} \right] \left[\frac{\partial \mathbf{r}^e}{\partial \mathbf{r}^n} \right] + \left[\frac{\partial \dot{\rho}_j}{\partial \mathbf{v}^e} \right] \left[\frac{\partial \mathbf{v}^e}{\partial \mathbf{r}^n} \right] \right\} \delta\mathbf{r}^n + \left[\frac{\partial \dot{\rho}_j}{\partial \mathbf{v}^e} \right] \left[\frac{\partial \mathbf{v}^e}{\partial \mathbf{v}^n} \right] \delta\mathbf{v}^n + c \cdot \delta\dot{b}_u + \nu_{\dot{\rho}}, \tag{D.20}$$

where $\delta\mathbf{v}^n$ is the n-frame user velocity error, $\delta\dot{b}_u$ is the error of the user clock bias rate, and $\nu_{\dot{\rho}}$ is a white noise process that accounts for the additional uncompensated errors. As explained on page 344, the ECEF position is independent of the n-frame velocities, so this Jacobian is a zero-matrix and has been omitted in the linearized pseudorange rate equation above. Parkinson and Spilker[7] neglect the position error terms in the pseudorange rate measurement above by implicitly assuming that the line of sight vector error is negligible. This assumption was first implemented, however the filter simulation quickly diverged making it evident that this was an invalid assumption for the hypersonic velocities simulated. After including these terms, the filter performed as expected.

The partial derivatives of the pseudorange rate with respect to ECEF position and velocity can be found to be

$$\left[\frac{\partial\dot{\rho}_j}{\partial\mathbf{r}^e}\right] = \frac{\left(\widehat{\mathbf{v}}^e - \mathbf{v}_j^e\right)^T}{||\mathbf{r}_j^e - \widehat{\mathbf{r}}^e||} + \frac{\left(\mathbf{v}_j^e - \widehat{\mathbf{v}}^e\right)\cdot\left(\mathbf{r}_j^e - \widehat{\mathbf{r}}^e\right)}{||\mathbf{r}_j^e - \widehat{\mathbf{r}}^e||^3}\left(\widehat{\mathbf{r}}_j^e - \mathbf{r}^e\right)^T \tag{D.21}$$

$$\left[\frac{\partial\dot{\rho}_j}{\partial\mathbf{v}^e}\right] = \frac{\left(\widehat{\mathbf{r}}^e - \mathbf{r}_j^e\right)^T}{||\mathbf{r}_j^e - \widehat{\mathbf{r}}^e||}. \tag{D.22}$$

The Jacobians of the ECEF velocity vector are found by taking the partial derivatives of

$$\mathbf{v}^e = C_n^e\mathbf{v}^n = \begin{pmatrix} -(\sin\phi\cos\lambda)v_N - (\sin\lambda)v_E - (\cos\phi\cos\lambda)v_D \\ -(\sin\phi\sin\lambda)v_N + (\cos\lambda)v_E - (\cos\phi\sin\lambda)v_D \\ (\cos\phi)v_N - (\sin\phi)v_D \end{pmatrix} \tag{D.23}$$

with respect to the navigation position and velocity states. The n-frame position to

ECEF velocity Jacobian is then

$$\left[\frac{\partial \mathbf{v}^e}{\partial \mathbf{r}^n}\right] = \begin{pmatrix} \partial v_N/\partial\phi & \partial v_N/\partial\lambda & \partial v_N/\partial h \\ \partial v_E/\partial\phi & \partial v_E/\partial\lambda & \partial v_E/\partial h \\ \partial v_D/\partial\phi & \partial v_D/\partial\lambda & \partial v_D/\partial h \end{pmatrix} \tag{D.24}$$

$$= \begin{pmatrix} -(\cos\phi\cos\lambda)v_N + (\sin\phi\cos\lambda)v_D & (\sin\phi\sin\lambda)v_N - (\cos\lambda)v_E + (\cos\phi\sin\lambda)v_D & 0 \\ -(\cos\phi\sin\lambda)v_N + (\sin\phi\sin\lambda)v_D & -(\sin\phi\cos\lambda)v_N - (\sin\lambda)v_E - (\cos\phi\cos\lambda)v_D & 0 \\ -(\sin\phi)v_N - (\cos\phi)v_D & 0 & 0 \end{pmatrix},$$

and the n-frame to ECEF velocity Jacobian is equal to the C_n^e transformation matrix:

$$\left[\frac{\partial \mathbf{v}^e}{\partial \mathbf{v}^n}\right] = C_n^e = \begin{pmatrix} -\sin\phi\cos\lambda & -\sin\lambda & -\cos\phi\cos\lambda \\ -\sin\phi\sin\lambda & \cos\lambda & -\cos\phi\sin\lambda \\ \cos\phi & 0 & -\sin\phi \end{pmatrix}. \tag{D.25}$$

The position transformation Jacobian in Eq. (D.20) is given in Eq. (D.17).

Because the author was unable to find a definitive pseudorange rate error budget, the total uncompensated error is estimated using the following assumptions. The pseudorange rate error, $\nu_{\dot{\rho}}$, is modeled as a white noise process with a standard deviation of 0.20 m/s. This value is estimated assuming that the user's GPS receiver can reliably measure the Doppler shift to within 1 Hz. The Doppler measurement is then scaled by c/L_1 to get a corresponding pseudorange rate error of 0.1903 m/s which is rounded to the above simulated value. Moreover, according to pg. 1-6 of the NAVSTAR GPS User Equipment Introduction,[176] the Precise Positioning System "receivers can achieve 0.2 metres per second 3-D velocity accuracy, but this is somewhat dependent on receiver design." Therefore, while the pseudorange rate error has been estimated less elegantly than the pseudorange UERE, it is deemed

suitable for this baseline simulation analysis and provides the desirable excellent integrated navigation performance.

D.3.4 Geometric Dilution of Precision

The effective error of the GPS measurements depend heavily on the orientation of the visible satellite-to-user line of sight vectors. The Geometric Dilution of Precision (GDOP) is a quantitative measurement of this phenomenon, and the sensed error at a given time is essentially the nominal error value multiplied by the GDOP.

The Geometric Dilution of Precision can be defined by starting with the pseudorange error perturbation, Eq. (D.15), and keeping the user position vector in ECEF coordinates so that

$$\delta\rho_j = \left[\frac{\partial\rho_j}{\partial\mathbf{r}^e}\right]\delta\mathbf{r}^e + c\cdot\delta b_u + \nu_\rho. \tag{D.26}$$

For N visible satellites and pseudorange measurements and rearranging slightly,

$$\delta\boldsymbol{\rho} - \boldsymbol{\nu}_\rho = \begin{pmatrix} \partial\rho_1/\partial\mathbf{r}^e & 1 \\ \vdots & \vdots \\ \partial\rho_N/\partial\mathbf{r}^e & 1 \end{pmatrix} \begin{pmatrix} \delta\mathbf{r}^e \\ c\cdot\delta b_u \end{pmatrix} \equiv G\delta\mathbf{x}_G, \tag{D.27}$$

where G is the *GPS geometry matrix* (because the partial derivatives are equal to the unit vector from the satellite to the user) and $\delta\mathbf{x}_G$ is the vector of position errors (including user clock bias in terms of meters). The position errors can then be found by taking the pseudo-inverse of G:

$$\delta\mathbf{x}_G = \left(G^TG\right)^{-1}G^T\left(\delta\boldsymbol{\rho} - \boldsymbol{\nu}_\rho\right). \tag{D.28}$$

The covariance of the position error (and clock bias) is then

$$E\left[\left(\delta\mathbf{x}_G\right)\left(\delta\mathbf{x}_G^T\right)\right] = \left(G^TG\right)^{-1}G^TE\left[\left(\delta\boldsymbol{\rho}-\boldsymbol{\nu}_\rho\right)\left(\delta\boldsymbol{\rho}-\boldsymbol{\nu}_\rho\right)^T\right]G\left(G^TG\right)^{-1}, \quad \text{(D.29)}$$

where the geometry matrix has been pulled out of the expectation operator because it contains no random component. Assuming the pseudorange perturbation and noise are uncorrelated between measurements and their variance is a constant, the expectation term can be rewritten as $\sigma^2 I$, where σ^2 is the constant variance and I is a 4×4 identity matrix. The position covariance can now be simplified to

$$E\left[\left(\delta\mathbf{x}_G\right)\left(\delta\mathbf{x}_G^T\right)\right] = \sigma^2\left(G^TG\right)^{-1}, \quad \text{(D.30)}$$

where $\left(G^TG\right)^{-1}$ is "the matrix of multipliers of ranging variance to give position variance." (Parkinson and Spilker,[7] pg. 474) The individual components of the matrix yield the dilutions of precision (DOPs) along its diagonal:

$$\left(G^TG\right)^{-1} = \begin{pmatrix} (r_1^e \text{ DOP})^2 & & & \text{covariance terms} \\ & (r_2^e \text{ DOP})^2 & & \\ & & (r_3^e \text{ DOP})^2 & \\ \text{covariance terms} & & & (\text{Time DOP})^2 \end{pmatrix}. \quad \text{(D.31)}$$

The GDOP is the total RMS of the DOPs and is calculated by taking the square root of the trace of $\left(G^TG\right)^{-1}$. Furthermore, the position dilution of precision (PDOP) can be found be taking the square root of the sums of the first three diagonal components, and the time DOP is the square root of the fourth diagonal element.

The GDOP is important as it states that for a given ranging error, the effective position (including clock bias) error is proportionally greater by the given GDOP

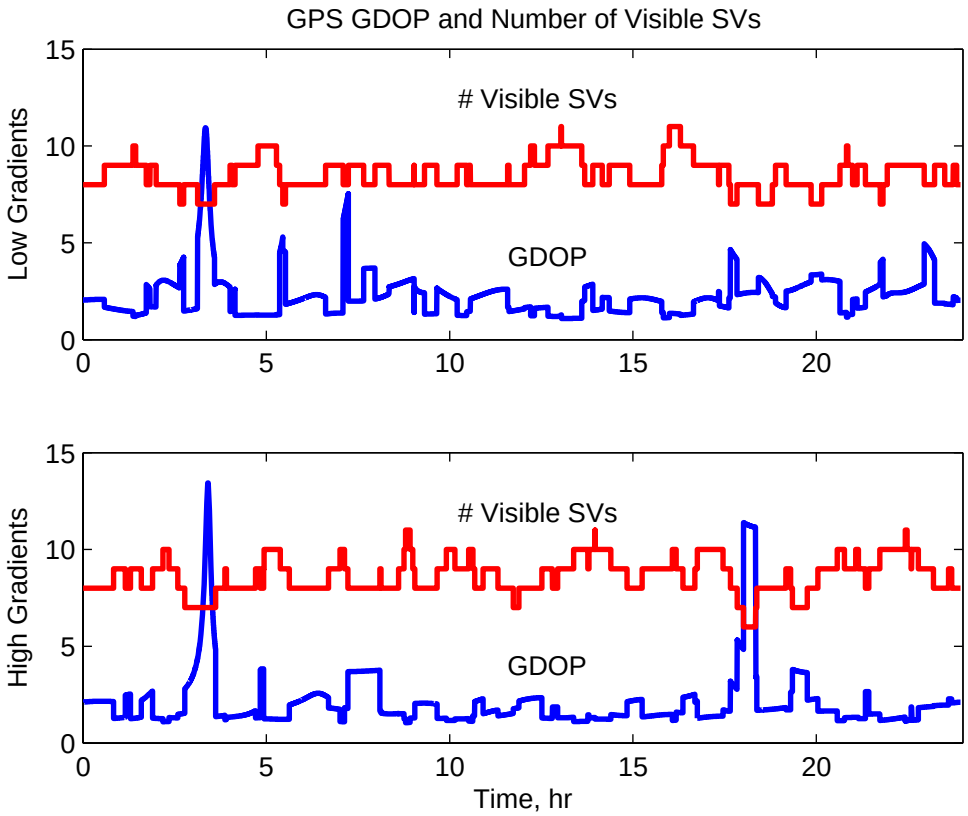

Figure D.4: Simulated GPS Geometric Dilution of Precision

value, as shown by Eq. (D.30). The GDOP for the two initial simulation positions given in Table D.3 over the course of two GPS orbits is shown in Fig. D.4. The number of visible satellites are also plotted to show the effect of a satellite going in and out of view. The GDOP spikes around four hours are characteristic of periods of poor satellite geometry even though seven satellites are visible. This results in approximately an order of magnitude greater position error than other simulation periods where the GDOP is much closer to unity. Furthermore, this underscores the need to simulate the GPS constellation at different times in their orbits to quantify the effect of time on navigation performance.

D.4 GPS Receiver Error Model

Two states are used to model the user's GPS receiver clock bias, b_u, and bias rate (drift), $\dot{b}_u$. These states both vary due to phase and frequency fluctuations in the receiver's clock oscillator or the atomic frequency standard.[1,2,7,9] These variations are modeled by white noise processes with phase and frequency power spectral densities (S_ϕ and S_f) estimated from the user's clock Allan variance parameters. The clock's dynamic model is therefore written as

$$\frac{d}{dt}\begin{pmatrix} b_u \\ \dot{b}_u \end{pmatrix} = \begin{pmatrix} 0 & 1 \\ 0 & 0 \end{pmatrix}\begin{pmatrix} b_u \\ \dot{b}_u \end{pmatrix} + \begin{pmatrix} \nu_\phi \\ \nu_f \end{pmatrix}. \tag{D.32}$$

The state transition matrix for the GPS receiver clock can be exactly calculated by its first-order Taylor series expansion:

$$\Phi_u = \begin{pmatrix} 1 & \Delta t \\ 0 & 1 \end{pmatrix}, \tag{D.33}$$

and used to solve for the discrete process noise matrix (Farrell and Barth,[2] pg. 152):

$$Q_{k,u} = \begin{pmatrix} S_\phi \Delta t + \frac{1}{3} S_f \Delta t^3 & \frac{1}{2} S_f \Delta t^2 \\ \frac{1}{2} S_f \Delta t^2 & S_f \Delta t \end{pmatrix}, \tag{D.34}$$

where Δt is the sampling period. The simulated values for the power spectral densities are then found by fitting the first component of $Q_{k,u}$ with the Allan clock error variance (Brown and Hwang,[9] pg. 430)

$$\frac{1}{2} h_0 \Delta t + 2 h_{-1} \Delta t^2 + \frac{2}{3} \pi^2 h_{-2} \Delta t^3, \tag{D.35}$$

at two sampling periods with the method of least-squares. The h terms above are the Allan variance parameters associated with the noise of a given clock type as

Table D.5: Simulated GPS Receiver Clock Parameters

Allan Variance Parameters			Power Spectral Densities	
h_0	h_{-1}	h_{-2}	$S_\phi, s^2/s$	$S_f, s^2/s^3$
2×10^{-19}	7×10^{-21}	2×10^{-20}	$1.00693069 \times 10^{-19}$	$4.03101008 \times 10^{-19}$

a function of sampling time. The least-squares formulation is then (Farrell and Barth,[2] pg. 153[†])

$$\begin{pmatrix} S_\phi \\ S_f \end{pmatrix} = \frac{1}{\Delta t_1 \Delta t_2^3 - \Delta t_2 \Delta t_1^3} \begin{pmatrix} \Delta t_2^3 & -\Delta t_1^3 \\ -3\Delta t_2 & 3\Delta t_1 \end{pmatrix} \begin{pmatrix} \Delta t_1 & \Delta t_1^2 & \Delta t_1^3 \\ \Delta t_2 & \Delta t_2^2 & \Delta t_2^3 \end{pmatrix} \begin{pmatrix} h_0/2 \\ 2h_{-1} \\ (2/3)\pi^2 h_{-2} \end{pmatrix}, \tag{D.36}$$

where Δt_1 and Δt_2 are the sampling periods to fit around. The simulated PSDs fit to sampling periods of $\Delta t_1 = 1/20$s and $\Delta t_2 = 5$s are given in Table D.5 along with the Allan variance parameters for the assumed temperature-compensated crystal (from Brown and Hwang,[9] pg. 431).

For consistency with standard GPS terminology, the actual clock states used in the simulation are scaled by the speed of light to states in terms of position and velocity instead of time bias and frequency drift. In order to correctly account for the scaling, the driving noise power spectral densities are multiplied by the speed of

[†]There is an error in the equation in Farrell and Barth. The coefficient to the h_{-2} term should be $\frac{2}{3}\pi^2$; the reference omitted the square on π.

light squared. Therefore, the clock states are implemented by

$$\begin{aligned} \frac{d}{dt}\begin{pmatrix} cb_u \\ c\dot{b}_u \end{pmatrix} &= \begin{pmatrix} 0 & 1 \\ 0 & 0 \end{pmatrix}\begin{pmatrix} cb_u \\ c\dot{b}_u \end{pmatrix} + \begin{pmatrix} c\nu_\phi \\ c\nu_f \end{pmatrix} \\ \dot{\mathbf{x}}_u &= F_u\mathbf{x}_u + \boldsymbol{\nu}_u, \end{aligned} \tag{D.37}$$

where the scaled driving noises have variances of

$$\sigma_\phi^2 = \frac{c^2 S_\phi}{\Delta t} = 0.18099684\left[\frac{m}{s}\right]^2 \tag{D.38}$$

$$\sigma_f^2 = \frac{c^2 S_f}{\Delta t} = 0.72457824\left[\frac{m}{s^2}\right]^2, \tag{D.39}$$

assuming the integration time step, $\Delta t = 1/20$s.

The clock noise states, $\boldsymbol{\nu}_u$, are simulated using a random Gaussian distribution and the variances above. The clock states, $\mathbf{x}_u$, are then numerically integrated as follows. The clock bias state, cb_u, uses a trapezoidal integration for the clock bias rate term and Euler integration for the noise term, so that

$$(cb_u)_{k+1} = (cb_u)_k + \frac{1}{2}\left((c\dot{b}_u)_{k+1} + (c\dot{b}_u)_k\right)\Delta t + (c\nu_\phi)_k\Delta t. \tag{D.40}$$

The clock bias rate uses Eulerian integration:

$$(c\dot{b}_u)_{k+1} = (c\dot{b}_u)_k + (c\nu_f)_k. \tag{D.41}$$

And substituting the new clock bias rate into the clock bias integration equation:

$$(cb_u)_{k+1} = (cb_u)_k + (c\dot{b}_u)_k\Delta t + (c\nu_f)_k\frac{\Delta t^2}{2} + (c\nu_\phi)_k\Delta t. \tag{D.42}$$

D.5 Summary

This section summarizes how this chapter is implemented into the overall Fortran simulation. The GPS update rate is first input by the program user. Then

for each simulation run, the main Fortran program randomly initializes a time offset so that the GPS constellation is arbitrarily positioned at a point in its orbit. The truth clock states are randomly initialized with variances of $(15\text{ m})^2$ and $(0.5\text{ m/s})^2$, and the initial filter covariance matrix, $P(t_0)$, uses the same values at the diagonal elements corresponding to these states. Also, the estimated clock states are both initialized to zero.

While no measurements are being made, the truth and estimated clock states are numerically integrated according to Eq. (D.41) and (D.42) using the scaled noise variances in Eq. (D.38) and (D.39). The Kalman filter covariance matrices are propagated using the state transition matrix of Eq. (D.33) and the process noise matrix of Eq. (D.34) multiplied by the speed of light squared (because of the unit conversion explained at the end of the last section).

When a GPS measurement is to be made, the Fortran GPS module first calculates the position of each satellite at the current simulation time plus additional time offset using Eq. (D.9). The user's truth and estimated ECEF position states are then calculated by Eq. (4.24) on page 144 or 343 using the current navigation frame truth and estimated position states, respectively. The visibility of each SV is determined by the discussion in Sec. D.3.1, particularly Eq. (D.13) using a zero-degree minimum elevation mask. Then, for each visibile satellite, the GDOP is calculated according to Sec. D.3.4 using the estimated ECEF user position states, and the velocities are calculated by Eq. (D.10).

The truth and estimated pseudoranges and (optionally) pseudorange rates are determined by Eq. (D.14) and Eq. (D.19) for each visible SV. The residuals are next

calculated by

$$\text{residual}_j = (\rho_j + \nu_\rho) - \widehat{\rho}_j, \tag{D.43}$$

where the first term on the right hand side is the simulated noisy j^{th} pseudorange measured by the GPS receiver, and $\widehat{\rho}_j$ is the j^{th} estimated pseudorange. The pseudorange rate residuals are similarly calculated. The variances for each measurement are $(3.6\text{m})^2$ and $(0.20\ \text{m/s})^2$. Lastly, the Kalman filter measurement matrices, H_{GPS}, are constructed using Eq. (D.15)–(D.17) for pseudorange, and Eq.(D.20)–(D.22), (D.17), and (D.24)–(D.25) for pseudorange rate. The measurement noise matrices, R_{GPS}, are diagonal matrices with the specified noise variances. The GPS module then passes the Kalman filter matrices and the measurement residuals to the main Fortran program which uses the Kalman filter subroutines to improve the estimated state vector according to App. C.

Appendix E

Additional Monte Carlo Results

This appendix supplements the results presented in Ch. 6 with additional hypersonic Monte Carlo simulations which were used in the sensitivity analyses of the aforementioned chapter. Each table in this appendix lists the mean radial spherical error (MRSE) for the position, velocity, and attitude states after three settling distances: 0 km, which is the MRSE value for the entire simulation duration; 100 km, which is the MRSE that neglects the initial filter transients; and 500 km, which approximates the steady state cruise errors. It should be noted that the tactical grade IMU cases do not typically reach a steady state yaw error by the 500 km settling distance, so the results for the tac. grade IMU simulations are not quite indicative of the true steady state attitude MRSE. (See Ch. 6 for further discussion.)

The current appendix is order as follows. Section E.1 summarizes the dead reckoning (free-inertial) hypersonic results. Section E.2 then lists the MRSE for the gravity gradiometer aided inertial navigation system simulations. And lastly, Sec. E.3 presents the baseline INS/Global Positioning System navigation results.

E.1 Dead Reckoning Results

The mean radial spherical error (MRSE) results for the 1,000 km dead reckoning (free-inertial) Monte Carlo simulations are shown in Tables E.1–E.4. The first two tables list the navigation grade IMU error accumulation due to the accelerometer, gyro, and gravity errors from over the high and low gravitational gradient variation trajectories. Tables E.3 and E.4 then summarize the tactical grade IMU dead reckoning errors for both the high and low Γ variation trajectories. Each table includes the Mach 6, 7, and 8 scramjet results computed from the 1,000-simulation Monte Carlo sets.

Table E.1: Dead Reckoning: Navigation Grade IMUs, High Γ Variation

	Settling Distance:		0 km		100 km		500 km	
M	State	Units	Error	Cov.	Error	Cov.	Error	Cov.
6	Pos.	m	37.603	616.54	40.535	679.67	64.539	1219.3
	Vel.	m/s	0.1592	3.1474	0.1722	3.3051	0.2821	4.6106
	Att.	$^\circ\times10^{-3}$	0.4693	83.459	0.5044	83.129	0.9010	80.446
7	Pos.	m	27.853	477.67	29.801	526.11	45.862	942.84
	Vel.	m/s	0.1304	2.8758	0.1404	3.0039	0.2249	4.0617
	Att.	$^\circ\times10^{-3}$	0.4142	84.335	0.4446	84.100	0.7936	82.147
8	Pos.	m	23.795	385.35	25.155	424.08	36.456	759.37
	Vel.	m/s	0.1147	2.6615	0.1229	2.7658	0.1921	3.6260
	Att.	$^\circ\times10^{-3}$	0.3731	84.927	0.3999	84.757	0.7132	83.308

Table E.2: Dead Reckoning: Navigation Grade IMUs, Low Γ Variation

	Settling Distance:		0 km		100 km		500 km	
M	State	Units	Error	Cov.	Error	Cov.	Error	Cov.
6	Pos.	m	40.337	616.09	43.365	679.13	68.483	1217.9
	Vel.	m/s	0.1730	3.1446	0.1852	3.3020	0.2860	4.6051
	Att.	$^\circ\times10^{-3}$	0.4625	83.348	0.4968	83.005	0.8874	80.213
7	Pos.	m	32.497	476.91	34.637	525.26	52.539	940.96
	Vel.	m/s	0.1519	2.8693	0.1618	2.9967	0.2434	4.0491
	Att.	$^\circ\times10^{-3}$	0.4177	84.253	0.4485	84.008	0.8005	81.978
8	Pos.	m	26.361	384.56	27.756	423.20	39.596	757.25
	Vel.	m/s	0.1272	2.6523	0.1346	2.7557	0.1948	3.6080
	Att.	$^\circ\times10^{-3}$	0.3725	84.860	0.3992	84.682	0.7117	83.171

Table E.3: Dead Reckoning: Tactical Grade IMUs, High Γ Variation

	Settling Distance:		0 km		100 km		500 km	
M	State	Units	Error	Cov.	Error	Cov.	Error	Cov.
6	Pos.	m	587.03	858.47	650.87	948.43	1163.03	1703.1
	Vel.	m/s	3.3720	4.9110	3.7191	5.2612	6.6611	8.1173
	Att.	$^\circ\times10^{-3}$	101.24	150.76	110.94	157.74	199.56	214.69
7	Pos.	m	402.25	624.50	445.58	689.21	793.21	1236.3
	Vel.	m/s	2.5937	4.1264	2.8577	4.3905	5.1105	6.5430
	Att.	$^\circ\times10^{-3}$	84.806	138.47	92.930	144.13	167.13	190.17
8	Pos.	m	291.01	481.03	322.09	530.36	571.58	950.66
	Vel.	m/s	2.1124	3.5942	2.3261	3.7997	4.1555	5.4744
	Att.	$^\circ\times10^{-3}$	76.327	129.38	83.637	134.05	150.43	172.03

Table E.4: Dead Reckoning: Tactical Grade IMUs, Low Γ Variation

	Settling Distance:		0 km		100 km		500 km	
M	State	Units	Error	Cov.	Error	Cov.	Error	Cov.
6	Pos.	m	600.86	857.51	665.92	947.31	1187.9	1700.7
	Vel.	m/s	3.4138	4.9042	3.7649	5.2536	6.7456	8.1035
	Att.	$^\circ\times10^{-3}$	100.97	150.64	110.64	157.61	199.01	214.44
7	Pos.	m	406.42	623.41	449.95	688.00	798.90	1233.8
	Vel.	m/s	2.6216	4.1164	2.8885	4.3796	5.1666	6.5234
	Att.	$^\circ\times10^{-3}$	86.438	138.38	94.729	144.03	170.36	189.99
8	Pos.	m	294.77	479.94	325.96	529.16	576.10	948.03
	Vel.	m/s	2.1049	3.5823	2.3168	3.7866	4.1368	5.4505
	Att.	$^\circ\times10^{-3}$	75.739	129.30	83.000	133.97	149.25	171.88

E.2 Gravity Gradiometer Aided Navigation

The hypersonic gravity gradiometer aided INS MRSE results are listed in Tables E.5–E.22 for the two GGI types, two simulated IMU specifications, two Γ variation trajectories, and three cruise Mach numbers. Each table includes the position, velocity, and attitude MRSEs for the three settling distances, three simulated GGI noise level standard deviations (σ_L = 0.001, 0.01, and 0.1 Eö; 1 Eö ≡ 10^{-9} s^{-2}), and three update rates (Δt = 1, 5, and 10 sec).

Tables E.5–E.7 on pg. 361–363 present the stabilized gradiometer, navigation grade inertial measurement unit INS results over the high gravitational gradient variation trajectory for the three simulated Mach numbers (6, 7, and 8). Tables E.8–E.10 on pg. 364–366 then present the same stabilized GGI, nav. grade IMU

configuration results as simulated over the low Γ variation trajectory.

Tables E.11–E.16 on pg. 367–372 next list the stabilized GGI, tactical grade IMU Monte Carlo simulation results. The first three tables correspond to the high gravitational gradient variation trajectory simulations at the three hypersonic velocities, and the latter three tables correspond to the low Γ variation trajectories.

Lastly, Tables E.17–E.22 summarize the simulated strapdown GGI, navigation grade IMU configuration's hypersonic navigation performance on pg. 373–378. Tables E.17–E.19 are for the high Γ variation trajectories, and Tables E.20–E.22 are for the low Γ variation trajectories with each table representing a single cruise Mach number.

Inertial navigation systems consisting of a strapdown GGI and tactical grade IMUs were simulated, but diverged almost instantly because of the numerical truncation issues discussed in Ch. 6. Therefore, full Monte Carlo simulations were not performed for this INS/GGI configuration.

Table E.5: INS/GGI: Stabilized GGI, Nav. Grade IMUs, High Γ Var., Mach 6

σ_L	Settling Distance:		0 km		100 km		500 km	
Δt	State	Units	Error	Cov.	Error	Cov.	Error	Cov.
.001	Pos.	m	1.2531	1.2989	1.3047	1.3507	0.3240	0.3233
1	Vel.	m/s	0.0329	0.7149	0.0218	0.7730	0.0061	0.0061
	Att.	$^\circ\times10^{-3}$	4.6307	44.066	4.1034	41.700	7.3813	7.5899
.001	Pos.	m	1.4827	1.5706	1.4659	1.5293	0.6709	0.6764
5	Vel.	m/s	0.0375	0.7315	0.0241	0.7756	0.0111	0.0113
	Att.	$^\circ\times10^{-3}$	6.7807	46.714	6.6872	43.694	12.032	12.702
.001	Pos.	m	1.6852	1.8337	1.6328	1.6632	0.9219	0.9355
10	Vel.	m/s	0.0378	0.7475	0.0258	0.7775	0.0145	0.0151
	Att.	$^\circ\times10^{-3}$	7.9106	48.414	8.1111	45.189	14.595	16.373
.01	Pos.	m	4.2590	6.3569	4.0783	6.3627	2.7380	2.7931
1	Vel.	m/s	0.0714	0.7733	0.0378	0.7900	0.0353	0.0384
	Att.	$^\circ\times10^{-3}$	11.114	54.886	11.960	51.867	21.525	31.614
.01	Pos.	m	6.2098	8.4138	5.7123	7.9871	5.8824	5.9503
5	Vel.	m/s	0.0946	0.8129	0.0543	0.8082	0.0649	0.0714
	Att.	$^\circ\times10^{-3}$	9.6797	59.181	10.526	56.611	18.943	41.637
.01	Pos.	m	7.5477	9.8941	6.9249	9.1992	8.2130	8.2657
10	Vel.	m/s	0.1063	0.8357	0.0668	0.8206	0.0870	0.0938
	Att.	$^\circ\times10^{-3}$	8.2927	60.526	9.0137	58.113	16.220	44.641
.1	Pos.	m	15.355	21.463	14.725	20.229	24.307	24.691
1	Vel.	m/s	0.1882	0.9465	0.1468	0.9010	0.2315	0.2438
	Att.	$^\circ\times10^{-3}$	5.2273	63.162	5.5696	61.019	10.019	49.365
.1	Pos.	m	28.506	36.364	29.453	35.596	50.802	52.640
5	Vel.	m/s	0.2869	1.0802	0.2663	1.0240	0.4466	0.4801
	Att.	$^\circ\times10^{-3}$	5.9907	64.981	6.4128	62.957	11.536	51.142
.1	Pos.	m	38.230	46.576	40.543	46.613	70.711	72.572
10	Vel.	m/s	0.3520	1.1616	0.3477	1.1072	0.5939	0.6404
	Att.	$^\circ\times10^{-3}$	7.3783	66.145	7.9951	64.196	14.385	52.246

Table E.6: INS/GGI: Stabilized GGI, Nav. Grade IMUs, High Γ Var., Mach 7

σ_L	Settling Distance:		0 km		100 km		500 km	
Δt	State	Units	Error	Cov.	Error	Cov.	Error	Cov.
.001	Pos.	m	1.2858	1.3474	1.3377	1.3996	0.3360	0.3366
1	Vel.	m/s	0.0344	0.7177	0.0221	0.7734	0.0069	0.0069
	Att.	$^\circ\times10^{-3}$	5.8014	45.380	5.4279	42.677	9.7653	9.9880
.001	Pos.	m	1.5576	1.6357	1.5396	1.5892	0.7060	0.7114
5	Vel.	m/s	0.0388	0.7362	0.0245	0.7766	0.0125	0.0132
	Att.	$^\circ\times10^{-3}$	8.3911	49.012	8.5468	45.838	15.379	17.710
.001	Pos.	m	1.7653	1.9214	1.7070	1.7306	0.9789	0.9873
10	Vel.	m/s	0.0388	0.7543	0.0265	0.7788	0.0163	0.0175
	Att.	$^\circ\times10^{-3}$	9.4599	51.125	9.9213	47.880	17.853	22.453
.01	Pos.	m	4.3398	6.4797	4.1528	6.4685	2.9415	2.9683
1	Vel.	m/s	0.0765	0.7823	0.0406	0.7936	0.0405	0.0446
	Att.	$^\circ\times10^{-3}$	10.628	57.784	11.490	55.045	20.678	38.059
.01	Pos.	m	6.4176	8.6453	5.9515	8.2043	6.2902	6.3438
5	Vel.	m/s	0.1030	0.8267	0.0609	0.8152	0.0778	0.0838
	Att.	$^\circ\times10^{-3}$	7.8673	61.192	8.5309	58.844	15.350	45.735
.01	Pos.	m	7.8314	10.207	7.2554	9.5085	8.6661	8.8306
10	Vel.	m/s	0.1166	0.8526	0.0760	0.8303	0.1037	0.1114
	Att.	$^\circ\times10^{-3}$	6.3584	62.100	6.8687	59.851	12.358	47.571
.1	Pos.	m	15.801	22.149	15.476	21.131	25.742	26.376
1	Vel.	m/s	0.2099	0.9780	0.1731	0.9279	0.2791	0.2972
	Att.	$^\circ\times10^{-3}$	5.1509	64.289	5.4837	62.220	9.8638	50.453
.1	Pos.	m	29.654	37.527	31.209	37.315	54.014	55.778
5	Vel.	m/s	0.3237	1.1297	0.3150	1.0749	0.5359	0.5817
	Att.	$^\circ\times10^{-3}$	7.9576	66.730	8.6592	64.820	15.580	52.815
.1	Pos.	m	38.213	47.951	41.029	48.672	71.806	76.289
10	Vel.	m/s	0.3784	1.2194	0.3855	1.1693	0.6626	0.7628
	Att.	$^\circ\times10^{-3}$	9.4384	68.321	10.346	66.528	18.617	54.658

Table E.7: INS/GGI: Stabilized GGI, Nav. Grade IMUs, High Γ Var., Mach 8

σ_L	Settling Distance:		0 km		100 km		500 km	
Δt	State	Units	Error	Cov.	Error	Cov.	Error	Cov.
.001	Pos.	m	0.9765	0.9817	0.9767	0.9747	0.3499	0.3538
1	Vel.	m/s	0.0371	0.7211	0.0224	0.7740	0.0077	0.0079
	Att.	$^\circ\times10^{-3}$	7.2219	47.151	7.0175	44.118	12.628	13.345
.001	Pos.	m	1.2578	1.3065	1.1955	1.1997	0.7512	0.7591
5	Vel.	m/s	0.0399	0.7399	0.0257	0.7780	0.0143	0.0154
	Att.	$^\circ\times10^{-3}$	9.7615	51.306	10.104	48.138	18.186	22.706
.001	Pos.	m	1.4293	1.6283	1.3431	1.3650	1.0406	1.0566
10	Vel.	m/s	0.0385	0.7599	0.0276	0.7806	0.0188	0.0204
	Att.	$^\circ\times10^{-3}$	10.532	53.342	11.159	50.227	20.084	27.343
.01	Pos.	m	5.1153	6.7624	4.9641	6.6903	3.1325	3.1783
1	Vel.	m/s	0.0841	0.7954	0.0452	0.7984	0.0486	0.0527
	Att.	$^\circ\times10^{-3}$	9.5473	60.050	10.348	57.546	18.625	42.745
.01	Pos.	m	7.3771	9.1563	6.9826	8.6860	6.7539	6.8215
5	Vel.	m/s	0.1146	0.8438	0.0718	0.8251	0.0964	0.1022
	Att.	$^\circ\times10^{-3}$	6.4039	62.521	6.9014	60.300	12.418	47.928
.01	Pos.	m	8.8600	10.834	8.3882	10.138	9.2846	9.4656
10	Vel.	m/s	0.1297	0.8716	0.0895	0.8430	0.1279	0.1357
	Att.	$^\circ\times10^{-3}$	5.4356	63.176	5.8384	61.017	10.504	49.014
.1	Pos.	m	15.837	22.842	15.785	22.040	27.348	27.852
1	Vel.	m/s	0.2330	1.0090	0.2029	0.9559	0.3341	0.3531
	Att.	$^\circ\times10^{-3}$	6.2879	65.533	6.7847	63.539	12.207	51.516
.1	Pos.	m	29.388	38.489	31.256	38.732	55.213	58.116
5	Vel.	m/s	0.3458	1.1746	0.3447	1.1221	0.5902	0.6742
	Att.	$^\circ\times10^{-3}$	9.9194	68.776	10.882	67.018	19.585	55.184
.1	Pos.	m	38.383	48.932	41.542	50.181	73.711	78.760
10	Vel.	m/s	0.3973	1.2677	0.4110	1.2219	0.7093	0.8633
	Att.	$^\circ\times10^{-3}$	11.307	70.738	12.459	69.141	22.424	57.892

Table E.8: INS/GGI: Stabilized GGI, Nav. Grade IMUs, Low Γ Var., Mach 6

σ_L	Settling Distance:		0 km		100 km		500 km	
Δt	State	Units	Error	Cov.	Error	Cov.	Error	Cov.
.001	Pos.	m	0.9714	0.9920	0.9788	0.9958	0.3229	0.3243
1	Vel.	m/s	0.0365	0.7155	0.0282	0.7730	0.0062	0.0062
	Att.	$^\circ\times10^{-3}$	4.5738	44.072	4.0177	41.595	7.2266	7.3473
.001	Pos.	m	1.2545	1.2819	1.2038	1.1952	0.6869	0.6849
5	Vel.	m/s	0.0403	0.7308	0.0311	0.7758	0.0114	0.0116
	Att.	$^\circ\times10^{-3}$	6.4881	46.504	6.3177	43.469	11.367	12.205
.001	Pos.	m	1.3947	1.5562	1.3151	1.3428	0.9489	0.9516
10	Vel.	m/s	0.0396	0.7465	0.0317	0.7778	0.0150	0.0155
	Att.	$^\circ\times10^{-3}$	7.6265	47.951	7.7610	44.766	13.965	15.426
.01	Pos.	m	5.0184	6.6512	4.9109	6.6363	2.8394	2.8668
1	Vel.	m/s	0.0747	0.7762	0.0430	0.7912	0.0374	0.0407
	Att.	$^\circ\times10^{-3}$	10.464	54.686	11.261	51.621	20.265	31.215
.01	Pos.	m	7.0229	8.8622	6.6195	8.4535	6.0551	6.1688
5	Vel.	m/s	0.0991	0.8159	0.0602	0.8115	0.0713	0.0777
	Att.	$^\circ\times10^{-3}$	9.9498	58.936	10.823	56.336	19.477	41.163
.01	Pos.	m	8.4670	10.418	7.9533	9.7743	8.4144	8.5652
10	Vel.	m/s	0.1100	0.8386	0.0715	0.8250	0.0933	0.1024
	Att.	$^\circ\times10^{-3}$	8.6197	60.312	9.3712	57.873	16.863	44.206
.1	Pos.	m	15.121	22.028	14.486	20.920	24.961	25.409
1	Vel.	m/s	0.1949	0.9523	0.1532	0.9094	0.2473	0.2615
	Att.	$^\circ\times10^{-3}$	5.4494	63.235	5.8115	61.097	10.454	49.428
.1	Pos.	m	28.994	37.422	30.018	36.815	52.933	54.276
5	Vel.	m/s	0.3040	1.0947	0.2839	1.0414	0.4873	0.5165
	Att.	$^\circ\times10^{-3}$	6.5818	65.271	7.0718	63.266	12.722	51.407
.1	Pos.	m	38.482	47.937	40.868	48.158	72.500	74.775
10	Vel.	m/s	0.3655	1.1804	0.3613	1.1292	0.6282	0.6857
	Att.	$^\circ\times10^{-3}$	7.9138	66.544	8.5915	64.624	15.458	52.666

Table E.9: INS/GGI: Stabilized GGI, Nav. Grade IMUs, Low Γ Var., Mach 7

σ_L	Settling Distance:		0 km		100 km		500 km	
Δt	State	Units	Error	Cov.	Error	Cov.	Error	Cov.
.001	Pos.	m	0.9950	1.0033	1.0017	1.0036	0.3399	0.3389
1	Vel.	m/s	0.0376	0.7182	0.0280	0.7734	0.0070	0.0071
	Att.	$^\circ\times10^{-3}$	5.5955	45.355	5.1643	42.526	9.2903	9.6843
.001	Pos.	m	1.2616	1.3115	1.2074	1.2176	0.7194	0.7258
5	Vel.	m/s	0.0416	0.7353	0.0316	0.7768	0.0132	0.0137
	Att.	$^\circ\times10^{-3}$	8.1191	48.665	8.2355	45.461	14.818	16.952
.001	Pos.	m	1.4334	1.6102	1.3542	1.3762	0.9989	1.0116
10	Vel.	m/s	0.0408	0.7533	0.0326	0.7792	0.0172	0.0183
	Att.	$^\circ\times10^{-3}$	9.2658	50.461	9.6888	47.214	17.434	21.079
.01	Pos.	m	5.1651	6.7707	5.0479	6.7403	2.9773	3.0544
1	Vel.	m/s	0.0806	0.7858	0.0454	0.7952	0.0439	0.0477
	Att.	$^\circ\times10^{-3}$	10.829	57.510	11.748	54.729	21.141	37.610
.01	Pos.	m	7.2413	9.0953	6.8573	8.6759	6.4223	6.5768
5	Vel.	m/s	0.1082	0.8303	0.0666	0.8193	0.0849	0.0921
	Att.	$^\circ\times10^{-3}$	8.1863	60.982	8.8848	58.610	15.986	45.397
.01	Pos.	m	8.6145	10.732	8.1227	10.086	8.8989	9.1391
10	Vel.	m/s	0.1203	0.8560	0.0806	0.8354	0.1126	0.1221
	Att.	$^\circ\times10^{-3}$	7.0102	61.951	7.5971	59.686	13.668	47.321
.1	Pos.	m	15.799	22.741	15.455	21.829	26.713	27.117
1	Vel.	m/s	0.2188	0.9855	0.1811	0.9378	0.3013	0.3182
	Att.	$^\circ\times10^{-3}$	5.5495	64.425	5.9248	62.364	10.657	50.595
.1	Pos.	m	29.544	38.573	31.115	38.497	54.941	57.351
5	Vel.	m/s	0.3347	1.1456	0.3255	1.0935	0.5645	0.6203
	Att.	$^\circ\times10^{-3}$	8.5104	67.140	9.2760	65.260	16.689	53.292
.1	Pos.	m	39.089	49.246	41.985	50.124	74.497	78.333
10	Vel.	m/s	0.3961	1.2381	0.4023	1.1909	0.7016	0.8068
	Att.	$^\circ\times10^{-3}$	10.072	68.833	11.047	67.080	19.878	55.332

Table E.10: INS/GGI: Stabilized GGI, Nav. Grade IMUs, Low Γ Var., Mach 8

σ_L	Settling Distance:		0 km		100 km		500 km	
Δt	State	Units	Error	Cov.	Error	Cov.	Error	Cov.
.001	Pos.	m	0.9724	1.0150	0.9729	1.0124	0.3558	0.3551
1	Vel.	m/s	0.0399	0.7210	0.0294	0.7740	0.0078	0.0081
	Att.	$^\circ\times10^{-3}$	6.9399	46.973	6.7099	43.908	12.072	12.997
.001	Pos.	m	1.2827	1.3400	1.2251	1.2400	0.7600	0.7656
5	Vel.	m/s	0.0425	0.7398	0.0316	0.7780	0.0150	0.0158
	Att.	$^\circ\times10^{-3}$	9.6522	51.051	10.012	47.842	18.017	22.279
.001	Pos.	m	1.4856	1.6611	1.4073	1.4078	1.0604	1.0679
10	Vel.	m/s	0.0423	0.7599	0.0339	0.7808	0.0195	0.0211
	Att.	$^\circ\times10^{-3}$	10.302	53.044	10.919	49.892	19.650	26.877
.01	Pos.	m	5.2330	6.8807	5.1124	6.8358	3.1665	3.2274
1	Vel.	m/s	0.0868	0.7954	0.0495	0.7993	0.0510	0.0550
	Att.	$^\circ\times10^{-3}$	9.6770	59.749	10.508	57.216	18.910	42.382
.01	Pos.	m	7.4060	9.3081	7.0380	8.8836	6.9301	6.9591
5	Vel.	m/s	0.1176	0.8449	0.0750	0.8275	0.1021	0.1076
	Att.	$^\circ\times10^{-3}$	6.6443	62.350	7.1724	60.117	12.904	47.810
.01	Pos.	m	8.8994	11.014	8.4681	10.377	9.5483	9.6757
10	Vel.	m/s	0.1316	0.8736	0.0922	0.8465	0.1349	0.1435
	Att.	$^\circ\times10^{-3}$	5.6786	63.071	6.1073	60.907	10.986	48.978
.1	Pos.	m	16.125	23.341	16.089	22.626	27.854	28.605
1	Vel.	m/s	0.2393	1.0178	0.2079	0.9669	0.3505	0.3766
	Att.	$^\circ\times10^{-3}$	6.6706	65.743	7.2092	63.766	12.970	51.780
.1	Pos.	m	30.430	39.384	32.424	39.743	57.274	59.608
5	Vel.	m/s	0.3569	1.1904	0.3559	1.1404	0.6186	0.7120
	Att.	$^\circ\times10^{-3}$	10.495	69.294	11.525	67.579	20.739	55.911
.1	Pos.	m	39.661	50.042	42.962	51.426	76.241	80.662
10	Vel.	m/s	0.4089	1.2843	0.4231	1.2409	0.7403	0.9024
	Att.	$^\circ\times10^{-3}$	12.008	71.324	13.240	69.779	23.827	58.794

Table E.11: INS/GGI: Stabilized GGI, Tac. Grade IMUs, High Γ Var., Mach 6

σ_L	Settling Distance:		0 km		100 km		500 km	
Δt	State	Units	Error	Cov.	Error	Cov.	Error	Cov.
.001	Pos.	m	1.3231	1.3759	1.3761	1.4306	0.5057	0.5057
1	Vel.	m/s	0.0431	0.7247	0.0312	0.7821	0.0233	0.0232
	Att.	$^\circ\times10^{-3}$	58.730	100.11	63.449	103.28	114.10	125.99
.001	Pos.	m	1.6710	1.7042	1.6602	1.6651	0.9825	0.9875
5	Vel.	m/s	0.0520	0.7448	0.0370	0.7877	0.0342	0.0344
	Att.	$^\circ\times10^{-3}$	58.215	101.20	63.016	104.17	113.32	127.66
.001	Pos.	m	1.8600	2.0077	1.8059	1.8369	1.3408	1.3292
10	Vel.	m/s	0.0559	0.7628	0.0414	0.7911	0.0413	0.0413
	Att.	$^\circ\times10^{-3}$	59.311	101.76	64.269	104.62	115.57	128.51
.01	Pos.	m	4.6339	6.6840	4.4683	6.7035	3.6301	3.6291
1	Vel.	m/s	0.0981	0.7963	0.0636	0.8121	0.0830	0.0828
	Att.	$^\circ\times10^{-3}$	62.651	103.48	68.178	106.20	122.61	131.39
.01	Pos.	m	6.9845	9.1623	6.5602	8.7890	7.6677	7.6952
5	Vel.	m/s	0.1402	0.8523	0.1025	0.8487	0.1524	0.1541
	Att.	$^\circ\times10^{-3}$	62.818	104.72	68.467	107.45	123.13	133.40
.01	Pos.	m	8.6750	10.989	8.1695	10.386	10.687	10.718
10	Vel.	m/s	0.1656	0.8883	0.1303	0.8759	0.2031	0.2065
	Att.	$^\circ\times10^{-3}$	60.505	105.34	65.957	108.10	118.61	134.27
.1	Pos.	m	18.629	24.653	18.384	23.769	30.930	31.226
1	Vel.	m/s	0.3263	1.0775	0.2985	1.0442	0.5054	0.5243
	Att.	$^\circ\times10^{-3}$	66.331	109.15	72.332	112.11	130.08	139.33
.1	Pos.	m	35.344	42.309	37.024	42.181	64.462	64.438
5	Vel.	m/s	0.5182	1.2996	0.5190	1.2660	0.9017	0.9308
	Att.	$^\circ\times10^{-3}$	68.834	113.91	75.068	117.22	134.99	146.39
.1	Pos.	m	46.740	54.223	49.943	55.065	87.681	87.634
10	Vel.	m/s	0.6310	1.4263	0.6500	1.3996	1.1383	1.1723
	Att.	$^\circ\times10^{-3}$	72.038	116.32	78.571	119.83	141.29	150.25

Table E.12: INS/GGI: Stabilized GGI, Tac. Grade IMUs, High Γ Var., Mach 7

σ_L	Settling Distance:		0 km		100 km		500 km	
Δt	State	Units	Error	Cov.	Error	Cov.	Error	Cov.
.001	Pos.	m	1.3945	1.4171	1.4525	1.4715	0.5079	0.5063
1	Vel.	m/s	0.0442	0.7271	0.0310	0.7821	0.0234	0.0233
	Att.	$^\circ\times10^{-3}$	54.575	95.312	58.850	97.720	105.81	114.45
.001	Pos.	m	1.7128	1.7546	1.6992	1.7097	1.0013	0.9952
5	Vel.	m/s	0.0536	0.7489	0.0376	0.7879	0.0351	0.0349
	Att.	$^\circ\times10^{-3}$	52.251	96.237	56.443	98.378	101.48	115.70
.001	Pos.	m	1.9323	2.0790	1.8793	1.8879	1.3612	1.3495
10	Vel.	m/s	0.0567	0.7690	0.0422	0.7918	0.0429	0.0425
	Att.	$^\circ\times10^{-3}$	53.352	96.701	57.830	98.717	103.98	116.33
.01	Pos.	m	4.6671	6.8126	4.4894	6.8206	3.8253	3.8064
1	Vel.	m/s	0.1059	0.8066	0.0704	0.8178	0.0948	0.0938
	Att.	$^\circ\times10^{-3}$	52.631	98.023	57.232	99.924	102.90	118.41
.01	Pos.	m	7.2763	9.4384	6.8759	9.0638	8.1560	8.1496
5	Vel.	m/s	0.1565	0.8724	0.1190	0.8637	0.1811	0.1825
	Att.	$^\circ\times10^{-3}$	55.267	99.266	60.220	101.20	108.27	120.15
.01	Pos.	m	8.8874	11.345	8.4168	10.752	11.084	11.325
10	Vel.	m/s	0.1844	0.9137	0.1494	0.8959	0.2371	0.2441
	Att.	$^\circ\times10^{-3}$	56.193	100.12	61.253	102.10	110.13	121.30
.1	Pos.	m	18.950	25.100	18.977	24.406	32.064	32.304
1	Vel.	m/s	0.3545	1.1144	0.3320	1.0779	0.5655	0.5829
	Att.	$^\circ\times10^{-3}$	59.555	105.03	64.935	107.36	116.75	128.42
.1	Pos.	m	34.952	42.736	37.007	43.067	64.393	65.950
5	Vel.	m/s	0.5373	1.3390	0.5458	1.3060	0.9509	0.9969
	Att.	$^\circ\times10^{-3}$	64.645	109.99	70.547	112.73	126.84	136.45
.1	Pos.	m	46.599	54.648	50.244	56.055	88.272	89.338
10	Vel.	m/s	0.6591	1.4677	0.6889	1.4434	1.2076	1.2444
	Att.	$^\circ\times10^{-3}$	65.068	112.29	71.030	115.23	127.71	140.38

Table E.13: INS/GGI: Stabilized GGI, Tac. Grade IMUs, High Γ Var., Mach 8

σ_L	Settling Distance:		0 km		100 km		500 km	
Δt	State	Units	Error	Cov.	Error	Cov.	Error	Cov.
.001	Pos.	m	1.0238	1.0623	1.0246	1.0605	0.5124	0.5089
1	Vel.	m/s	0.0466	0.7303	0.0310	0.7823	0.0236	0.0235
	Att.	$^\circ\times10^{-3}$	47.931	91.931	51.553	93.689	92.692	106.02
.001	Pos.	m	1.3676	1.4381	1.3118	1.3403	1.0111	1.0140
5	Vel.	m/s	0.0533	0.7520	0.0375	0.7888	0.0360	0.0363
	Att.	$^\circ\times10^{-3}$	46.739	92.644	50.427	94.161	90.664	106.86
.001	Pos.	m	1.6187	1.7986	1.5422	1.5468	1.3841	1.3869
10	Vel.	m/s	0.0559	0.7741	0.0426	0.7933	0.0452	0.0452
	Att.	$^\circ\times10^{-3}$	46.451	92.978	50.213	94.397	90.274	107.27
.01	Pos.	m	5.5411	7.1543	5.4245	7.1197	4.0157	4.0148
1	Vel.	m/s	0.1151	0.8221	0.0783	0.8260	0.1086	0.1095
	Att.	$^\circ\times10^{-3}$	48.273	94.297	52.529	95.620	94.449	109.11
.01	Pos.	m	8.2062	9.9848	7.8933	9.6023	8.4953	8.5383
5	Vel.	m/s	0.1702	0.8939	0.1327	0.8791	0.2071	0.2112
	Att.	$^\circ\times10^{-3}$	49.109	95.930	53.496	97.341	96.178	111.38
.01	Pos.	m	10.014	11.969	9.6483	11.396	11.678	11.788
10	Vel.	m/s	0.2009	0.9370	0.1670	0.9139	0.2687	0.2768
	Att.	$^\circ\times10^{-3}$	50.440	97.020	54.978	98.505	98.849	112.94
.1	Pos.	m	18.562	25.474	18.772	24.956	32.705	33.025
1	Vel.	m/s	0.3676	1.1412	0.3495	1.1016	0.5985	0.6217
	Att.	$^\circ\times10^{-3}$	55.383	102.44	60.408	104.36	108.61	121.44
.1	Pos.	m	35.079	43.085	37.546	43.795	66.500	66.991
5	Vel.	m/s	0.5603	1.3682	0.5772	1.3357	1.0080	1.0448
	Att.	$^\circ\times10^{-3}$	61.055	107.07	66.696	109.41	119.93	129.40
.1	Pos.	m	45.921	54.914	49.862	56.770	88.660	90.360
10	Vel.	m/s	0.6795	1.4980	0.7169	1.4758	1.2592	1.2972
	Att.	$^\circ\times10^{-3}$	62.306	109.20	68.049	111.75	122.37	133.22

Table E.14: INS/GGI: Stabilized GGI, Tac. Grade IMUs, Low Γ Var., Mach 6

σ_L	Settling Distance:		0 km		100 km		500 km	
Δt	State	Units	Error	Cov.	Error	Cov.	Error	Cov.
.001	Pos.	m	1.0699	1.0826	1.0847	1.0931	0.5017	0.4988
1	Vel.	m/s	0.0454	0.7250	0.0346	0.7820	0.0232	0.0232
	Att.	$^\circ\times10^{-3}$	60.112	99.734	64.988	102.82	116.86	125.15
.001	Pos.	m	1.3865	1.4356	1.3410	1.3593	0.9764	0.9792
5	Vel.	m/s	0.0528	0.7438	0.0395	0.7876	0.0345	0.0345
	Att.	$^\circ\times10^{-3}$	60.145	100.79	65.136	103.72	117.13	126.84
.001	Pos.	m	1.6137	1.7503	1.5440	1.5489	1.3260	1.3213
10	Vel.	m/s	0.0550	0.7616	0.0423	0.7912	0.0418	0.0416
	Att.	$^\circ\times10^{-3}$	58.692	101.30	63.577	104.14	114.32	127.64
.01	Pos.	m	5.4416	7.0280	5.3717	7.0429	3.6341	3.6588
1	Vel.	m/s	0.0990	0.7994	0.0641	0.8136	0.0859	0.0865
	Att.	$^\circ\times10^{-3}$	59.232	103.39	64.438	106.07	115.88	131.18
.01	Pos.	m	7.7770	9.6410	7.4369	9.3079	7.7802	7.7959
5	Vel.	m/s	0.1430	0.8560	0.1044	0.8528	0.1622	0.1637
	Att.	$^\circ\times10^{-3}$	62.767	104.77	68.392	107.50	122.99	133.44
.01	Pos.	m	9.5300	11.519	9.1229	10.989	10.744	10.847
10	Vel.	m/s	0.1688	0.8919	0.1331	0.8809	0.2140	0.2184
	Att.	$^\circ\times10^{-3}$	63.951	105.47	69.727	108.23	125.39	134.41
.1	Pos.	m	18.174	25.055	17.891	24.280	31.132	31.584
1	Vel.	m/s	0.3316	1.0843	0.3032	1.0536	0.5239	0.5446
	Att.	$^\circ\times10^{-3}$	67.543	109.53	73.669	112.52	132.48	139.87
.1	Pos.	m	34.651	42.976	36.255	42.964	64.141	65.278
5	Vel.	m/s	0.5227	1.3113	0.5219	1.2803	0.9159	0.9604
	Att.	$^\circ\times10^{-3}$	69.363	114.36	75.664	117.71	136.06	147.11
.1	Pos.	m	46.324	55.103	49.517	56.075	88.024	88.882
10	Vel.	m/s	0.6384	1.4419	0.6577	1.4180	1.1609	1.2093
	Att.	$^\circ\times10^{-3}$	73.264	116.78	79.936	120.32	143.75	151.00

Table E.15: INS/GGI: Stabilized GGI, Tac. Grade IMUs, Low Γ Var., Mach 7

σ_L	Settling Distance:		0 km		100 km		500 km	
Δt	State	Units	Error	Cov.	Error	Cov.	Error	Cov.
.001	Pos.	m	1.0732	1.0880	1.0834	1.0943	0.4997	0.5013
1	Vel.	m/s	0.0477	0.7275	0.0355	0.7820	0.0232	0.0233
	Att.	$^\circ\times10^{-3}$	51.086	95.050	54.992	97.384	98.865	113.87
.001	Pos.	m	1.4101	1.4508	1.3611	1.3663	0.9988	0.9921
5	Vel.	m/s	0.0545	0.7478	0.0404	0.7880	0.0357	0.0353
	Att.	$^\circ\times10^{-3}$	53.171	95.955	57.448	98.075	103.28	115.19
.001	Pos.	m	1.6341	1.7867	1.5639	1.5639	1.3495	1.3486
10	Vel.	m/s	0.0568	0.7677	0.0439	0.7920	0.0436	0.0433
	Att.	$^\circ\times10^{-3}$	52.543	96.380	56.876	98.407	102.25	115.81
.01	Pos.	m	5.4598	7.1478	5.3621	7.1511	3.8303	3.8534
1	Vel.	m/s	0.1067	0.8106	0.0702	0.8201	0.0991	0.0994
	Att.	$^\circ\times10^{-3}$	54.200	98.032	58.986	99.926	106.05	118.43
.01	Pos.	m	8.0740	9.9015	7.7839	9.5654	8.2502	8.2545
5	Vel.	m/s	0.1573	0.8765	0.1196	0.8681	0.1901	0.1931
	Att.	$^\circ\times10^{-3}$	56.157	99.459	61.202	101.40	110.03	120.44
.01	Pos.	m	9.8845	11.855	9.5303	11.330	11.448	11.452
10	Vel.	m/s	0.1884	0.9172	0.1539	0.9009	0.2520	0.2560
	Att.	$^\circ\times10^{-3}$	54.527	100.37	59.405	102.37	106.80	121.67
.1	Pos.	m	18.711	25.506	18.694	24.897	32.553	32.651
1	Vel.	m/s	0.3616	1.1203	0.3386	1.0859	0.5864	0.6004
	Att.	$^\circ\times10^{-3}$	60.411	105.44	65.873	107.80	118.43	129.08
.1	Pos.	m	35.586	43.425	37.718	43.852	66.796	66.820
5	Vel.	m/s	0.5581	1.3507	0.5672	1.3200	0.9971	1.0257
	Att.	$^\circ\times10^{-3}$	64.907	110.41	70.837	113.19	127.36	137.18
.1	Pos.	m	46.713	55.545	50.404	57.067	89.629	90.614
10	Vel.	m/s	0.6673	1.4833	0.6965	1.4615	1.2289	1.2810
	Att.	$^\circ\times10^{-3}$	65.971	112.72	72.032	115.71	129.51	141.17

Table E.16: INS/GGI: Stabilized GGI, Tac. Grade IMUs, Low Γ Var., Mach 8

σ_L	Settling Distance:		0 km		100 km		500 km	
Δt	State	Units	Error	Cov.	Error	Cov.	Error	Cov.
.001	Pos.	m	1.0823	1.0935	1.0908	1.0963	0.5094	0.5050
1	Vel.	m/s	0.0494	0.7300	0.0360	0.7822	0.0237	0.0236
	Att.	$^\circ\times10^{-3}$	48.022	91.710	51.664	93.444	92.878	105.66
.001	Pos.	m	1.4272	1.4685	1.3787	1.3774	1.0121	1.0120
5	Vel.	m/s	0.0552	0.7518	0.0405	0.7888	0.0366	0.0368
	Att.	$^\circ\times10^{-3}$	46.707	92.485	50.373	93.985	90.554	106.63
.001	Pos.	m	1.6427	1.8272	1.5719	1.5855	1.3873	1.3873
10	Vel.	m/s	0.0574	0.7741	0.0446	0.7935	0.0460	0.0462
	Att.	$^\circ\times10^{-3}$	45.922	92.848	49.678	94.259	89.300	107.11
.01	Pos.	m	5.5815	7.2673	5.4870	7.2597	4.0456	4.0461
1	Vel.	m/s	0.1162	0.8229	0.0785	0.8277	0.1133	0.1140
	Att.	$^\circ\times10^{-3}$	48.178	94.329	52.430	95.657	94.254	109.21
.01	Pos.	m	8.3029	10.109	8.0238	9.7708	8.5573	8.6143
5	Vel.	m/s	0.1709	0.8958	0.1324	0.8823	0.2126	0.2192
	Att.	$^\circ\times10^{-3}$	51.206	96.131	55.814	97.562	100.34	111.73
.01	Pos.	m	10.059	12.101	9.7358	11.582	11.811	11.891
10	Vel.	m/s	0.2032	0.9393	0.1690	0.9177	0.2798	0.2862
	Att.	$^\circ\times10^{-3}$	50.756	97.294	55.301	98.806	99.414	113.41
.1	Pos.	m	18.877	25.778	19.119	25.325	33.298	33.380
1	Vel.	m/s	0.3786	1.1467	0.3604	1.1089	0.6249	0.6378
	Att.	$^\circ\times10^{-3}$	56.281	102.83	61.392	104.79	110.37	122.13
.1	Pos.	m	35.560	43.677	38.063	44.471	67.381	67.894
5	Vel.	m/s	0.5732	1.3803	0.5904	1.3499	1.0368	1.0740
	Att.	$^\circ\times10^{-3}$	60.758	107.48	66.361	109.87	119.31	130.16
.1	Pos.	m	46.409	55.697	50.392	57.653	89.584	91.632
10	Vel.	m/s	0.6804	1.5131	0.7173	1.4931	1.2654	1.3322
	Att.	$^\circ\times10^{-3}$	64.644	109.66	70.643	112.26	127.02	134.09

Table E.17: INS/GGI: Strapdown GGI, Nav. Grade IMUs, High Γ Var., Mach 6

σ_L	Settling Distance:		0 km		100 km		500 km	
Δt	State	Units	Error	Cov.	Error	Cov.	Error	Cov.
.001	Pos.	m	11.729	10.620	10.244	9.5024	17.445	7.2003
1	Vel.	m/s	0.1392	0.7848	0.0637	0.7904	0.0957	0.0435
	Att.	$^\circ\times10^{-3}$	4.5092	23.133	2.2844	22.997	3.5618	1.4451
.001	Pos.	m	14.505	12.739	13.552	11.453	23.442	10.885
5	Vel.	m/s	0.1354	0.8057	0.0734	0.7985	0.1127	0.0595
	Att.	$^\circ\times10^{-3}$	4.9722	23.969	3.1423	23.489	5.0903	2.3304
.001	Pos.	m	15.450	13.848	14.979	12.437	26.155	12.697
10	Vel.	m/s	0.1229	0.8203	0.0758	0.8021	0.1152	0.0662
	Att.	$^\circ\times10^{-3}$	4.8798	24.509	3.4646	23.734	5.7539	2.7714
.01	Pos.	m	13.394	18.565	13.347	17.384	22.260	20.979
1	Vel.	m/s	0.1071	0.8422	0.0651	0.8154	0.0873	0.0882
	Att.	$^\circ\times10^{-3}$	3.6818	24.929	2.5823	24.229	3.6387	3.6432
.01	Pos.	m	19.559	25.050	20.161	24.114	34.501	33.108
5	Vel.	m/s	0.1217	0.8730	0.0808	0.8311	0.1161	0.1142
	Att.	$^\circ\times10^{-3}$	3.9487	25.629	2.8725	24.541	4.0807	4.2050
.01	Pos.	m	24.451	29.499	25.619	28.813	44.376	41.580
10	Vel.	m/s	0.1317	0.8901	0.0945	0.8416	0.1391	0.1328
	Att.	$^\circ\times10^{-3}$	4.0718	25.992	3.0613	24.696	4.4083	4.4844
.1	Pos.	m	45.886	54.123	49.582	55.404	88.854	88.671
1	Vel.	m/s	0.1820	0.9656	0.1570	0.8985	0.2519	0.2387
	Att.	$^\circ\times10^{-3}$	4.7328	27.550	3.6868	25.701	6.0294	6.2251
.1	Pos.	m	77.306	89.088	84.900	94.007	152.44	158.22
5	Vel.	m/s	0.2413	1.0449	0.2381	0.9754	0.3985	0.3887
	Att.	$^\circ\times10^{-3}$	6.1010	29.794	5.5657	27.791	9.4547	9.9866
.1	Pos.	m	92.553	111.81	102.00	119.20	183.19	203.57
10	Vel.	m/s	0.2709	1.0917	0.2767	1.0251	0.4683	0.4854
	Att.	$^\circ\times10^{-3}$	6.7348	31.167	6.4908	29.228	11.145	12.574

Table E.18: INS/GGI: Strapdown GGI, Nav. Grade IMUs, High Γ Var., Mach 7

σ_L	Settling Distance:		0 km		100 km		500 km	
Δt	State	Units	Error	Cov.	Error	Cov.	Error	Cov.
.001	Pos.	m	11.104	10.476	9.8557	9.4242	16.766	7.0500
1	Vel.	m/s	0.1413	0.7926	0.0656	0.7923	0.0999	0.0473
	Att.	$^\circ\times10^{-3}$	4.3016	23.080	2.2747	23.040	3.6024	1.5143
.001	Pos.	m	13.900	12.470	13.257	11.288	22.912	10.536
5	Vel.	m/s	0.1368	0.8140	0.0761	0.8004	0.1170	0.0630
	Att.	$^\circ\times10^{-3}$	4.8303	23.947	3.2593	23.545	5.3360	2.4235
.001	Pos.	m	15.110	13.582	15.007	12.291	26.152	12.367
10	Vel.	m/s	0.1236	0.8296	0.0795	0.8042	0.1228	0.0699
	Att.	$^\circ\times10^{-3}$	4.3971	24.516	3.2534	23.769	5.3480	2.8284
.01	Pos.	m	13.988	18.801	14.209	17.863	23.748	21.796
1	Vel.	m/s	0.1110	0.8534	0.0694	0.8200	0.0955	0.0964
	Att.	$^\circ\times10^{-3}$	3.5192	24.753	2.4831	24.156	3.5028	3.5073
.01	Pos.	m	20.658	26.176	21.625	25.643	37.226	35.859
5	Vel.	m/s	0.1292	0.8886	0.0905	0.8404	0.1330	0.1323
	Att.	$^\circ\times10^{-3}$	3.8057	25.499	2.7287	24.466	3.9343	4.0662
.01	Pos.	m	25.999	31.048	27.575	30.847	47.922	45.251
10	Vel.	m/s	0.1423	0.9081	0.1088	0.8538	0.1672	0.1569
	Att.	$^\circ\times10^{-3}$	3.9337	25.916	2.9311	24.647	4.2702	4.3911
.1	Pos.	m	47.962	57.258	52.234	59.408	93.650	95.971
1	Vel.	m/s	0.1960	0.9921	0.1789	0.9232	0.2935	0.2901
	Att.	$^\circ\times10^{-3}$	4.9006	27.748	3.8088	25.888	6.2745	6.5618
.1	Pos.	m	78.696	95.330	86.691	101.56	155.67	171.91
5	Vel.	m/s	0.2675	1.0880	0.2723	1.0217	0.4604	0.4854
	Att.	$^\circ\times10^{-3}$	6.1600	30.271	5.6886	28.297	9.6896	10.899
.1	Pos.	m	93.744	118.30	103.55	127.03	185.99	217.69
10	Vel.	m/s	0.3018	1.1446	0.3159	1.0832	0.5398	0.6034
	Att.	$^\circ\times10^{-3}$	7.0573	31.695	6.9041	29.799	11.894	13.602

Table E.19: INS/GGI: Strapdown GGI, Nav. Grade IMUs, High Γ Var., Mach 8

σ_L	Settling Distance:		0 km		100 km		500 km	
Δt	State	Units	Error	Cov.	Error	Cov.	Error	Cov.
.001	Pos.	m	12.367	11.018	11.476	9.9472	19.885	8.0657
1	Vel.	m/s	0.1544	0.8020	0.0853	0.7962	0.1172	0.0552
	Att.	$^\circ\times10^{-3}$	4.4648	23.126	2.8837	23.246	4.2404	1.9055
.001	Pos.	m	15.171	13.361	14.918	12.306	26.187	12.310
5	Vel.	m/s	0.1518	0.8221	0.0964	0.8066	0.1360	0.0755
	Att.	$^\circ\times10^{-3}$	4.2822	23.834	3.1523	23.709	4.7159	2.7391
.001	Pos.	m	16.482	14.483	16.675	13.419	29.393	14.311
10	Vel.	m/s	0.1408	0.8363	0.0994	0.8111	0.1406	0.0838
	Att.	$^\circ\times10^{-3}$	3.8930	24.307	3.0941	23.857	4.6375	3.0061
.01	Pos.	m	13.895	19.934	14.363	19.224	24.855	23.918
1	Vel.	m/s	0.1185	0.8676	0.0780	0.8294	0.1070	0.1142
	Att.	$^\circ\times10^{-3}$	3.5846	24.570	2.5018	24.104	3.2687	3.4106
.01	Pos.	m	21.052	27.579	22.285	27.402	39.203	38.684
5	Vel.	m/s	0.1406	0.9051	0.1037	0.8532	0.1532	0.1569
	Att.	$^\circ\times10^{-3}$	4.0411	25.220	2.8674	24.415	3.8765	3.9705
.01	Pos.	m	25.159	32.570	26.891	32.803	47.607	48.427
10	Vel.	m/s	0.1488	0.9256	0.1182	0.8683	0.1796	0.1855
	Att.	$^\circ\times10^{-3}$	4.0596	25.603	2.9650	24.615	4.1312	4.3304
.1	Pos.	m	49.816	60.139	54.530	63.026	98.044	102.57
1	Vel.	m/s	0.2150	1.0186	0.2047	0.9496	0.3394	0.3466
	Att.	$^\circ\times10^{-3}$	5.0269	27.976	3.9617	26.101	6.5785	6.9411
.1	Pos.	m	78.404	99.729	86.566	106.91	155.69	181.59
5	Vel.	m/s	0.2929	1.1317	0.3047	1.0695	0.5201	0.5838
	Att.	$^\circ\times10^{-3}$	6.2973	30.657	5.8815	28.707	10.090	11.632
.1	Pos.	m	88.244	121.32	97.586	130.84	175.51	224.55
10	Vel.	m/s	0.3205	1.1950	0.3393	1.1390	0.5813	0.7134
	Att.	$^\circ\times10^{-3}$	6.6646	32.032	6.4966	30.163	11.191	14.253

Table E.20: INS/GGI: Strapdown GGI, Nav. Grade IMUs, Low Γ Var., Mach 6

σ_L	Settling Distance:		0 km		100 km		500 km	
Δt	State	Units	Error	Cov.	Error	Cov.	Error	Cov.
.001	Pos.	m	16.736	12.817	15.795	11.646	27.817	10.743
1	Vel.	m/s	0.1507	0.7932	0.0747	0.7985	0.1204	0.0606
	Att.	$^\circ\times10^{-3}$	5.5260	23.231	3.4075	23.336	4.8853	2.1038
.001	Pos.	m	27.762	17.487	28.071	16.522	50.143	19.522
5	Vel.	m/s	0.1597	0.8131	0.0956	0.8088	0.1578	0.0814
	Att.	$^\circ\times10^{-3}$	5.7841	24.086	4.0349	23.907	6.0346	3.1310
.001	Pos.	m	34.850	20.555	36.120	19.789	64.642	25.399
10	Vel.	m/s	0.1630	0.8266	0.1109	0.8145	0.1859	0.0926
	Att.	$^\circ\times10^{-3}$	5.7427	24.532	4.2648	24.113	6.2382	3.5023
.01	Pos.	m	30.791	37.114	32.988	37.826	58.910	57.459
1	Vel.	m/s	0.1341	0.8678	0.1011	0.8449	0.1597	0.1522
	Att.	$^\circ\times10^{-3}$	4.3583	25.368	3.4604	24.846	4.7248	4.7618
.01	Pos.	m	48.175	55.893	52.358	58.402	93.832	94.657
5	Vel.	m/s	0.1744	0.9180	0.1472	0.8837	0.2413	0.2300
	Att.	$^\circ\times10^{-3}$	5.5147	26.683	4.6128	25.968	6.8237	6.7813
.01	Pos.	m	58.321	67.103	63.606	70.744	114.09	116.99
10	Vel.	m/s	0.1971	0.9460	0.1738	0.9070	0.2891	0.2790
	Att.	$^\circ\times10^{-3}$	6.0139	27.524	5.1380	26.720	7.7761	8.1360
.1	Pos.	m	90.808	122.70	99.781	132.15	179.53	227.86
1	Vel.	m/s	0.2657	1.0718	0.2551	1.0193	0.4308	0.5219
	Att.	$^\circ\times10^{-3}$	7.5158	31.939	6.6880	30.654	11.441	15.149
.1	Pos.	m	89.802	166.73	98.804	180.82	177.73	315.34
5	Vel.	m/s	0.2597	1.1657	0.2557	1.1131	0.4297	0.7051
	Att.	$^\circ\times10^{-3}$	6.8928	35.035	6.3846	33.646	10.840	20.532
.1	Pos.	m	84.666	180.80	93.196	196.29	167.60	342.94
10	Vel.	m/s	0.2499	1.1996	0.2496	1.1481	0.4171	0.7629
	Att.	$^\circ\times10^{-3}$	6.1561	35.914	5.8084	34.522	9.7851	22.109

Table E.21: INS/GGI: Strapdown GGI, Nav. Grade IMUs, Low Γ Var., Mach 7

σ_L	Settling Distance:		0 km		100 km		500 km	
Δt	State	Units	Error	Cov.	Error	Cov.	Error	Cov.
.001	Pos.	m	17.857	13.173	17.279	12.152	30.535	11.657
1	Vel.	m/s	0.1582	0.8009	0.0815	0.8010	0.1328	0.0658
	Att.	$^\circ\times10^{-3}$	5.3710	23.212	3.4249	23.407	5.0142	2.2169
.001	Pos.	m	30.343	18.481	31.280	17.788	55.909	21.800
5	Vel.	m/s	0.1744	0.8235	0.1121	0.8139	0.1878	0.0920
	Att.	$^\circ\times10^{-3}$	5.4181	24.008	3.8370	23.915	5.7317	3.1305
.001	Pos.	m	38.831	21.978	41.050	21.551	73.584	28.572
10	Vel.	m/s	0.1809	0.8397	0.1361	0.8217	0.2304	0.1075
	Att.	$^\circ\times10^{-3}$	5.1474	24.483	4.0197	24.106	6.1252	3.4762
.01	Pos.	m	33.584	39.647	36.310	40.899	64.936	63.044
1	Vel.	m/s	0.1514	0.8903	0.1219	0.8623	0.1985	0.1888
	Att.	$^\circ\times10^{-3}$	4.3859	25.354	3.4727	24.957	4.9292	4.9571
.01	Pos.	m	50.680	59.498	55.327	62.732	99.201	102.57
5	Vel.	m/s	0.1975	0.9501	0.1743	0.9115	0.2903	0.2912
	Att.	$^\circ\times10^{-3}$	5.5170	26.881	4.5459	26.269	6.8538	7.3190
.01	Pos.	m	60.548	71.466	66.332	75.954	118.99	126.52
10	Vel.	m/s	0.2215	0.9833	0.2055	0.9407	0.3466	0.3547
	Att.	$^\circ\times10^{-3}$	6.1351	27.847	5.2935	27.128	8.1956	8.8647
.1	Pos.	m	82.158	124.57	90.409	134.71	162.65	232.54
1	Vel.	m/s	0.2727	1.1192	0.2668	1.0679	0.4533	0.6295
	Att.	$^\circ\times10^{-3}$	7.1033	32.266	6.2155	30.964	10.633	15.707
.1	Pos.	m	75.095	158.09	82.684	171.70	148.69	298.79
5	Vel.	m/s	0.2520	1.2072	0.2515	1.1576	0.4228	0.7945
	Att.	$^\circ\times10^{-3}$	6.0438	34.694	5.5046	33.233	9.2896	19.790
.1	Pos.	m	70.082	168.51	77.204	183.11	138.77	319.00
10	Vel.	m/s	0.2397	1.2406	0.2429	1.1926	0.4062	0.8464
	Att.	$^\circ\times10^{-3}$	5.5213	35.355	5.1550	33.877	8.6051	20.949

Table E.22: INS/GGI: Strapdown GGI, Nav. Grade IMUs, Low Γ Var., Mach 8

σ_L	Settling Distance:		0 km		100 km		500 km	
Δt	State	Units	Error	Cov.	Error	Cov.	Error	Cov.
.001	Pos.	m	18.948	13.630	18.783	12.758	33.302	12.747
1	Vel.	m/s	0.1662	0.8087	0.0916	0.8044	0.1511	0.0728
	Att.	$^\circ\times10^{-3}$	5.0291	23.172	3.1762	23.456	4.7050	2.2858
.001	Pos.	m	34.199	19.541	35.953	19.108	64.368	24.178
5	Vel.	m/s	0.1949	0.8348	0.1389	0.8209	0.2360	0.1063
	Att.	$^\circ\times10^{-3}$	5.2052	23.933	3.7671	23.920	5.6605	3.1211
.001	Pos.	m	41.521	23.393	44.352	23.283	79.512	31.693
10	Vel.	m/s	0.2018	0.8537	0.1625	0.8310	0.2786	0.1269
	Att.	$^\circ\times10^{-3}$	5.1076	24.458	4.1260	24.115	6.2961	3.4723
.01	Pos.	m	35.201	41.704	38.255	43.401	68.468	67.616
1	Vel.	m/s	0.1685	0.9128	0.1419	0.8810	0.2335	0.2290
	Att.	$^\circ\times10^{-3}$	4.4146	25.392	3.4656	25.089	5.1002	5.1848
.01	Pos.	m	53.276	62.397	58.394	66.225	104.72	108.98
5	Vel.	m/s	0.2217	0.9813	0.2049	0.9398	0.3467	0.3551
	Att.	$^\circ\times10^{-3}$	5.7894	27.100	4.7768	26.549	7.3772	7.8135
.01	Pos.	m	62.383	74.728	68.537	79.877	122.99	133.72
10	Vel.	m/s	0.2482	1.0187	0.2381	0.9741	0.4062	0.4310
	Att.	$^\circ\times10^{-3}$	6.2644	28.147	5.4253	27.464	8.6084	9.4613
.1	Pos.	m	71.488	122.86	78.717	133.15	141.60	229.75
1	Vel.	m/s	0.2664	1.1578	0.2629	1.1083	0.4454	0.7168
	Att.	$^\circ\times10^{-3}$	6.3558	32.340	5.4502	30.981	9.2523	15.735
.1	Pos.	m	61.617	148.17	67.863	161.01	121.98	279.42
5	Vel.	m/s	0.2389	1.2399	0.2409	1.1930	0.4037	0.8612
	Att.	$^\circ\times10^{-3}$	5.3044	34.249	4.7899	32.707	7.9991	18.841
.1	Pos.	m	62.495	156.54	68.916	170.15	123.83	295.48
10	Vel.	m/s	0.2423	1.2741	0.2490	1.2292	0.4180	0.9109
	Att.	$^\circ\times10^{-3}$	5.1465	34.808	4.8173	33.251	7.9939	19.819

E.3 Global Positioning System Aided Navigation

The baseline hypersonic INS/GPS Monte Carlo simulation results are summarized in Tables E.23–E.34.

Tables E.23–E.25 list the MRSE results for the Mach 6, 7, and 8 cases with navigation grade IMUs and GPS pseudorange, ρ, and pseudorange rate, $\dot{\rho}$, updates at intervals of 1 to 300 seconds. Tables E.26–E.28 on pg. 383-385 summarize the tactical grade IMU, ρ and $\dot{\rho}$ results as GPS updates are simulated every 1–300 seconds.

Tables E.29–E.34 list the pseudorange-only INS/GPS results for the hypersonic Monte Carlo simulations. The first half of the tables, on pg. 386–388, are performed with the simulated navigation grade IMU specifications. And Tables E.32–E.34 on pg. 389–391 list the tactical grade IMU, pseudorange-only INS simulations for the Mach 6, 7, and 8 cases.

All INS/GPS simulations are performed over the high gravitational gradient variation trajectories since the low Γ variation trajectories produce essentially the same GPS visibility and geometric dilution of precision (GDOP) values as the high Γ trajectories, as shown in Sec. D.3. Therefore, the INS/GPS navigation performance should be nearly identical between the two trajectories.

Table E.23: INS/GPS: ρ & $\dot{\rho}$ Updates, Nav. Grade IMUs, Mach 6

	Settling Distance:		0 km		100 km		500 km	
Δt	State	Units	Error	Cov.	Error	Cov.	Error	Cov.
1	Pos.	m	1.0153	0.5806	1.0771	0.6039	0.1663	0.1357
	Vel.	m/s	0.1927	0.2094	0.2074	0.2259	0.0032	0.0029
	Att.	$^\circ\times10^{-3}$	3.5271	41.958	3.0019	40.874	5.3976	5.3941
10	Pos.	m	1.2715	0.7988	1.2421	0.7429	0.4642	0.3948
	Vel.	m/s	0.2113	0.2222	0.2175	0.2287	0.0072	0.0065
	Att.	$^\circ\times10^{-3}$	4.5543	43.681	4.2191	41.671	7.5889	7.5228
30	Pos.	m	1.6828	1.3727	1.3366	0.9194	0.9005	0.6841
	Vel.	m/s	0.2223	0.2472	0.2120	0.2308	0.0122	0.0102
	Att.	$^\circ\times10^{-3}$	5.5208	46.314	5.4406	42.562	9.7880	9.8346
60	Pos.	m	2.4643	2.5036	1.3077	1.0611	1.1323	0.9879
	Vel.	m/s	0.2375	0.2713	0.2128	0.2327	0.0151	0.0143
	Att.	$^\circ\times10^{-3}$	6.0396	47.918	6.6964	43.683	12.048	12.652
90	Pos.	m	2.8265	2.6694	1.6654	1.2651	1.5420	1.3510
	Vel.	m/s	0.2465	0.2706	0.2213	0.2325	0.0200	0.0189
	Att.	$^\circ\times10^{-3}$	7.1277	48.894	7.9054	44.791	14.225	15.355
120	Pos.	m	3.1126	3.0220	1.9793	1.6316	2.0355	2.0056
	Vel.	m/s	0.2494	0.2793	0.2244	0.2413	0.0248	0.0285
	Att.	$^\circ\times10^{-3}$	5.6479	51.756	6.2606	48.050	11.264	22.974
180	Pos.	m	11.106	12.080	10.916	11.746	18.190	20.310
	Vel.	m/s	0.3209	0.3696	0.3052	0.3414	0.1851	0.2174
	Att.	$^\circ\times10^{-3}$	4.5634	61.997	5.0503	59.655	9.0826	46.199
240	Pos.	m	23.191	23.167	24.354	24.053	42.451	42.454
	Vel.	m/s	0.4246	0.4606	0.4203	0.4427	0.3931	0.4001
	Att.	$^\circ\times10^{-3}$	5.8967	64.220	6.5311	62.127	11.747	50.222
300	Pos.	m	31.562	42.041	33.561	45.032	59.069	80.218
	Vel.	m/s	0.4825	0.5798	0.4822	0.5754	0.4828	0.6434
	Att.	$^\circ\times10^{-3}$	5.5397	65.586	6.1345	63.591	11.033	51.624

Table E.24: INS/GPS: ρ & $\dot{\rho}$ Updates, Nav. Grade IMUs, Mach 7

	Settling Distance:		0 km		100 km		500 km	
Δt	State	Units	Error	Cov.	Error	Cov.	Error	Cov.
1	Pos.	m	0.8455	0.5903	0.8878	0.6121	0.1574	0.1398
	Vel.	m/s	0.1983	0.2137	0.2133	0.2300	0.0033	0.0031
	Att.	$^\circ\times10^{-3}$	3.8905	42.456	3.3065	41.081	5.9456	5.8611
10	Pos.	m	1.3752	0.8313	1.3505	0.7700	0.5407	0.4261
	Vel.	m/s	0.2039	0.2237	0.2076	0.2283	0.0090	0.0076
	Att.	$^\circ\times10^{-3}$	5.4510	44.839	5.1901	42.500	9.3365	9.5509
30	Pos.	m	1.5499	1.3799	1.1710	0.9195	0.8136	0.7112
	Vel.	m/s	0.2244	0.2480	0.2124	0.2302	0.0130	0.0119
	Att.	$^\circ\times10^{-3}$	6.5897	47.657	6.8312	43.927	12.290	13.102
60	Pos.	m	2.4149	2.2778	1.4855	1.1235	1.2897	1.0805
	Vel.	m/s	0.2342	0.2650	0.2103	0.2298	0.0189	0.0171
	Att.	$^\circ\times10^{-3}$	7.4678	49.486	8.2850	45.462	14.908	16.781
90	Pos.	m	2.9581	2.6011	1.9840	1.4404	1.8732	1.6322
	Vel.	m/s	0.2573	0.2777	0.2316	0.2422	0.0255	0.0249
	Att.	$^\circ\times10^{-3}$	7.7110	51.502	8.5540	47.755	15.391	22.059
120	Pos.	m	3.0919	2.8461	2.1925	1.7505	2.3539	2.2219
	Vel.	m/s	0.2482	0.2752	0.2239	0.2408	0.0300	0.0347
	Att.	$^\circ\times10^{-3}$	5.4358	55.547	6.0259	52.369	10.840	32.277
180	Pos.	m	14.377	14.707	14.725	14.959	25.043	26.091
	Vel.	m/s	0.3767	0.4082	0.3659	0.3880	0.2840	0.3053
	Att.	$^\circ\times10^{-3}$	5.4406	64.566	6.0259	62.500	10.837	50.581
240	Pos.	m	26.145	25.994	27.859	27.499	48.990	48.660
	Vel.	m/s	0.4703	0.4977	0.4720	0.4878	0.4897	0.4863
	Att.	$^\circ\times10^{-3}$	6.6106	65.302	7.3276	63.290	13.180	51.365
300	Pos.	m	29.752	64.824	31.769	70.655	55.436	126.34
	Vel.	m/s	0.4479	0.7566	0.4454	0.7759	0.4270	1.0132
	Att.	$^\circ\times10^{-3}$	4.7688	69.240	5.2797	67.513	9.4946	55.742

Table E.25: INS/GPS: ρ & $\dot{\rho}$ Updates, Nav. Grade IMUs, Mach 8

	Settling Distance:		0 km		100 km		500 km	
Δt	State	Units	Error	Cov.	Error	Cov.	Error	Cov.
1	Pos.	m	0.9622	0.5905	1.0141	0.6103	0.1789	0.1487
	Vel.	m/s	0.1968	0.2104	0.2108	0.2256	0.0038	0.0035
	Att.	$^\circ\times10^{-3}$	4.4477	43.108	3.8104	41.461	6.8537	6.7323
10	Pos.	m	1.1600	0.8466	1.1092	0.7793	0.5429	0.4498
	Vel.	m/s	0.2114	0.2272	0.2148	0.2301	0.0097	0.0087
	Att.	$^\circ\times10^{-3}$	6.7862	46.227	6.6718	43.646	12.005	12.208
30	Pos.	m	1.9290	1.4572	1.5304	0.9671	0.9382	0.7807
	Vel.	m/s	0.2315	0.2504	0.2165	0.2303	0.0158	0.0140
	Att.	$^\circ\times10^{-3}$	7.8858	49.351	8.4014	45.692	15.119	17.080
60	Pos.	m	2.5532	2.2038	1.7487	1.2356	1.4404	1.2615
	Vel.	m/s	0.2454	0.2686	0.2206	0.2354	0.0222	0.0214
	Att.	$^\circ\times10^{-3}$	9.1541	51.822	10.158	48.112	18.282	22.583
90	Pos.	m	2.8408	2.4777	2.0405	1.5070	1.9100	1.7485
	Vel.	m/s	0.2515	0.2789	0.2268	0.2455	0.0286	0.0294
	Att.	$^\circ\times10^{-3}$	7.2581	54.453	8.0517	51.108	14.489	29.156
120	Pos.	m	5.1623	5.4951	4.6559	4.8938	7.1414	7.9608
	Vel.	m/s	0.2785	0.3165	0.2585	0.2881	0.0998	0.1173
	Att.	$^\circ\times10^{-3}$	4.4391	59.660	4.9161	56.974	8.8425	40.150
180	Pos.	m	16.510	16.777	17.233	17.465	29.480	30.614
	Vel.	m/s	0.4178	0.4437	0.4113	0.4302	0.3642	0.3831
	Att.	$^\circ\times10^{-3}$	6.7129	65.682	7.4417	63.686	13.388	51.515
240	Pos.	m	22.716	36.251	24.158	39.086	42.094	69.547
	Vel.	m/s	0.4401	0.6058	0.4381	0.6099	0.4248	0.7061
	Att.	$^\circ\times10^{-3}$	5.8799	68.180	6.5165	66.368	11.722	54.344
300	Pos.	m	32.998	85.686	35.535	94.040	62.54	168.49
	Vel.	m/s	0.4395	0.9194	0.4357	0.9598	0.4049	1.3491
	Att.	$^\circ\times10^{-3}$	3.7842	73.128	4.1873	71.742	7.5293	61.532

Table E.26: INS/GPS: ρ & $\dot{\rho}$ Updates, Tac. Grade IMUs, Mach 6

	Settling Distance:		0 km		100 km		500 km	
Δt	State	Units	Error	Cov.	Error	Cov.	Error	Cov.
1	Pos.	m	1.1096	0.6226	1.1786	0.6472	0.2357	0.2116
	Vel.	m/s	0.2057	0.2196	0.2207	0.2361	0.0130	0.0127
	Att.	$^\circ\times10^{-3}$	58.597	98.863	63.113	102.35	113.49	124.20
10	Pos.	m	1.4541	0.8889	1.4315	0.8332	0.6415	0.5557
	Vel.	m/s	0.2182	0.2332	0.2227	0.2385	0.0220	0.0214
	Att.	$^\circ\times10^{-3}$	58.819	99.965	63.534	103.22	114.25	125.83
30	Pos.	m	1.8339	1.5308	1.4421	1.0466	1.0820	0.9521
	Vel.	m/s	0.2380	0.2600	0.2224	0.2398	0.0316	0.0304
	Att.	$^\circ\times10^{-3}$	59.788	101.18	64.886	103.82	116.68	126.97
60	Pos.	m	2.8754	2.8610	1.6789	1.3774	1.6798	1.5718
	Vel.	m/s	0.2575	0.2877	0.2274	0.2446	0.0453	0.0447
	Att.	$^\circ\times10^{-3}$	59.393	102.18	64.760	104.56	116.46	128.37
90	Pos.	m	3.5836	3.4358	2.4028	1.9909	2.8881	2.6856
	Vel.	m/s	0.2745	0.3019	0.2447	0.2595	0.0680	0.0666
	Att.	$^\circ\times10^{-3}$	59.042	102.98	64.373	105.47	115.76	130.08
120	Pos.	m	7.5166	7.5455	6.8036	6.6463	10.945	11.152
	Vel.	m/s	0.3491	0.3749	0.3268	0.3411	0.2208	0.2262
	Att.	$^\circ\times10^{-3}$	61.312	105.51	66.868	108.18	120.25	133.84
180	Pos.	m	31.672	31.541	33.758	33.299	59.538	59.114
	Vel.	m/s	0.6227	0.6566	0.6355	0.6551	0.7996	0.7968
	Att.	$^\circ\times10^{-3}$	65.757	110.82	71.701	113.89	128.94	141.69
240	Pos.	m	53.853	50.643	58.373	54.497	103.74	97.221
	Vel.	m/s	0.8192	0.8214	0.8535	0.8381	1.1879	1.1220
	Att.	$^\circ\times10^{-3}$	70.645	112.98	77.071	116.21	138.60	144.95
300	Pos.	m	79.024	83.950	86.273	91.462	153.84	163.74
	Vel.	m/s	0.9895	1.0497	1.0406	1.0904	1.5111	1.5624
	Att.	$^\circ\times10^{-3}$	71.162	114.82	77.631	118.20	139.61	147.89

Table E.27: INS/GPS: ρ & $\dot{\rho}$ Updates, Tac. Grade IMUs, Mach 7

	Settling Distance:		0 km		100 km		500 km	
Δt	State	Units	Error	Cov.	Error	Cov.	Error	Cov.
	Pos.	m	0.8448	0.6190	0.8864	0.6419	0.2273	0.2090
1	Vel.	m/s	0.2051	0.2153	0.2195	0.2307	0.0129	0.0127
	Att.	$^\circ\times10^{-3}$	49.379	94.176	52.828	97.010	94.972	113.08
	Pos.	m	1.2727	0.8790	1.2359	0.8162	0.6082	0.5476
10	Vel.	m/s	0.2143	0.2328	0.2170	0.2361	0.0220	0.0214
	Att.	$^\circ\times10^{-3}$	51.267	95.147	55.186	97.660	99.220	114.31
	Pos.	m	1.8464	1.5253	1.4645	1.0484	1.0640	0.9437
30	Vel.	m/s	0.2338	0.2616	0.2181	0.2408	0.0317	0.0303
	Att.	$^\circ\times10^{-3}$	52.478	96.194	56.933	98.105	102.36	115.15
	Pos.	m	2.9395	2.6398	1.9315	1.4369	1.9255	1.6422
60	Vel.	m/s	0.2665	0.2880	0.2366	0.2490	0.0492	0.0462
	Att.	$^\circ\times10^{-3}$	53.318	97.030	58.145	98.723	104.54	116.33
	Pos.	m	4.4633	4.2712	3.6240	3.2581	5.1615	5.0088
90	Vel.	m/s	0.2981	0.3256	0.2724	0.2902	0.1213	0.1211
	Att.	$^\circ\times10^{-3}$	55.153	98.446	60.167	100.25	108.18	118.52
	Pos.	m	8.0701	8.0768	7.6707	7.5506	12.515	12.803
120	Vel.	m/s	0.3752	0.3991	0.3581	0.3726	0.2738	0.2811
	Att.	$^\circ\times10^{-3}$	57.211	101.13	62.404	103.15	112.20	122.64
	Pos.	m	31.716	31.481	33.962	33.502	59.872	59.422
180	Vel.	m/s	0.6650	0.6949	0.6823	0.7016	0.8758	0.8694
	Att.	$^\circ\times10^{-3}$	60.609	106.55	66.094	109.00	118.83	130.79
	Pos.	m	57.174	57.189	62.255	62.091	110.92	110.89
240	Vel.	m/s	0.8701	0.8962	0.9099	0.9262	1.2780	1.2801
	Att.	$^\circ\times10^{-3}$	63.780	109.24	69.620	111.91	125.18	135.23
	Pos.	m	78.038	96.760	85.400	106.03	152.13	189.96
300	Vel.	m/s	1.0128	1.1543	1.0684	1.2122	1.5615	1.7881
	Att.	$^\circ\times10^{-3}$	63.888	110.70	69.728	113.51	125.37	137.68

Table E.28: INS/GPS: ρ & $\dot{\rho}$ Updates, Tac. Grade IMUs, Mach 8

	Settling Distance:		0 km		100 km		500 km	
Δt	State	Units	Error	Cov.	Error	Cov.	Error	Cov.
1	Pos.	m	1.0085	0.6247	1.0643	0.6462	0.2400	0.2145
	Vel.	m/s	0.2000	0.2160	0.2132	0.2308	0.0130	0.0127
	Att.	$^\circ\times10^{-3}$	45.699	90.855	48.730	93.182	87.610	105.07
10	Pos.	m	1.2069	0.9133	1.1569	0.8446	0.6479	0.5656
	Vel.	m/s	0.2170	0.2353	0.2186	0.2368	0.0227	0.0219
	Att.	$^\circ\times10^{-3}$	48.046	91.764	51.656	93.694	92.880	105.99
30	Pos.	m	1.9185	1.5571	1.5177	1.0597	1.1516	0.9738
	Vel.	m/s	0.2358	0.2607	0.2184	0.2384	0.0332	0.0316
	Att.	$^\circ\times10^{-3}$	47.854	92.678	51.902	94.035	93.323	106.61
60	Pos.	m	2.9568	2.5538	2.1535	1.5688	2.1568	1.8963
	Vel.	m/s	0.2609	0.2874	0.2340	0.2519	0.0568	0.0532
	Att.	$^\circ\times10^{-3}$	46.984	93.332	51.224	94.517	92.097	107.46
90	Pos.	m	4.8598	4.7534	4.2319	4.0276	6.3613	6.4023
	Vel.	m/s	0.3241	0.3447	0.3021	0.3148	0.1637	0.1679
	Att.	$^\circ\times10^{-3}$	47.948	95.610	52.266	96.965	93.973	110.74
120	Pos.	m	12.869	12.827	13.156	13.006	22.368	22.565
	Vel.	m/s	0.4536	0.4793	0.4473	0.4650	0.4362	0.4427
	Att.	$^\circ\times10^{-3}$	52.335	99.249	57.059	100.89	102.59	116.28
180	Pos.	m	31.637	32.036	34.038	34.329	59.816	60.900
	Vel.	m/s	0.6769	0.7170	0.6973	0.7292	0.8950	0.9147
	Att.	$^\circ\times10^{-3}$	58.800	103.74	64.210	105.78	115.46	123.63
240	Pos.	m	51.035	57.997	55.520	63.195	98.385	112.88
	Vel.	m/s	0.8548	0.9264	0.8920	0.9628	1.2266	1.3421
	Att.	$^\circ\times10^{-3}$	58.527	105.76	63.888	107.97	114.87	127.11
300	Pos.	m	89.218	118.92	97.933	130.88	174.56	234.72
	Vel.	m/s	1.1044	1.3274	1.1693	1.4075	1.7276	2.1370
	Att.	$^\circ\times10^{-3}$	61.095	109.35	66.738	111.91	120.01	133.51

Table E.29: INS/GPS: ρ Updates, Nav. Grade IMUs, Mach 6

	Settling Distance:		0 km		100 km		500 km	
Δt	State	Units	Error	Cov.	Error	Cov.	Error	Cov.
	Pos.	m	5.7337	2.9529	5.9940	2.9678	1.2628	1.0801
1	Vel.	m/s	0.0550	0.7373	0.0283	0.7786	0.0184	0.0175
	Att.	$^\circ\times10^{-3}$	8.5429	48.760	8.6979	45.839	15.652	17.935
	Pos.	m	6.9961	4.3938	6.8666	4.0566	3.4967	3.0628
10	Vel.	m/s	0.0747	0.7764	0.0429	0.7915	0.0452	0.0428
	Att.	$^\circ\times10^{-3}$	11.746	55.214	12.588	52.394	22.654	32.738
	Pos.	m	9.0135	6.6522	8.7520	5.3034	6.2100	5.2876
30	Vel.	m/s	0.0718	0.8354	0.0566	0.8039	0.0712	0.0661
	Att.	$^\circ\times10^{-3}$	11.261	58.193	12.480	55.419	22.461	39.118
	Pos.	m	10.070	10.867	9.8697	6.6449	8.5678	7.7020
60	Vel.	m/s	0.0671	0.9110	0.0697	0.8158	0.0946	0.0885
	Att.	$^\circ\times10^{-3}$	10.182	59.675	11.301	57.091	20.339	42.503
	Pos.	m	11.880	11.895	11.811	7.8020	11.550	9.7868
90	Vel.	m/s	0.0777	0.9195	0.0815	0.8253	0.1157	0.1065
	Att.	$^\circ\times10^{-3}$	8.7932	60.582	9.7577	58.121	17.559	44.546
	Pos.	m	12.780	13.097	12.770	9.1506	12.993	12.245
120	Vel.	m/s	0.0852	0.9304	0.0898	0.8374	0.1308	0.1294
	Att.	$^\circ\times10^{-3}$	6.7070	61.278	7.4391	58.907	13.385	46.002
	Pos.	m	15.024	39.844	15.360	39.181	18.405	66.673
180	Vel.	m/s	0.0938	1.1736	0.0991	1.1091	0.1461	0.6587
	Att.	$^\circ\times10^{-3}$	1.9838	66.883	2.1874	64.952	3.9310	52.433
	Pos.	m	17.499	87.837	18.049	92.682	22.807	163.05
240	Vel.	m/s	0.1029	1.5607	0.1094	1.5430	0.1662	1.4802
	Att.	$^\circ\times10^{-3}$	1.0613	73.096	1.1632	71.708	2.0874	61.543
	Pos.	m	18.788	132.14	19.601	141.79	26.505	251.38
300	Vel.	m/s	0.1143	1.8582	0.1222	1.8749	0.1906	2.0820
	Att.	$^\circ\times10^{-3}$	0.9091	76.269	0.9939	75.185	1.7829	66.917

Table E.30: INS/GPS: ρ Updates, Nav. Grade IMUs, Mach 7

	Settling Distance:		0 km		100 km		500 km	
Δt	State	Units	Error	Cov.	Error	Cov.	Error	Cov.
1	Pos.	m	5.8780	3.0802	6.1105	3.0814	1.4060	1.1771
	Vel.	m/s	0.0607	0.7435	0.0309	0.7803	0.0225	0.0209
	Att.	$^\circ\times10^{-3}$	10.077	51.500	10.472	48.545	18.846	23.953
10	Pos.	m	7.5515	4.6390	7.4026	4.2807	3.9170	3.4009
	Vel.	m/s	0.0809	0.7870	0.0469	0.7959	0.0533	0.0506
	Att.	$^\circ\times10^{-3}$	11.414	58.079	12.276	55.469	22.093	38.894
30	Pos.	m	8.9762	6.7441	8.7676	5.3157	6.5078	5.4300
	Vel.	m/s	0.0754	0.8500	0.0642	0.8084	0.0842	0.0738
	Att.	$^\circ\times10^{-3}$	9.7306	60.325	10.777	57.827	19.395	43.674
60	Pos.	m	10.696	10.257	10.500	6.7629	9.1676	7.9058
	Vel.	m/s	0.0726	0.9153	0.0761	0.8219	0.1068	0.0992
	Att.	$^\circ\times10^{-3}$	8.3040	61.522	9.2145	59.171	16.580	46.260
90	Pos.	m	11.768	11.502	11.754	8.1620	11.880	10.523
	Vel.	m/s	0.0866	0.9281	0.0915	0.8362	0.1337	0.1263
	Att.	$^\circ\times10^{-3}$	6.6073	62.122	7.3284	59.842	13.185	47.372
120	Pos.	m	12.517	12.513	12.633	9.2943	13.807	12.525
	Vel.	m/s	0.0942	0.9362	0.1001	0.8452	0.1499	0.1431
	Att.	$^\circ\times10^{-3}$	4.6282	62.793	5.1280	60.603	9.2241	48.869
180	Pos.	m	14.746	49.744	15.037	50.993	17.627	87.982
	Vel.	m/s	0.0947	1.3228	0.1005	1.2777	0.1498	0.9802
	Att.	$^\circ\times10^{-3}$	1.3737	71.404	1.5122	69.863	2.7158	58.892
240	Pos.	m	16.743	100.78	17.325	107.78	22.295	190.25
	Vel.	m/s	0.1037	1.7541	0.1105	1.7606	0.1686	1.8798
	Att.	$^\circ\times10^{-3}$	0.9397	78.138	1.0295	77.243	1.8465	70.280
300	Pos.	m	16.041	130.31	16.582	140.24	21.235	248.31
	Vel.	m/s	0.1002	1.8757	0.1067	1.8937	0.1628	2.0901
	Att.	$^\circ\times10^{-3}$	0.7743	78.392	0.8452	77.523	1.5148	70.751

Table E.31: INS/GPS: ρ Updates, Nav. Grade IMUs, Mach 8

	Settling Distance:		0 km		100 km		500 km	
Δt	State	Units	Error	Cov.	Error	Cov.	Error	Cov.
1	Pos.	m	5.4744	3.0245	5.6716	3.0270	1.3097	1.1960
	Vel.	m/s	0.0615	0.7475	0.0300	0.7816	0.0227	0.0230
	Att.	$^\circ\times10^{-3}$	11.075	54.109	11.620	51.247	20.914	29.566
10	Pos.	m	7.4604	4.6138	7.3223	4.2442	3.9691	3.4374
	Vel.	m/s	0.0849	0.7951	0.0505	0.7989	0.0591	0.0554
	Att.	$^\circ\times10^{-3}$	10.051	60.153	10.799	57.719	19.437	43.045
30	Pos.	m	8.4087	7.1502	8.2802	5.6041	6.9087	5.8526
	Vel.	m/s	0.0760	0.8676	0.0697	0.8147	0.0947	0.0848
	Att.	$^\circ\times10^{-3}$	7.7684	61.939	8.5997	59.631	15.476	46.718
60	Pos.	m	10.739	10.128	10.679	7.2131	10.395	8.7704
	Vel.	m/s	0.0844	0.9238	0.0893	0.8322	0.1307	0.1179
	Att.	$^\circ\times10^{-3}$	6.4071	62.810	7.1061	60.596	12.787	48.352
90	Pos.	m	12.428	11.411	12.452	8.6520	12.854	11.310
	Vel.	m/s	0.0999	0.9378	0.1065	0.8479	0.1616	0.1478
	Att.	$^\circ\times10^{-3}$	5.4215	63.282	6.0101	61.114	10.813	49.081
120	Pos.	m	13.734	18.903	13.899	17.039	15.428	26.525
	Vel.	m/s	0.1013	1.0309	0.1079	0.9516	0.1639	0.3476
	Att.	$^\circ\times10^{-3}$	3.5153	65.912	3.8913	63.921	6.9989	51.541
180	Pos.	m	14.781	56.458	15.156	59.002	18.387	102.41
	Vel.	m/s	0.0956	1.4501	0.1015	1.4210	0.1517	1.2464
	Att.	$^\circ\times10^{-3}$	1.2162	75.676	1.3381	74.534	2.4027	65.857
240	Pos.	m	16.037	92.621	16.362	98.999	19.229	174.17
	Vel.	m/s	0.0974	1.7381	0.1036	1.7417	0.1558	1.8198
	Att.	$^\circ\times10^{-3}$	0.8875	79.727	0.9721	78.997	1.7437	73.227
300	Pos.	m	15.870	146.70	16.209	158.94	19.259	282.02
	Vel.	m/s	0.0950	1.9308	0.1009	1.9545	0.1515	2.1790
	Att.	$^\circ\times10^{-3}$	0.6715	80.379	0.7320	79.718	1.3110	74.468

Table E.32: INS/GPS: ρ Updates, Tac. Grade IMUs, Mach 6

	Settling Distance:		0 km		100 km		500 km	
Δt	State	Units	Error	Cov.	Error	Cov.	Error	Cov.
1	Pos.	m	6.1444	3.1146	6.4395	3.1375	1.5785	1.3797
	Vel.	m/s	0.0686	0.7505	0.0406	0.7904	0.0410	0.0395
	Att.	$^\circ\times10^{-3}$	62.797	101.82	68.052	104.80	122.38	128.86
10	Pos.	m	8.2561	4.8787	8.1887	4.5618	4.8311	3.9098
	Vel.	m/s	0.1030	0.7989	0.0692	0.8123	0.0932	0.0824
	Att.	$^\circ\times10^{-3}$	63.846	103.53	69.427	106.34	124.86	131.67
30	Pos.	m	9.6738	7.2846	9.4505	5.9720	7.4679	6.5207
	Vel.	m/s	0.1157	0.8672	0.0961	0.8343	0.1417	0.1251
	Att.	$^\circ\times10^{-3}$	62.667	104.40	68.388	107.05	122.99	132.84
60	Pos.	m	12.057	12.015	11.835	7.9115	11.373	10.045
	Vel.	m/s	0.1387	0.9558	0.1274	0.8630	0.1981	0.1814
	Att.	$^\circ\times10^{-3}$	61.470	105.02	67.058	107.71	120.59	133.77
90	Pos.	m	14.147	14.070	14.140	10.227	15.503	14.184
	Vel.	m/s	0.1719	0.9867	0.1637	0.8975	0.2630	0.2495
	Att.	$^\circ\times10^{-3}$	62.182	105.74	67.832	108.47	121.98	134.75
120	Pos.	m	19.468	20.116	20.134	17.015	26.984	26.531
	Vel.	m/s	0.2616	1.0839	0.2642	1.0062	0.4443	0.4605
	Att.	$^\circ\times10^{-3}$	68.238	109.02	74.466	111.97	133.92	139.11
180	Pos.	m	63.737	83.014	69.541	86.989	117.59	152.62
	Vel.	m/s	0.7959	1.7888	0.8576	1.7928	1.5118	1.9036
	Att.	$^\circ\times10^{-3}$	75.996	123.86	82.949	128.04	149.17	163.18
240	Pos.	m	118.44	154.82	130.21	166.68	225.95	295.97
	Vel.	m/s	1.2884	2.4213	1.4044	2.4955	2.4943	3.1559
	Att.	$^\circ\times10^{-3}$	85.052	132.23	92.955	137.23	167.18	178.59
300	Pos.	m	189.50	241.57	209.15	263.08	367.88	469.52
	Vel.	m/s	1.8557	3.0311	2.0348	3.1736	3.6318	4.3763
	Att.	$^\circ\times10^{-3}$	94.237	140.22	103.11	146.06	185.46	193.93

Table E.33: INS/GPS: ρ Updates, Tac. Grade IMUs, Mach 7

	Settling Distance:		0 km		100 km		500 km	
Δt	State	Units	Error	Cov.	Error	Cov.	Error	Cov.
	Pos.	m	6.4903	3.1435	6.7685	3.1578	1.6236	1.4001
1	Vel.	m/s	0.0737	0.7550	0.0421	0.7912	0.0430	0.0411
	Att.	$^\circ\times10^{-3}$	52.241	96.691	56.462	98.835	101.51	116.56
	Pos.	m	8.2089	4.8668	8.1591	4.5423	4.8222	3.9436
10	Vel.	m/s	0.1098	0.8080	0.0757	0.8168	0.1050	0.0909
	Att.	$^\circ\times10^{-3}$	55.871	97.965	60.713	99.925	109.16	118.43
	Pos.	m	10.186	7.6940	10.046	6.3402	8.2014	7.1209
30	Vel.	m/s	0.1240	0.8879	0.1088	0.8468	0.1659	0.1490
	Att.	$^\circ\times10^{-3}$	53.376	98.784	58.185	100.66	104.61	119.47
	Pos.	m	12.129	11.778	12.058	8.4607	12.403	10.988
60	Vel.	m/s	0.1532	0.9708	0.1469	0.8818	0.2331	0.2168
	Att.	$^\circ\times10^{-3}$	55.166	99.552	60.160	101.47	108.16	120.51
	Pos.	m	15.173	15.034	15.516	12.096	19.259	17.571
90	Vel.	m/s	0.2107	1.0263	0.2113	0.9437	0.3485	0.3347
	Att.	$^\circ\times10^{-3}$	56.485	101.30	61.602	103.34	110.76	122.89
	Pos.	m	20.581	20.547	21.493	18.289	29.872	28.842
120	Vel.	m/s	0.3058	1.1246	0.3168	1.0536	0.5385	0.5486
	Att.	$^\circ\times10^{-3}$	60.353	105.50	65.813	107.85	118.33	129.11
	Pos.	m	65.260	84.052	71.076	88.821	118.68	155.76
180	Vel.	m/s	0.8604	1.8885	0.9319	1.9045	1.6439	2.0863
	Att.	$^\circ\times10^{-3}$	71.762	120.57	78.416	124.32	141.01	155.38
	Pos.	m	133.05	173.27	146.43	187.94	254.47	334.23
240	Vel.	m/s	1.4506	2.6366	1.5884	2.7361	2.8272	3.5799
	Att.	$^\circ\times10^{-3}$	81.341	130.68	89.037	135.49	160.12	174.78
	Pos.	m	125.72	189.31	138.37	205.70	240.63	366.09
300	Vel.	m/s	1.4457	2.6940	1.5824	2.7992	2.8152	3.6867
	Att.	$^\circ\times10^{-3}$	80.152	130.08	87.724	134.83	157.76	173.61

Table E.34: INS/GPS: ρ Updates, Tac. Grade IMUs, Mach 8

	Settling Distance:		0 km		100 km		500 km	
Δt	State	Units	Error	Cov.	Error	Cov.	Error	Cov.
	Pos.	m	5.8145	3.1507	6.0425	3.1574	1.6854	1.4473
1	Vel.	m/s	0.0758	0.7596	0.0439	0.7927	0.0467	0.0435
	Att.	$^\circ\times10^{-3}$	48.233	92.998	52.090	94.511	93.657	107.48
	Pos.	m	8.5636	4.9282	8.4419	4.5952	4.7636	4.0728
10	Vel.	m/s	0.1161	0.8187	0.0815	0.8230	0.1148	0.1020
	Att.	$^\circ\times10^{-3}$	49.537	94.103	53.826	95.458	96.778	108.90
	Pos.	m	9.7680	7.8781	9.6873	6.4150	8.4260	7.3441
30	Vel.	m/s	0.1301	0.9080	0.1203	0.8574	0.1856	0.1680
	Att.	$^\circ\times10^{-3}$	50.373	95.009	54.931	96.339	98.771	110.05
	Pos.	m	13.291	11.998	13.338	9.2909	14.277	12.469
60	Vel.	m/s	0.1788	0.9936	0.1783	0.9085	0.2898	0.2645
	Att.	$^\circ\times10^{-3}$	50.010	96.389	54.510	97.812	98.006	112.00
	Pos.	m	15.867	15.156	16.248	12.812	20.017	18.872
90	Vel.	m/s	0.2371	1.0539	0.2434	0.9758	0.4060	0.3918
	Att.	$^\circ\times10^{-3}$	53.753	98.838	58.626	100.45	105.41	115.64
	Pos.	m	26.862	29.905	28.437	29.216	41.732	48.458
120	Vel.	m/s	0.4015	1.2765	0.4254	1.2239	0.7347	0.8485
	Att.	$^\circ\times10^{-3}$	57.305	105.31	62.547	107.48	112.46	126.30
	Pos.	m	65.493	86.432	71.395	92.009	119.38	161.56
180	Vel.	m/s	0.8905	1.9625	0.9686	1.9871	1.7118	2.2229
	Att.	$^\circ\times10^{-3}$	67.304	117.58	73.609	120.98	132.37	148.90
	Pos.	m	92.039	135.98	100.91	147.03	172.71	260.57
240	Vel.	m/s	1.1728	2.3885	1.2817	2.4605	2.2738	3.0722
	Att.	$^\circ\times10^{-3}$	71.857	123.08	78.670	127.07	141.48	159.58
	Pos.	m	105.18	185.25	115.63	201.73	200.01	359.01
300	Vel.	m/s	1.2368	2.5613	1.3534	2.6521	2.4029	3.4112
	Att.	$^\circ\times10^{-3}$	70.362	123.12	77.023	127.11	138.52	159.66

BIBLIOGRAPHY

[1] Jekeli, C., *Inertial Navigation Systems with Geodetic Applications*, Walter de Gruyter, New York, 2001.

[2] Farrell, J. A. and Barth, M., *The Global Positioning System & Inertial Navigation*, McGraw-Hill, New York, 1999.

[3] Chatfield, A., *Fundamentals of High Accuracy Inertial Navigation*, AIAA, Reston, VA, 1997.

[4] Titterton, D. H. and Weston, J. L., *Strapdown Inertial Navigation*, AIAA, Reston, VA, 2nd ed., 2004.

[5] Levine, S. A. and Gelb, A., "Effect of Deflections of the Vertical on the Performance of a Terrestrial Inertial Navigation System," *Journal of Spacecraft and Rockets*, Vol. 6, No. 9, 1969, pp. 978–984, See also AIAA 1968–847.

[6] Ritland, J. T., "Survey of Aided-Inertial Navigation Systems for Missiles," *AIAA Guidance, Navigation and Control Conference*, Boston, MA, Aug. 14-16, 1989, AIAA 1989–3497.

[7] Parkinson, B. W. and Spilker, Jr., J. J., editors, *Global Positioning System: Theory and Applications Volume I*, AIAA, Washington, DC, 1996.

[8] Parkinson, B. W. and Spilker, Jr., J. J., editors, *Global Positioning System: Theory and Applications Volume II*, AIAA, Washington, DC, 1996.

[9] Brown, R. G. and Hwang, P. Y. C., *Introduction to Random Signals and Applied Kalman Filtering*, Wiley, New York, 3rd ed., 1997.

[10] Thompson, E., Henry, K., and Williams, L., "Guinness World Records Recognizes NASA Speed Record," Press release: 04-279, NASA, Aug. 30, 2004.

[11] Thompson, E., Henry, K., and Williams, L., "Faster than a Speeding Bullet: Guiness Recognizes NASA Scramjet," Press release: 05-156, NASA, June 20, 2005.

[12] Marshall, L., Bahm, C., Corpening, G., and Sherrill, R., "Overview With Results and Lessons Learned of the X-43A Mach 10 Flight," *AIAA/CIRA 13th International Space Planes and Hypersonics Systems and Technologies Conference*, Capua, Italy, May 16-20, 2005, AIAA 2005–3336.

[13] Boyce, R., Gerard, S., and Paull, A., "The HyShot Scramjet Flight Experiment—Flight Data and CFD Calculations Compared," *12th AIAA International Space Planes and Hypersonic Systems and Technologies*, Norfolk, Virginia, Dec. 15-19, 2003, AIAA 2003–7029.

[14] Smart, M. K., Hass, N. E., and Paull, A., "Flight Data Analysis of the HyShot 2 Scramjet Flight Experiment," Vol. 44, No. 10, Oct. 2006, See also AIAA 2005–3354.

[15] Centre of Hypersonics, "HyShot," *The University of Queensland, Australia*, cited 24 Jan. 2007 <http://www.uq.edu.au/hypersonics/index.html?page =19501>.

[16] "Air-Breathing, Scramjet-Powered Vehicle Tested," News release, DARPA, Dec. 15, 2005, cited 24 Jan. 2007 <http://www.darpa.mil/body/news/2005/ hyfly_test.pdf>.

[17] Jackson, K. Y., "Scramjet Engine Gears up for Flight Tests," news@afrl Features, AFRL, March 2006, cited 24 Jan. 2007 <http://www.afrl.af.mil/news/ mar06/features/flight_tests.pdf>.

[18] Shachtman, N., "Hypersonic Cruise Missile: America's New Global Strike Weapon," *Popular Mechanics*, Jan. 2007, cited 24 Jan. 2007 <http://www.popularmechanics.com/technology/military_law/4203874 .html>.

[19] Matthews, R., *Mobile Gravity Gradiometry*, Ph.D. thesis, The University of Western Australia, Dept. of Physics, 2002.

[20] Gleason, D. M., "Passive Airborne Navigation and Terrain Avoidance Using Gravity Gradiometry," *AIAA Journal of Guidance, Control, and Dynamics*, Vol. 18, No. 6, 1995, pp. 1450–1458.

[21] Király, P., "Eötvoös and STEP," *Proceedings of the STEP (Satellite Test of the Equivalence Principle) Symposium (esa WPP-115)*, Noordwijk, Netherlands, July 1996, pp. 399–406.

[22] Gray, S. D., Parmentola, J. A., and LeSchack, R., "Estimating the Weight of Very Heavy Objects with a Gravity Gradiometer," *Journal of Physics D: Applied Physics*, Vol. 28, 1995, pp. 2378–2388.

[23] Brezezowski, S. J. and Heller, W. G., "Gravity Gradiometer Survey Errors," *Geophysics*, Vol. 53, No. 10, Oct. 1988, pp. 1355–1361.

[24] Kalman, R. E., "A New Approach to Linear Filtering and Prediction Problems," *Transactions of the ASME. Series D, Journal of Basic Engineering*, Vol. 82, 1960, pp. 35–45.

[25] Kalman, R. E. and Bucy, R. S., "New Results in Linear Filtering and Prediction Theory," *Transactions of the ASME. Series D, Journal of Basic Engineering*, Vol. 83, 1961, pp. 95–107.

[26] Pelka, E. J. and DeBra, D. B., "Effects of Relative Instrument Orientation upon Gravity Gradiometer System Performance," *AIAA Journal of Guidance, Control, and Dynamics*, Vol. 1, No. 2, Jan.–Feb. 1979, pp. 18–24, See also AIAA 1977–1070.

[27] Trageser, M. B., "US Patent 3,731,537: Gravity Gradiometer," Filed June 22, 1970, Issued May 8, 1973.

[28] Trageser, M. B., "Feasibility Model Gravity Gradiometer Test Results," *AIAA Guidance and Control Conference*, Aug. 20–22, 1975, AIAA 1975–1093.

[29] Metzger, E. H., "Recent Gravity Gradiometer Developments," *AIAA Guidance and Control Conference*, Buffalo, NY, Aug. 8–10 1977, AIAA-1977-1081.

[30] Trageser, M. B., "Inertial Technology for the Future. Part II: Floated Gravity Gradiometer," *IEEE Transactions on Aerospace and Electronic Systems*, Vol. AES–20, July 1984, pp. 417–419.

[31] Grubin, C., "A Three-Axis Gravity Gradiometer," *AIAA Guidance and Control Conference*, Boulder, CO, Aug. 6–8, 1979, AIAA 1979–1756.

[32] Bell, C. C., Forward, R. L., and Morris, J. R., "Mass Detection by Means of Measuring Gravity Gradients," *AIAA Second Annual Meeting*, San Francisco, CA, July 26–29 1965, AIAA-1965-403.

[33] Berman, D., "Nonideal Behavior of Rotating Gravitational Mass Sensors," *AIAA Journal*, Vol. 5, No. 5, May 1967, pp. 1000–1008.

[34] Berman, D., "Effects of Mechanical Imperfections on Performance of a Rotating Gravity Gradiometer," *AIAA Journal of Spacecraft and Rockets*, Vol. 5, No. 10, Oct. 1968, pp. 1193–1198.

[35] Metzger, E. H. and Jircitano, A., "Inertial Navigation Performance Improvement using Gravity Gradient Matching Techniques," *AIAA Guidance and Control Conference*, Boston, MA, Aug. 20–22, 1975, pp. AIAA 1975–1092.

[36] Affleck, C. A. and Jircitano, A., "Passive Gravity Gradiometer Navigation System," *Proceedings of IEEE's Position Location and Navigation Symposium (PLANS)*, Las Vegas, NV, March 20–23, 1990, pp. 60–66.

[37] Jircitano, A. and Dosch, D. E., "Gravity Aided Inertial Navigation System (GAINS)," *Proceedings of the 47th Annual Meeting of the Institute of Navigation*, Washington, DC, June 10–12, 1991, pp. 221–229.

[38] Jekeli, C., "A Review of Gravity Gradiometer Survey System Data Analyses," *Geophysics*, Vol. 58, No. 4, Apr. 1993, pp. 508–514.

[39] Hofmeyer, G. M. and Affleck, C. A., "US Patent 5,357,802: Rotating Accelerometer Gradiometer," Filed May 7, 1993, Issued Oct. 25, 1994.

[40] Zorn, A. H., "A Merging of System Technologies: All-Accelerometer Inertial Navigation and Gravity Gradiometry," *Proceedings of 2002 IEEE Position, Location, and Navigation Symposium*, Palm Springs, CA, Apr. 15–18, 2002, pp. 66–73.

[41] Zorn, A. H., "GPS-Aidied All-Acceleromer Inertial Navigation," *ION GPS 2002, 15th International Technical Meeting of the Satellite Division of The Institute of Navigation*, Portland, OR, Sept. 24–27, 2002.

[42] Vajda, S. and Zorn, A., "Survey of Existing and Emerging Technologies for Strategic Submarine Navigation," *Proceedings of 1998 IEEE Position, Location, and Navigation Symposium (PLANS)*, Palm Springs, CA, Apr. 20–23, 1998, pp. 309–315.

[43] Richman, J., "Use of Multiple Inertial Systems to Correct for the Effects of Gravitational Anomalies," *AIAA Journal of Guidance, Control, and Dynamics*, Vol. 8, No. 4, July–Aug. 1985, pp. 426–432, See also AIAA 1983–2196.

[44] Dransfield, M. H. and Lee, J. B., "The FALCON® Airborne Gravity Gradiometer Survey Systems," *Abstracts from the ASEG-PESA Airborne Gravity 2004 Workshop Record*, Sydney, Australia, Aug. 15, 2004, pp. 15–19.

[45] Difrancesco, D., "Advances and Challenges in the Development and Deployment of Gravity Gradiometer Systems," *EGM 2007 International Workshop*, Capri, Italy, Apr. 15–18, 2007.

[46] Romaides, A. J., Battis, J. C., Sands, R. W., Zorn, A., Benson, D. O., and DiFransesco, D. J., "A Comparison of Gravimetric Techniques for Measuring Subsurface Void Signals," *Journal of Applied Physics D*, Vol. 34, No. 3, Feb. 2001.

[47] Murphy, C. A., "The Air-FTG™Airborne Gravity Gradiometer System," *Abstracts from the ASEG-PESA Airborne Gravity 2004 Workshop Record*, Sydney, Australia, Aug. 15, 2004, pp. 7–14.

[48] Hatch, D., "Evaluation of a Full Tensor Gravity Gradiometer for Kimberlite Exploration," *Abstracts from the ASEG-PESA Airborne Gravity 2004 Workshop Record*, Sydney, Australia, Aug. 15, 2004, pp. 73–79.

[49] BHP Billiton, "Orion Operations : Falcon™," cited 16 Oct. 2007 <http://falcon.bhpbilliton.com/falcon/>.

[50] van Leeuwen, E. H., "BHP Develops Worlds First Airborne Gravity Gradiometer for Mineral Exploration," *Preview*, No. 86, June 2000.

[51] Lee, J. B., Downey, M. A., Turner, R. J., Boggs, D. B., Maddever, R. A. M., and Dransfield, M. H., "First Test Survey Results from the FALCON Helicopter-borne Airborne Gravity Gradiometer System," *Extended Abstracts*

of the Australian Earth Sciences Convention (AESC) 2006, Melbourne, Australia, 2006.

[52] Bell Geospace, "Bell Geospace – 3D FTG Geophysical Surveys – Airborne and Marine Gravity Gradiometry," cited 16 Oct. 2007 <http://www.bellgeo.com/index.html>.

[53] Hammmond, S. and Murphy, C., "Air-FTG^{TM}: Bell Geospace's Airborne Gravity Gradiometer – A Description and Case Study," *Preview*, Aug. 2003, pp. 24–26, cited 16 Oct. 2007 <http://www.bellgeo.com/doc/Preview_Article.pdf>.

[54] Hinks, D., McIntosh, S., and Lane, R., "A Comparison of the Falcon® and Air-FTG^{TM}Airborne Gravity Gradiometer Systems at the Kokong Test Block, Botswana," *Abstracts from the ASEG-PESA Airborne Gravity 2004 Workshop Record*, Sydney, Australia, Aug. 15, 2004, pp. 125–134.

[55] ARKeX, "ARKeX – Airborne Geophysical Surveying," cited 16 Oct. 2007 <http://www.arkex.com>.

[56] Energy Ventures, "Energy Ventures invests in ArkeX, a company with a unique airborne exploration technology," Dec. 12, 2005.

[57] ARKeX, "ARKeX to double survey capacity," Oct. 4, 2006.

[58] Chan, H. A. and Paik, H. J., "Superconducting Gravity Gradiometer for Sensitive Gravity Measurements. I. Theory," *APS Physical Review D*, Vol. 35, No. 12, Jun. 1987, pp. 3551–3571.

[59] Chan, H. A., Moody, M. V., and Paik, H. J., "Superconducting gravity gradiometer for sensitive gravity measurements. II. Experiment," *APS Physical Review D*, Vol. 35, No. 12, Jun. 1987, pp. 3572–3597.

[60] Moody, M. V., Chan, H. A., and Paik, H. J., "Superconducting Gravity Gradiometer for Space and Terrestrial Applications," *AIP Journal of Applied Physics*, Vol. 60, No. 12, Dec. 1986, pp. 4308–4315.

[61] Paik, H. J., Leung, J.-S., Morgan, S. H., and Parker, J., "Global Gravity Survey by an Orbiting Gravity Gradiometer," *EOS Transactions of the American Geophysical Union*, Vol. 69, Nov. 29, 1988, pp. 1601–1611.

[62] Moody, M. V., Paik, H. J., and Canavan, E. R., "Three-axis Superconducting Gravity Gradiometer for Sensitive Gravity Experiments," *AIP Review of Scientific Instruments*, Vol. 73, No. 11, Nov. 2002, pp. 3957–3974.

[63] "Superconducting Gravity Gradiometers (SGGs)," *The University of Maryland, Department of Physics*, cited 24 Jan. 2007 <http://www.physics.umd.edu/GRE/NASA_SGG.pdf>.

[64] Moody, M. V., Paik, H. J., and Canavan, E. R., "Principle and Performance of a Superconducting Angular Accelerometer," *AIP Review of Scientific Instruments*, Vol. 74, No. 3, Mar. 2003, pp. 1310–1318.

[65] Moody, M. V. and Paik, H. J., "A Superconducting Gravity Gradiometer for Inertial Navigation," *IEEE Position Location and Navigation Symposium (PLANS) 2004*, Apr. 26–29, 2004, pp. 775–781.

[66] "Superconducting Gravity Gradiometer for Moving-Base Applications," *The University of Maryland, Department of Physics*, cited 24 Jan. 2007 <http://www.physics.umd.edu/GRE/Moving_base_SGG.pdf>.

[67] Lumley, J. M., White, J. P., Barnes, G., Huang, D., and Paik, H. J., "A Superconducting Gravity Gradiometer Tool for Exploration," *Abstracts from the ASEG-PESA Airborne Gravity 2004 Workshop Record*, Sydney, Australia, Aug. 15, 2004, pp. 21–39.

[68] Gedex, "GEDEX – Catalyst for Discovery," cited 16 Oct. 2007 <http://www.gedex.ca/>.

[69] Gedex, "High Definition Airborne Gravity Gradiometer Gedex HD-AGG^{TM}," cited 16 Oct. 2007 <http://www.gedex.ca/pdf/tech2.pdf>.

[70] "Award Winning Technology "Sees" Deep Beneath the Earth's Surface," *Mining Magazine*, Jan. 2007, pp. 51.

[71] Soteroff, G., "De Beers and Gedex Inc. Sign Strategic Agreement," Tech. rep., Gedex, June 28, 2006.

[72] Smith, M., "Exploration with Gravitas," *New Technology Magazine*, Jan./Feb. 2007, pp. 7–8.

[73] Buckler, G., "Eye in the Sky Spots Diamonds in the Rough," *The Globe and Mail*, Mar. 20, 2007.

[74] European Space Agency, *GOCE Mission Requirements Document*, Apr. 14, 2000, GO-RS-ESA-SY-0001, cited 24 Jan. 2007 <http://esamultimedia.esa.int/docs/GO-RS-ESA-SY-0001.PDF>.

[75] European Space Agency, *GOCE System Critical Design Review (CDR) – Executive Summary*, May 2005, cited 24 Jan. 2007 <http://esamultimedia.esa.int/docs/GOCE_System_Critical_ Design_ Review.pdf>.

[76] "GRACE - Gravity Research and Climate Experiment," *University of Texas at Austin*, cited 24 Jan. 2007 <http://www.csr.utexas.edu/grace/>.

[77] Gravitec Instruments Pty Ltd., "Gravity Gradiometers & Magnetic Gradiometers: Gravitec Instruments, Western Australia," cited 12 Oct. 2007 <http://www.gravitec.co.nz/>.

[78] McRae, W., "New Australian Instruments and Missions Working Group," cited 16 Oct. 2007 <http://plasma.newcastle.edu.au/~david/niam/gravity.html>.

[79] Veryaskin, A., "String Gravity Gradiometer: Noise Error Analysis and Applications," *Geophysical Research Abstracts, EGS - AGU - EUG Joint Assembly*, Vol. 5, Apr. 6–11, 2003, EAE03-A-01650.

[80] "QinetiQ, Gravitec, and Shell to Develop Gravity Sensor," *Society of Exploration Geophysicists – The Leading Edge*, Vol. 26, No. 9, Sept. 2007, pp. 1221, 1223, 1225, cited 16 Oct. 2007 <http://www.edge-online.org/pdf/pdf-archive-2007/tle2609r1221.pdf>.

[81] Chu, S., Cohen-Tannoudji, C., and Phillips, W. D., "For development of methods to cool and trap atoms with laser light," 1997, cited 16 Oct. 2007 <http://nobelprize.org/nobel_prizes/physics/laureates/1997/>.

[82] Cornell, E. A., Ketterie, W., and Wieman, C. E., "For the achievement of Bose-Einstein condensation in dilute gases of alkali atoms, and for early fundamental studies of the properties of the condensates," 2001, cited 16 Oct. 2007 <http://nobelprize.org/nobel_prizes/physics/laureates/2001/>.

[83] Bongs, K., Fixler, J., Foster, G., Young, B., and Kasevich, M., "Atom Inferometer-Based Inertial Force Sensors," *AIAA Guidance, Navigation, and Control Conference and Exhibit*, Monterey, CA, Aug. 5–8, 2002, pp. AIAA 2002–5053.

[84] Maleki, L., Yu, N., and Kohel, J., "Quantum Gravity Gradiometer for Sub-Surface Imaging," *AIAA Space 2004 Conference and Exhibit*, San Diego, CA, Sep. 28–30, 2004, pp. AIAA 2004–5906.

[85] Yu, N., Kohel, J. M., Kellogg, J. R., and Maleki, L., "Development of an atom-interferometer gravity gradiometer for gravity measurement from space," *Applied Physics B*, Vol. 84, 2006, pp. 647–652.

[86] Gerber, M. A., "Propagation of Gravity Gradiometer Errors in an Airborne Intertial Navigation System," *AIAA Guidance and Control Conference*, Boston, MA, Aug. 20–22, 1975, AIAA 1975–1089.

[87] Grubin, C., "Accuracy Improvement in a Gravity Gradiometer-Aided Cruise Inertial Navigator Subjected to Deflections of the Vertical," *AIAA Guidance and Control Conference*, Boston, MA, Aug. 20–22, 1975, AIAA 1975–1090.

[88] Heller, W. G. and Jordan, S. K., "Error Analysis of Two New Gradiometer-Aided Inertial Navigation Systems," *AIAA Journal Journal of Spacecraft and Rockets*, Vol. 13, No. 6, 1976, pp. 340–347, See also AIAA 1975–1091.

[89] Zondek, B., "Improved Orbit Estimation by Satellite-Mounted Gravity Gradiometers," *AIAA Journal of Guidance and Control*, Vol. 2, No. 3, May–June 1979, pp. 173–178.

[90] Wells, E. M. and Breakwell, J. V., "Real-Time Gravity Gradiometer Utilization to Improve INS Accuracy," *AIAA Journal of Guidance, Control, and Dynamics*, Vol. 5, No. 2, Mar.–Apr. 1982, pp. 113–117, See also AIAA 1980–1722.

[91] Hopkins, J., "The Global Positioning System versus Gravity Disturbance Modeling in an Inertial Navigation System," *19th AIAA Aerospace Sciences Meeting*, St. Louis, MO, Jan. 12–15, 1981, AIAA 1981–87.

[92] Shingu, H., "On the Application of Gravity Gradiometer for Inertial Navigation System," *AAS Advances in the Astronautical Science, Spaceflight Mechanic*, Vol. 95, No. 1, 1997, pp. 431–442.

[93] Shingu, H., "An Onboard Measurement System of Gravity Gradients Using Inertial Accelerometers," TR–1333T, National Aerospace Library, Tokyo, Japan, Sept. 1997.

[94] Jekeli, C., "Precision Free-Inertial Navigation with Gravity Compensation by an Onboard Gradiometer," *Journal of Guidance, Control, and Dynamics*, Vol. 29, No. 3, May-June 2006, pp. 704–713.

[95] Kwon, J. H. and Jekeli, C., "Gravity Requirements for Compensation of Ultra-Precise Inertial Navigation," *The Journal of Navigation*, Vol. 58, 2005, pp. 479–492.

[96] Jordan, S. K., "Moving-Base Gravity Gradiometer Surveys and Interpretation," *Geophysics*, Vol. 43, No. 1, Feb. 1978, pp. 94–101.

[97] Jekeli, C., "Airborne Gravimetry Using INS/GPS and Gravity Gradiometers," *ION 60th Annual Meeting / U.S. Air Force Research Laboratory Sensors Directorate*, Dayton, OH, June 7–9, 2004.

[98] Jekeli, C., "Airborne Gradiometry Error Analysis," *Surveys in Geophysics*, Vol. 27, 2006, pp. 257–275.

[99] Jekeli, C., "Statistical Analysis of Moving-Base Gravimetry and Gravity Gradiometry," Report no. 466, Laboratory for Space Geodesy and Remote Sensing Research, Ohio State University, Columbus, OH, 2003.

[100] Metzger, E. H. and Jircitano, A., "Inertial Navigation Performance Improvement using Gravity Gradient Matching Techniques," *AIAA Journal Journal of Spacecraft and Rockets*, Vol. 13, No. 6, 1976, pp. 323–324.

[101] Jircitano, A. and Dosch, D. E., "US Patent 5,339,684: Gravity Aided Inertial Navigation System," Filed Dec. 10, 1991, Issued Aug. 23, 1994.

[102] Zhang, F., Chen, X., Sun, M., Yan, M., and Yang, D., "Simulation Study of Underwater Passive Navigation System Based on Gravity Gradient," *Proceedings of the 2004 IEEE International Geoscience and Remote Sensing Symposium (IGARSS)*, Vol. 5, Sep. 20–24, 2004, pp. 3111–3113.

[103] Archibald, J. B., *Two Novel Approaches to Navigation using the Earth's Gravity and Magnetic Fields*, Ph.D. thesis, State Univ. of New York at Buffalo, Amherst, NY, 1993.

[104] Roberson, R. E., "Gravity Gradiometer Determination of the Vertical," *American Rocket Society*, Vol. 31, 1961, pp. 1509–1515.

[105] Diesel, J. W., "A New Approach to Gravitational Gradient Determination of the Vertical," *AIAA Journal*, Vol. 2, No. 7, July 1964, pp. 1189–1196.

[106] Parmentola, J., "The Gravity Gradiometer as a Verification Tool," *Science & Global Security*, Vol. 2, 1990, pp. 43–57.

[107] Friedlander, A. L., Davis, D. R., and Heppenheimer, T. A., "Measurement Error Analysis in Determination of Small-Body Gravity Fields," *AIAA Journal of Spacecraft*, Vol. 12, No. 6, June 1975, pp. 325–326, See also AIAA 1974–218.

[108] Chen, J.-H., Lee, S.-C., and DeBra, D. B., "Gyroscope Free Strapdown Inertial Measurement Unit by Six Linear Accelerometers," *AIAA Journal of Guidance, Control, and Dynamics*, Vol. 17, No. 2, Mar.–Apr. 1994, pp. 286–290.

[109] Heiskanen, W. A. and Moritz, H., *Physical Geodesy*, W. H. Freeman and Co., San Francisco, CA, 1967.

[110] Jekeli, C. and Zhu, L., "Comparison of Methods to Model the Gravitational Gradients from Topographic Data Bases," *Geophysical Journal International*, Vol. 166, No. 3, Sept. 2006, pp. 999–1014.

[111] Tscherning, C. C., "Computation of the Second-Order Derivatives of the Normal Potential Based on the Representation by a Legendre Series," *Manuscripta Geodaetica*, Vol. 1, 1976, pp. 71–92, cited 6 Mar. 2007 <http://www.gfy.ku.dk/~cct/mg2.pdf>.

[112] Macrobert, T. M., *Spherical Harmonics: An Elementary Treatise on Harmonic Functions with Applications*, Pergamon Press, New York, 3rd ed., 1967.

[113] "Department of Defense World Geodetic System 1984, Its Definition and Relationships With Local Geodetic Systems," TR8350.2, National Imagery and Mapping Agency, 4 July 1997.

[114] Lemoine, F. G., Kenyon, S. C., Factor, J. K., Trimmer, R. G., Pavlis, N. K., Chinn, D. S., Cox, C. M., Klosko, S. M., Luthcke, S. B., Torrence, M. H., Wang, Y. M., Williamson, R. G., Pavlis, E. C., Rapp, R. H., and Olson, T. R., "The Development of the Joint NASA GSFC and the National Imagery and

Mapping Agency (NIMA) Geopotential Model EGM96," NASA/TP –1998-206861, NASA, July 1998.

[115] Vallado, D., *Fundamentals of Astrodynamics and Applications*, Microcosm Press, El Segundo, CA, 2nd ed., 2001.

[116] Laprise, R., "The resolution of global spectral models," *Bulletin American Meteorological Society*, Vol. 73, No. 9, Sept. 1992, pp. 1453–1454.

[117] Reigber, C., Jochmann, H., Wnsch, J., Petrovic, S., Schwintzer, P., Barthelmes, F., Neumayer, K.-H., König, R., Förste, C., Balmino, G., Biancale, R., Lemoine, J.-M., Loyer, S., and Perosanz, F., "Earth Gravity Field and Seasonal Variability from CHAMP," *Earth Observation with CHAMP – Results from Three Years in Orbit*, Springer Verlag, 2004, pp. 25–30.

[118] Tapley, B., Ries, J., Bettadpur, S., Chambers, D., Cheng, M., Condi, F., Gunter, B., Kang, Z., Nagel, P., Pastor, R., Pekker, T., Poole, S., and Wang, F., "GGM02 – An Improved Earth Gravity Field Model from GRACE," *Journal of Geodesy*, 2005.

[119] Tscherning, C. C., "On the Chain-Rule Method for Computing Potential Derivatives," *Manuscripta Geodaetica*, Vol. 1, 1976, pp. 125–141, cited 24 Jan. 2007 <http://www.gfy.ku.dk/~cct/mg1.pdf>.

[120] "Software used in the Research and Production of Geoid Models at NGS," *National Geodetic Survey / National Oceanic and Atmospheric Administration*, cited 2 Aug. 2007 <http://www.ngs.noaa.gov/GEOID/RESEARCH_SOFTWARE/geopot97.v0.4e.f>.

[121] Smith, D. A., "There is No Such Thing as "The" EGM96 Geoid: Subtle Points on the Use of a Global Geopotential Model," *International Geoid Service Bulletin*, No. 8, Milan, Italy, 1998, pp. 17–28, cited 24 Jan. 2007 <http://www.ngs.noaa.gov/PUBS_LIB/EGM96_GEOID_PAPER/egm96_geoid_paper.html>.

[122] Tscherning, C. C. and Poder, K., "Some Geodetic Applications of Clenshaw Summation," *Bollettino di Geodesia e Scienze Affini*, Vol. XLI, No. 4, 1982, pp. 349–375, cited 24 Jan. 2007 <http://www.gfy.ku.dk/~cct/tscherning13.pdf>.

[123] "Software used in the Research and Production of Geoid Models at NGS," *National Geodetic Survey / National Oceanic and Atmospheric Administration*, cited 2 Aug. 2007 <http://www.ngs.noaa.gov/GEOID/RESEARCH_SOFTWARE/research_software.html>.

[124] Wieczorek, M., "SHTOOLS – Tools for working with spherical harmonics," Jan. 2006, cited 7 Mar. 2007 <http://www.ipgp.jussieu.fr/~wieczor/SHTOOLS/SHTOOLS.html>.

[125] Holmes, S. A. and Featherstone, W. E., "A Unified Approach to the Clenshaw Summation and the Recursive Computation of Very High Degree and Order Normalized Associated Legendre Functions," *Journal of Geodesy*, Vol. 76, 2002, pp. 279–299, DOI 10.1007/s00190-002-0216-2.

[126] National Oceanic and Atmospheric Administration, NASA, and United States Air Force, *U.S. Standard Atmosphere, 1976*, Wiley-Interscience, Washington, DC, 1976.

[127] Boeing, "Technical Specifications – 747 Classics," *Commercial Airplanes - 747 Classics Technical Specs*, cited 6 Nov. 2007 <http://www.boeing.com/commercial/747family/pf/pf_classics.html>.

[128] Cessna, "Model >> Grand Caravan – Performance," *Cessna Caravan. Sure Thing*, cited 6 Nov. 2007 <http://grandcaravan.cessna.com/performance.chtml>.

[129] Waltrup, P. J., Billig, F. S., and Stockbridge, R. D., "Engine Sizing and Integration Techniques for Hypersonic Airbreathing Missile Applications," *AGARD Ramjets and Ramrockets for Military Applications*, CP–307, Paper 8, March 1982.

[130] Fry, R. S., "A Century of Ramjet Propulsion Technology Evolution," *Journal of Propulsion and Power*, Vol. 20, No. 1, 2004, pp. 27–58.

[131] Waltrup, P. J., White, M. E., Zarlingo, F., and Gravlin, E. S., "History of U.S. Navy Ramjet, Scramjet, and Mixed-Cycle Propulsion Development," *Journal of Propulsion and Power*, Vol. 18, No. 1, 2002, pp. 14–27, also AIAA Paper 1996–3152, July 1996.

[132] Andrews, E. H., "Scramjet Development and Testing in the United States," *10th AIAA/NAL-NASDA-ISAS International Space Planes and Hypersonic Systems and Technologies Conference*, Kyoto, Japan, Apr. 24–27,, 2001, AIAA 2001–1927.

[133] Anderson, Jr., J. D., *Modern Compressible Flow with Historical Perspective*, McGraw-Hill, New York, 3rd ed., 2003.

[134] Hood, C., "Cone Flow," Oct. 28, 2001, cited 19 Oct. 2007 <http://ucsu.colorado.edu/~hoodcr/conep/cone.html>.

[135] Starkey, R. P., *Investigation of Air-Breathing Hypersonic Missile Configurations Within External Box Constraints*, Ph.D. thesis, The University of Maryland, College Park, Dept. of Aerospace Engineering, 2000.

[136] Billig, F. S., Corda, S., and Pandolfini, P. P., "Design Techniques for Dual Mode Ram-Scramjet Combustors," *AGARD Hypersonic Combined Cycle Propulsion*, CP–479, Paper 23, Dec. 1990.

[137] Waltrup, P. J., "Upper Bounds on the Flight Speed of Hydrocarbon-Fueled Scramjet-Powered Vehicles," *AIAA Journal of Propulsion and Power*, Vol. 17, No. 6, Nov.–Dec. 2001, pp. 1199–1204.

[138] Edwards, T., "Liquid Fuels and Propellants for Aerospace Propulsion: 1903-2003," *AIAA Journal of Propulsion and Power*, Vol. 19, No. 6, Nov.–Dec. 2003, pp. 1089–1107.

[139] Horning, D. C., "A Study of the High-Temperature Autoignition and Thermal Decomposition of Hydrocarbons," TSD–135, Stanford Univ., Dept. Mech. Eng., Palo Alto, CA, June 2001.

[140] Heiser, W. and Pratt, D., *Hypersonic Airbreathing Propulsion*, AIAA, Washington, DC, 1994.

[141] Jensen, G. E. and Netzer, D. W., editors, *Tactical Missile Propulsion*, AIAA, Washington, DC, 1996.

[142] Waltrup, P. J., White, M. E., Zarlingo, F., and Gravlin, E. S., "History of U.S. Navy Ramjet, Scramjet, and Mixed-Cycle Propulsion Development," *AIAA Journal of Propulsion and Power*, Vol. 18, No. 1, Jan.–Feb. 2002, pp. 14–27.

[143] Torge, W., *Geodesy*, Walter de Gruyter, Berlin, 3rd ed., 2001.

[144] Abzug, M. J., *Computational Flight Dynamics*, AIAA Education Series, Reston, VA, 1998.

[145] Phillips, W. F., Hailey, C. E., and Gebert, G. A., "Review of Attitude Representations Used for Aircraft Kinematics," *AIAA Journal of Aircraft*, Vol. 38, No. 4, July–Aug. 2001, pp. 718–737, See also AIAA 2000–4302, Jan. 2000.

[146] Phillips, W. F., Hailey, C. E., and Gebert, G. A., "Errata: Review of Attitude Representations Used for Aircraft Kinematics," *AIAA Journal of Aircraft*, Vol. 40, No. 1, Jan–Feb. 2003, pp. 223.

[147] Chapra, S. C. and Canale, R. P., *Numerical Methods for Engineers with Programming and Software Applications*, WCB/McGraw Hill, New York, 3rd ed., 1998.

[148] Weinreb, A. and Bar-Itzhack, I. Y., "The Psi-Angle Error Equation in Strapdown Inertial Navigation Systems," *IEEE Transactions on Aerospace and Electronic Systems*, Vol. AES–14, No. 3, May 1978, pp. 539–542, See also "Weinred" because of typo in publication.

[149] Benson, Jr., D. O., "A Comparison of Two Approaches to Pure-Inertial and Doppler-inertial Error Analysis," *IEEE Transactions on Aerospace and Electronic Systems*, Vol. AES–11, No. 4, July 1975, pp. 447–455.

[150] Britting, K. R., *Inertial Navigation Systems Analysis*, Wiley-Interscience, New York, 1971.

[151] Friedland, B., "Analysis Strapdown Navigation Using Quaternions," *IEEE Transactions on Aerospace and Electronic Systems*, Vol. AES–14, No. 5, Sept. 1978, pp. 764–768.

[152] Shibata, M., "Error Analysis Strapdown Inertial Navigation Using Quaternions," *AIAA Journal of Guidance, Control and Dynamics*, Vol. 9, No. 3, May–June 1986, pp. 379–381.

[153] Goshen-Meskin, D. and Bar-Itzhack, I. Y., "Unified Approach to Inertial Navigation System Error Modeling," *AIAA Journal of Guidance, Control, and Dynamics*, Vol. 15, No. 3, May–June 1992, pp. 648–653, See also AIAA 1990–3367, Aug. 1990.

[154] Baziw, J. and Leondes, C. T., "In Flight Alignment and Calibration of Inertial Measurement Units – Part 1: General Formulation," *IEEE Transactions on Aerospace and Electronic Systems*, Vol. AES–8, No. 4, July 1972, pp. 439–499.

[155] Shin, E.-H., *Accuracy Improvement of Low Cost INS/GPS for Land Applications*, Master's thesis, University of Calgary, Department of Geomatics Engineering, Calgary, Alberta, December 2001.

[156] Honeywell Aerospace, "Avionics & Electronics," *Honeywell International, Inc.*, cited 15 Aug. 2006 <http://www.honeywell.com/sites/aero/Avionics_Electronics.htm>.

[157] Honeywell, "Accelerometer," *Honeywell International, Inc.*, cited 15 Aug. 2006 <http://www.inertialsensor.com/>.

[158] Northrop Grumman, "Navigation Systems," *Northrup Grumman*, cited 15 Aug. 2006 <http://www.nsd.es.northropgrumman.com/Automated/categories/Navigation_Systems.html>.

[159] Kearfott Guidance & Navigation Corporation, "Air," *Astronautics Corporation of Amertica*, cited 15 Aug. 2006 <http://www.kearfott.com/products/air.htm>.

[160] Systron Donner Inertial Division, "Products Center," *BEI Technologies, Inc.*, cited 15 Aug. 2006 <http://www.systron.com/products.asp>.

[161] Gesellschaft für inertiale Mess-, Automatisierungs- und Regelsysteme (iMAR), "Inertial Navigation, Navigation Systems, Gyro Technology, Stabilization, Surveying, Gyroscope Stabilization, Inertial Surveying, Guidance and Control in Industry, Geodesy, Research and Military Applications by iMAR GmbH," *iMAR*, cited 15 Aug. 2006 <http://www.imar-navigation.de/imar.htm>.

[162] Gaylor, D., "Simulation of an Unaided INS in Orbit," Tech. rep., Univ. of Texas, Nov. 27, 2002.

[163] Richeson, J. A. and Pines, D. J., "GPS Denied Inertial Navigation Using Gravity Gradiometry," *AIAA Guidance, Navigation and Control Conference and Exhibit*, Hilton Head, SC, Aug. 20–23, 2007, AIAA 2007–6791.

[164] Richeson, J. A., "Gravity Gradiometer Aided Inertial Navigation Wiithin Non-GNSS Environments," *ION GNSS 2007*, Ft. Worth, TX, Sept. 25–28, 2007.

[165] Northrop Corp., "Gravity Compensation for INS Demonstration Program," Tr–85–1156, avionics lab, AFWAL, Wright Patterson, AFB, OH, Feb. 1986.

[166] DARPA–FALCON, "Force Application and Launch from CONUS (FALCON)," *Broad Agency Announcement 03-25, DARPA*, Arlington, VA, July, 29, 2003.

[167] Jordan, S. K., Moonan, P. J., and Weiss, D. J., "State-Space Models of Gravity Disturbance Gradients," *IEEE Transactions on Aerospace and Electronic Systems*, Vol. AES–17, No. 5, Sept. 1981, pp. 610–619.

[168] Bose, S. C. and Mortensen, R. E., "Comments on 'State-Space Models of Gravity Disturbance Gradients'," *IEEE Transactions on Aerospace and Electronic Systems*, Vol. AES–20, No. 2, Mar. 1984, pp. 202–203.

[169] Gerber, M. A., "Expanded Third-Order Markov Undulation Model," *AIAA Journal of Guidance and Control*, Vol. 4, No. 5, Sept.–Oct. 1981, pp. 495–501.

[170] Koehler, G. F., "Comment on 'Expanded Third-Order Markov Undulation Model'," *AIAA Journal of Guidance*, Vol. 5, No. 6, Nov.–Dec. 1982, pp. 597.

[171] Baumgartner, S. L. and Heller, W. G., "Comment on 'Expanded Third-Order Markov Undulation Model'," *AIAA Journal of Guidance*, Vol. 5, No. 6, Nov.–Dec. 1982, pp. 597–599.

[172] Goldenberg, F., "Geomagnetic Navigation Beyond the Magnetic Compass," *IEEE/ION Position Location and Navigation Symposium (PLANS) 2006*, Apr. 25–27, 2006, pp. 684–694.

[173] Chen, C.-T., *Linear System Theory and Design*, Oxford, New York, 1984.

[174] Wiener, N., *Extrapolation, Interpolation, and Smoothing of Stationary Time Series*, Wiley, New York, 1949.

[175] "Navstar GPS Space Segment / Navigation User Interfaces," Interface Control Document ICD-GPS-200, Rev. C, GPS Joint Program Office, 12 Aug. 2000.

[176] "NAVSTAR GPS User Equipment Introduction (Public Release Version)," Tech. rep., Sept. 1996, cited 20 June 2007 <http://www.navcen.uscg.gov/pubs/gps/gpsuser/gpsuser.pdf>.